R-06-23

Regional hydrogeological simulations using CONNECTFLOW

Preliminary site description Laxemar subarea – version 1.2

Lee Hartley, Fiona Hunter, Peter Jackson, Rachel McCarthy
Serco Assurance

Björn Gylling, Niko Marsic
Kemakta Konsult AB

April 2006

Svensk Kärnbränslehantering AB
Swedish Nuclear Fuel
and Waste Management Co
Box 5864
SE-102 40 Stockholm Sweden
Tel 08-459 84 00
+46 8 459 84 00
Fax 08-661 57 19
+46 8 661 57 19

ISSN 1402-3091
SKB Rapport R-06-23

Regional hydrogeological simulations using CONNECTFLOW

Preliminary site description Laxemar subarea – version 1.2

Lee Hartley, Fiona Hunter, Peter Jackson, Rachel McCarthy
Serco Assurance

Björn Gylling, Niko Marsic
Kemakta Konsult AB

April 2006

Summary

Svensk Kärnbränslehantering AB (The Swedish Nuclear Fuel and Waste Management Co, SKB) is responsible for managing and disposing of the radioactive waste from nuclear power plants in Sweden. SKB carries out site investigations in two different candidate areas with the objective of describing the in situ conditions for a bedrock repository for spent nuclear fuel. The two candidate areas are in the municipalities of Östhammar and Oskarshamn.

An integral component of the site characterisation work is the development of site descriptive models. These comprise basic models in three dimensions with an accompanying text description. Central in the modelling work is the geological model, which provides the geometrical context in terms of a model of deformation zones and the rock mass between the zones. Using the geological and geometrical description models as a basis, descriptive models for other geo-disciplines (hydrogeology, hydrogeochemistry, rock mechanics, thermal properties and transport properties) will be developed. In addition, a description is provided of the surface ecological system, which partly constitutes the interface between the geosphere and the biosphere. Great care is taken to arrive at a general consistency in the description of the various models, and to assess uncertainties and possible needs of alternative models.

A numerical model is developed on a regional-scale (hundreds of square kilometres) to understand the zone of influence for groundwater flow that affects the Laxemar subarea. Transport calculations are then performed by particle tracking from a local-scale release area (tens of square kilometres) to identify potential discharge areas for the site. The transport from the two site-scale release areas (a few square kilometres) at the Laxemar subarea and at the Simpevarp subarea are also considered more specifically and using greater grid resolution.

The main objective of this study is to support the development of a preliminary Site Description of the Laxemar subarea on a regional-scale based on the available data of November 2004 (Data Freeze L1.2). A more specific objective of this study is to assess the role of both known and less quantified hydrogeological conditions in determining the present-day distribution of saline groundwater in the Laxemar subarea on a regional-scale. An improved understanding of the palaeo-hydrogeology is necessary in order to gain credibility for the Site Description in general and the hydrogeological description in particular. This is to serve as a basis for describing the present hydrogeological conditions on a local-scale, as well as predictions of future hydrogeological conditions. Another objective is to assess the flow-paths from the local-scale model domain, based on the present-day flow conditions, to assess the distribution of discharge and recharge areas connected to the flow at the approximate repository depth to inform the Preliminary Safety Evaluation.

Significant new features incorporated in the modelling include: a depth variation in hydraulic properties within the deformation zones; a dependence on rock domain and depth in the rock mass properties in regional-scale models; a more detailed model of the overburden in terms of a layered system of spatially variable thickness made up of several different types of Quaternary deposits has been implemented; and several variants on the position of the watertable have been tried. The motivation for introducing a dependence on rock domain was guided by the hydrogeological interpretation with the aim of honouring the observed differences in hydraulic properties measured at the boreholes. Hydraulic data was available for several new boreholes in the Simpevarp subarea, such as KLX03, KLX04 and KLX05, together with some re-interpretation of data from older boreholes such as KLX01, KLX02,

KSH01A and KAV01. By selecting representative boreholes for each rock domain and using previously developed techniques for conditioning hydrogeological discrete fracture network models (Hydro-DFN), a parameterisation of the fractured bedrock is derived for each rock domain along with equivalent porous medium properties on various scales. However, there are only one or two boreholes within each rock domain and hence it is difficult to quantify the variability within domains compared to that between rock domains.

The main conclusions from the groundwater modelling are:

- The fracture size distributions for open fractures were derived within this study due to problems of coordination with the final Geo-DFN. The values derived are broadly consistent with the final values derived in the final Geo-DFN, but it does leave an uncertainty as to the most representative model for fracture size distribution. However, it is felt that ultimately the calculation of flow within the Hydro-DFN is less sensitive once all other parameters – open fracture intensity and transmissivity – have been constrained by conditioning on hydrogeological data.
- Three different relationships between transmissivity and size have been considered, and all three can be made to give a reasonable match to the hydrogeological data. The semi-correlated model (i.e. a log-normal stochastic variation, but with a mean transmissivity that increases with fracture size) gives a slightly better match and more realistic relationship.
- Matching hydraulic data for all boreholes gives higher values for the median effective hydraulic conductivity, $\log(K_{eff})$ above –300 m, than below –300 m elevation. Median $\log(K_{eff})$ in the Ävrö granite (RD A) is between –6.6 to –7.1 above –300 m, and –8.0 to –8.5 below –300 m elevation. A decrease in hydraulic conductivity with depth has been interpreted in rock domain A at Laxemar, and rock domains B and C at Simpevarp, but not in rock domain A at Äspö and Ävrö. Rock domain A has the highest conductivity, followed by rock domain MD, and rock domains B and C at Simpevarp have the lowest.
- Anisotropy in block-scale properties has been calculated for the Laxemar subarea with a strike NW-SE to WNW-ESE, which corresponds with the direction of maximum horizontal stress. Further, the hydraulic data from individual fractures suggests a possible anisotropy in the transmissivity between fracture orientations. Sub-vertical fracture sets oriented with strike SW-NE or N-S have potentially lower transmissivity than sub-horizontal fractures ones oriented NW-SE.
- The regional-scale domain used in S1.2, which was based on several water catchments, has been confirmed as adequate for stable predictions of both chemistry in boreholes and flow-paths to study the recharge and discharge areas relevant to the Laxemar and Simpevarp release areas.
- The flow boundary conditions on the top surface of the model have a considerable impact on the results and a watertable several metres below the topographic surface often gives the best calibration results against borehole hydrogeochemistry. Using a lower watertable below the topographic surface was found to be a vital ingredient in achieving a calibrated model. Other ways of applying a lower watertable were considered using a specified flux type boundary condition. This suggested a potential groundwater recharge of a few tens of mm/year would give a reasonable match. It is suggested that this be compared with the potential recharge calculated by the SurfaceNet Group.
- Another key step in the calibration against hydrogeochemistry was to introduce anisotropy between the transmissivity of the fracture sets. This was implemented as a reduction in the transmissivity in SW-NE and N-S sets by a factor 10. This makes physical sense since both sets are oriented perpendicular to the maximum horizontal stress, and is supported by hydraulic data.

- A further step in achieving a calibrated model was in the transport parameters. It was necessary to delay deep infiltration of meteoric waters by choosing a diffusion accessible porosity at the high end of measured values and allowing good access to this porosity by setting a flow-wetted surface of the bedrock around 1 m^2/m^3 or more. This suggests that advective flow occurs in fractures with transmissivities below the detection limit of PFL-anomalies and has a significant effect on solute transport under natural flow conditions over hundreds to thousands of years, enhancing the effect of rock matrix diffusion.
- The distribution of salinity is broadly confirmed by the ChemNet Group and adds credibility to the modelling results.
- It is worth noting that all initial attempts to calibrate homogeneous models for hydraulic conductivity using depth dependency trends based on the PSS data resulted in a poor match against the hydro-geochemical data. For such models, a calibration could only be achieved by using a hydraulic conductivity in the deep rock over an order of magnitude less than measured values. In contrast, the Hydro-DFN gave heterogeneous hydraulic properties resulting in a model that is consistent with packer-test conductivities and gives a reasonable match with hydrogeochemistry.
- Sensitivities of the palaeo-hydrogeology to the various model components can be ranked as follows. The sensitivity to the surface flow boundary condition, anisotropy and flow-wetted surfaces are high. More moderate sensitivities were found for HCD depth dependence, HCD stochastic variability and kinematic porosity, transmissivity model and DFN realisation. Low sensitivities were found to the initial condition, domain, deformation zone confidence, diffusion accessible porosity, bedrock kinematic porosity, overburden properties and diffusion coefficient.
- Close to the surface at –10 m the flows are mainly downwards (recharge) at a rate of around 0.01 to 0. 1 m/year, reducing to about 0.001 to 0.01 m/year at –100 m elevation. The discharge is directed to the Baltic Sea in the eastern part of the modelled area and around deformation zones and valleys onshore. In the deformation zones, the vertical Darcy velocity is around 0.1 m/year. The flow-field near the surface is very heterogeneous indicating localised flow cells. At –500 m, the flow-rates are generally around 0.01–0.0001 m/year in both the recharge and discharge areas. The flow-field also tends to be more homogeneous at this depth. At –1,000 m, the flow-rates are generally less than 0.0001 m/year.

A series of transport calculations were performed for each of the variants considered to provide guidance for the Preliminary Safety Evaluation (PSE). Based on these results, the following conclusions are drawn:

- The characteristics of the two different release areas, Laxemar and Simpevarp, are quite different. Even though there are some particles with very high F-factors in Laxemar, the median value of the F-factor at Laxemar is one order of magnitude lower, with a median $\mathrm{Log}_{10}(F_r)$ of 5.5 year/m, than in the Simpevarp subarea with median $\mathrm{Log}_{10}(F_r)$ of 6.7 year/m. This is expected as the effective conductivity of the rock is lower around Simpevarp. The areas containing particles with high F-factors generally coincide with recharge areas.
- The path-length of the released particles is generally quite short. Localised flows are present as a result of the topography and the heterogeneous bedrock. Most released particles exit inside or very close to the local-scale release area. The exit locations are located close to the shoreline and in the valleys with lower topographic elevation in the area. Due to the topographic elevation, most of the Laxemar release area is beneath a recharge area.

- The recharge areas (obtained by back-tracking of particles in the velocity-field until they reach the surface) are associated with several topographic highs both inside and outside the local-scale release area. The recharge area for the Laxemar release area is mostly directly above the site. A few recharge areas that influence the Laxemar release area are located at hills several kilometres to the west and southwest. All the major islands (Äspö, Ävrö and Hålö) together with the Simpevarp peninsula act as recharge areas.
- The predominant exit locations of the particles released from the Laxemar subarea are the valleys north and south of the Laxemar release area and close to the shoreline between Äspö and Hålö. There is only one very minor discharge area at the centre of the Laxemar release area, associated with a small stream. Compared to the Simpevarp release area, the particles released from the Laxemar release area go more northerly. The main exit locations for the particles released from the Simpevarp release area are found around the Simpevarp peninsula and north of Hålö.

This study has suggested some issues on which to focus further acquisition of site data:

- The use of inclined boreholes with different trends would provide a better basis for studies of relative anisotropy between fracture sets.
- Flow data from other boreholes with PFL-anomaly and PSS data will help to bound the variability of hydraulic properties within the main rock domains, and hence bound the uncertainty in properties extrapolated from boreholes to rock domains.
- PSS 5 m interval data from another borehole at Laxemar would help to confirm whether the fracture transmissivity displays a bi-modal behaviour as partly suggested by the lower section of KLX04, or whether this was just a unique feature in KLX04.
- The performance of cross-hole/interference tests as a basis for testing the Hydro-DFN models developed is important for the process of confidence building. However, it is accept that the hydraulic response in such tests often tends to be dominated by a few transmissive features rather than measure the background fracture system, and so careful planning is required. Vertical cross-hole or intra-hole tests could also help compare vertical flow with horizontal cross-hole and radial flow.
- The importance of the position of the watertable suggests that more data should be acquired on the surface hydrology in terms of groundwater levels and the potential groundwater recharge into the deep bedrock. This suggests further cooperation between the HydroNet and SurfaceNet Groups.
- More hydrogeochemical data around repository depth between –300 m to –600 m would assist the regional model calibration around repository depth, and help inform of depth dependency in hydraulic properties. Of particular interest is to confirm the existence of Glacial water (or low $\delta^{18}O$) at these depths as it would suggest greater heterogeneity and possibly lower vertical hydarulic conductivities. Appropriate locations for acquiring such data would under recharge areas where one expects vertical flushing by Meteoric water. The existence of a Littorina signature is of more interest in lower lying areas in the valleys to the north and south of the Laxemar subarea, in the topographic low at the centre of the site and in the south east corner of the Laxemar subarea. More data on the deep brine would help identify the lower extent of groundwater flow. Possibly this could be aided by a 3D profile of salinity interpreted from transient electromagnetic remote sensing data.
- The ChemNet group has started to provide information on the chemistry in the diffusion accessible porosity and to compare this with that in the fracture system. This is encouraged, and further work will help to address uncertainties in the exchange between the two porosities and transport parameters such as flow-wetted surface.

- It is also recommended that steps be taken to avoid some of the problems encountered in the coordination of the Geo-DFN and the Hydro-DFN. This could be achieved by tighter integration between Geology and Hydrogeology. In particular, evidence from the hydrogeological data that may address uncertainties in the geological data should be incorporated in the Geo-DFN.

Contents

Glossary of abbreviations and symbols

For clarity, the SKB advised terminology for referring to fracture size is as follows.

r — Equivalent fracture radius (m)
Fractures are modelled as squares. However, an equivalent fracture radius, $r = \sqrt{\frac{A}{\pi}}$, where A is fracture area, is used to describe fracture size throughout this report.

k — The shape parameter for a general power-law distribution

k_r — The shape parameter for the power-law distribution for fracture radii (see Subsection 3.3.1)

x_0 — The location parameter of a general power-law distribution (m)

r_0 — The location parameter of the power-law distribution for fracture radii (see Subsection 3.3.1) (m)

Other abbreviations and notation used are:

a_r — Fracture surface area per unit volume (2×P32) ($m^2\ m^{-3}$)

BC — Boundary condition

CPM — Continuum porous medium

DFN — Discrete fracture network

DZ — Deformation zone

ECPM — Equivalent continuum porous medium

e_t — Fracture transport aperture (m)

F_r — F-factor in the rock (year/m)

F1.2 — Forsmark version 1.2

FWS — Flow-wetted surface, same as a_r ($m^2\ m^{-3}$)

GWF — Groundwater flow

HCD — Hydraulic conductor domains

HRD — Hydraulic rock domains

HSD — Hydraulic soil domains

IC — Initial condition

IFZ — Implicit fracture zone

K — Hydraulic conductivity (m/s)

K_{eff} — Effective isotropic hydraulic conductivity (m/s)

K_{hmax} — Maximum horizontal hydraulic conductivity (m/s)

K_{hmin} — Minimum horizontal hydraulic conductivity (m/s)

K_x — Hydraulic conductivity in the E-W direction (m/s)

K_y Hydraulic conductivity in the N-S direction (m/s)

K_z Hydraulic conductivity in the vertical direction (m/s)

KAV Cored borehole at Ävrö

KAS Cored borehole at Äspö

KLX Cored borehole at Laxemar

k_r fit A fracture size model based on fixing r_0 at 0.28 m and matching k_r to the L1.2 structural model

KSH Cored borehole at Simpevarp

L1.2 Laxemar version 1.2

L_r Path-length in the rock (m)

M3 Mixing and mass-balance modelling

n_e Kinematic porosity (–)

$n_{e,b}$ Kinematic porosity for a model block (–)

n_m Matrix porosity (–)

P10 Linear fracture intensity: number of fractures per metre along a borehole (m^{-1})

$P10_c$ Linear fracture intensity of connected fractures: number of connected fractures per metre along a borehole (m^{-1})

$P10_{corr}$ Terzaghi corrected linear fracture intensity: 'true' number of fractures per metre along a borehole corrected for the bias introduced by the angle of the borehole made with fractures (m^{-1})

$P10_{PFL}$ Linear fracture intensity of PFL-anomalies: number of PFL anomalies per metre along a borehole (m^{-1})

P21 Area fracture intensity: total fracture trace lengths per square metre of outcrop ($m\ m^{-2}$)

P32 Volumetric fracture intensity: total fracture surface area per cubic metre of rock ($m^2\ m^{-3}$)

$P32_c$ Volumetric fracture intensity of connected fractures: total connected fracture surface area per cubic metre of rock ($m^2\ m^{-3}$)

PDF Probability distribution function

PFL Posiva flow-log

PFL-f Posiva flow-anomaly logging is made with a test section length of 1 m and a step length of 0.1 m

PFL-s Posiva flow section logging is made with a test section length of 5 m and a step length of 0.5 m

PM Performance measure

PSE Preliminary safety evaluation

PSS Pipe-string system

Q Groundwater flux ($m^3 s^{-1}$)

q Darcy velocity ($m\ s^{-1}$)

RD Rock domain

r_{min} Minimum fracture radius used in DFN simulations (m)

RVS	Rock visualisation sytem (a tool used by SKB for their structural modelling)
RMD	Rock matrix diffusion
S1.2	Simpevarp version 1.2
SDM	Site descriptive modelling
t_r	Travel-time in the rock (year)
TDS	Total dissolved solids
U_r	Initial Darcy velocity in the rock (m/year)
μ	Mean of normal distribution
σ	Standard deviation of normal distribution

1 Introduction

1.1 Background

The company Svensk Kärnbränslehantering AB (Swedish Nuclear Fuel and Waste Management Co, SKB) is responsible for managing and disposing of the radioactive waste from nuclear power plants in Sweden. SKB carries out site investigations in two different candidate areas with the objective of describing the in situ conditions for a bedrock repository for spent nuclear fuel. The two candidate areas are in the municipalities of Östhammar and Oskarshamn. The site characterisation work is divided into two phases, an initial site investigation phase (IPLU) and a complete site investigation phase (KPLU) /SKB 2001/. The results of IPLU are used as a basis for deciding on a subsequent KPLU phase. On the basis of the KPLU investigations a decision is made as to whether detailed characterisation will be performed (including sinking of a shaft).

An integrated component in the site characterisation work is the development of site descriptive models. These comprise basic models in three dimensions with an accompanying text description. Central in the modelling work is the geological model, which provides the geometrical context in terms of a model of deformation zones and the rock mass between the zones. Using the geological and geometrical description models as a basis, descriptive models for other geo-disciplines (hydrogeology, hydrogeochemistry, rock mechanics, thermal properties and transport properties) will be developed /SKB 2000/. In addition, a description is provided of the surface ecological system, which partly constitutes the interface between the geosphere and the biosphere. Great care is taken to arrive at a general consistency in the description of the various models, and to assess uncertainty and possible needs of alternative models /Andersson 2003/.

A numerical model is developed on a regional-scale (hundreds of square kilometres) to understand the zone of influence for groundwater flow that affects the Laxemar subarea. Transport calculations are then performed by particle tracking from a local-scale release area (tens of square kilometres) to identify potential discharge areas for the site. The transport from the two site-scale release areas (a few square kilometres) at the Laxemar subarea and at the Simpevarp subarea are also considered more specifically and using greater grid resolution.

Descriptive model versions are produced at specified times which are adapted to the needs of the primary users, i.e. repository design and safety assessment. These specified times define a “data freeze” which singles out the database that should inform the model version in question. The data used in this study is based on Laxemar Data Freeze 1.2. The results of the descriptive modelling also serve to guide priorities and act as a stimulus for review and feedback on the ongoing site characterisation.

1.2 Scope and objectives

The main objective of this study is to support the development of a preliminary Site Description of the Laxemar subarea on a regional-scale based on the available data of November 2004 (Data Freeze L1.2) and the Site Description for Simpevarp version 1.2 (S1.2) /SKB 2005/.

A more specific objective of this study is to assess the role of both known and less quantified hydrogeological conditions in determining the present-day distribution of saline groundwater in the Laxemar subarea on a regional-scale. An improved understanding of the palaeo-hydrogeology is necessary in order to gain credibility for the Site Description in general and the hydrogeological description in particular. This is to serve as a basis for describing the present hydrogeological conditions on a local-scale as well as predictions of future hydrogeological conditions.

The main objective implies a testing of:

- geometrical alternatives in the structural geology and bedrock fracturing,
- variants in the initial and boundary conditions, and
- parameter uncertainties (i.e, uncertainties in the hydraulic property assignment).

Another specific objective is to assess the flow-paths from the local-scale model domain, based on the present-day flow conditions. This allows assessment of the distribution of discharge and recharge areas connected to the flow at the approximate repository depth. However, these results are just preliminary indications within the local-scale area. The subsequent SR-Can Safety Assessment calculation, not part of this study, with transient boundary conditions, more detailed local-scale modelling and representation of the particle release points may show different results.

1.3 Setting and limitations

The Simpevarp area is located in the province of Småland, within the municipality of Oskarshamn, and immidiately adjacent to the Oskarshamn nuclear power plant, cf Figure 1-1. The Simpevarp area (including the Simpevarp and Laxemar subareas) is located close to the shoreline of the Baltic Sea. The eastern-most part (Simpevarp subarea) includes the Simpevarp peninsula and the islands Hålö and Ävrö. The island of Äspö, under which the Äspö Hard Rock Laboratory (Äspö HRL) is developed, is located some two kilometres north of the Simpevarp peninsula. The area of the Laxemar subarea covers some 12.5 km^2 whereas the Simpevarp subarea is approximately 6.6 km^2.

One important issue to confirm is whether the model domain used in S1.2 is sufficient to simulate regional-scale flow and solute transport at the Laxemar area. In the CONNECTFLOW S1.2 modelling studies, the domain was chosen on the basis of surface water catchments in the area with dimensions 21 km, 13 km and 2.3 km in the Easting (x), Northing (y), and Elevation (z) directions respectively. To check this, studies are made here of the recharge and discharge areas that influence the site area.

An updated geological model of the deformation zones was produced for L1.2, and the hydrogeological properties of the zones were re-interpreted. Significantly, these updates introduced the concept of depth dependence in hydraulic properties based on evidence from the site. In terms of the rock mass, depth dependence in the hydraulic conductivity was also interpreted along with a dependence on rock domain. Hence, a significantly more complex model of the hydrogeological properties is required for L1.2 than was implemented in S1.2. The motivation being to honour the observed differences in hydraulic properties measured at the boreholes. However, there are only one or two boreholes within each rock domain and hence it is difficult to quantify the variability within domains compared to that between rock domains.

Figure 1-1. *The Laxemar subarea (within the grey boundary centre-left), and the Simpevarp subarea (within the grey boundary centre-right). The positions of cored boreholes are shown.*

A large amount of additional hydraulic data was acquired from boreholes in the Laxemar area, such as KLX03 and KLX04 together with some re-interpretation of data from older boreholes such as KLX01, KLX02, KSH01A and KAV01. Using previously developed techniques for conditioning hydrogeological fracture models (Hydro-DFN), a parameterisation of the fractured bedrock is required for each rock domain along with equivalent porous medium properties on various scales. It is important that this methodology be implemented in a systematic way that addresses uncertainties associated with the assumptions made in interpreting the data, such as the relationship between fracture transmissivity and size, and anisotropy. The update in hydro-geochemical data represented only a small increase in that available from S1.2. However, some important new information was introduced that suggested that there is a diffusive equilibrium between the groundwater in the fracture system and the pore-water in the tighter background rock. This is signigicant, since this may help to constrain transport properties. The hydro-geochemical information is used to calibrate simulations of palaeo-hydrogeology and to help understand the key sensitivities of present-day chemistry profiles observed in the boreholes.

Other new information that is considered here is more complex models of the overburden in terms of a layered system of spatially variable thickness made of several different types of Quaternary deposits. This is to give greater consistency with surface hydrology and aid the study of discharge to the biosphere.

Studies of flow-paths, including the locations of recharge and discharge areas pertinent to the site, are required. This is done by particle-tracking, both with the flow-velocity to identify discharge areas and against the flow-velocity to identify recharge areas. Particles release points are located on a dense array of points within the local-scale release area of 7.8 km and 3.2 km in the x,y-directions.

1.4 Organisation of work and layout of report

The numerical modelling was performed by two separate modelling teams. The work presented in this report was conducted by The CONNECTFLOW Team involving modelling experts from Serco Assurance and Kemakta Konsult. The CONNECTFLOW code and the visualisation software GeoVisage are developed by Serco Assurance /Serco Assurance 2005abc/. A complementary interpretation of a hydrogeological DFN has been performed by the DarcyTools Team based on the KLX04 borehole /Follin et al. 2006/.

This report presents the development of a Hydro-DFN for Laxemar, simulations of regional-scale variable-density groundwater flow, and transport calculations. Many simulations of regional-scale groundwater flow were performed to develop a model calibrated to the hydro-geochemical information and to provide a sensitivity analysis. Chapter 2 presents the overall modelling methodology, the model specifications and the deliverables on groundwater flow and particle tracking. Chapter 3 describes the methodology for deriving the Hydro-DFN parameters and its application to Laxemar. In Chapter 4 these parameters are used to study block-scale hydraulic properties required by Design and the regional-scale modelling. Chapter 5 gives more specific information on the overall approach to modelling groundwater flow at Laxemar and the various assumptions and uncertainties. The methods and data available for calibrating the regional flow models are detailed in Chapter 6. Chapter 7 presents the results for the calibration of the regional flow model and variants against the hydrogeochemistry and hydraulic data in boreholes. The results for the simulations of reference waters at the present-day are illustrated in Chapter 8. Further results for the groundwater flow patterns, discharge areas and reference water distributions for each variant considered are included in Chapter 0. Finally, Section 9.1 concludes the study.

2 Model set-up and specifications

2.1 Modelling methodology

The modelling methodology used in this study is based on the use of the Discrete Fracture Network (DFN) concept, which explicitly represents fractures within a rock mass and calculates flows through the individual fractures and between fractures at intersections. Using DFN models it is possible to integrate statistically-generated, smaller-scale fracture sets with large-scale deterministic features. From these DFN models, it is then possible to generate Equivalent Continuum Porous Medium (ECPM) models by converting the flow properties of blocks of the fracture network into the equivalent properties for a porous medium block of the same size. This effectively 'smears' the flow from the fractures intersecting a block boundary across the whole of the block face.

Serco Assurance's CONNECTFLOW software was used to carry out the modelling as it allows both DFN and ECPM representations to be used independently or combined in a single model. GeoVisage, a 3D visualisation tool developed by Serco Assurance, was used to visualise the models and to perform calculations relating to fracture clustering and intensity.

The models generated in this study have been used to calculate the flow of groundwater at Laxemar and also the transport of dissolved species in the groundwater. An option in CONNECTFLOW that allows the mixing of various groundwater 'end members' (groundwaters with defined compositions) to be tracked has enabled calculations of geochemical mixing in density dependent flow. From these models, the flow-field at the present-day has been used to track particles released from potential repository locations at Laxemar to the model boundary, from which transport performance measures are derived.

The regional groundwater models are constructed from the following three hydrogeological units:

HCD Hydraulic Conductor Domains – deterministically represented deformation zones of generally relatively high conductivity.

HRD Hydraulic Rock Domains – the bedrock between the deformation zones.

HSD Hydraulic Soil Domains – the surface hydrological units.

This distinction is made because different modelling concepts, field investigations, and interpretation techniques are applied to each.

The following sections describe the main concepts and assumptions used in the Laxemar 1.2 modelling study.

2.2 Discrete fracture network (DFN) model representation

The discrete fracture network (DFN) concept assumes that flow through a fractured rock is predominantly through an inter-connected network of flow-conductive fractures with groundwater moving from one fracture to another at the intersections between them. The properties of the network are usually characterized in terms of:

- Spatial distribution (e.g. Poisson, fractal, clustered around points or lineaments).
- Fracture intensity (and its spatial variation).
- Number of fracture orientation sets.

The properties of individual fractures are primarily:

- Either deterministic or stochastic.
- Size (radius).
- Orientation (strike and dip).
- Transmissivity (and possibly spatial variability within the plane).
- Transport aperture.
- Storativity.

In CONNECTFLOW, fractures are rectangular, or may be right-angle triangles where a complex surface has been triangulated into many pieces. For stochastic fractures, the properties are sampled from Probability Distribution Functions (PDFs) specified for each fracture set. The properties may be sampled independently or correlated. For the work reported here, the stochastic fractures were modelled as squares.

The purposes of the Hydro-DFN modelling exercise were:

- Checking the modelled fracture size and orientations distributions in the boreholes (based on the Geo-DFN) derived from core data.
- Deriving transmissivity distributions to match the observed flows in the Posiva Flow-Log (PFL) and Pipe-String System (PSS) data.
- Deriving the statistical distributions of ECPM properties on specified block scales for addressing design issues using flux-based upscaling.
- Creating realisations of the regional-scale ECPM model based on upscaling regional-scale DFN models.

The DFN concept is very useful since it naturally reflects the individual flow conduits in fractured rock, and the available field data. However, to understand flow and transport on the regional-scale it is often necessary to consider larger-scale bulk properties in the context of an ECPM concept. This requires methods to (i) convert the properties of a network of discrete fractures of lengths less than the continuum blocks into ECPM block properties, known as upscaling, and (ii) represent larger scale features such as deformation zones by appropriate properties in a series of continuum blocks, i.e. a downscaling method. The implementation of upscaling and downscaling in CONNECTFLOW is described in Sections 2.3 and 2.4, respectively.

Another useful facility in DFN modelling is the analysis of network connectivity. In CONNECTFLOW the fractures that are either isolated or form dead-ends (only one-way in) can be deleted to allow calculation of statistics such as P10 and P32 for the connected fracture network only. Use was made of this facility in this work to calculate the connected P10, $P10_c$, and to make estimates of the flow-wetted surface.

2.3 Fracture representation as equivalent continuum porous medium (ECPM) flow properties

In order to assess the implications of the DFN model for flow and transport on the regional-scale, it is often necessary for practical reasons to convert the DFN model to an ECPM model with appropriate properties. The resulting parameters are a directional hydraulic conductivity tensor, fracture kinematic porosity and other transport properties (such as the fracture surface area per unit volume). These peroperties are determined for blocks of a given scale as defined by ECPM model element/cell size or by the length of packer-intervals for comparison with field data. In this work, 100 m and 20 m scales are studied for comparison with the packer-interval data, and as required by the Repository Design Team. In CONNECTFLOW, a flux-based upscaling method is used that requires several flow calculations through a DFN model in different directions.

Figure 2-1 shows an illustration of how flow is calculated in a DFN model (a 2D network is shown for simplicity). To calculate equivalent hydraulic conductivity for the block shown, the flux through the network is calculated for a linear head gradient in each of the axial directions. Due to the variety of connections across the network, several flow-paths are possible, and this may result in cross-flows non-parallel to the head gradient. Cross-flows are a common characteristic of DFN models and can be approximated in an ECPM by an anisotropic hydraulic conductivity. In 3D, CONNECTFLOW uses a six component symmetric hydraulic conductivity tensor. The fluxes through each face of the block are calculated for each head gradient direction. The hydraulic conductivity tensor is then derived by a least-squares fit to these flux responses for the fixed head gradients. Other authors /La Pointe et al. 1995/ have only considered the components of the equivalent hydraulic conductivity parallel to the coordinate axes using a head difference between opposite faces and no-flow on the other faces. This leads to a very poor representation of blocks in which the network connections, and hence flow, are mostly between adjacent faces rather than between opposite faces. The effective permeability assigned to such blocks may be essentially zero, even though the flow-paths through the block may contribute significantly to the overall flow through the network.

In 3D, the blocks must be hexahedra (cuboids), but the upscaling method can be applied to an array of sub-blocks within a much larger DFN domain by performing the upscaling on each sub-block in sequence. The upscaling method is typically used in one of two ways:

1. To obtain the statistical distribution of hydraulic conductivity on a given block scale, a DFN model is generated for a much larger domain, and then ECPM properties are calculated for an array of sub-blocks of equal size and shape to give an ensemble of properties.
2. To obtain an ECPM model for a local- or regional-scale grid, a DFN model is generated within the grid domain, and the upscaling is performed within each grid element to derive the ECPM properties element by element.

A detailed description of the upscaling method for calculating the ECPM hydraulic conductivity tensor is given in /Jackson et al. 2000/. Briefly, the method can be summarised by the following steps:

- Define a sub-block within a DFN model.
- Identify the fractures that are either completely inside or cut the block.
- Calculate the connections between these fractures and their connection to the faces of the block.

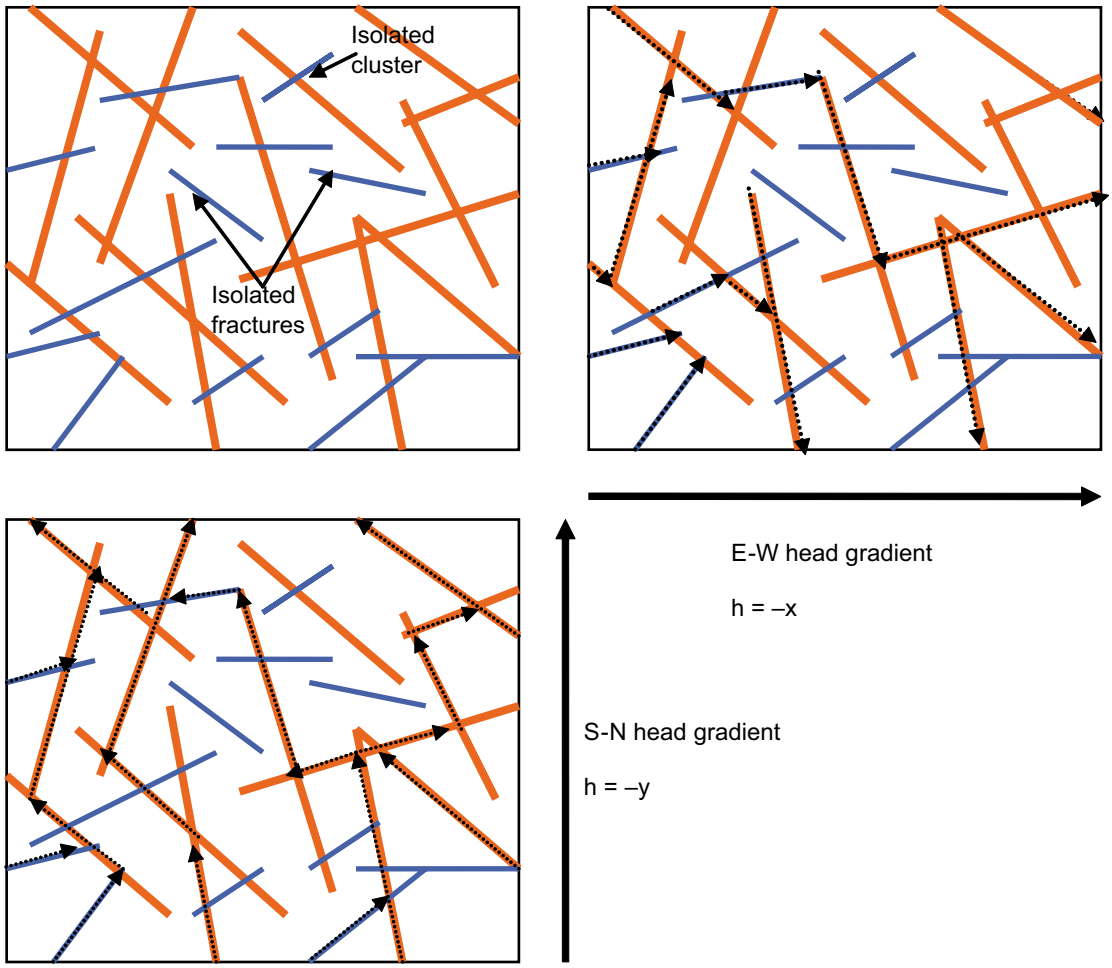

Figure 2-1. *2D illustration of flow through a network of fractures. A random network of fractures with variable size and transmissivity is shown top left (orange fractures are large transmissivity, blue are low). Top right: flow paths for a linear head gradient E-W decreasing along the x-axis. Bottom left: flow paths through the network for a linear head gradient S-N decreasing along the y-axis.*

- Specify a linear head gradient parallel to each coordinate axis on all the faces of the block.
- Calculate the flow through the network and the flux through each face of the block for each axial head gradient.
- Fit a symmetric anisotropic hydraulic conductivity tensor that best fits (least-squares) the flux response of the network.
- Fracture kinematic porosity is calculated as the sum (over all fractures that are connected on the scale of the block) of fracture area within the block multiplied by the transport aperture of the fracture divided by the block volume.

Hence, to calculate the ECPM properties for a finite-element grid with 1 million elements, say, involves 3 times 1 million DFN flow calculations. One important aspect of this approach is that the properties are calculated on a particular scale, that of the blocks, and that a connectivity analysis of the network is performed only on the scale of the block. Bulk flows across many blocks will depend on the correlation and variability of properties between blocks.

One refinement of the upscaling methodology is to simulate flow through a slightly larger domain than the block size required for the ECPM properties, but then to calculate the flux responses through the correct block size. The reason for this is to avoid over-prediction of hydraulic conductivity from flows through fractures that just cut the corner of the block but that are unrepresentative of flows through the in situ fracture network. This is the method used in this study and is illustrated in Figure 2-2. The area around the block is known as a 'guard-zone', and an appropriate choice for its thickness is about half a fracture length, and should be varied to check for convergence. The problem is most significant in sparse heterogeneous networks in which the flux through the network of fractures is affected by 'bottlenecks' through low transmissivity fractures, and is quite different to the flux through single fractures.

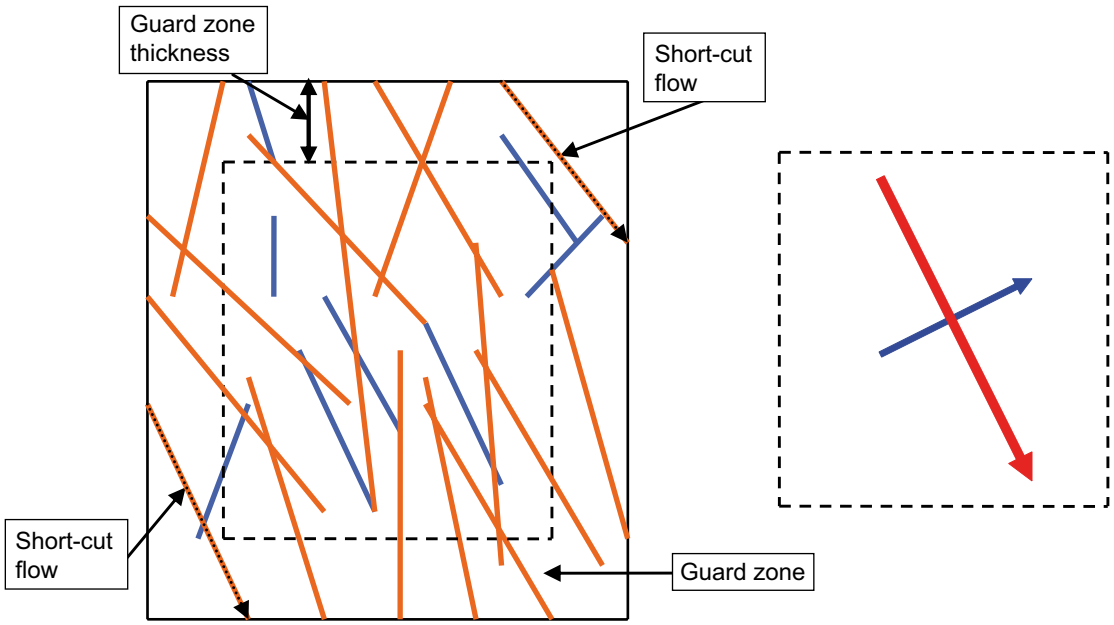

Figure 2-2. *2D sketch of how block-scale hydraulic conductivity can be over-estimated using a linear head gradient when high transmissivity fractures cut across a corner of the block. By simulating flow through a larger domain, but only calculating the flux through the required block size (dashed block) then fluxes more consistent with flow through an in situ network are obtained. The ECPM hydraulic conductivities are then calculated for the dashed block to give principal components (right). The red arrow is the maximum component, blue the minimum.*

2.4 Implicit representation of fracture zones (the 'IFZ' method)

For Laxemar 1.2, the basic concept is that fractures exist on a continuous range of length scales (see /Bour et al. 2002/ for example), which motivates a methodology to generate sub-lineament-scale fractures stochastically on scales between tens of metres and about 1 km, and then combine this DFN by superposition with the larger scale deterministic deformation zones. In CONNECTFLOW, the approach taken was to create one or more realisations of the stochastic network on the regional-scale and then, using the upscaling methods described above, to convert this to a realisation of the ECPM model, minus the deformation zones. That is, at this point the ECPM model was only an equivalent representation of the stochastic network. The ECPM model was then modified to incorporate the structural model in terms of the geometry and properties of a set of large-scale deformation zones using the Implicit Fracture Zone (IFZ) method in CONNECTFLOW as described in /Marsic et al. 2001/. The reason for this approach was that it was then relatively quick to combine different scenarios for the deformation zones with the stochastic DFN model without having to repeat the computationally expensive upscaling step.

The IFZ downscaling method identifies which elements are crossed by a fracture zone and combines a hydraulic conductivity tensor associated with the fracture zone with a hydraulic conductivity tensor for the background stochastic network. For each element crossed by the fracture zone, the following steps are performed:

- The volume of intersection between the fracture zone and the element is determined.
- The hydraulic conductivity tensor of the background rock is calculated in the coordinate system of the fracture zone.
- The combined conductivity tensor of the background rock and the fracture zone is calculated in the coordinate system of the fracture zone.
- The effective hydraulic conductivity tensor that includes the effect of the fracture zone is determined in the original coordinate system.

The methodology is illustrated diagrammatically in Figure 2-3. In 3D, the resultant hydraulic conductivity is a 6-component symmetric tensor in the Cartesian coordinate system. The tensor can be diagonalised to give the principal components and directions of anisotropy.

Similarly, a combined scalar block-scale porosity is calculated for the element as a weighted combination of the fracture zone porosity and the background block-scale porosity. The weighting is based on either the relative volume or on the hydraulic conductivity weighted volume (hydraulic conductivity multiplied by the volume of the feature within the element). The latter weighting can be suitable for transport since it weights the combined porosity toward the fracture zone porosity if this is of a relatively high hydraulic conductivity. The result of this step is to produce a spatial distribution of ECPM element properties (hydraulic conductivity tensor and porosity) that represent the combined influence of both the deterministic fractures zones and background stochastic fractures.

It should be noted that the term "background conductivity" here means the equivalent conductivity of the stochastic fracture network. No extra component for matrix conductivity or micro-fracturing is added. However, the stochastic DFN is necessarily truncated in some way, e.g. based on fracture size, which consequently means that some elements may include a connected network of fractures, or may only be connected in some directions. To avoid this just being a result of the choice of truncation limit and chance, a minimum block conductivity and porosity is set for any elements that have zero properties following the fracture upscaling and IFZ methods. Appropriate minimum values are derived from the

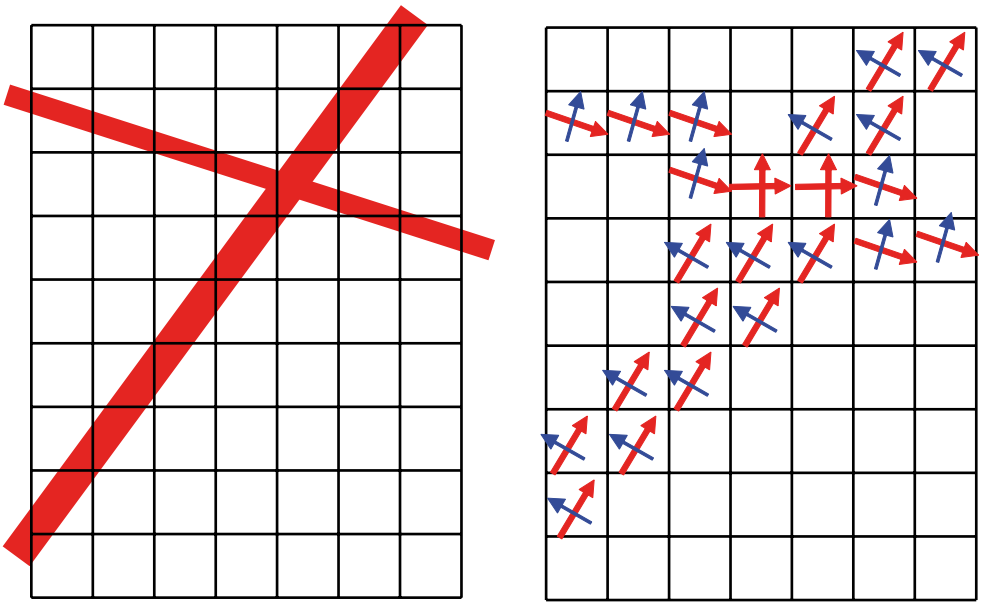

Figure 2-3. *Schematic illustration of the modification of the hydraulic conductivity tensor by the IFZ method. A finite-element grid crossed obliquely by two fracture zones of different thickness (left). The effect on the equivalent porous medium hydraulic conductivity is shown right. Elements with a large IFZ effect are coloured pink. Ones with a lesser effect, where the fracture zone only crosses one corner, are coloured orange. The principal directions of the resultant anisotropic hydraulic conductivity tensor are shown by arrows (red for major component, blue for minor).*

block-scale property studies by calculating the minimum values that occur when the DFN is truncated at very small fractures relative to the block size. Such values correspond to the limit when the properties are essentially free from the truncation effect.

2.5 Variable density groundwater flow and salt transport

An option was added to CONNECTFLOW for the earlier Forsmark version 1.2 modelling to model flow in a porous medium for groundwater of variable salinity, where the salinity arises from a number of groundwater constituents. This can be modelled either in terms of transport of mass fractions of each of the basic hydro-geochemical constituents (such as chloride, sodium, oxygen isotope ratio), which are taken to be conservative, or in terms of transport of fractions of selected reference waters. Either way, the transport equations are coupled with the overall mass conservation equation for groundwater.

The first approach would involve solving transport equations for each of the major ions and isotopic values with the transient groundwater flow, including a coupling back to the flow via spatial variations in groundwater density due to its varying composition. Since the raw hydrogeochemistry is analysed in terms of concentrations of major ions, then this option appears attractive as it models what is measured. However, the model would need to be formulated in terms of individual ion concentration of the initial groundwaters and the surface waters as they evolve in time. This would not be straightforward since the hydro-geochemical conceptual understanding and data have been developed in terms of the mixing of fractions of well-defined reference waters. In consequence it is more practical to use the option for transport of reference water fractions, since the boundary conditions for the flow modelling are most naturally expressed in the terms of the reference waters. This

option makes the approximation that the geochemical composition of a mixture of reference waters can be related linearly to the compositions of the individual reference waters (i.e. no reactions), and that transport properties of the major ions (e.g. diffusivities) are similar. The option also provides a very user-friendly way of presenting the results of multi-component groundwater flow calculations, which are given directly in terms of the selected reference waters for direct comparison with the Mixing and mass-balance modelling (M3) geochemical analysis /Laaksoharju et al. 1999/. In addition, the assumed linear relationship between reference water mixing fractions and groundwater composition can be used to obtain the concentrations of the basic geochemical constituents for direct comparison with measurements of groundwater chemistry. This option has been used in the ECPM regional-scale model. A simplified representation in terms of four reference waters (Meteoric, Littorina, Glacial, and Brine) was used (see Section 5.3).

Transport of fractions of reference waters can be modelled using the same equations used to model transport of groundwater constituents (the various ionic species, oxygen and hydrogen isotope ratios) provided that it is assumed that the constituents have the same dispersion, matrix diffusion and sorption properties. This may be a good approximation for dispersion, which may be largely determined by the variations in groundwater velocity within and between pores. However, the self-diffusion coefficients for the various constituents differ by a factor of about 2, and so the effective (or intrinsic) diffusion coefficients would be expected to differ by a similar factor, or even more, if anion exclusion is significant. If differences of this order are considered important, then the standard transport equations can only be used to model the transport of constituents. For this work, it has been assumed that these factor differences in diffusion rates are relatively unimportant, and hence we can work in terms of mixing fractions.

However, the following point should be noted. Because of the linearity of the transport equations (in the assumed absence of reactions), linear combinations of the constituents also satisfy transport equations. Transport equations for the fractions of reference waters can still be written down, therefore, even if the diffusion coefficients for the different constituents are different. However, the key point is that each equation no longer involves only a single reference water, but the equations are coupled. For the case where diffusion coefficients are very differnet, it would probably be best to carry out the transport calculations in terms of constituents, translating between reference waters and constituents before and after the calculations if necessary.

It should also be noted that if the constituents have different transport properties, it is also necessary to account for the constraint of electro-neutrality.

It is also possible to model diffusion of the reference waters, or constituents, between groundwater flowing in fractures and immobile water in the rock matrix between the fractures (Rock-Matrix Diffusion or RMD). The numerical approach used /Hoch and Jackson 2004/ is based on a method developed by /Carrera et al. 1998/, enhanced to enable potentially larger time steps to be taken. The approach combines an approximation that is accurate for small times with one that is accurate for long times, to give a representation of the diffusion into the rock matrix that is accurate for all times. At early times, the diffusion is represented in terms of the inverse of the square root of time, and at long times it is represented as a series of decaying exponentials. The approach is very efficient computationally, although it is necessary to make the assumption that the groundwater density does not vary in the rock matrix at each location.

2.6 Boundary condition concepts

Simulating the palaeo-hydrogeology for Laxemar 1.2 requires modelling of the evolution of groundwater flow and solute transport during the post-glacial period up to the present-day. A key issue in this exercise is how to represent the time-varying boundary conditions for both flow and solutes or reference waters.

For flow, there are two main possibilities onshore: either specified head, or a flux type boundary condition. For specified head, the model is assumed to be fully saturated, and hence head is equal to the height of the topographic surface at that time according to the sea-level transgression. Offshore it is most natural to use a specified head type boundary condition. Here, the head is equal to the depth of the sea multiplied by the relative salinity of the Baltic Sea, and both the salinity of the Baltic and sea depth alter in time.

Specified head boundary conditions are straightforward to implement numerically by setting the value at nodes on the surface to the required head at each time-step. For the flux type boundary condition, it is more complicated because in reality, the flux through the top surface will vary spatially, both in magnitude and direction since in some areas groundwater is recharging and in others it is discharging. This distribution of flux varies according to the amount of potential groundwater recharge and the hydraulic properties. It is also going to change in time as the shoreline retreats. The approach taken in CONNECTFLOW is to define the recharge flux, R, into or out of the model as a function of the current head, h, in the model, the topographic surface height, z, and the potential groundwater recharge, R_p. The maximum potential groundwater recharge is equal to the precipitation minus evapotranspiration and surface run-off. Surface run-off is subtracted because we are only interested in the potential recharge to the sub-surface. The Appropriate functions for the flux, R, must have certain characteristics. For recharge areas, the head, h, or watertable, is below ground surface and so the recharge must be equal to the full recharge, R_p. In discharge areas, the watertable is just above ground surface and so head is just above ground surface, which can be achieved by taking a suitably large flux out of the model, i.e. a negative value of R, whenever the head goes above ground surface. The standard function used in CONNECTFLOW is:

$$R = \begin{cases} R_p & h \le z - \varepsilon \\ -R_p (h - z)/\varepsilon & h > z - \varepsilon \end{cases},$$

where ε is a small number. This function implies that if the watertable is more than ε below the topographic surface then recharge equals the full potential groundwater recharge. Above that, the recharge reduces until the watertable is at the surface. If the watertable is above the topographic surface, then recharge becomes negative, i.e. discharge, and an appropriate flux of groundwater is taken from the model to reduce the head until the watertable is restored to the topographic height. Hence, this boundary condition is a non-linear equation (the flux depends on the free-variable head) that ensures a specified flux if the watertable is low and a specified head where the watertable is at or above ground surface. The non-linearity requires that multiple iterations of the groundwater flow equations be performed at each time-step to reach convergence, which implies longer run times for this boundary condition. The topographic surface is not constant in time due to post-glacial rebound and marine transgressions, and hence $z = z(t)$. Newton-Raphson iteration was used to achieve convergence of the non-linear equations at each time-step. This technique works best for systems with smooth gradients. The standard function given above for flux has a discontinuous derivative at $h = z–\varepsilon$ and this led to a slow rate of convergence; typically 3–5 Newton-Raphson iterations were required at each time-step. Hence, an alternative smooth function for recharge was tried:

$$R = R_p \times \left(\exp\left(\frac{h - z}{0.5} \right) - 1 \right).$$

This has similar characteristics to the standard function, but has smooth derivatives around $h = z$. It was found to always converge in 2 Newton-Raphson iterations for the time-step used, and hence gave quicker and more robust solutions. There are other candidates for this function, such as a modification to the standard function but using a hyperbola to give a smooth transition around $h = z$.

It should be noted with this model that groundwater that discharges through the top surface exits the model and does not enter a separate surface model that allows recharge downstream. Alternative approaches, are to couple the groundwater model to a surface Hydrology model, such as MIKE-SHE /Werner et al. 2005/, or to add a surface layer with very high hydraulic conductivity to model the surface flow explicitly. In the second of these approaches, a flux is specified over the onshore region not covered by lakes, a head is specified in the sea and lakes, and the unsaturated flow equations should be solved in the near-surface layers. In this case, the flux should be set to precipitation minus evapotranspiration, and these in principle can vary spatially. Whichever approach is used it must be implemented in the context of an environment changing in time.

For solutes, the boundary conditions are generally a specified value where there is an advective flow into the model (recharge area), or an outflow condition where there is flow out (discharge). Because the flows are transient, the areas of recharge and discharge evolve in time, and hence it is important to have an automatic way of determining the recharge and discharge areas. The difficulty in achieving this is that it requires mixing a Neumann (flux) type boundary condition on outflow with a Dirichlet (head) type boundary condition on inflow; and since the recharge/discharge areas change in time, the type of boundary condition has to be changed in time. Our solution is to specify a flux of solute through the top surface that changes depending on the direction of flow across the surface. Where an inflow of groundwater at a specified input concentration is required (i.e. a Dirichlet condition), flux is equated to a penalty weight function based on the difference between solute concentration in the model and the required input concentration. Therefore, the flux of solute out of the model, F_c, is then given by the equation:

$$F_c = \begin{cases} (q \times n)\, c & q \times n \geq 0 \\ (c - c_0)/\delta & q \times n < 0 \end{cases},$$

where $q \times n$ is the advective flux out of the model, i.e. the groundwater flow, q, in the direction parallel to the outward normal to the surface, n, c is the solute concentration or mixing fraction, and δ is a small number. For $q \times n \geq 0$ the flux corresponds to an outflow condition, for $q \times n < 0$ a specified value condition, $c = c_0$, is implemented as a penalty function such that solute is removed if $c > c_0$, and injected if $c < c_0$. This effectively ensures that $c \approx c_0$.

2.7 Transport performance measures: canister flux (q_r), travel time (t_r), path-length (L_r) and F-factor (F_r)

One objective of the site descriptive modelling is to understand groundwater pathways from a local-scale area to the surface. The approach taken is to track particles moving with the advective flow velocity from a range of release points until they reach the top surface. Although it would be possible in CONNECTFLOW to track particles as they move through a velocity field that evolves in time, it is preferred here to only use the velocity field from

the present-day. This is mainly because particle tracks released in a transient velocity field would be sensitive to both the release time and the kinematic porosity, making it more difficult to interpret the results due to the added uncertainties. One uncertainty that it is important to address here is the effect of the stochastic DFN on regional-scale pathways. Hence, several realisations of the DFN model, and hence the ECPM model, will be considered here to quantify the sensitivity of transport performance measures to particular realisations. The four performance measures required are:

1. Travel-time, $t_r = \sum_l \frac{n_f \delta l}{q}$, where δl is the length of a step in distance along the path, l denotes steps along a path, for example through one finite-element, n_e is the kinematic porosity, and q the Darcy velocity.
2. Initial Darcy velocity at the release point (Canister flux), $U_r = U_{0,r}$.
3. Path-length, $L_r = \sum_l \delta l$.
4. F-factor, $F_r = \sum_l \frac{a_r \delta l}{q}$, where a_r is the fracture surface area per unit volume.

The approach to calculating the performance measures is to release a large number of particles distributed evenly (fixed spacing) over the local-scale area and use these to produce ensemble statistics for the performance measures, as well as locating the discharge areas. No attempt is made to avoid starting particles in either deterministic deformation zones or high transmissivity stochastic fractures. In reality, such features are likely to be avoided during repository construction, and hence the current modelling approach will tend to track particles starting in a wider range of possible fracture transmissivities than might be encountered in reality.

As well as tracking particles forwards with the advective velocity field, it is also possible to track them backwards against the flow direction to identify the source of groundwater recharge. This is done by following particles along the reverse flow vector upstream ignoring any convergence of flow from several sources, so that the approach tends to identify concentrated areas of recharge.

2.8 Modelling strategy

A key philosophy in developing the groundwater models described here has been to calibrate model parameters against field data within a margin appropriate to the quality and availability of the data. Equally, it is important that any variants considered in order to quantify uncertainties are also calibrated to data, rather than being arbitrary parameter variations, so that in a sense they are equally possible realisations. As such, many models have been created during this study, but in the reporting we focus on the combinations of parameters and conditions that give predictions consistent with field data. The variants reported here are therefore the ones that have been constructed to demonstrate the uncertainties that remain in the model concepts and parameters, and consequent model predictions, due to the lack of constraint by the available data. These variants are used to quantify sensitivities and form the basis for recommending important uncertainties that should be propagated to the SR-Can Assessment calculations.

3 Assessment of hydrogeological discrete fracture network (Hydro-DFN) model

The current site characterisation of the Simpevarp and Laxemar subareas using the Laxemar 1.2 data freeze (or 'L1.2') has provided a geologically derived DFN model (denoted the 'Geo-DFN model' /Hermansson et al. 2005/) of fracture geometrical data (orientation and intensities) based on outcrop data, borehole data and the RVS deformation zone model. However, for the hydrogeological modelling it is necessary to integrate the Geo-DFN with hydraulic data, namely the Posiva Flow-Log (PFL) data and the double-packer injection test data, known as Pipe-String System (PSS) data. In doing so, it has been necessary to make some practical simplifications to derive a satisfactory hydrogeological DFN model – known as the Hydro-DFN – suitable for GroundWater Flow (GWF) modelling. Having derived a Hydro-DFN, block-scale properties on a 100 m and 20 m scale were calculated to be used for regional GWF property assignment, and also for repository design issues.

The hydraulic data used in this work comes from the following types of hydraulic test /Rhen et al. 2006/:

- After completion of core drilling, the Posiva Flow Log (PFL) is generally applied in the cored borehole. The section logging (PFL-s) is made with a test section length of 5 m and a step length of 0.5 m, with the purpose of measuring transmissivity in 5 m sections and indicating flowing sections with a resolution of 0.5 m, useful for planning the hydrogeochemistry sampling and the flow-anomaly logging. The flow-anomaly logging (PFL-f) is made with a test section length of 1 m and a step length of 0.1 m when moving the test section along the borehole, with the purpose of identifying individual flowing fractures.
- Subsequently to PFL measurements, injection tests with the Pipe String System (PSS) are made starting with 100 m test sections, then 20 m sections within all 100 m sections with flow-rates above the measurement limit, and then 5 m sections in the borehole section 300–700 m in all 20 m sections with flow-rates above measurement limit.
- In percussion boreholes, generally 100–200 m long, pumping tests of the entire boreholes are made, and sometimes they are also flow logged with an Impeller Meter. A majority of the percussion holes have been aimed to intersect the deformation zones.

This data formed the basis for a series of data analyses and modelling tasks to interpret a Hydro-DFN. The work reported here on the Hydro DFN includes:

- Simulating the DFN model(s) based on the delivery from Geology. In particular, testing different relationships between fracture transmissivity and size, as well as relationships between fracture intensities and size. Calibrating the hydraulic parameters against hydraulic data from borehole tests to evaluate the agreement in transmissivities with the measured transmissivities (PFL-f and PSS hydraulic test data). This involved performing flow simulations based on flow through a fracture network with radial flow boundary conditions.
- A summary of hydraulic data for each borehole (Laxemar subarea: KLX02, KLX03, KLX04, Simpevarp subarea: KSH01A, KSH02, KAV01, KAV04A/B). In the case of KLX03, KLX04, KSH01A and KAV04A, DFN simulations of the PFL-f and PSS tests (where applicable) were carried out for various transmissivity models to compare

modelled transmissivities with the measurements. The quality of the match was measured in several ways. For the PSS tests, the model predictions of the transmissivities of 5 m intervals were compared with the 5 m interval tests or 20 m intervals depending on data availability. For the PFL-f tests, simulated flow-rates in individual fractures were compared against the distribution of flow anomalies seen in the boreholes. Further, by grouping flows into 5 m intervals to give a distribution of interval transmissivities it was possible to cross-compare the simulations against both the PFL-f and PSS interval data . Finally, the total measured transmissivity, and number of PSS 5 m intervals without any flow were compared. In addition, for the PFL-f tests, statistics for the flow anomalies within each set were compared. The flow simulations considered alternative transmissivity models and were used to identify parameter ranges that could reproduce the observed flows.

- Based on a collation of the information from the group of Laxemar and Simpevarp boreholes, recommendations are made for the DFN definition to be applied in the regional and site-scale GWF modelling.

The work reported here on the block properties for the Laxemar and Simpevarp subareas includes:

- Estimation of anisotropy in horizontal and vertical directions.
- Calculation of the statistics of the hydraulic conductivity of 100 m and 20 m blocks.
- Evaluation of the effects of fracture size-truncation as well as other numerical sensitivities.
- Recommendations for block/element-background properties for the regional-scale GWF modelling. This used for the regional-scale DFN models where for practical reasons a minimum fracture size, r_{min}, has to be chosen perhaps much greater than r_0. For a stochastic DFN model this can lead to a small number elements having a sparse network and corresponding low or zero equivalent hydraulic conductivity. In these elements it is appropriate to assign a minimum hydarulic conductivity based on block properties that have been evaluated with a much lower fracture size truncation.
- Calculation of kinematic porosity based on fracture transport aperture = function (Transmissivity) relationship from Äspö Task Force 6c /Dershowitz et al. 2003/.
- Calculation of the block properties for the alternative transmissivity models.

SKB have suggested a consistent terminology to be used for describing DFN models as given in the Glossary at the beginning of this report.

The Geo-DFN defines an orientation model for fracture sets that is based on outcrop mapping analysis. /Hermansson et al. 2005/ report three regional sub-vertical fracture sets (Set_A, Set_B and Set_C), one local sub-horizontal set (Set_d), and one local sub-vertical set (Set_f for Laxemar subarea, and Set_e for Simpevarp subarea. This classification and the implementation of the orientation model in the Hydro-DFN are discussed further in Section 3.4.

The initial development of a Hydro-DFN model proved problematic using the original delivery of the Geo-DFN model in April 2005. Attempts were made at developing a Hydro-DFN model based on applying the Geo-DFN, honouring all the various geometrical parameters specified, such as set classification, fracture-radius distributions, P32 values and orientations. However, problems were encountered in the integration of the hydraulic data with the power-law size distribution parameters as specified for some sets due to either very small or large values of the location parameter of the power-law, r_0. For instance, small r_0 values gave few large sub-vertical fractures in Set_A despite it being the dominant set in the

local-scale RVS deformation zone model. Conversely, high r_0 values for Set_B and Set_C seemed unrealistic given the minimum measured outcrop fracture trace length was 0.5 m (see Subsection 3.4.1 and outcrop maps in Figure 3-41). Some improvements were made by holding the power-law slope, k_r, at the values specified in the Geo-DFN but modifying r_0 so as to ensure the P32 for fractures greater than 1 km in length was consistent with the Rock Visualisation System (RVS) L1.2 deterministic deformation zone model. This provided a basis for an exercise to match the hydraulic data in boreholes KLX03, KLX04 and KSH01A. However, fracture networks generated were characterised by many small fractures that resulted in a more connected and homogeneous network than was suggested by the hydraulic data. This characteristic was due to the relatively high power-law slopes, k_r around 3.0 or more, as suggested in the Geo-DFN. This compares with slopes in the range 2.6–2.9 interpreted in S1.2.

In consequence, we reassessed the fracture size distribution by fixing r_0 at 0.28 m – equivalent to a length of 0.5 m for square fractures – and calculating values of k_r for each set that gave a consistent match between the P32 of open and partly-open fractures seen at the borehole scale and the P32 for deterministic deformation zones in the L1.2 local-scale RVS deformation zone model. An r_0 of 0.28 m was assumed on the basis that it is equivalent to the minimum trace length of 0.5 m used in mapping outcrops. A subsequent analysis of the connectivity of the resulting fracture network (see Section 3.10) indicated that this choice of r_0 was sufficient to generate a well inter-connected network of open fractures. It was necessary to make this re-interpretation of the fracture size distributions in August 2005 to complete the Hydro-DFN analysis. However, this was prior to corrections being made to the final Geo-DFN model issued in September 2005. The result is that Hydro-DFN models reported here are consistent with final Geo-DFN in terms of fracture sets, orientations, borehole fracture intensities, and proportions between sets, but the power-law fracture size distributions differ slightly. The differences arise partly from the use of different deformation zone models: The S1.2 RVS DZ model was used for the Geo-DFN model whereas the L1.2 RVS DZ model was used for the analysis described in this report. More significantly, different assumptions were made in matching the power-law slopes to the fracture intensities at the borehole-scale and to those given by the local-scale RVS DZ model. From a hydrogeological viewpoint, we chose to match the fracture intensity of open and partly-open fractures at the borehole-scale to the local-scale deformation zone model, whereas the updated Geo-DFN chose to match the fracture intensity of open and sealed fractures at the borehole-scale to the local-scale deformation zone. Consequently, we derive slightly lower values of the power-law slope, k_r, for r_0 of 0.28 m than in the September issue of the Geo-DFN. For brevity we only report our final Hydro-DFN results using the values of k_r that we interpreted in this work. The details of the power-law fitting are given in Subsection 3.4.1.

3.1 Methodology

As part of the S1.2 modelling, a methodology was developed and tested using data from the Simpevarp SDM /Hartley et al. 2005a/, and further developed for the Forsmark version 1.2 SDM modelling /Hartley et al. 2005b/. The approach has been refined further for Laxemar version 1.2 data. The current workflow used for the L1.2 data can be summarised by the following steps:

1. Analyse fracture intensity for a possible depth trend in flowing fractures (no depth trend had been interpreted in the Geo-DFN based on all fractures).
2. Use fracture size distribution from Geo-DFN (this had to be re-analysed as described above).

3. Generate five realisations of the DFN model around the borehole and check the modelled P10 of open fractures in the borehole against that in the field-data assuming an r_0 of 0.28 m. Adjust Terzaghi (/Terzaghi 1965/) corrected P10, $P10_{corr}$, if necessary. The borehole is treated as a line for the Terzaghi correction (Subsection 3.3.3).
4. Cross check P21 distribution quantitatively with outcrop maps. The P21 distribution corresponding to the matched P10 has been simulated for all (open and sealed) fractures for comparison with the outcrop maps. That is, separate DFN simulations that include all fractures are performed to check P10 and P21 in addition to the Hydro-DFN simulations of flow where only the conductive fractures are considered.
5. Define alternative transmissivity concepts (uncorrelated: log-normal; correlated: direct T vs. r correlation; semi-correlated: correlated but with log-normal perturbation).
6. For each T concept, use DFN flow simulations to match the interpreted distribution of transmissivity for 5 m intervals. To allow a direct comparison to be made between DFN flow simulation results, PFL-f data, and PSS data, the transmissivity of flow anomalies given by the PFL-f data was grouped into 5 m intervals.
7. For the PFL-f data the distribution of flow-rates, Q, from individual flow anomalies is also compared to the model. The dependence on fracture orientation is considered by comparing the distributions of Q within each fracture set.
8. For each T concept, identify possible ranges of parameters i.e. uncertainties.
9. For each T concept, calculate block-scale directional permeability and porosity.

The ambition of this modelling was to demonstrate one or more matches to the observations in the boreholes in a statistical sense based on statistical distributions of quantities such as transmissivity, rather than to reproduce very specific and perhaps localised characteristics seen in each borehole. The rationale behind this approach is that we are aiming to make conclusions that can be applied over very large volumes. The Geo-DFN advocates a link between fracture intensity and rock domain, and hence we also seek to define Hydro-DFN properties for each of the main rock domains within the Laxemar and Simpevarp subareas. Later in this study the Hydro-DFN is used to parameterise the regional-scale GWF models, and hence it is most important to understand the hydrogeological DFN characteristics and their uncertainties in a broad sense.

3.2 Modelling assumptions and input data

This study focused on the new data available from the Laxemar subarea (KLX03 and KLX04), and updated/new data from the Simpevarp subarea (KSH01A and KAV04A/B). However, the full collation of data included:

- The borehole core-logs that record all the fractures identified in the cores (and cross-checked with the BIPS borehole image logs) along with a comprehensive set of fracture classifications (Laxemar subarea: KLX01, KLX02, KLX03, KLX04; and Simpevarp subarea: KSH01A, KSH02, KAV01, KAV04A,B).
- The PFL flow anomalies including the flow-rates and head changes for each feature (Laxemar subarea: KLX02, KLX03, KLX04; and Simpevarp subarea: KSH01A, KSH02, KAV01, KAV04A,B).
- Double-packer injection test data (PSS) for Laxemar subarea:
  - KLX04 (5 m, 20 m and 100 m intervals).
  - KLX02 (PSS and older hydraulic tests) (5 m, 20 m, 100 m, 1,000 m intervals).
  - KLX01 (Injection tests, 3 m, 30 m, 100 m, 500 m, 1,000 m intervals).

- Double-packer injection test data (PSS) for Simpevarp subarea:
  – KSH01A (5 m, 20 m, 100 m, 1,000 m intervals).
  – KSH03A (limited data from injection tests, 100 m intervals).
- Rock domain data in boreholes.
- Location of deformation zones in each borehole and specification as either deterministic in the RVS DZ model or stochastic from single-hole interpretations.
- The Geo-DFN model of fracture characterisation /Hermansson et al. 2005/, which considers Laxemar subarea and Simpevarp subarea separately, and includes an analysis of the outcrops and boreholes followed by derivation of a DFN statistical model.

The following assumptions have been made:

- Deformation zones identified from single-hole interpretations represent a swarm of fractures, but these are modelled and characterised as a single large stochastic feature.
- All deformation zones are open or partly-open (see Subsection 3.4.1).
- Fractures exist on all scales with stochastic fractures ranging in radii from r_0 to 564 m. The maximum radius for stochastic fractures is set to be the minimum size interpreted in the RVS deformation zone model. These have lengths down to 1 km, which for an equivalent area corresponds to a radius of 564 m (see conversion formula in the Glossary). The power-law parameters have been chosen to ensure the density of stochastic fracture and deterministic fractures are consistent (see Subsection 3.4.1).
- Fracture sets can be categorised according to orientation and size groupings (based on Geo-DFN; see Section 3.4 and /Hermansson et al. 2005/).
- Open and partly open fractures have constant aperture. Sealed fractures make no contribution to the hydraulic system.

3.3 Conceptual models with potential alternatives

Few characteristics of the DFN can be determined uniquely and directly and so it is necessary to assume a framework of conceptual models, and then derive parameters that best match observed data.

3.3.1 Continuous power-law fracture size distribution

One of the most difficult characteristics of fractures to measure directly in the sub-surface rock is fracture size. Fracture trace length can be measured on outcrops for fractures on the scale of metres to tens of metres, and data is available for lineaments on the scale of 1 km to several kilometres, but this leaves a gap between the scales. (The minimum lineament length is 1 km in the local-scale RVS deformation zone model, and 1.6 km in the regional-scale deformation zone model). A widely used assumption is one of a continuous scale of fracturing that spans all scales in a continuous manner which can be described by a power-law relationship between fracture intensity and fracture size. A schematic illustration of such a relationship is shown in Figure 3-1, which also includes a lognormal distribution plot for comparison. The lognormal distribution is another commonly used model for fracture size.

The key parameters for a power-law distribution for fracture radius are the shape parameter (k_r) and the location parameter (r_0). The distribution, $f(r)$, is often defined only in a truncated range, between r_{min} and r_{max}.

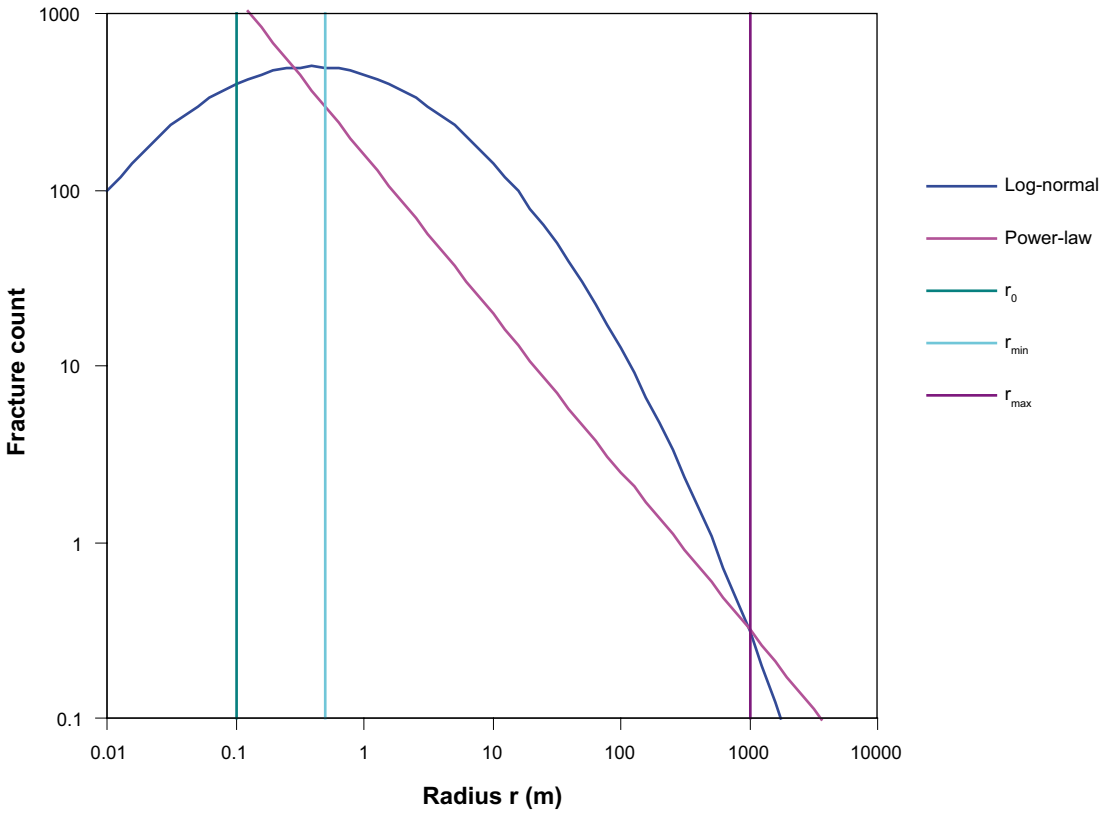

Figure 3-1. *Example of a power-law and lognormal model of fracture size distribution. Also shown is an example of the location radius, r_0, which depends on the resolution of the fracture observation technique. When a fracture network is simulated, for practical reasons it is often necessary to truncate the power-law distribution and these parameters will be referred to as r_{min} and r_{max}.*

$$f(r) = \frac{k_r r_0^{k_r}}{r^{k_r+1}} \quad , \tag{1}$$

where $r_{max} \geq r \geq r_{min}$, $r_0 > 0$, and $k_r > 0$.

In the groundwater flow modelling for L1.2, it was assumed that fractures of radius greater than 564 m would be modelled deterministically having been detected as lineaments or deformation zones and included in the RVS DZ model, while fractures less than 564 m in radius would be modelled stochastically based on the Hydro-DFN model developed here. The figure 564 m is derived from the minimum length interpreted in the local-scale RVS DZ model being 1 km, which for an equivalent area has radius 564 m (see the Glossary).

3.3.2 Stochastic lineament swarms represented as planar features

Large fractures with radii of the order of 100 m may exist as single breaks. However, it is more common that discontinuities with radii greater than about 30 m exist as deformation zones. On an outcrop, the trace of these features will be observed as 'lineament swarms'. A number of deformation zones are observed in the boreholes, and hence it is useful to characterise these features to get some indication of the thickness and fracture intensities within these zones. However, at this stage, deformation zones with radius less then 564 m will be approximated as large stochastic fracture planes with a continuous range of fracture sizes as shown in Figure 3-2. It is important that data such as fracture intensity and the

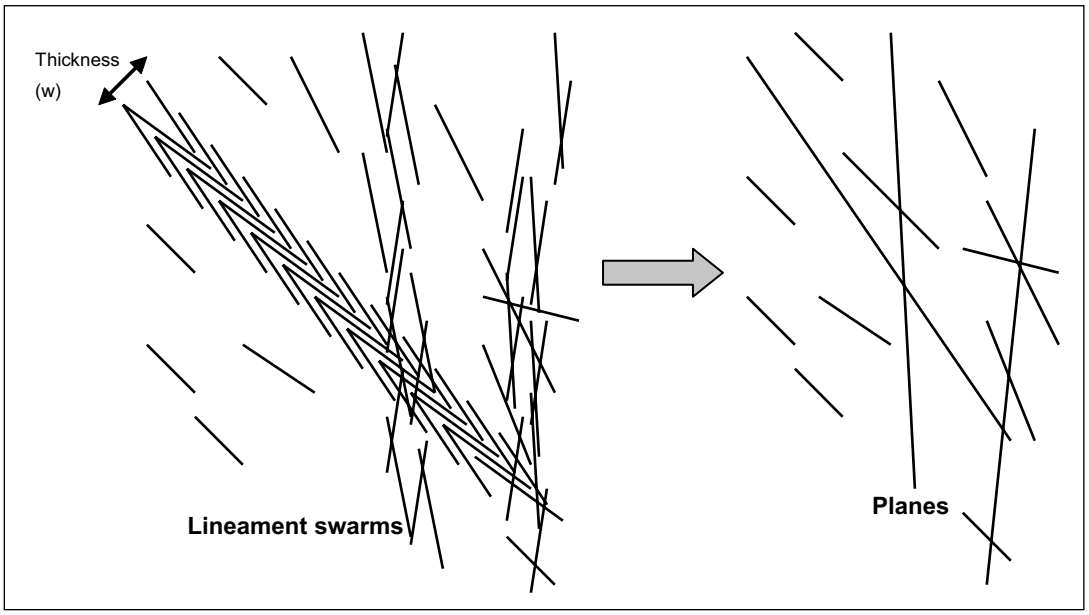

Figure 3-2. *Representation of lineament swarms as stochastic planar features using the power-law distribution.*

PFL flow anomalies are handled consistently with this concept. Also, transport parameters such as kinematic porosity and flow-wetted surface may have to be enhanced in the larger fractures to reflect their zone characteristic.

3.3.3 Fracture intensity and Terzaghi correction

The potential bias arising from observing fractures cutting boreholes of varying trajectory was removed by correcting for the orientation of fractures relative to the trajectory of the borehole in which they were observed /Terzaghi 1965/. The sketch in Figure 3-3 illustrates the issue in an idealised case. Note that the borehole is treated as a line, not as a cylinder, for the Terzaghi correction. For sub-vertical fractures, a vertical borehole will cut fractures at an average separation of s that is much larger than the true separation, t. The ratio of s/t = $1/\cos(\vartheta)$, where ϑ is the angle between the fracture pole and the borehole trajectory. For an inclined borehole near-orthogonal to the fractures, the angle is much smaller and so s/t is close to 1. However, for a horizontal borehole parallel to the fracture strike, s/t would again be large. The implication is that care must be taken when combining fracture statistics e.g. fracture intensities or counts from boreholes of varying orientation. In this illustration, P10 is $1/s$ while $P10_{corr}$ is $1/t$. In reality, each fracture has a different orientation and the borehole trajectory may vary down-hole. Hence, the average orientation of the entire core was used to determine the angle between each fracture pole and the borehole trajectory ϑ, and a correction, $1/\cos(\vartheta)$, was calculated for every fracture. This correction was used as a weighting when calculating statistics such as mean fracture poles, and $P10_{corr}$, and when plotting density contours on stereonets. In addition, the orientation correction was used when calculating the percentage of fractures in each orientation set. Rather than just counting the number of fractures in each set, a weighted percentage was calculated by weighting each fracture by $1/\cos(\vartheta)$ (the maximum weight was arbitrarily set to 7 to avoid excessively large values where ϑ is near to 90°).

An alternative correction factor is proposed by /Darcel et al. 2004/ for the case where the fractures encountered in the borehole are dominated by small ones, the lengths of which are comparable to the borehole diameter. Based on a power-law length model they propose a

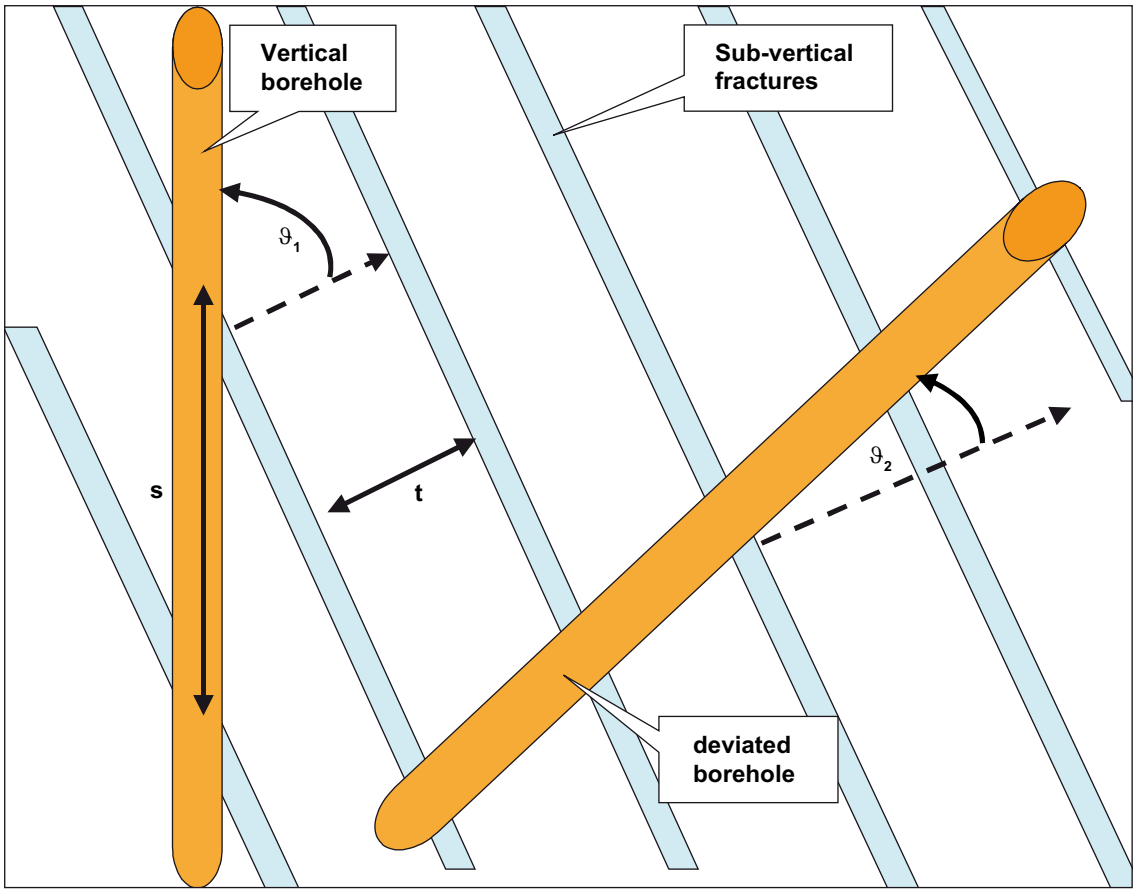

Figure 3-3. *Example of Terzaghi correction for different borehole orientations. The angles* ϑ_1 *and* ϑ_2 *are shown between the fracture pole (dotted arrow) and two different borehole orientations. The Terzaghi correction is proportional to 1/cos(*ϑ*).*

correction factor around $1/(\cos(\vartheta))^3$ for Simpevarp, which emphasises the sub-vertical fractures more, and would perhaps give more consistency when comparing the relative intensity of fracture sets when measured in boreholes against outcrops. However, this approach has not been used in this study.

3.3.4 Fracture transmissivity models

In the Simpevarp version 1.2 modelling, a direct correlation between fracture transmissivity and fracture radius was assumed. In order to illustrate the implications of this assumption, three alternative concepts for fracture transmissivity, T, and its relationship to fracture radius, r, were considered in this study for L1.2 (as shown in Figure 3-4):

- Uncorrelated: Log-normal distribution for T,

  $$T = 10^{\mu + \sigma N'(0,1)}, \quad (2)$$

  where μ is the mean of $\log_{10}(T)$, σ is the standard deviation of $\log_{10}(T)$, and N'(0,1) is a normalised normal distribution, truncated between –2 and +2.
- Correlated: power-law relation between T and r,

  $$T = a \times r^b, \quad (3)$$

  where a and b are the factor and exponent respectively describing the power-law relation.

- Semi-correlated: Random lognormal distribution about a mean that is based on a correlation,

$$T = 10^{\log\left(a \times r^{b}\right) + \sigma\, N'(0,1)}, \quad (4)$$

where a and b are the factor and exponent respectively of the deterministic part of the relation between r and T, σ is the standard deviation of $\log_{10}(T)$, and N'(0,1) is a normalised normal distribution, truncated between –2 and +2.

Each of these concepts has an associated set of parameters, and it is the objective of the Hydro-DFN to explore what ranges of parameters are required in the DFN simulations to give a match to the hydrogeological data. Note that the correlated case and the semi-correlated case are considered independently of each other and so the values of the parameters a and b will not necessarily be the same for these two cases.

The correlated relationship was proposed in /Dershowitz et al. 2003/ One argument for it is that, at least for deformation zones, the zone width often increases with length, and thus generally the number of individual conductive fractures associated with zone. If the transmissivity distribution for individual fracture is the same, then based on the above assumption it follows that the effective transmissivity for the fracture zone should increase with the length of the fracture zone.

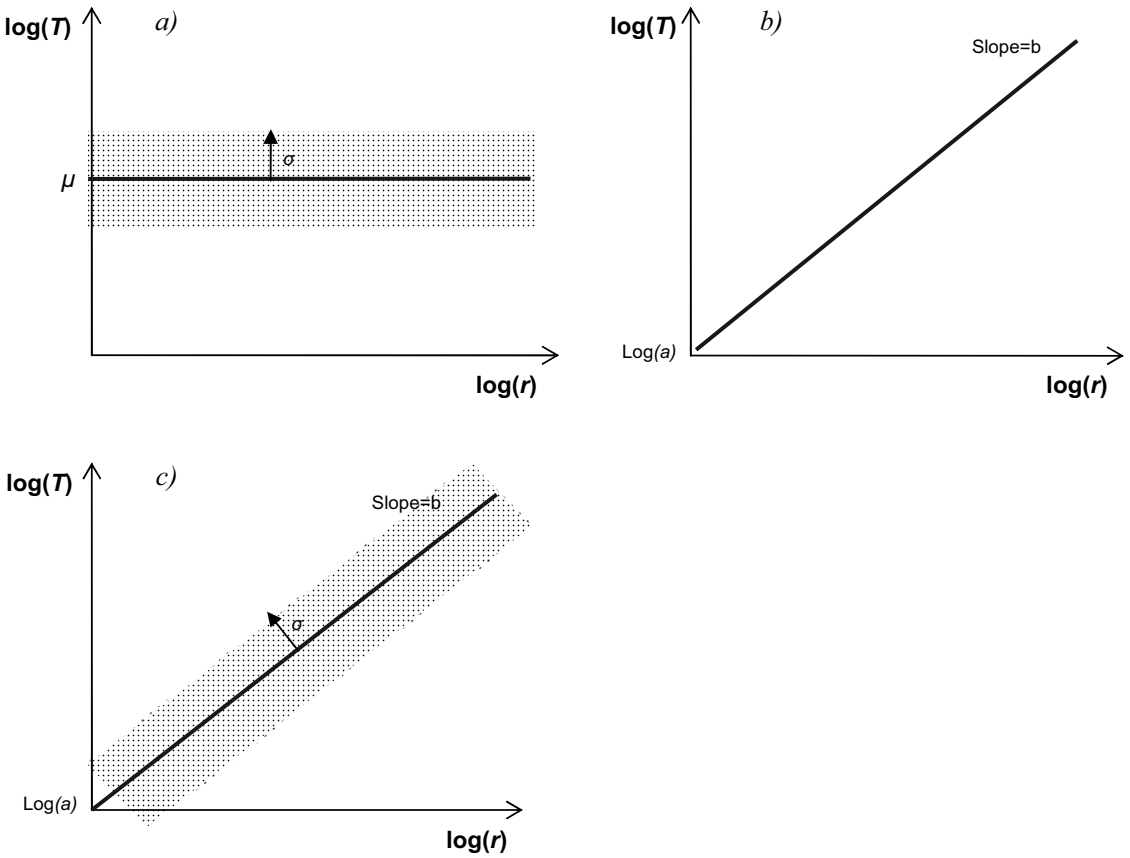

Figure 3-4. *Schematic of transmissivity models: a) Uncorrelated, b) correlated, and c) semi-correlated. Note that for the Hydro-DFN models, the values of the parameters a and b used for the semi-correlated case are not necessarily the same as those used for the correlated case.*

3.3.5 Fracture aperture models and kinematic porosity

The kinematic porosity, n_e, was derived based on fracture transport apertures as described in Section 2.3. It is required as part of the block properties as these are needed in the regional GWF modelling. There is no new data such as tracer test to try to interpret and so the model for the porosity of an individual fracture will be based on Äspö Task Force 6c results /Dershowitz et al. 2003/. This approximates a direct correlation between the transport aperture e_t, and the transmissivity, such that:

$$e_t = a \times T^b \,. \tag{5}$$

The values suggested from Äspö Task Force 6c are $a = 0.46$, $b = 0.5$. For a given block-scale, fracture kinematic porosity, n_e, is calculated as the sum of fracture area multiplied by transport aperture, e_t, over fractures in the block divided by the block volume.

3.4 Analysis of geological data and Geo-DFN model

The Geo-DFN model, described in detail in /Hermansson et al. 2005/, was used as the guide for the orientation of each fracture set, fracture size distribution, and fracture intensity. /Hermansson et al. 2005/ provide overall P32 values for 'all' and 'open' fractures for each rock domain, classified into five different fracture sets for each subarea. For the boreholes considered during the development of the Geo-DFN, this classification was used to assign each fracture to a fracture set.

The fracture set classification was defined by /Hermansson et al. 2005/ following an analysis of outcrop data for each subarea (See Section 3.9 for examples of the set classification on two of the outcrops). /Hermansson et al. 2005/ classify each set as either regional or local in nature, i.e. whether they have an association to regional structures or have a more restricted localised expresssion. The regional sets, Set_A, Set_B and Set_C, consist of sub-vertical fractures, follow a power-law scaling relationship between outcrop scale and lineament-scale, and are observed in both Laxemar and Simpevarp subareas. The local sets, Set_e and Set_f, are observed in outcrops as weakly defined and diffuse sets and are each confined to a single subarea. A local sub-horizontal set is defined as Set_d in both subareas, although the set properties are not the same for both subareas. Section 3.9 demonstrates that the set classification does seem to define distinct and consistent orientation sets in each outcrop, but that the relative distribution varies considereable between the outcrops, perhaps because of the limited size of outcrops mapped, only about 20 m across. Set_A and Set-C are most prevalent in the RVS deformation zones model in the Laxemar subarea, while the boreholes suggest very similar relative fracture intensities for the sub-vertical sets in Rock domain A.

When generating fractures stochastically in the Hydro-DFN, we sample orientations from the statistical models as given in the Geo-DFN. However, for some analytical steps, and in particular for assigning a fracture set to the measured PFL-anomalies and flow model output, it is necessary to be able to determine which set a fracture belongs to given it's trend and plunge (or dip and azimuth). To do this an approximated fracture set division was produced to match the Geo-DFN fracture set classification. The stereonet program used (DIPS) only allows division of the stereonet into segments or circles. As a result, an approximation of the Geo-DFN fracture set classification was required to allow each measured PFL-anomaly, and each fracture resulting from the flow model, to be assigned to one particular set.

As an illustration of the Geo-DFN fracture set classification and the approximated classification, stereonet plots of the orientation of fractures recorded in the core-log for boreholes KLX04 and KSH01A are illustrated in Figure 3-5 and Figure 3-6 respectively. In these figures, the Geo-DFN fracture set classification is indicated by the coloured symbols used for each fracture, and the approximated classification is superimposed as a grid of segments. (Note that two or three segments or circles for each fracture set were needed in DIPS to produce the closest approximation to the Geo-DFN fracture set classification). The approximated classification illustrated in Figure 3-5 is used for Laxemar subarea and the approximated classification illustrated in Figure 3-6 is used for Simpevarp subarea.

The trend and plunge limits for the approximated classifications illustrated in Figure 3-5 and Figure 3-6 are summarised in Table 3-1 and Table 3-2 respectively. These hard sector divisions are used for assigning measured PFL-anomalies, and fracture flow model output to a particular fracture set; they are not used to provide parameters for fracture generation in the models.

The locations of the cored boreholes, KLX03, KLX04, KSH01A and KAV04, for which Hydro-DFN models were developed are shown in Figure 3-7 along with rock domains and the outcrops ASM000208 and ASM000209.

Table 3-1. Hydro-DFN classification of the fractures sets for Laxemar subarea. Fracture sets are reported as the trend and plunge of the fracture pole. This hard-sector approximation of the Geo-DFN classification is required to classify each PFL-anomaly and flow model output using the DIPS software.

Set	Strike description	Trend (°)	Plunge (°)
Set_A (regional set)	ENE-WSW	308–005	0–35
		130–185	0–50
Set_B (regional set)	N-S	065–130	0–50
		260–308	0–35
Set_C (regional set)	NW-SE	005–065	0–35
		185–230	0–35
Set_d (sub horizontal)	Horizontal	065–185	50–90
		185–280	60–90
		280–065	35–90
Set_f (local set)	NW-SE	230–260	0–35
		185–280	35–60

Table 3-2. Hydro-DFN classification of the fractures into sets for Simpevarp subarea. Fracture sets are reported as the trend and plunge of the fracture pole. This hard-sector approximation of the Geo-DFN classification is required to classify each PFL-anomaly and flow model output using the DIPS software.

Set	Strike description	Trend (°)	Plunge (°)
Set_A (regional set)	ENE-WSW	130–170	0–40
		305–000	0–45
Set_B (regional set)	NNE-SSW	095–130	0–40
		225–305	0–20
		245–305	20–40
Set_C (regional set)	WNW-ESE	170–235	0–20
		170–245	20–40
		000–040	0–45
Set_d (sub horizontal)	Horizontal	095–170	40–90
		170–095	45–90
Set_e (local set)	NNW-SSE	235–255	0–20
		040–095	0–45

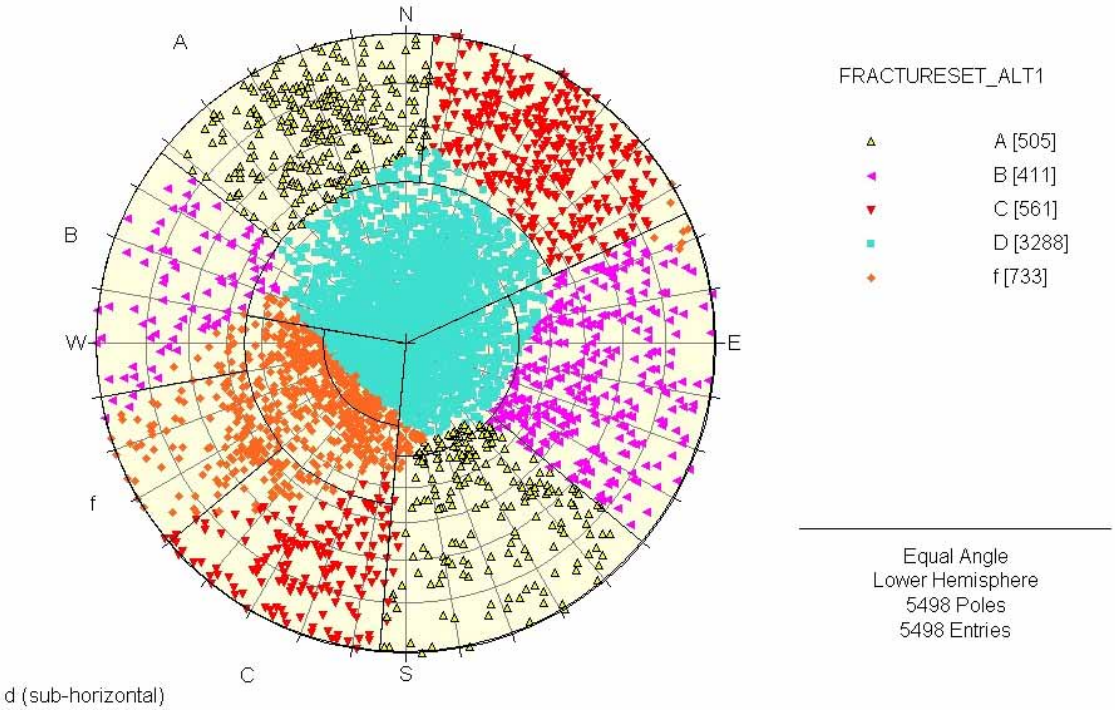

Figure 3-5. *Geo-DFN classification of each fracture set for Laxemar subarea (KLX04) is shown by the coloured symbols. For the purposes of the Hydro-DFN (e.g. assigning PFL flow anomalies into each fracture set) an approximated grid of segments, drawn in black, has been superimposed.*

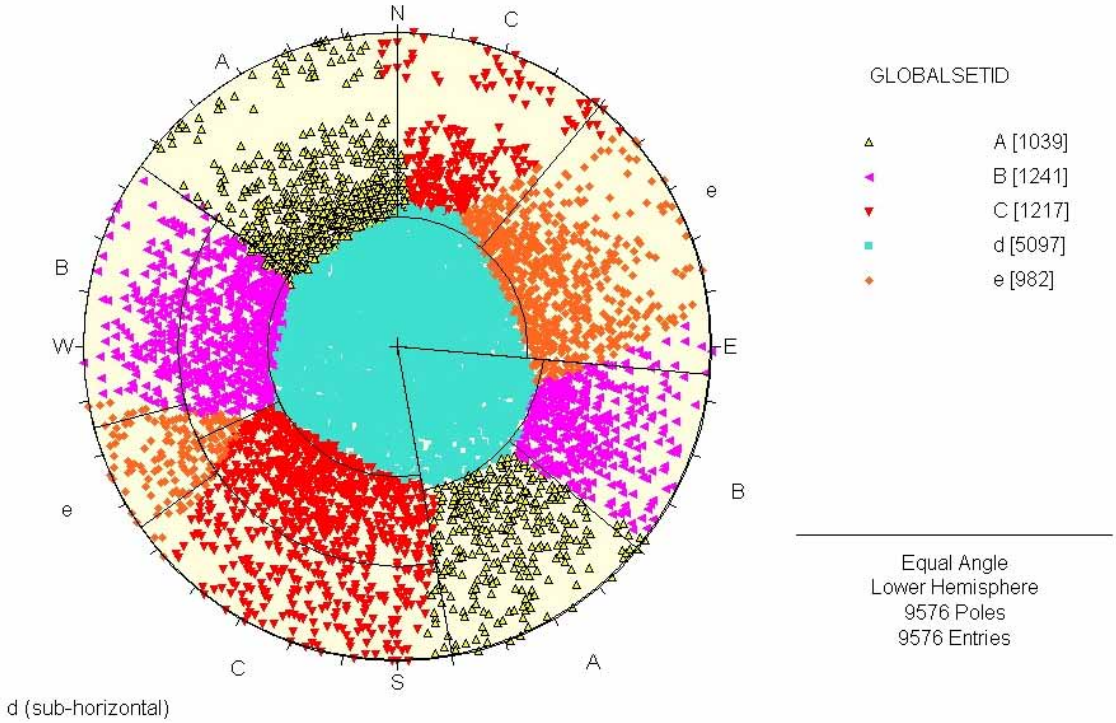

Figure 3-6. *Geo-DFN classification of each fracture set for Simpevarp subarea (KSH01A) is shown by the coloured symbols. For the purposes of the Hydro-DFN (e.g. assigning PFL flow anomalies into each fracture set) an approximated grid of segments, drawn in black, has been superimposed.*

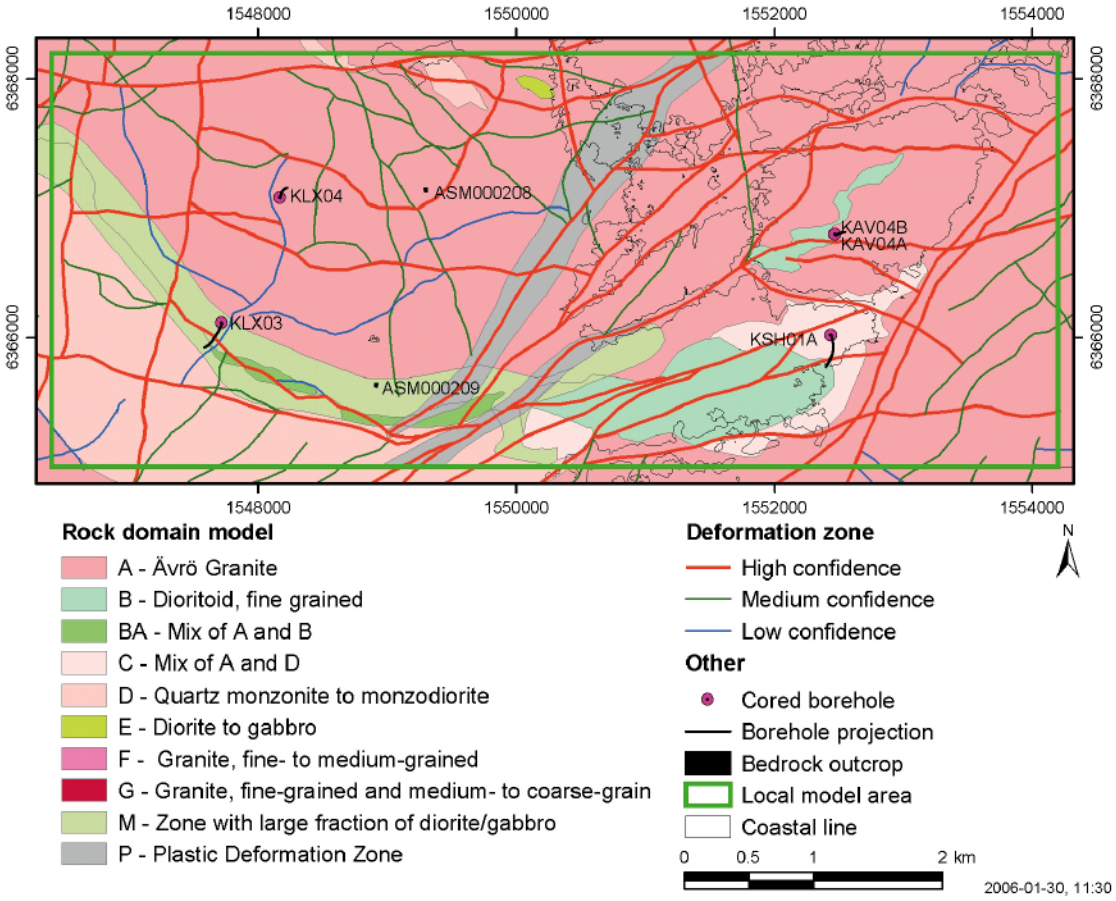

Figure 3-7. *Geology of the local model showing the locations of the evaluated boreholes: KLX03, KLX04, KSH01A and KAV04A/B and the outcrop areas.*

3.4.1 Fracture size distribution

In the April 2005 delivery of the Geo-DFN, it was reported that within the Laxemar subarea, it was difficult to find one set of parameters (r_0, k_r) for fracture size distribution that would constitute a self-consistent model of fracture size for outcrop, borehole and trace length data over all scales. Instead, they reported a range of k_r and r_0 values for each fracture set. Initial modelling of the Hydro-DFN incorporated this uncertainty by maintaining two cases at either extreme of the fracture-size distribution. Hence, the set of parameter values consisting of the lower limits of the k_r ranges for each fracture set, with corresponding r_0 values were referred to as 'Geo-DFN min'. Similarly, the set of parameter values consisting of the upper limits of the k_r ranges for each fracture set, with corresponding r_0 values, were referred to as 'Geo-DFN max'. For the Simpevarp subarea, it was more straightforward since a single set of parameters (r_0, k_r) that match borehole, outcrop and deformation zone intensity, though not outcrop trace length, for each set were provided in the Geo-DFN. These were referred to as the 'Geo-DFN match' case. The parameters defined for the power-law distributions of fracture radius for the Laxemar and Simpevarp subareas are detailed in Table 3-3 and Table 3-4. It should be noted that differences in k_r as small as 0.2–0.3 can have significant impact on flow in a DFN, especially around a k_r of 3. For $k_r > 3$, one expects the hydraulic properties to be controlled by the smallest fractures in the system, while for $k_r < 3$ one expects the hydraulic properties to be controlled also by larges fractures /De Dreuzy et al. 2001/.

Table 3-3. Power-law parameters for fracture size distribution for two bounding cases for Rock domain A in the Laxemar subarea in the April 2005 delivery of the Geo-DFN.

Set	Geo-DFN min		Geo-DFN max	
	k_r	r_0	k_r	r_0
Set_A	2.73	0.02	2.93	0.12
Set_B	2.96	1.69	3.12	3.66
Set_C	2.92	1.02	3.20	4.44
Set_d	2.90	0.21	2.90	0.21
Set_f	3.60	0.40	3.60	0.40

Table 3-4. Power-law parameters for fracture size distribution for Rock domain B in the Simpevarp subarea in the April 2005 delivery of the Geo-DFN.

Set	k_r match	r_0 match
Set_A	3.22	0.40
Set_B	3.01	0.29
Set_C	3.02	0.31
Set_d	3.10	0.15
Set_e	3.27	0.21

A notable characteristic of these parameters is the high values of the slope, k_r, compared to S1.2 where values around 2.7 to 2.9 were derived. In addition, some rather high values of r_0 are implied for Set_B and Set_C. These parameters created significant problems in trying to integrate the hydraulic data with the Geo-DFN. Firstly, the small r_0 values for Set_A gave few large sub-vertical fractures in this set despite it being the dominant set in the local-scale deformation zone model. Conversely, the high r_0 for Set_B and Set_C seemed unrealistic given the minimum measured outcrop fracture trace length was 0.5 m. In addition, the April 2005 Geo-DFN for the Laxemar subarea specified an exponential distribution as the preferred model for fracture size for the sub-horizontal set (Set_d). However, this description would provide no fractures larger than 10 m, which is inconsistent with the RVS L1.2 deformation zone model, which includes a gently dipping zone (ZSMNW928A) transecting KLX04, and with the observation that most flowing features are observed to have a sub-horizontal orientation (compare with Figure 3-8). Therefore, it was decided to use a power-law distribution for Set_d for Laxemar subarea.

Given these problems, the derivation of the fracture size distribution was re-analysed within the Hydro-DFN study. The methodology used was to import the 3D local-scale RVS deformation zone model into a DFN model and calculate the P32 for each fracture set, and then the match the power-law size distribution to both this fracture intensity and the fracture intensity observed in an appropriate borehole as provided in the Geo-DFN. A P32 for the deformation zone model was calculated separately for the Laxemar and Simpevarp subareas since the Geo-DFN specifies different fracture set classifications in each subarea. Although this approach is consistent with the Geo-DFN, the relative fracture intensites of the sub-vertical sets for the deformation zone model as reported in the April 2005 Geo-DFN could not be reproduced.

Table 3-5 compares the P32 calculated here for the local-scale RVS deformation zone model against that given in the April 2005 Geo-DFN. Using the L1.2 deformation zone model, P32 is given for the Laxemar and Simpevarp subareas separately as well as for the combined area. Although the total P32 are consistent, the distribution between the

Table 3-5. Fracture intensity, P32, calculated for the local-scale RVS deformation model calculated for the L1.2 model and as given in the Geo-DFN as of April 2005.

Set	L1.2 DZ: P32 (m^2/m^3)	April 2005 Geo-DFN DZ P32 (m^2/m^3)	L1.2 DZ (Laxemar): P32 (m^2/m^3)	L1.2 DZ (Simpevarp): P32 (m^2/m^3)
Set_A	$2.60\ 10^{-3}$	$6.00\ 10^{-4}$	$1.98\ 10^{-3}$	$2.76\ 10^{-3}$
Set_B	$9.33\ 10^{-4}$	$2.15\ 10^{-3}$	$9.91\ 10^{-4}$	$9.79\ 10^{-4}$
Set_C	$1.26\ 10^{-3}$	$1.98\ 10^{-3}$	$2.01\ 10^{-3}$	$9.62\ 10^{-3}$
Total	$4.80\ 10^{-3}$	$4.73\ 10^{-3}$	$4.98\ 10^{-3}$	$4.71\ 10^{-3}$

sets is very different. For example, we found that Set_A has the highest fracture intensity ($2.6\ 10^{-3}$ m^2/m^3), but the April 2005 Geo-DFN identifies this as a very minor set. The cause was traced to problems in implementing the deformation zone analysis in the April 2005 Geo-DFN, which led to the difficulties in matching a power-law distribution within the April 2005 Geo-DFN.

In this study, we fixed r_0 as 0.28 m (since this is equivalent to the 0.5 m minimum trace length measured on the outcrop) and calculated k_r values to match the borehole fracture intensity to the deformation zones. That is, the local-scale deformation zone model was imported into a DFN model and the fracture intensity per unit volume (P32) was calculated for each of the regional fracture sets (Set_A, Set_B and Set_C), considering Laxemar and Simpevarp subareas separately. Then a value of k_r was fitted (assuming a fixed r_0 of 0.28 m) to give a power-law model that had total fracture intensity equal to the borehole P32 (based on open and partly-open fractures only) and a P32 for the truncated range r = 564–5,641 m equal to the P32 calculated for the deformation zone model. This assumes that all defomation zones are open or partly-open. This procedure was followed for each of the three vertical sets since these are the ones represented in the RVS deformation zone model. There are one or two sub-horizontal deformation zones, but these are probably largely under-represented due to their uncertain surface expression. Hence, for Set_d, k_r was set to the average value for the sub-vertical sets (see below). The power-law parameters for the local sub-vertical sets Set_e (Simpevarp subarea) and Set_f (Laxemar subarea) were maintained at the values given in the April 2005 Geo-DFN since these were not subject to the errors in analysing the RVS deformation zone model. Table 3-6 gives the power-law slope values derived for the three vertical sets for Rock domain A in the Laxemar subarea and for Rock domain B in the Simpevarp subarea. The derived k_r values are significantly lower than those given in the April 2005 Geo-DFN and in line with those used in S1.2.

In the procedure described above, the borehole fracture intensity for Laxemar was taken from KLX04, and that for Simpevarp was taken from KSH01A. The same approach was used to obtain values for the combined Rock domain M(A), M(D) and D in the Laxemar subarea using the borehole fracture intensity from KLX03 and for Rock Domain A at Simpevarp using KAV04A.

Although for pragmatic reasons we had to derive our own size distributions in the absence of an updated Geo-DFN, it is interesting to compare those derived with the final Geo-DFN /Hermansson et al. 2005/ as given in Table 3-7. A single set of parameters is given in the final Geo-DFN since a consistent match to borehole, outcrop and deformation zones was possible. It can be seen that the power-law slopes have been revised downwards and the r_0 values are similar, though generally a little higher with the 0.28 m we assumed, and hence a radius limit around 0.3–0.4 m may be physical character of the fractures in the field. The differences are due to the choice to match the borehole P32 for only open and partly open fractures in our work compared to all fractures (open and sealed) in the final Geo-DFN, and the extra constraint in the Geo-DFN of varying r_0 to match the outcrop.

Table 3-6. Power-law slopes k_r derived in the Hydro-DFN for Rock domain A in the Laxemar subarea (based on KLX04) and Rock domain B in the Simpevarp subarea (based on KSH01A).

Set	Laxemar RD A (KLX04)		Simpevarp RD B (KSH01A)	
	k_r	r_0 (m)	k_r	r_0 (m)
Set_A	2.73	0.28	2.77	0.28
Set_B	2.83	0.28	2.91	0.28
Set_C	2.73	0.28	2.92	0.28

Table 3-7. Power-law slopes k_r derived in the final Geo-DFN for Rock domain A in the Laxemar subarea (based on KLX04) and Rock domain B in the Simpevarp subarea (based on KSH01A). Data from /Hermansson et al. 2005/.

Set	Laxemar RD A (KLX04)		Simpevarp RD B (KSH01A)	
	k_r	r_0 (m)	k_r	r_0 (m)
Set_A	2.85	0.33	2.93	0.37
Set_B	3.04	0.98	2.84	0.40
Set_C	3.01	0.86	2.88	0.37

3.5 Analysis of hydrogeological data

To help interpret the flow data measured by the Posiva Flow Log (PFL), borehole fractures that correspond to the depths at which flow anomalies have been identified in the PFL tests have been identified by /Forssman et al. 2005ab/. The methodology followed by Forsmann and co-authors when assigning a fracture orientation to each flow anomaly is described below.

For each anomaly, the fracture (or fractures) most ‘consistent’ with the anomaly is (are) selected. If there is more than one equally consistent fracture associated with an anomaly, then the orientations of each of the fractures are used. Generally, there are only one or two consistent fractures, but sometimes there are 3–5 equally consistent fractures. The assumptions made by Forsmann and co-authors when correlating the Boremap data to the PFL-anomalies were:

- As a first assumption, the open and partly-open fractures as well as crush zones are assumed to be possible flowing features. This is an important assumption on which all subsequent analysis relies. Alternative possibilities, which were not considered in this work, include the suggestion that sealed fractures could contain flow. For instance, fractures that are considered sealed when viewed from the Boremap data within the diameter of the borehole may have a conductive (flowing) section further away from the borehole.
- It is assumed that the precision of the position (L) in the borehole of the PFL-anomaly is not on the 1 dm level. If an open, partly-open fracture or crush zone is within ± 0.5 m of a PFL-anomaly it is assumed that it can correspond to the PFL-anomaly (in a few cases larger differences have been accepted). The nearest distance in dm from the fractures trace (a sinus-shape line) on the borehole wall to depth L is judged and documented in the database (PFL-anom. Confidence) and the actual deviation (Deviation fr. L (+downwards, 1 dm)) of the open, partly-open fractures or crush zones from L, defined positive if the fracture is located below (higher value) L.

- A few **sealed fractures** were indicated as possible flowing features if the core has been broken AND adjusted secup (Boremap) ≈ *L* (Borehole length) for the PFL-anomaly AND that no open fracture was < 0.6 m from *L* OR that the nearest open fracture is positioned closer than 0.6 m but matches another anomaly very well. When interpreting these broken/sealed fractures, only the ones located ± 0.1 m from the anomaly have been mapped. These are fractures considered to be very uncertain and may be excluded from the analysis. "PFL-Confidence" is set to zero (0) in the database for these cases.
- Occasionally, several **open fractures** are within ± 0.1–0.2 m of *L* for the PFL-anomaly and it is judged that one or all of them may be flowing features. If "FRACT_INTERPRET" is used in the database, the "Certain, Probable, Possible" entries can be used to decide whether one is more likely to be the flowing feature. In a few cases, the mapped open fractures are so close (< 1 cm) that possibly one could consider them as one fracture. In some cases where open fractures have been identified within ± 0.1–0.2 m of *L*, there may be more open fractures at a distance ± 0.2–0.5 m that are not included in the database as possible flowing features.
- In a few cases several PFL-anomalies may be connected to a single geological feature, generally a crush zone but sometimes also an open fracture.
- Some open, possibly flowing, fractures have very high amplitudes, stretching over up to several meters of the borehole wall. These fractures can, because of their shape, have an influence on the flow conditions quite a long distance from the level indicated by the fractures "secup"-value. When evaluating the data, these fractures are given a lower "PFL-confidence" than suggested only by the distance between the fractures secup and the level of the PFL-anomaly. If the fracture cuts the level of the PFL-anomaly, the PFL-confidence is set to one (1, which is the highest confidence), independent of how long the distance between the secup value and the level of the anomaly is. In consequence, some fractures with high amplitudes that almost (± 0.2 m) cut the PFL-anomaly level are also included in the analysis. The PFL-confidence has been set to 2 in these cases.

In this study, the flowing features in each borehole have been examined for the magnitude of transmissive features, and the fractures associated with each flowing feature have been assigned to a fracture set and plotted against elevation. In addition, the flow anomaly orientations corresponding to all identified fractures have been plotted on a stereonet and coloured according to the magnitude of the transmissivity associated with the anomaly. The PSS data has also been plotted where available. An example of this analysis is given in Subsection 3.5.1 for KLX04 since this borehole has a complete set of hydrogeological data (both PFL-f and PSS data are available). The equivalent analyses for KLX02, KLX03, KAV01, KAV04A, KSH01A and KSH02 are presented in Appendix A. A summary of the hydraulic data for all cored boreholes is given in Subsection 3.5.2.

3.5.1 KLX04, Orientation and transmissivity of PFL-anomalies

The orientations of features located closest to each PFL-anomaly have been plotted for KLX04 (Figure 3-8 to Figure 3-10). All features within 0.5 m of each PFL-anomaly are shown, including sealed fractures and fractures associated with deformation zones. Where there is more than one feature associated with an anomaly, the orientation of each feature has been plotted separately. The data points are coloured by the measured transmissivity. In these plots, the simplified fracture set classification described in Section 3.4 is superimposed. These figures indicate that the dominating conductive fractures are sub-horizontal or steeply dipping features with strike to the NW. However, sub-horizontal features are over-represented in these plots due to the higher likelihood of these fractures intersecting the borehole. The transmissivity of each flowing feature has been plotted against elevation for the PFL-anomalies (Figure 3-11), and for the PSS data (Figure 3-12). Flow is noted

throughout the borehole, with the most transmissive flows observed in the sub-horizontal set (Set_d) and Set_C (sub-vertical). Flow is greatest at shallow elevations (< 350 m). The PSS data shows flow at most elevations, which is consistent with the PFL-f data.

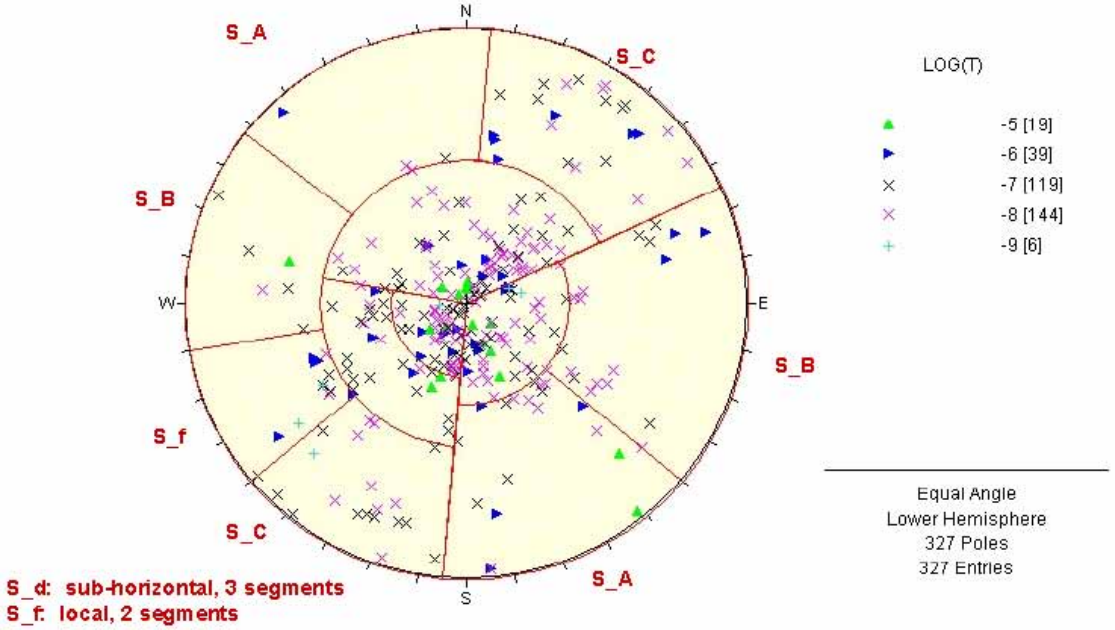

Figure 3-8. *Orientations of the pole to fractures associated with PFL-anomalies in KLX04, for all fractures (including DZ's). Fractures are coloured by magnitude of the transmissivity of the PFL-anomaly. The set divisions and the names of each set are superimposed in red.*

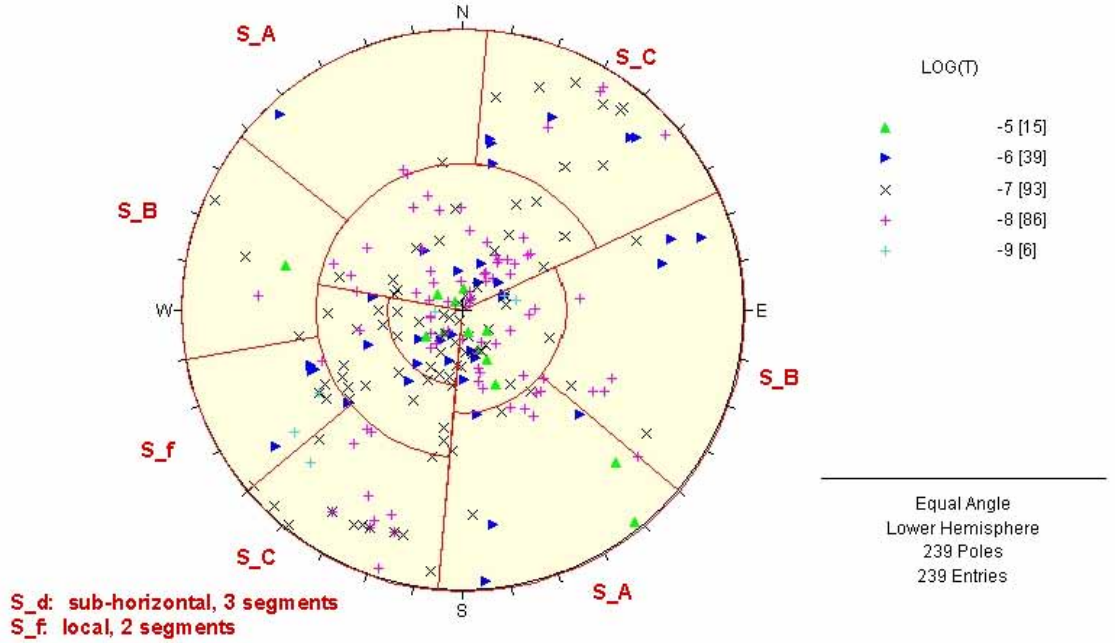

Figure 3-9. *Orientations of the pole to fractures associated with PFL-anomalies in KLX04, for all fractures (excluding DZ's). Fractures are coloured by magnitude of the transmissivity of the PFL-anomaly. The set divisions and the names of each set are superimposed in red.*

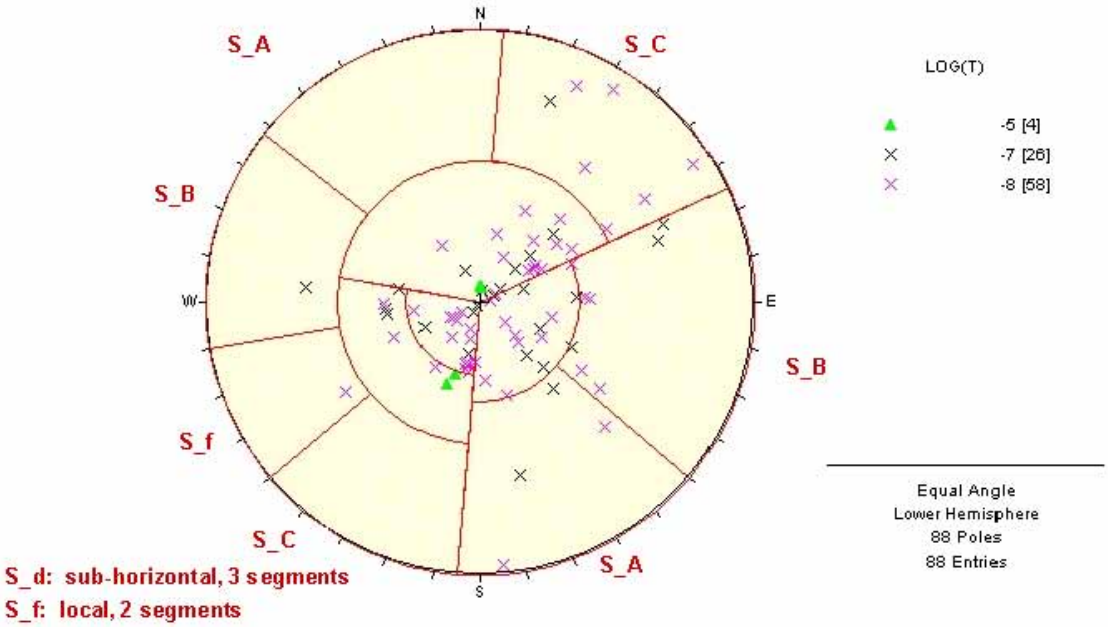

Figure 3-10. *Orientations of the pole to fractures associated with PFL-anomalies in KLX04, for deformation zones (DZ1 to DZ6). Fractures are coloured by magnitude of the transmissivity of the PFL-anomaly. The set divisions and the names of each set are superimposed in red.*

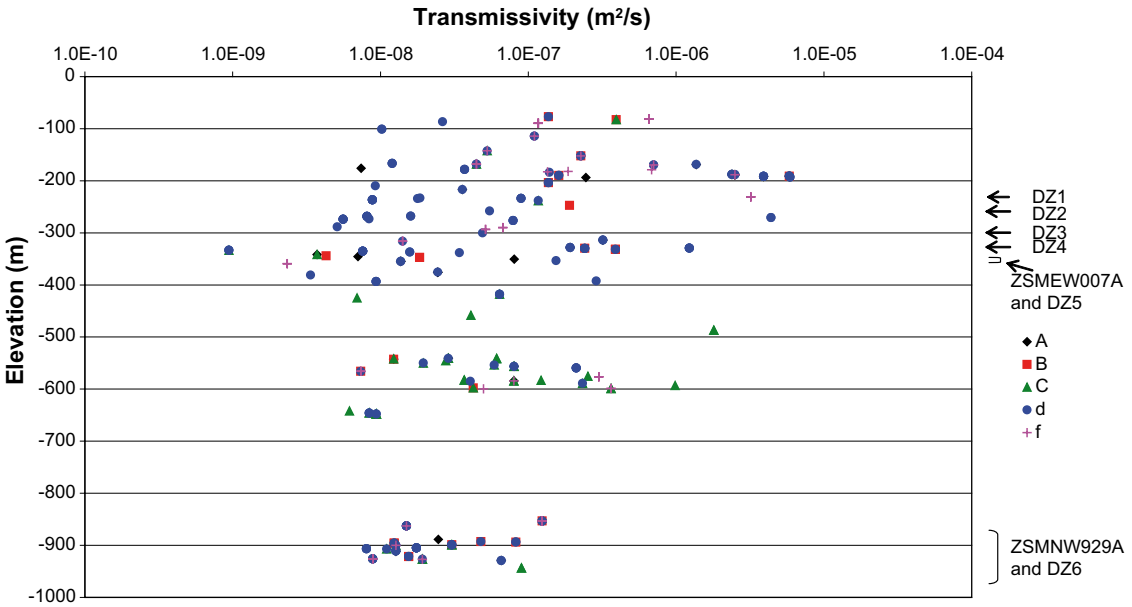

Figure 3-11. *Transmissivity of PFL-anomalies against elevation for KLX04. Each PFL-anomaly is coloured by fracture set. The colouring depends on the orientation of the closest fracture(s). Hence, one PFL-anomaly may have more than one associated orientation if there are several close fractures.*

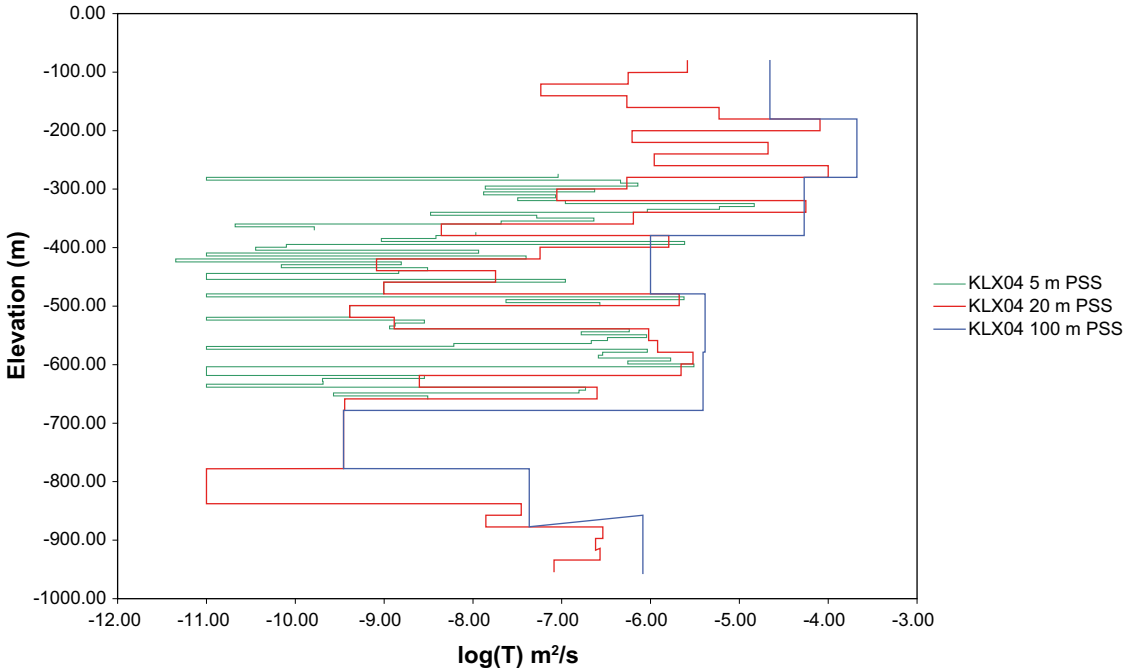

Figure 3-12. *Transmissivity of 5 m, 20 m and 100 m borehole intervals with measurable flow recorded by PSS in KLX04.*

3.5.2 Summary of hydrogeological data

The Laxemar subarea shows highest flows at depths shallower than about –300 m elevation, with the most transmissive features oriented sub-horizontally (Set_d) or with a NW strike (Set_C) for KLX03 and KLX04. However, KLX02 shows the most transmissive flows with sub-vertical NS strike (Set_B) at shallow depths (< –300 m), and deeper flows generally sub-horizontal (Set_d). This corresponds well with the dominance of steeply dipping conductive features with strike to the NW seen at the Äspö HRL /SKB 2005/, but the Äspö HRL has a larger contrast between the different fracture sets. However, the sub-horizontal fracture set at Äspö is much less permeable (perhaps a factor 1/100) than the sub-vertical fracture set, as shown by /Rhén et al. 1997, Rhén and Forsmark 2001/.

The Simpevarp subarea shows that the most transmissive flows are sub-horizontal (Set_d) or orientated with strike to the SE (Set_C or Set_e). Flow is observed at all depths, possibly with greater flow at shallower depths in some boreholes. Overall, the Simpevarp subarea provides lower transmissivity flows than Laxemar subarea.

Because the boreholes are vertical, there is a natural bias toward intersecting more sub-horizontal fractures and their associated flow, while flow in sub-vertical fractures is under-sampled. Clearly, inclined boreholes would assist in establishing the true extent of this bias, but in the meantime it is possible to quantify how sensitive flow is to different assumptions about the hydraulics of the sub-vertical fracture sets by performing sensitivity studies as is reported in Subsection 3.8.2.

Brief summaries of the hydraulic data in the boreholes and how these vary between the different boreholes are given for the PFL-anomalies in Table 3-8 to Table 3-11. The numbers of PFL-anomalies given in these tables are based on the raw data. Later, as described in Section 3.8, PFL-anomalies that are associated with the same deformation zone are amalgamated and counted as one anomaly to be consistent with the concept described in

Subsection 3.3.2, but at this stage, total numbers of PFL-anomalies are given. The total transmissivities are calculated by summing all *T* values over the entire borehole length. The mean hydraulic conductivity, *K*, is obtained by dividing the total T by the borehole length.

For Table 3-8 and Table 3-9 a depth division was made at –335 m elevation based on KLX04 where there seems to be a distinct change in the frequency of high flows. However, this varies from about –200 m to –350 m elevation between boreholes.

The equivalent summaries for the PSS flows are given in Table 3-12 for all intervals and in Table 3-13 for intervals that do not traverse RVS deformation zones. Here, it is not known how many flow fractures there are within a packer interval. However, the minimum packer interval length is generally 5 m, so for flow to occur in a 5 m interval there must be at least one flowing fracture. Hence, it is assumed that for each 5 m interval with flow there is one fracture, for each 20 m interval there are 4 fractures and so on.

In Table 3-8, Table 3-9, Table 3-11 and Table 3-13 the transmissivity and section lengths associated with the RVS DZ model are excluded

Table 3-8. Summary of PFL-anomalies above an elevation of –335 m for Laxemar subarea. Borehole sections that traverse deterministic RVS DZs are excluded.

Subarea	Borehole	No of PFL-anomalies	Borehole length (m)	$P10_{PFL}$ (m^{-1})	Total T ($m^2\ s^{-1}$)	Mean K ($m\ s^{-1}$)
Laxemar	KLX02	37	122	0.30	$2.5\ 10^{-5}$	$2.0\ 10^{-7}$
subarea	KLX03	25	217	0.12	$1.5\ 10^{-5}$	$6.9\ 10^{-8}$
	KLX04	60	251	0.24	$5.4\ 10^{-5}$	$2.2\ 10^{-7}$

Table 3-9. Summary of PFL-anomalies below an elevation of –335 m for Laxemar subarea. Sections of the boreholes that traverse deterministic RVS DZs are not included.

Subarea	Borehole	No of PFL-anomalies	Borehole length (m)	$P10_{PFL}$ (m^{-1})	Total T ($m^2\ s^{-1}$)	Mean K ($m\ s^{-1}$)
Laxemar	KLX02	37	854	0.04	$1.8\ 10^{-6}$	$2.1\ 10^{-9}$
subarea	KLX03	30	644	0.05	$6.3\ 10^{-6}$	$9.7\ 10^{-9}$
	KLX04	46	537	0.09	$7.1\ 10^{-6}$	$1.3\ 10^{-8}$

Table 3-10. Summary of PFL-anomalies. $P10_{PFL}$ is the number of flowing PFL-anomalies per unit length of borehole.

Subarea	Borehole	No of PFL-anomalies	Borehole length (m)	$P10_{PFL}$ (m^{-1})	Total T ($m^2\ s^{-1}$)	Mean K ($m\ s^{-1}$)
Laxemar	KLX02	102	1,144	0.09	$2.8\ 10^{-5}$	$2.4\ 10^{-8}$
subarea	KLX03	55	860	0.06	$2.1\ 10^{-5}$	$2.5\ 10^{-8}$
	KLX04	129	872	0.15	$6.5\ 10^{-5}$	$7.4\ 10^{-8}$
Simpevarp	KSH01A	82	624	0.13	$5.0\ 10^{-6}$	$8.0\ 10^{-9}$
subarea	KSH02	82	912	0.09	$7.0\ 10^{-6}$	$7.7\ 10^{-9}$
	KAV01	181	581	0.31	$3.3\ 10^{-5}$	$5.7\ 10^{-8}$
	KAV04A	134	792	0.17	$1.8\ 10^{-5}$	$2.2\ 10^{-8}$
	KAV04B	54	75	0.72	$3.9\ 10^{-5}$	$5.2\ 10^{-7}$

Table 3-11. Summary of PFL-anomalies. $P10_{PFL}$ is the number of flowing PFL-anomalies per unit length of borehole. Borehole sections that traverse deterministic RVS DZs are excluded.

Subarea	Borehole	No of PFL-anomalies	Borehole length (m)	$P10_{PFL}$ (m^{-1})	Total T ($m^2\ s^{-1}$)	Mean K ($m\ s^{-1}$)
Laxemar	KLX02	74	976	0.08	$2.6\ 10^{-5}$	$2.7\ 10^{-8}$
subarea	KLX03	55	860	0.06	$2.1\ 10^{-5}$	$2.5\ 10^{-8}$
	KLX04	106	788	0.13	$6.1\ 10^{-5}$	$7.8\ 10^{-8}$
Simpevarp	KSH01A	68	481	0.14	$4.0\ 10^{-6}$	$8.3\ 10^{-9}$
subarea	KSH02	82	912	0.09	$7.0\ 10^{-6}$	$7.7\ 10^{-9}$
	KAV01	117	416	0.28	$1.3\ 10^{-5}$	$3.1\ 10^{-8}$
	KAV04A	126	742	0.17	$1.6\ 10^{-5}$	$2.2\ 10^{-8}$
	KAV04B	54	75	0.72	$3.9\ 10^{-5}$	$5.2\ 10^{-7}$

Table 3-12. Summary of PSS anomalies for 5 m, 20 m and 100 m intervals. $P10_{PSS}$ is the number of flowing intervals per unit length, assuming one fracture per 5 m interval, four fractures per 20 m interval and twenty fractures per 100 m interval.

Borehole	Interval (m)	No of intervals	No of flowing intervals	No of non-flowing intervals	Borehole length (m)	$P10_{PSS}$ (m^{-1})	Total *T* ($m^2\ s^{-1}$)	Mean K ($m\ s^{-1}$)
KAV01	2	175	175	0	415.9	0.17	$8.2\ 10^{-5}$	$2.0\ 10^{-7}$
KAV01	10	69	69	0	690.0	0.20	$2.5\ 10^{-4}$	$3.6\ 10^{-7}$
KAV01	1,000	1	1	0	686.9	0.20	$3.8\ 10^{-5}$	$5.6\ 10^{-8}$
KAV02	2	41	41	0	81.0	0.20	$9.0\ 10^{-5}$	$1.1\ 10^{-6}$
KLX01	3	197	197	0	585.0	0.20	$9.2\ 10^{-5}$	$1.6\ 10^{-7}$
KLX01	30	20	20	0	599.1	0.20	$9.3\ 10^{-5}$	$1.6\ 10^{-7}$
KLX01	100	3	3	0	377.0	0.16	$4.7\ 10^{-5}$	$1.2\ 10^{-7}$
KLX01	500	1	1	0	377.0	0.20	$1.2\ 10^{-5}$	$3.2\ 10^{-8}$
KLX01	1,000	1	1	0	702.1	0.20	$8.0\ 10^{-5}$	$1.1\ 10^{-7}$
KLX02	5	49	35	14	245.0	0.14	$4.5\ 10^{-5}$	$1.8\ 10^{-7}$
KLX02	20	48	48	0	800.0	0.20	$2.2\ 10^{-4}$	$2.8\ 10^{-7}$
KLX02	100	11	11	0	1,700.5	0.13	$3.0\ 10^{-4}$	$1.8\ 10^{-7}$
KLX02	1,000	1	1	0	1,497.6	0.13	$1.3\ 10^{-4}$	$8.6\ 10^{-8}$
KLX03	100	9	9	0	897.4	0.20	$3.0\ 10^{-5}$	$3.3\ 10^{-8}$
KLX04	5	77	64	13	385.4	0.17	$3.8\ 10^{-5}$	$9.9\ 10^{-8}$
KLX04	20	44	41	3	877.8	0.19	$2.8\ 10^{-4}$	$3.2\ 10^{-7}$
KLX04	100	9	9	0	881.0	0.20	$3.0\ 10^{-4}$	$3.4\ 10^{-7}$
KLX05	100	11	11	0	1,000.2	0.20	$6.9\ 10^{-5}$	$6.9\ 10^{-8}$
KSH01A	5	80	58	22	400.0	0.15	$1.8\ 10^{-6}$	$4.4\ 10^{-9}$
KSH01A	20	45	45	0	896.0	0.20	$1.4\ 10^{-5}$	$1.6\ 10^{-8}$
KSH01A	100	9	9	0	896.0	0.20	$1.2\ 10^{-5}$	$1.4\ 10^{-8}$
KSH01A	1,000	1	1	0	990.9	0.20	$2.8\ 10^{-6}$	$2.8\ 10^{-9}$
KSH02	5	80	80	0	400.0	0.20	$1.3\ 10^{-6}$	$3.2\ 10^{-9}$
KSH02	20	45	45	0	900.0	0.20	$8.3\ 10^{-6}$	$9.2\ 10^{-9}$
KSH02	100	9	9	0	895.5	0.20	$4.4\ 10^{-6}$	$5.0\ 10^{-9}$
KSH02	1,000	1	1	0	921.1	0.20	$2.9\ 10^{-6}$	$3.1\ 10^{-9}$
KSH03A	100	10	7	3	983.2	0.14	$4.0\ 10^{-4}$	$4.1\ 10^{-7}$

Table 3-13. Summary of PSS anomalies for 5 m, 20 m and 100 m intervals. $P10_{PSS}$ is the number of flowing intervals per unit length, assuming one fracture per 5 m interval, four fractures per 20 m interval and twenty fractures per 100 m interval. Sections of the boreholes that traverse deterministic RVS DZs are not included.

Borehole	Interval (m)	No of intervals	No of flowing intervals	No of non-flowing intervals	Borehole length (m)	$P10_{PSS}$ (m^{-1})	Total *T* ($m^2\ s^{-1}$)	Mean K ($m\ s^{-1}$)
KAV01	2	155	155	0	375.9	0.16	4.1E–05	1.1E–07
KAV01	10	48	48	0	480.0	0.20	2.7E–05	5.6E–08
KAV01	1,000	1	1	0	686.9	0.29	3.8E–05	5.6E–08
KAV02	2	41	41	0	81.0	0.20	9.0E–05	1.1E–06
KLX01	3	197	197	0	585.0	0.20	9.2E–05	1.6E–07
KLX01	30	20	20	0	599.1	0.20	9.3E–05	1.6E–07
KLX01	100	3	3	0	377.0	0.16	4.7E–05	1.2E–07
KLX01	500	1	1	0	377.0	0.27	1.2E–05	3.2E–08
KLX01	1,000	1	1	0	702.1	0.28	8.0E–05	1.1E–07
KLX02	5	49	35	14	245.0	0.14	4.5E–05	1.8E–07
KLX02	20	37	37	0	581.0	0.25	2.2E–04	3.8E–07
KLX02	100	11	11	0	1,700.5	0.13	3.0E–04	1.8E–07
KLX02	1,000	1	1	0	1,497.6	0.13	1.3E–04	8.6E–08
KLX03	100	9	9	0	897.4	0.20	3.0E–05	3.3E–08
KLX04	5	75	62	13	375.4	0.17	2.3E–05	6.2E–08
KLX04	20	37	34	3	740.9	0.18	2.3E–04	3.1E–07
KLX04	100	9	9	0	881.0	0.20	3.0E–04	3.4E–07
KLX05	100	11	11	0	1,000.2	0.22	6.9E–05	6.9E–08
KSH01A	5	59	42	17	315.0	0.13	9.6E–08	3.1E–10
KSH01A	20	39	39	0	776.0	0.20	1.3E–05	1.6E–08
KSH01A	100	9	9	0	896.0	0.20	1.2E–05	1.4E–08
KSH01A	1,000	1	1	0	990.9	0.20	2.8E–06	2.8E–09
KSH02	5	80	80	0	400.0	0.20	1.3E–06	3.2E–09
KSH02	20	45	45	0	900.0	0.20	8.3E–06	9.2E–09
KSH02	100	9	9	0	895.5	0.20	4.4E–06	5.0E–09
KSH02	1,000	1	1	0	921.1	0.22	2.9E–06	3.1E–09
KSH03A	100	10	7	3	983.2	0.14	4.0E–04	4.1E–07

3.6 Simulations for assessment of DFN properties

The primary reasons for performing DFN simulations are to:

1. Check that the Hydro-DFN model defines a self-consistent set of fracture intensities (P32), fracture size distributions and fracture set definitions that can be applied in to reproduce the observed P10 of open fractures seen in the boreholes. Also, that the simulated relative intensities between the sets are consistent with the data. The Geo-DFN was used for the fracture set definitions, but, as detailed in Subsection 3.4.1, the fracture intensities and fracture size distributions were adapted to provide a set of self-consistent input parameters.

2. Condition the P32 for open conductive features and the fracture transmissivity parameters against the PFL-f and PSS 5 m interval transmissivity data, where available, using DFN flow simulations.

3. For the PFL-f data, compare both the distribution of transmissivity and flow-rate for flowing features. Check the simulated flux of water (Q) for each fracture set as well as the total simulated flux.

The initial step was to use a DFN model to simulate the fracturing around a borehole and check the modelled open P10 against that in the core-log. To do this, several realisations of the Hydro-DFN model of all open and partly-open fractures in each borehole are generated. The Geo-DFN fracture intensity P32 (m^2/m^3) of the open fractures is used as input to the DFN model. The Geo-DFN fracture intensity provides 'global' fracture intensities for Simpevarp and Laxemar subareas respectively; hence a perfect match to an individual borehole is not expected. Then the simulated frequency of open fractures in the borehole (P10) is checked against the observation. Both the total simulated P10 in the borehole and the proportions of P10 in each fracture set are taken into consideration. In the case that the 'open P32' does not give an accurate estimate of measured P10 for open fractures in the borehole, then P32 can be adjusted to get a better match. This 'fine-tuning' is considered for the overall fracture intensity and for the individual sets where the relative proportion of fractures intercepted by the borehole in each set differs significantly between the model and the measurement. However, in the case of KLX04 and KLX03, fine tuning has not been considered necessary.

The second step, which is to condition the DFN models based on transmissivity distributions from PFL-f and PSS data, is discussed in Section 3.7. The final step, to compare flow-rates from PFL-f data, for both the individual fracture sets and the overall distribution, is described in Section 3.8.

For the Laxemar version 1.2 data freeze, new data was available for KLX03 (PFL-f data) and KLX04 (both PFL-f and PSS) data. Hence, work concentrated on these boreholes for Laxemar subarea. New data was also available for KAV04A/B for the Simpevarp subarea, and the Geo-DFN model was updated for the Simpevarp subarea after the Laxemar 1.2 data freeze. As a result, KAV04A/B was investigated and KSH01A was re-investigated, using the new Geo-DFN model for the Simpevarp subarea.

3.6.1 DFN simulations for KLX04

For the simulations, KLX04 was modelled as vertical with length of 885 m (the length range over which fracture data was collected, elevation of –77 m to –962 m). The fracture sets, orientation and fracture intensities were taken directly from the Geo-DFN, but the fracture-size was re-analysed as described in Subsection 3.4.1. Based on the Geo-DFN set classification, five sets of fractures were used to model the DFN, all having a range of radii between r_0 and r_{max} (564 m), with a power-law distribution. The fracture sets were sub-divided into sets of smaller-scale ($r < 5.6$ m) and larger-scale ($r > 5.6$ m) fractures. The model domain was a 400 m square cross-section surrounding the borehole, and 1,088 m long. Smaller-scale fractures were generated within a 40 m square horizontal cross-section around the borehole, extending to 20 m above and below the top and bottom of the borehole. Larger-scale fractures were generated within a region around the borehole with a 1,200 m square horizontal cross-section, extending to 500 m above and below the top and bottom of the borehole. It was necessary to do this, as generating the small-scale fractures throughout the whole model domain would lead to an impractical and unnecessarily large model. It was found in convergence tests for the block-scale hydraulic conductivity studies reported in Chapter 4 that a minimum fracture radius around 1 m is appropriate for a 20 m block and a minimum radius of about 6 m for a 100 m block. Concersely, an appropriate domain for modelling flow of fracture sizes down to about 1 m is 20 m and for 6 m it should

be at least 100 m. The mean fracture intensity, P32, for open fractures in Rock domain A provided by the Geo-DFN was used as a starting point for the calibration against hydraulic data. A summary of the DFN parameters used in the simulations is given in Table 3-14.

To check the validity of the P32 values and relative intensities used for the fracture sets in the model, five DFN realisations were generated, and the simulated P10 for open fractures taken over the length of the borehole was compared with the observed value for KLX04. Five realisations were performed as a compromise between computational time required and statistical convergence. (Future work should include a more detailed investigation into statistical convergence.) The simulated P10 in KLX04 for the mean of five simulations is reported in Table 3-15, and compared to the observed P10. Overall, the match of simulated P10 to the observed P10 is reasonable, but 11% below the observation. The comparison for the individual sets suggests that Set_d and especially Set_C are under-estimated, while Set_f is over-estimated. Note that about 50% of both the observed and simulated fractures are in Set_d, (sub-horizontal).

As an example, two realisations of the DFN model are shown in Figure 3-13 with all fractures included within a 1,088 m long and a 400 m diameter model domain surrounding KLX04. The smaller-scale fractures (fracture radii between r_0 and 5.6 m) generated only within a region with a 40 m square horizontal cross-section around KLX04 are shown in Figure 3-14. Similar models were used to perform the flow simulations described in Section 3.7.

Table 3-14. Description of 'k_r fit' DFN parameters used for simulation of fractures in KLX04, Rock Domain A.

Fracture set name	Orientation set pole: (trend, plunge), concentration	Fracture radius model power-law (r_0, k_r)	Intensity P_{32} (m^2/m^3); valid radius interval (r_{min}, r_{max})	Relative intensity of P32	Transmissivity model T (m^2/s)
Set_A	(338.1, 4.5) 13.06	(0.28, 2.73)	All = 8.36, open = 3.4; (0.28, 564)	0.18	–
Set_B	(100.4, 0.2) 19.62	(0.28, 2.83)		0.19	
Set_C	(212.9, 0.9) 10.46	(0.28, 2.73)		0.19	
Set_d	(3.3, 62.1) 10.13	(0.28, 2.76)		0.27	
Set_f	(243, 24.4) 23.52	(0.40, 3.6)		0.17	

Table 3-15. Comparison of observed P10 and proportions of P10 for open fractures in KLX04, with the mean of 5 realisations of simulated P10. The observed P10 does not include deterministic RVS DZs.

KLX04	Observed P10	Simulated P10	% model/observed
Set_A	0.16	0.15	89%
Set_B	0.11	0.11	98%
Set_C	0.23	0.15	66%
Set_d	0.89	0.74	83%
Set_f	0.15	0.24	157%
Total	1.55	1.38	89%

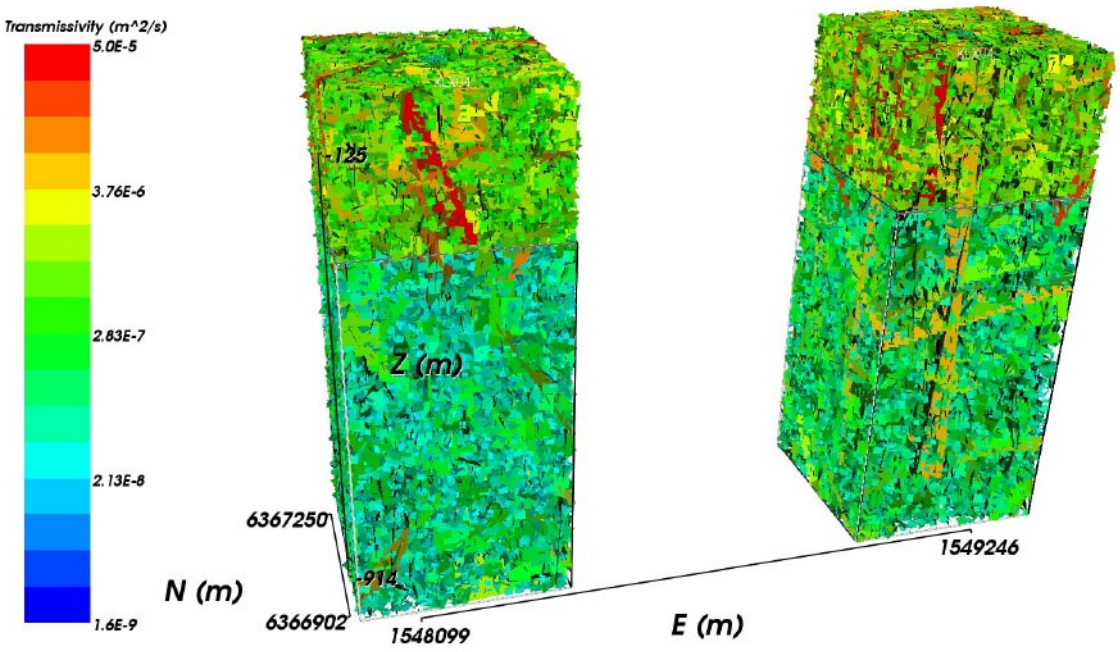

Figure 3-13. *Two realisations of the DFN for a domain of 400 m square cross-section and 1,088 m length around borehole KLX04. All fractures are shown and coloured by log(T) (in this case T is correlated to r using a power-law distribution). The right-hand realisation is translated 1 km east.*

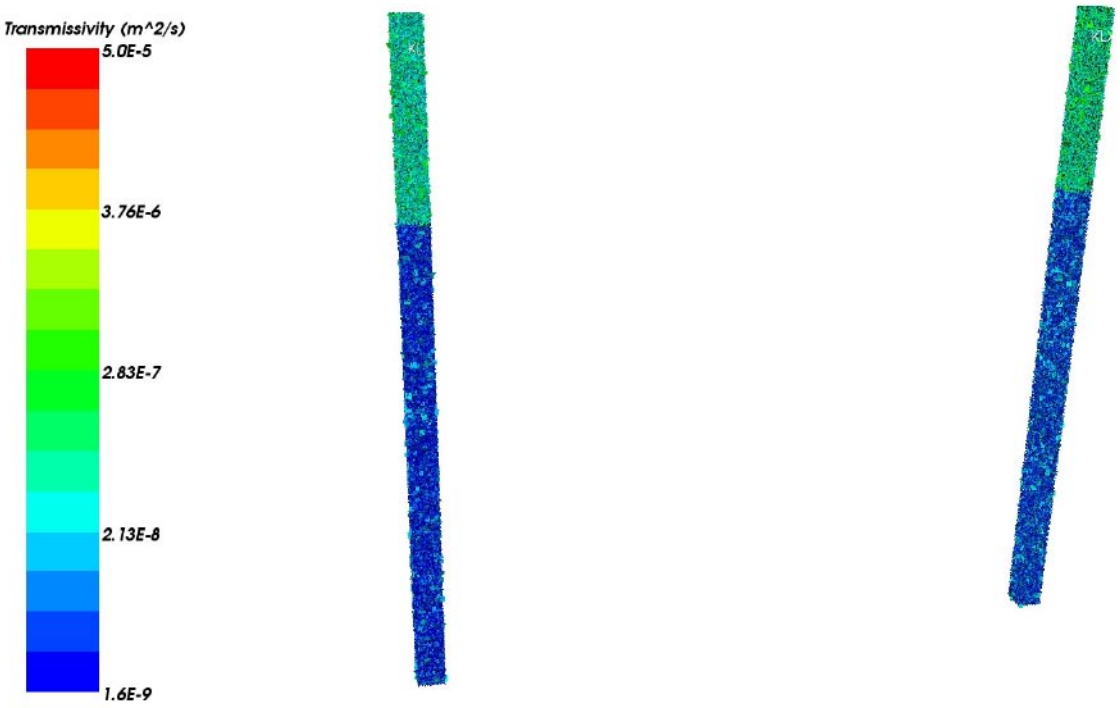

Figure 3-14. *Small-scale fractures generated within a region of 40 m square cross-section around borehole KLX04. Fractures are coloured by log(T) (in this case T is correlated to r using a power-law distribution). The right-hand realisation is translated 1 km east.*

3.7 Conditioning transmissivity against PFL-f and PSS data

Clearly the choice of statistical distribution used for transmissivity is a key assumption in interpreting the flow test-data. Three alternative transmissivity concepts were considered (as shown in Subsection 3.3.4). For each of these concepts an associated set of parameters are required in the DFN simulations to give a match to the distribution of flow-rates, Q, seen in the PFL-f data. It would be preferable to match Q rather than T from the PFL-f data because firstly it is Q that is measured not T (T is inferred from Q based on the Dupuit formula /Marsily 1986/), and secondly a fracture intersecting the borehole may have a substantial T value, but zero Q if it is not connected to the network. Matching Q necessitates performing flow calculations for flow to the borehole.

Building from experiences of Simpevarp version 1.2 and Forsmark version 1.2 /Hartley et al. 2005ab/, the approach of calibrating models against transmissivity measurements (from both PSS and PFL-f data) was taken, with simultaneous checking against flow-rate data, Q, from PFL tests. The PSS hydraulic data generally has a lower measurement limit than the PFL-f method, and therefore in order to get a handle on the lower flow-rates, the model has been fitted against both PFL-f and PSS data. Since the PSS data is only available as the transmissivity of 5 m intervals rather than flow-rates in individual fractures, it was necessary to compare simulated flow-rates in fractures in a consistent way. This was achieved by firstly inferring a transmissivity for each flowing fracture that intersects the borehole in the model using Dupuit's formula and then grouping them into 5 m intervals to compare with the shortest PSS interval length. Likewise, the transmissivity of PFL-anomalies was converted in the same way for comparison. The extent of the 5 m PSS data does not tend to cover the entire borehole, so when doing the comparison with the model simulations, one has to be careful to compare consistent lengths of borehole. Also, for some borehole sections we only have PSS 20 m data. The same methodology can be used for these sections, although in such long intervals the flow is less likely to represent flow from individual fractures, so it is less useful in calibrating a distribution for the transmissivity of individual fractures.

Once the model had been calibrated against T values for PSS and PFL-f, then the calibration was cross-checked using flow-rate, Q, of individual fractures from the PFL-f analyses. Here the simulated flowing fractures were compared against measured flow in each fracture set, as well as the overall flow-rate distribution.

For the Laxemar version 1.2 data freeze, PFL-anomaly data was available for KLX02 to KLX04, KAV01, KAV04A/B, KSH01A and KSH02. PSS packer-test data was available for KLX01 to KLX04, KSH01A to KSH03A, and KAV01 to KAV04A, although some PSS data is older and some boreholes are only covered by lower resolution intervals (e.g. 100 m intervals). To give the best match to the lower end of measured flow anomalies, both PFL-f and PSS data were matched (where 5 m PSS data were available). This would allow a fit of the model to the largest number of observations, in particular those observations with the lowest flow-rates (measured by PSS). This required that the PFL-anomaly data be grouped into 5 m intervals. Then, flow simulations were carried out to find the best match of the model to the transmissivity distribution by cross-checking against the flow-rate distribution, Q.

The flow simulations were performed using the following assumptions:

- Zero head on the vertical and top boundary. The vertical boundaries were 200 m away from the borehole. The top boundary was 50 m above the top of the borehole. A no-flow boundary was used on the base of the model, 50 m below the base of the borehole.
- A uniform drawdown of 10 m was specified throughout the length of the borehole.

- Fractures with radius less than 0.56 m were discarded to make the flow calculations tractable.
- Small fractures with radius less than 5.6 m were generated only within a 40 m diameter region surrounding the borehole. Small fractures are expected to have limited effect on large-scale flows due to their limited connectivity. Small fractures may contribute significantly to flow if there is no correlation between transmissivity and length and the network is well connected.
- The modelled transmissivity ($m^2\ s^{-1}$) can be calculated from the modelled flow-rate Q ($m^3\ s^{-1}$) into the borehole, and hence the transmissivity can be compared with that calculated from the PFL differencing.
- Because of the consistent difference in flow distributions for the upper and lower parts of the borehole, the intensity of open fractures and the transmissivity parameters were calibrated as independent values for each part. An appropriate choice for the depth of this transition varies from borehole to borehole between about –200 m and –350 m elevation. For simplicity, it was assumed that –300 m elevation was a suitable position for a step change in properties for all boreholes. Hence, the result is a set of best-fit Hydro-DFN parameters calibrated for above and below –300 m elevation.
- Using the best-fit parameters determined by matching the transmissivity, the modelled flow-rate Q [m^3/s] into the borehole was calculated and checked against Q from the PFL differencing.

Further, in matching T the objective is only to match statistically the distribution of T rather than necessarily the actual intervals where the flows occur or reproduce any clustering of flow anomalies that may arise around DZs, for example. Also, the minimum transmissivity associated with a PSS flow interval is about $1\ 10^{-11}\ m^2\ s^{-1}$, which is a function of the detection limit, but it is assumed that smaller fracture flows that are not detected by this equipment may exist. (The minimum flow associated with a PFL flow-anomaly is $3\ 10^{-8}\ m^3\ s^{-1}$, which corresponds to a detection limit (transmissivity) of about $3\ 10^{-9}\ m^2\ s^{-1}$). Hence, we will aim to match the part of the T distribution that has been measured, but not worry about the distribution of T below the detection limit.

One important uncertainty that needs to be considered in matching the flow-tests is the percentage of open and partly-open fractures that contribute to flow given the uncertainties in their characterisation from core. Hence, as well as varying the T parameters, we can also vary the percentage of open $P10_{corr}$ that is used.

The next step was to compare the distribution of transmissivities, T, simulated in the DFN models, which are described in Section 3.6, to give a distribution of fitted transmissivities for 5 m intervals for comparison with the PSS data and grouped PFL-f data. This is a very simplified approach since it relies on a number of assumptions, but nonetheless yields a useful comparison of simulated and observed transmissivities in the boreholes. The assumptions include:

- The measured and simulated transmissivities can be compared as simple distributions without concern for spatial bias.
- The transmissivity of the modelled fractures can be derived from a simulated radial flow system, and compared with the measured transmissivity derived from a spherical flow system.

3.7.1 Conditioning transmissivity for KLX04

The modelling approach taken was to perform flow simulations in a DFN model using CONNECTFLOW. In CONNECTFLOW, the connectivity between fractures, boreholes and boundaries is established and then flow is calculated through each fracture connected to the network using the finite-element method and applying Darcy's law. The flow-rate, Q, into the borehole from each connected fracture intersecting the borehole is then derived. The steady-state head distribution was calculated using a Pre-Conditioned Conjugate Gradient (PCCG) iterative solver with a low convergence criterion so as to obtain an accurate solution despite the large heterogeneity in the DFN models. This gave a relative mass balance (i.e. residual flux/total flux) of less than 10^{-8}. Figure 3-15 gives an example of the head distribution in a flow model. Here, fractures are coloured by the average head on the fracture. Most are red since we only see the fractures on the outside of the model and these are connected to the high head, 0 m, on the external boundaries. Fractures that are coloured grey do not carry flow since they are isolated from the network or are dead-ends. They are coloured grey since there is no water in them, and hence no head can be calculated in them. The fractures connected to the borehole see the greatest drawdown, and Figure 3-16 shows only the fractures connected to the borehole or that have a significant drawdown (> 1 m). Figure 3-17 shows the same information as Figure 3-15, but on a vertical slice through the borehole to reveal the head distribution inside the model. This shows that significant drawdown is quite localised with the drawdown reducing to modtly less than 1 m within a twenty metres of the borehole. This also shows that the match gives a higher fracture intensity of open fractures in the top part of the borehole above –300 m elevation and hence more connectivity as shown by the larger size of voids below –300 m elevation.

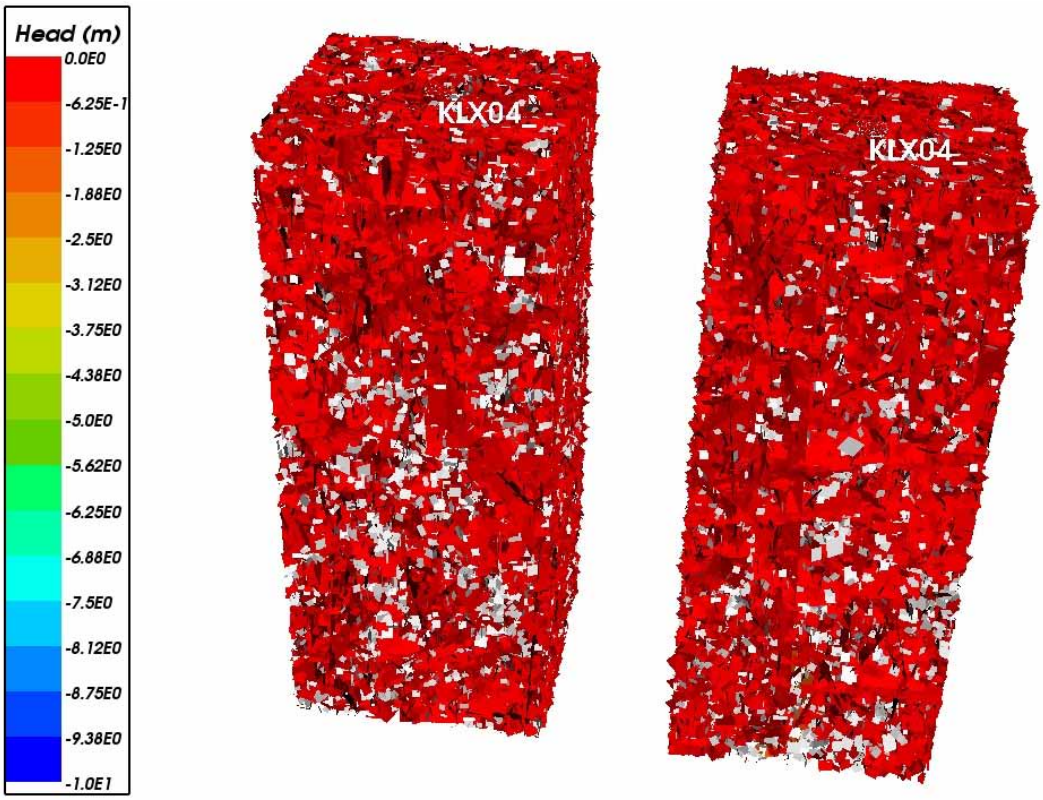

Figure 3-15. *Two realisations of the DFN model for a region of 400 m square cross-section around KLX04 used in the PFL-f/PSS simulation. The example shows the final matched case for a semi-correlated transmissivity model. Fractures are coloured by the average head on the fracture, or grey where they are either isolated or dead-ends.*

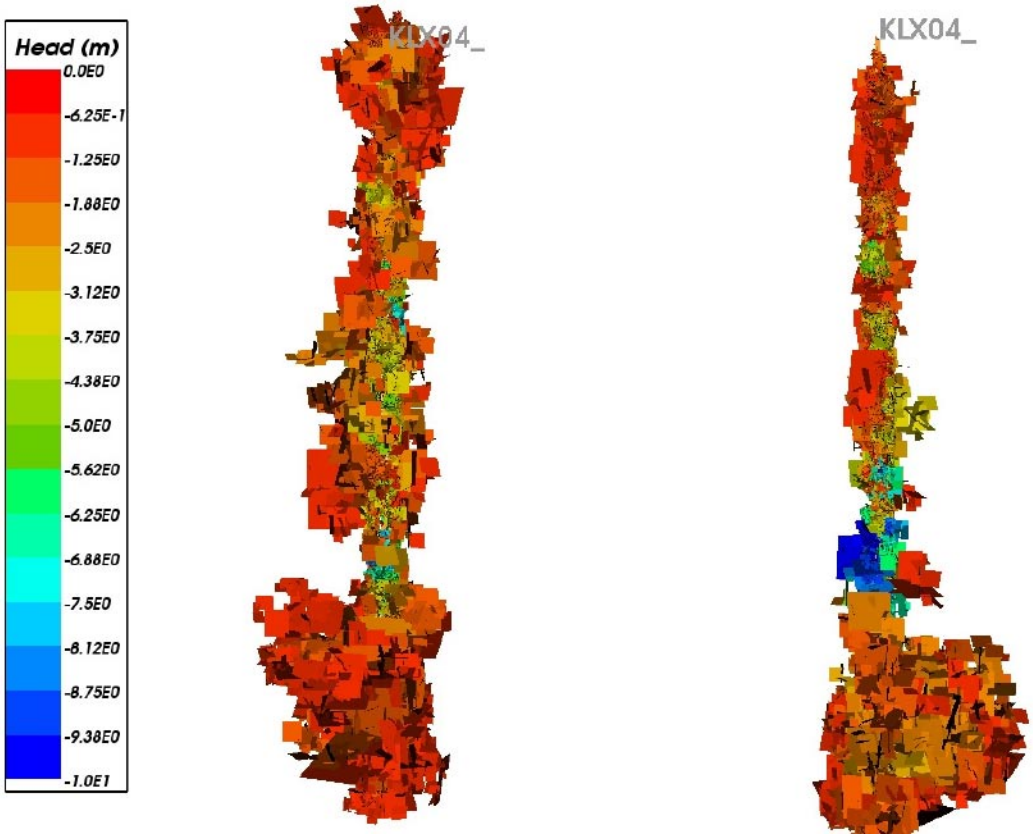

Figure 3-16. *Two DFN realisations as for Figure 3-15, but showing only the fractures around the borehole with a significant drawdown (> 1 m). Fractures coloured blue have the highest drawdown.*

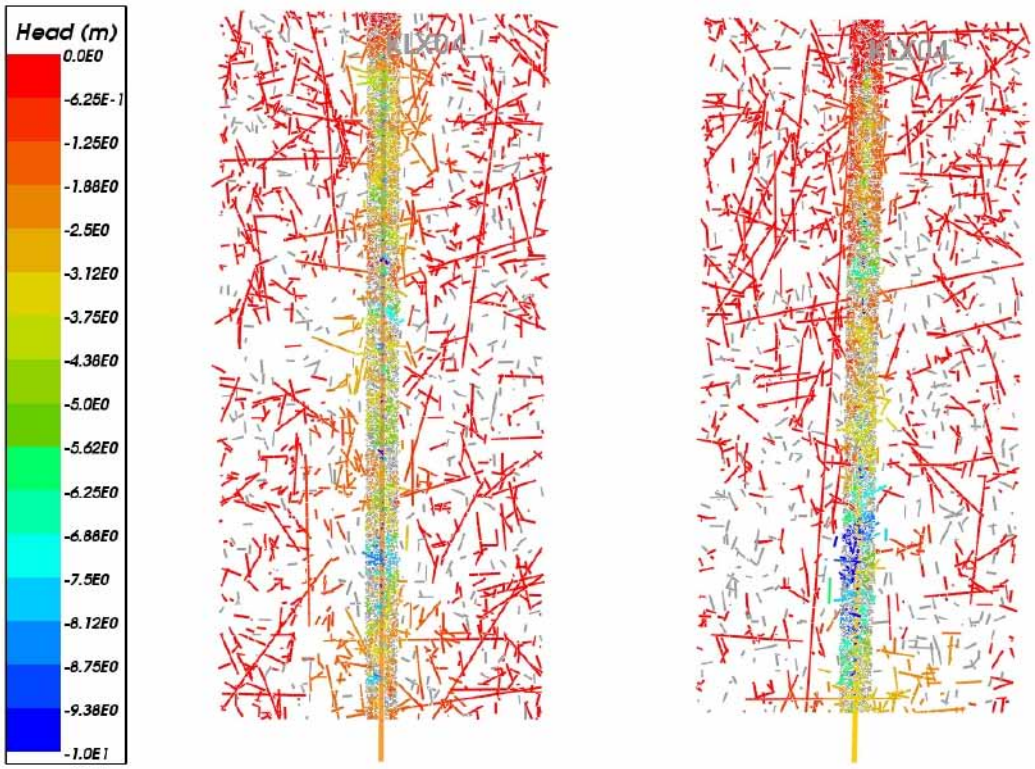

Figure 3-17. *Two DFN realisations as for Figure 3-15, but showing the head in fractures on a vertical slice E-W through the borehole. Fractures coloured grey are not connected in the network.*

For the upper and lower sections of the borehole (above and below –300 m elevation), parameters for the transmissivity models were fitted to both the PFL-f and the 5 m interval PSS results by a trial and error process. Parameters were chosen to provide good fits to both the total transmissivity of flowing features in the borehole and a histogram of transmissivities (fitting the values above detection limits for the flow-tests). To allow comparison of the simulation results to the PSS and PFL-f data simultaneously, the results were converted into compatible formats. The transmissivities for the PFL-anomalies were grouped into 5 m intervals and summed to match those of the PSS tests. Transmissivities for the simulated flow results were calculated following the same method used to calculate transmissivities from the flow test data; these were grouped and summed as for the PFL-f data. The transmissivity for the 5 m interval was then plotted as a histogram. Five realisations were simulated for each fit to give a reasonable representation of the variability predicted.

As a starting point, simulations were made with the fracture intensity, P32, based on 100% of all open and partly-open fractures. This predicted that every 5 m interval would have flow, but in fact the PFL-f data indicates that about 70% of intervals below –300 m elevation have flow below the PFL-f detection limit, and the PSS data, which has a lower detection limit, indicates that about 45% of intervals below –300 m have flow below the PSS detection limit. Above –300 m elevation, the PFL-f data suggests only 9% of 5 m intervals have flow below the detection limit (There is no PSS 5 m test scale data above –300 m elevation). Hence, the connectivity of the network had to be reduced, especially below –300 m elevation. A match to the percentage of non-flowing 5 m intervals in the PSS data below –300 m elevation was achieved by reducing the P32 to 35% of the P32 for open and partly-open fractures given in the Geo-DFN for Rock domain A at Laxemar. For the region above –300 m elevation, the P32 was only reduced to 50% of the P32 for open and partly-open fractures. Hence, we try to explain the higher flows at the top of the borehole by having higher fracture connectivity, though we also must have a higher fracture transmissivity in the top section. Figure 3-18 to Figure 3-23 show the distributions of interval transmissivity for the different borehole sections and transmissivity versus radius relationships.

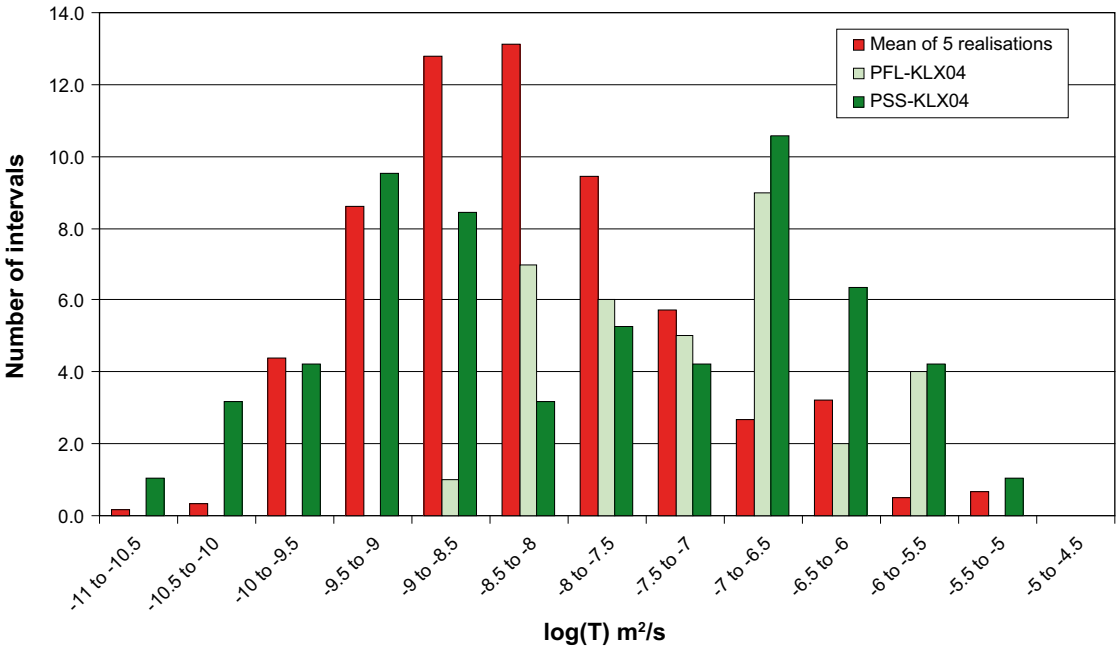

Figure 3-18. *Histogram of Log(T) in 5 m intervals for the mean of 5 realisations of the correlated T distribution compared with the PFL-anomaly and PSS data for KLX04 below –300 m. This case is based on 35% of open and partly-open fractures.*

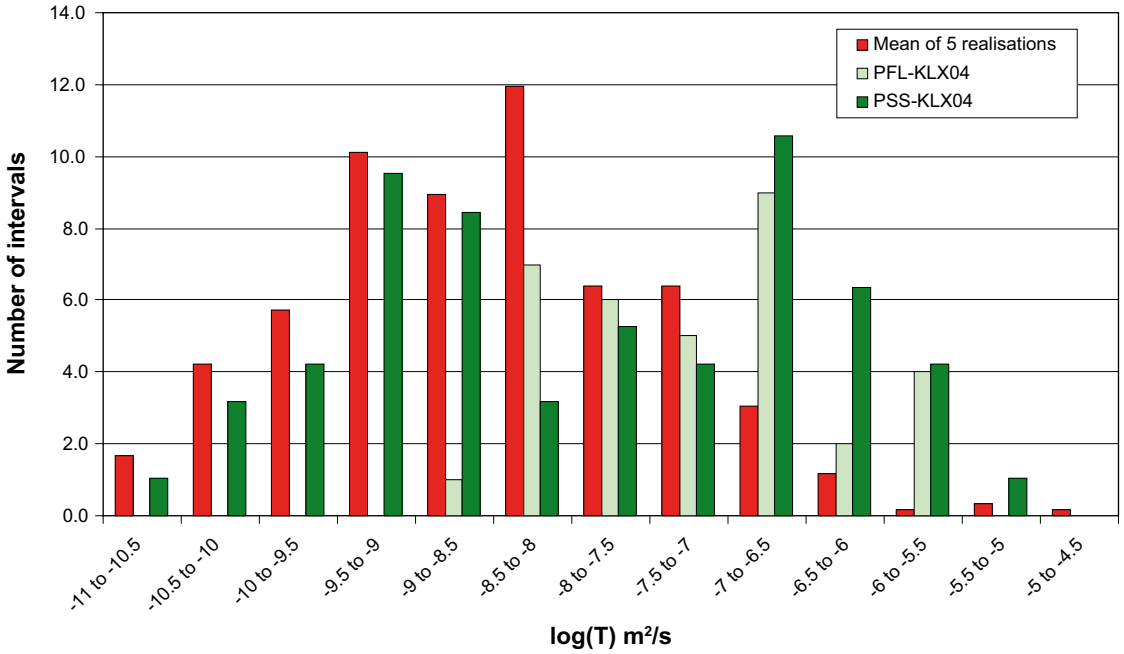

Figure 3-19. *Histogram of Log(T) in 5 m intervals for the mean of 5 realisations of the semi-correlated T distribution compared with the PFL-anomaly and PSS data for KLX04 below –300 m. This case is based on 35% of open and partly-open fractures.*

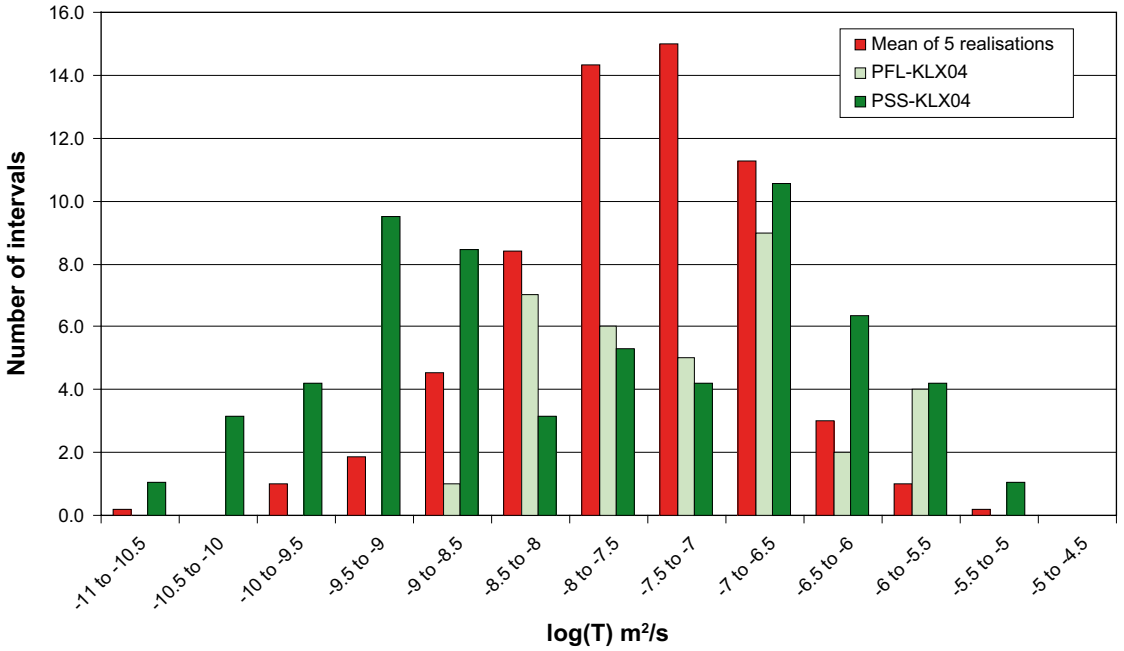

Figure 3-20. *Histogram of Log(T) in 5 m intervals for the mean of 5 realisations of the uncorrelated T distribution compared with the PFL-anomaly and PSS data for KLX04 below –300 m. This case is based on 35% of open and partly-open fractures.*

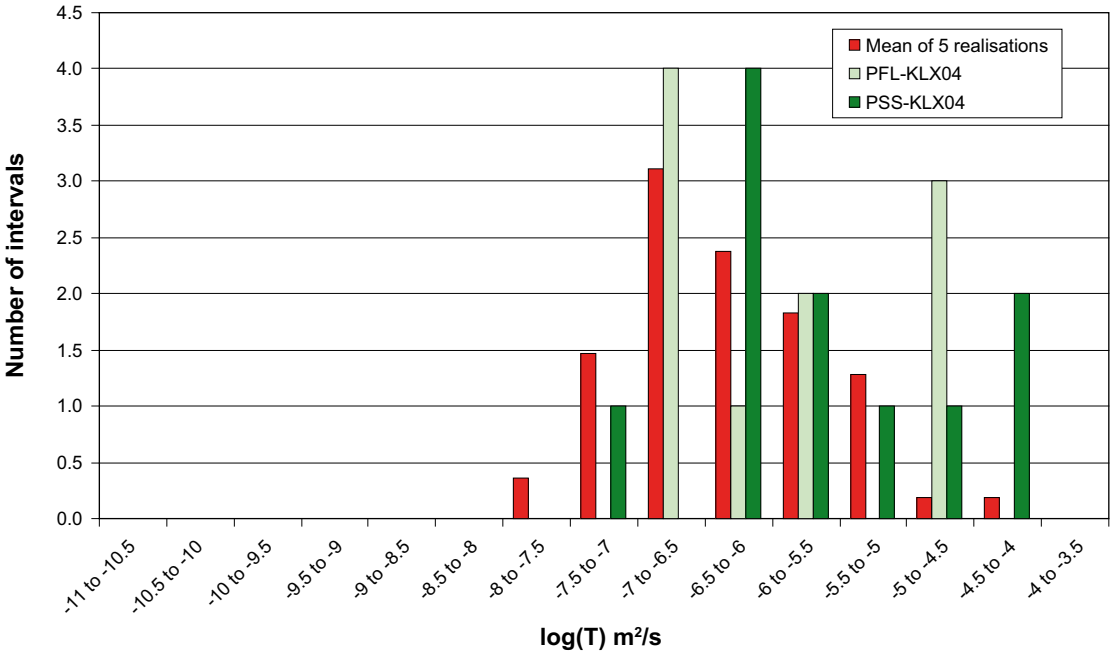

Figure 3-21. *Histogram of Log(T) in 20 m intervals for the mean of 5 realisations of the correlated T distribution compared with the PFL-anomaly and PSS data for KLX04 above –300 m. This case is based on 50% of open and partly-open fractures.*

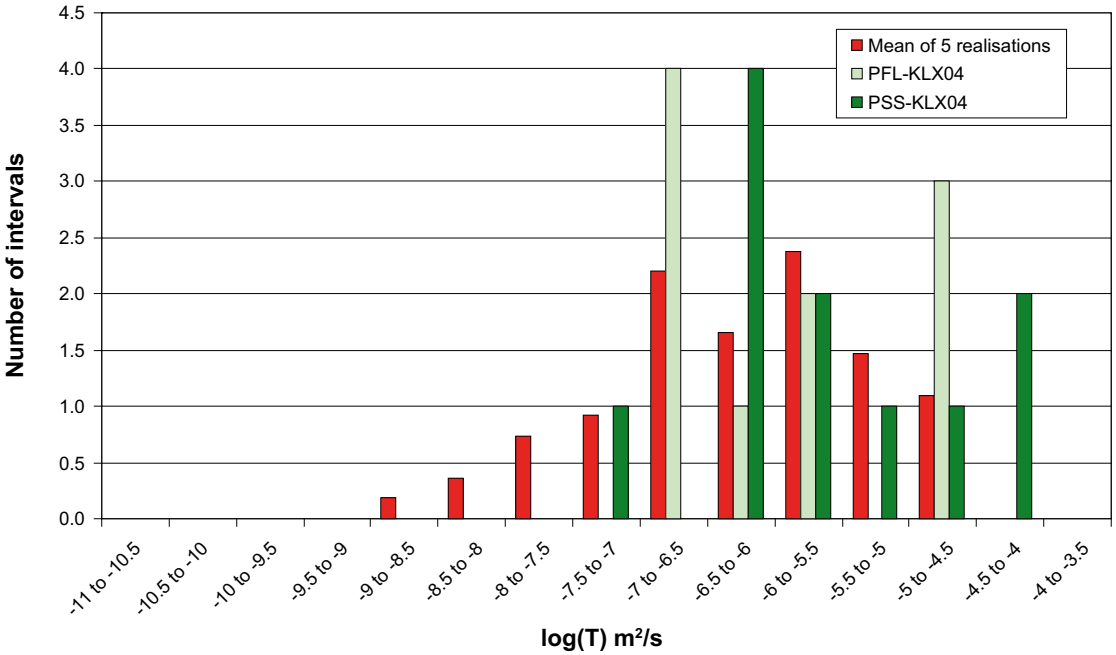

Figure 3-22. *Histogram of Log(T) in 20 m intervals for the mean of 5 realisations of the semi-correlated T distribution compared with the PFL-anomaly and PSS data for KLX04 above –300 m. This case is based on 50% of open and partly-open fractures.*

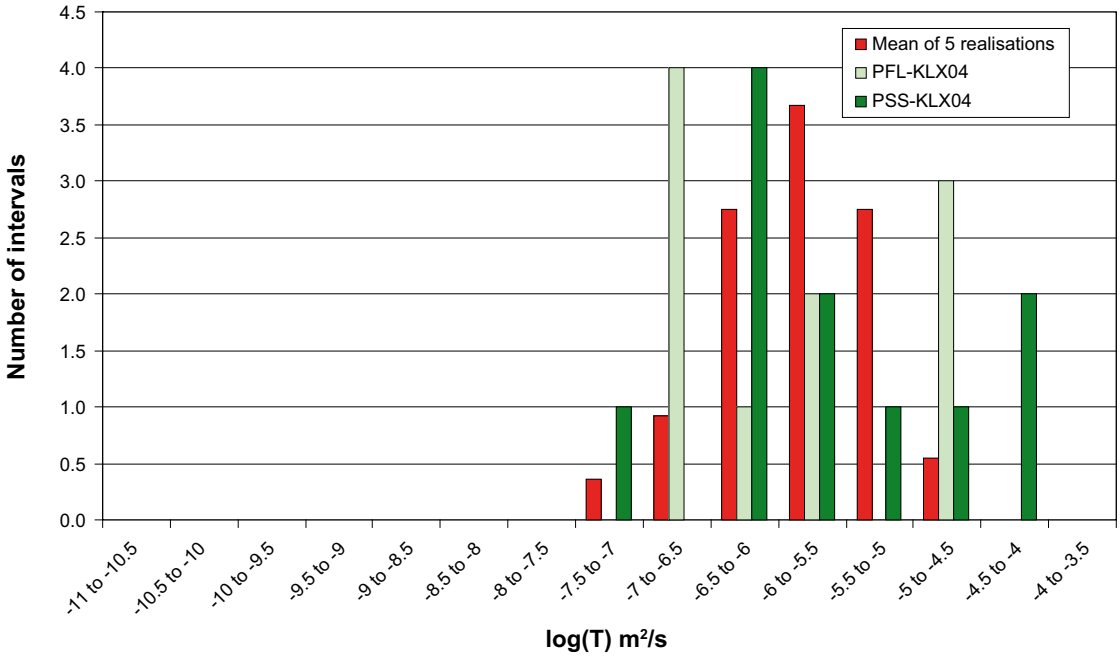

Figure 3-23. *Histogram of Log(T) in 20 m intervals for the mean of 5 realisations of the uncorrelated T distribution compared with the PFL-anomaly and PSS data for KLX04 above –300 m. This case is based on 50% of open and partly-open fractures.*

Using the same geometrical parameters from the Geo-DFN and P32 values for the upper and lower bedrock sections, transmissivity distributions were matched for the correlated, semi-correlated and uncorrelated models. The main objectives of the matching process relate to the average total flow over 5 realisations, with the aim of qualitatively matching the distribution of transmissivity between borehole intervals. Other objective measures were comparisons of the distribution of Q against PFL-f data, overall and for individual fracture sets as described in Section 3.8.

For the lower section of bedrock below –300 m elevation, the transmissivity distribution of 5 m intervals derived from both the PFL-f and PSS data is compared with the mean distribution from 5 realisations. By the mean distribution we mean the average frequency within each bin. PSS was available for fewer intervals than for the PFL-f data, and so the frequencies obtained from the PSS data were multiplied by (number of PFL intervals/ number of PSS intervals) to allow direct comparison with the PFL-f data and simulations.

In our model we assume that fractures can be approximated as continuous in scale according to the power-law, and try different relationships between transmissivity and size. The transmissivities of intervals shown for the model are based on values interpreted from the simulated flow-rates, Q, into the borehole rather than just being the input transmissivity of fractures intersected by the borehole. This is an important point, since a small fracture may have a high transmissivity for the uncorrelated model, but the actual flow-rate into the borehole may be low because there is limited supply of water due to its poor connectivity. Generally, we find that flow-rates are as or more sensitive to fracture size as transmissivity, since large fractures are more connected and hence have a higher likelihood for large supply of water. Therefore, the shapes of the distributions of interval transmissivity here are strongly dependent on the fracture size distribution and fracture intensity rather than the fracture transmissivity relationship. Still, the shape of the distributions seems to be better represented in the correlated and semi-correlated cases than in the uncorrelated case, and the semi-correlated appears to give the best match, and is more realistic.

It is seen later in Section 4.4 that the distribution of block scale hydraulic conductivity has a dependence on the relationship between fracture transmissivity and size, at least for 20 m blocks with a significantly lower standard deviation for an uncorrelated model than a directly correlated one.

For the lower section of bedrock, below –300 m elevation, Figure 3-18 to Figure 3-20 show the comparison for the final matched models for each transmissivity model. One problem in matching this section is that the data shows a bi-modal type behaviour with a high mode just over 10^{-7} m^2/s and a lower one at around 10^{-9} m^2/s.

The high values are clustered in specific sections at about –300 m, –540 m to –605 m and –900 m elevation where the highest and lowest clusters are close to deterministic deformations, but the high flow seems to occur just outside the single-hole interpretations of the deformation zones. Whereas the high flows around –540 m to –605 m are not associated with any interpreted deformation zone. This may be observed in Figure 3-24. The strike of the fractures associated with the PFL-anomalies in this interval are generally steeply dipping with a strike oriented NW-SE, i.e. Set_C and Set_f. The consistency in orientation of fractures associated with flow-anomalies may suggest that they belong to a deformation zone not identified in the single-hole interpretations, perhaps because it is more diffuse compared to some of the thin stochastic deformation zones nearer the surface. This is an important observation since it suggests that the single-hole interpretations of deformation zones in the boreholes may be an under-estimate due to not integrating the hydraulic data. It is also creates a dilemma for our conceptualisation and modelling. One course of action would be to interpret this as an additional stochastic deformation zone, and then following our methodology we would amalgamate the flow-rate and transmissivity associated with the flow-anomalies into a single stochastic feature. This would result in a single very high value in the observed distribution of flow and transmissivity to match our simulations to. The drawback is that we would then diverge from the single-hole interpretations provided. Instead, we have retained the PFL-anomalies associated with this interval as individual flow-rate and transmissivity values in the observed distribution. The implication of this approach is that it results in the bi-modal distribution of observed flow-rates and transmissivities as seen in Figure 3-18, for example, which is difficult to match based on our modelling assumption of a continuous distribution of fractures as determined by size and transmissivity.

Given that this is a single feature in a single borehole, it is hard to assess the wider consequences. Such features are not so apparent in the other boreholes analysed. It remains to be seen if such features occur in future borehole interpretations. One recommendation is that the hydraulic data be better integrated in the single-hole interpretation process. However, if such features occur in several boreholes, then it would motivate a consideration of more sophisticated fracture concepts than the single continuous distribution.

In the upper borehole section, above –300 m elevation, only 20 m interval PSS data was available and so the amount of data for this part of the calibration is more limited as shown in Figure 3-21 to Figure 3-23. These really just show that the model is in the right kind of area and the PFL-f data of individual flows must be used to supplement the match as described in the next section.

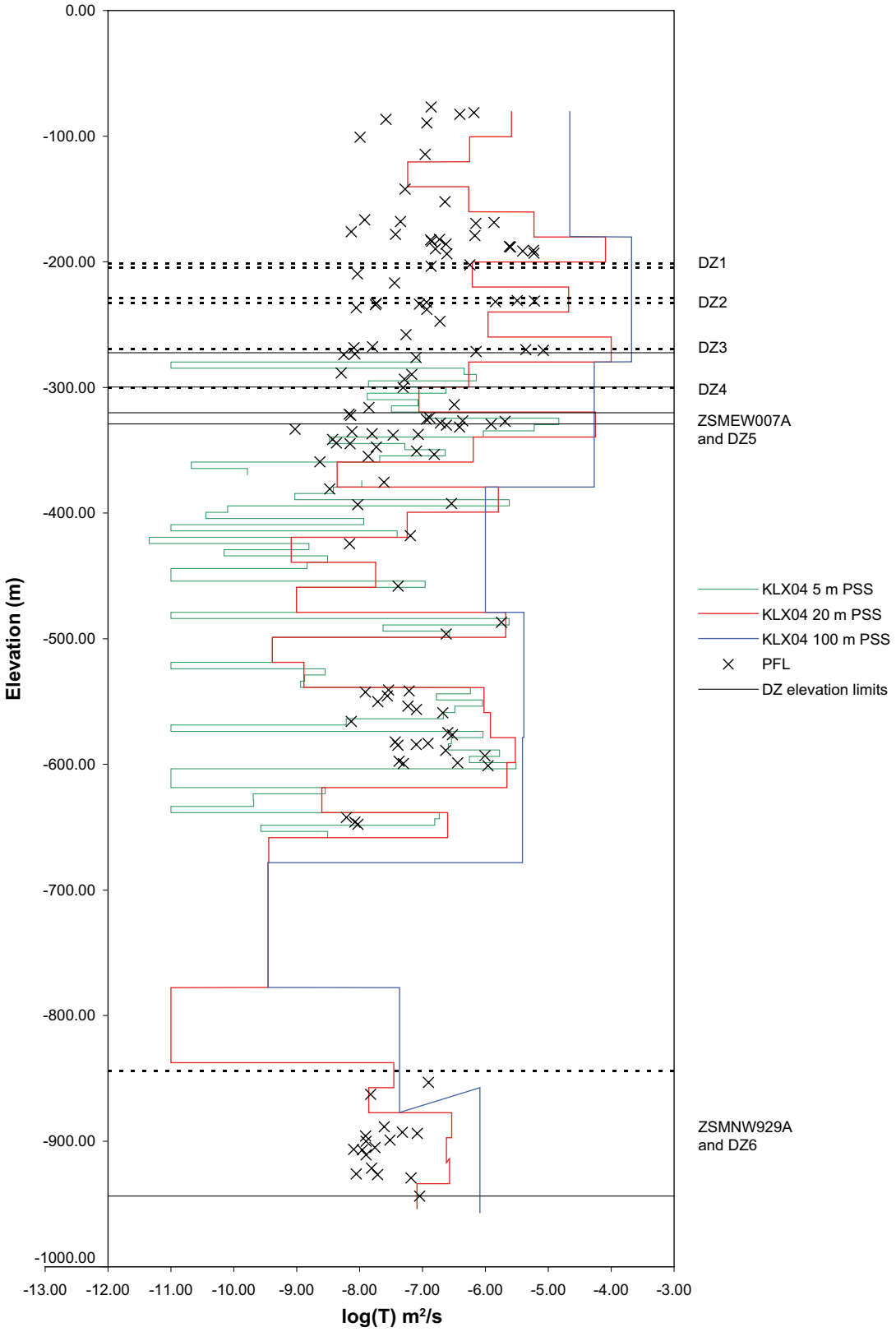

Figure 3-24. *Transmissivity of 5 m, 20 m and 100 m borehole intervals with measurable flow recorded by PSS in KLX04, and transmissivity of PFL-anomalies.*

3.8 Checking the simulated flow-rate distribution against PFL-f data

After the transmissivity has been matched to both PFL-f and PSS data (this allows a best fit to both the maximum data and the lowest measurement limit), then the best case of simulated flow-rate, Q, is checked against the measured PFL flow anomalies. This has been considered in several ways:

- The total simulated flow-rate has been checked against the measured flow-rate, bearing in mind that the PSS data has been matched first. Primary matching to the PSS data with its lower measurement limit will provide a poorer match for the measured PFL flow anomalies.
- The simulated distribution of Q was checked against the measured distribution of PFL flow anomalies.
- The distribution of Q for each fracture set was compared to the measured PFL flow anomalies for each fracture set. In addition, selected realisations have been plotted on a stereonet to check if the simulated orientation of flowing fractures corresponds to the orientation of measured flow anomalies.

Checking the best fit T model parameters determined by matching the simulated T to PFL-f and PSS data requires that the flow anomaly data must be processed in two important ways:

- Firstly, the actual drawdown in the boreholes is of the order of 10 m but varies considerably down the borehole, generally decreasing down the hole. Hence, the effective drawdown associated with the flow-rate measured from each anomaly is not constant, and so there is some bias. Since we want to match Q as a distribution, it is important to remove this bias by renormalizing Q: $Q_{unbiased} = Q \times 10/\Delta h$, where Δh is the measured drawdown, and 10 m is the drawdown used in the simulations.
- Secondly, for self-consistency, if several PFL-anomalies are associated with a deformation zone, then the Q values for the anomalies are amalgamated into a single data point since the DFN model conceptualises the deformation zones as single large stochastic fracture.

3.8.1 Checking the simulated flow-rate against PFL-f data for KLX04

The best fit parameters for each transmissivity model have been checked against the distribution of flow-rate for individual PFL-anomalies, an example is shown for the lower section of KLX04 with the correlated case in Figure 3-25. These show that the simulated flow-rate distribution is a reasonable match against the PFL flow anomalies in the range above the detection limit around $3\ 10^{-8}$ m^3/s. The rest of the distribution below this limit was matched on the basis of the PSS data as discussed in the previous section. Again there is a bit of difficulty in matching the maximum frequency observed in the PFL-f data at around 10^{-6} m^3/s, which is associated with the PFL-anomalies between –540 m and –605 m. Since Q is proportional to T, then for the correlated model Q is correlated to r, and so the distribution of Q resembles the wedge-shape associated with the power-law size distribution. As such, it will never predict peaks at intermediate flow-rates. Consequently, the simulated flow distribution for the correlated case (and the semi-correlated case, see Figure 3-32) must include higher flows than those measured by PFL-f in order to match the total flow measured by PFL-f. In contrast, the uncorrelated case, shown in Figure 3-36, gives a maximum frequency around the correct value for Q although too many flowing fractures overall.

The orientation of the simulated flowing features in each fracture set has also been compared to the orientation of the closest features to each PFL-anomaly, an example is shown for the lower section of KLX04 with the correlated case in Figure 3-26. The plots show the

point of the median, minimum and maximum flow-rate associated with each set. The spread in the PFL-f data is clearly limited by the lower detection limit at about $\log(Q) = -7.5$ m^3 s^{-1}, and so only that part of the simulated flow-rates above this limit is used for comparison. The numbers of flow-anomalies in each set for the observed data and the simulations are shown to the right of the distribution. For the simulations, this is the mean of five realisations, and so it is not just an integer number. As can be seen, the data predicts a spread of flow-rates over about 1.5 to 3 orders of magnitude, and this is similar in the simulations. Corresponding plots for the semi-correlated and uncorrelated cases are given in Figure 3-33 and Figure 3-37.

For the lower section of the borehole, the data suggests that the high flows are predominantly in Set_C and Set_d, and 77% of the anomalies belong to these two sets. It should be noted that the division in the data between Set_C and Set_f is just based on the hard sectors shown in Figure 3-5, while in reality one would expect higher flow in Set_C since these are the more extensive fractures. The simulations predict about the right numbers of flow-anomalies and flow-rates in Set_d and Set_B. The simulated numbers of flow-anomalies and flow rates in Set_A are a little high. However, flow in Set_C is under-simulated. This again relates to the high flows between –540 m and –605 m that correspond to Set_C and probably reflects that a higher than average percentage of the open fractures seen in core-logs in this interval are associated with flow-anomalies. If we had treated this interval as a stochastic deformation zone and amalgamated the flow data, then the number of flows in the set would be more consistent with the simulation, although the flow-rate would be much higher. Hence, the importance of Set_C for flow is under-estimated in the model for KLX04. A more consistent prediction would be made if the transmissivity of Set_C were increased by one order of magnitude. The maximum flow-rate in Set_A in KLX04 is over-predicted by about half an order of magnitude. Also, considering KLX03 and KSH01A in Appendix B, PFL-f data suggests that there is very little flow in Set_A and Set_B. Hence, a reduction in transmissivity in Set_A and Set_B of about 0.5–1.0 orders of magnitude may improve the model overall. Such anisotropy would make the model more complex, but it is perhaps more realistic to expect a lower transmissivity in Set_A and Set_B, which are orthogonal to the maximum regional stress, while Set_C is parallel. An investigation of anisotropic transmissivity is described in Subsection 3.8.2 and should be considered as an alternative Hydro-DFN model. Anisotropic transmissivity needs to be explored in future as more PFL-f data is made available.

Similar plots are shown for the upper section of KLX04 in Figure 3-28 and Figure 3-29 for the correlated case, Figure 3-34 and Figure 3-35 for the semi-correlated case, and Figure 3-38 and Figure 3-39 for the uncorrelated case. The match is perhaps better for this section and the general distribution between sets is reasonable although the data is quite sparse for the sub-vertical sets, and Set_d completely dominates.

One realisation of the simulated flowing features is plotted as a stereonet in Figure 3-27 for below –300 m, Figure 3-30 for above –300 m elevation, and Figure 3-31 for the complete length of the borehole. Only simulated fractures with flow above the detection limit, about $\log(Q) = -7.5$ m^3 s^{-1}, are shown. Figure 3-31 can be compared with the measured flows for all fractures, excluding RVS DZs, given in Figure 3-9.

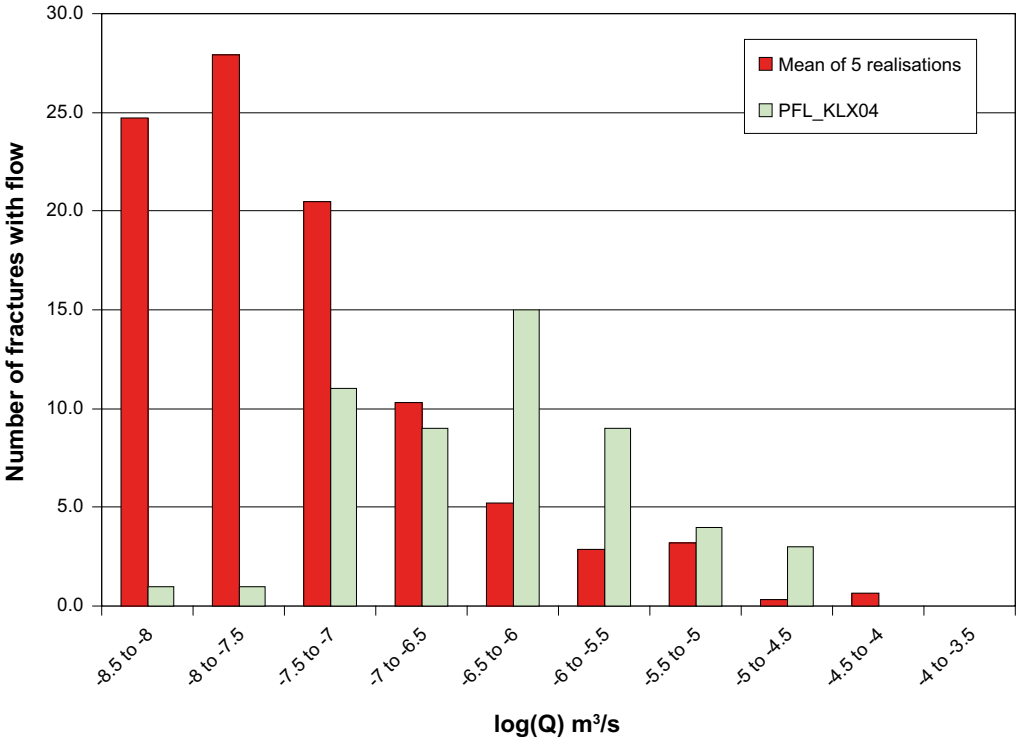

Figure 3-25. *Histogram of Log(Q) flow-rate to borehole, for the mean of five realisations compared to the PFL-anomaly data for KLX04 below –300 m. Here, the correlated T distribution is used from the matched PFL-f and PSS transmissivity with 35% of P32.*

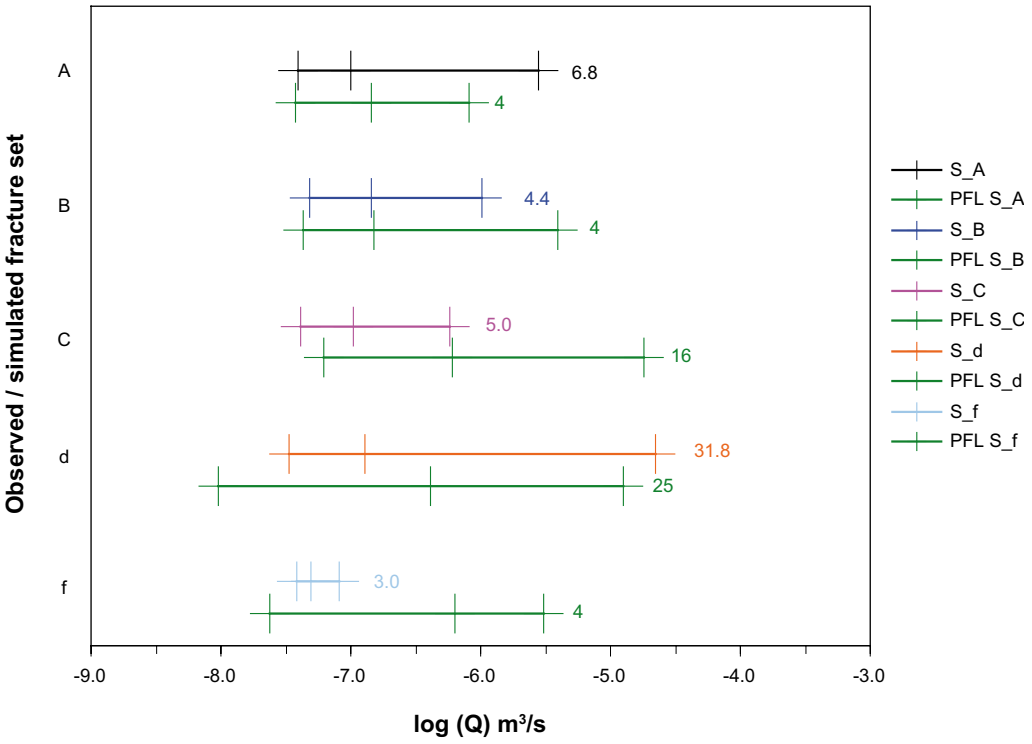

Figure 3-26. *Plot of Log(Q) flow-rate to borehole, for the mean of five realisations compared to the PFL-anomaly data for KLX04 below –300 m. The flow in each fracture set is shown, with vertical bars marking the minimum, median and maximum flow-rates. The number of fractures in the set is given to the right of each plot. Here, the correlated T distribution is used from the matched PFL-f and PSS transmissivity with 35% of P32.*

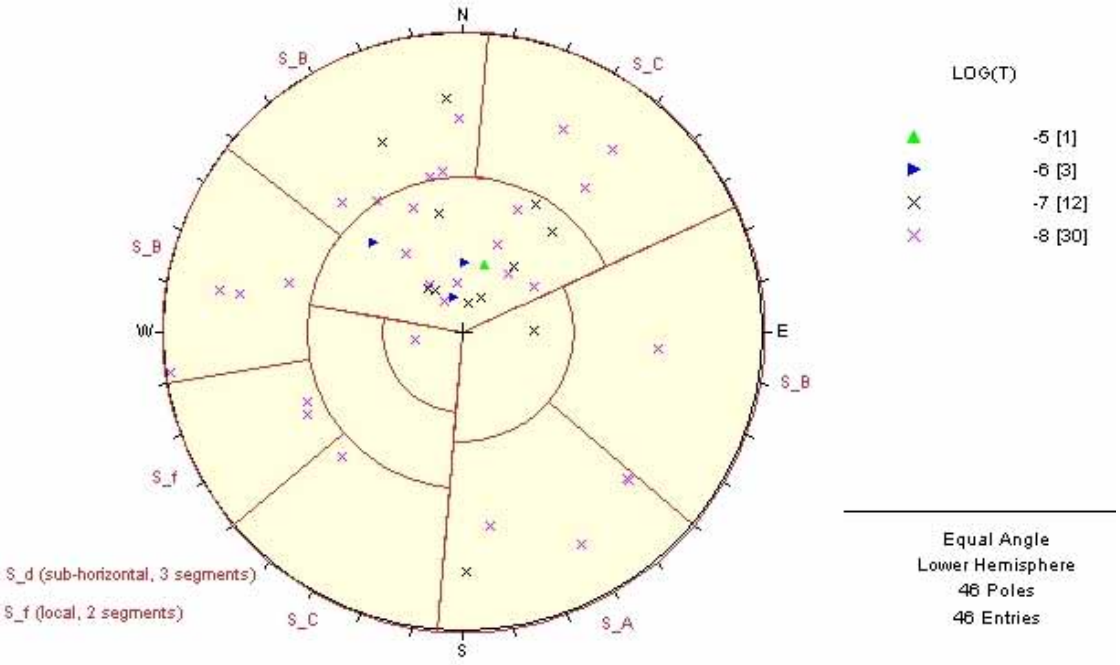

Figure 3-27. *Orientations of the simulated flowing features for the correlated case for KLX04 below –300 m. One realisation is shown as an illustration. Symbols are coloured according to log of transmissivity of each flowing feature (m^2 s^{-1}).*

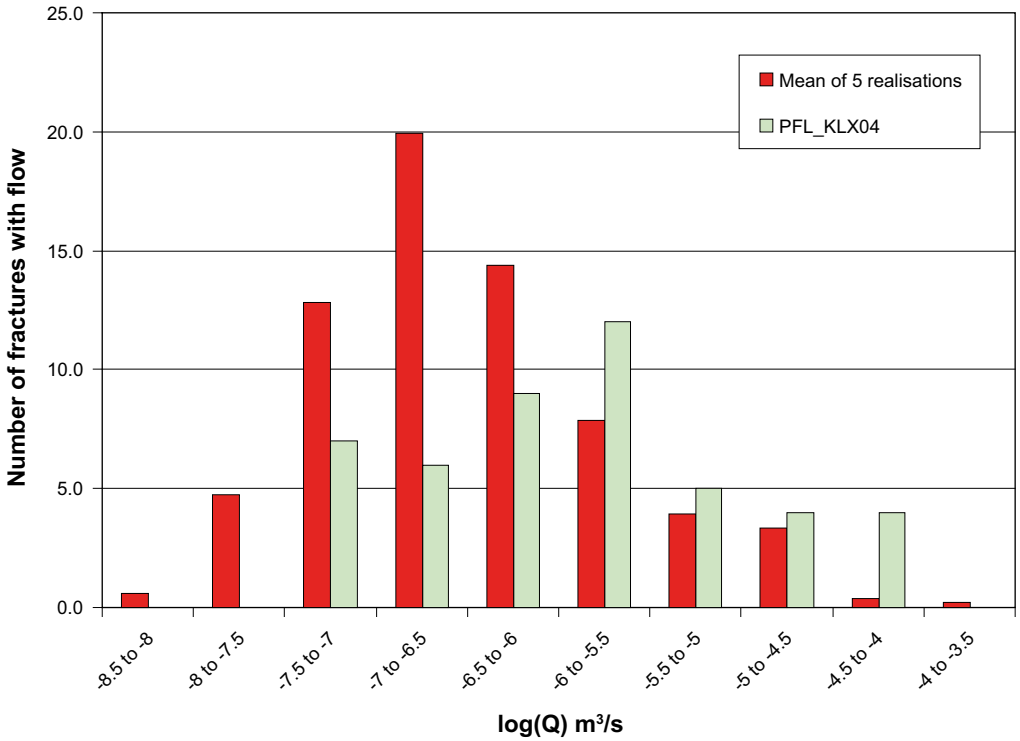

Figure 3-28. *Histogram of Log(Q) flow-rate to borehole, for the mean of five realisations compared to the PFL-anomaly data for KLX04 above –300 m. Here, the correlated T distribution is used from the matched PFL-f and PSS transmissivity with 35% of P32.*

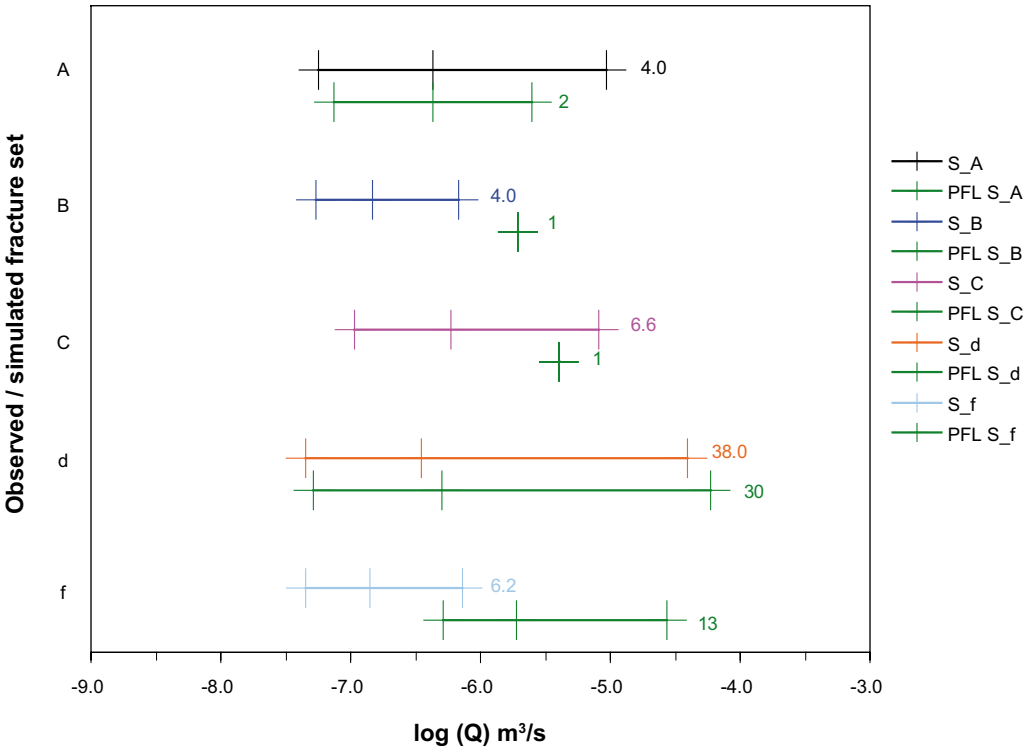

Figure 3-30. *Orientations of the simulated flowing features for the correlated case for KLX04 above –300 m. One realisation is shown. Symbols are coloured according to log of transmissivity of each flowing feature (m^2 s^{-1}).*

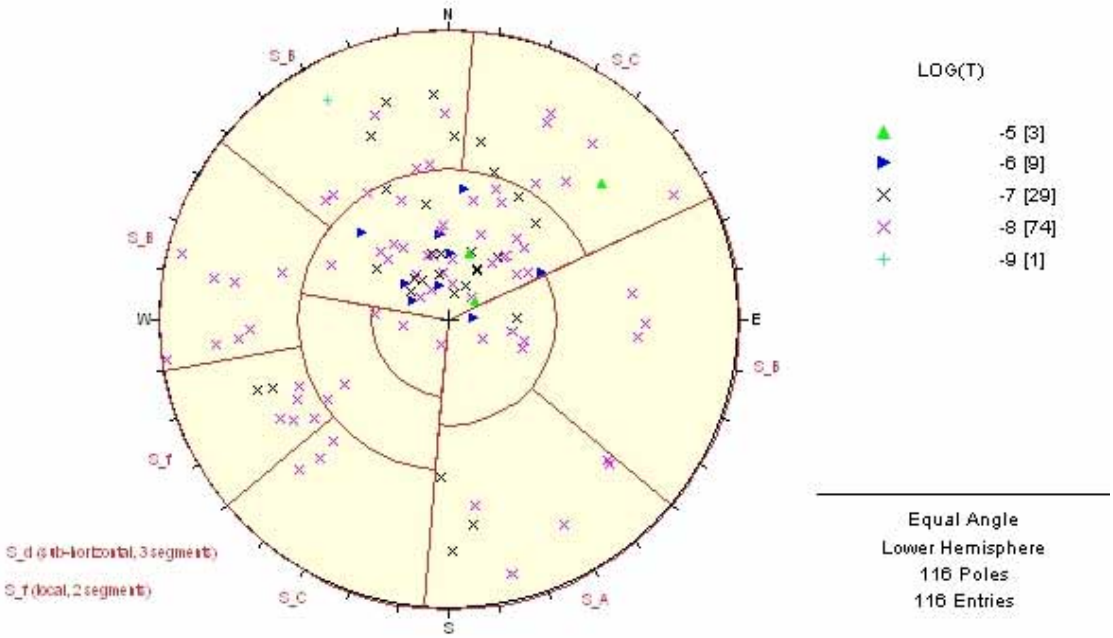

Figure 3-29. *Plot of Log(Q) flow-rate to borehole, for the mean of five realisations compared to the PFL-anomaly data for KLX04 above –300 m. The flow in each fracture set is shown, with vertical bars marking the minimum, median and maximum flow-rates. The number of fractures in the set is given to the right of each plot. Here, the correlated T distribution is used from the matched PFL-f and PSS transmissivity with 35% of P32.*

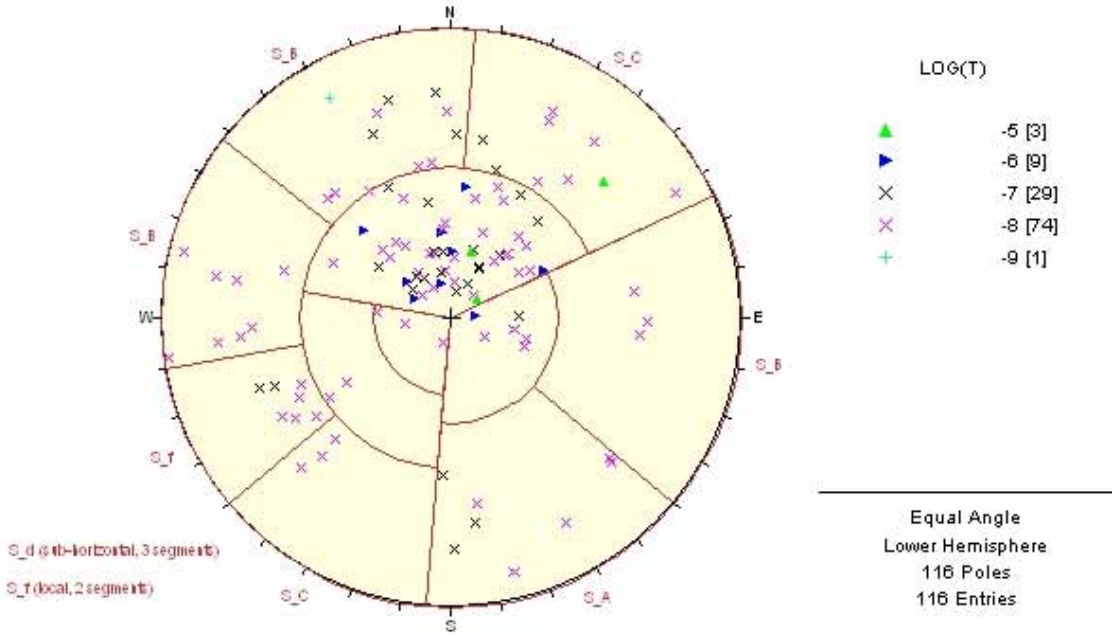

Figure 3-31. *Orientations of the simulated flowing features for the correlated case for the complete length of KLX04. One realisation is shown. Symbols are coloured according to log of transmissivity of each flowing feature (m^2 s^{-1}).*

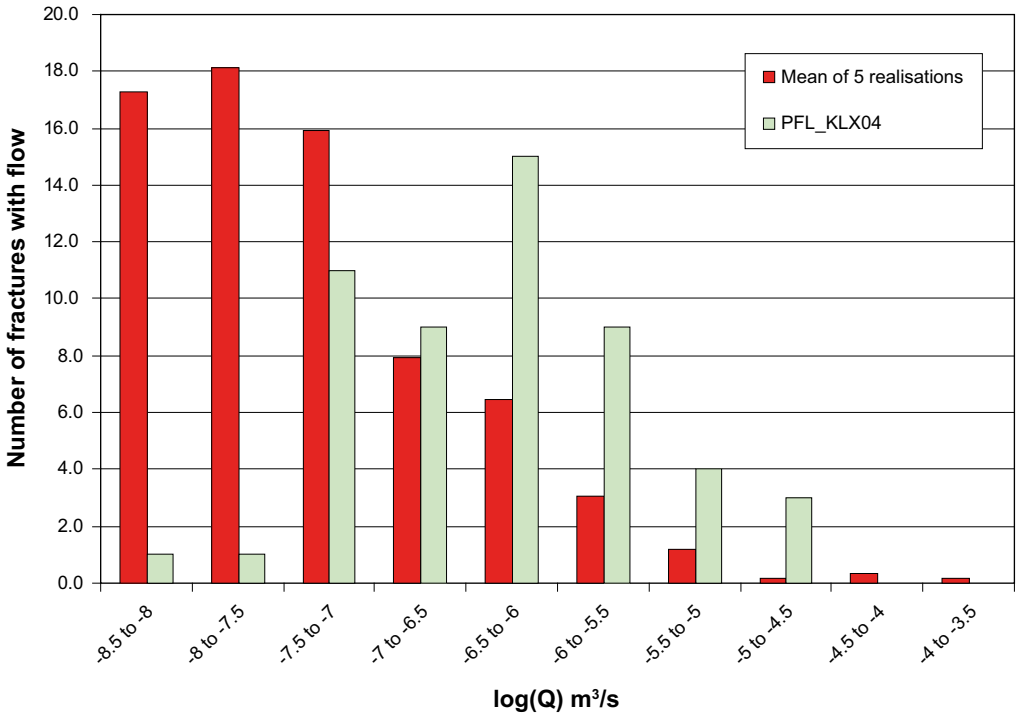

Figure 3-32. *Histogram of Log(Q) flow-rate to borehole, for the mean of five realisations compared to the PFL-anomaly data for KLX04 below –300 m. Here, the semi-correlated T distribution is used from the matched PFL-f and PSS transmissivity with 35% of P32.*

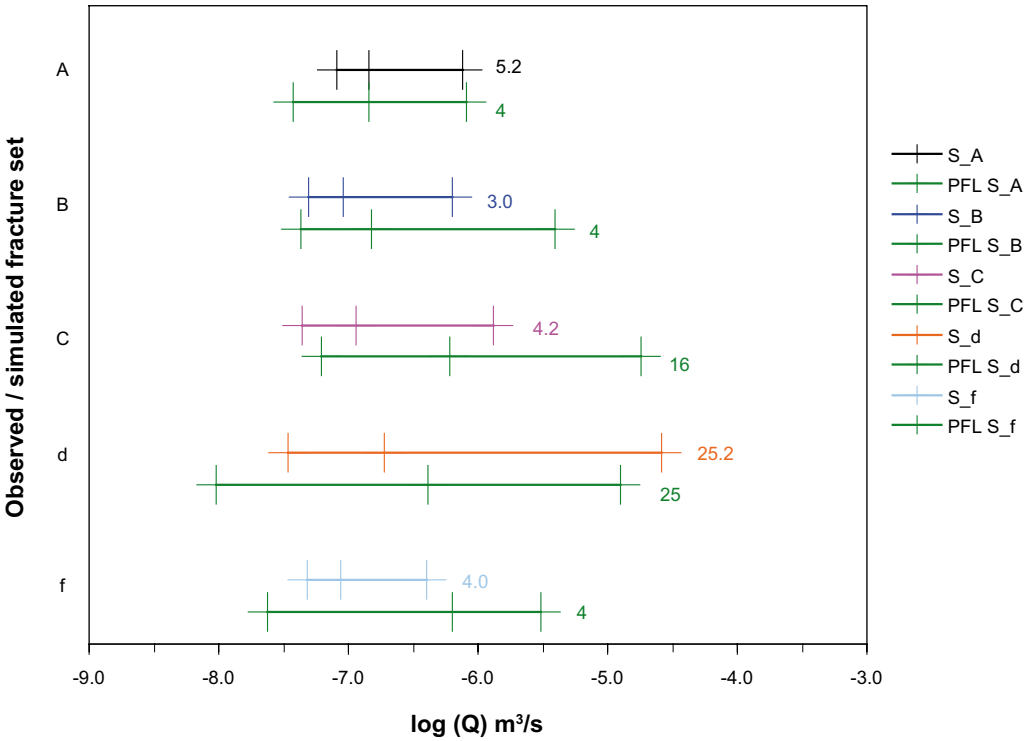

Figure 3-33. *Plot of Log(Q) flow-rate to borehole, for the mean of five realisations compared to the PFL-anomaly data for KLX04 below –300 m. The flow in each fracture set is shown, with vertical bars marking the minimum, median and maximum flow-rates. The number of fractures in the set is given to the right of each plot. Here, the semi-correlated T distribution is used from the matched PFL-f and PSS transmissivity with 35% of P32.*

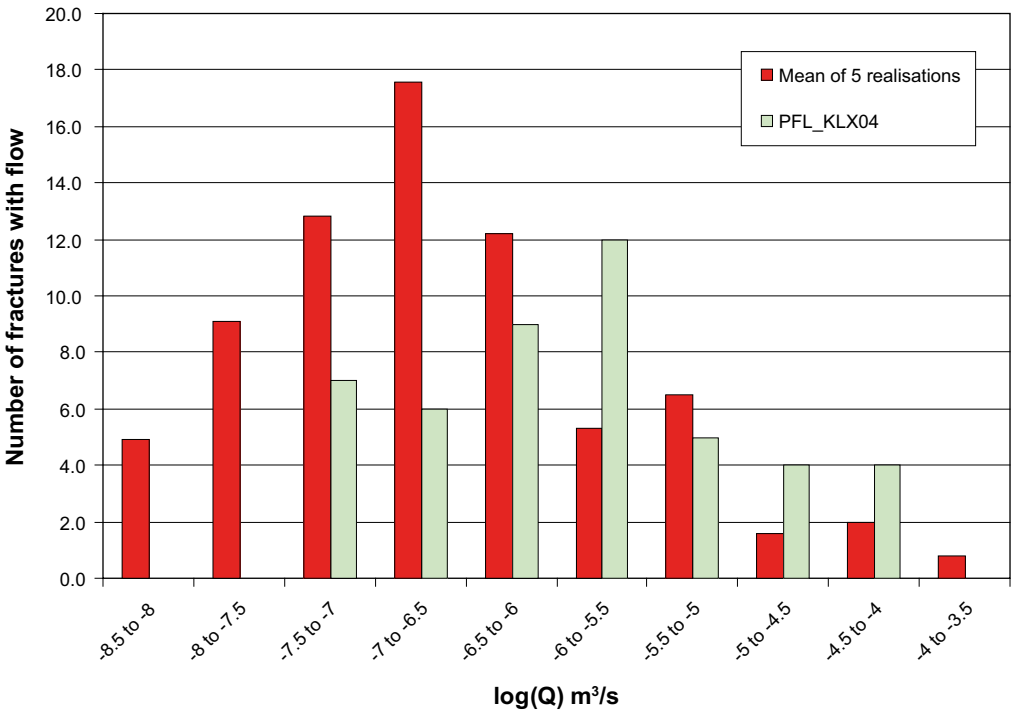

Figure 3-34. *Histogram of Log(Q) flow-rate to borehole, for the mean of five realisations compared to the PFL-anomaly data for KLX04 above –300 m. Here, the semi-correlated T distribution is used from the matched PFL-f and PSS transmissivity with 50% of P32.*

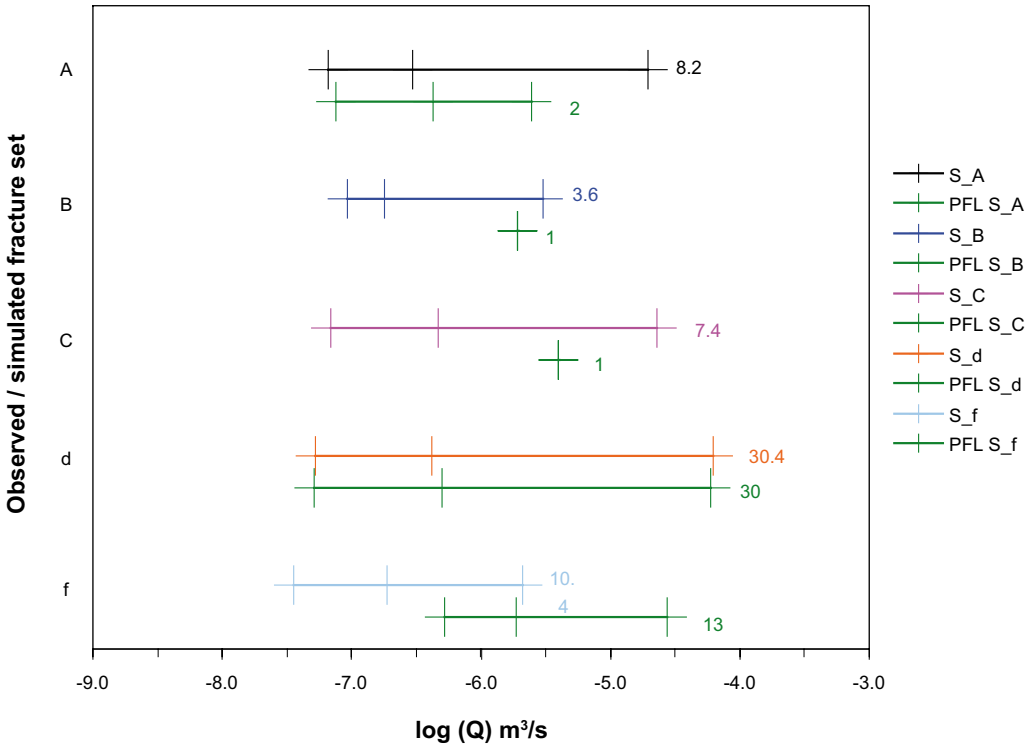

Figure 3-35. *Plot of Log(Q) flow-rate to borehole, for the mean of five realisations compared to the PFL-anomaly data for KLX04 above –300 m. The flow in each fracture set is shown, with vertical bars marking the minimum, median and maximum flow-rates. The number of fractures in the set is given to the right of each plot. Here, the semi-correlated T distribution is used from the matched PFL-f and PSS transmissivity with 50% of P32.*

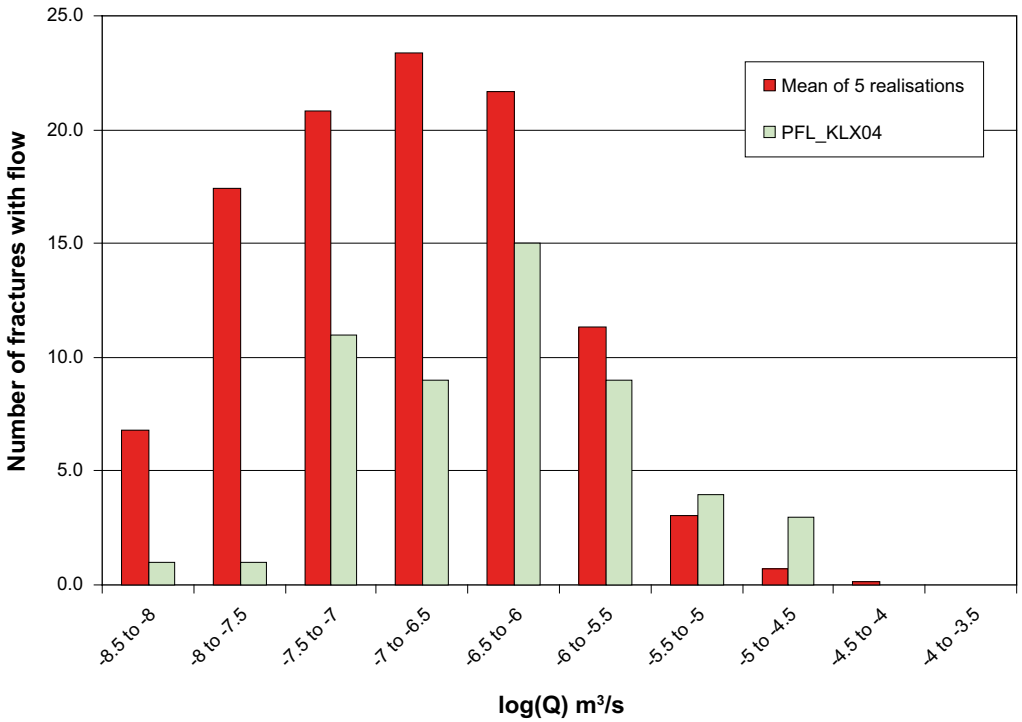

Figure 3-36. *Histogram of Log(Q) flow-rate to borehole, for the mean of five realisations compared to the PFL-anomaly data for KLX04 below –300 m. Here, the uncorrelated T distribution is used from the matched PFL-f and PSS transmissivity with 35% of P32.*

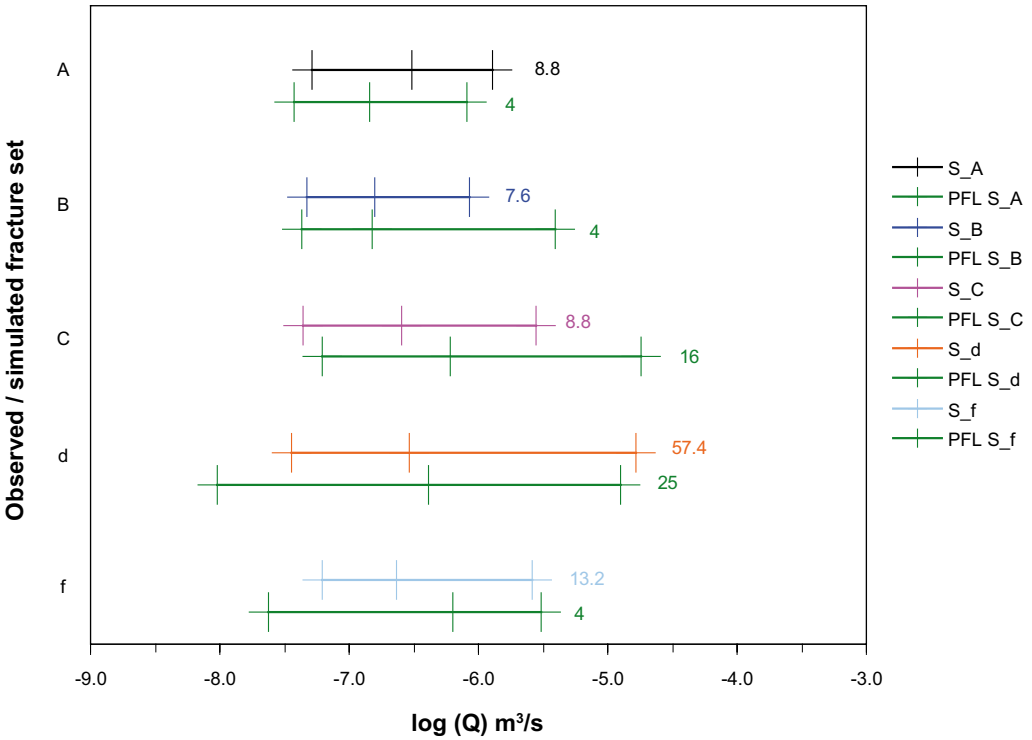

Figure 3-37. *Plot of Log(Q) flow-rate to borehole, for the mean of five realisations compared to the PFL-anomaly data for KLX04 below –300 m. The flow in each fracture set is shown, with vertical bars marking the minimum, median and maximum flow-rates. The number of fractures in the set is given to the right of each plot. Here, the uncorrelated T distribution is used from the matched PFL-f and PSS transmissivity with 35% of P32.*

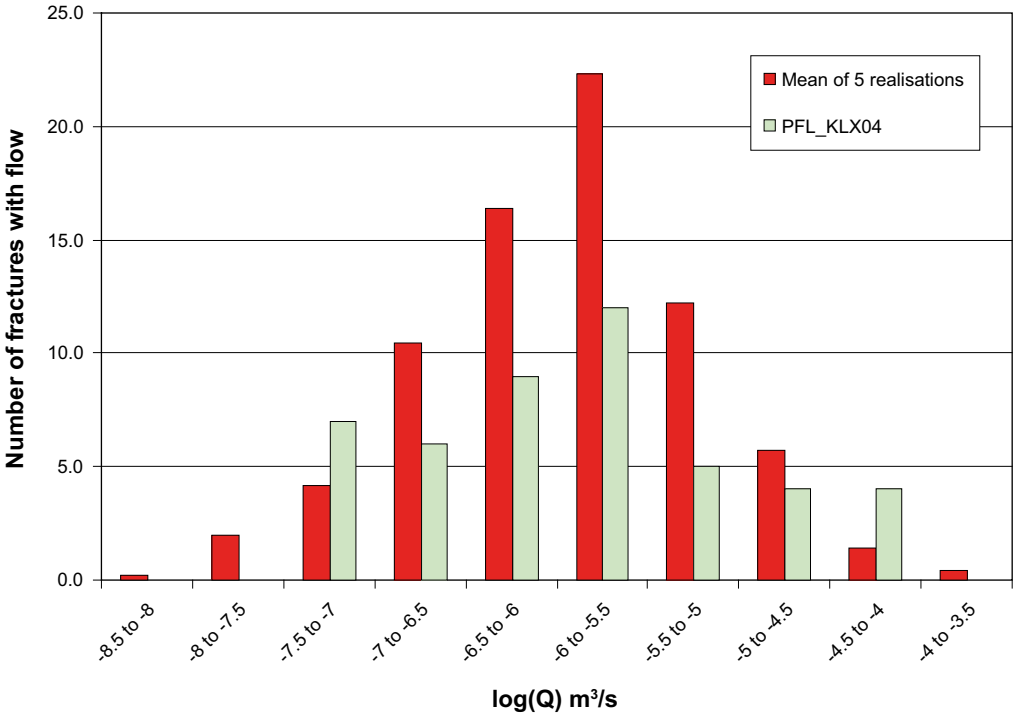

Figure 3-38. *Histogram of Log(Q) flow-rate to borehole, for the mean of five realisations compared to the PFL-anomaly data for KLX04 above –300 m. Here, the uncorrelated T distribution is used from the matched PFL-f and PSS transmissivity with 50% of P32.*

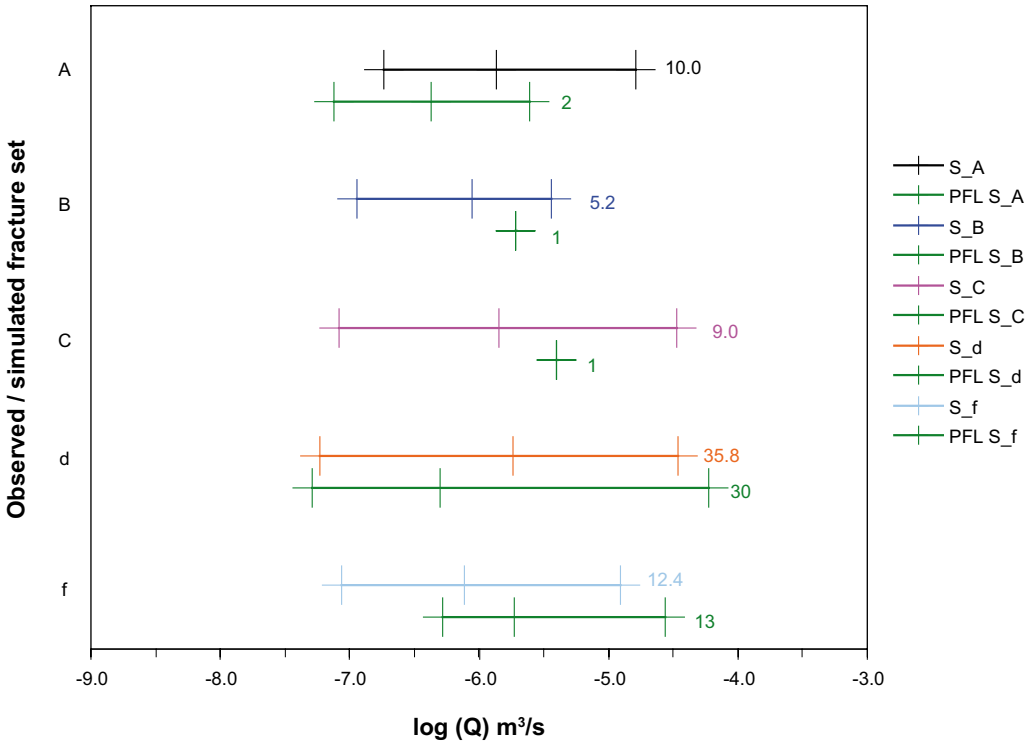

Figure 3-39. *Plot of Log(Q) flow-rate to borehole, for the mean of five realisations compared to the PFL-anomaly data for KLX04 above –300 m. The flow in each fracture set is shown, with vertical bars marking the minimum, median and maximum flow-rates. The number of fractures in the set is given to the right of each plot. Here, the uncorrelated T distribution is used from the matched PFL-f and PSS transmissivity with 50% of P32.*

3.8.2 Sensitivity to anisotropy in transmissivity between fracture sets

Investigations of hydrogeological properties at the Äspö Hard Rock Laboratory /Rhén et al. 1997/ found strong anisotropy in the hydraulic conductivity at depth with about two orders of magnitude higher hydraulic conductivity in the direction WNW-NW compared to NE. The direction of maximum hydraulic conductivity corresponded with the maximum horizontal stress direction, which is similar to the maximum stress direction in the Simpevarp subarea. Therefore, it was considered relevant to perform some preliminary investigations into the possible role of anisotropy in the transmissivity between different fracture sets at Laxemar. Example cases for KLX03 and KLX04 were considered for the semi-correlated T-model. Two scenarios were considered. The first scenario, Anisotropic 1, reduced the transmissivity of Set_A and Set_B by one order of magnitude, while the second, Anisotropic 2, considered an increase in transmissivity of Set_C by one order of magnitude in addition to the reduction in transmissivity of Set_A and Set_B by one order of magnitude. The basis for these scenarios comes from a consideration of all the boreholes analysed as discussed in Subsection 3.8.1, not just KLX03 and KLX04. However, we focus on KLX03 and KLX04 as these are used to guide groundwater flow modelling around the potential repository area.

A comparison is made between the simulated cases and the PFL-f data in Table 3-16 for the sections of KLX04 below and above –300 m elevation. Due to large variations between realiations for the semi-corrleated transmissivity model, 10 realisations were performed for each case. For each section and each set, the numbers of fractures with flows above the detection limit was recorded along with the total flow in the set. Based on the measured data, a detection limit of $\log_{10}(Q) = -7.5$ m^3s^{-1} was used. The average number of fractures

Table 3-16. Comparison of anisotropy in transmissivity between different fracture sets for KLX04. PFL-f refers to the measured data; Isotropic refers to the semi-correlated base case (mean of 10 realisations); Anisotropic 1 has a reduction of one order of magnitude of transmissivity for Set_A and Set_B (mean of 10 realisations); Anisotropic 2 has an increase in transmissivity of one order of magnitude for Set_C in addition to a reduction of one order of magnitude in transmissivity for Set_A and Set_B (mean of 10 realisations). A detection limit of $\log_{10}(Q) = -7.5$ m^3 s^{-1} has been assumed for the model cases, to match the measured data.

Below –300 m	PFL-f		Isotropic		Anisotropic 1		Anisotropic 2	
	log (Total Q)	N(flow)	log (Total Q)	N(flow)	log (Total Q)	N(flow)	log (Total Q)	N(flow)
Set_A	–5.9	4	–5.5	5	–6.6	1	–6.5	2
Set_B	–5.4	4	–5.7	3	–6.9	1	–6.9	1
Set_C	–4.4	16	–5.5	5	–5.8	4	–5.1	7
Set_d	–4.4	25	–4.4	25	–4.5	20	–4.5	22
Set_f	–5.4	4	–6.2	4	–6.3	3	–6.4	3
Total	–4.0	53	–4.3	42	–4.5	29	–4.3	35
Above –300 m								
Set_A	–5.6	2	–4.5	8	–5.5	5	–5.5	4
Set_B	–5.7	1	–5.2	5	–6.2	2	–6.1	2
Set_C	–5.4	1	–4.9	6	–5.1	6	–4.3	7
Set_d	–3.6	30	–3.8	35	–3.9	29	–3.9	31
Set_f	–4.0	13	–5.4	9	–5.6	8	–5.5	8
Total	–3.5	47	–3.5	63	–3.7	50	–3.6	52

across the realisations was taken as the arithmetic mean, while the total flow was taken as the geometric mean. The table shows that flow to the vertical KLX04 borehole is dominated by the sub-horizontal Set_d and the associated Set_f. In fact, making a distinction between Set_d and Set_f based on hard sectors is probably unhelpful for this analysis, and they could be merged into a single sub-horizontal set. The numbers of features and flow magnitude from the sub-vertical sets is generally small, apart from Set_C in the lower section of KLX04. This is associated with the feature between –540 m and –605 m not identified in the single-hole interpretations. One notable point is that making order of magnitude changes to the transmissivity in the chosen sets only affects the total flow by at most 0.2 in log-space. This weak sensitivity to anisotropy in the simulations makes it hard to calibrate variations in transmissivity between sets. Further, the numbers of flowing features modelled in Set_A, Set_B and Set_C are small, making it hard to make meaningful statistical comparisons. Hence, it is difficult to promote one variant over another with certainty without data from boreholes in other orientations.

Anyhow, for the upper section of the borehole, the Anisotropy 1 model seems to give an improvement in predicting the low numbers of PFL-anomalies and flow in Set_A and Set_B. For the lower section, the reduction in Set_A and Set_B is perhaps too much, and the increase in Set_C too little. As mentioned before, the feature between –540 m and –605 m is associated with Set_C and makes matching of this section difficult. The results for the two anisotropic cases suggest that the changes to Set_A and Set_B almost completely remove flow from these sets. This is interesting because this is the observation made in KLX03, as shown in Table 3-17. There are no flow-anomalies in these sets for the lower section of KLX03, and only 1 anomaly in each set for the upper section. The Anisotropic 2 case provides the better match the lower section of KLX03, and the Anisotropic 1 case for the upper section.

Table 3-17. Comparison of anisotropy in transmissivity between different fracture sets for KLX03. PFL-f refers to the measured data; Isotropic refers to the semi-correlated base case (mean of 10 realisations); Anisotropic 1 has a reduction of one order of magnitude of transmissivity for Set_A and Set_B (mean of 10 realisations); Anisotropic 2 has an increase in transmissivity of one order of magnitude for Set_C in addition to a reduction of one order of magnitude in transmissivity for Set_A and Set_B (mean of 10 realisations). A detection limit of $\log_{10}(Q) = -7.5$ m^3s^{-1} has been assumed for the model cases, to match the measured data.

Below –300 m	PFL-f		Isotropic		Anisotropic 1		Anisotropic 2	
	log (Total Q)	N(flow)	log (Total Q)	N(flow)	log (Total Q)	N(flow)	log (Total Q)	N(flow)
Set_A	N/A	0	–6.2	2	–7.1	2	–7.1	2
Set_B	N/A	0	–6.4	1	–7.1	0	–7.3	0
Set_C	–5.4	6	–6.0	2	–6.2	2	–5.4	2
Set_d	–5.2	11	–4.6	15	–4.9	13	–4.7	13
Set_f	–5.4	2	–6.9	1	–7.7	1	–7.7	1
Total	–4.8	19	–4.5	21	–4.6	18	–4.5	18
Above –300 m								
Set_A	–6.7	1	–5.3	3	–6.3	2	–6.2	2
Set_B	–7.4	1	–6.6	3	–7.5	2	–7.4	2
Set_C	–6.3	4	–5.8	3	–6.0	3	–5.2	3
Set_d	–3.88	19	–4.0	20	–4.1	18	–4.0	19
Set_f	N/A	0	–7.5	1	–7.3	0	–7.1	0
Total	–3.8	25	–3.6	30	–3.8	25	–3.5	18

The results for the two anisotropic cases suggest that the reduction in transmissivity in Set_A and Set_B is reasonable, while the increase in transmissivity in Set_C gives some improvement to the match in the lower sections of KLX03 and KLX04.

These results are tentative given the data available for Laxemar v 1.2. However, the anisotropy variants considered here show some possibility to give an improved match to the PFL-f data, and it is recommended that the effects of anisotropy between the fracture sets be considered in the regional-scale flow modelling later in this report to scope its effect on larger scale flows.

3.8.3 Conclusions

For KLX04, the transmissivity distributions given by the PSS and PFL-f data for the bed-rock section below –300 m indicate a bi-modal type behaviour. Plotting the data against elevation shows that the high values are clustered within specific sections of the borehole. Some of these are within deterministic deformations, but the highest flows occur just outside the single-hole interpretations of the RVS deformation zones. In addition, the high flows around –540 m and –605 m are not associated with any interpreted deformation zone. To match the total flow using the correlated and semi-correlated simulation cases, the simulated flow distribution must include higher flows than those observed in the PFL-f data. As a result, the match between simulations and PFL-f/PSS data for the distribution of flow is poor for the higher flows although the total flow is a good match. For the section above –300 m, a good match between the simulations and PFL-f/PSS data is achieved.

The results for the two anisotropic cases considered for KLX03 and KLX04 suggest that a reduction in transmissivity in Set_A and Set_B. The PFL-f data suggests that there is very little flow in Set_A and Set_B. The isotropic case over-predicts the flow-rates in the sets.

A reduction in transmissivity in Set_A and Set_B of about 0.5–1.0 orders of magnitude improves the model overall. The simulations under-predict flow in Set_C for the lower parts of KLX03 and KLX04. An increase in transmissivity by one order of magnitude in Set_C gives some improvement in the lower sections of KLX03 and KLX04, if on the low side.

For KSH01A, for the section below –300 m, the simulations predict higher flow-rates than the PFL-f data. However, the simulated flow-rate distribution for the section above –300 m is a reasonable match to the PFL-f data. For both the upper and lower sections of KSH01A, the simulations over-predict the flow rates in Set_d and Set_A.

For KAV04A, the simulated flow-rate distribution is reasonably well matched against the PFL flow anomalies. For the section below –300 m the simulations are reasonable in predicting higher flows for Set_A and Set_d. However, flow-rates in Set_B and Set_C are over-predicted. The simulations for the section above –300 m, the flow-rate in Set_C is over-predicted.

3.9 Simulated outcrops and P21 for Laxemar subarea

DFN models were set up to simulate the detailed fracture mapping outcrops ASM000209 and ASM000208 in Laxemar subarea. Each outcrop was simulated by taking a horizontal slice through a DFN model with a rectangular horizontal cross-sectional area equal to the area of the outcrop. All fractures (open, partly open and sealed) were simulated using model parameters for KLX04 (see Table 3-14) and a minimum fracture radius, r_{min}, of r_0. In subsequent calculations of fracture trace length statistics, traces of length less than 0.5 m were excluded since this is the minimum trace length recorded in the outcrop data.

The outcrop data was analysed using the stereonet program DIPS. For each of the outcrops ASM000209 and ASM000208, the fracture set classification for Laxemar subarea (see Figure 3-5) was used in DIPS to assign fracture traces to the fracture sets Set_A, Set_B, Set_C, Set_d and Set_f. This analysis was performed to allow fracture trace plots and statistics obtained from the model and the data to be compared. However, inconsistencies between the data and the model in terms of the characteristic features of different sets (e.g. relative size and intensity) are expected, as discussed below.

In the Geo-DFN, analyses were performed for six detailed fracture mapping outcrops, including ASM000209 and ASM000208, in the Laxemar and Simpevarp subareas. For each outcrop, local fracture sets were identified, primarily on the basis of feature orientation. To simplify the orientation model, local outcrop sets with similar strikes were then combined to generate the ‘domain-scale’ orientation model, which defines the fracture sets Set_A, Set_B, Set_C, Set_d, Set_f and Set_e. However, this simplified orientation model may not capture localised phenomena. For example, it is noted in the Geo-DFN report that although Set_f is observed as a weakly defined and diffuse set in most of the outcrops, it has a higher intensity in areas surrounding ASM000209 and makes a very strong showing in ASM000209. This will not be reproduced in the simulations since Set_f, which is local to Laxemar subarea and does not appear in the RVS DZ model, is assigned a relatively low intensity and a fracture size distribution that has a strong bias towards smaller-scale fractures.

Therefore, to compare fracture trace plots and statisitics by fracture set, it would be ideal to revert to the local outcrop sets defined in the Geo-DFN. For outcrop ASM000209, four local outcrop sets are defined in the Geo-DFN. This local set classification can be approximated by combining Set_C and Set_f to form one local set. For outcrop ASM000208, five local outcrop sets are defined in the Geo-DFN. However, although Set_A corresponds roughly

to a local outcrop set, the remaining local outcrop sets cannot be matched by combining 'domain-scale' fracture sets. Therefore, for this outcrop, the fracture trace plots and statistics obtained from the model and the data for each individual set (except for Set_A) are not expected to compare very well.

The model and the fracture trace plot for outcrop ASM000209 are illustrated in Figure 3-40 for all fracture orientations and Figure 3-41 for individual fracture sets. Note that for the DFN model plots, fracture traces with lengths less than 0.5 m have not been excluded. Even so, these plots indicate that the model over-represents the number of fracture traces in all sets except Set_B, although under-representation of the sub-horizontal set Set_d in the outcrop data is expected. It is noted that this outcrop is located on the edge of the mixed rock domain in the south of the Laxemar subarea which has lower fracture intensity, and so a comparison with the Hydro-DFN defined for KLX03 might be more conistent. For outcrop ASM000208, the model and the fracture trace plot for all fracture orientations are shown in Figure 3-42. This also shows that the model over-represents the intensity of fracture traces.

Fracture trace statistics for ASM000209 and ASM000208 are summarised in Table 3-18 and Table 3-19 respectively. The simulated P21 values are significantly higher than the P21 values calculated from the data. This is partly due to under-representation of sub-horizontal fractures (Set_d) in the data. However, the Hydro-DFN model has been defined on the basis of a 'domain-scale' orientation model and the data for one borehole, KLX04, and so should not necessarily be expected to capture localised phenomena observed on the outcrop scale.

Table 3-18. Outcrop ASM000209: Summary of fracture trace statistics obtained from the data and from the DFN model.

Fracture set	Fracture count		Fracture trace length (m)						P21 (m m^{-2})	
			Max		Mean		S.D.			
	Model	Data	Model	Data	Model	Data	Model	Data	Model	Data
Set_A	518	228	13.8	3.9	1.2	1.1	1.3	0.6	1.4	0.6
Set_B	616	319	16.5	12.2	1.1	1.6	1.3	1.5	1.5	1.2
Set_C and Set_f	1,055	431	13.7	9.5	1.2	1.4	1.0	1.0	2.7	1.3
Set_d	508	52	8.5	1.8	1.1	0.9	1.0	0.3	1.3	0.1
All sets	2,697	1,030	16.5	12.2	1.1	1.4	1.1	1.1	6.9	3.2

Table 3-19. Outcrop ASM000208: Summary of fracture trace statistics obtained from the data and from the DFN model.

Fracture set	Fracture count		Fracture trace length (m)						P21 (m m^{-2})	
			Max		Mean		S.D.			
	Model	Data	Model	Data	Model	Data	Model	Data	Model	Data
Set_A	371	381	11.8	7.0	1.1	1.3	1.2	0.8	1.3	1.5
Set_B	467	155	17.7	5.5	1.1	1.4	1.4	1.0	1.6	0.6
Set_C	413	108	8.6	7.8	1.1	1.1	0.9	0.8	1.4	0.4
Set_d	363	283	8.0	5.2	1.1	1.1	1.0	0.6	1.3	0.9
Set_f	388	126	7.6	7.0	1.1	1.4	0.7	1.0	1.3	0.5
All sets	2,002	1,053	17.7	7.8	1.1	1.2	1.1	0.8	6.8	3.9

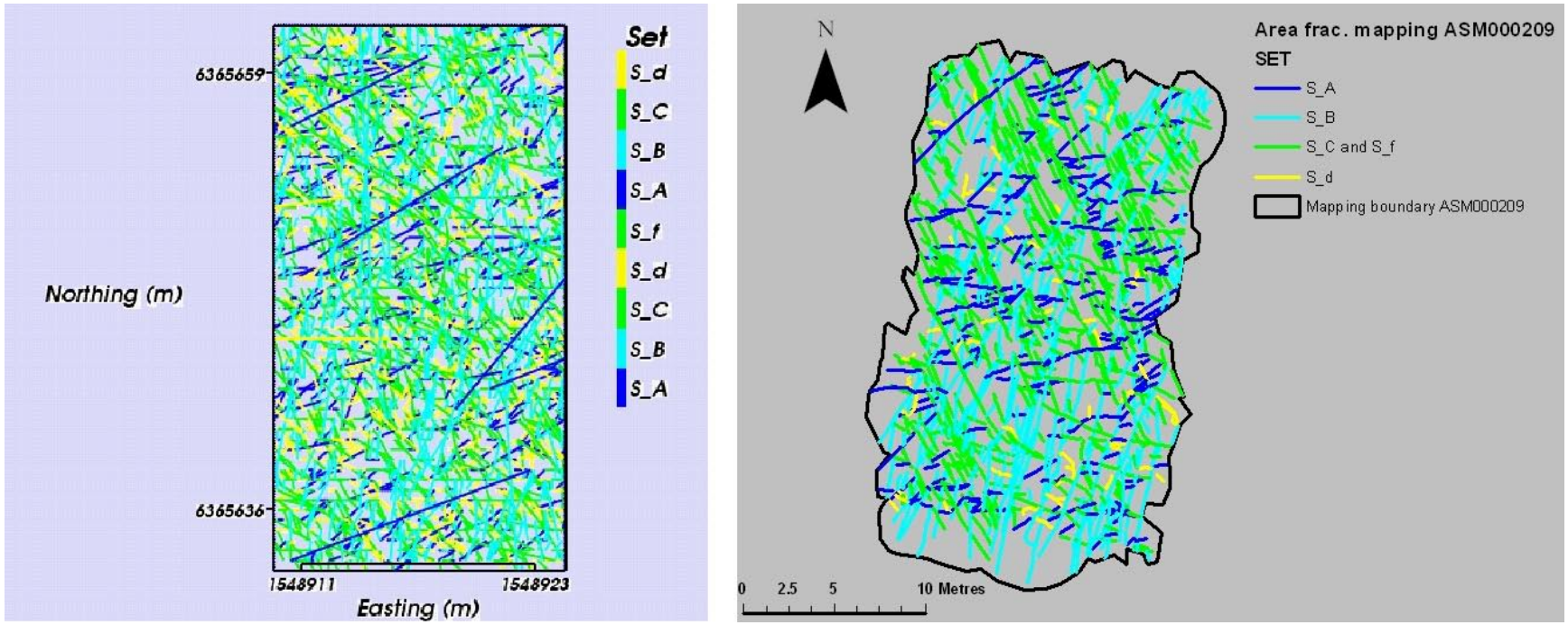

Figure 3-40. *Outcrop ASM000209: Horizontal slice through the Hydro-DFN model using the 'k_r fit' parameters (left), and trace plot for the outcrop (right). Fracture traces on the horizontal slice are coloured according to fracture set as defined in the model: S_A (global set Set_A), S_B (global set Set_B), S_C (global set Set_C), S_d (sub-horizontal set Set_d), S_f (local set Set_f). S_C and S_f have been combined here to match the classification of local sets for this outcrop as defined in the Geo-DFN. In the legend for the left-hand figure, each fracture set (except S_f) appears twice because each was defined for two size ranges (0.28 m to 5.6 m and 5.6 m to 562 m). S_f only appears once because it contains no fractures with radii in the upper range 5.6 m to 562 m. Note that the outcrop model plot (left) includes traces with length less than 0.5 m, whilst the minimum trace length in the outcrop trace plot (right) is 0.5 m.*

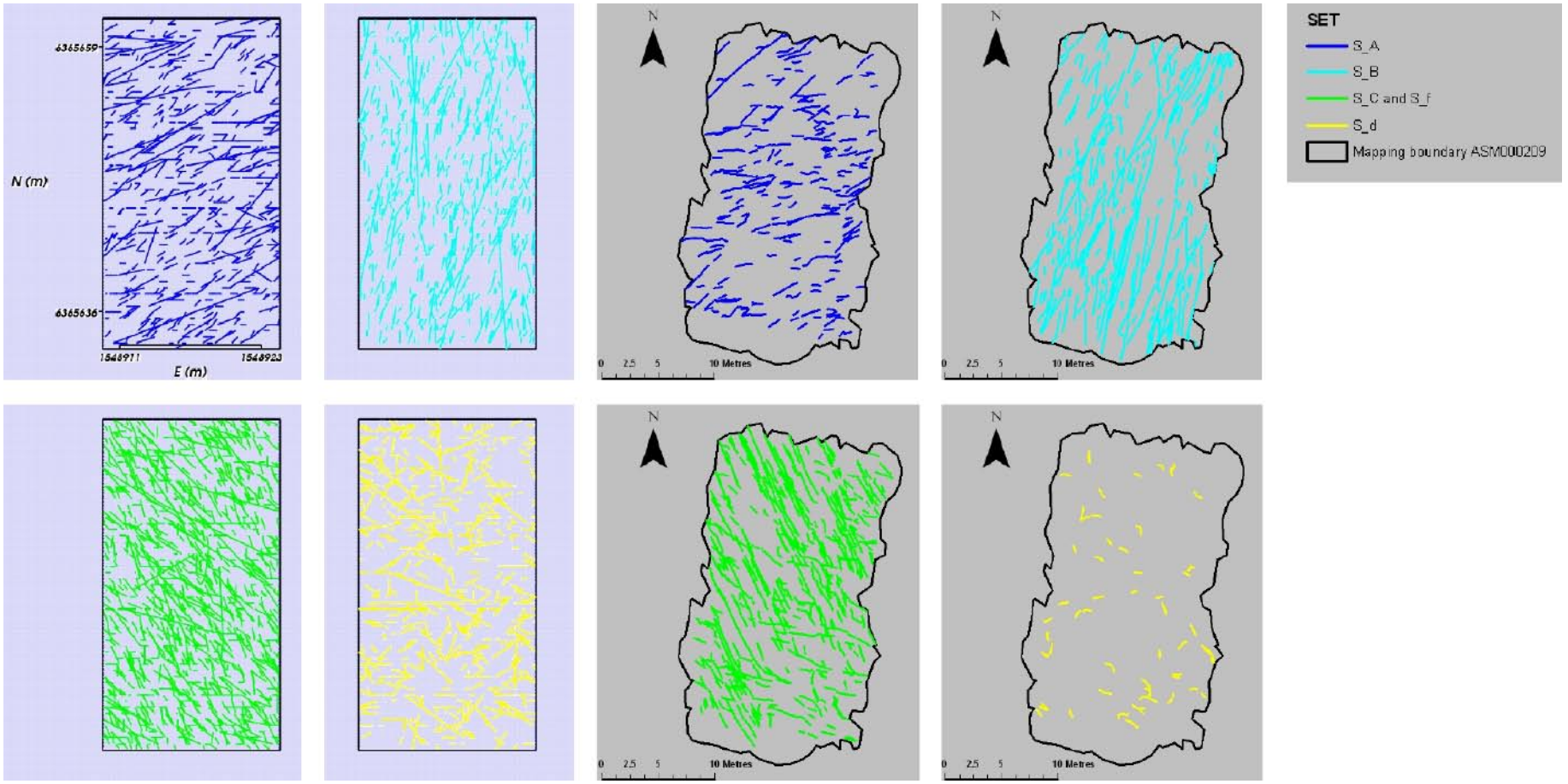

Figure 3-41. *Outcrop ASM000209: Fracture traces on horizontal slices through the Hydro-DFN model using the 'k_r fit' parameters (left), and trace plots for outcrop ASM000209 (right). Note that the outcrop model plots (left) include traces with length less than 0.5 m, whilst the minimum trace length in the outcrop trace plots (right) is 0.5 m.*

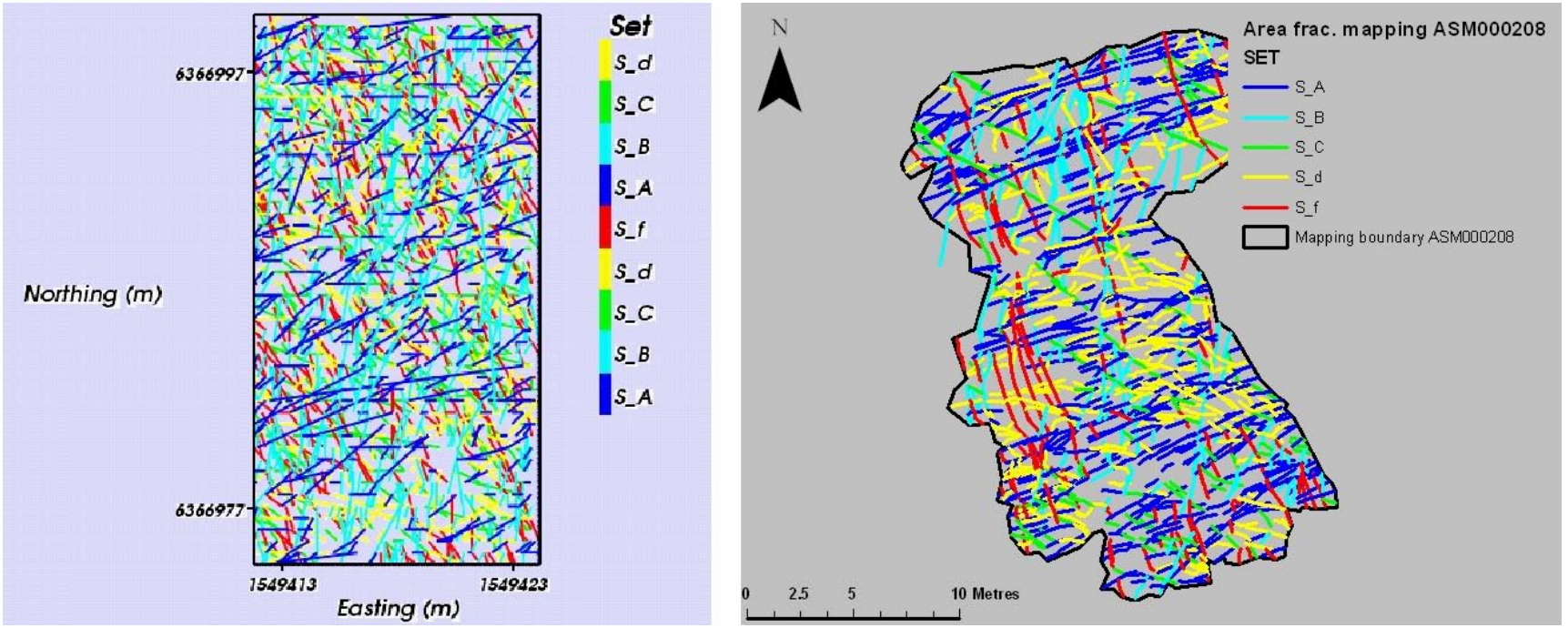

Figure 3-42. *Outcrop ASM000208: Horizontal slice through the Hydro-DFN model using the 'k_r fit' parameters (left), and trace plot for the outcrop (right). Fracture traces on the horizontal slice are coloured according to fracture set as defined in the model: S_A (global set Set_A), S_B (global set Set_B), S_C (global set Set_C), S_d (sub-horizontal set Set_d), S_f (local set Set_f). In the legend for the left-hand figure, each fracture set (except S_f) appears twice because each was defined for two size ranges (0.28 m to 5.6 m and 5.6 m to 562 m). S_f only appears once because it contains no fractures with radii in the upper range 5.6 m to 562 m. Note that the outcrop model plot (left) includes traces with length less than 0.5 m, whilst the minimum trace length in the outcrop trace plot (right) is 0.5 m.*

3.10 Checking the connectivity of the fracture network for KLX04

The connectivity of the fracture network resulting from the use of the 'k_r fit' parameter values (r_0, k_r) and the scaled P32 determined by conditioning the transmissivity against PFL-f and PSS data was assessed by calculating 'P32 connected' ($P32_c$) values (an example for KLX04 is shown in Table 3-20). These $P32_c$ quantities will be used to guide the choice of value used for the flow-wetted-surface parameter in the regional modelling (see Subsection 5.10.2). One realisation was performed using the scaled P32 determined as the best match in conditioning the transmissivity for each borehole. Fracture radii between r_0 and 564 m were generated over the whole model domain; a 100×100×100 m model region was defined. The intersections between fractures and between fractures and the domain boundary were then calculated. All isolated fractures, i.e. those without any connection to the boundary, were removed and the P32 of the remaining network was calculated to give a 'P32 connected'. The results are summarised in Table 3-20.

Table 3-20. Model input P32 and connected $P32_c$ for Laxemar KLX04 DFN model.

Case	Input P32	$P32_c$	% connected
'k_r fit above –300 m elevation'	1.70	1.51	86%
'k_r fit below –300 m elevation'	1.19	0.87	71%

3.11 Model parameters of the Hydro-DFN models with uncertainties

To recapitulate, Table 3-21 lists the sources of data used in deriving and conditioning the Hydro-DFN, and indicates the purpose to which each type of data is put.

In order to aid design issues, calculations of block properties such as hydraulic conductivity are required over the whole Oskarsham area. Hence, a Hydro-DFN model needs to be derived that captures the broad features of each subarea, but not necessarily all the localised characteristics of particular boreholes. It was assumed that the three proposed transmissivity models can be used as alternative cases with the parameterisation derived from the analysis of the PFL-f and PSS data.

Table 3-21. Summary of data usage in deriving the Hydro-DFN.

Data	Hydro-DFN Usage
Geo-DFN model	Classification of fracture sets; fracture orientation distributions; open fracture intensities for rock domains; relative fracture intensity of each set for open fractures; fracture intensity initial guess for intensity of flow conducting fractures.
RVS Deformation zones	Derivation of P32 for fractures larger than r = 560 m used in fitting values for k_r for sub-vertical sets.
Outcrop data (ASM000208 and ASM000209)	Checking P21 for sets on a horizontal slice.
PFL-f data	Conditioning simulations of radial flow to borehole (total flux and distribution of Qs); numbers of PFL-anomaly in each set for conditioning flows as divided by set and studying anisotropy; lumping interpreted T values into 5 m intervals to check conditioning on PSS 5 m intervals.
PSS 5 m interval interpreted T values	Conditioning P32 of flow conducting fractures against numbers of 5 m intervals without flow; distribution of T for 5 m intervals.

3.11.1 Model parameters

On the basis of the above assumptions, Hydro-DFN base case parameters for Laxemar subarea were derived for KLX04 and KLX03. For the Simpevarp subarea, Hydro-DFN base case parameters were derived for KSH01A and KAV04A/B.

Three transmissivity models were considered. Summary tables of 'k_r fit' parameter values for KLX04, KLX03, KSH01A and KAV04A matched to hydraulic data are presented below in Table 3-22 to Table 3-25. The fracture orientation parameters are taken directly from the Geo-DFN. For fracture intensity, the mean P32 values for open fractures given in the Geo-DFN (where fractures labelled as open or partly open in borehole data were considered to be open fractures) were reduced to achieve a match to the hydraulic data and so the resulting P32 values are expressed as a percentage of the Geo-DFN mean P32 values.

Based on the studies of anisotropy in Subsection 3.8.2, a variant is included in Table 3-26 for the Hydro-DFN in Rock Domain A based on KLX04. The semi-correlated *T* model is used with a reduction in the transmissivity of fracture sets Set_A and Set_B by a factor of 10. For the regional modelling described in Chapters 5–9, anisotropy in transmissivity was introduced in the same way for all the underlying Hydro-DFN models. In addition, a variant in which the transmissivity of fracture set Set_C is increased by an order of magnitude is also recommended when quantifying the effects of uncertainty.

Table 3-22. Description of the Hydro-DFN input parameters using the 'k_r fit' parameters for KLX04 matched to all hydraulic data (Rock Domain A), with all other parameters taken from the Geo-DFN. The recommended transmissivity model is highlighted in bold.

Fracture set name	Orientation set pole: (trend, plunge), concentration	Fracture radius model power-law (r_0, k_r)	Intensity P_{32} (m^2/m^3); valid radius interval (r_{min}, r_{max})	Relative intensity of P32	Transmissivity model T (m^2/s)
Set_A	(338.1, 4.5) 13.06	(0.28, 2.73)	Above –300 m: 50% of open = 1.70	0.18	Correlated (above –300 m): *(a,b)* (3.2 10^{-8}, 1.2)
Set_B	(100.4, 0.2) 19.62	(0.28, 2.83)	Below –300 m: 35% of open = 1.19	0.19	Correlated (below –300 m): *(a,b)* (3.2 10^{-9}, 1.2)
Set_C	(212.9, 0.9) 10.46	(0.28, 2.73)	(0.56, 564)	0.19	Uncorrelated (above –300 m): *(μ, σ)* (–6.0, 0.9)
Set_d	(3.3, 62.1) 10.13	(0.28, 2.76)		0.27	Uncorrelated (below –300 m): *(μ, σ)* (–6.7, 0.9)
Set_f	(243, 24.4) 23.52	(0.40, 3.6)		0.17	**Semi-correlated (above –300 m): *(a,b,σ)* (3.5 10^{-8}, 1.0, 0.9)**
					Semi-correlated (below –300 m): *(a,b,σ)* (3.5 10^{-9}, 1.0, 0.9)

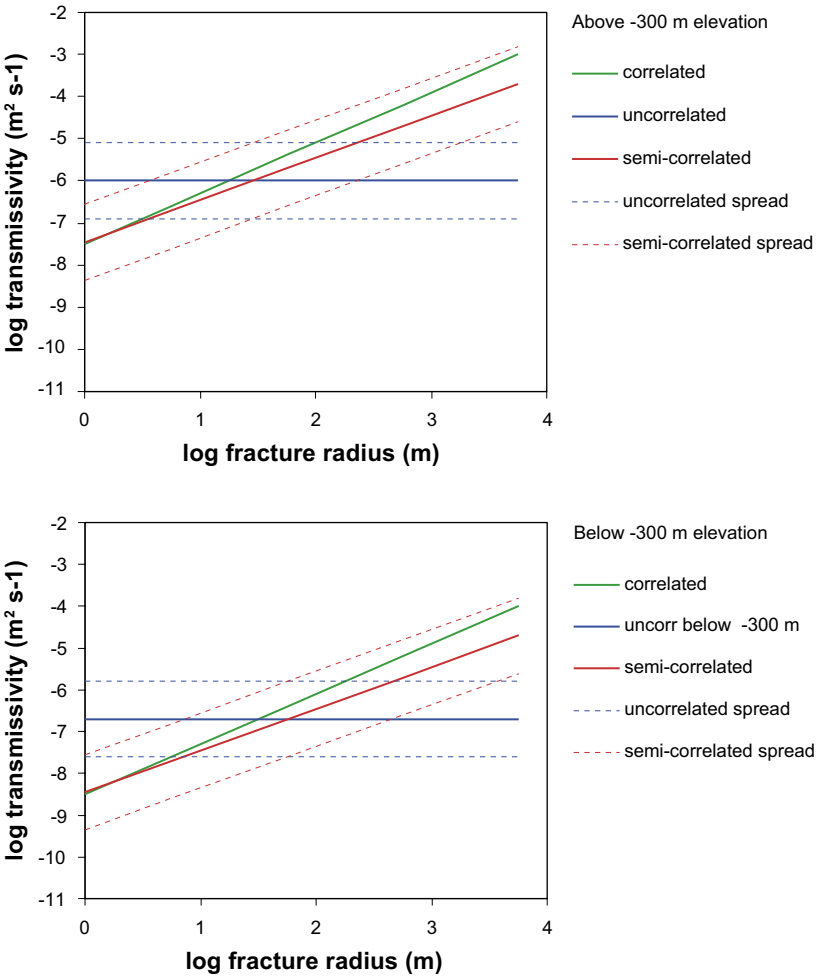

Figure 3-43. *Transmissivity model relationships for KLX04 (Table 3-22). For the uncorrelated and semi-correlated cases, the mean $log_{10}(T)$, μ, and the spread, defined as $\mu \pm \sigma$, where σ is the standard deviation of $log_{10}(T)$, are plotted.*

Table 3-23. Description of the Hydro-DFN input parameters using the 'k_r fit' parameters for KLX03 (Rock Domains: M(A), M(D) and D), with all other parameters taken from the Geo-DFN. The recommended transmissivity model is highlighted in bold.

Fracture set name	Orientation set pole: (trend, plunge), concentration	Fracture radius model power-law (r_0, k_r)	Intensity P_{32} (m^2/m^3); valid radius interval (r_{min}, r_{max})	Relative intensity of P32	Transmissivity model T (m^2/s)
Set_A	(338.1, 4.5) 13.06	(0.28, 2.63)	Above –300 m: 60% of open = 0.84	0.22	Correlated (above –300 m): *(a,b)* (2.0 10^{-8}, 1.2)
Set_B	(100.4, 0.2) 19.62	(0.28, 2.68)	Below –300 m: 30% of open = 0.42	0.15	Correlated (below –300 m): *(a,b)* (2.0 10^{-9}, 1.0)
Set_C	(212.9, 0.9) 10.46	(0.28, 2.59)	(0.56, 564)	0.17	Uncorrelated (above –300 m): *(μ, σ)* (–6.4, 1.3)
Set_d	(3.3, 62.1) 10.13	(0.28, 2.63)		0.36	Uncorrelated (below –300 m): *(μ, σ)* (–7.0, 1.3)
Set_f	(243, 24.4) 23.52	(0.40, 3.6)		0.09	**Semi-correlated (above –300 m): *(a,b,σ)* (1.8 10^{-8}, 1.0, 0.9)**
					Semi-correlated (below –300 m): *(a,b,σ)* (3.5 10^{-9}, 1.0, 0.9)

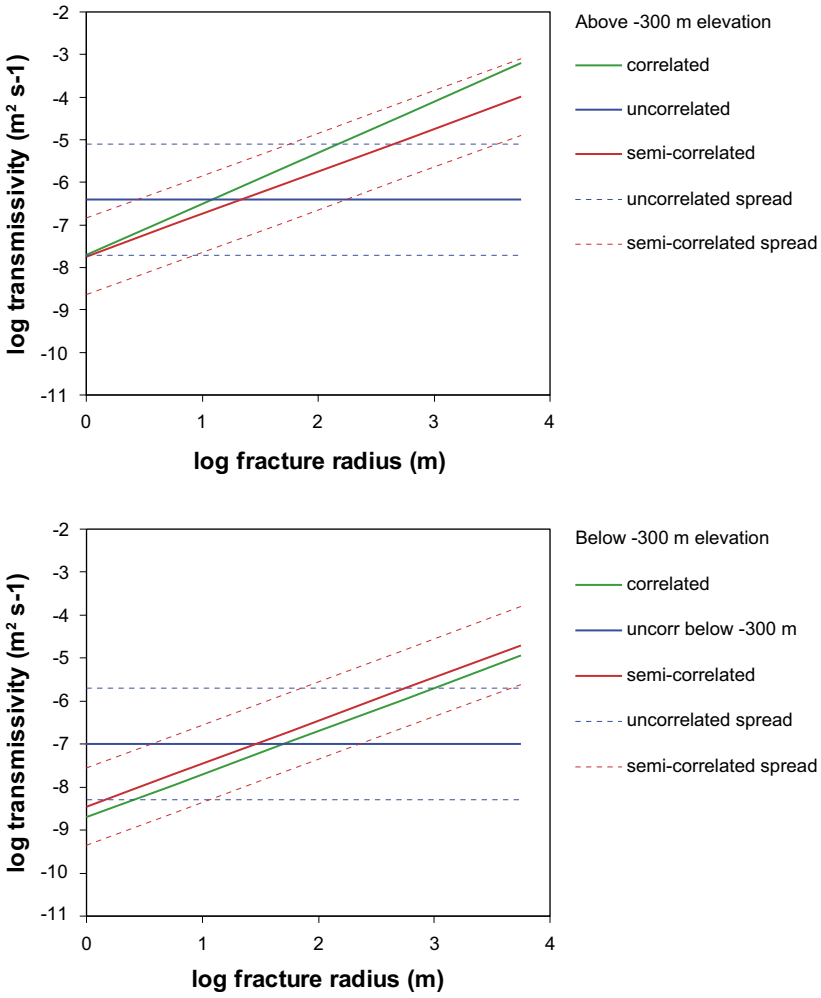

Figure 3-44. *Transmissivity model relationships for KLX03 (Table 3-23). For the uncorrelated and semi-correlated cases, the mean $log_{10}(T)$, μ, and the spread, defined as $\mu \pm \sigma$, where σ is the standard deviation of $log_{10}(T)$, are plotted.*

Table 3-24. Description of the Hydro-DFN input parameters using the 'k$_r$ fit' parameters for KSH01A (Rock Domains: B and C), with all other input parameters taken from the Geo-DFN. The recommended transmissivity model is highlighted in bold.

Fracture set name	Orientation set pole: (trend, plunge), concentration	Fracture radius model power-law (r_0, k_r)	Intensity P_{32} (m^2/m^3); valid radius interval (r_{min}, r_{max})	Relative intensity of P32	Transmissivity model T (m^2/s)
Set_A	(330.3, 6.1) 16.80	(0.28, 2.77)	Above –300 m: 27% of open = 1.40	0.24	Correlated (above –300 m): *(a,b)* (5.3 10^{-8}, 1.0)
Set_B	(284.6, 0.6) 10.78	(0.28, 2.91)	Below –300 m: 27% of open = 1.40	0.15	Correlated (below –300 m): *(a,b)* (1.2 10^{-10}, 1.0)
Set_C	(201.8, 3.7) 14.60	(0.28, 2.92)	(0.56, 564)	0.26	Uncorrelated (above –300 m): *(μ, σ)* (–6.5, 1.0)
Set_d	(84.6, 81.8) 6.98	(0.28, 2.87)		0.26	Uncorrelated (below –300 m): *(μ, σ)* (–8.7, 1.0)
Set_f	(67.1, 15.5) 11.73	(0.21, 3.27)		0.10	**Semi-correlated (above –300 m): *(a,b,σ)* (1.4 10^{-8}, 1.2, 0.9)**
					Semi-correlated (below –300 m): *(a,b,σ)* (1.6 10^{-10}, 0.8, 0.9)

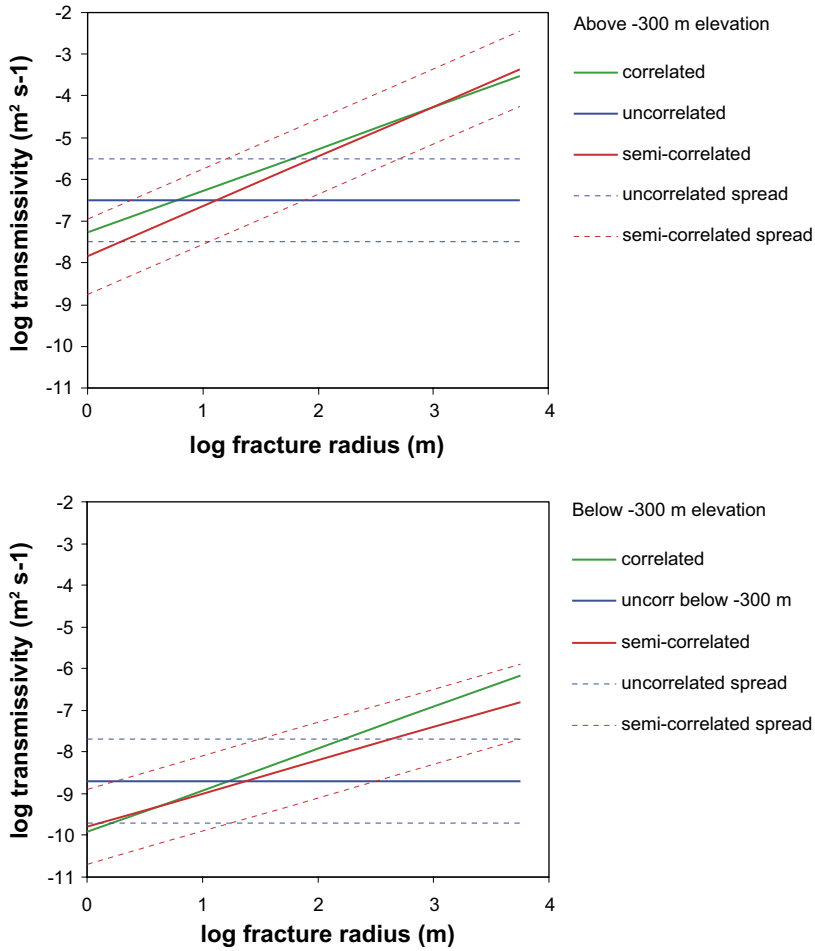

Figure 3-45. *Transmissivity model relationships for KSH01A (Table 3-24). For the uncorrelated and semi-correlated cases, the mean $log_{10}(T)$, μ, and the spread, defined as $\mu \pm \sigma$, where σ is the standard deviation of $log_{10}(T)$, are plotted.*

Table 3-25. Description of the Hydro-DFN input parameters using the 'k_r fit' parameters for KAV04A (Rock Domains: A and C around Ävrö and Äspö), with all other input parameters taken from the Geo-DFN. The recommended transmissivity model is highlighted in bold.

Fracture set name	Orientation set pole: (trend, plunge), concentration	Fracture radius model power-law (r_0, k_r)	Intensity P_{32} (m^2/m^3); valid radius interval (r_{min}, r_{max})	Relative intensity of P32	Transmissivity model T (m^2/s)
Set_A	(330.3, 6.1) 16.80	(0.28, 2.78)	Above –300 m: 28% of open = 1.43	0.24	Correlated (above –300 m): *(a,b)* (5.3 10^{-8}, 1.0)
Set_B	(284.6, 0.6) 10.78	(0.28, 2.87)	Below –300 m: 22% of open = 1.13	0.16	Correlated (below –300 m): *(a,b)* (3.5 10^{-8}, 1.0)
Set_C	(201.8, 3.7) 14.60	(0.28, 2.90)	(0.56, 564)	0.22	Uncorrelated (above –300 m): *(μ, σ)* (–6.3, 1.0)
Set_d	(84.6, 81.8) 6.98	(0.28, 2.85)		0.27	Uncorrelated (below –300 m): *(μ, σ)* (–6.1, 0.8)
Set_f	(67.1, 15.5) 11.73	(0.21, 3.27)		0.11	**Semi-correlated (above –300 m): *(a,b,σ)* (4.5 10^{-8}, 0.7, 0.9)**
					Semi-correlated (below –300 m): *(a,b,σ)* (7.5 10^{-8}, 0.7, 0.9)

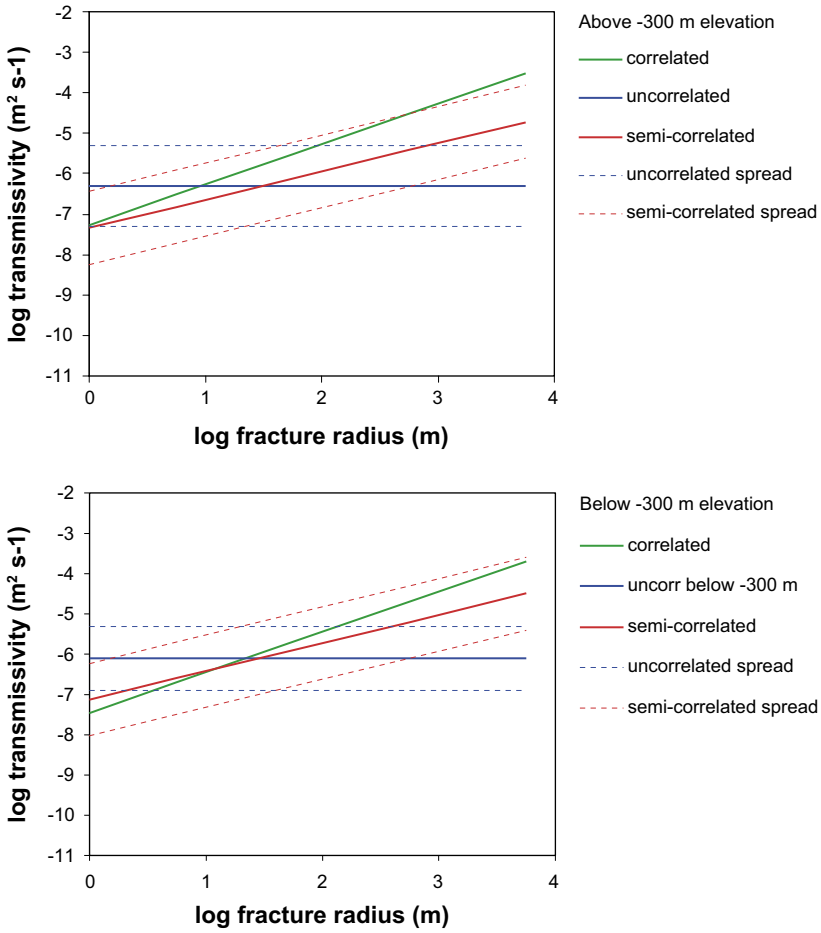

Figure 3-46. *Transmissivity model relationships for KAV04A (Table 3-25). For the uncorrelated and semi-correlated cases, the mean $log_{10}(T)$, μ, and the spread, defined as $\mu \pm \sigma$, where σ is the standard deviation of $log_{10}(T)$, are plotted.*

Table 3-26. Anisotropy of transmissivity between fracture sets: Description of the Hydro-DFN variant case input parameters using the 'k_r fit' parameters for KLX04 matched to all hydraulic data (Rock Domain A), with all other parameters taken from the Geo-DFN.

Fracture set name	Orientation set pole: (trend, plunge), concentration	Fracture radius model power-law (r_0, k_r)	Intensity P_{32} (m^2/m^3); valid radius interval (r_{min}, r_{max})	Relative intensity of P32	Semi-correlated transmissivity model parameters *(a,b,σ)*
Set_A	(338.1, 4.5) 13.06	(0.28, 2.73)	Above –300 m: 50% of open = 1.70	0.18	(3.5 10^{-9}, 1.0, 0.9) z > –300 (3.5 10^{-10}, 1.0, 0.9) z < –300
Set_B	(100.4, 0.2) 19.62	(0.28, 2.83)	Below –300 m: 35% of open = 1.19	0.19	
Set_C	(212.9, 0.9) 10.46	(0.28, 2.73)	(0.56, 564)	0.19	(3.5 10^{-8}, 1.0, 0.9) z > –300 (3.5 10^{-9}, 1.0, 0.9) z < –300
Set_d	(3.3, 62.1) 10.13	(0.28, 2.76)		0.27	
Set_f	(243, 24.4) 23.52	(0.40, 3.6)		0.17	

3.11.2 Evaluation of uncertainties

The key uncertainties in the Hydro-DFN model and the manner in which they have been addressed are summarised below.

- The correlation between transmissivity and size. This has been addressed here by considering three alternative transmissivity models.
- Extrapolation of borehole data. The spatial variability between boreholes means the uncertainty in how representative it is to extrapolate a single borehole to an entire rock domain needs to be quantified. For example, comparing KLX04 in the Ävrö granite with more recent data since the L1.2 data freeze from KLX08 would suggest that the values might be about half an order of magnitude too high compared to the bedrock away from large deformation zones. It is difficult to address this question directly until more boreholes have been analysed so as to make a statistical analysis meaningful. However, some progress can be made by testing the validity of block-scale hydraulic properties derived from the Hydro-DFN in the regional groundwater flow modelling that follows in Chapters 5–9. There, simulations of palaeo-hydrogeology of the Holocene period (last ten thousand years) are used to test whether our understanding of site conditions and model parameters can result in predictions of the present-day hydrogeochemistry that are consistent with site data from boreholes. If the hydraulic properties predicted by the Hydro-DFN results in models that are inconsistent with the site hydrogeochemistry, it indicates that the boreholes analysed here may not be representative of the general charcateristics of bedrock fracturing.
- Anisotropy in transmissivity between fracture sets. The PFL-f data gives some indication that the sub-vertical sets Set_A and Set_B are 0.5 to 1.0 orders of magnitude lower in transmissivity than Set_C and Set_d. Further, Set_C could have transmissivity 0.5 to 1.0 orders of magnitude higher than Set_d. At the moment these results are speculative being based on an analysis of KLX04 only. However, it should be understood that we may have under-estimated the importance of anisotropy in opting for a simplified model with the same transmissivity relationships for all sets. A preliminary investigation has been carried out to consider anisotropy in transmissivity between fracture sets in KLX04, but it is recommended that more consideration be given in the future to hydraulic anisotropy between fracture sets when analysing PFL-f data from additional boreholes. Also, the quantity of flow data from sub-vertical fractures is limited in vertical boreholes such as KLX04. The use of inclined boreholes with different trends may inform more on the anisotropy between sets. Again, with the current data it is difficult to establish the importance of anisotropy, but regional modelling can be used to quantify its effect on groundwater flow and chemical composition. Simulations that considered anisotropy between fracture sets are reported in Chapters 5–9.
- Depth dependency. Because of the consistent difference in flow distributions for the upper and lower parts of the borehole, the intensity of open fractures and the transmissivity parameters were calibrated as independent values for each part. An appropriate choice for the depth of this transition varies from borehole to borehole between about –200 m and –350 m elevation. For simplicity, it was assumed that –300 m elevation was a suitable position for a step change in properties for all boreholes. Hence, the result is a set of best-fit Hydro-DFN parameters calibrated for above and below –300 m elevation. However, it is difficult to establish the importance of the choice of position of the step change at this stage. In addition, hydrogeological data for some boreholes, e.g. KLX04, suggest that a further step change in properties with a depth of transition between –600 m and –700 m may be justified. Regional modelling may be used to test the effect of depth trends on predictions of the present-day hydrogeochemistry. Simulations that include step changes in properties at –200 m elevation and –600 m elevation are reported in Chapters 5–9.

4 Assessment of hydraulic block properties

The objectives for the hydraulic block property task can be summarised as follows:

- Estimate anisotropy and calculate the statistics of the hydraulic conductivity of 100 m and 20 m blocks using the results of the Hydro-DFN modelling work that was specified by an SKB Task Description and is described in Chapter 3 of this report.
- Calculate the statistics of the hydraulic conductivity of 100 m and 20 m blocks.
- Include DFN porosity based on the 'aperture = function(Transmissivity)' relationship from Äspö Task 6
- Evaluate the effects of size-truncation of stochastic features on cell-background properties to motivate the minimum fracture size that can be used in the regional DFN models.

4.1 Methodology

To calculate Equivalent Continuum Porous Medium (ECPM) block properties (directional hydraulic conductivity and porosity) based on an underlying DFN model, the following modelling steps are performed:

1. A fracture network is calculated stochastically by generating fractures within a domain that is much larger than the required block size (1,000 m for a 100 m block and 200 m for a 20 m block was used here).
2. The fracture domain is split into sub-blocks of a selected scale (20 m or 100 m).
3. Simulations of flow through the DFN model are performed in each of the axial directions. For the flow simulations, a linear pressure gradient is specified parallel to each of the axial directions and imposed on all six faces of a cube to allow a general symmetric hydraulic conductivity tensor (6 components) to be calculated.
4. For each set of the three axial pressure gradients, the flux through each of the six faces of the block is computed. Based on these 18 flux responses for the 3 pressure gradients, a full symmetric 3D hydraulic conductivity tensor is fitted based on a least-squares optimisation.
5. An enhancement to this methodology is to introduce a guard zone as described in Section 2.3. This involves dividing the domain of fractures into blocks larger than the size on which the properties are required, simulating flow through the larger block, but then only calculating the flux through the central cube of the required size. This has the advantage that flows are calculated through the fractures 'in situ', i.e. within a network, and avoids overestimating hydraulic conductivity due to flows through fractures that cut across edges or corners of the block and do not represent flows within a network.
6. The hydraulic conductivity is calculated for 100 m and 20 m blocks, and different fracture size truncations are considered. To obtain the results presented in Section 4.4, a minimum fracture radius r_{min} of 1.13 m was used for the 20 m block calculations, and r_{min} was set to 5.64 m for the 100 m block calculations, i.e. the minimum fracture radius was about an eighteenth of the block length-scale. For calculating the 100 m block hydraulic conductivity, fractures are generated in a 1,000 m cube that is split into

an array of 9×9×9 (729 blocks in total) overlapping cubes of side 300 m (i.e. the guard zone thickness is 100 m) for use in the flow simulations. For each block, the hydraulic conductivity is then calculated on the basis of the flux through the central 100 m block within the 300 m cube, so as to avoid problems with high flows through the corner or edge of a cube that may be unrepresentative of flow in a network.

7. Hydraulic conductivities are then calculated as a Cumulative Distribution Function (CDF) of the values for an ensemble of 729 blocks.
8. For a 20 m block, fractures are generated in a 200 m cube and an array of 9×9×9 (729 blocks in total) cubes of side 80 m (i.e. the guard zone thickness is 30 m).
9. Anisotropy is studied in several ways. The overall hydraulic conductivity is calculated as the geometric mean of the axial components. A principal component analysis is used to derive the maximum and minimum horizontal hydraulic conductivities together with the strike of the maximum hydraulic conductivity for each of the 729 blocks. This shows how much anisotropy can be expected in any given block and whether there is a general trend toward certain directions over all blocks.
10. Fracture (kinematic) porosity is calculated by summing the fracture area multiplied by transport aperture for each connected fracture within each block and dividing by the block volume.

4.2 Modelling assumptions and input data

The remit for this study, as specified by SKB's Design Team, was to calculate the statistics of the hydraulic conductivity tensor of 20 m and 100 m blocks using the results of the work specified by the SKB Task Description, which are summarised in Subsection 3.11.1. This analysis was performed for all the Hydro-DFN models described in Subsection 3.11.1 except for the case with anisotropy of transmissivity between fracture sets.

The main modelling assumptions in the study performed here are:

1. The hydraulic conductivity in the host rock is completely dominated by the connected fracture system and hence can be modelled by the DFN concept.
2. Flow within fractures can be approximated by Darcy's law.
3. The heterogeneity between blocks on a specified scale can be modelled by calculating the hydraulic conductivity of an array of sub-blocks within a much larger domain (as big as the largest stochastic fracture, and ten times the block size) and using this as an ensemble.
4. Each borehole (KLX03, KLX04, KSH01A and KAV04A) was upscaled separately and the results can be used to represent different rock domains in the regional modelling.
5. Fracture transmissivity can be described by one of three alternative models.
6. Fracture kinematic porosity (transport aperture) is correlated to fracture transmissivity.

4.3 Simulations for assessment of hydraulic block properties

An example of a DFN model that was used to calculate hydraulic properties for a 20 m block is shown in Figure 4-1. This was for a case with a semi-correlated transmissivity distribution matched to the KLX04 hydraulic data. Here, the DFN is created within a 200 m domain, which is sub-divided into overlapping cubes with side 80 m for flow simulations. Hydraulic properties are then calculated on the basis of the flux through the central 20 m block. Clearly, blocks cut by a large fracture, here coloured red, will have a high hydraulic conductivity.

Figure 4-2 shows an example of a DFN model that was used to calculate hydraulic properties for a 100 m block.

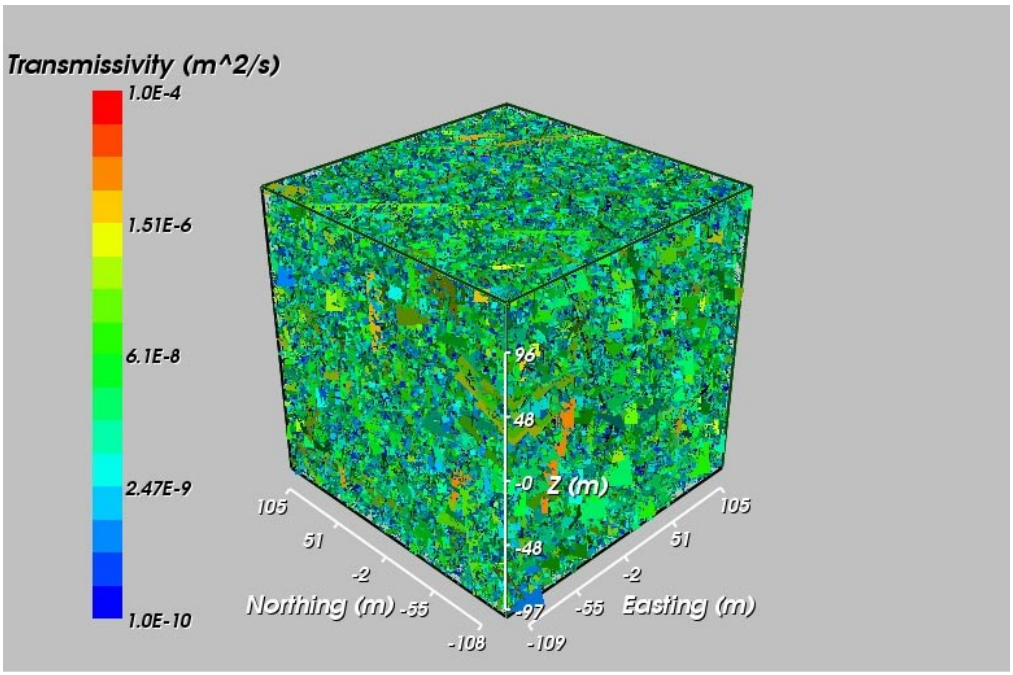

Figure 4-1. *KLX04 DFN model simulation for a 200 m domain that was used to calculate hydraulic block properties for 20 m blocks. The example shown here is for the semi-correlated transmissivity model, 'k_r fit', below –300 m for KLX04.*

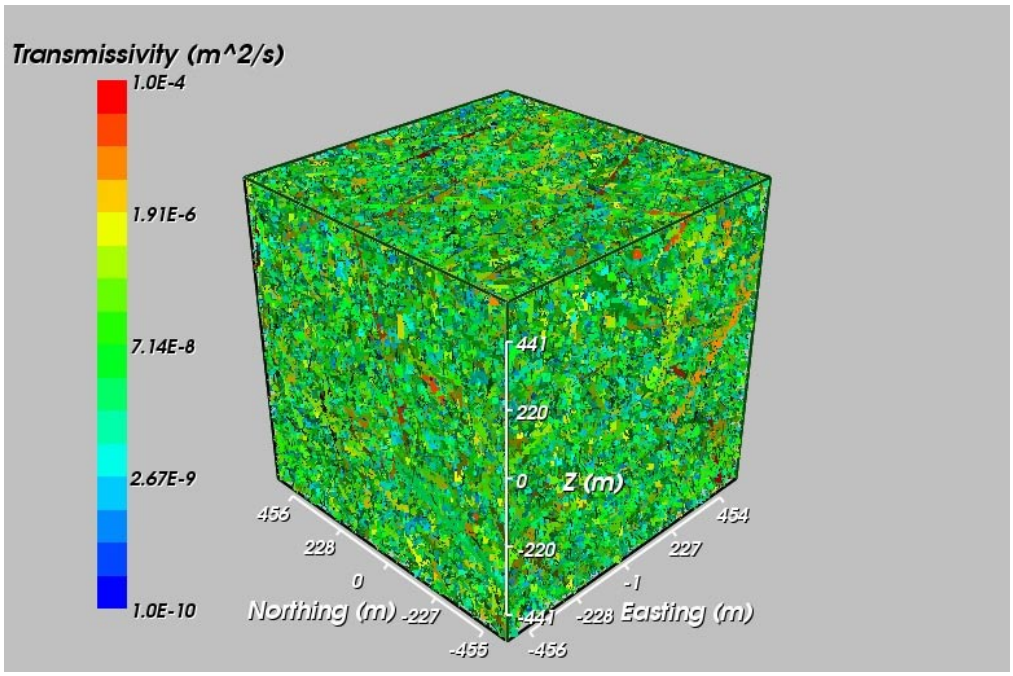

Figure 4-2. *KLX04 DFN model simulation for a 1,000 m domain used to calculate hydraulic block properties for 100 m blocks. The example shown here is for the semi-correlated transmissivity model, 'k_r fit', below –300 m for KLX04.*

4.4 Model parameters for block properties with uncertainties

Using the DFN model, as described by the parameters in Table 3-22 to Table 3-25, simulations were performed for the 100 m and 20 m block sizes and for the three different transmissivity models. All three transmissivity models were propagated to the block scale modelling in order to quantify the sensitivity to the assumption of a relationship between fracture transmissivity and fracture size, and to see if there are any distinct differences between the models that may point toward one model being more realistic.

4.4.1 Block properties for KLX04

Investigations during the course of this work showed that the size of the guard zone surrounding each block can affect the block properties. As described in Section 2.3, the guard zone is the model volume surrounding the central block in which the block properties are calculated. For instance, for the 20 m block properties, flow is simulated across many 80 m blocks but block properties are only calculated through a smaller central cube within this block, of size 20 m in this case. For the 100 m blocks, flow is simulated through 300 m blocks, but the properties are only calculated through the central 100 m block. This allows flows to be calculated 'in situ' and avoids over-estimating the hydraulic conductivity due to flows through fractures that cut across edges or corners of the block and do not represent flows within a network.

Sensitivity cases were carried out to test the size of the guard zone. The 20 m block is expected to be more sensitive to the guard zone than the 100 m block due to the smaller size of the 20 m block and therefore more chance of flow taking a 'shortcut' across the edge or corner of the 20 m block. Results for an example using the semi-correlated case

are summarised in Table 4-1. This shows that for the 20 m block, K_{eff} is not very sensitive to the size of the guard zone. For the 100 m block, there is a consistent but slight decrease in the percentiles of $Log_{10}(K_{eff})$ with increasing guard zone size. Future sensitivity investigations should consider the effect of increasing the number of blocks by using a larger model domain. As a result of this sensitivity analysis, all cases were carried out using a guard zone of 30 m on all faces of a 20 m block and 100 m on all faces of a 100 m block.

Table 4-2 and Table 4-3 show results for the 'k_r fit' cases matched to all hydraulic data for KLX04, above –300 m and below –300 m elevation, respectively. The results are given in terms of percentiles (10, 25, 50, 75 and 90), as well as the mean and one standard deviation of the sample, to capture the distribution of K_{eff}, the geometric mean of the axial components of the hydraulic conductivity tensor.

Table 4-1. Investigation of the sensitivity of the guard zone on K_{eff} for the semi-correlated case, KLX04 (Rock domain A,) below –300 m for 20 m blocks and 100 m blocks, 'k_r fit' case.

Scale (m)	Guard zone (m)	r_{min} (m)	$Log_{10}(K_{eff})$ m/s						
			10-percentile	25-percentile	50-percentile	75-percentile	90-percentile	Mean	1 s.d.
20	10	1.13	–9.85	–9.24	–8.51	–7.71	–7.28	–8.54	1.00
20	20	1.13	–9.84	–9.25	–8.40	–7.71	–7.36	–8.51	0.97
20	30	1.13	–9.76	–9.10	–8.34	–7.77	–7.49	–8.50	0.89
20	40	1.13	–9.86	–9.18	–8.34	–7.83	–7.58	–8.58	0.95
100	50	5.64	–8.88	–8.59	–8.15	–7.69	–7.27	–8.12	0.62
100	100	5.64	–9.08	–8.73	–8.25	–7.75	–7.30	–8.21	0.69
100	150	5.64	–9.14	–8.77	–8.30	–7.85	–7.50	–8.30	0.65
100	200	5.64	–9.18	–8.78	–8.35	–7.83	–7.24	–8.28	0.71

Table 4-2. Comparison of K_{eff} for KLX04 (Rock domain A) above –300 m for 20 m blocks and 100 m blocks in the 'k_r fit' case.

T model	Scale (m)	Guard zone (m)	r_{min} (m)	Log10(K_{eff}) m/s						
				10-percentile	25-percentile	50-percentile	75-percentile	90-percentile	Mean	1 s.d.
Corr	20	30	1.13	–7.75	–7.27	–6.48	–5.77	–5.56	–6.57	0.83
Corr	100	100	5.64	–7.07	–6.86	–6.62	–6.37	–6.17	–6.62	0.34
Uncorr	20	30	1.13	–7.24	–7.01	–6.77	–6.55	–6.34	–6.79	0.37
Uncorr	100	100	5.64	–7.50	–7.31	–7.10	–6.87	–6.62	–7.08	0.34
Semi-corr	20	30	1.13	–7.78	–7.22	–6.80	–6.50	–6.23	–6.91	0.60
Semi-corr	100	100	5.64	–7.36	–7.10	–6.74	–6.32	–5.86	–6.68	0.57

Table 4-3. Comparison of K_{eff} for KLX04 (Rock domain A) below –300 m for 20 m blocks and 100 m blocks in the 'k_r fit' case.

T model	Scale (m)	Guard zone (m)	r_{min} (m)	Log10(K_{eff}) m/s						
				10-percentile	25-percentile	50-percentile	75-percentile	90-percentile	Mean	1 s.d.
Corr	20	30	1.13	–9.64	–9.12	–8.00	–6.85	–6.64	–8.06	1.19
Corr	100	100	5.64	–8.62	–8.30	–7.93	–7.54	–7.22	–7.92	0.51
Uncorr	20	30	1.13	–8.78	–8.36	–7.90	–7.58	–7.29	–7.99	0.59
Uncorr	100	100	5.64	–8.76	–8.55	–8.22	–7.89	–7.63	–8.21	0.45
Semi-corr	20	30	1.13	–9.76	–9.10	–8.34	–7.77	–7.49	–8.50	0.89
Semi-corr	100	100	5.64	–9.08	–8.72	–8.24	–7.74	–7.29	–8.21	0.69

Calculation of K_{eff} below –300 m shows values of about 1 to 1.5 orders of magnitude lower than above –300 m elevation, which is in agreement with lower measured hydraulic conductivity at depth. Generally, it is expected that the mean log(K_{eff}) should scale with increasing block size, e.g. a smaller (20 m) block should generate smaller values of log(K_{eff}) than an 100 m block. Likewise, the spread is expected to decrease with increasing block size. For example, the likelihood of one fracture dominating a 20 m block is much greater than for a 100 m block, leading to greater heterogeneity and therefore increased spread in the smaller scale. Averaging over many 20 m blocks, of which a few are dominated by a large flow, will give a smaller log(K_{eff}) than the 100 m block. In contrast, averaging over the 100 m blocks, which is more likely to capture several highly transmissive fractures, will give a greater log(K_{eff}). Overall, the calculations show that the mean log(K_{eff}) scales with block size (or gives similar values) for the correlated and semi-correlated case. In all cases (correlated, semi-correlated and uncorrelated), the spread decreases with increasing block size.

The results for the 'k_r fit' cases are also presented in Table 4-4 and Table 4-5 in terms of the individual axial components of hydraulic conductivity (K_x, K_y and K_z); the median ratios of maximum horizontal and minimum horizontal conductivities (K_{hmax}/K_{hmin}); the median ratios of maximum horizontal and vertical conductivities (K_{hmax}/Kz); and the strike of any general trend in the maximum horizontal conductivity (strike of K_{hmax}). The ratios of anisotropy are calculated block-by-block and then the median is computed over the ensemble of 729 blocks. K_{hmin} and K_{hmax} are the minimum and maximum horizontal components of the hydraulic conductivity tensor respectively. Hence the median ratio K_{hmax}/K_{hmin} shows the local block anisotropy in the horizontal direction, while the median ratio of K_{hmax}/K_z shows the local block anisotropy between the horizontal and vertical directions. The final column, strike of K_{hmax}, shows whether regional anisotropy is present, deduced from the overall strike of the maximum horizontal component of the hydraulic conductivity tensor. On the local scale for KLX04 above –300 m elevation, the ratio of K_{hmax} to K_{hmin} is generally around 1.9 to 3.9, and 2.7 to 5.0 below –300 m elevation, showing clear local anisotropy. The ratio of K_{hmax} to K_z is between 1.1 and 1.5 for both cases, showing slight local block anisotropy between the vertical and horizontal directions. However, a different picture is observed on the regional scale. For all cases, regional anisotropy is clearly oriented towards a NW-SE strike direction, between about 080° to 130°.

The corresponding fracture (kinematic) porosity percentiles (10, 25, 50, 75 and 90) are given in Table 4-6 and Table 4-7. The porosity for hydraulic data matched to KLX04 above –300 m, 'k_r fit', gives median $\log_{10}$(porosity) between –3.8 and –3.4 for the 20 m block, and between –4.5 and –3.9 for below –300 m elevation.

Table 4-4. Comparison of anisotropy KLX04 (Rock domain A) above –300 m for 20 m blocks and 100 m blocks in the k_r fit case.

T model	Scale (m)	Guard zone (m)	r_{min} (m)	Median Log10(K_x) m/s	Median Log10(K_y) m/s	Median Log10(K_z) m/s	Median ratio K_{hmax}/K_{hmin}	Median ratio K_{hmax}/K_z	Strike of K_{hmax} (by eye)
Corr	20	30	1.13	–6.38	–6.46	–6.63	3.27	1.44	120–130
Corr	100	100	5.64	–6.66	–6.66	–6.59	2.08	1.19	80–100
Uncorr	20	30	1.13	–6.76	–6.85	–6.67	2.70	1.07	70–110
Uncorr	100	100	5.64	–7.08	–7.18	–7.04	1.93	1.12	70–110
Semi-corr	20	30	1.13	–6.83	–6.95	–6.69	3.89	1.14	90–110
Semi-corr	100	100	5.64	–6.67	–6.86	–6.68	2.50	1.29	80–100

Table 4-5. Comparison of anisotropy KLX04 (Rock domain A) below –300 m for 20 m blocks and 100 m blocks in the k_r fit case.

T model	Scale (m)	Guard zone (m)	r_{min} (m)	Median Log10(K_x) m/s	Median Log10(K_y) m/s	Median Log10(K_z) m/s	Median ratio K_{hmax}/K_{hmin}	Median ratio K_{hmax}/K_z	Strike of K_{hmax} (by eye)
Corr	20	30	1.13	–7.97	–7.99	–8.09	4.71	1.53	100–130
Corr	100	100	5.64	–7.83	–8.05	–7.90	2.67	1.40	90–100, 120–130
Uncorr	20	30	1.13	–7.92	–8.00	–7.84	3.78	1.23	90–100
Uncorr	100	100	5.64	–8.20	–8.35	–8.12	2.54	1.12	80–100
Semi-corr	20	30	1.13	–8.35	–8.51	–8.27	5.00	1.19	90–110
Semi-corr	100	100	5.64	–8.22	–8.46	–8.12	3.42	1.18	80–110

Table 4-6. Comparison of kinematic porosity (n_e) for KLX04 (Rock domain A) above –300 m for 20 m blocks and 100 m blocks in the k_r fit case.

T model	Scale (m)	Guard zone (m)	r_{min} (m)	Log10(n_e) – 10-percentile	25-percentile	50-percentile	75-percentile	90-percentile
Corr	20	30	1.13	–3.89	–3.86	–3.81	–3.77	–3.73
Corr	100	100	5.64	–4.14	–4.12	–4.09	–4.07	–4.04
Uncorr	20	30	1.13	–3.46	–3.45	–3.44	–3.43	–3.42
Uncorr	100	100	5.64	–4.04	–4.03	–4.01	–4.00	–3.98
Semi-corr	20	30	1.13	–3.83	–3.81	–3.78	–3.76	–3.74
Semi-corr	100	100	5.64	–4.10	–4.07	–4.03	–3.99	–3.94

Table 4-7. Comparison of kinematic porosity (n_e) for KLX04 (Rock domain A) below –300 m for 20 m blocks and 100 m blocks in the k_r fit case.

T model	Scale (m)	Guard zone (m)	r_{min} (m)	Log10(n_e) – 10-percentile	25-percentile	50-percentile	75-percentile	90-percentile
Corr	20	30	1.13	–4.55	–4.50	–4.46	–4.40	–4.35
Corr	100	100	5.64	–4.71	–4.69	–4.65	–4.61	–4.58
Uncorr	20	30	1.13	–3.92	–3.91	–3.90	–3.88	–3.87
Uncorr	100	100	5.64	–4.51	–4.50	–4.48	–4.46	–4.44
Semi-corr	20	30	1.13	–4.49	–4.47	–4.44	–4.41	–4.38
Semi-corr	100	100	5.64	–4.78	–4.75	–4.70	–4.65	–4.61

Some examples of the calculations of the resultant model parameters for the hydraulic block properties are shown in Figure 4-3 to Figure 4-6 for the 100 m block. Figure 4-3 and Figure 4-4 show the *x* (East-West) hydraulic conductivity for the uncorrelated *T* model case.

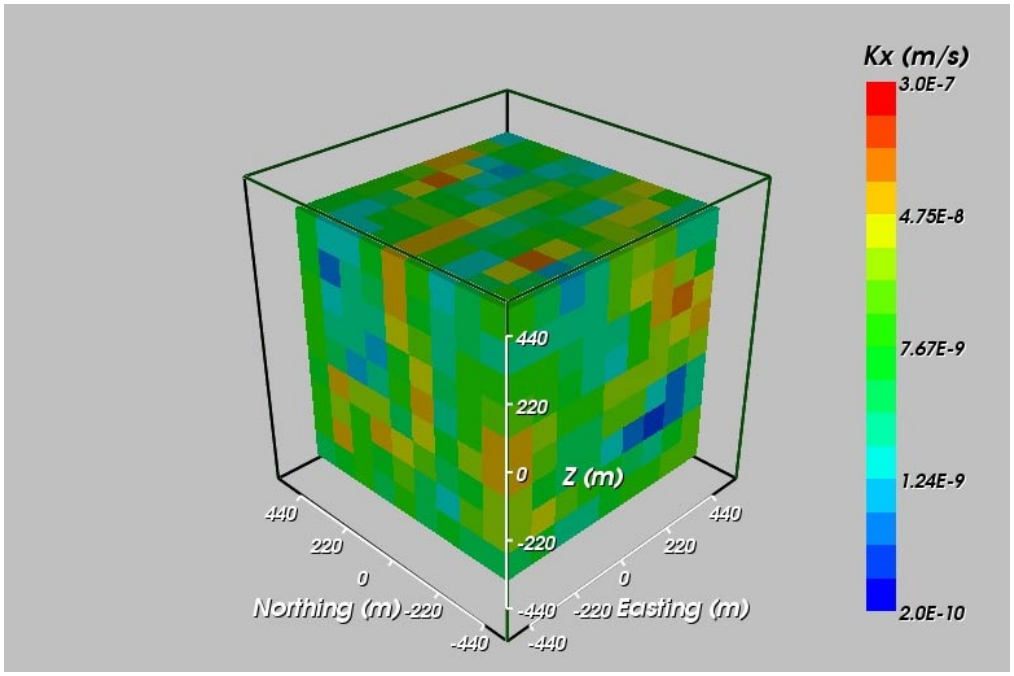

Figure 4-3. *Calculated hydraulic conductivity in the East-West direction for a 9×9×9 array of 100 m blocks for the KLX04 DFN with an uncorrelated T model, 'k_r fit below –300 m'. Model input parameters shown in Table 3-22.*

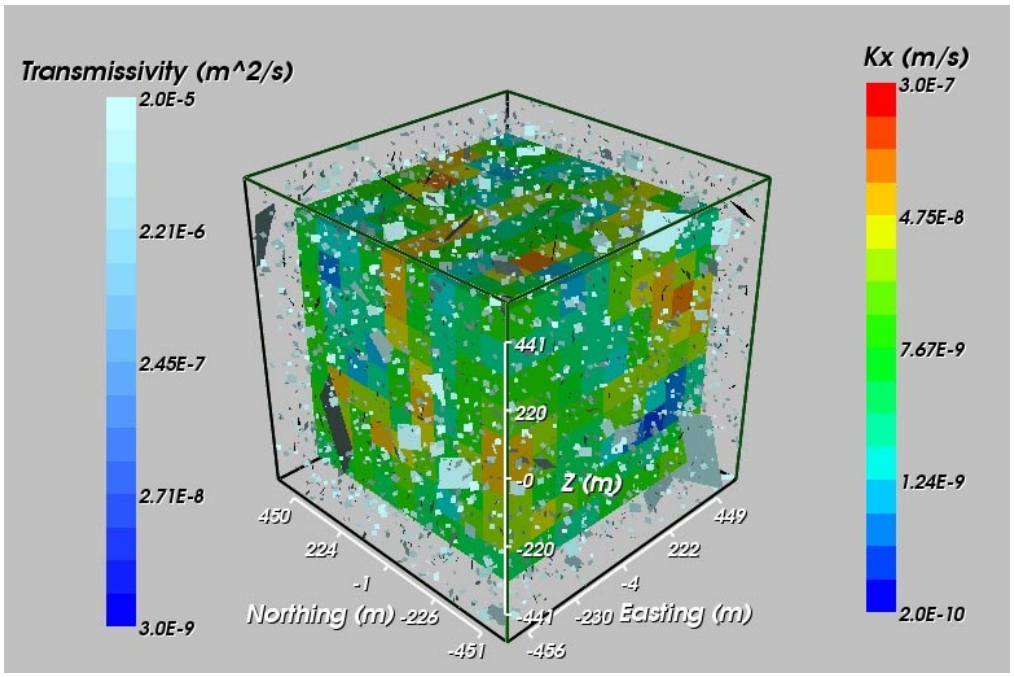

Figure 4-4. *Calculated hydraulic conductivity in the East-West direction for a 9×9×9 array of 100 m blocks for the KLX04 DFN with an uncorrelated T model, 'k_r fit below –300 m'. Fractures with large transmissivity are superimposed. Model input parameters shown in Table 3-22.*

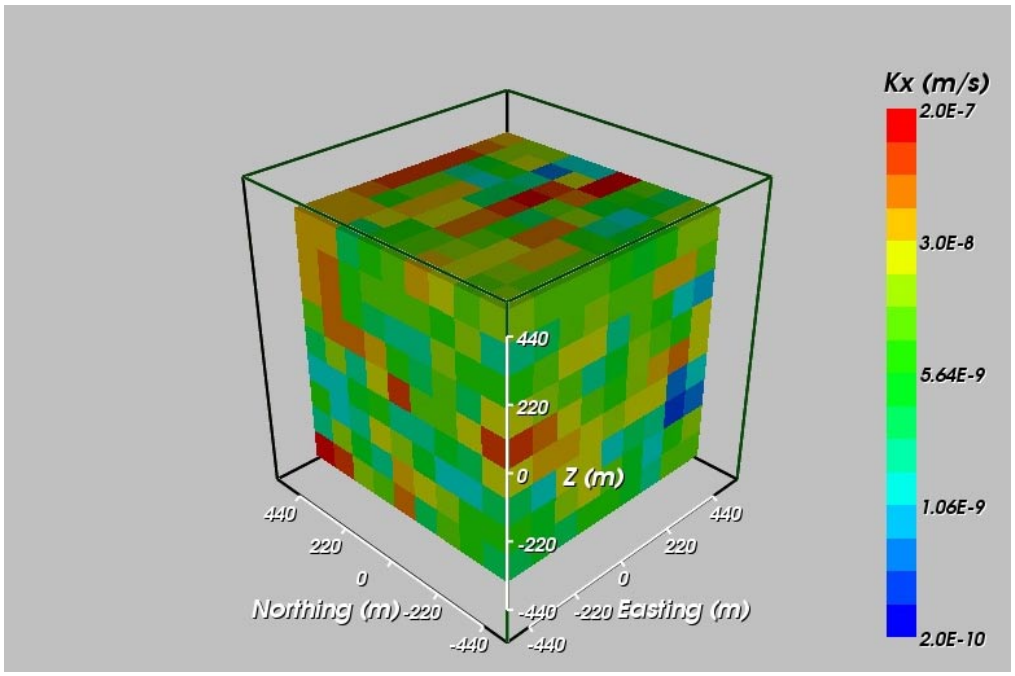

Figure 4-5. *Calculated hydraulic conductivity in the East-West direction for a 9×9×9 array of 100 m blocks for the KLX04 DFN with a correlated T model, 'k_r fit below –300 m'. Model input parameters shown in Table 3-22.*

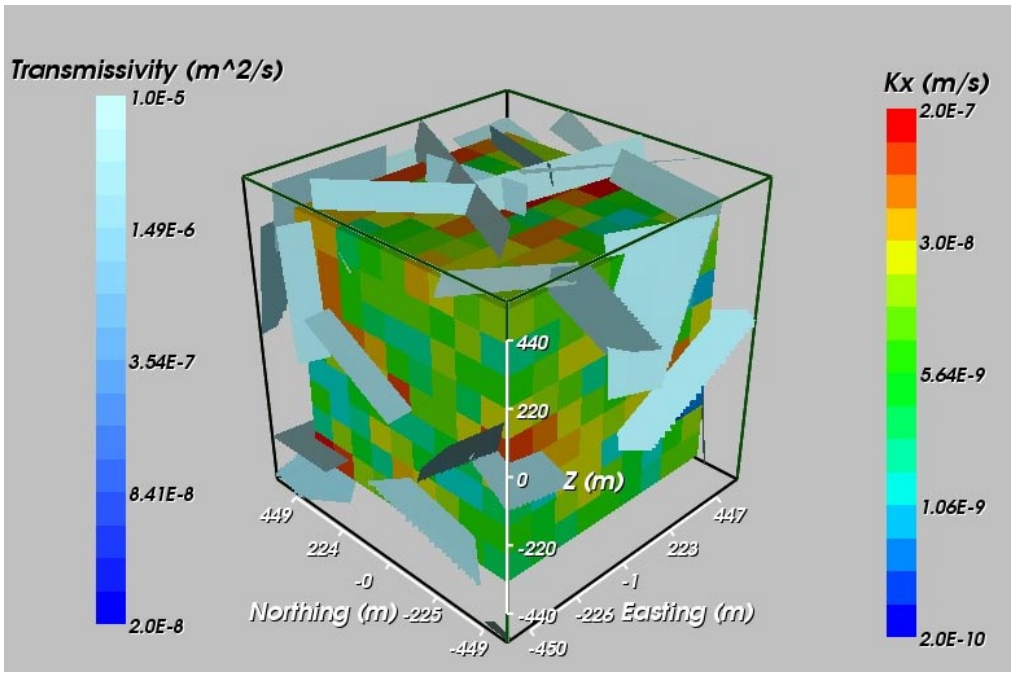

Figure 4-6. *Calculated hydraulic conductivity in the East-West direction for a 9×9×9 array of 100 m blocks for the KLX04 DFN with a correlated T model, 'k_r fit below –300 m'. Fractures with large transmissivity are superimposed. Model input parameters shown in Table 3-22.*

In Figure 4-4, fractures with large (> 8 10^{-6} m^2s^{-1}) transmissivity are superimposed. This case demonstrates some characteristic features particular to the uncorrelated model. There is considerable heterogeneity, and there is little correlation between adjacent blocks. This stems from the fact that high transmissivity fractures can be any size. In addition, due to the power-law size distribution, many of the high *T* fractures are relatively small, and so only affect 1 or 2 blocks. It is rare that a large fracture is generated with a high *T* and so there are few, if any, continuous lineaments of high hydraulic conductivity.

Figure 4-5 and Figure 4-6 show the corresponding plots for the case with a correlated *T* model (Figure 4-6 shows fractures with large, > 1 10^{-6} m^2s^{-1}, transmissivity). A clear difference here is the much greater correlation between blocks due to the effect of larger fractures having relatively higher transmissivity.

Example cases of the distribution of block-scale hydraulic conductivities and the maximum horizontal hydraulic conductivities are presented in Figure 4-7 to Figure 4-18 for the 'k_r fit' input parameters.

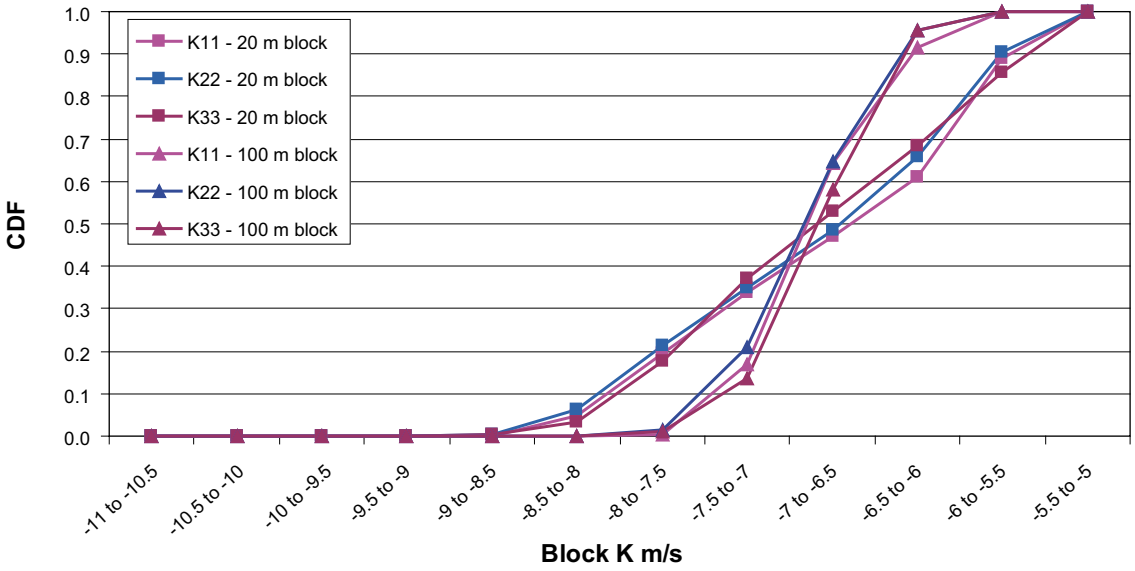

Figure 4-7. *Hydraulic conductivity distribution for 'k_r fit' case for hydraulic data above –300 m KLX04, correlated transmissivity model. K11, K22, K33 correspond to Kx (Easting), Ky (Northing) and Kz (vertical), respectively. Model input parameters shown in Table 3-22.*

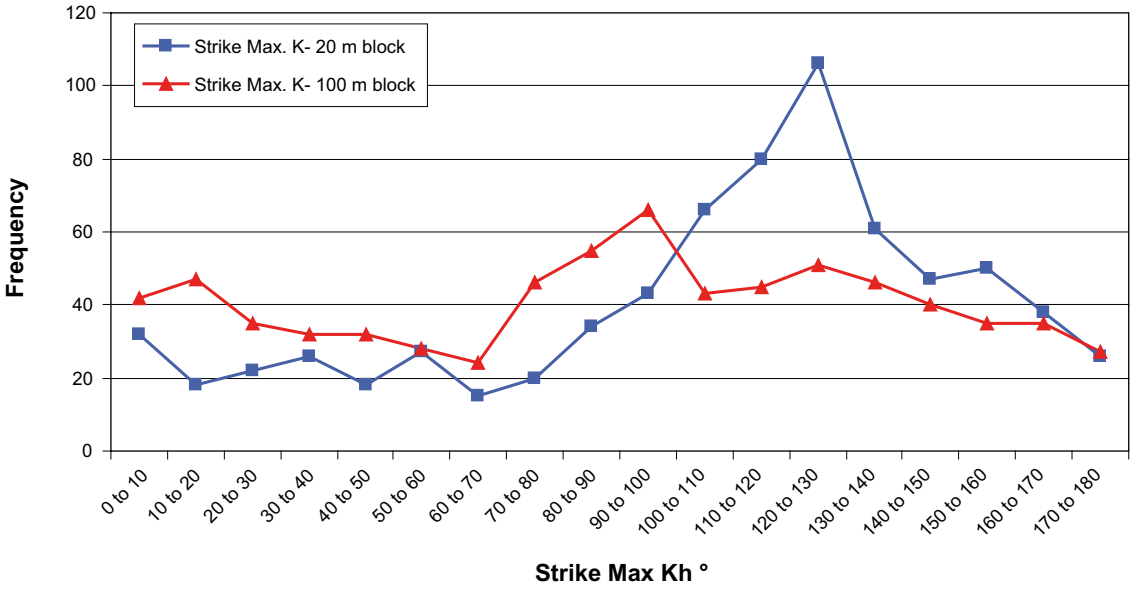

Figure 4-8. *Distribution of the maximum horizontal hydraulic conductivity for the 'k_r fit' case of correlated transmissivity model hydraulic data above –300 m for KLX04. Model input parameters shown in Table 3-22.*

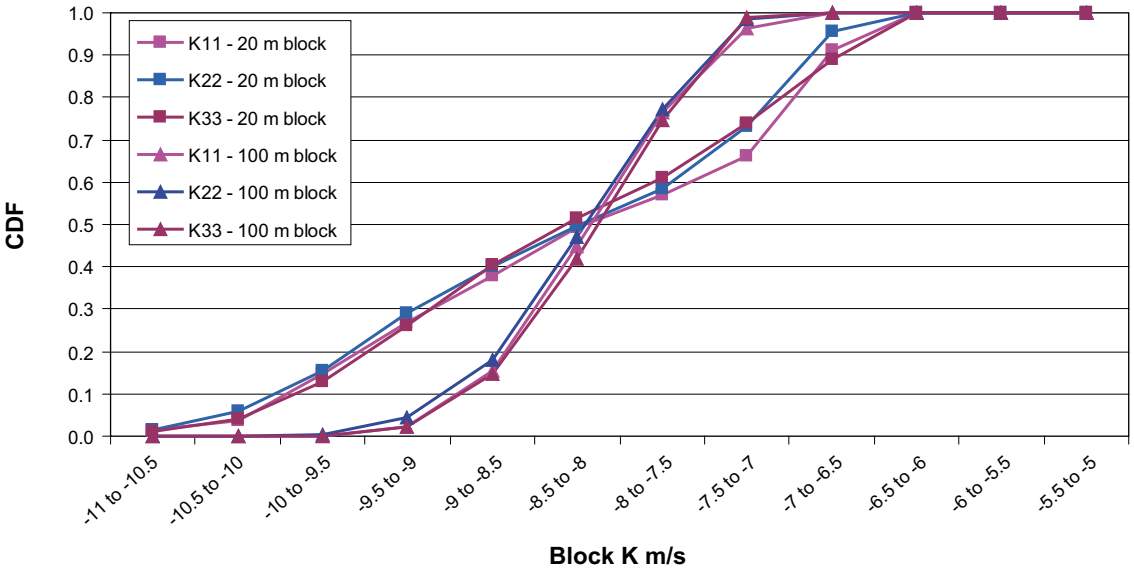

Figure 4-9. *Hydraulic conductivity distribution for 'k_r fit' case for hydraulic data below –300 m KLX04, correlated transmissivity model. K11, K22, K33 correspond to Kx (Easting), Ky (Northing) and Kz (vertical), respectively. Model input parameters shown in Table 3-22.*

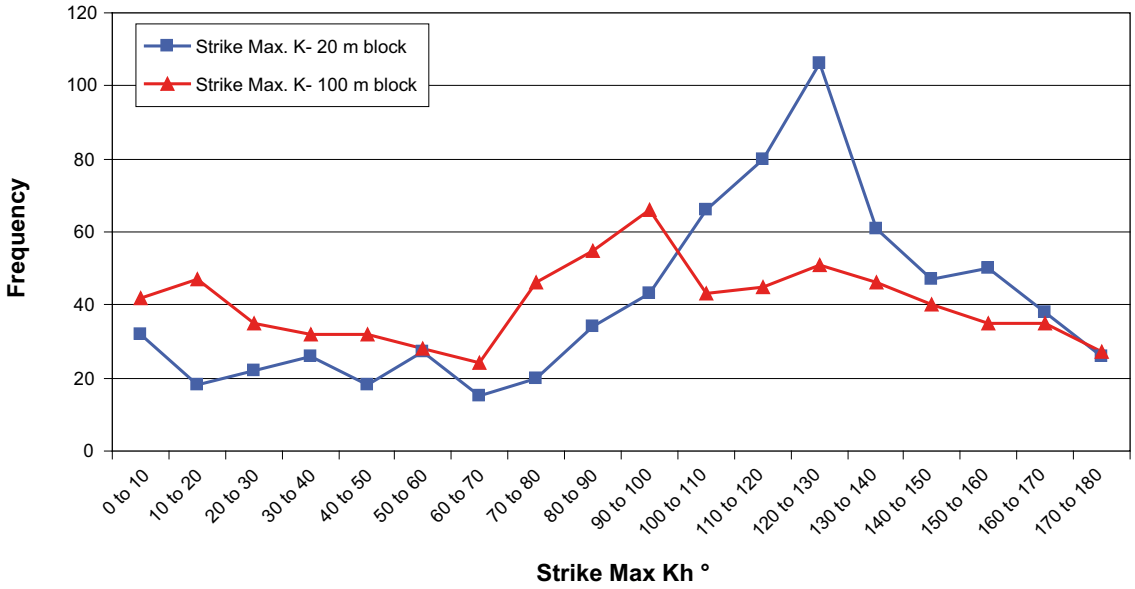

Figure 4-10. *Distribution of the maximum horizontal hydraulic conductivity for the 'k_r fit' case of correlated transmissivity model hydraulic data below –300 m for KLX04. Model input parameters shown in Table 3-22.*

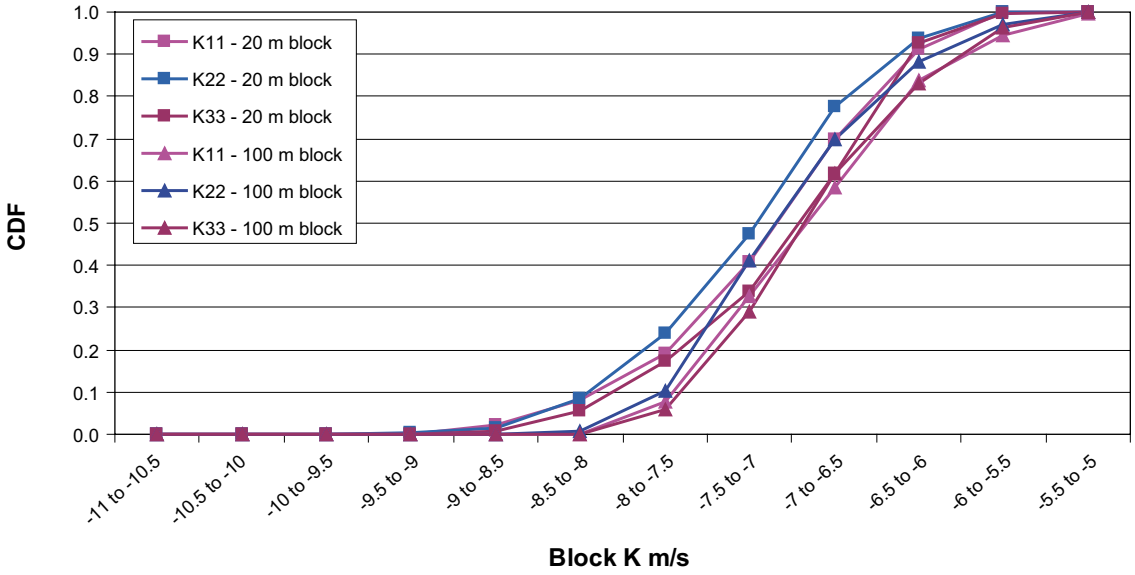

Figure 4-11. *Hydraulic conductivity distribution for 'k_r fit' case for hydraulic data above –300 m KLX04, semi-correlated transmissivity model. K11, K22, K33 correspond to Kx (Easting), Ky (Northing) and Kz (vertical), respectively. Model input parameters shown in Table 3-22.*

Figure 4-12. *Distribution of the maximum horizontal hydraulic conductivity for the 'k_r fit' case of semi-correlated transmissivity model hydraulic data above –300 m for KLX04. Model input parameters shown in Table 3-22.*

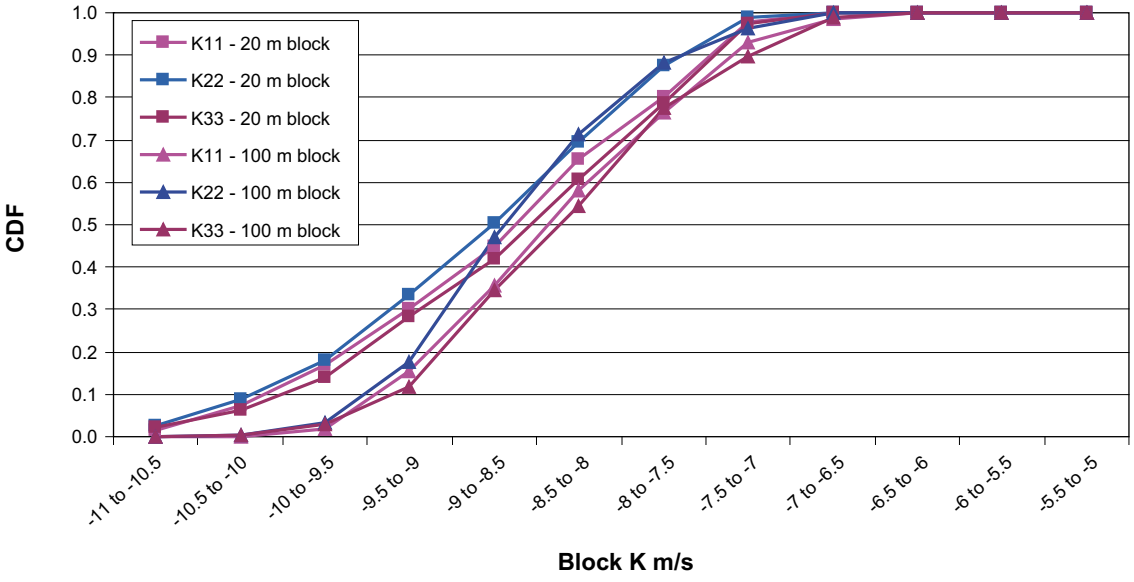

Figure 4-13. *Hydraulic conductivity distribution for 'k_r fit' case for hydraulic data below –300 m KLX04, semi-correlated transmissivity model. K11, K22, K33 correspond to Kx (Easting), Ky (Northing) and Kz (vertical), respectively. Model input parameters shown in Table 3-22.*

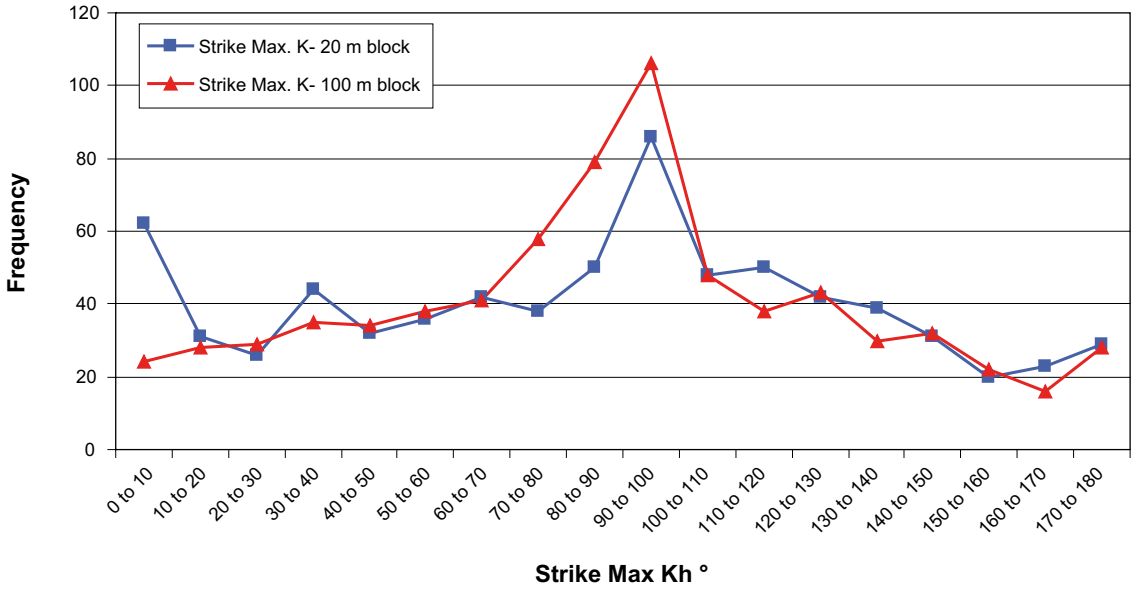

Figure 4-14. *Distribution of the maximum horizontal hydraulic conductivity for the 'k_r fit' case of semi-correlated transmissivity model hydraulic data below –300 m for KLX04. Model input parameters shown in Table 3-22.*

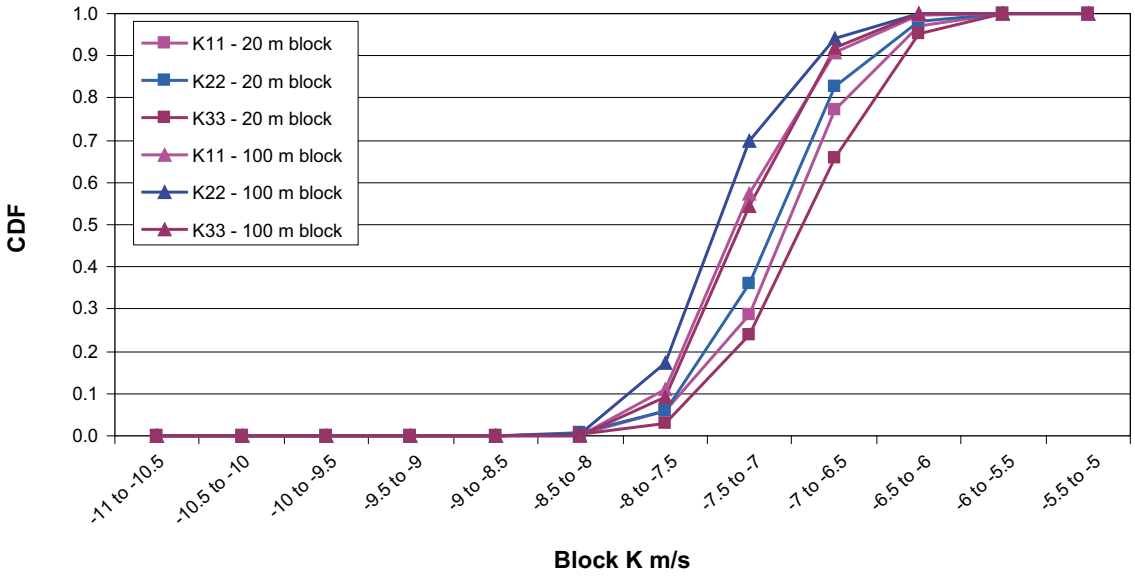

Figure 4-15. *Hydraulic conductivity distribution for 'k_r fit' case for hydraulic data above –300 m KLX04, uncorrelated transmissivity model. K11, K22, K33 correspond to Kx (Easting), Ky (Northing) and Kz (vertical), respectively. Model input parameters shown in Table 3-22.*

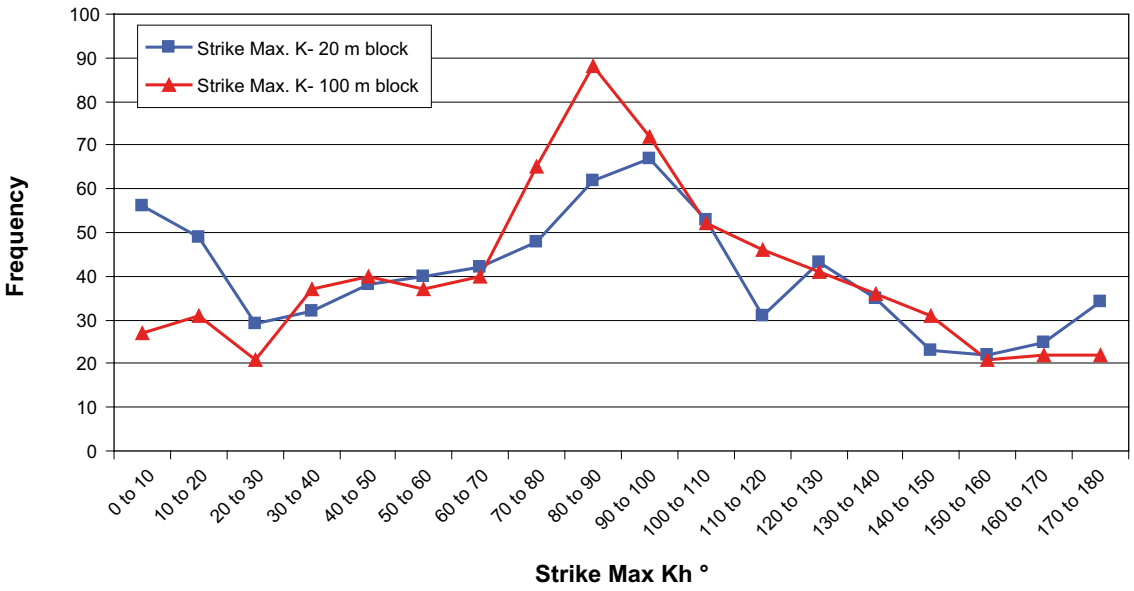

Figure 4-16. *Distribution of the maximum horizontal hydraulic conductivity for the 'k_r fit' case of uncorrelated transmissivity model hydraulic data above –300 m for KLX04. Model input parameters shown in Table 3-22.*

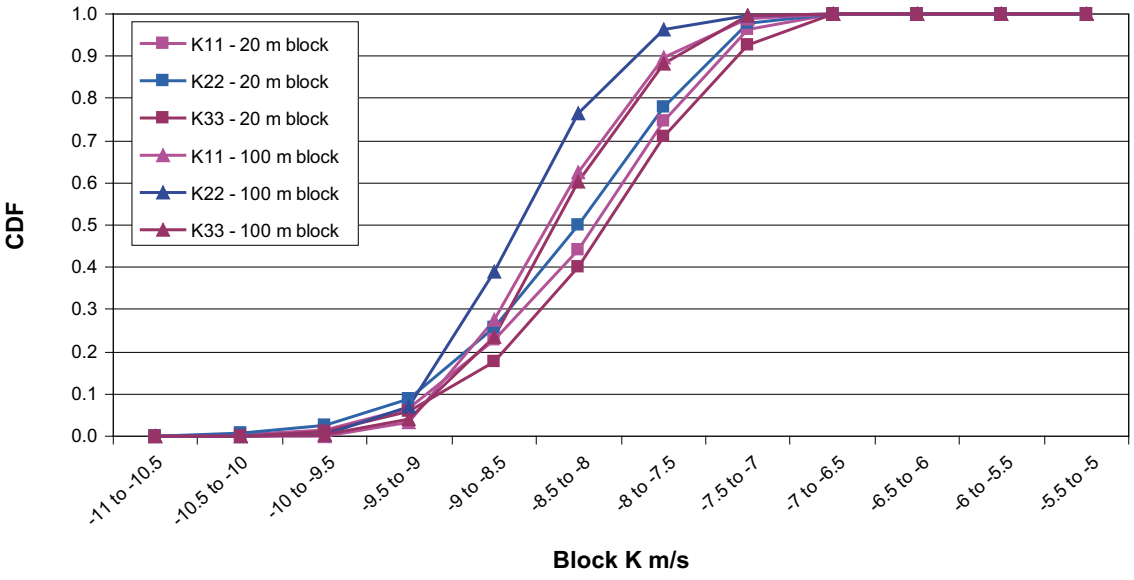

Figure 4-17. *Hydraulic conductivity distribution for 'k_r fit' case for hydraulic data below –300 m KLX04, uncorrelated transmissivity model. K11, K22, K33 correspond to Kx (Easting), Ky (Northing) and Kz (vertical), respectively. Model input parameters shown in Table 3-22.*

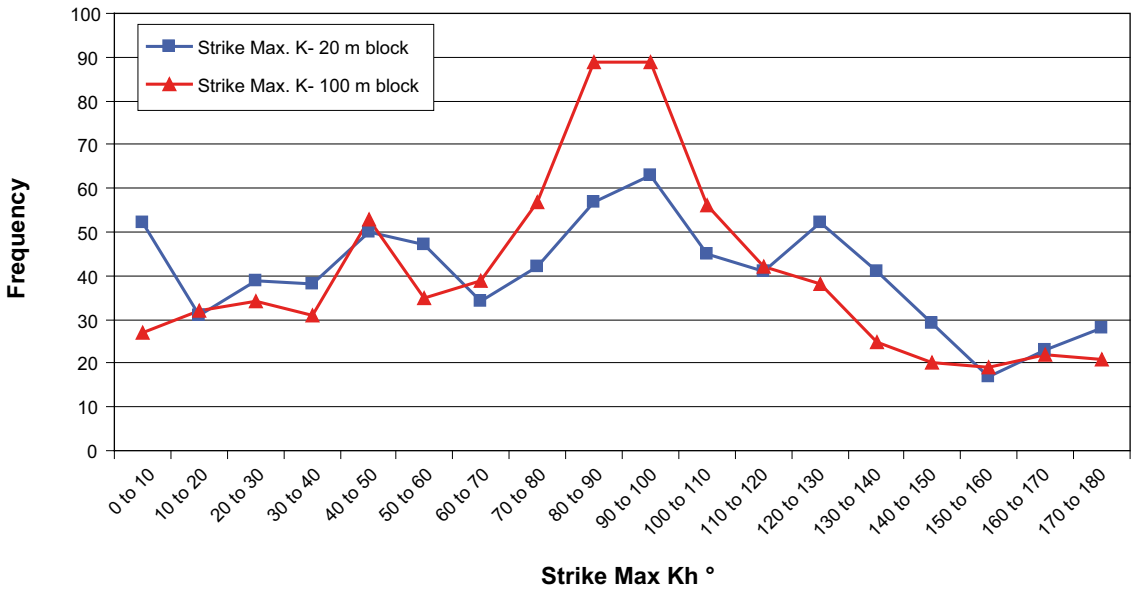

Figure 4-18. *Distribution of the maximum horizontal hydraulic conductivity for the 'k_r fit' case of uncorrelated transmissivity model hydraulic data below –300 m for KLX04. Model input parameters shown in Table 3-22.*

4.4.2 Block properties for KLX03

The resulting effective hydraulic conductivities, anisotropy and fracture porosities for KLX03 are shown in Table 4-8 to Table 4-13. For detailed explanations of how the parameters describe the results, see Subsection 4.4.1.

Table 4-10 and Table 4-11 show results for the 'k_r fit' cases matched to all hydraulic data for KLX03, above –300 m and below –300 m elevation, respectively. Calculation of K_{eff} below –300 m shows values of about 2 orders of magnitude lower than above –300 m elevation, which is in agreement with lower measured hydraulic conductivity at depth. The calculations show that the mean log(K_{eff}) scales with block size for all cases, and the spread decreases with increasing block size. Table 4-12 and Table 4-13 show clear local anisotropy with the ratio of K_{hmax} to K_{hmin} around 2.8 to 6.8 above –300 m elevation, and 4.4 to 9.9 below –300 m elevation. The ratio of K_{hmax} to K_z is between 1.3 and 1.7 for both cases, showing slight local block anisotropy between the vertical and horizontal directions. For all cases, regional anisotropy is clearly orientated towards a WNW-ESE strike direction, between about 050° to 130°, which is similar to KLX04.

The corresponding fracture (kinematic) porosity percentiles (10, 25, 50, 75 and 90) are given in Table 4-12 and Table 4-13. The porosity for hydraulic data matched to KLX03 above –300 m, 'k_r fit', gives median $\log_{10}$(porosity) between –4.1 and –3.8 for the 20 m block, and between –4.9 and –4.3 for below –300 m elevation.

Table 4-8. Comparison of K_{eff} for KLX03 (Rock domains M(A), M(D), and D) above –300 m for 20 m blocks and 100 m blocks in the k_r fit case.

T model	Scale (m)	Guard zone (m)	r_{min} (m)	Log10(K_{eff}) m/s						
				10-percentile	25-percentile	50-percentile	75-percentile	90-percentile	Mean	1 s.d.
Corr	20	30	1.13	–8.82	–7.88	–7.08	–6.49	–6.11	–7.28	1.06
Corr	100	100	5.64	–7.46	–7.18	–6.86	–6.59	–6.35	–6.89	0.43
Uncorr	20	30	1.13	–9.13	–8.58	–7.84	–7.31	–6.80	–7.98	1.08
Uncorr	100	100	5.64	–8.26	–7.98	–7.66	–7.35	–7.09	–7.67	0.45
Semi-corr	20	30	1.13	–9.51	–8.79	–7.99	–7.31	–6.88	–8.11	1.05
Semi-corr	100	100	5.64	–8.04	–7.69	–7.26	–6.83	–6.40	–7.25	0.63

Table 4-9. Comparison of K_{eff} for KLX03 (Rock domains M(A), M(D), and D) below –300 m for 20 m blocks and 100 m blocks in the k_r fit case.

T model	Scale (m)	Guard zone (m)	r_{min} (m)	Log10(K_{eff}) m/s						
				10-percentile	25-percentile	50-percentile	75-percentile	90-percentile	Mean	1 s.d.
Corr	20	30	1.13	–23.00	–12.17	–9.25	–8.32	–7.89	–9.75	2.46
Corr	100	100	5.64	–10.67	–9.81	–9.22	–8.73	–8.43	–9.34	0.86
Uncorr	20	30	1.13	–23.00	–14.63	–10.24	–9.06	–8.50	–10.33	2.15
Uncorr	100	100	5.64	–10.71	–10.02	–9.39	–8.85	–8.30	–9.50	1.01
Semi-corr	20	30	1.13	–23.00	–16.60	–10.29	–8.58	–7.84	–10.36	2.93
Semi-corr	100	100	5.64	–10.58	–9.88	–9.14	–8.34	–7.87	–9.19	1.16

Table 4-10. Comparison of anisotropy KLX03 (Rock domains M(A), M(D), and D) above –300 m for 20 m blocks and 100 m blocks in the k_r fit case.

T model	Scale (m)	Guard zone (m)	r_{min} (m)	Median Log10(K_x) m/s	Median Log10(K_y) m/s	Median Log10(K_z) m/s	Median ratio K_{hmax}/K_{hmin}	Median ratio K_{hmax}/K_z	Strike of K_{hmax} (by eye)
Corr	20	30	1.13	–7.03	–7.23	–7.06	6.80	1.51	50–100
Corr	100	100	5.64	–6.84	–6.88	–6.91	2.68	1.49	70–110
Uncorr	20	30	1.13	–7.88	–7.90	–7.87	5.25	1.66	70–100
Uncorr	100	100	5.64	–7.62	–7.74	–7.61	2.75	1.28	60–110
Semi-corr	20	30	1.13	–8.00	–7.99	–8.00	6.19	1.49	100–120
Semi-corr	100	100	5.64	–7.15	–7.44	–7.20	3.50	1.28	70–100

Table 4-11. Comparison of anisotropy KLX03 (Rock domains M(A), M(D), and D) below –300 m for 20 m blocks and 100 m blocks in the k_r fit case.

T model	Scale (m)	Guard zone (m)	r_{min} (m)	Median Log10(K_x) m/s	Median Log10(K_y) m/s	Median Log10(K_z) m/s	Median ratio K_{hmax}/K_{hmin}	Median ratio K_{hmax}/K_z	Strike of K_{hmax} (by eye)
Corr	20	30	1.13	–9.19	–9.37	–9.25	8.60	1.25	50–130
Corr	100	100	5.64	–9.19	–9.25	–9.26	4.39	1.68	70–110
Uncorr	20	30	1.13	–10.20	–10.14	–10.31	6.06	1.48	70–90
Uncorr	100	100	5.64	–9.36	–9.52	–9.40	5.41	1.73	30–130
Semi-corr	20	30	1.13	–10.30	–10.37	–10.28	9.90	1.06	80–120
Semi-corr	100	100	5.64	–9.09	–9.21	–9.05	6.59	1.59	70–140

Table 4-12. Comparison of kinematic porosity (n_e) for KLX03 (Rock domains M(A), M(D), and D) above –300 m for 20 m blocks and 100 m blocks in the k_r fit case.

T model	Scale (m)	Guard zone (m)	r_{min} (m)	Log10(n_e) –				
				10-percentile	25-percentile	50-percentile	75-percentile	90-percentile
Corr	20	30	1.13	–4.14	–4.06	–4.00	–3.94	–3.89
Corr	100	100	5.64	–4.26	–4.22	–4.19	–4.17	–4.14
Uncorr	20	30	1.13	–3.79	–3.77	–3.75	–3.73	–3.70
Uncorr	100	100	5.64	–4.25	–4.23	–4.22	–4.20	–4.19
Semi-corr	20	30	1.13	–4.19	–4.16	–4.12	–4.08	–4.05
Semi-corr	100	100	5.64	–4.33	–4.29	–4.24	–4.17	–4.12

Table 4-13. Comparison of kinematic porosity (n_e) for KLX03 (Rock domains M(A), M(D), and D) below –300 m for 20 m blocks and 100 m blocks in the k_r fit case.

T model	Scale (m)	Guard zone (m)	r_{min} (m)	Log10(n_e) –				
				10-percentile	25-percentile	50-percentile	75-percentile	90-percentile
Corr	20	30	1.13	–5.07	–5.01	–4.93	–4.84	–4.78
Corr	100	100	5.64	–5.28	–5.24	–5.20	–5.15	–5.11
Uncorr	20	30	1.13	–4.38	–4.36	–4.34	–4.32	–4.31
Uncorr	100	100	5.64	–4.82	–4.80	–4.78	–4.75	–4.72
Semi-corr	20	30	1.13	–4.85	–4.81	–4.76	–4.69	–4.64
Semi-corr	100	100	5.64	–5.01	–4.96	–4.90	–4.85	–4.81

4.4.3 Block properties for KSH01A

The resulting effective hydraulic conductivities, anisotropy and fracture porosities for KSH01A are shown in Table 4-14 to Table 4-19. For detailed explanations of how the parameters describe the results, see Subsection 4.4.1. Table 4-14 and Table 4-15 show results for the 'k_r fit' cases matched to all hydraulic data for KSH01A, above –300 m and below –300 m elevation, respectively. Calculation of K_{eff} below –300 m shows values of about 2 orders of magnitude lower than above –300 m elevation, which is in agreement with lower measured hydraulic data at depth. The calculations show that the mean log(K_{eff}) scales with block size (or similar values) for the semi-correlated case. The spread decreases with increasing block size for all cases.

Table 4-16 and Table 4-17 show clear local anisotropy with the ratio of K_{hmax} to K_{hmin} at around 3.6 to 6.4 above –300 m elevation, and 3.2 to 5.6 below –300 m elevation. The ratio of K_{hmax} to K_z is between 1.1 and 1.5, for both cases, showing slight local block anisotropy between the vertical and horizontal directions. For most cases, regional anisotropy is clearly orientated towards a W-E strike direction, between about 070° to 100°.

The corresponding fracture (kinematic) porosity percentiles (10, 25, 50, 75 and 90) are given in Table 4-18 and Table 4-19. The porosity for hydraulic data matched to KSH01A above –300 m, k_r fit, gives median $\log_{10}$(porosity) between –4.1 and –3.7 for the 20 m block, and between –5.3 and –4.8 for below –300 m elevation.

Table 4-14. Comparison of K_{eff} for KSH01A (Rock domains B and C) above –300 m for 20 m blocks and 100 m blocks in the k_r fit case.

T model	Scale (m)	Guard zone (m)	r_{min} (m)	Log10(K_{eff}) m/s						
				10-percentile	25-percentile	50-percentile	75-percentile	90-percentile	Mean	1 s.d.
Corr	20	30	1.13	–8.49	–7.93	–7.01	–6.15	–5.90	–7.10	1.00
Corr	100	100	5.64	–7.97	–7.70	–7.25	–6.76	–6.47	–7.24	0.57
Uncorr	20	30	1.13	–8.77	–8.37	–7.94	–7.51	–7.19	–7.96	0.62
Uncorr	100	100	5.64	–8.87	–8.58	–8.24	–7.90	–7.67	–8.25	0.46
Semi-corr	20	30	1.13	–9.13	–8.45	–7.66	–7.05	–6.69	–7.79	0.93
Semi-corr	100	100	5.64	–8.45	–8.09	–7.62	–6.97	–6.50	–7.51	0.78

Table 4-15. Comparison of K_{eff} for KSH01A (Rock domains B and C) below –300 m for 20 m blocks and 100 m blocks in the k_r fit case.

T model	Scale (m)	Guard zone (m)	r_{min} (m)	Log10(K_{eff}) m/s						
				10-percentile	25-percentile	50-percentile	75-percentile	90-percentile	Mean	1 s.d.
Corr	20	30	1.13	–11.12	–10.56	–9.65	–8.78	–8.53	–9.73	1.00
Corr	100	100	5.64	–10.60	–10.33	–9.88	–9.39	–9.10	–9.87	0.57
Uncorr	20	30	1.13	–10.94	–10.54	–10.11	–9.68	–9.36	–10.13	0.62
Uncorr	100	100	5.64	–11.04	–10.75	–10.41	–10.07	–9.84	–10.42	0.46
Semi-corr	20	30	1.13	–11.37	–10.78	–10.12	–9.63	–9.32	–10.24	0.79
Semi-corr	100	100	5.64	–10.96	–10.66	–10.28	–9.73	–9.33	–10.18	0.65

Table 4-16. Comparison of anisotropy KSH01A (Rock domains B and C) above –300 m for 20 m blocks and 100 m blocks in the k_r fit case.

T model	Scale (m)	Guard zone (m)	r_{min} (m)	Median Log10(K_x) m/s	Median Log10(K_y) m/s	Median Log10(K_z) m/s	Median ratio K_{hmax}/K_{hmin}	Median ratio K_{hmax}/K_z	Strike of K_{hmax} (by eye)
Corr	20	30	1.13	–7.14	–7.08	–6.90	4.19	1.39	70–90
Corr	100	100	5.64	–7.18	–7.40	–7.19	3.55	1.15	40–90
Uncorr	20	30	1.13	–7.90	–8.08	–7.83	4.69	1.28	70–100
Uncorr	100	100	5.64	–8.17	–8.35	–8.24	3.20	1.46	70–100
Semi-corr	20	30	1.13	–7.61	–7.88	–7.55	6.39	1.43	40–90
Semi-corr	100	100	5.64	–7.51	–7.82	–7.53	4.93	1.28	70–90

Table 4-17. Comparison of anisotropy KSH01A (Rock domains B and C) below –300 m for 20 m blocks and 100 m blocks in the k_r fit case.

T model	Scale (m)	Guard zone (m)	r_{min} (m)	Median Log10(K_x) m/s	Median Log10(K_y) m/s	Median Log10(K_z) m/s	Median ratio K_{hmax}/K_{hmin}	Median ratio K_{hmax}/K_z	Strike of K_{hmax} (by eye)
Corr	20	30	1.13	–9.77	–9.72	–9.53	4.19	1.39	0–10, 70–90
Corr	100	100	5.64	–9.81	–10.03	–9.82	3.55	1.15	40–100
Uncorr	20	30	1.13	–10.07	–10.25	–10.00	4.68	1.28	70–100
Uncorr	100	100	5.64	–10.34	–10.52	–10.41	3.20	1.46	70–100
Semi-corr	20	30	1.13	–10.11	–10.33	–10.02	5.61	1.36	50–90
Semi-corr	100	100	5.64	–10.16	–10.45	–10.19	4.31	1.29	70–90

Table 4-18. Comparison of kinematic porosity (n_e) for KSH01A (Rock domains B and C) above –300 m for 20 m blocks and 100 m blocks in the k_r fit case.

T model	Scale (m)	Guard zone (m)	r_{min} (m)	Log10(n_e) – 10-percentile	25-percentile	50-percentile	75-percentile	90-percentile
Corr	20	30	1.13	–4.04	–3.99	–3.94	–3.88	–3.84
Corr	100	100	5.64	–4.38	–4.35	–4.31	–4.26	–4.22
Uncorr	20	30	1.13	–3.75	–3.74	–3.73	–3.71	–3.70
Uncorr	100	100	5.64	–4.39	–4.38	–4.37	–4.35	–4.33
Semi-corr	20	30	1.13	–4.11	–4.09	–4.06	–4.03	–3.99
Semi-corr	100	100	5.64	–4.39	–4.36	–4.31	–4.25	–4.19

Table 4-19. Comparison of kinematic porosity (n_e) for KSH01A (Rock domains B and C) below –300 m for 20 m blocks and 100 m blocks in the k_r fit case.

T model	Scale (m)	Guard zone (m)	r_{min} (m)	Log10(n_e) – 10-percentile	25-percentile	50-percentile	75-percentile	90-percentile
Corr	20	30	1.13	–5.36	–5.31	–5.25	–5.20	–5.16
Corr	100	100	5.64	–5.69	–5.67	–5.63	–5.57	–5.53
Uncorr	20	30	1.13	–4.83	–4.82	–4.81	–4.80	–4.79
Uncorr	100	100	5.64	–5.48	–5.47	–5.45	–5.43	–5.42
Semi-corr	20	30	1.13	–5.23	–5.22	–5.20	–5.17	–5.14
Semi-corr	100	100	5.64	–5.62	–5.60	–5.57	–5.52	–5.49

4.4.4 Block properties for KAV04A

The resulting effective hydraulic conductivities, anisotropy and fracture porosities for KAV04A are shown in Table 4-20 to Table 4-25. For detailed explanations of how the parameters describe the results, please see Subsection 4.4.1. Table 4-20 and Table 4-21 show results for the 'k_r fit' cases matched to all hydraulic data for KAV04A, above –300 m and below –300 m elevation, respectively. Calculation of K_{eff} below –300 m give values that are slightly lower than those above –300 m elevation, which is in agreement with lower measured hydraulic conductivity at depth. The calculations show that the mean log(K_{eff}) does not scale with block size (or similar values) for any of the *T* model cases. However, as expected, the spread decreases with increasing block size for all cases.

Table 4-22 and Table 4-23 show clear local anisotropy with the ratio of K_{hmax} to K_{hmin} at around 2.9 to 4.8 above –300 m elevation, and 3.1 to 5.8 below –300 m elevation. The ratio of K_{hmax} to K_z is between 1.1 and 1.5, for both cases, showing slight local block anisotropy between the vertical and horizontal directions. For most cases, regional anisotropy is clearly orientated towards a ENE-WSW strike direction, between about 040° to 100°.

The corresponding fracture (kinematic) porosity percentiles (10, 25, 50, 75 and 90) are given in Table 4-24 and Table 4-25. The porosity for hydraulic data matched to KAV04A above –300 m, k_r fit, gives median $\log_{10}$(porosity) between –4.0 and –3.6 for the 20 m block, and between –4.0 and –3.7 for below –300 m elevation.

Table 4-20. Comparison of K_{eff} for KAV04A (Rock domain A within Ävrö region) above –300 m for 20 m blocks and 100 m blocks in the k_r fit case.

T model	Scale (m)	Guard zone (m)	r_{min} (m)	Log10(K_{eff}) m/s						
				10-percentile	25-percentile	50-percentile	75-percentile	90-percentile	Mean	1 s.d.
Corr	20	30	1.13	–8.29	–7.82	–6.90	–6.13	–5.88	–6.99	0.95
Corr	100	100	5.64	–7.85	–7.56	–7.14	–6.72	–6.44	–7.15	0.52
Uncorr	20	30	1.13	–8.46	–8.08	–7.69	–7.27	–6.85	–7.68	0.61
Uncorr	100	100	5.64	–8.50	–8.22	–7.92	–7.60	–7.33	–7.91	0.44
Semi-corr	20	30	1.13	–8.77	–8.25	–7.66	–7.22	–6.95	–7.77	0.70
Semi-corr	100	100	5.64	–8.48	–8.21	–7.84	–7.36	–7.03	–7.78	0.58

Table 4-21. Comparison of K_{eff} for KAV04A (Rock domain A within Ävrö region) below –300 m for 20 m blocks and 100 m blocks in the k_r fit case.

T model	Scale (m)	Guard zone (m)	r_{min} (m)	Log10(K_{eff}) m/s						
				10-percentile	25-percentile	50-percentile	75-percentile	90-percentile	Mean	1 s.d.
Corr	20	30	1.13	–9.14	–8.35	–7.17	–6.20	–5.99	–7.40	1.28
Corr	100	100	5.64	–8.57	–8.20	–7.70	–7.05	–6.67	–7.65	0.70
Uncorr	20	30	1.13	–8.94	–8.47	–7.88	–7.35	–6.99	–7.99	1.08
Uncorr	100	100	5.64	–8.87	–8.53	–8.16	–7.77	–7.48	–8.16	0.53
Semi-corr	20	30	1.13	–9.31	–8.76	–7.88	–7.22	–6.91	–8.04	1.12
Semi-corr	100	100	5.64	–8.84	–8.48	–8.06	–7.58	–7.17	–8.03	0.65

Table 4-22. Comparison of anisotropy KAV04A (Rock domain A within Ävrö region) above –300 m for 20 m blocks and 100 m blocks in the k_r fit case.

T model	Scale (m)	Guard zone (m)	r_{min} (m)	Median Log10(K_x) m/s	Median Log10(K_y) m/s	Median Log10(K_z) m/s	Median ratio K_{hmax}/K_{hmin}	Median ratio K_{hmax}/K_z	Strike of K_{hmax} (by eye)
Corr	20	30	1.13	–7.02	–6.98	–6.81	4.24	1.39	40–50, 70–80
Corr	100	100	5.64	–7.10	–7.26	–7.09	3.34	1.19	40–90
Uncorr	20	30	1.13	–7.70	–7.73	–7.57	4.49	1.34	70–80
Uncorr	100	100	5.64	–7.86	–7.99	–7.94	2.89	1.54	50–90
Semi-corr	20	30	1.13	–7.64	–7.84	–7.60	4.84	1.34	40–80
Semi-corr	100	100	5.64	–7.74	–7.99	–7.79	3.63	1.25	70–90

Table 4-23. Comparison of anisotropy KAV04A (Rock domain A within Ävrö region) below –300 m for 20 m blocks and 100 m blocks in the k_r fit case.

T model	Scale (m)	Guard zone (m)	r_{min} (m)	Median Log10(K_x) m/s	Median Log10(K_y) m/s	Median Log10(K_z) m/s	Median ratio K_{hmax}/K_{hmin}	Median ratio K_{hmax}/K_z	Strike of K_{hmax} (by eye)
Corr	20	30	1.13	–7.27	–7.26	–7.14	4.79	1.42	80–90
Corr	100	100	5.64	–7.64	–7.77	–7.60	4.16	1.19	50–60
Uncorr	20	30	1.13	–7.92	–7.95	–7.82	5.02	1.35	90–100
Uncorr	100	100	5.64	–8.07	–8.23	–8.14	3.14	1.50	50–90
Semi-corr	20	30	1.13	–7.84	–8.01	–7.77	5.81	1.51	40–80
Semi-corr	100	100	5.64	–8.00	–8.23	–8.01	4.45	1.31	80–90

Table 4-24. Comparison of kinematic porosity (n_e) for KAV04A (Rock domain A within Ävrö region) above –300 m for 20 m blocks and 100 m blocks in the k_r fit case.

T model	Scale (m)	Guard zone (m)	r_{min} (m)	Log10(n_e) – 10-percentile	25-percentile	50-percentile	75-percentile	90-percentile
Corr	20	30	1.13	–4.02	–3.97	–3.92	–3.87	–3.83
Corr	100	100	5.64	–4.35	–4.32	–4.29	–4.23	–4.19
Uncorr	20	30	1.13	–3.63	–3.63	–3.61	–3.60	–3.59
Uncorr	100	100	5.64	–4.26	–4.25	–4.23	–4.21	–4.20
Semi-corr	20	30	1.13	–4.02	–4.01	–4.00	–3.98	–3.96
Semi-corr	100	100	5.64	–4.43	–4.41	–4.38	–4.34	–4.31

Table 4-25. Comparison of kinematic porosity (n_e) for KAV04A (Rock domain A within Ävrö region) below –300 m for 20 m blocks and 100 m blocks in the k_r fit case.

T model	Scale (m)	Guard zone (m)	r_{min} (m)	Log10(n_e) – 10-percentile	25-percentile	50-percentile	75-percentile	90-percentile
Corr	20	30	1.13	–4.12	–4.06	–4.01	–3.96	–3.93
Corr	100	100	5.64	–4.55	–4.52	–4.48	–4.41	–4.35
Uncorr	20	30	1.13	–3.72	–3.71	–3.70	–3.69	–3.68
Uncorr	100	100	5.64	–4.35	–4.34	–4.32	–4.30	–4.28
Semi-corr	20	30	1.13	–4.02	–4.00	–3.99	–3.97	–3.95
Semi-corr	100	100	5.64	–4.43	–4.41	–4.38	–4.35	–4.31

4.4.5 Evaluation of uncertainties

The sensitivity of the block-scale properties with regard to the following has been considered:

- The effect of the size of the guard zone has been considered for both the 20 m and 100 m blocks.
- The effect of the lower fracture size limit was considered for both the 20 m block and the 100 m block during a previous study /Hartley et al. 2005a/. In general, the calculations described in this report for the 20 m block have been run with r_{min} of 1.13 m, which is much smaller than the block size but the calculations are still computationally feasible.
- The relationship between fracture size and transmissivity.

4.5 Conclusions from block property study

Results obtained from the 'k_r fit' cases considered for above –300 m and below –300 m elevation are referred to in this section. The following conclusions can be drawn from the study of block properties:

- Matching hydraulic data for all boreholes gives higher values for the median effective hydraulic conductivity, log(K_{eff}), above –300 m, than for log(K_{eff}) below –300 m elevation.
- The mean effective hydraulic conductivity, K_{eff}, for the 20 m block-scale is either lower than or not significantly different from the mean K_{eff} for the 100 m block scale for (i) the semi-correlated cases for each borehole (above and below –300 m); and (ii) all cases (correlated, uncorrelated, semi-correlated) considered for KLX03 above and below –300 m.
- In all cases and all boreholes, the spread of the effective hydraulic conductivity is higher for the 20 m block-scale than for the 100 m block-scale because there is a greater amount of averaging over individual fractures on the 100 m scale.
- Sensitivity cases have been considered for the guard zone size (this is defined as half the difference between the length dimension of the volume in which fractures are generated and the length dimension of the smaller volume in which block properties are calculated). Smaller (20 m blocks) are more sensitive to the size of the guard zone. As a result of this investigation it was found that the 20 m block requires a 30 m guard zone and the 100 m block requires a 100 m guard zone.
- Regional anisotropy with strike towards NW-SE has been shown for all cases for KLX04. This direction is parallel to the regional maximum horizontal in situ stress. For KLX03, the regional anisotropy has WNW-ESE strike direction. For KSH01A, the regional anisotropy has W-E strike direction. For KAV04A, the regional anisotropy has an ENE-WSW strike direction.
- As expected, lower kinematic porosity values are obtained in the simulations matched to hydraulic data below –300 m than above –300 m elevation.

5 Regional model – general conditions

Modelling of groundwater flow and transport for the regional area that includes the Simpevarp and Laxemar subareas is described in this section. The overall aim is to assess the uncertainties of the hydrogeological properties and conditions at Laxemar subarea. A primary objective in this is to assess the role of known and unknown hydrogeological conditions for the present-day distribution of saline groundwater at the Laxemar subarea. An improved understanding of the palaeo-hydrogeology is necessary in order to gain credibility for the Site Descriptive Model in general and the Site Hydrogeological Description in particular. The numerical models developed are then to serve as a basis for describing the present hydrogeological conditions, as well as predictions of future hydrogeological conditions and transport pathways in the forthcoming SR-Can Safety Assessment study for Laxemar.

The overall aim implies a testing of the following modelling components:

- Structural geology with geometrical alternatives.
- Bedrock fracturing.
- Initial and boundary conditions variants.
- Parameter uncertainties (i.e, uncertainties in the hydraulic property assignment).

Another specific objective is to assess the flow-paths from the local-scale model domain, based on the present-day flow conditions. This will allow the distribution of discharge and recharge areas associated with the flow at approximate repository depth to be assessed. (The subsequent Safety Assessment calculation, not part of this study, under future flow conditions and more detailed selection of particle release points may of course show different results.) This aspect is necessary in order to evaluate the impact on the groundwater flow-field of the specified components and to promote proposals of further investigations of the hydrogeological conditions at the site.

5.1 Model assumptions and input sata

The simulations of how flow and reference waters have evolved in the post-glacial period up to the present-day are modelled using CPM (Continuum Porous Medium) and ECPM (Equivalent Continuum Porous Medium) models with fixed hydraulic properties, but with boundary conditions that change with time. In the base case, the head on the top surface was set to the topographic height (relative to sea level), which evolves in time due to post-glacial rebound. Offshore, the head was equal to the depth of the sea multiplied by the relative salinity of the Baltic Sea, and here both the salinity of the Baltic and sea depth varies in time. Simulations were started at 8000 BC (approximately when the glaciers in the area melted) with an assumed initial distribution of the reference water fractions, and run until the present-day. The start date was chosen well before the Littorina sea phase, and when the land around Laxemar rose briefly before temporarily becoming submerged again (see Section 5.7). The key assumptions in the modelling and the possible alternatives are:

- The deformation zone model provided by Geology represents possible hydraulically active features. Where no direct observation has been made of a deformation zone's properties, then it has been assumed vertical in the provided deformation zone model.

In the regional modelling described here, the transmissivity is assumed to decrease with depth using a step function as the reference case. Alternatives include removing low-confidence lineaments, different depth profiles of transmissivity within the zones, adjusting the depth trend within zones where a direct measurement(s) of transmissivity has been made, or sampling the unknown parameters stochastically.

- The regional-scale model may be divided into five rock domains. For each rock domain, the Hydro-DFN models developed for the appropriate borehole (KLX04, KLX03, KSH01A or KAV04A) can then be extrapolated over the extent of the rock domain. According to the Hydro-DFN models, there is a step-change in hydraulic properties at an elevation of about –300 m. The step-change is maintained in the regional-scale model although at an elevation of –200 m. Alternatives include several different Hydro-DFN models based on different assumptions about a transmissivity dependence on fracture size, a different elevation chosen for the step-change in hydraulic properties, or an additional reduction in hydraulic conductivity below about –600 m.
- The hydrogeochemistry measurements are represented by two alternative analyses. Either in terms of 4 reference water types (Brine, Littorina, Meteoric and Glacial) with fractions computed on the basis of the M3 analysis /Laaksoharju et al. 1999/, or as individual ions and isotope ratios as calibration targets. The latter has proved to be a useful complement to the reference water analysis because of the inherent uncertainties associated with the principal component analysis used in the M3 analysis. An appropriate time to start the simulations is 8000 BC, at which time the groundwater is assumed to be a mixture of Glacial and Brine reference waters with specified mixing fraction spatial distributions. Variants include different distributions for initial mixing fractions.
- Surface groundwaters are appropriate mixtures of Glacial and Littorina waters during the early Baltic Ice Lake, Yoldia Sea, and Ancylus Lake periods. The surface groundwaters then switch to a mixture of Meteoric water and Littorina during the Littorina Sea and current Baltic Sea phases. The history of sea-water salinity has been provided and this is used to determine the relative fractions of Littorina and Meteoric reference waters at the top surface of the model offshore. The surface water composition is implemented as boundary conditions on the reference water transport equations.
- As a starting point the surface flow condition is that onshore, the head equals the evolving topographic surface as provided by ice-sheet and sea-level modelling. Alternatively, the head is set equal to an estimated watertable based on water levels in groundwater wells in the area. Finally, a third option considered was to specify a flux type boundary condition using a model of recharge that is a function of the calculated head, and potential groundwater recharge.

5.2 Conceptual model

The primary concepts used in the regional-scale groundwater flow modelling are:

- The current hydrogeological and hydro-geochemical situation at Laxemar has arisen due to natural transient processes that have evolved over the post-glacial period.
- The hydrogeochemistry can be modelled in terms of four reference waters (Brine, Glacial, Littorina and Meteoric) using the reference water fractions as conservative tracers. Alternatively, major ions and isotopes can be used as calibration targets.
- The natural transient processes (land-rise, marine transgressions, dilution/mixing of sea water) can be modelled by appropriate choice of flow and reference water boundary conditions.

- The spatial variability of hydraulic properties can be represented in an ECPM model by appropriate upscaling of bedrock fracturing and downscaling of deformation zones on a suitable grid resolution.
- The properties of the Hydraulic Rock Domain (HRD) are represented as an ECPM under-pinned by a regional-scale stochastic DFN model. The HRD properties (hydraulic conductivity tensor and porosity) are calculated explicitly for each element in the ECPM model by an upscaling method. Alternatively, a CPM model based on median values from the Hydro-DFN can be used. In both case a depth dependency is considered.
- For the Hydraulic Conductor Domains (HCD), the properties (transmissivity and porosity) are assumed to have depth dependence over each deformation zone. The thickness is constant and a depth dependency is considered.
- For the Hydraulic Soil Domains (HSD), a three layer model is used with the properties (hydraulic conductivity, thickness, and porosity) held constant over the whole top surface of the model. As an alternative, a detailed heterogeneous model (delivered by SurfaceNet /Nyman 2005/) still using three layers, but with variable thickness and properties as defined by 6 different soil domains.

Sections 5.3–5.9 give details of the actual concepts, parameters values, and variants considered in the regional-scale groundwater flow modelling.

5.3 Concepts for reference water transport

Based on the analysis of Hydrogeochemistry /SKB 2004, 2006/, groundwater compositions were described using a simplified system of four reference waters, which have been used previously in M3 geochemical modelling:

- **Brine water** represents the sampled deep brine type (Cl = 47,000 mg/L) of water found in KLX02. An old age for the Brine is suggested by the measured ^{36}Cl values indicating a minimum residence time of 1.5 Ma for the Cl component.
- **Glacial water** /SKB 2006/ represents a possible melt-water composition from the last glaciation > 11,000 BC. Sampled modern glacial melt water from Norway is used for the major elements and the $\delta^{18}O$ isotope value (−21‰ SMOW) is based on measured values of $\delta^{18}O$ in surficial calcite coatings (subglacial $CaCO_3$ deposits precipitates on present rock surface on the Swedish west coast /Tullborg and Larson 1984/. The δD value (−158‰ SMOW) is a modelled value based on the equation ($\delta D = 8 \times \delta^{18}O + 10$ for the meteoric water line /Craig 1961/.
- **Littorina water** represents modelled Littorina water.
- **Meteoric water** corresponds to a shallow groundwater sampled in the percussion-drilled borehole HAS05 (sampled between –32 and –80 m elevation) representing the shallow end member for the local hydro-geochemical model in Laxemar and Simpevarp subareas (Gurban 2005, written communication).

The major ion components and stable isotope composition for the selected reference waters are given in Table 5-1.

In the modelling, the groundwater density and viscosity vary spatially in three dimensions based on equations of state that are a function of total groundwater salinity, total pressure, and temperature. The salinity for a given water composition is just the sum over reference waters of the product of the reference water fraction and the salinity of that reference water.

Table 5-1. Groundwater analytical or modelled data used as reference waters for Laxemar /SKB 2004/.

	Cl (g/L)	Na (g/L)	K (g/L)	Ca (g/L)	Mg (g/L)	HCO_3 (g/L)	SO_4 (g/L)	δD (‰)	$\delta^{18}O$ (‰)
Brine	47.2	8.5	0.045	19.3	0.002	0.014	0.906	–44.9	–8.9
Littorina	6.5	3.674	0.134	0.151	0.448	0.093	0.890	–38.0	–4.7
Meteoric water	0.119	0.237	0.004	0.025	0.006	0.372	0.118	–73.8	–9.9
Glacial	0.001	0	0	0	0	0	0.001	–158.0	–21.0

The salinities for the reference waters were calculated from the Total Dissolved Solids (TDS, g L^{-1}) using:

Salinity = TDS / density,

where density is a function of salinity (and temperature, and total pressure). It was assumed that the data given in Table 5-1 were obtained under laboratory conditions. Therefore, it was assumed that the data correspond to a temperature of 20°C and pressure of one atmosphere. The density and viscosity were obtained using empirical correlations for NaCl brines (See /SKB 2004, Kestin et al. 1981/). This corresponds to representing transport of equivalent NaCl for each water. The approximation made is reasonable, but it will lead to the density and salinity being slightly under-estimated for a Ca-rich solution such as the Brine reference water.

Assuming a pressure profile down-core (surface ~ 1 atm to ~ 25 MPa at depth), a salinity profile (surface 0‰ to 72.3‰ (brine) at depth), and a temperature range (surface 6°C; geothermal gradient 0.01°C m^{-1}; i.e. ~ 30°C at bottom of model), the groundwater density (ρ) can be calculated from the equation of state. At the surface, the density is around 1,000 kg m^{-3}; and at depth the density is around 1,056 kg m^{-3} (the greatest model depth is 2,300 m). The groundwater viscosity (μ) can be similarly calculated. At the surface, the viscosity is around 1.3×10^{-3} Pa s^{-1} and at depth, the viscosity at depth is around 0.9×10^{-3} Pa s^{-1}.

The equations used to represent the transport of fractions of reference waters, with rock-matrix diffusion, are:

$$\frac{\partial(\phi_f \rho)}{\partial t} + \nabla \cdot (\rho \mathbf{q}) = 0 \qquad \text{(Mass conservation for groundwater)}$$

$$\frac{\partial(\phi_f \rho \sigma_i)}{\partial t} + \nabla \cdot (\rho \sigma_i \mathbf{q}) = \nabla \cdot (\phi_f \rho \mathbf{D} \nabla \sigma_i) + \zeta \rho D_{\text{int}} \left.\frac{\partial \sigma_i'}{\partial w}\right|_{w=0} \qquad \text{(Transport of reference waters)}$$

$$\alpha_i \frac{\partial \sigma_i}{\partial t} = D_{\text{int}} \frac{\partial^2 \sigma_i'}{\partial w^2} \qquad \text{(Rock-matrix diffusion)}$$

where σ_i is the mass fraction of reference water i in the water in the fracture system (mobile water); σ_i' is the mass fraction of reference water i in the water in the matrix (immobile water); $\boldsymbol{q}$ is the Darcy velocity:

$$\mathbf{q} = -\frac{k}{\mu}(\nabla p + \rho \mathbf{g}).$$

$\boldsymbol{D}$ is the dispersion tensor; ϕ_f is the kinematic porosity, ρ is the groundwater density, ζ is the specific surface area of the fractures D_{int} is the intrinsic (or effective) diffusion coefficient, α_i is the capacity factor for the rock matrix (which allows for sorption), w is a coordinate into the rock matrix, k is the permeability, μ is the fluid viscosity, p is residual pressure, t is time, and $\boldsymbol{g}$ is gravitational acceleration. All parameters use SI units.

In fact, the transport equations for the fractions of reference waters are not all independent. Since the sum of the reference water fractions must be equal to one, then it is not necessary to solve explicitly the transport equation for the final reference water. It can simply be evaluated as the remaining water fraction once the other reference water fractions have been computed at each time-step.

5.4 Porosity terms and concepts

Groundwater flow and transport depend on the total connected porosity. This can be categorised in various ways. The most important distinction for groundwater flow and transport is the distinction between the kinematic, or flowing, porosity and the diffusion accessible porosity. The kinematic porosity is the porosity accessible to flowing groundwater, and the diffusion accessible porosity is the rest of the total connected porosity. In some rocks, such as some porous sandstones, groundwater flow may occur in most of the connected porosity and the diffusion accessible porosity may be relatively negligible. However, in fractured rocks, most of the flow may occur in the fractures, which may provide the dominant contribution to the kinematic porosity. The diffusion accessible porosity may then play a very important role in solute transport.

The diffusion accessible porosity may include contributions from the inter-granular porosity and from micro-fractures. The latter may, indeed, provide the dominant contribution to the diffusion accessible porosity. The diffusion accessible porosity may also include contributions from fractures in which there is negligible flow (which would typically be a subset of the smaller fractures) and from regions of nearly immobile water in the larger fractures (resulting from constrictions in fracture aperture or the presence of gouge material). In practice, it may be difficult to make a clear distinction between the fractures carrying flow and those in which the groundwater is immobile.

CONNECTFLOW allows the modelling of groundwater flow and solute transport in fractured rocks accounting for flow and solute transport by advection, dispersion and diffusion through the kinematic porosity together with diffusion of solute between the groundwater in the kinematic porosity and immobile groundwater in the diffusion accessible porosity. Processes such as radioactive decay and sorption can also be taken into account. The process of diffusion between groundwater in the kinematic porosity and the diffusion accessible porosity (RMD) can lead to a significant retardation of solute migration relative to migration in the kinematic porosity alone. CONNECTFLOW uses the simplest model of RMD which represents the process in terms of a 1D model of diffusion between groundwater flowing in infinite, parallel, equidistant, constant-aperture, planar fractures and immobile groundwater in the intervening rock.

This model is a considerable simplification of the physical process. It is recognised that the groundwater flows in irregular channels that only occupy parts of fracture planes and the groundwater velocity varies within a fracture and from fracture to fracture. Solute migrating through the fractures will therefore diffuse away from different fractures at different times, and the diffusion will be 3D rather than 1D. However, effective parameters for the model can be chosen to give a good overall representation of diffusion away from fractures both at early times and in the long-time limit when solute has diffused into (or out of) all of the diffusion accessible porosity, although the model is unlikely to give an accurate representation of diffusion at intermediate times.

More complicated models could readily be envisaged, and implemented. For example, models could be developed in terms of 1D diffusion in different geometries, such as cylindrical or spherical geometries. Models could also be developed in which the contribution to the diffusion accessible porosity from immobile water in fractures was distinguished from the contribution from micro-fractures and inter-granular porosity in the rock between the fractures. A range of variants of such models could be considered from diffusion in series or in parallel between the kinematic porosity and the two components of the diffusion accessible porosity. Such models could be implemented in CONNECTFLOW.

However, the simple RMD model currently used in CONNECTFLOW is preferred because it would be very difficult, if not impossible, to adequately characterise experimentally the parameters of the more complicated models, whereas most of the parameters of the simple model can in principle be measured experimentally or justified on the basis of experimental data. These parameters are:

(i) the effective (or intrinsic) diffusion coefficient (for diffusion in the diffusion accessible porosity),

(ii) the diffusion accessible porosity,

(iii) the maximum distance available for diffusion into the diffusion accessible porosity,

(iv) the area of fracture surface per unit volume (the flow-wetted surface per unit volume) over which there may be diffusion between the groundwater flowing in the fractures and the diffusion accessible porosity,

(v) the kinematic porosity.

The effective diffusion coefficient and the diffusion accessible porosity on a small scale can be measured in diffusion experiments for example. The diffusion accessible porosity cannot be measured directly on large length scales, but has to be upscaled from the small scale on the basis of a model for the connectivity of the pores in the matrix. Electrical resistivity measurements may be used to support the model of the connectivity. Measurements of the total porosity (for example using drying experiments) may also support the values for the diffusion accessible porosity, at least, by providing an upper bound.

The fracture spacing will be based on information about the fracture network. This may be derived from the value of P32. The maximum distance available for diffusion into the diffusion accessible porosity can be based on the spacing of the fractures (if it is considered that all of the rock between the fractures is potentially accessible) or based on the dimensions of alteration halos around fractures (if it is considered that only the rock within a limited distance of fractures is accessible).

The flow-wetted surface per unit volume cannot be measured directly. It can be estimated on the basis of DFN models of the flowing conductive network of fractures, for example. This is discussed further in Subsection 5.10.2.

Measurement of the kinematic porosity is difficult, particularly in fractured rocks. In practice, it may be necessary to infer the kinematic porosity on the basis of DFN models of the flowing fractures (see Section 2.3 and Subsection 3.3.5), for example. However, in some circumstances, the value of the kinematic porosity may not have a large impact on solute transport. If the travel-times are long enough that sufficient diffusion accessible porosity is accessed by RMD, then what matters may be the portion of the diffusion accessible porosity accessed, and it may be easier to justify the appropriate value for this than the appropriate value for the kinematic porosity.

5.5 Topography and model domain

New topographic and bathymetric data (DEM) were supplied for Laxemar v1.2 on a 10 m scale covering the entire regional-scale model as defined in the TD. This fine-scale data was used both to define the model area and to set boundary conditions on the top surface. The reference case model domain was based on regional water divides associated with River catchments. A smaller regional model domain was used for scoping calculations based on 'apparent' local water divides identified in the S1.2 modelling. In CONNECTFLOW, it is possible to construct unstructured meshes with irregular boundaries, and hence it is possible to choose boundaries that follow water divides. Figure 5-1 shows the extent of the topographic data along with the regional scale area as proposed in the TD. Also, the large regional model (black curve) and the alternative smaller regional model (red) used for initial calibration modelling are superimposed. The TD definition of the local model (large white rectangle) area together with the Laxemar and Simpevarp release areas (white) are also shown for orientation.

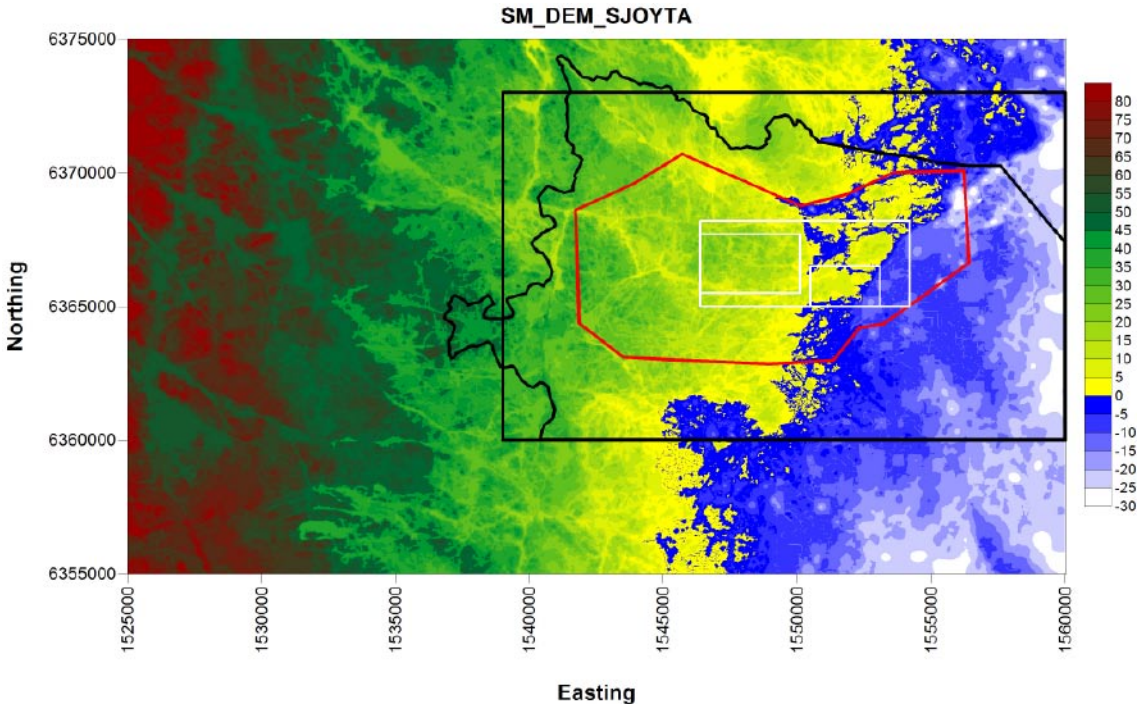

Figure 5-1. *Overview of available data: 10 m topographic and bathymetric data (sm_dem_sjoyta). The regional scale area as defined in the TD (black rectangle), the large regional model (black curve) and the alternative smaller regional model (red) used for calibration modelling are superimposed. The TD definition of the local model area (large white rectangle) together with the Laxemar and Simpevarp release areas (white) are shown for orientation.*

Several variants of the possible Digital Elevation Map (DEM) data for current day groundwater levels were delivered:

- Topography including lake surfaces.
- Simulated DEM for the watertable. An interpolation based on groundwater level measurements, water courses, lakes and peat lands. The measurements from groundwater wells are mostly located in low-lying areas, and so there is likely to be a bias toward low water levels. Hence, this is assumed to be the lowest possible watertable. The aim is to smooth out the topographic variations and thereby decrease the amount of water entering through the top surface of the model, see Figure 5-2. Figure 5-3 shows the elevation difference between the topographic DEM using the lake surfaces and the simulated DEM for the watertable. A value equal to zero, indicating no difference, is found off-shore and for all areas corresponding to water courses, lakes and peat lands. The other areas show positive values, i.e. the watertable has been lowered compared to the topography, as expected. This case is considered to be the minimum possible watertable elevation, and is probably unrealistically low.

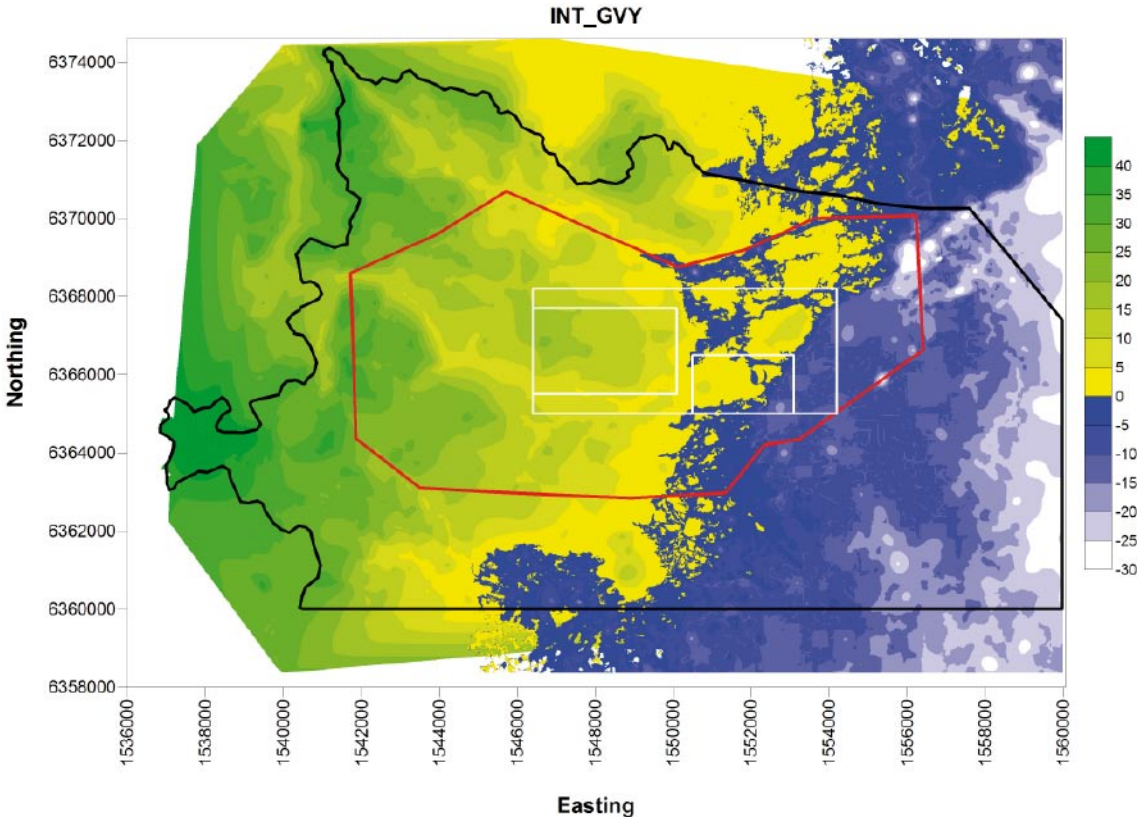

Figure 5-2. *Elevation map of the simulated DEM for the interpolated surface between water courses, lakes and peat lands, which is assumed to be the lowest possible watertable. The large regional model (black) and the smaller regional model (red) used for calibration modelling are superimposed. The TD definition of the local model area (large white rectangle) together with the Laxemar and Simpevarp release areas (white) are shown for orientation.*

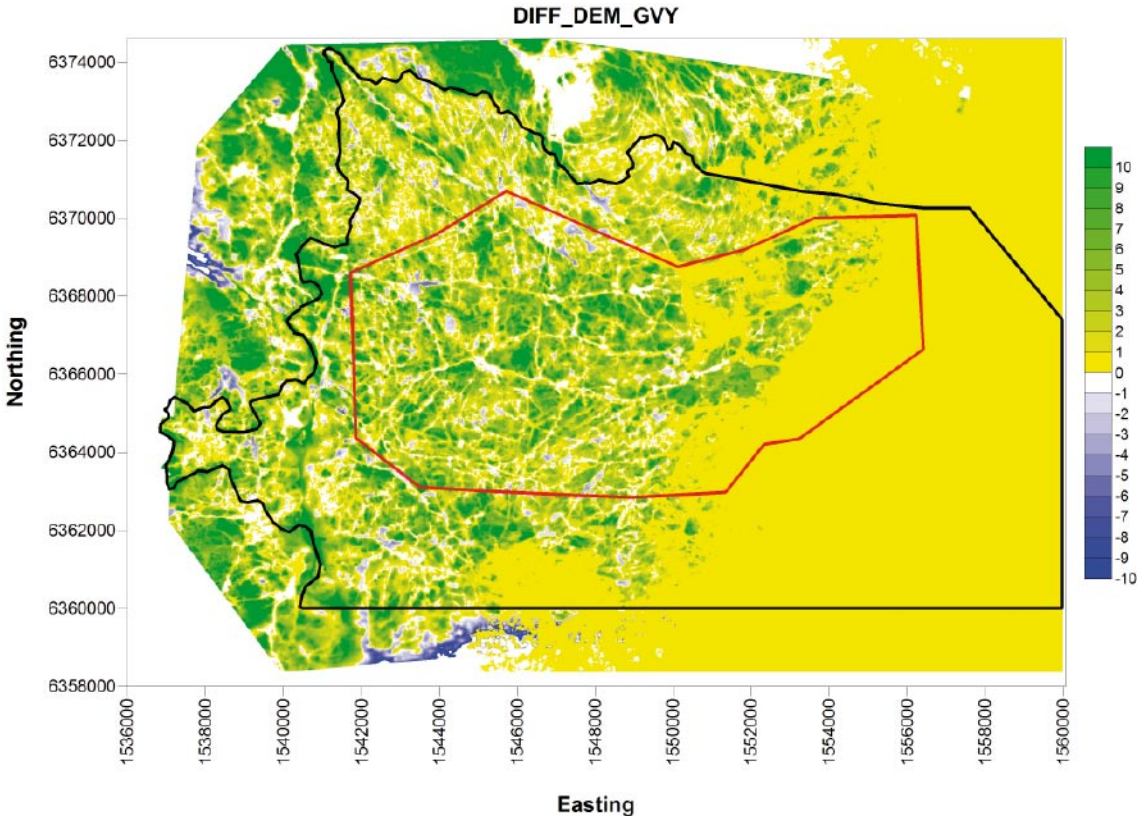

Figure 5-3. *Elevation map of the difference between the topographic DEM and the simulated DEM for the interpolated watertable between water courses, lakes and peat lands, which is assumed to be the maximum possible watertable. The large regional-scale model (black) and smaller regional model (red) used for calibration modelling are superimposed.*

- Additional variants of the simulated watertable data. In the top picture in Figure 5-4 (est_gvy_03) the elevation of the lowest possible watertable has been increased by 30% of the difference between the topographic data and the simulated watertable. This should be a more realistic simulation of the watertable. The lower picture Figure 5-4 (est_gvy_06) shows a data set using an increase equal to 60% of the difference.
- Finally, a watertable can be calculated by groundwater simulation given a specified maximum potential groundwater recharge through the top surface, as described in Section 2.6.

All topographic data was supplied as a data set combined with the bathymetric data in the sea.

The work of selecting a model domain involves finding natural, well defined features where the hydrological conditions are well understood. Such features are regional and local water-divides that can be created by long ridges or hills and deep valleys, often in combination with larger regional deformation zones.

It was decided that the large regional model boundary from Simpevarp v1.2 /Hartley et al. 2005a/ should be reused for Laxemar v1.2. The large regional model domain follows regional and local water-divides where available. Reaching out in the Baltic Sea, the model boundary mainly follows large regional deformation zones, and the model is extended enough to the east so as not to cause any boundary effects. This model domain covers the whole regional-scale area, although some areas outside of regional or local water divides were removed, and no-flow boundaries were set on the lateral sides along these water divides (See Figure 5-5). However, modelling transient flow coupled to transport of four reference waters creates significant computational demands, and hence it became necessary to

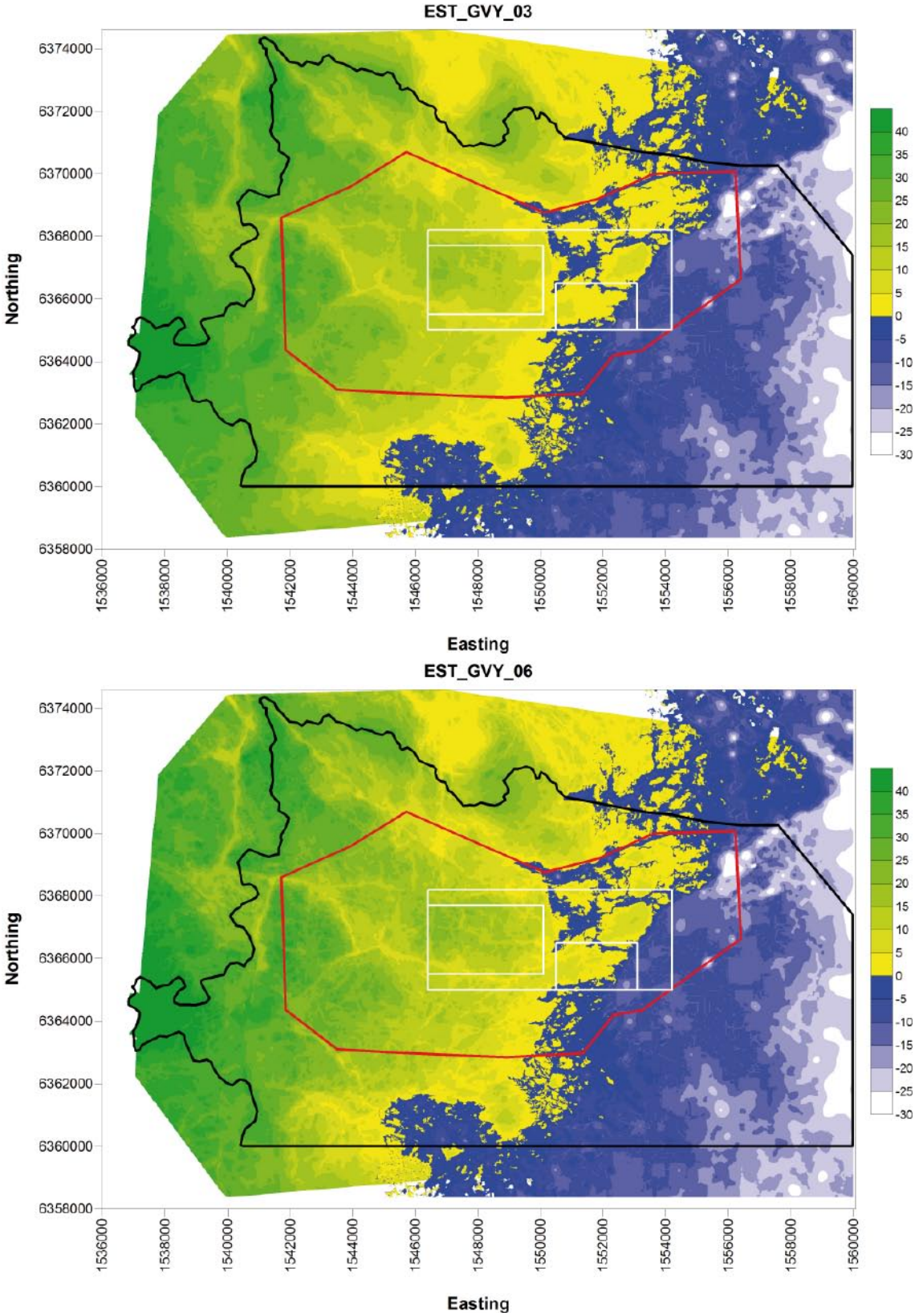

Figure 5-4. *Elevation map of the simulated DEM increased by 30% (top: est_gvy_03.xyz) or 60% (bottom: est_gvy_06.xyz) of the difference between the topographic data and the simulated DEM for the watertable (est_gvy_03.xyz). The large regional model (black) and the alternative smaller regional model (red) used for calibration modelling are superimposed. The TD definition of the local model area (large white rectangle) together with the Laxemar and Simpevarp release areas (white) are shown for orientation.*

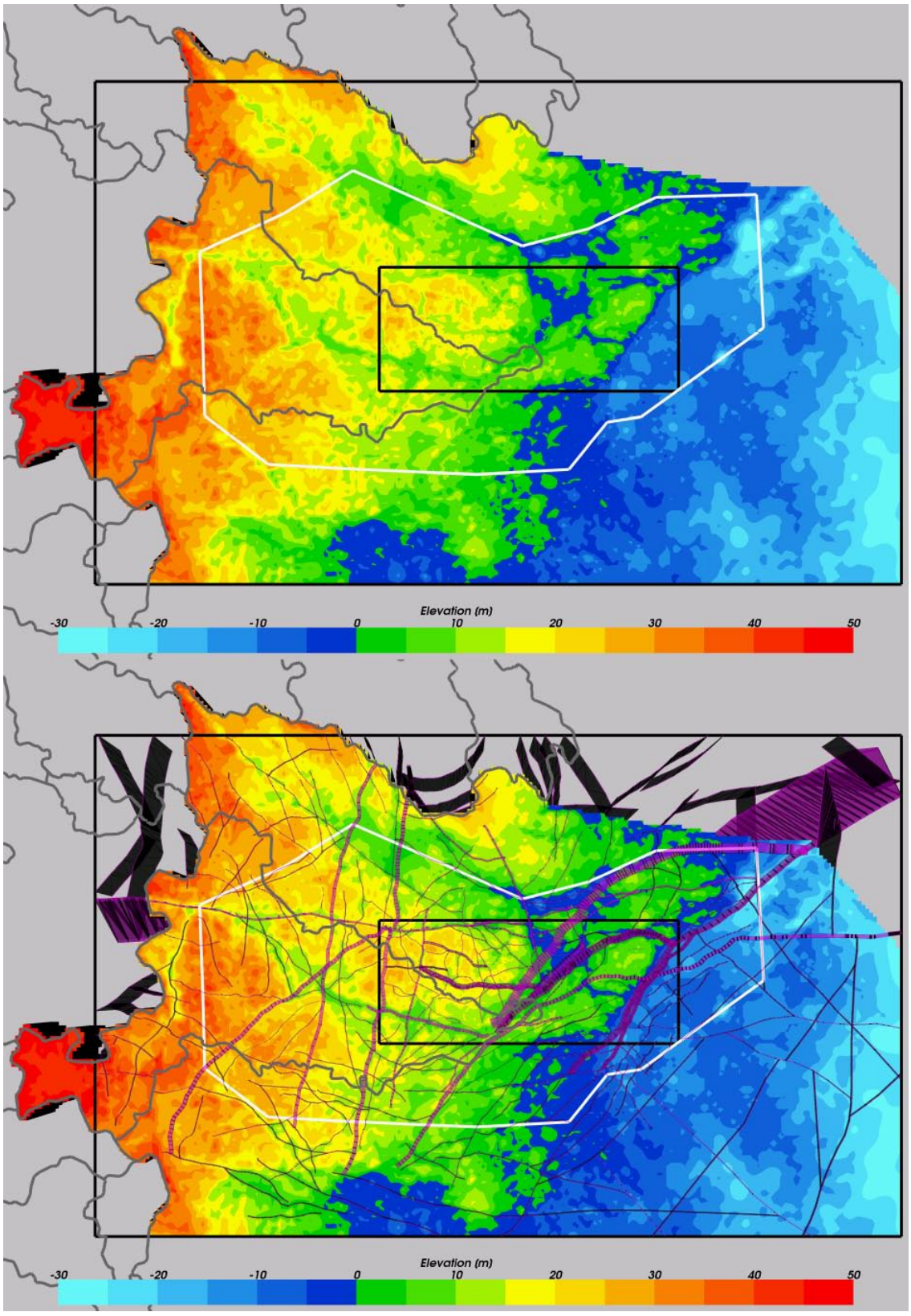

Figure 5-5. *Topographic elevation map of the Laxemar v1.2 regional model domain. The TD definitions of the regional model (large black rectangle) and the local model (small black rectangle) areas are superimposed together with the alternative smaller regional model used for calibration modelling (white). The water divides are shown as grey lines. In the lower plot, the HCD model is superimposed, coloured purple.*

use an additional smaller model domain for the initial calibration phase of the model where many realisations and variants were performed. The model boundary chosen was based on the results from Simpevarp v1.2 /Hartley et al. 2005a/, where a comprehensive sensitivity analysis was performed with the aim of finding a minimum sized regional model for which stable calibration results could be obtained, see Figure 5-5.

5.6 Selection of grid resolution

Based on the requirements of Design, hydraulic properties were calculated on a 20 m and 100 m block-scale as described in Chapter 4. The SKB Task Description for the regional-scale modelling specified a 100 m grid resolution. For practical reasons of model size, greater resolution over the whole regional model would be prohibitive for transient multi-component reference water transport problems. However, it is possible to increase the refinement in restricted areas to get a better resolution of geological structures and simulated processes. Figure 5-6 shows the location of refined areas around Laxemar, Simpevarp and Ävrö, as well as the alternative smaller regional model. The refined areas have a grid resolution of 50 m, and everything outside of these areas has a grid resolution of 100 m. The Ävrö area is only refined in a few variants in order to investigate the impact on the chemistry calibration for the boreholes in these areas.

Figure 5-7 shows the resolution of the hydraulic conductivity of a CPM over the local-scale area for a case with homogenous HRD and deterministic HCD features. Figure 5-8 is the same plot with the HCD deformation zones superimposed as semi-transparent volumes.

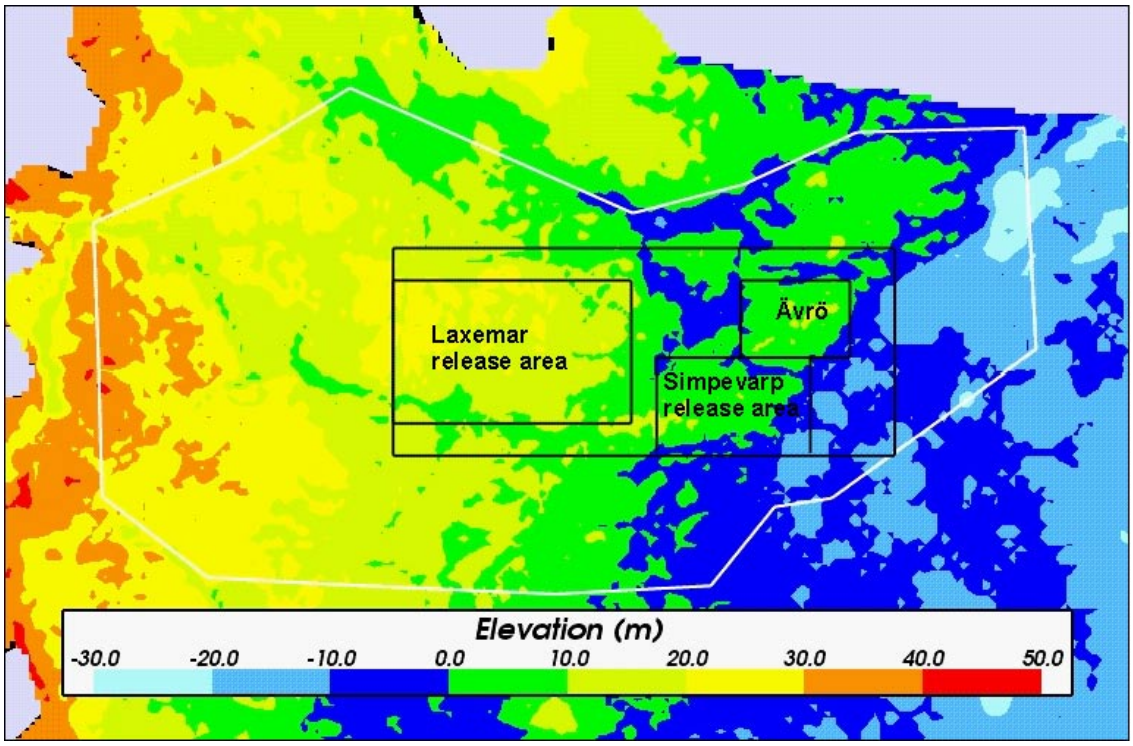

Figure 5-6. *Close-up view of the Laxemar v1.2 refined areas and alternative smaller regional model domain (white), coloured according to elevation. 50 m elements are used in the three refined areas. The Laxemar and Simpevarp areas are also used for releasing particles when calculating flow-paths and performance statistics. The refined area of Ävrö is used in some variants to improve the local calibration.*

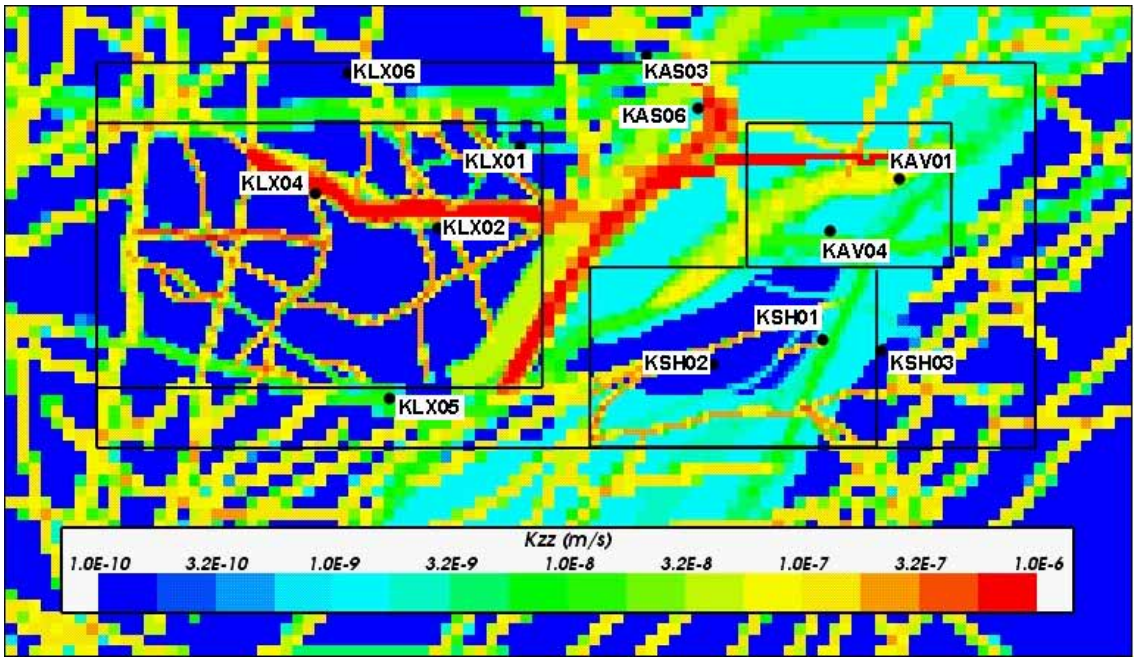

Figure 5-7. *Vertical hydraulic conductivity Kzz (m/s) on a horizontal slice at z = –500 m showing the representation of the HRD (homogeneous case) and HCD on the regional- and site-scales using an embedded grid. Boreholes are superimposed in black.*

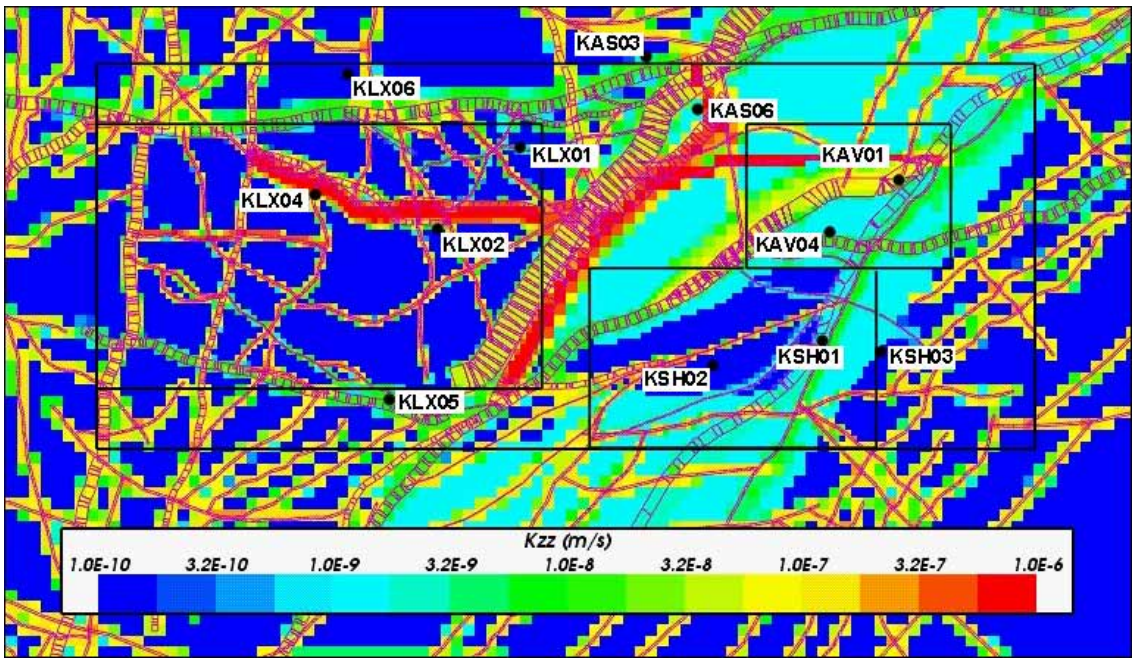

Figure 5-8. *Vertical hydraulic conductivity Kzz (m/s) on a horizontal slice at z = –500 m showing the representation of the HRD (homogeneous case) and HCD on the regional- and site-scales using an embedded grid with the deformation zones superimposed and shown semi-transparent (purple). Boreholes are superimposed in black.*

The embedded 50 m grids for the Laxemar and Simpevarp site-scale release areas can be seen in these plots. It can be seen that representation of the deformation zones outside the refined areas is quite coarse and there is a potential for zones to be smeared out sufficiently to create artificial connections between zones (the downscaling method for mapping the deformation zone properties onto a grid is described in Section 2.4). Therefore, the 50 m refinement is used to an elevation of –1,000 m in the Laxemar and Simpevarp site-scale release areas. At the interface between the two levels of refinement, internal boundary conditions are imposed to ensure continuity of variables (pressure, and reference water fractions) and conservation of mass and reference water flux (see Section 2.6). The improved refinement clearly gives a better representation of the deformation zones within the refined areas. Previous sensitivity studies (Simpevarp v1.2) using transport statistics as a performance measure suggested that the finer 50 m grid would reveal a bi-modal type behaviour that is not apparent for the coarser 100 m grid. This bi-modal behaviour is caused by a better distinction in the 50 m grid case between particles starting in a deformation zone and particles starting in the surrounding rock.

5.7 Initial and boundary conditions

The boundary conditions used must represent the transient processes of shore displacement due to post-glacial rebound and the variations in the salinity of the Baltic Sea. The general modelling approach was to hold the model domain fixed (i.e. same x, y and z coordinates), but modify the head and salinity on the top surface in time.

The evolution of shore displacement over the post-glacial period is shown in Figure 5-9 and compared with that used in the Simpevarp v1.2 modelling /Hartley et al. 2005a/. The shore displacement data used for Laxemar v1.2 covers the time period from 10,000 BC until present and includes very sharp changes early on, although it is smoother than the curves used for Simpevarp v1.2. The early sharp changes in shoreline correspond to rapid melting of the glacier. The simulations were started at 8000 BC, well before the start of the Littorina phase and after the initial rapid changes in sea-levels that resulted in the area around Laxemar beginning to rise out of the sea. The uncertainty in the shoreline displacement curve is about ± 1 m for the last few thousand years. The uncertainty in the shore dsiplacement curve around –9000 AD to –7000 AD has some influence on an appropiate start time and initial conditions. For the L1.2 curve, some areas of the studied area in the far west of the model emerge from Ancylus Ice Lake and so are briefly exposed to infiltration by meteoric water before the advance of the shoreline and onset of the Littorina phase. Hence, there is some uncertainty about shoreline and surface waters during these early phases. However, these the effects on hydrogeochemistry are expected to be small compared to those arise as a consequence of the density turnover resulting from the Littorina phase and later flushing by Meteoric water as the whole Laxemar subarea became terrestrial.

The salinity progress in the Baltic Sea at Oskarshamn is shown in Figure 5-10 /Westman et al. 1999/. The data used in the modelling is represented by the blue line. The maximum and minimum values along the curve are also presented in orange to give an indication of uncertainty. The present-day salinity at Oskarshamn (6.8‰) is represented by a straight blue line in the figure. One notable difference from the salinity curve used for S1.2 is the lack here of an earlier saline spike associated with the Yoldia Sea around –9000 AD at a time when the whole area studied would have been covered by the sea and hence a potential density turnover occurring prior to the later density turnover associated with the Littorina sea stage. However, the Yolida phase was short-lived and of uncertain salinity.

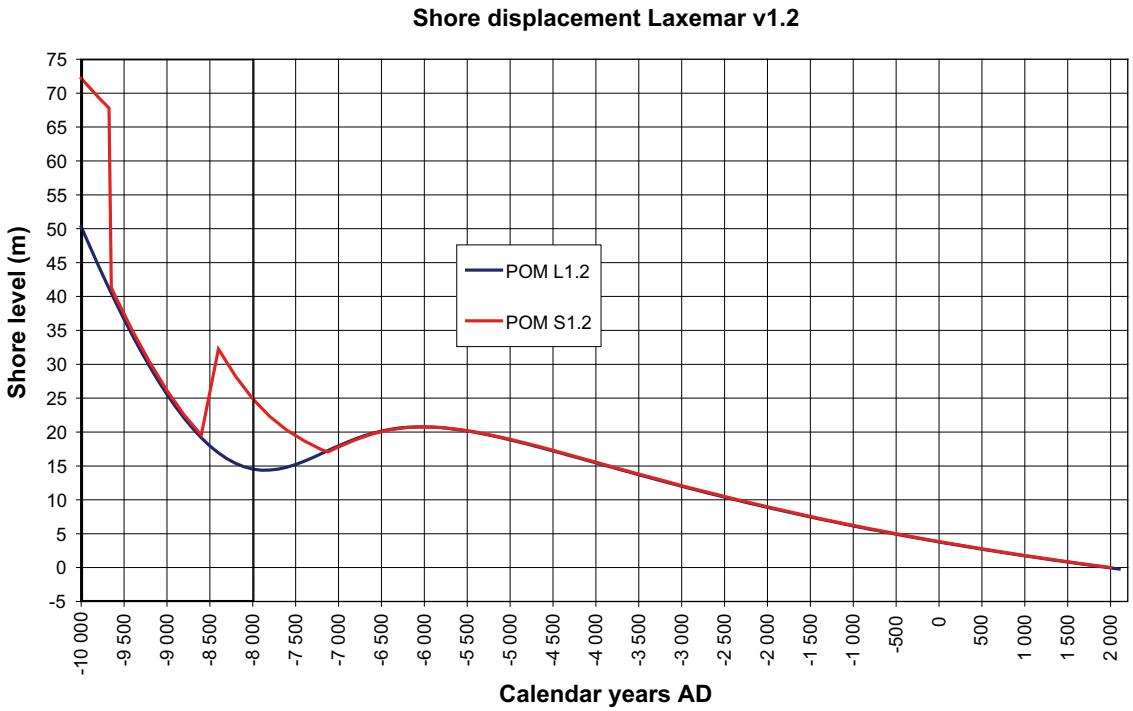

Figure 5-9. *The shore displacement used for Laxemar v1.2 (blue). The data used for Simpevarp v1.2 are shown for comparison (red). Only data from –8000 AD and onwards are used.*

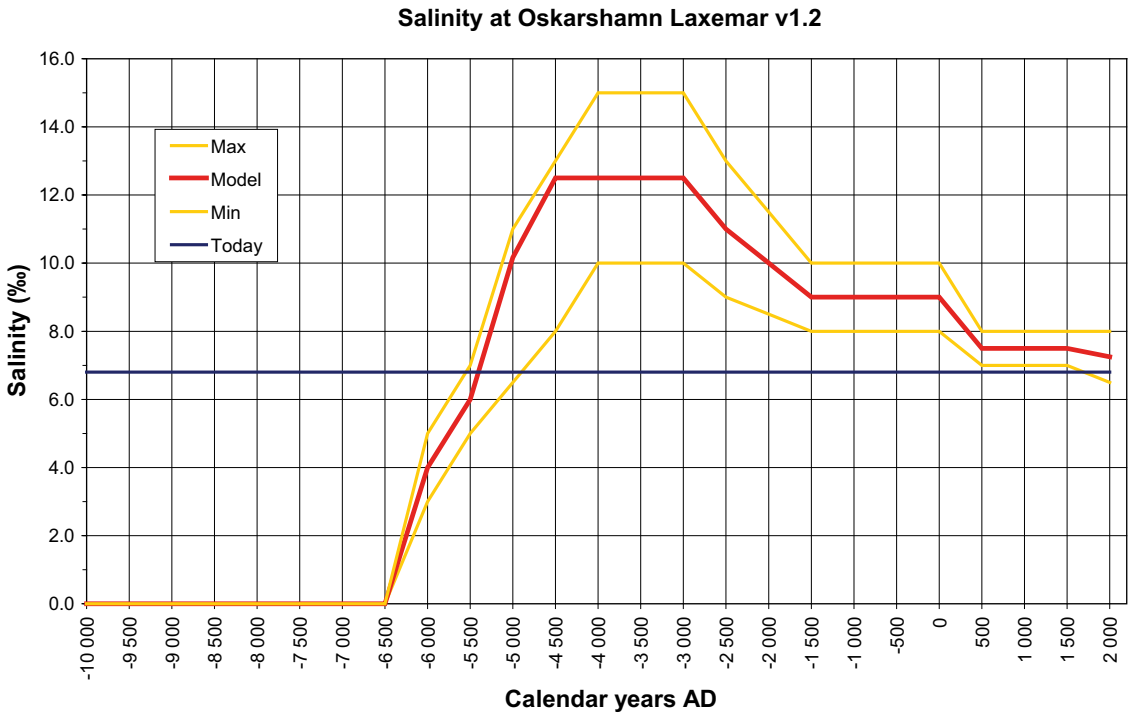

Figure 5-10. *The salinity progress in the southern Baltic Sea. The red line shows the data used in the model and the orange lines indicate the maximum and minimum intervals. The present-day salinity is indicated by the blue line.*

The evolution of salinity in the Baltic informs how the Glacial, Littorina and Meteoric reference waters have mixed in differing fractions over time. It is also important to have a more general hypothesis of the evolution of surface and sub-surface reference waters. The current understanding is illustrated in Figure 5-11 /SKB 2006/.

In the reference case, the head on the top surface was set to the topographic height, which evolves in time due to changes in the height relative to the shoreline (see Figure 5-9). Offshore, the head was equal to the depth of the sea multiplied by the relative density of the Baltic Sea to freshwater.

Other variants considered were to use a simulated DEM for the watertable, calculating the head on the top surface. The watertable is based on measurement data in the area and an assumed varying offset from the surface. The watertable for past times was approximated as the present-day watertable minus the shoreline displacement. A third alternative was to use a flux type top surface pressure boundary condition, as defined in Section 2.6, with a potential groundwater recharge of 165 mm/year (as specified in the SKB Task Description) and calculate the evolving watertable at each time-step.

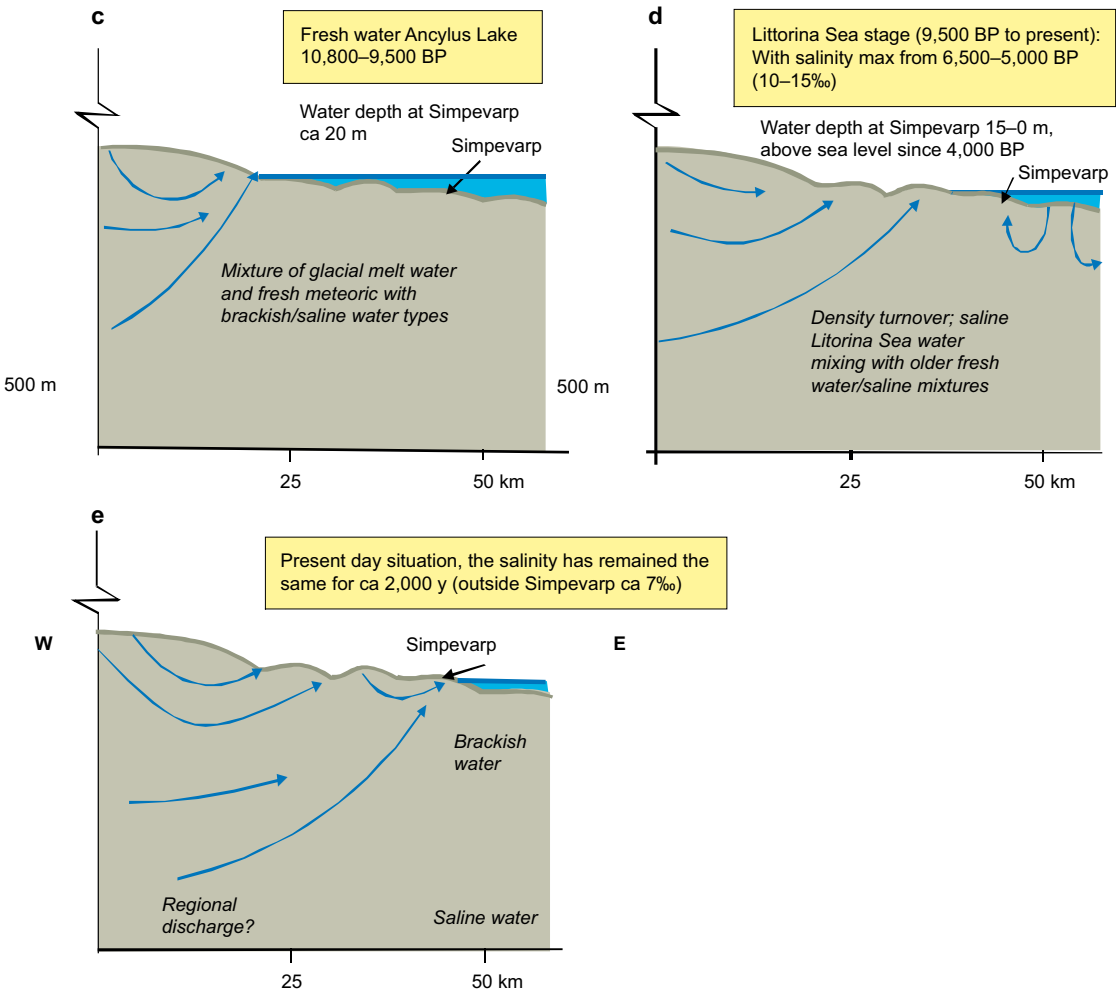

Figure 5-11. *Hydro-chemistry scenario for evolution of reference water transport from 10,800 BP to present-day showing 5 distinct stages as proposed for Simpevarp v1.2 /Laaksoharju et al. 2004/.*

Based on the surface hydro-chemistry concept shown in Figure 5-11, the definition of reference water boundary conditions was specified according to the following stages:

- Ancylus Ice Lake: Full Meteoric water onshore; Full Glacial water offshore.
- Littorina Sea to present-day: Full Meteoric water onshore; offshore a mixture of Marine and Meteoric reference waters according to the ratio of TDS shown in Figure 5-10 to the TDS of the Littorina reference water.

The boundary conditions on the sides are no-flow and zero flux of reference waters. At the bottom of the model, at z = –2,300 m, there is a no-flow condition and groundwater is set to pure Brine, i.e Brine fraction = 1.0, all other fractions = 0.

The initial conditions for the reference waters assume a profile of Brine at depth and Glacial water at the surface, with a start time of –8000 AD. The results from Simpevarp v1.2 suggest a piecewise linear initial condition (IC 1) with full Glacial water down to 700 m depth, and then a gradual rise in Brine to full Brine at 1,500 m depth. This profile, illustrated in Figure 5-12, was based on the present-day profile of Brine and Glacial water in KLX02, the only borehole deep enough to measure the full Brine reference water.

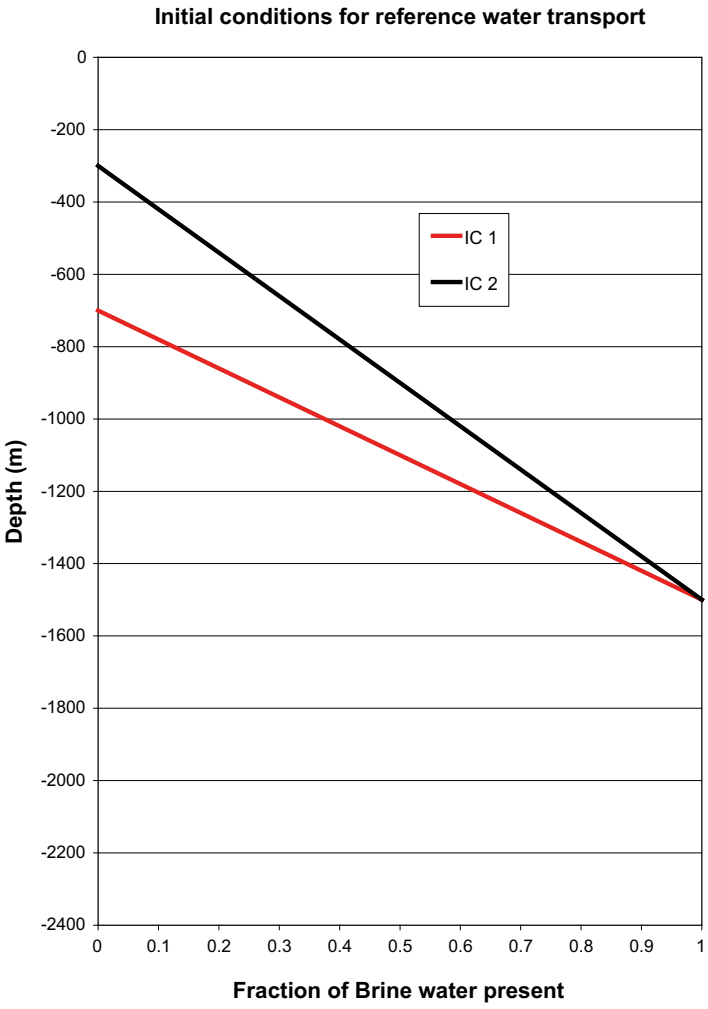

Figure 5-12. *Initial conditions for reference water transport, at –8000 AD. For IC 1 (the reference case), the water is pure Glacial above –700 m. There is then a linear transition between Glacial and Brine water toward pure Brine below –1,500 m. For IC 2, the water is pure Glacial above –300 m, with a linear transition between Glacial and Brine water toward pure Brine below –1,500 m.*

An alternative initial condition (IC 2) with full Glacial to 300 m depth increasing to full Brine at 1,500 m depth was tested in an attempt to improve the calibration of Cl in bore-holes KLX01 and KSH01A where saline water is found above 600 m depth.

The initial condition for flow is calculated by holding the reference water fractions fixed, and calculating the flow-field that is at hydrostatic equilibrium at the initial time of 8000 BC.

5.8 HCD model

This section includes a description of the HCD model, which is based on a data delivery from Geology, and a summary of the calibration of the HCD model against PSS data and chemistry data.

The data delivery from Geology included the following.

- Rock Visualisation System (RVS) data file in XML format.
- Supporting documents and spreadsheets defining:
  - Properties (transmissivity and kinematic porosity) for deformation zones.
  - Three different depth dependency models.

The HCD model contains 37 zones that have been classified as high confidence zones. 65 zones are classified as intermediate confidence zones, and in total there are 200 DZs in the data set. This is illustrated in Figure 5-13. Hydraulic thickness is based on geological estimates of the width of the DZ. If no value is given by the geologist, the thickness is approximated with a default value of 20 m. For 24 of the zones, an explicit transmissivity is estimated on the basis of the hydraulic tests in the HCDs.

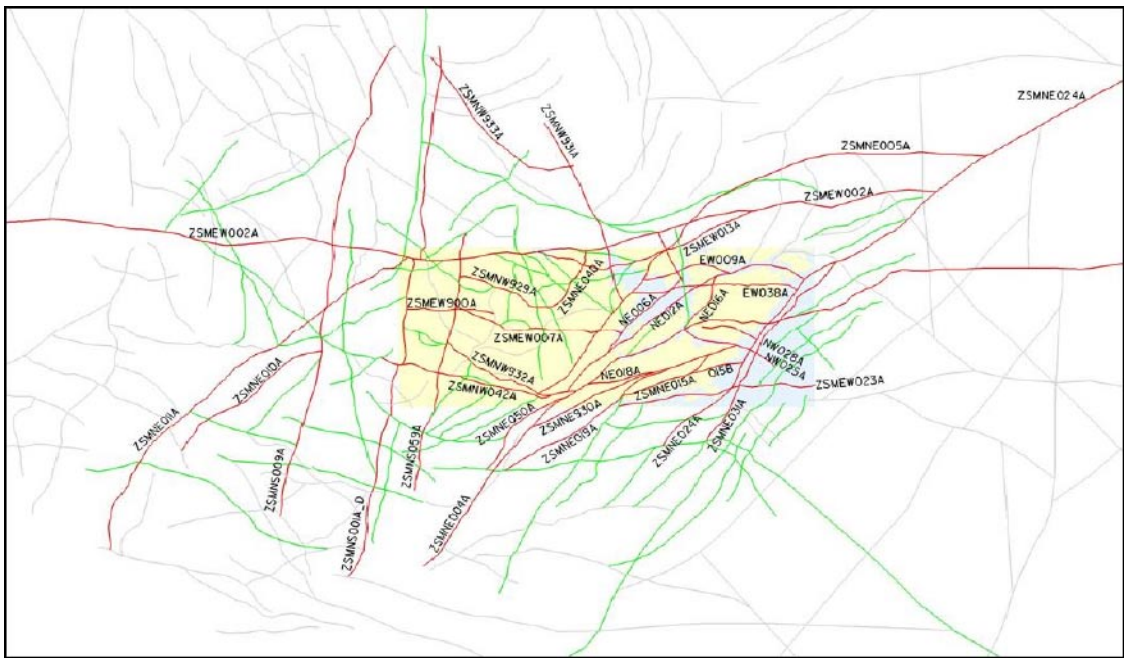

Figure 5-13. *HCD for regional-scale modelling. Deformation zones coloured red have been verified and are high confidence. Lineaments are coloured green and have intermediate or low confidence.*

5.8.1 Transmissivity

According to the SKB Task Description and associated data set, all RVS Deformation Zones (DZs) are assumed to have a depth dependency and continuous variation of properties within each RVS DZ as the reference case. The depth dependency models are illustrated in Figure 5-14 and may also be summarised as:

- Step change:
  - $-300 \leq z \leq 0$: $T = 2.0\ 10^{-5}$ m^{2}s^{-1}
  - $-600 \leq z \leq -300$: $T = 1.2\ 10^{-5}$ m^{2}s^{-1}
  - $-2{,}100 \leq z \leq -600$: $T = 7.1\ 10^{-7}$ m^{2}s^{-1}
- Power-law:
  - Bounded power function: $T = a(-z)^b$
  - $a = 0.219$, $b = -1.783$
  - Min(T) = 10^{-9} and Max(T) = 10^{-3} m^2/s
- Exponential:
  - Bounded exponential function: $T = ae^{-bz}$
  - $a = 6.24\times10^{-5}$, $b = -0.00519$
  - Min(T) = 10^{-9} and Max(T) = 10^{-3} m^2/s

For RVS DZs with one or more measured transmissivities, the geometric mean T and the representative 'mean elevation' of these observations are used to modify the suggested depth trend curves for transmissivity (T) defined above, by adding/subtracting a number to/from the given equation so that it passes through the given point. For RVS DZs without any measurements, the given depth trends for T are used. Global maximum and minimum T values are also provided and these are used to limit the resulting T values.

To implement the depth trend for the step change model, the zones are divided into three horizontal segments. For the other depth dependency models, deformation zones are divided into 10 horizontal segments.

After the depth trends are implemented, the values are calibrated against PSS data. Where there is a discrepancy between the modelled and observed transmissivity, the zones are modified indvidually to obtain a better match. Based on the data, intersections of the bore-holes with the deformation zones were identified and the intersected horizontal segment of the zone was calibrated against corresponding PSS data. For each intersected deformation zone, the depth trend curve was adjusted such it passes through the interpreted transmissivity at the "mean elevation" in the provided data file. For those RVS DZs where no PSS data is available, the transmissivity curves follow the provided "average" depth dependency curve. In the calibration step, only the horizontal segment with the PSS data was modified, whilst checking that the transmissivities remained within the suggested range. An example of the calibration step is shown in Figure 5-15. The available 100 m PSS data for KLX01–06, KSH01A–03A, and KAV04A were used. For KAV01A, 100 m interval PSS data was approximated from the 10 m PSS data by grouping the 10 m intervals into 100 m intervals and summing the transmissivity values.

The deformation zones are usually divided into triangles. Presently, no tool has been developed to identify all of the triangles within a given radius of the calibration point. In the current study, a horizontal segment of the deformation zone is modified to fit the calibration value, i.e. only the horizontal segment with the PSS data is modified. The same technique was used for all three depth model concepts, i.e. the step change, the power-law and the exponential function.

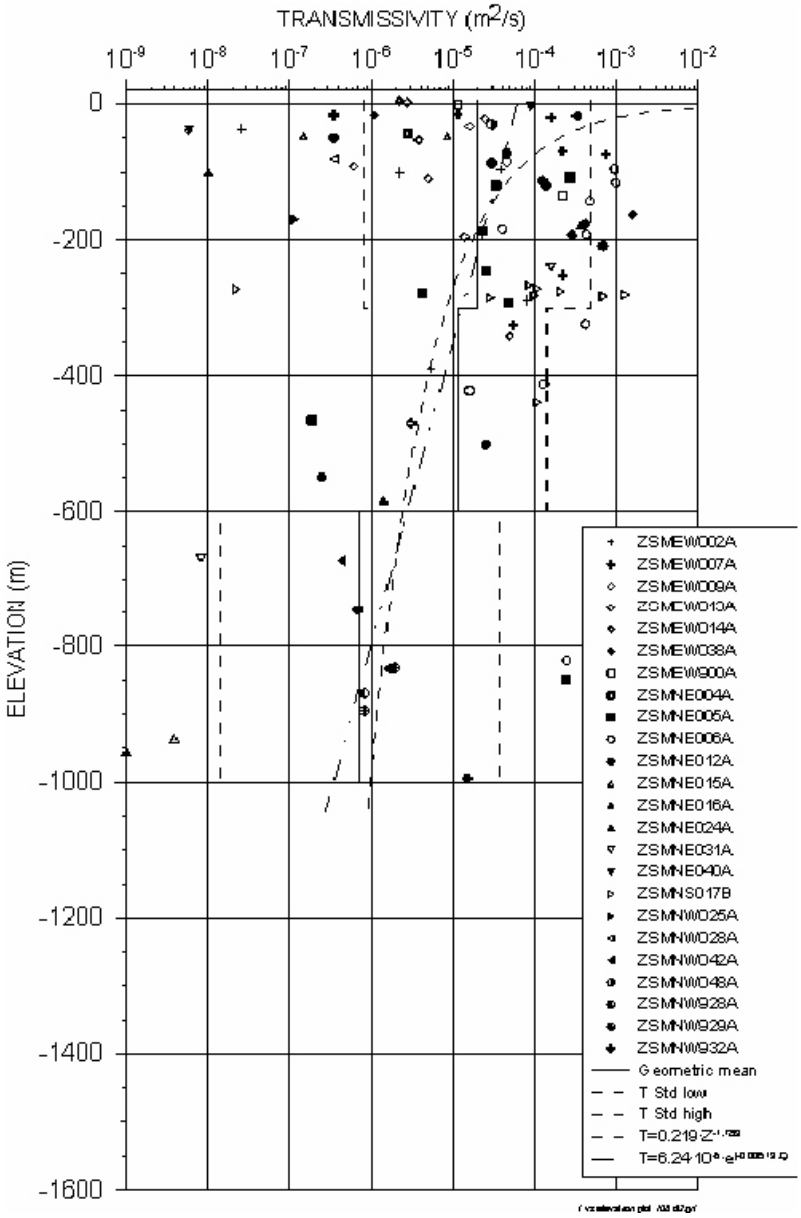

Figure 5-14. *Zone transmissivity values versus depth and three interpreted depth dependency models (given in the legend where Z (= –z) is the depth): Step change (Geometric mean); Power-law (T = 0.219 (–z)$^{-1.783}$); Exponential (T = 6.24 10^{-5} e$^{-0.00519\ z}$).*

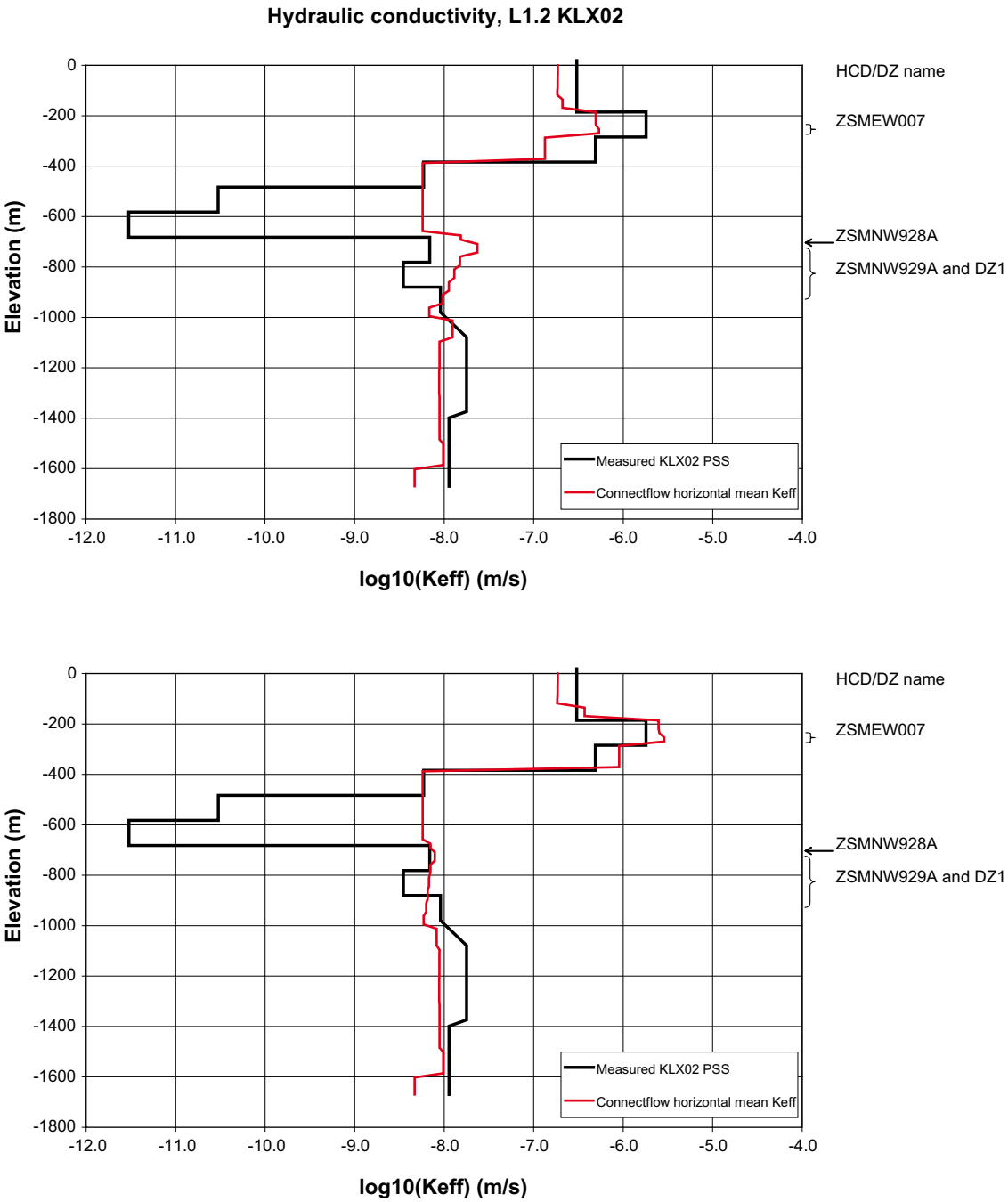

Figure 5-15. *Example of calibration of hydraulic properties for zones intersecting KLX02. Top: before calibration; bottom: after calibration.*

An example of the implementation of the HCD model is illustrated in Figure 5-16. It is also stipulated that all HCDs should be in hydraulic contact with the overburden (the modelled HSD). The high confidence zones are listed in Table 5-2.

After the first calibration step based on hydraulic data, the HCD models are refined even further based on comparisons of simulation results and chemistry data.

The HCD models described above, consisting of 25 HCDs with properties based on hydraulic tests in the HCDs, are considered as the reference case HCD models for the three depth dependency models. Due to the uncertainties in the HCD model, the following variants were considered.

- Confidence levels: Model only HCD with high and intermediate confidence of existence.
- Model including HCDs with stochastic properties.

Based on the calibrated reference case HCD models, variants in which the low confidence zones were omitted were constructed. One example is shown in Figure 5-17. HCD models have also been constructed using stochastic properties for the deformation zones. An example is shown in Figure 5-18.

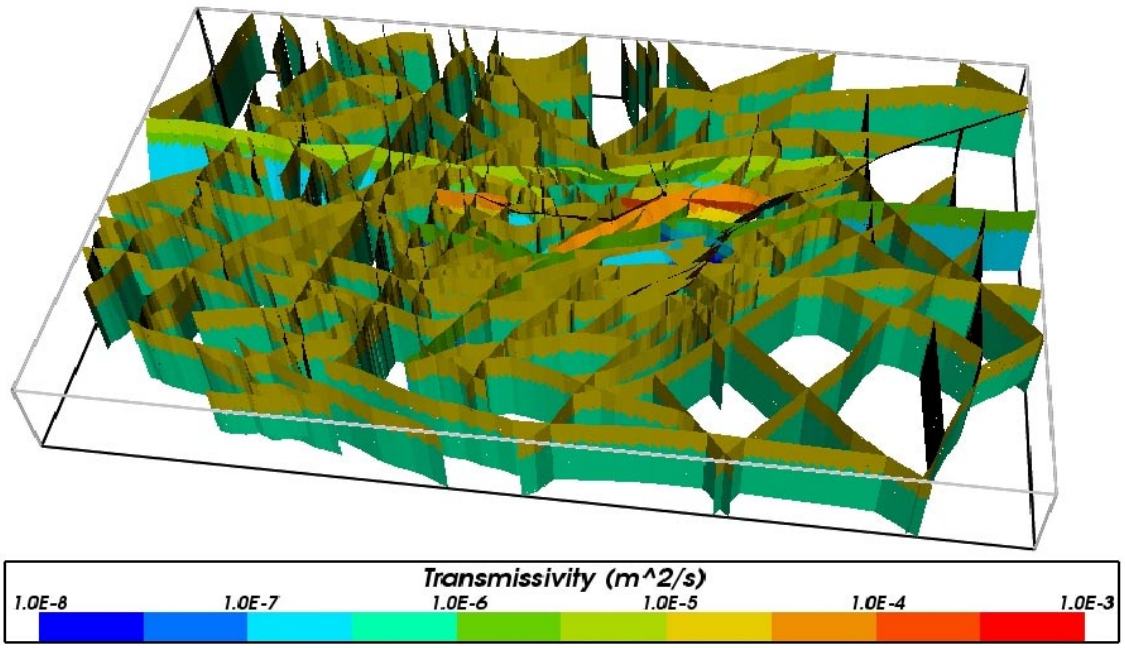

Figure 5-16. *HCD for regional-scale modelling in 3D. The zones are coloured by transmissivity, where red is high and blue is low.*

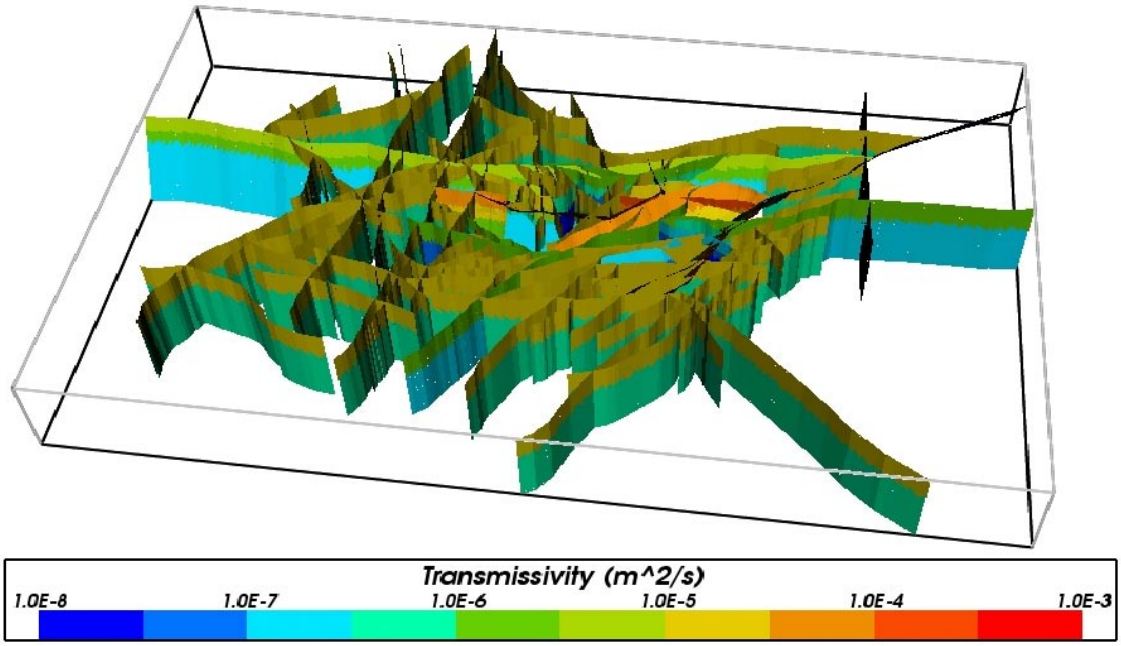

Figure 5-17. *Example of a HCD model with high (37) and intermediate (65) confidence zones, i.e. 102 deformation zones. The zones are coloured by transmissivity, where red is high and blue is low.*

Table 5-2. Hydraulic properties for high confidence zones based on hydraulic tests in the HCDs. The values are taken from the upper part of the step change model before calibration.

DZ-ID	Hydraulic thickness *W* (m)	Transmissivity *T* (m^2/s)
ZSMEW002A	100	3.93E–06
ZSMEW007A	50	4.58E–05
ZSMEW009A	12	1.21E–05
ZSMEW013A	45	1.20E–06
ZSMEW023A	20	2.00E–05
ZSMEW038A	10	1.21E–04
ZSMEW900A	20	5.07E–05
ZSMNE004A	100	2.80E–06
ZSMNE005A	250	2.21E–05
ZSMNE006A	130	2.21E–04
ZSMNE010A	10	2.00E–05
ZSMNE011A	100	2.00E–05
ZSMNE012A	120	3.53E–05
ZSMNE015A	10	1.08E–07
ZSMNE015B	5	2.00E–05
ZSMNE016A	15	2.48E–06
ZSMNE018A	50	2.00E–05
ZSMNE019A	5	2.00E–05
ZSMNE024A	80	4.52E–07
ZSMNE031A	15	1.92E–06
ZSMNE040A	20	7.28E–07
ZSMNE050A	50	2.00E–05
ZSMNE930A	5	2.00E–05
ZSMNS001A	100	2.00E–05
ZSMNS001B	100	2.00E–05
ZSMNS001C	100	2.00E–05
ZSMNS001D	100	2.00E–05
ZSMNS009A	80	2.00E–05
ZSMNS017B	20	1.04E–04
ZSMNS059A	50	2.00E–05
ZSMNW025A	10	1.16E–07
ZSMNW028A	10	3.55E–07
ZSMNW042A	80	4.25E–07
ZSMNW929A	50	3.50E–05
ZSMNW931A	50	2.00E–05
ZSMNW932A	10	1.48E–06
ZSMNW933A	40	2.00E–05

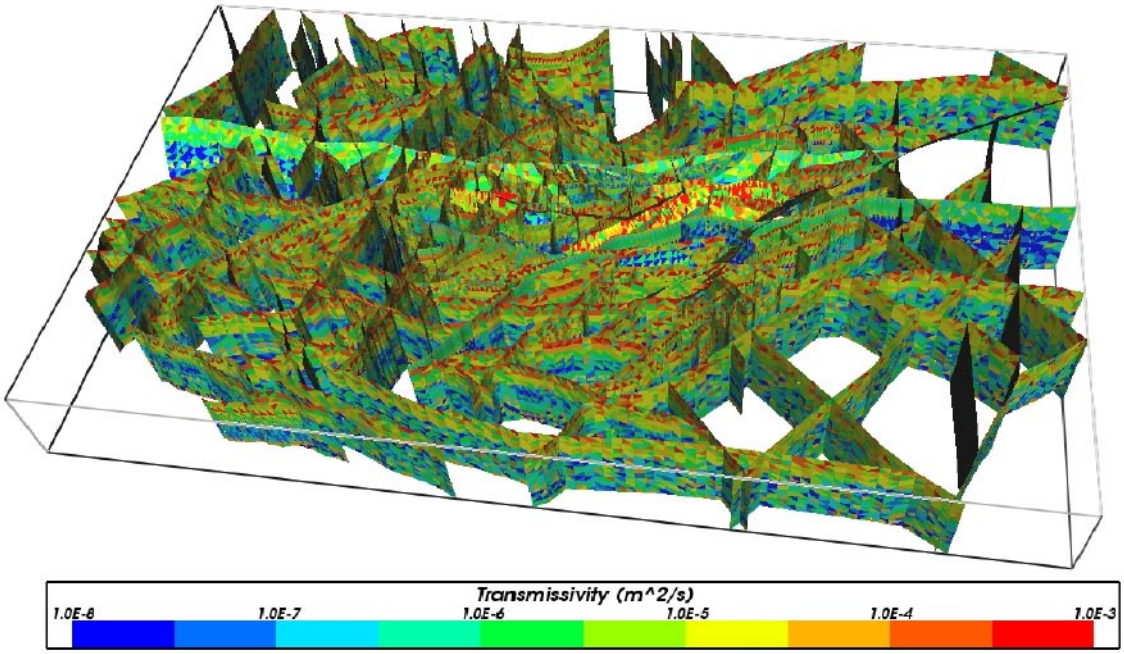

Figure 5-18. *HCD model with all zones and stochastic hydraulic properties. The zones are coloured by transmissivity, where red is high and blue is low.*

5.8.2 Kinematic porosity

Different options for the kinematic porosity of the zones were also tested. Initially, the proposed function in the data delivery, where the kinematic porosity is a function of transmissivity and the thickness of the zones, was used. Since T is depth dependent, the kinematic porosity will also be depth dependent. However, the comparisons against chemistry data suggested that the porosities needed to be increased to obtain a better match. Therefore, two alternative approaches were tested. In the first, the values obtained from the function proposed in the data delivery were scaled such that they fall in the range 10^{-2} to 10^{-6}. This was achieved by dividing each value by the maximum porosity value given by the function and then multiplying by 10^{-2}. The choice of 10^{-2} is arbitrary. This procedure was repeated for all three depth dependency models. This approach also gives a depth dependent porosity model.

In the second alternative approach, the porosity is based on the thickness, W, of the zones such that thick zones have a higher kinematic porosity than thin zones. This concept is not depth dependent.

In summary, the tested approaches for the kinematic porosity of the zones are:

- Data delivery: $n_e = 0.46\ T^{0.5}/W$, where W is the thickness of zone.
- Alternative case: Porosities as for 1. but then scaled such that the max porosity is 10^{-2}, and the minimum is about 10^{-6}.
- Alternative case: Porosity 10^{-3} for $W < 100$ m and 10^{-2} for $W \geq 100$ m.

5.9 HRD and DFN model

The Hydraulic Rock Domain (HRD) model for L1.2, as provided by Geology, is illustrated in Figure 5-19 and Figure 5-20. To create a simplified HRD model, domains with similar properties were grouped and the HRDs listed below were defined. Original HRD names and groupings are given in brackets.

- HRD(A) (A – Ävrö granite).
- HRD(A2) (A in an area east of Äspö that forms a more conductive part of HRD(A)).
- HRD(B,C) (B and C).
- HRD(D,E,M) (M, BA, D and E).
- HRD(F,G) (F and G).

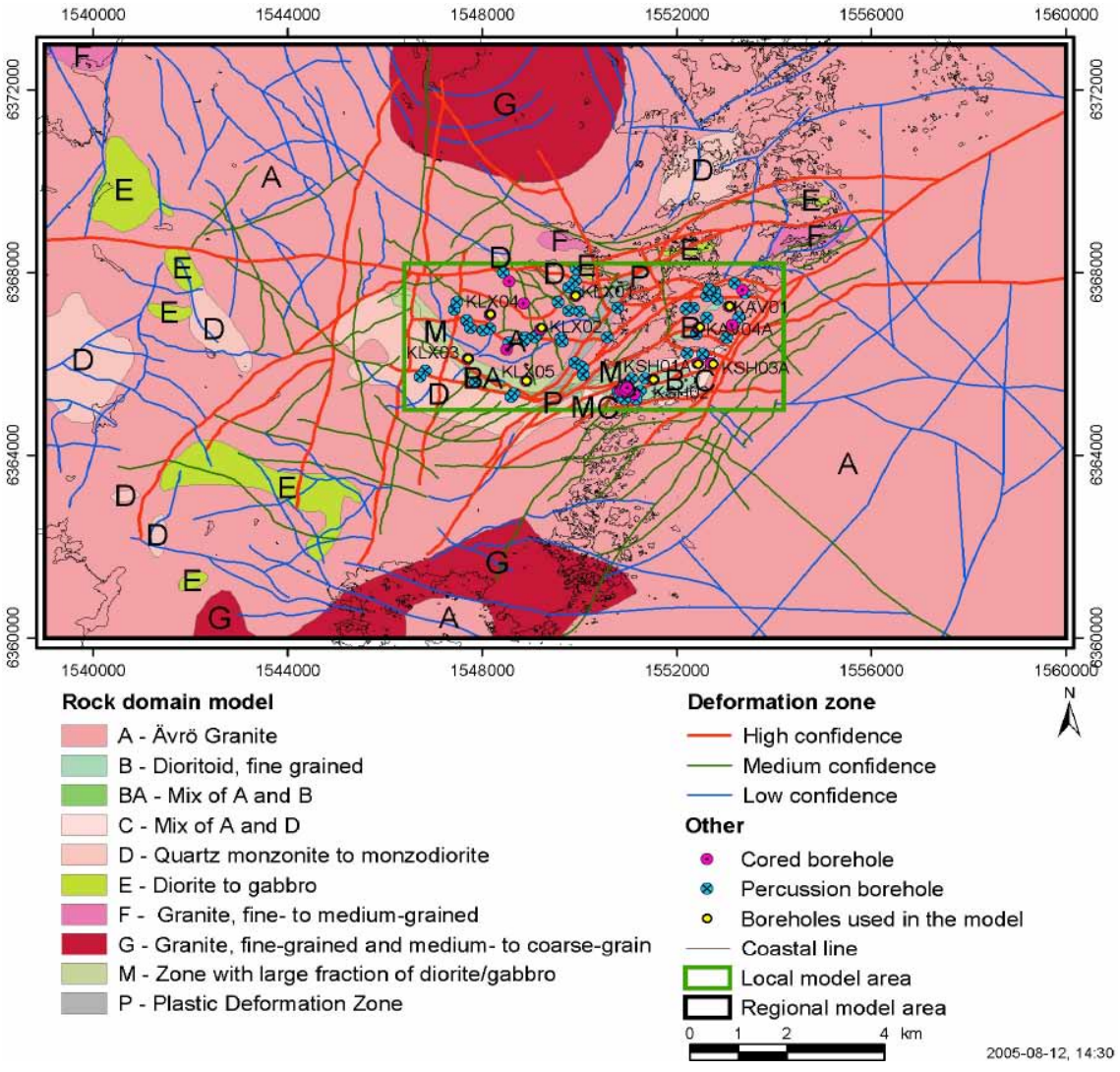

Figure 5-19. *Rock domain model for the regional model area.*

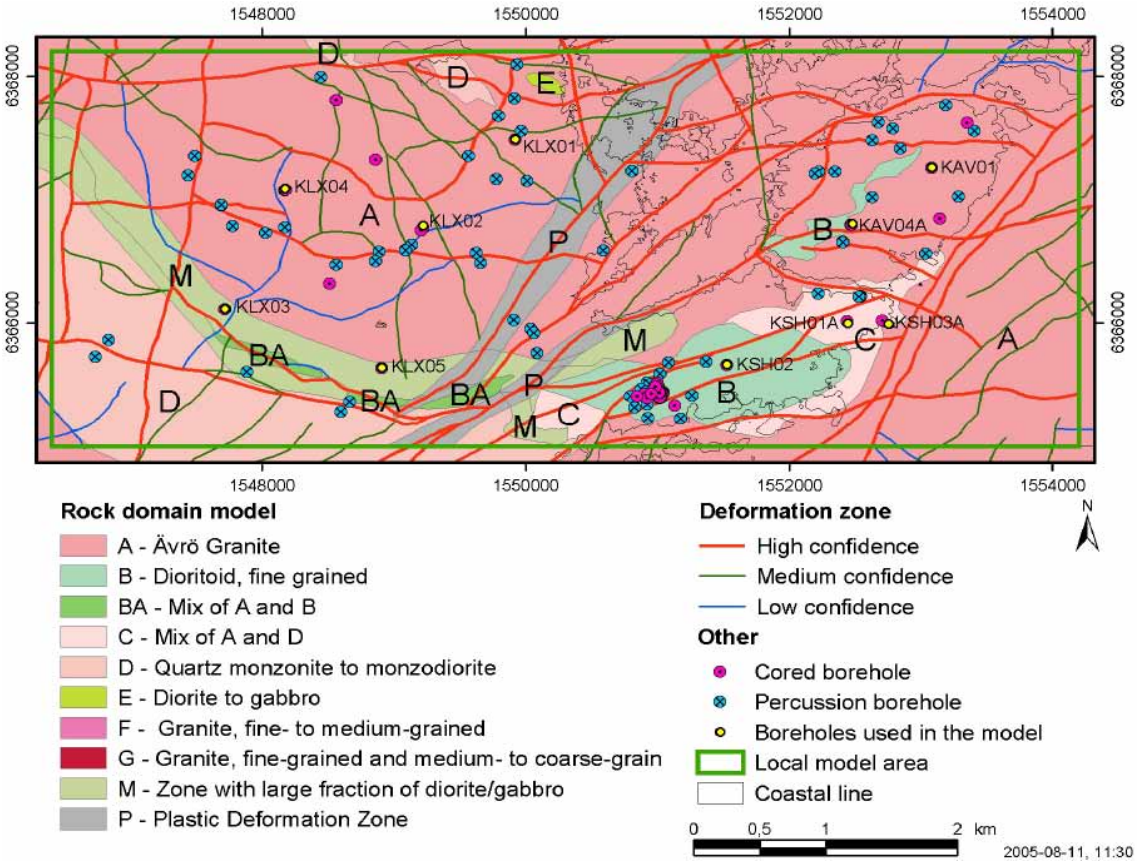

Figure 5-20. *Rock domain model for the local model area.*

The domain was also subdivided into four layers according to the elevation intervals 0 m to –100 m, –100 m to –300 m, –300 m to –600 m, and –600 m to the bottom of the model (elevation –2,100 m). A dummy HRD was added as an extra layer at the bottom of the model (elevation –2,100 to –2,300 m) to act as a buffer between the bottom of the HCDs and the lower boundary of the model. The extent of the regional model domain is based on the water catchment area, as discussed in Section 5.5. The resulting model is illustrated in Figure 5-21.

A smaller regional model domain bounded by large (> 1 km) deformation zones was also defined (see Section 5.5). This is illustrated in Figure 5-22. The locations of the boreholes considered in the model calibration are also shown in Figure 5-22. Figure 5-23 provides a close-up view of the borehole locations and the surrounding HCDs.

The treatment of HRD properties started with simple homogeneous models and gradually developed to include more sophisticated concepts such as DFN-derived properties for the different rock domains. This strategy was adopted so that simple models with few parameters could be used for quantifying parameter sensitivities prior to incorporating more complexity such as stochastic DFN models.

Several variants were considered during this process, these are summarised below.

- **HRD1: Homogeneous**. The rock mass is simulated with a fixed background conductivity for each HRD and for each depth interval. The background conductivities are based on 100 m and 20 m PSS data for each of the HRDs.

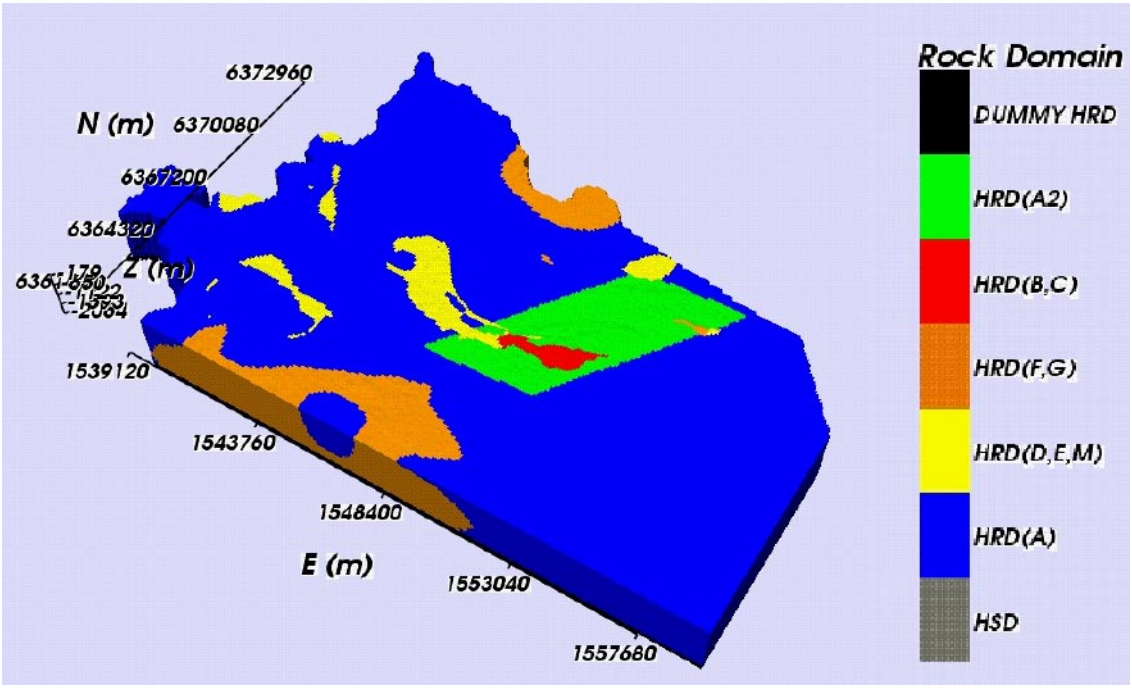

Figure 5-21. *HRD model. The regional model domain is divided into the HRDs: HRD(A), HRD(A2), HRD(B,C), HRD(D,E,M) and HRD(F,G). The key gives the name of the HRD and the depth interval. The HRD in the depth interval 2,100 m to 2,300 m provides a buffer between the bottom of the HCDs and the bottom of the model. The HSD layers have been removed.*

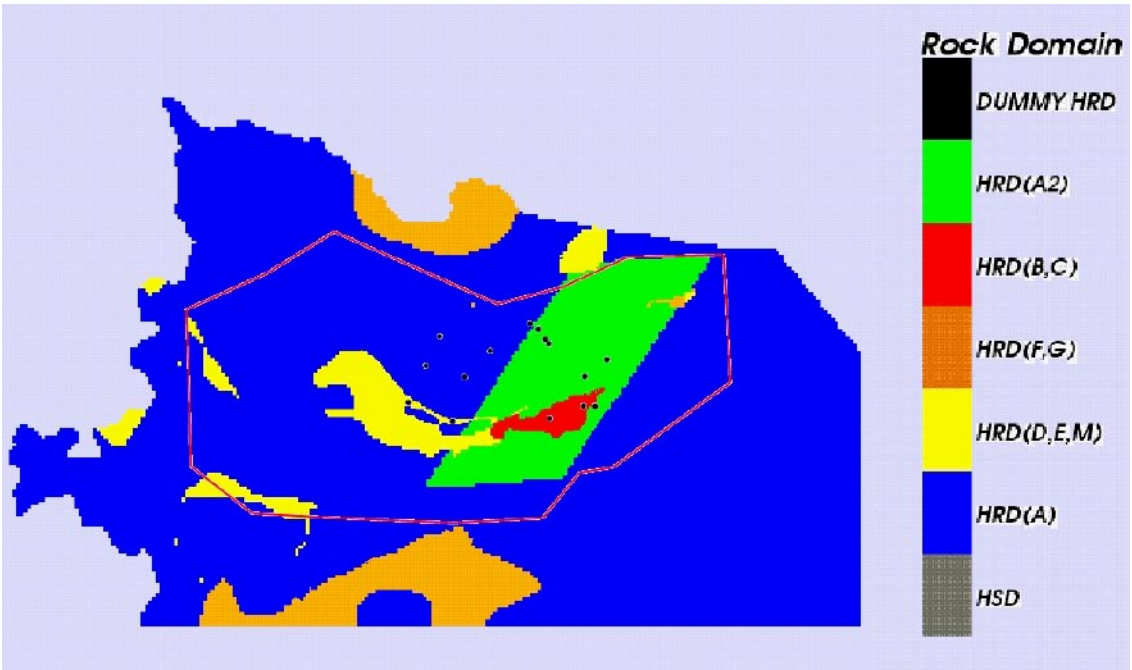

Figure 5-22. *Plan view of HRD model showing the small regional inner model domain (red line) and the boreholes (black dots) considered in the model calibration. The HSD layers have been removed.*

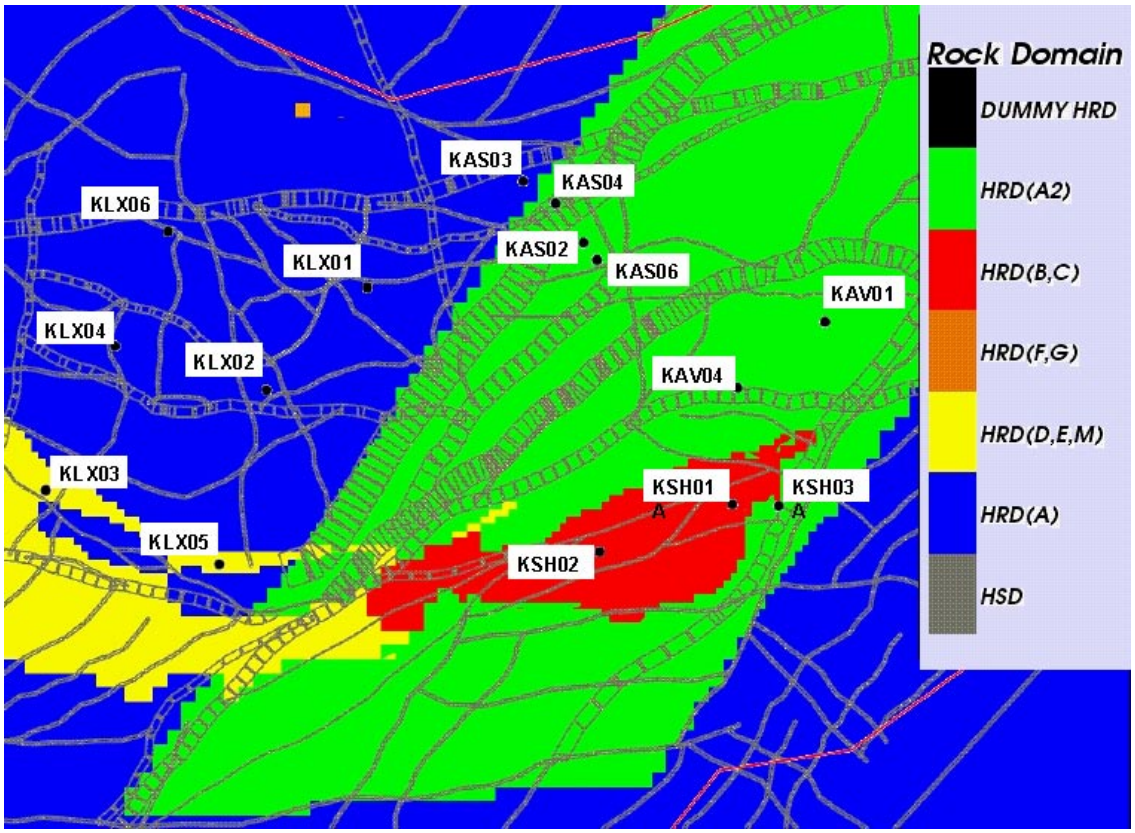

Figure 5-23. *Zoomed-in view of the borehole locations and surrounding HRDs and HCDs. The HSD layers have been removed.*

- **HRD2: Homogeneous**. The rock mass is simulated with a fixed background conductivity for each HRD and for each depth interval. The background conductivities are based on the 50th percentile block-scale properties provided by the Hydro-DFN base case in Section 4.4 for each HRD.
- **HRD3: Stochastic DFN, semi-correlated**. The rock mass of the entire model domain is simulated as a heterogeneous DFN. Each HRD is associated with five fracture sets according to the Hydro-DFN base case with a semi-correlated *T* model, with a change in properties at –300 m elevation. This had This is a more sophisticated model that incorporates the details of the Hydro-DFN developed in Chapter 3 and Chapter 4.
- **HRD4: Stochastic DFN, correlated.** The rock mass of the entire model domain is simulated as a heterogeneous DFN. Each HRD is associated with five fracture sets according to the Hydro-DFN base case with a correlated *T* model, with a change in properties at –300 m elevation. This is a more sophisticated model that incorporates the details of the Hydro-DFN developed in Chapter 3 and Chapter 4.
- **HRD5: Stochastic DFN, uncorrelated.** The rock mass of the entire model domain is simulated as a heterogeneous DFN. Each HRD is associated with five fracture sets according to the Hydro-DFN base case with an uncorrelated *T* model, with a change in properties at –300 m elevation. This is a more sophisticated model that incorporates the details of the Hydro-DFN developed in Chapter 3 and Chapter 4.
- **HRD6: Depth trend function, power-law**. The rock mass is simulated with a step function based on a power-law trend for conductivity. The Laxemar and Ävrö HRDs (HRD(A), HRD(D,E,M), HRD(F,G), and HRD(A2)) are assigned the same depth trend, and the Simpevarp HRD, HRD(B,C), is assigned a different depth trend.

- **HRD7: Depth trend function, exponential.** The rock mass is simulated with a continuous exponential depth dependency for conductivity. The Laxemar and Ävrö HRDs (HRD(A), HRD(D,E,M), HRD(F,G), and HRD(A2)) are assigned the same depth trend and the Simpevarp HRD, HRD(B,C), is assigned a different depth trend.

Each of the above variants provides properties for HRD(A), HRD(A2), HRD(B,C) and HRD(D,E,M). HRD(F,G) is assumed to be 10 times as conductive as HRD(A) in all cases.

The simulation cases based on HRD1, HRD3 and HRD7 formed the main focus of the study.

5.9.1 HRD1: Homogeneous HRD models with hydraulic properties based on PSS data

A fixed background conductivity was assigned according to both the HRD and four elevation intervals (0 m to –100 m, –100 m to –300 m, –300 m to –600 m, –600 m to the bottom of the model).

Hydraulic properties were based on a statistical analysis of the 20 m and 100 m PSS data. It was assumed that an appropriate value for the effective conductivity of the rock is the geometric mean of PSS interval measurements. For each subarea, two alternative step models were considered: Step model A, which is based on 20 m data; and Step model B, which is based on 100 m data.

The PSS data indicates depth dependence for Laxemar. This trend is stronger in the 20 m interval data, although there is considerable uncertainty associated with the geometric means at greater depths due to the small number of measurements taken. On the basis of this data, two alternative step models for the hydraulic conductivity for HRD(A) were considered. The 20 m and 100 m PSS data are plotted with the step models in Figure 5-24.

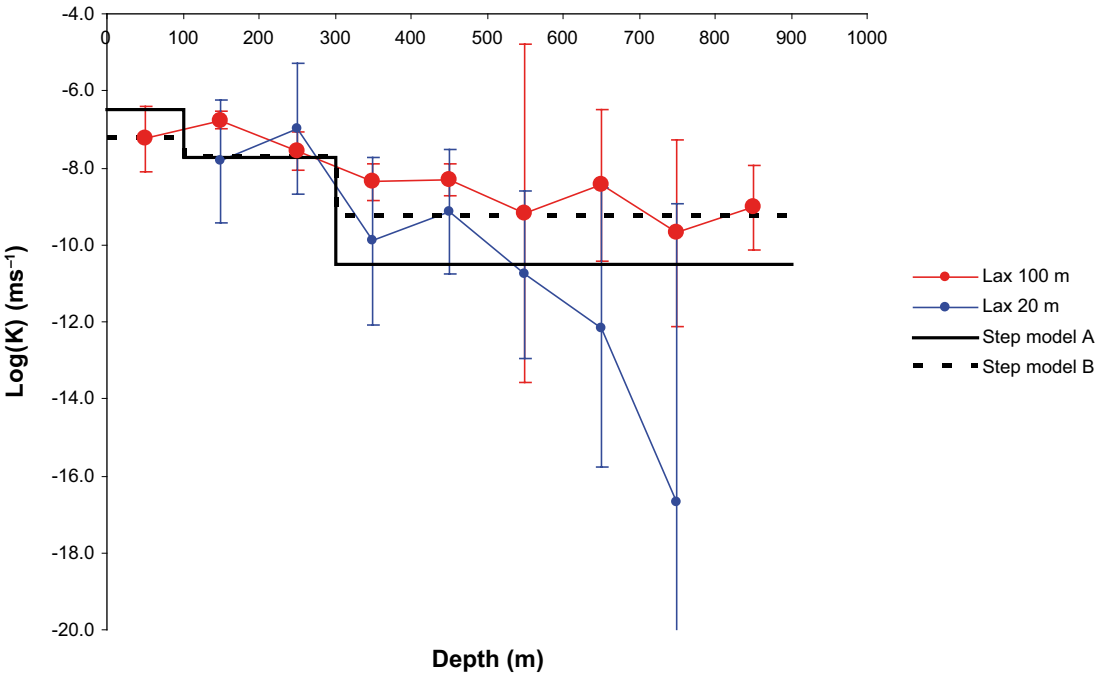

Figure 5-24. *Plots of 20 m and 100 m PSS data for Laxemar subarea, and the step models for background conductivity used for HRD(A) in the basecase HRD model, HRD1.*

For HRD(D,E,M), 20 m PSS data was not available. However, analysis of the 100 m interval PSS suggests that HRD(A) is about half an order of magnitude more permeable than HRD(D,E,M), which is about half an order of magnitude more permeable than HRD(B,C). The available 20 m data for HRD(A) and HRD(B,C) appears to be consistent with this. Therefore, HRD(D,E,M) was assigned a conductivity half an order of magnitude lower than that for HRD(A).

The 20 m data for Simpevarp showed very little variation with depth. The 100 m data suggests depth dependence but there is considerable uncertainty in the estimates of geometric mean. Two alternative step models are plotted with the PSS data in Figure 5-25.

The 20 m data for Ävrö show a marked decrease at depths of around 400–600 m. However, there are relatively few measurements at such depths, and the uncertainties in the estimated means are relatively large. For the 100 m interval data, there are very few 100 m interval measurements below a depth of 100 m. The uncertainties in the top 100 m are relatively large but suggest a higher conductivity for the top 100 m. Two alternative step models were considered, one based on the 20 m data and the other based on the 100 m data. These are plotted with the 20 m PSS data in Figure 5-26.

The hydraulic conductivities for each HRD and each depth interval are given in Table 5-3.

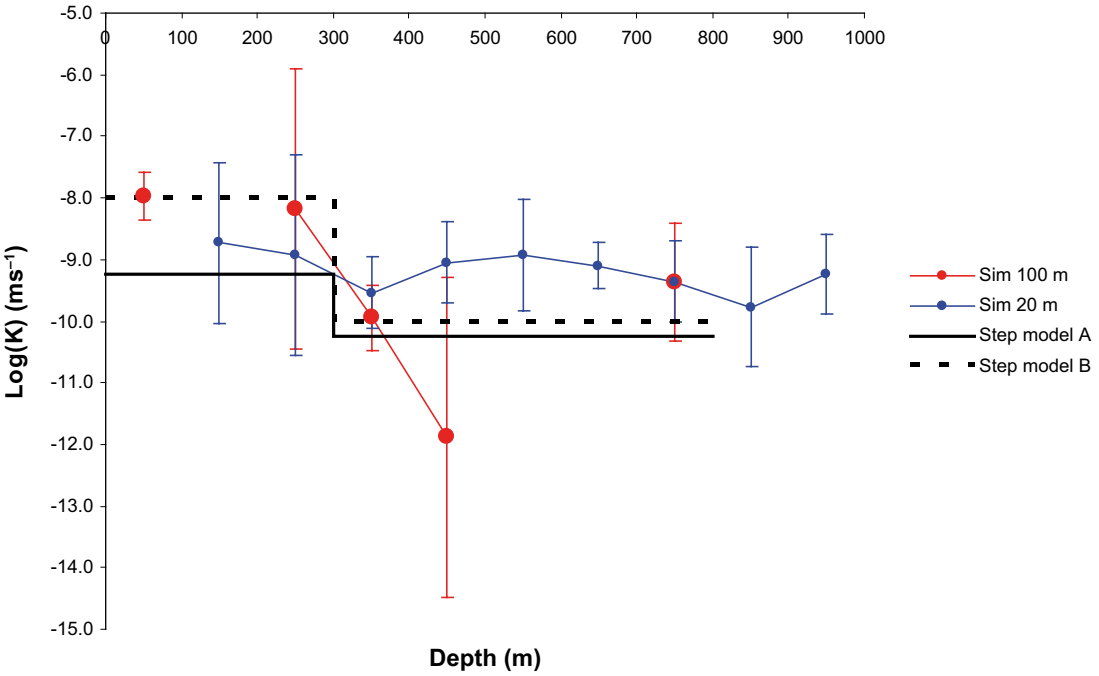

Figure 5-25. *Plots of 20 m and 100 m PSS data for Simpevarp subarea, and the step models for background conductivity used for HRD(B,C) in the basecase HRD model, HRD1.*

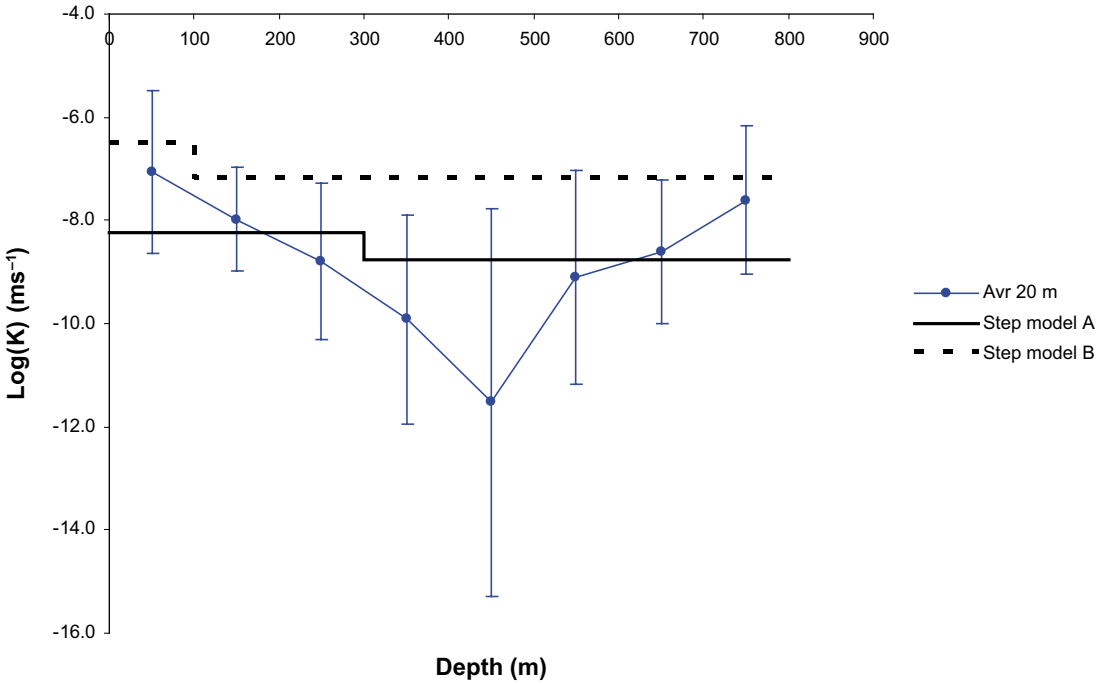

Figure 5-26. *Plots of 20 m PSS data for Ävrö subarea, and the step model for background conductivity used for HRD(A2) in the basecase HRD model, HRD1.*

Table 5-3. Hydraulic conductivities for the HRDs and three depth intervals.

	HRD	Step model	Log10(K)		
			0–100 m depth	100 m–300 m depth	> 300 m depth
Laxemar	HRD(A)	A	–6.50	–7.75	–10.50
	HRD(A)	B	–7.25	–7.75	–9.25
	HRD(D,E,M)	A	–7.00	–8.25	–11.00
	HRD(D,E,M)	B	–7.75	–8.25	–9.75
Simpevarp	HRD(B,C)	A	–9.25	–9.25	–10.25
	HRD(B,C)	B	–8.00	–10.00	–10.00
Ävrö	HRD(A2)	A	–8.25	–8.25	–8.75
	HRD(A2)	B	–6.50	–7.20	–7.20

5.9.2 HRD6 and HRD7: Depth trend functions

Two depth trend functions were considered:

- an exponential (HRD7), $K = ae^{-bz}$,
- a power-law relation (HRD6), $K = a(-z)^b$.

The values for a and b are given in Table 5-4 for the exponential depth trend and Table 5-5 for the power-law depth trend.

These trends are compared with the step models HRD1 and HRD2 in Figure 5-27.

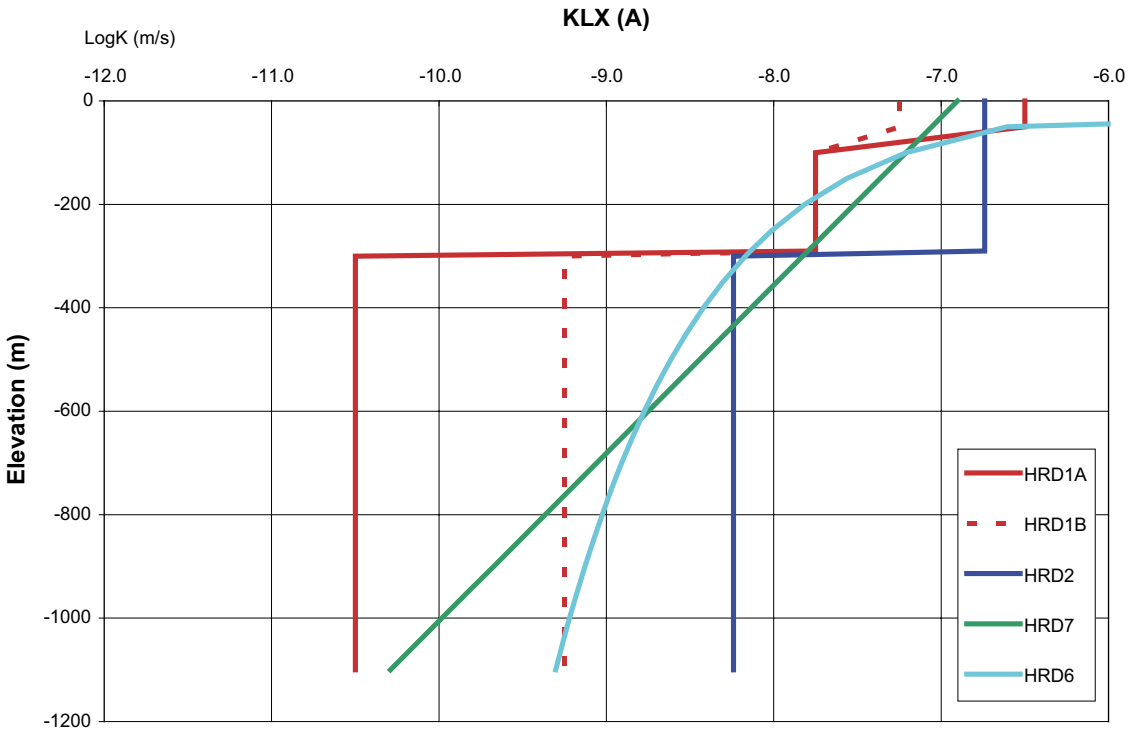

Figure 5-27. *Comparison of the depth trend in conductivity HRD(A) for the homogeneous (step model) cases HRD1A, HRD1B and HRD2, and the depth trend functions for cases HRD6 and HRD7.*

Table 5-4. Values for the exponential depth trend coefficients a and b for each HRD.

HRD	*a*	*b*
HRD(A)	$1.25\ 10^{-7}$	$-7.09\ 10^{-3}$
HRD(D,E,M)	$3.96\ 10^{-7}$	$-7.09\ 10^{-3}$
HRD(B,C)	$9.54\ 10^{-9}$	$-8.57\ 10^{-3}$
HRD(A2)	$3.00\ 10^{-8}$	$-3.00\ 10^{-3}$
HRD(F,G)	$1.25\ 10^{-6}$	$-7.09\ 10^{-3}$

Table 5-5. Values for the power-law depth trend coefficients a and b for each HRD.

HRD	*a*	*b*
HRD(A)	$6.46\ 10^{-4}$	–2.01
HRD(D,E,M)	$6.46\ 10^{-4}$	–2.01
HRD(B,C)	$2.70\ 10^{-3}$	–2.81
HRD(A2)	$3.00\ 10^{-6}$	–1.00
HRD(F,G)	$6.46\ 10^{-3}$	–2.01

5.9.3 HRD2, HRD3, HRD4, and HRD5: HRD models based on the Hydro-DFN

The Hydro-DFN was used in two different ways:

- as the basis for simple homogeneous regional-scale models by using the 50th percentile block-scale properties (HRD2),
- stochastic regional-scale DFN modelling (HRD3, HRD4, HRD5).

Hydro-DFN models were defined for four boreholes that traverse different rock domains in the Laxemar, Simpevarp and Ävrö subareas. For the models described in this section, each rock domain in the simplified HRD model (see Figure 5-21) is associated with one of the Hydro-DFN models.

The HRDs are listed below, each is followed by the borehole for which the associated Hydro-DFN model was defined and, in brackets, the rock domains (as defined by the rock domain model illustrated in Figure 5-20) traversed by the borehole. The Hydro-DFN parameters are given in Chapter 0.

- HRD(A) and HRD(F,G): KLX04 (Laxemar RD A).
- HRD(A2): KAV04A (Ävrö RDs A and C).
- HRD(B,C): KSH01A (Simpevarp RDs B and C).
- HRD(D,E,M): KLX03 (Laxemar RDs M(A), M(D) and D).

For the Hydro-DFN, two intervals were considered separately, above –300 m and below –300 m, to reflect a depth trend observed in the PFL-f and PSS data for Laxemar subarea, with flow occurring mainly in the region above –300 m. However, there is some uncertainty in the choice of the elevation of –300 m as the level for the step change in properties. Measurements taken for boreholes that are known not to intersect large deformation zones in the upper part of the borehole, e.g. KLX03 and KLX05, suggest that a higher elevation, –200 m say, could be used. This is considered in the regional modelling. Also there is an uncertainty in extrapolating the properties of a whole rock domain from a single borehole. Considerations of the variability of the mean measured 100 m PSS interval data without deformation zones within the Laxemar subarea suggests a variability of about half an order of magnitude between boreholes, and KLX04 is probably toward the high-end compared with newer boreholes such as KLX08.

In the development of the Hydro-DFN for KLX04, a preliminary investigation of anisotropy in transmissivity between fracture sets was also performed (see Subsection 3.8.2). For the regional modelling, several simulation cases were performed that included this anisotropy in transmissivity between fracture sets for all HRDs.

For HRD3, HRD4 and HRD5, the concept was to generate stochastic realisations of the DFN model on the regional-scale, based on the Hydro-DFN described in Chapter 3, with variants parameterised in Chapter 0 and using the upscaling method defined in Section 2.3 to obtain ECPM properties.

The transport aperture was calculated using $e_t = aT^b$, $a = 0.46$, $b = 0.5$ (see Sub-section 3.3.5). The kinematic porosity, $n_{e,b}$, for a block was then calculated as the sum of products of connected fracture area within the block and the transport aperture, and then divided by the volume of the block.

Figure 5-6 shows the different areas on the L1.2 model relating to different grid refinement. Based on the findings of block-scale upscaling in a previous study /Hartley et al. 2005a/, the minimum fracture length sampled should be no more than one quarter the element size. Hence, r_{min} = 14 m was used (equivalent to a fracture length of 25 m) throughout the regional domain. The full regional DFN model, which has over ten million fractures, is too large to visualise and so the smaller regional domain is shown here as an illustration. The DFN generation region is shown in Figure 5-28 for the smaller regional domain. One realisation of the regional-scale DFN model is shown in Figure 5-29 as the full 3D model in plan view, and as a horizontal cross-section at z = –500 m (i.e. a trace map) in Figure 5-30. It is apparent from this cross-section that different fracture parameters – mainly fracture intensity and transmissivity – are used in different rock domains (see Figure 5-22). Note that based on a regional-scale connectivity analysis, the isolated fractures, isolated fracture clusters and dead-end fractures are removed, so the fractures shown are only those that form part of the connected network. Even for a Poisson spatial process this results in a heterogeneous distribution of connected fractures. The equivalent plot with the deterministic HCD model superimposed is shown in Figure 5-31.

As an illustration of how the DFN fits onto the ECPM grid, Figure 5-32 shows a close-up plan view of a slice through the DFN and finite-element grid. The finite-elements are cubes, but the visualisation tool draws a slice through them as 2 triangles. It can be seen that some elements are not cut by a fracture (at least in this 2D view), some have several fractures and some larger stochastic fractures cut many elements. This is all due to the stochastic nature of the DFN model.

Fractures were generated in the extended regional model domain and upscaling was performed. The upscaled conductivity, K_x, is shown in Figure 5-33 and Figure 5-34. The block-scale porosity is shown in Figure 5-35 and Figure 5-36, and the flow-wetted-surface is shown in Figure 5-37 and Figure 5-38.

A relatively high r_{min} of 14 m was used for practical reasons. This means that a few elements will have no fractures and hence zero hydraulic conductivity and kinematic porosity. This is potentially non-conservative and so a background hydraulic conductivity needs to be specified that has equivalent properties of the fracture network for fractures with a radius less than r_{min}. We have some handle on appropriate properties for the background from the block-scale modelling of Chapter 4 where block-scale properties were calculated for 100 m blocks for $r_{\min}$ = 5.6 m. Based on the minimum values calculated in the block-scale upscaling, a minimum hydraulic conductivity for a block was estimated as $1\ 10^{-10}$ m/s, and a minimum porosity of 10^{-5}. In CONNECTFLOW, the background properties were implemented such that if the ECPM properties based on the stochastic DFN for an element fell below these minimum values, then the ECPM values were reset to the minimum.

There is a level of uncertainty in the hydraulic properties for the rock domains. The properties for HRD(A) are based largely on KLX04. However, if other boreholes in HRD(A) (KLX02, KLX06, KLX08) are considered, a decrease in conductivity by a factor of half an order of magnitude for the deeper parts (below depth 300 m) of HRD(A), and possibly also HRD(A2), is justified. In addition, data from boreholes that do not intersect large DZs in the upper part of the borehole, e.g. KLX03 and KLX05, suggest that for the underlying step models incorporated in the Hydro-DFN, the step-change could be modelled with increased hydraulic conductivity in the depth interval 0–200 m instead of 0–300 m.

In order to perform sensitivity tests on the DFN input, several DFN models were created. These are listed in Table 5-6 with names that denote the transmissivity model used and the realisation number.

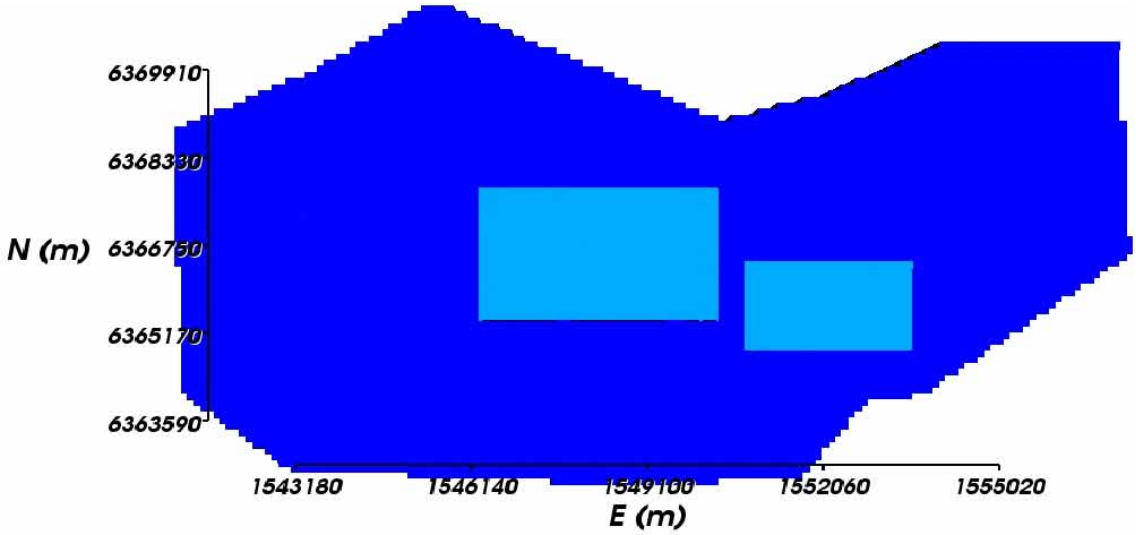

Figure 5-28. *DFN generation region for the small regional-scale domain. r_{min} was set to 14 m throughout the model region. The grid resolution is 50 m in the site-scale areas (coloured light blue), and 100 m in the regional-scale area (dark blue).*

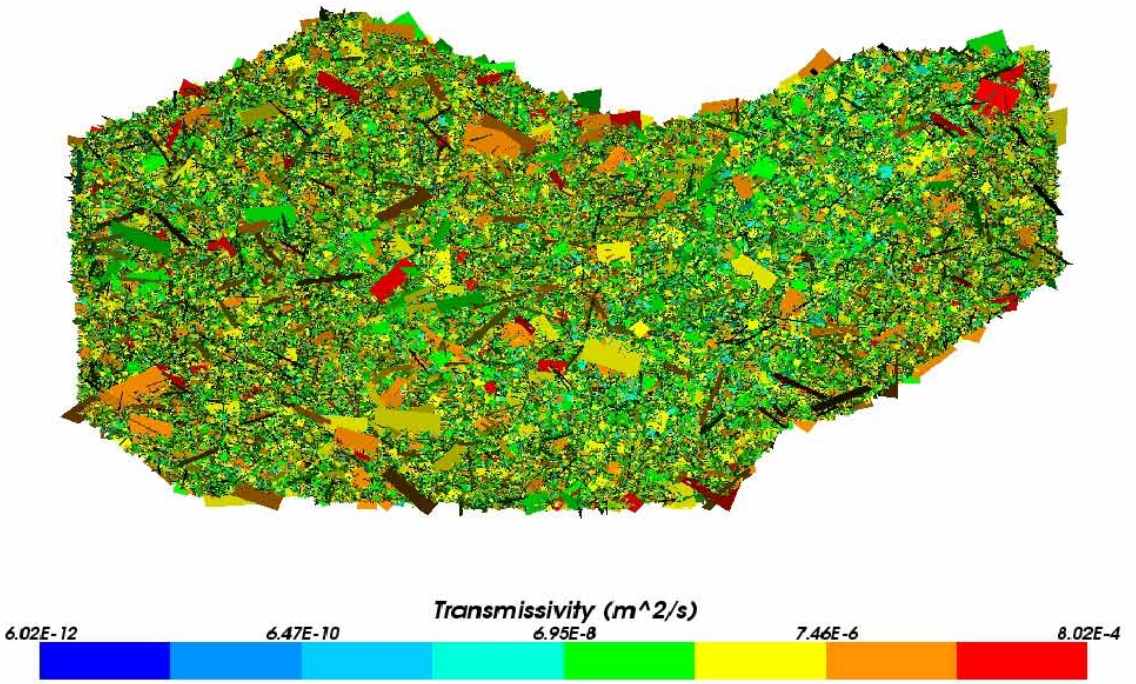

Figure 5-29. *DFN model for the small regional-scale domain showing all stochastic fractures (in 3D) coloured by Log(transmissivity).*

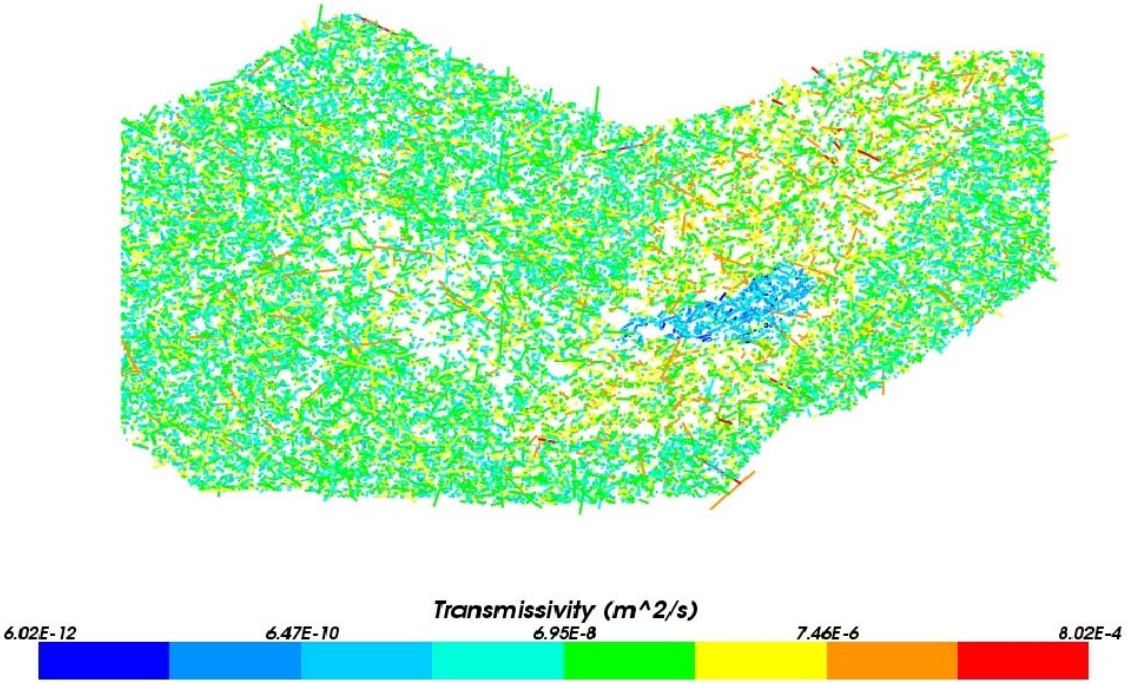

Figure 5-30. *DFN model for the small regional-scale domain showing stochastic fractures cutting a horizontal slice at z = –500 m coloured by Log(transmissivity).*

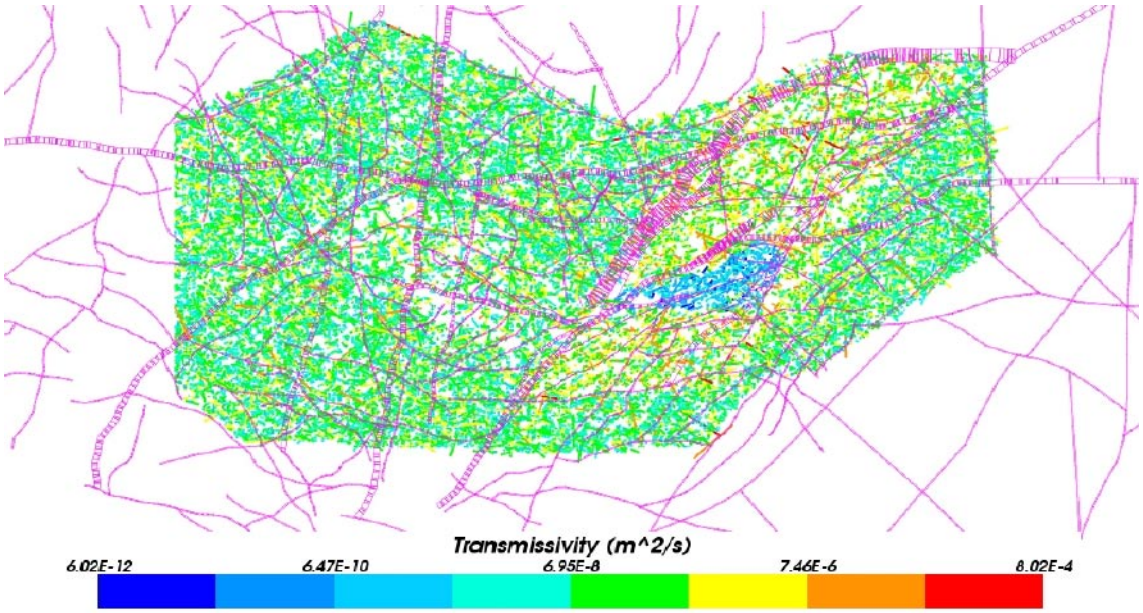

Figure 5-31. *DFN model for the small regional-scale domain showing stochastic fractures cutting a horizontal slice at z = –500 m coloured by Log(transmissivity) and the HCD model superimposed (purple).*

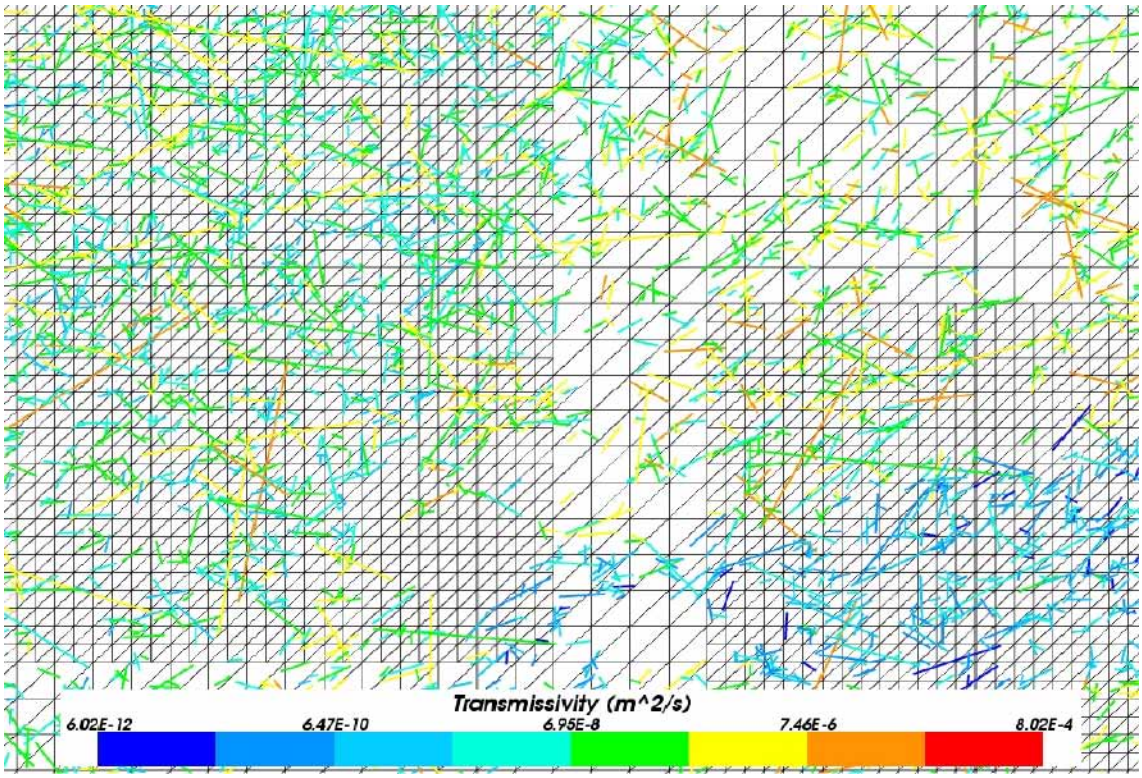

Figure 5-32. *A part of the DFN model as shown on a slice through the fractures coloured by Log(transmissivity) and the 100 m and 50 m finite-element grid (coloured black and each element drawn as 2 triangles).*

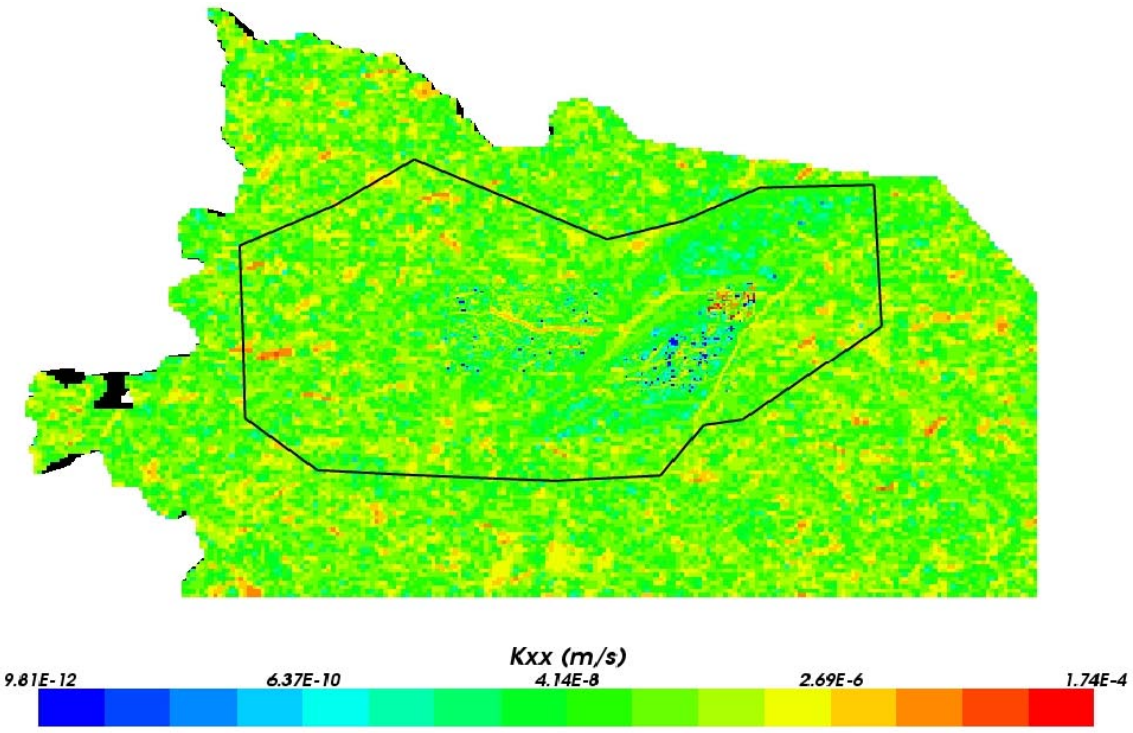

Figure 5-33. *Regional-scale ECPM model showing upscaled conductivity on the the top of the HRD and the outline of the smaller regional model domain (black line).*

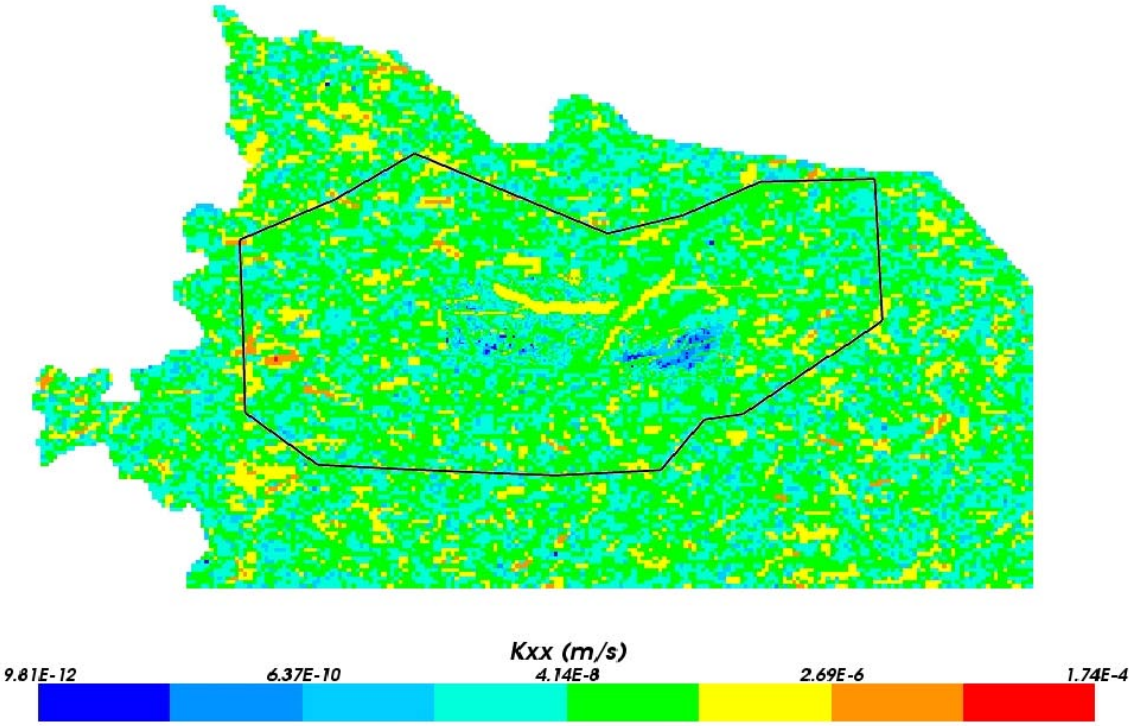

Figure 5-34. *Regional-scale ECPM model showing upscaled conductivity on a horizontal slice, z = –500 m, through the model, and the outline of the smaller regional model domain (black line).*

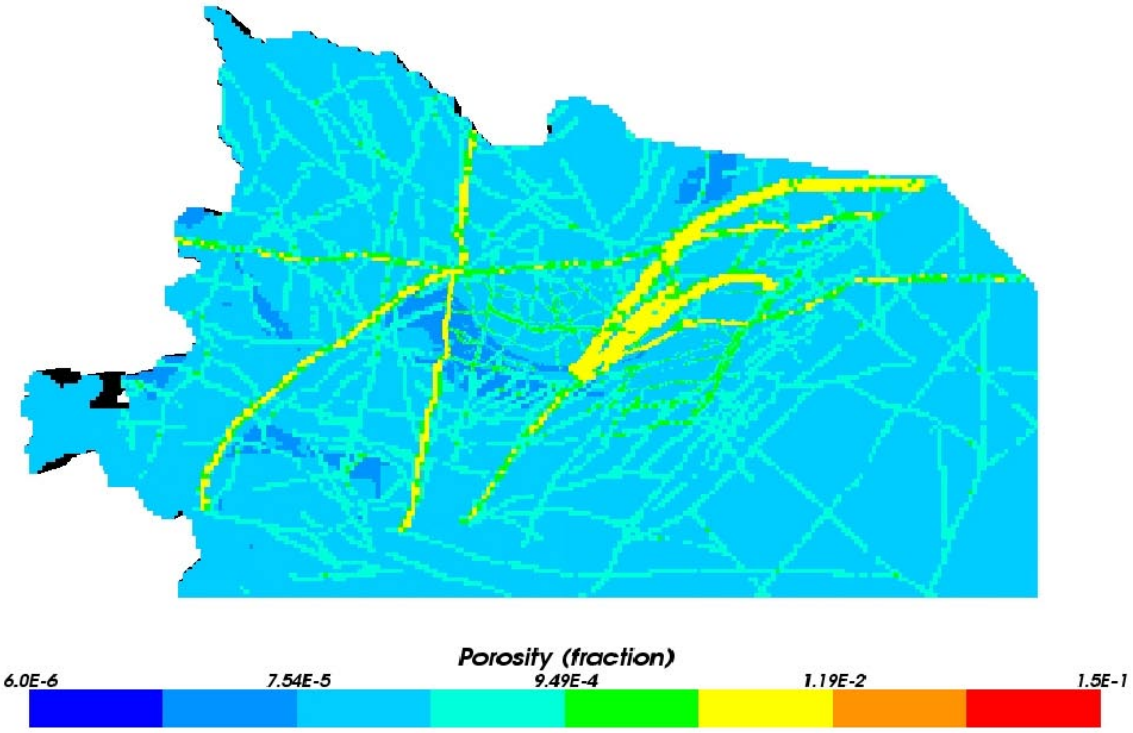

Figure 5-35. *Block-scale kinematic porosity shown at the top of HRD on a plan view of the regional-scale ECPM model.*

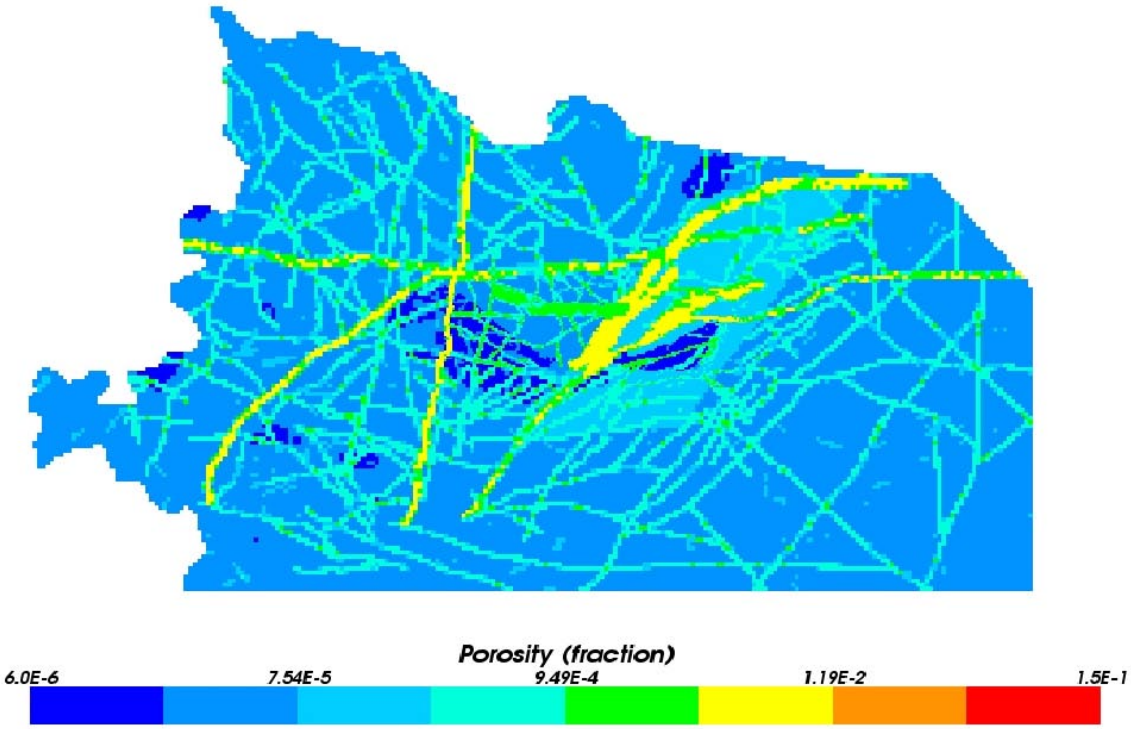

Figure 5-36. *Block-scale kinematic porosity on a horizontal slice z = –500 m through the regional-scale ECPM model.*

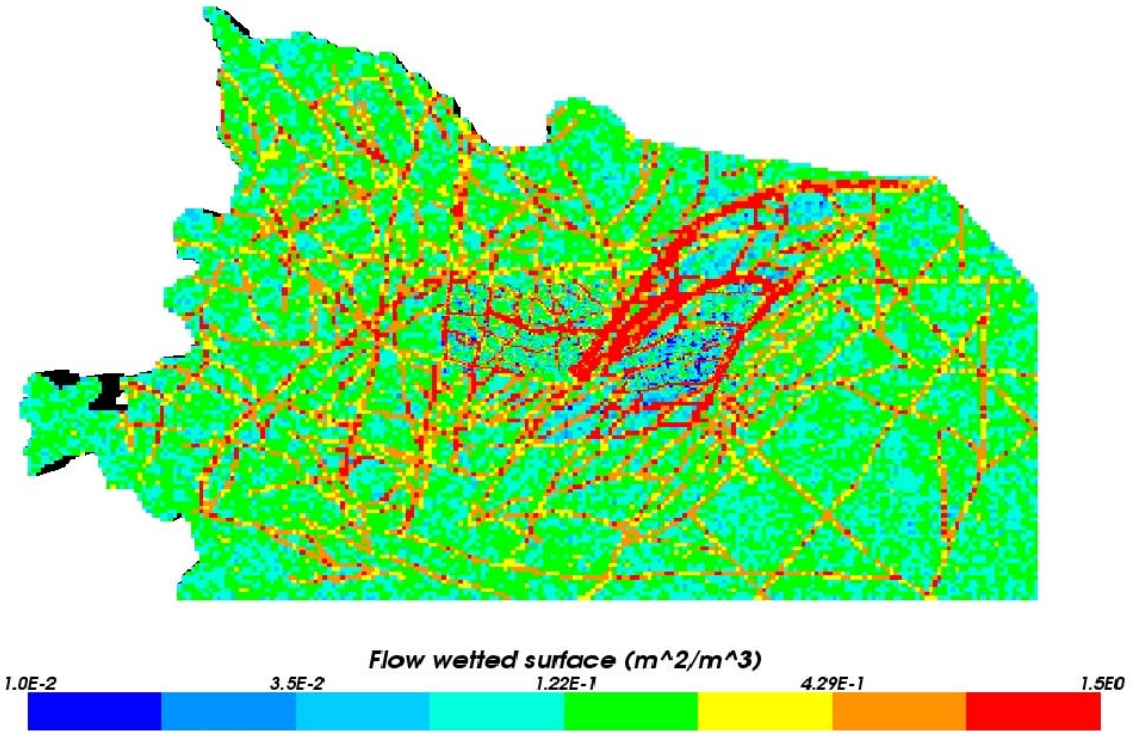

Figure 5-37. *Block scale flow-wetted surface used in the transport calculations on the top surface of the HRDs.*

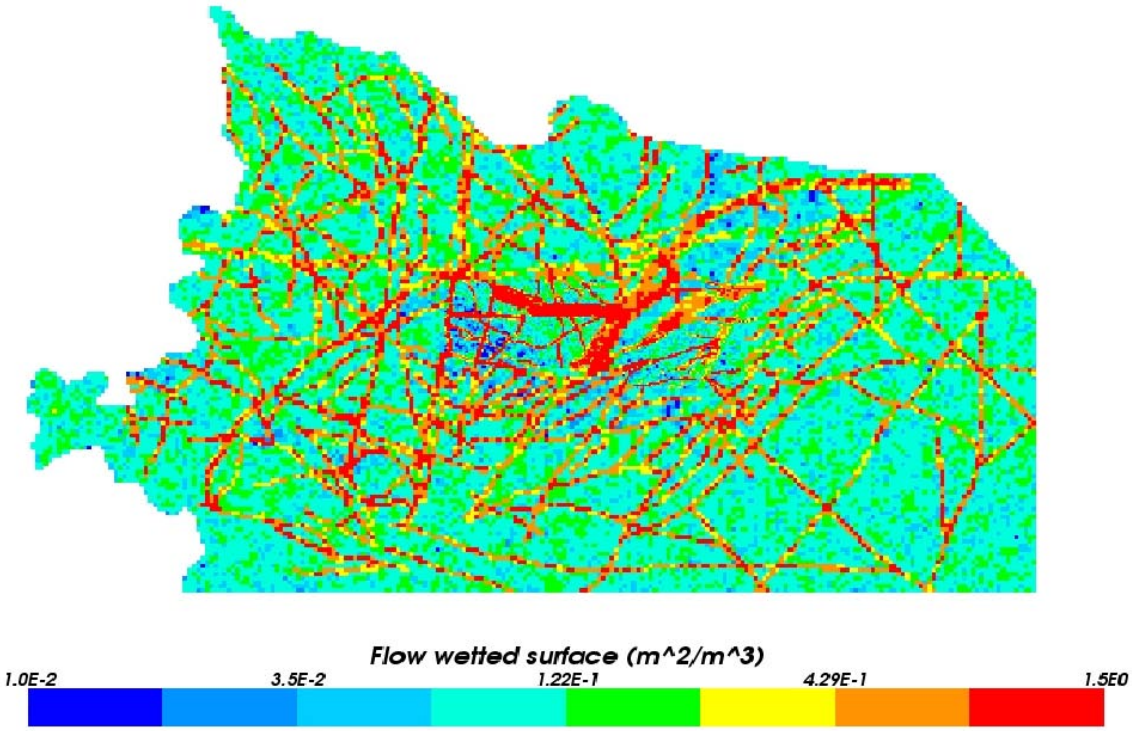

Figure 5-38. *Block scale flow-wetted surface a_r on a horizontal slice z = –500 m through the regional-scale ECPM model.*

Table 5-6. DFN variants created and their parameters.

DFN Case	Seed	Fracture model	r_{min}
HRD3a	101	CONNECTFLOW interpretation –T/r semi-correlated	14 m
HRD3b	201	CONNECTFLOW interpretation – T/r semi-correlated	14 m
HRD3c	301	CONNECTFLOW interpretation – T/r semi-correlated	14 m
HRD4	101	CONNECTFLOW interpretation – T/r correlated	14 m
HRD5	101	CONNECTFLOW interpretation – T/r uncorrelated	14 m

5.10 Transport properties

The choice of diffusion accessible porosity and intrinsic diffusion coefficient are discussed in Subsection 5.10.1, and calculation of the flow-wetted surface parameter, a_r, is described in Subsection 5.10.2.

The hydraulic and transport properties for the HRD1 case are summarised in Table 5-7. Mostly, the same transport parameters were used in the final Reference Case model (see Table 7-2).

5.10.1 Diffusion accessible porosity and intrinsic diffusivity

Two sources were considered to guide the choice of values for the diffusion accessible porosity and intrinsic diffusion coefficient, /Byegård and Gustavsson 2006/ and /SKB 2004/. Table 5-8 and Table 5-9 summarise the values for diffusion accessible porosity and diffusion coefficient respectively.

Table 5-7. Hydraulic and transport properties used in the HRD1 case.

Property	Value	Comment
Block-scale hydraulic conductivity (ms^{-1})	$1\ 10^{-11}$–$3.2\ 10^{-7}$	Based on PSS 20 m and 100 m intervals
Block-scale fracture kinematic porosity n_e	$1\ 10^{-4}$ above –300 m elevation $1\ 10^{-5}$ below –300 m elevation	Based on block-scale kinematic porosity for 20 m which includes fractures down r_{min} = 1.1 m
Diffusion accessible porosity n_m	Base-case: $5.9\ 10^{-3}$ Variant: $3.6\ 10^{-3}$	/Byegård and Gustavsson 2006/ maximum value
Dispersion lengths	a_l = 40 m, a_t = 5 m	Minimal values for grid size
Flow-wetted-surface area per unit volume a_r ($m^2\ m^{-3}$)	Base-case: 1.0–2.0 above –300 m elevation 1.0 below –300 m elevation	Values based on approximate calibration against hydrogeochemistry
	Variant: 0.6–1.9 above –300 m elevation 0.2–0.6 below –300 m elevation	RD and depth dependent, based on PFL-f data
Intrinsic diffusivity D_e (m^2s^{-1})	Base-case: $1.5\ 10^{-13}$ Variant: $3.1\ 10^{-13}$	/Byegård and Gustavsson 2006/

Table 5-8. Values for diffusion acccessible porosity (%) reported by two different sources. n denotes the number of samples used in the measurements.

Source	Rock	
	Avro Granite (A)	Quartz monzodiorite (D)
/Byegård and Gustavsson 2006/	(0.36 ± 0.23 (n = 71, of which KLX02 = 42 and KLX04 = 29)	0.17 ± 0.08 (n = 19)
/Laaksoharju et al. 2005/	0.71 ± 0.2 (n = 9)	0.32 ± 0.18 (n = 7)

Table 5-9. Values for the diffusion coefficient, D_e ($m^2\ s^{-1}$), reported by two different sources. n denotes the number of samples used in the measurements.

D_e ($m^2\ s^{-1}$)	Avro Granite (A)
/Byegård and Gustavsson 2006/ (D_e for HTO)	$1.51\ 10^{-13}$ (n = 3, on KLX04, no temp given)
/Laaksoharju et al. 2006/ (D_e for Cl)	$3.1\ 10^{-13}$ (on KLX03–7, data for 20°C)

For the diffusion accessible porosity, the L1.2 hydrogeochemical report /SKB 2006/ provides values for KLX03 whilst /Byegård and Gustavsson 2006/ report updated values for KLX02 and KLX04. The values given by /SKB 2006/ are significantly higher than the values reported in /Byegård and Gustavsson 2006/. This may be due to differences in how the porosity measurements are performed. For the measurements reported in /SKB 2006/, a drying temperature of 105°C and a drying time of up to 170 days were used, whereas Byegård et al used 70°C as a drying temperature and a drying time of, on average, 3–4 days. However, it is believed that all reported values are within the general uncertainty bounds associated with porosity measurements.

The diffusion coefficients are harder to compare, since they have been carried out and reported by different methods and for different elements. /Byegård and Gustavsson 2006/ report a formation factor of $(6.7 \pm 1.2)\ 10^{-5}$ (n = 3) for HTO through-diffusion. The relation $D_e = D_0 \times F$, where F is the formation factor, D_0 (m^2/s) is the free ion coefficient, and D_0(HTO) = $2.25\ 10^{-9}$ m^2/s (from literature), is used to obtain $D_e = 1.51\ 10^{-13}$ m^2/s. This compares to a value of $3.1\ 10^{-13}$ m^2/s for Cl at 20°C given by /Laaksoharju et al. 2006/, which is stated to be in excellent agreement with reported literature data of $3.9\ 10^{-13}$ m^2/s.

The dispersion lengths used to model hydrodynamic dispersion are chosen to be small relative to the element size. This is because the dispersion due to heterogeneity on the macro-scale (larger than an element size) will be occur explicitly due to the spatial variablity in the hydraulic conductivity field that arise naturally from the stochastic Hydro-DFN model that underlies the element property assignment. Further hydrodynamic dispersion may occur on the micro-scale (sub-element scale) which can be represented implicitly through the dispersion tensor term in the reference water transport equations. The values for dispersion lengths are chosen to be about the minimum possible without introducing numerical problems. Hence, the longitudinal dispersion length is about the size of the elements in the local-scale, and the transverse dispersion is one tenth of this.

5.10.2 Fracture connectivity and flow-wetted surface (FWS)

The flow-wetted-surface, or a_r, is required to calculate the F-factor along flow-paths in continuum models. It is also used in the calculation of rock matrix diffusion (RMD) for the reference water transport. There are several possible approaches to estimating a_r. One possibility is to obtain a value by calibrating the models of palaeo-hydrogeology in terms of the RMD process to estimate a value of a_r that gives a reasonable reproduction of the measured hydrogeochemistry data. Two other possible approaches are either to perform a connectivity analysis of the Hydro-DFN to calculate the fracture intensity of the connected network, $P32_c$, or to use the hydraulic PFL-f data directly.

Starting with the latter approach, the vertical frequency of PFL-anomalies, $P10_{PFL}$, as well as other hydraulic statistics are summarised for each borehole above and below –300 m in Table 5-10 and Table 5-11 respectively. The numbers of PFL-anomalies given in these tables are based on the raw data. Strictly, to be consistent with the concept described in Subsection 3.3.2 and Section 3.8, PFL-anomalies that are associated with the same deformation zone should be amalgamated and counted as one anomaly, but this was not done for the calculations reported in this section. The total transmissivities are calculated by summing all T values over the entire borehole length. The mean hydraulic conductivity, K, is obtained by dividing the total T by the borehole length.

Two formulae are then needed to estimate a_r. Firstly, $a_r = 2 \times P32_c$, where $P32_c$ is the connected fracture intensity. The factor 2 comes from the two rock surfaces either side of the fracture at which matrix diffusion and sorption can take place. Secondly, $P32_c = \alpha \times P10_c$ relates the areal fracture intensity of connected fractures to the vertical frequency of connected fractures, $P10_c$. The factor α is a function of the geometrical parameters of the DFN model. For example, for a single horizontal set, α would be 1.0.

The other approach is to use the relationship $a_r = 2 \times P32_c$, and calculate $P32_c$ from a connectivity analysis of the Hydro-DFN model. In performing the connectivity analysis, it is informative to calculate both $P32_c$ and the vertical frequency of connected fractures, $P10_c$, since this gives an estimate of the number of connected fractures intersecting a vertical deposition hole. $P32_c$ is calculated by generating a network of fractures within a given block-size, removing all isolated fractures and isolated clusters that have no connection to the boundary, removing all dead-end fractures (those with only one intersection), and then the surface area per volume of the remaining fractures is calculated. To calculate $P10_c$, fractures are generated within a given block-size, all isolated and dead-end fractures are removed, and then an array of 25 equally spaced vertical boreholes is used to sample the fracture spacing in the block. This means the total simulated core length is 25 multiplied by the block size. $P10_c$ is then calculated as the average connected fracture frequency over the 25 simulated cores. The calculated $P32_c$ and $P10_c$ can be sensitive to the block size and minimum fracture size truncation used since they both affect connectivity. In modelling studies for the Forsmark area /Hartley et al. 2006/, these parameters were varied to quantify

Table 5-10. Summary table of PFL-anomalies above –300 m. $P10_{PFL}$ is the number of flowing PFL-anomalies per unit length of borehole.

Borehole	Number of PFL-anomalies	Borehole length (m)	$P10_{PFL}$ (m^{-1})	Total transmissivity ($m^2\ s^{-1}$)	Mean K ($m\ s^{-1}$)
KAV01	106	220	0.48	1.3E–05	5.9E–08
KAV04A	43	185	0.23	4.6E–06	2.5E–08
KLX02	32	99	0.32	2.4E–05	2.4E–07
KLX03	25	217	0.12	1.5E–05	6.9E–08
KLX04	53	218	0.24	5.2E–05	2.4E–07
KSH01A	60	209	0.29	4.0E–06	1.9E–08
KSH02	18	214	0.08	3.1E–06	1.5E–08

Table 5-11. Summary table of PFL-anomalies below –300 m. $P10_{PFL}$ is the number of flowing PFL-anomalies per unit length of borehole.

Borehole	Number of PFL-anomalies	Borehole length (m)	$P10_{PFL}$ (m^{-1})	Total transmissivity ($m^2\ s^{-1}$)	Mean K ($m\ s^{-1}$)
KAV01	11	197	0.06	1.0E–07	5.1E–10
KAV04A	83	556	0.15	1.2E–05	2.1E–08
KLX02	42	877	0.05	2.7E–06	3.1E–09
KLX03	30	644	0.05	6.3E–06	9.7E–09
KLX04	53	570	0.09	9.4E–06	1.6E–08
KSH01A	8	272	0.03	1.0E–08	3.7E–11
KSH02	64	698	0.09	3.9E–06	5.6E–09

sensitivities. It was found that $P32_c$ generally reduces with block-size and the addition of smaller scale fractures made a limited impact on $P32_c$ for the sparse networks at Forsmark. Here, the network is more connected, and so the choice of fracture radius truncation, r_{min}, has a greater impact on $P32_c$. Here, a fracture size truncation of $r_{min} = 0.5$ m was used compared to r_0 of 0.28 m for Set_A-Set_d. This was close to the lower limit for what was computationally feasible for a 200 m block.

Using the Hydro-DFN models for boreholes KLX03, KLX04, KAV04 and KSH01A, the connected $P32_c$ above and below –300 m is calculated as presented in Table 5-12. The table gives the input P32 before removing unconnected and dead-end fractures, for $r_{min} = 0.5$ m, followed by $P32_c$. The connected network varies between 40% in the lower part of KLX03 to 80% in the upper section of KLX04. The average vertical fracture spacing for each borehole above and below –300 m is given in Table 5-13. The factors $P32_c/P10_c$ for each borehole above and below –300 m are summarised in Table 5-14. The average of these factors is 2.5.

It is useful to try to illustrate the fracture connectivity graphically also. Figure 5-39 shows an example of a DFN model generated in a 200 m cube according to the Hydro-DFN for KLX04 above –300 m. The left picture shows all fractures that are generated on a 2D vertical slice, and the right picture shows the same fracture network on the same slice, but with isolated fractures and clusters removed. Only isolated fractures are removed here, dead-ends remain. There are areas that are devoid of connected fractures, and a clear pattern is seen that all of the large fractures (coloured green to red) remain, but only those small fractures (coloured blue) that intersect or hang-off the large fractures are retained. The pattern of connected fracturing shown here also illustrates that intact ‘matrix’ blocks between

Table 5-12. Calculation of $P32_c$ for 200 m block-size and and fracture radius truncations r_{min} = 0.5 m.

	KLX03	KLX04	KAV04A	KSH01A
Input P32 (m^2 m^{-3}) above –300 m	0.50	1.07	0.77	0.74
Output $P32_c$ (m^2 m^{-3}) above –300 m	0.31	0.86	0.55	0.52
Input P32 (m^2 m^{-3}) below –300 m	0.22	0.72	0.59	0.75
Output $P32_c$ (m^2 m^{-3}) below –300 m	0.09	0.50	0.37	0.53

Table 5-13. Average vertical fracture spacing, $1/P10_c$, in a connected network for a block-size of 200 m and fracture radius truncations r_{min} = 0.5 m.

	KLX03	KLX04	KAV04	KSH01A
$1/P10_c$ (m) above –300 m	8	3	5	5
$1/P10_c$ (m) below –300 m	26	5	7	5

Table 5-14. Factor $P32_c/P10_c$ for a connected network for a 200 m block-size and fracture radius truncations r_{min} = 0.5 m.

	KLX03	KLX04	KAV04	KSH01A
$P32_c/P10_c$ above –300 m	2.5	2.5	2.7	2.7
$P32_c/P10_c$ below –300 m	2.2	2.3	2.5	2.7

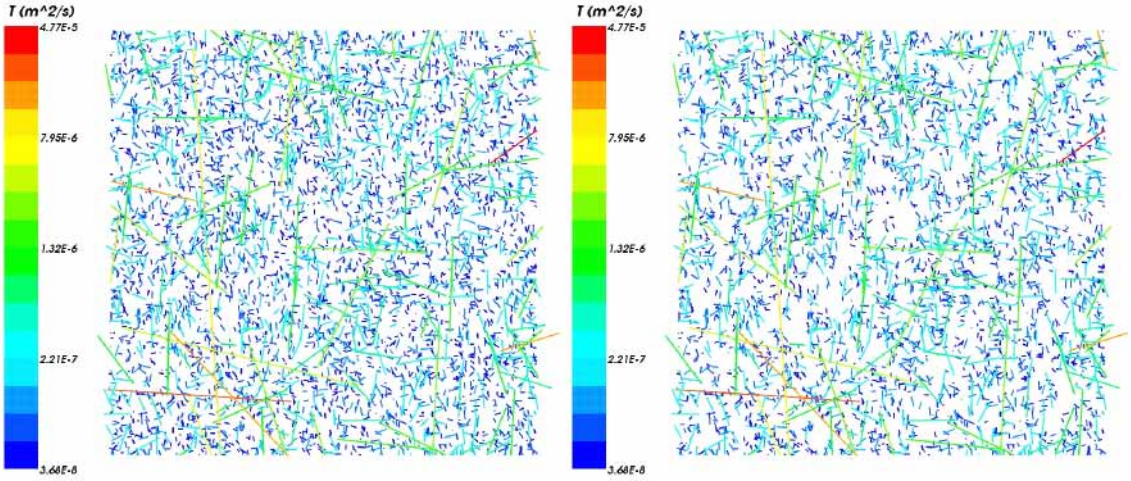

Figure 5-39. *An example of fracture connectivity in a 200 m cube using the fracture network defined for KLX04 above –300 m (see Table 3-22). Left: a 2D vertical slice through the network showing all fractures; right: 2D vertical slice after removing isolated fractures.*

the interconnected networks are heterogeneous in size and shape. This is consistent with observed variability in the length of sections of broken and unbroken core seen in boreholes and the distribution of flow anomalies. In addition, since matrix block size has a strong influence on the effectiveness of the RMD process, then spatial variations in block size will lead to spatial variations in the effectiveness of RMD. Hence, the degree of equilibrium between fracture and matrix hydrogeochemistry will vary spatially depending on the local

degree of fracture connectivity. This suggests that we have to be cautious not to assume that the interpretation of a few hydro-chemical samples can necessarily be extrapolated over the whole Laxemar subarea.

Values for a_r for each borehole above and below –300 m may now be calculated using the $P32_c$ values in Table 5-12, and using the $P10_{PFL}$ values in Table 5-10 and Table 5-11 along with the average value for α of 2.5. The a_r values are summarised in Table 5-15. The vertical frequency of connected fractures, $P10_c$ may also be compared directly with $P10_{PFL}$ in Table 5-16. The a_r values calculated using $P32_c$ are generally similar to the a_r values calculated using $P10_{PFL}$ for all boreholes above and below –300 m, except for KLX04 below –300 m and KSH01A below –300 m where they are higher. Correspondingly, $P10_{PFL}$ similar to $P10_c$ values for all boreholes except for KLX04 below –300 m and KSH01A below –300 m. In KLX03 and KLX04 both approaches give consistent values, predict a much higher a_r in KLX04 than in KLX03, and higher values above –300 m than below. It should be noted that the a_r values given by the model are sensitive to the choice of r_{min}, and if all fractures were included down to r_0, then a_r would increase.

For the regional modelling, a_r values were calculated for each rock domain and for the depth intervals above and below –300 m by taking an average over the $P10_{PFL}$ values for each borehole in the HRD, weighted by borehole length. These a_r values are given in Table 5-17. For example, for HRD(A), data from boreholes KLX02 and KLX04 is available. Therefore, the length weighted average a_r may be calculated as:

$$a_r = 2\alpha\left(\frac{L^{\mathrm{KLX02}} P10_{\mathrm{PFL}}^{\mathrm{KLX02}} + L^{\mathrm{KLX04}} P10_{\mathrm{PFL}}^{\mathrm{KLX02}}}{L^{\mathrm{KLX02}} + L^{\mathrm{KLX04}}}\right),$$

and for HRD(A) above –300 m, KLX04 has a $P10_{PFL}$ of 0.24 m^{-1} over a 218 m length of borehole, and KLX02 has a $P10_{PFL}$ of 0.32 m^{-1} over a 99 m length of borehole. Therefore, for HRD(A), the average a_r is 1.4 m^2 m^{-3}.

Table 5-15. Comparison of a_r values calculated in two different ways based on the Hydro-DFN model and the PFL-f data.

Elevation interval	Borehole	a_r (m^2 m^{-3})	
		$a_r = 2\times P32_c$ (model)	$a_r = 2\times\alpha\times P10_{PFL}$ (PFL)
Above –300 m elevation	KAV04A	1.1	1.2
	KLX04	1.7	1.2
	KLX03	0.6	0.6
	KSH01A	1.0	1.5
Below –300 m elevation	KAV04A	0.7	0.8
	KLX04	1.0	0.5
	KLX03	0.2	0.2
	KSH01A	1.0	0.1

Table 5-16. Comparison of $P10_{PFL}$ and $P10_c$.

Elevation interval	Borehole	P10	
		$P10_c$ (model)	$P10_{PFL}$ (PFL)
Above –300 m elevation	KAV04A	0.20	0.23
	KLX04	0.35	0.24
	KLX03	0.13	0.12
	KSH01A	0.20	0.29
Below –300 m elevation	KAV04A	0.14	0.15
	KLX04	0.20	0.09
	KLX03	0.04	0.05
	KSH01A	0.20	0.03

Table 5-17. Average, minimum and maximum a_r values for each rock domain, calculated from PFL-anomaly data.

	Rock domain	Average a_r (m^2 m^{-3})	Min a_r (m^2 m^{-3})	Max a_r (m^2 m^{-3})
Above –300 m elevation	HRD(A2)	1.9	1.2	2.4
	HRD(A), HRD(F,G)	1.4	1.2	1.6
	HRD(D,E,M)	0.6	0.6	0.6
	HRD(B,C)	0.9	0.4	1.5
Below –300 m elevation	HRD(A2)	0.6	0.3	0.8
	HRD(A), HRD(F,G)	0.3	0.2	0.5
	HRD(D,E,M)	0.2	0.2	0.2
	HRD(B,C)	0.4	0.1	0.5

5.11 HSD model

The overburden in the Simpevarp area is dominated by sandy till but in several valleys the till is overlain by clay deposits, and on top of hills the thickness of the till is small or the rock is out-cropping. In minor parts of the area, eskers with coarse-grained material are found.

As a reference case in this Laxemar 1.2 modelling, it is assumed that the entire area is covered by a 3 m thick layer of silty till, with the upper 1 m more porous due to soil forming processes. This was represented explicitly in the model as three very thin layers of finite-elements of thickness 1 m at the top surface of the model. The HSD properties within each layer are uniform. The HSD overlays all HCDs providing a hydraulic contact between the soil layers and the deformation zones.

A heterogenous model for the distribution of Quaternary Deposits (QD) was also provided /Nyman 2005/. The QD depth model is based on three layers, Z1, Z2 and Z3. The upper layer (Z1) is characterised by the impact of surface processes, e.g. roots and biological activity. The bottom layer (Z3) is characterised by contact with the bedrock and is dominated by till. The middle layer (Z2) is assumed to have different hydraulic qualities to the upper and bottom layers and is dominated by clay. The soil type assigned to QD layer Z1 at a certain location is taken directly from detailed maps of QD. The soil types assigned to QD layers Z2 and Z3 at a certain location also depend on the soil type in QD layer Z1.

Three additional layers, M1, M2 and M3, are superimposed on the layers Z1, Z2, Z3 as illustrated in Figure 5-40. Layer M1 corresponds to peat, M2 to glacio-fluvial sediments, M3 to artificial fill. All layers can have thickness zero.

Four QD maps were provided, which indicate the soil type at each node on a uniform grid with 10 m spacing. In addition, stratigraphy maps were provided for the top surface and for each of the six layers Z1, Z2, Z3, M1, M2 and M3. These maps provide the surface topography (with lake bathymetry) and depths of the layers on a uniform grid with 10 m spacing. Twelve different soil types were defined for the current study.

The regional model is composed of 100 m and 50 m elements and so the QD distribution and stratigraphy had to be mapped on to these elements in some way. Firstly, to set the soil type of each element, the QD maps were used to assign the most frequently occurring soil type within each 100 m or 50 m element to the entire element. The CONNECTFLOW implementation of the QD maps is illustrated in Figure 5-41. The soil type was used to set the QD in the layers Z1, Z2 and Z3 based on the 'stratigraphy rules' of /Werner et al. 2005/. For each node on the top surface of the regional model domain, the elevation was then approximated by taking a linear interpolation of the elevations of the four corners of the appropriate cell in the stratigraphy maps. The stratigraphy maps for the six layers were used in a similar way to assign a thickness to each element corresponding to each layer. The resulting model is illustrated in Figure 5-42. For the bedrock soil type in the QD maps, the QD for layer Z1 is till with a thickness of 0.1 m and so all of the areas that appear orange (indicating bedrock) in Figure 5-41 are green (indicating till) in Figure 5-42. The data provided specifies mostly Gytta under the sea as a default, although where data is available from ship traverses, shown as long thin strips offshore in Figure 5-41 and Figure 5-42, the QD is either Clay or Till.

Two vertical cross-sections through the regional model with the overburden model are shown in Figure 5-43 and Figure 5-44. These figures illustrate the thinner surface layers on top of hills and thicker surface layers in valleys. Figure 5-44 is magnified to show the QD layering in the valleys.

The properties of the two HSD layers for the homogenous HSD model and for the twelve soil types for the heterogeneous HSD model are summarised in Table 5-18. These properties are taken from the draft report /Werner et al. 2005/. For the heterogeneous HSD model, the thickness of a soil type depends on which of the layers, Z1, Z2, Z3, M1, M2 or M3, it lies in. Z1 is up to 0.5 m thick; Z2 is up to 3.8 m thick; Z3 is at least 3.6 m thick; M1 has a thickness of 0.9 m; M2 has a thickness of 5.0 m or 15 m; and M3 has a thickness of 4 m. Comparing these hydraulic conductivities with those of the homogeneous HRD model (see Figure 5-24 to Figure 5-26 or Table 5-3) shows that they are generally higher than the HRD, and even the Clay has a similar hydraulic conductivity to the Laxemar HRD near the surface. Comparing with the HCD, only the Gytta, Gytta clay and Clay (lower) have a lower hydraulic conductivity than the HCD. Hence, the overburden is not expected to affect infiltration to the deep bedrock significantly. The hydraulic conductivity of the clay would have to be reduced by about an order of magnitude for it to act as a semi-impermeable cover.

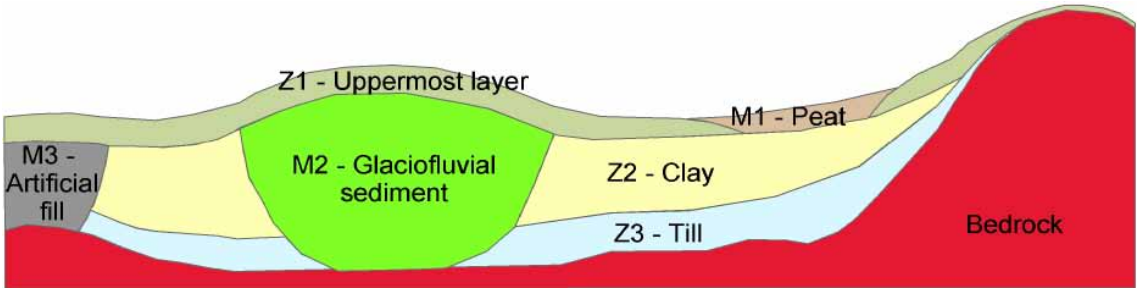

Figure 5-40. *Illustration of the layers Z1, Z2 and Z3, and M1, M2 and M3 in the overburden model. From /Nyman 2005/.*

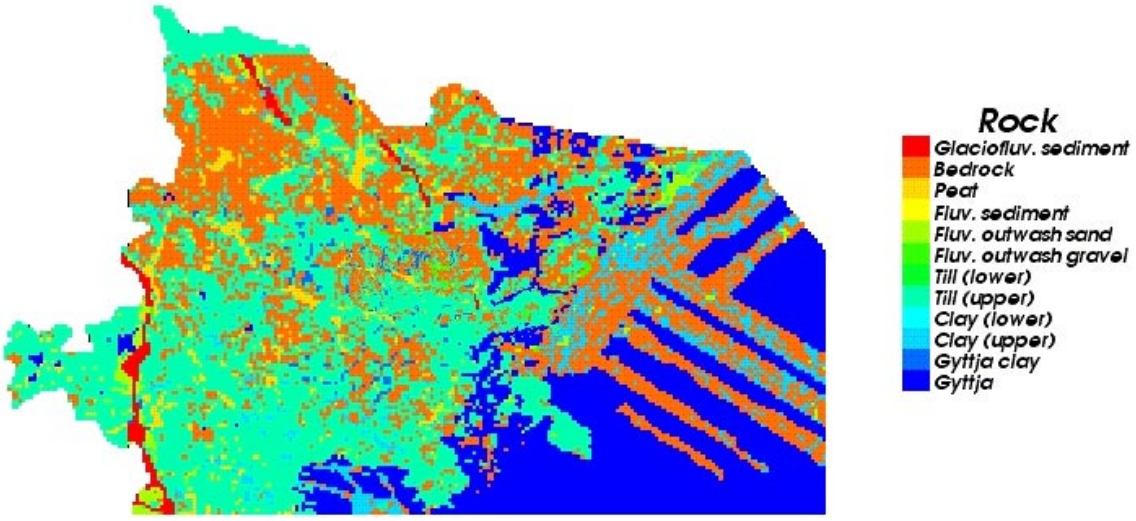

Figure 5-41. *The CONNECTFLOW implementation of the QD map for the extended regional model domain. The long thin strips offshore correspond to data available from ship traverses.*

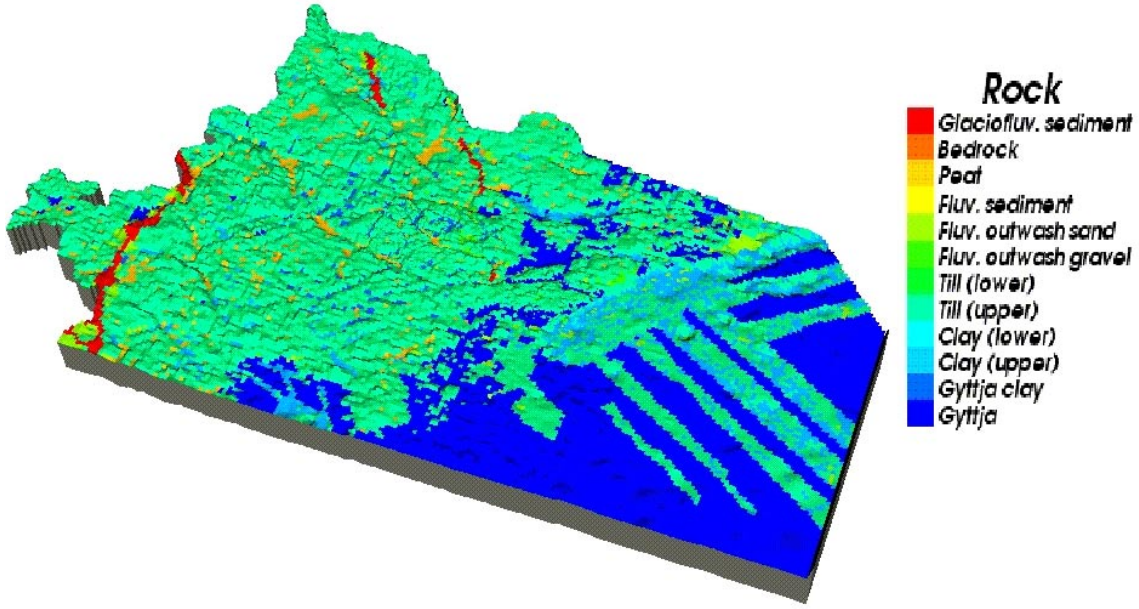

Figure 5-42. *The overburden model for the extended regional model domain. The HRD layers are only shown to a depth of approximately 100 m. The model has been stretched in the z-direction to exaggerate the surface topography.*

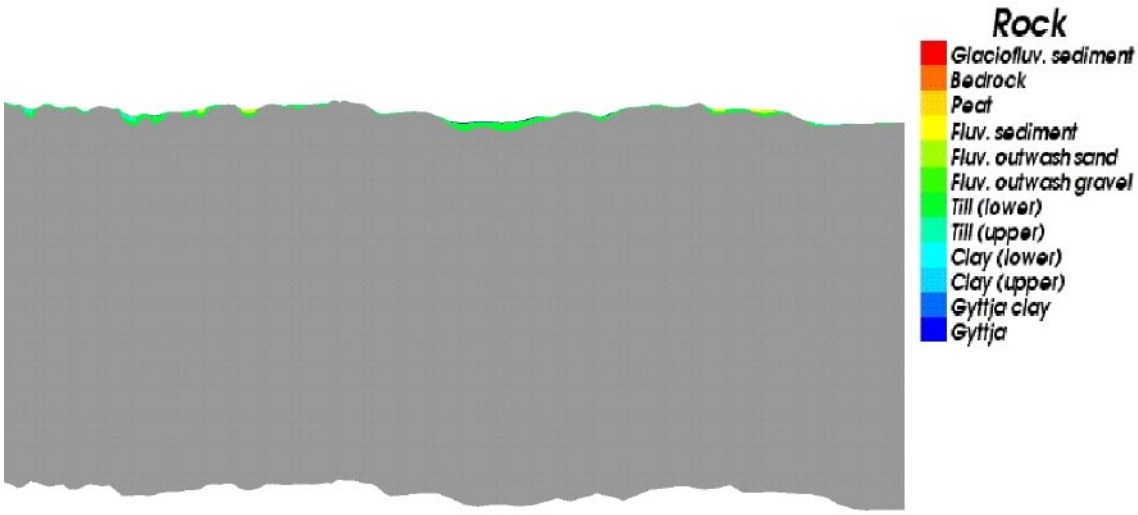

Figure 5-43. *Cross-section through the regional model illustrating thicker QD layers in valleys, and thinner layers on top of hills. HRD layers are coloured grey. The model has been stretched 10:1 in the z-direction to exaggerate the surface topography.*

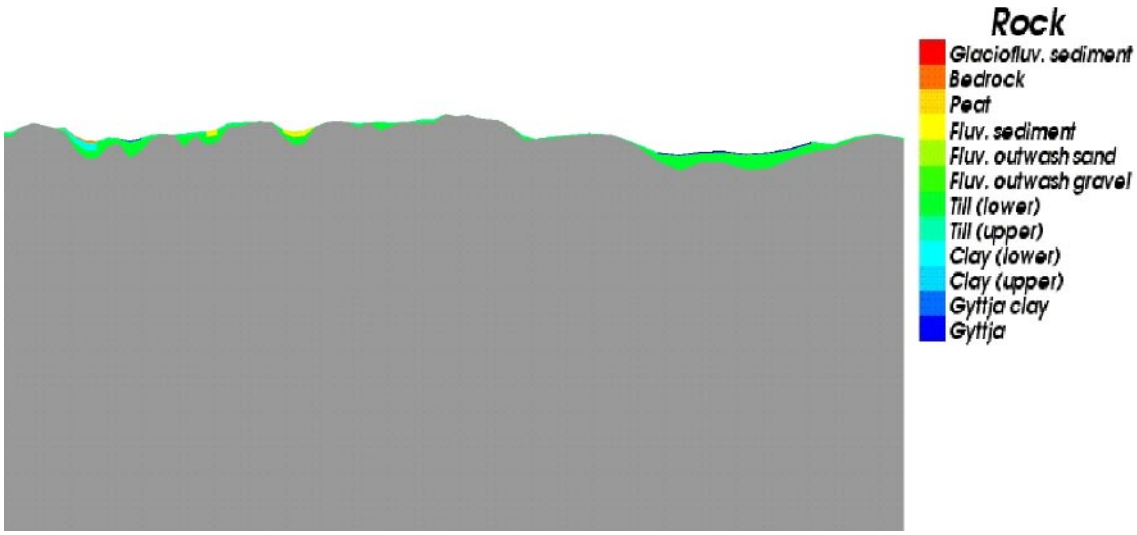

Figure 5-44. *Magnified cross-section through the regional model illustrating the QD layering in the valleys. HRD layers are coloured grey. The model has been stretched 10:1 in the z-direction to exaggerate the surface topography.*

Table 5-18. Surface hydraulic domain properties (from /Werner et al. 2005/).

HSD case	Geological description	Hydraulic thickness (m)	Hydraulic conductivity (m/s)	Kinematic porosity
HSD1	Till/artificial fill , near surface	1	$4\ 10^{-5}$	$1.5\ 10^{-1}$
	Till/artificial fill, below HSD1	2	$4\ 10^{-5}$	$5\ 10^{-2}$
HSD2	Gyttja	–	$1\ 10^{-8}$	$3\ 10^{-2}$
	Gyttja clay	–	$1\ 10^{-7}$	$3\ 10^{-2}$
	Clay (upper)	–	$1\ 10^{-6}$	$3\ 10^{-2}$
	Clay (lower)	–	$1\ 10^{-8}$	$3\ 10^{-2}$
	Till (upper)	–	$4\ 10^{-5}$	$1.5\ 10^{-1}$
	Till (lower)	–	$4\ 10^{-5}$	$5\ 10^{-2}$
	Fluv. outwash gravel	–	$1\ 10^{-4}$	$2.5\ 10^{-1}$
	Fluv. outwash sand	–	$1\ 10^{-4}$	$2.5\ 10^{-1}$
	Fluv. sediment	–	$1\ 10^{-6}$	$3\ 10^{-2}$
	Peat	–	$1.5\ 10^{-6}$	$2.4\ 10^{-1}$
	Bedrock	–	$1.05\ 10^{-7}$	$5\ 10^{-3}$
	Glaciofluv. sediment	–	$1\ 10^{-4}$	$2.5\ 10^{-1}$

6 Regional model – calibration targets

The primary data used for calibration of the hydrogeological model concepts and parameters was the hydrogeochemistry data available from boreholes in the regional model area. More precisely, this includes the salinity profiles, ratios of environmental isotopes (Oxygen-18 and Deuterium) and mixing fractions of the reference waters, along the trend and plunge of KLX01, KLX02, KLX03 (no mixing ratios), KLX04 (no mixing ratios), KSH01A, KSH02, KSH03A, KAV01, KAV04, KAS02, KAS03, KAS04 and KAS06, under present-day conditions.

In addition, the SKB Task Description requested visualisation of the evolution of reference water fractions on a series of vertical sections through the model as a more qualitative calibration of the overall evolution of the hydrogeological situation.

The reference water transport modelling facility in CONNECTFLOW when used in conjunction with RMD calculates a mixing fraction for both the fracture system and the matrix. Hence, in theory it would be possible to calibrate the model against hydrogeochemistry data from both the flowing features (as is acquired currently) and that from the much tighter matrix. However, techniques are only just being developed to acquire and analyse groundwater samples taken from the rock matrix /SKB 2006/. Data reported from KLX03 suggests the hydro-geochemical composition in fracture and matrix porewater volumes are broadly consistent suggesting a diffusive equilibrium.

Another possible calibration test is to compare the hydraulic conductivity along the boreholes in the model with the long interval PSS data. The grid resolution is either 50 m or 100 m, and hence given the choice of PSS interval data we have, 5 m, 20 m or 100 m, it seems appropriate to compare with the 100 m interval PSS data. However, it must be pointed out that the model is stochastic with Hydro-DFN properties for each HRD extrapolated for the interpreted boreholes, but without local conditioning of the hydraulic conductivities at the boreholes (except for the HCD). Therefore, this comparison should only be done in a qualitative sense by comparing the overall magnitude of hydraulic conductivity, for example.

6.1 Salinity profiles in boreholes

6.1.1 Data

The list of boreholes for which data is available is given in Table 6-1, and includes their positions and amount of data available. Figure 6-1 shows the relative location of these boreholes with reference to the road network. In addition, matrix porewater data has been reported for KLX03 /SKB 2006/. A depth profile of 14 matrix porewater samples have been reported for major ion concentrations and 11 of these samples reported for $\delta^{18}O$ and δD. /SKB 2006/ show that matrix pore water and fracture (formation) water are in equilibrium above –450 m elevation. Below this depth it is more uncertain.

The hydrogeochemical data are reported as either ‘representative’ or ‘less representative but suitable when used with caution’ /Laaksoharju et al. 2006/. A representative sample shows a complete set of elemental and isotopic analyses as well as having < 5% charge balance and contains < 1% drilling fluid.

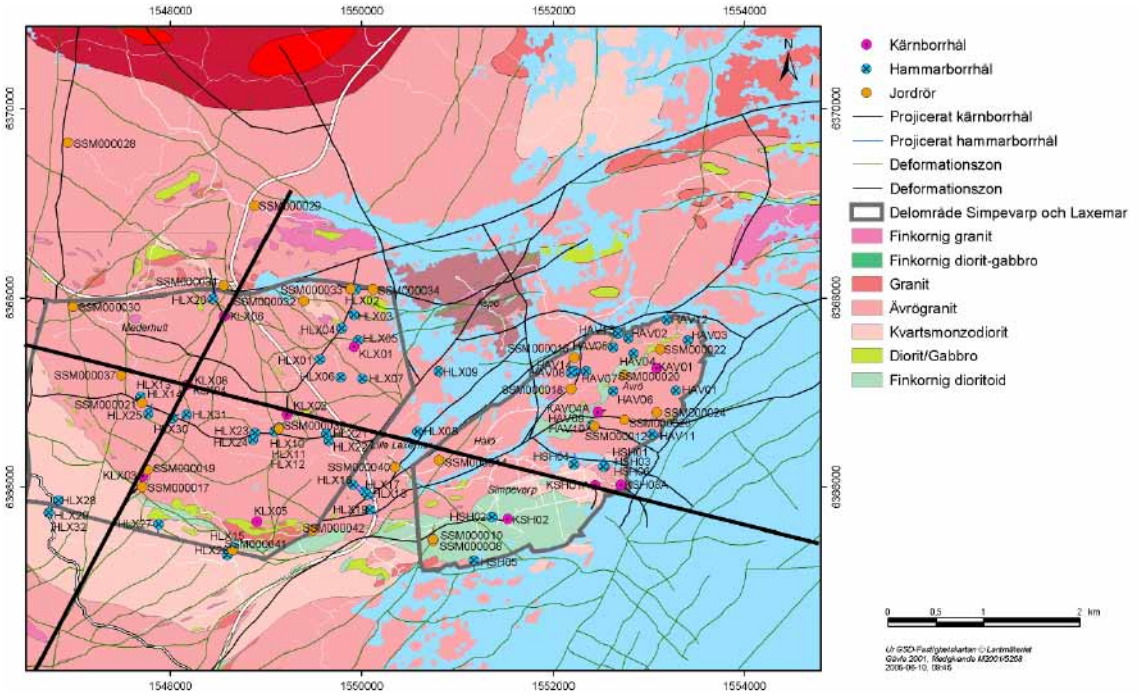

Figure 6-1. *Map showing the location of the sampling points and boreholes in the Simpevarp and Laxemar subareas. The positions of the WNW-ESE and NNE-SSW transect profiles used for presenting results in later chapters are marked in black.*

Table 6-1. Coordinates of the boreholes used as calibration targets. The amount and coverage of hydrogeochemistry data is also indicated.

Name	Easting	Northing	Adjacent percussion boreholes	Number of data points (representative/less suitable/ total nr)	Highest elevation of data (m)	Lowest elevation of data (m)
KLX01	1549923	6367486	HLX10	(0/3/3)	–257	–673
KLX02	1549224	6366769		(0/9/9)	–2	–1,531
KLX03	1547719	6366113		(2/2/4)	–137	–923
KLX04	1548172	6367077		(0/3/3)	–82	–944
KSH01A	1552443	6366014	HSH03	(0/3/3)	–153	–544
KSH02	1551529	6365658	HSH02	(1/1/2)	–415	–571
KSH03A	1552711	6366019		(0/1/1)	–39	–39
KAV01	1553085	6367258	HAV04, HAV05	(0/1/1)	–645	–675
KAV04	1552475	6366796	HAV06, HAV07	(1/0/1)	–40	–40
KAS02	1551420	6367796		(5/0/5)	–200	–881
KAS03	1551005	6368217		(2/5/7)	–122	–914
KAS04	1551185	6368121		(2/0/2)	–276	–377
KAS06	1551509	6367621		(3/1/4)	–200	–433

6.1.2 Calibration targets

Salinity gives an indication of the balance in driving forces between hydraulic gradients at the surface and buoyancy effects of the dense brine, and how this balance has changed over time due to land-rise. Hence, it acts as a natural tracer for transient variable-density flow.

However, by including the mixing fractions of reference waters, a more stringent calibration of the hydrogeological properties and boundary conditions is possible since it introduces freshwater tracers of varying age, such as the Glacial and Meteoric water, and the less dense Littorina waters.

The salinity for a given water composition in the model is calculated as the sum of the products of each reference water fraction and the salinity of that reference water. The salinities for the reference waters were calculated from the TDS based on Table 5-1.

6.1.3 Uncertainties in data

Data from more boreholes is available for calibration in Laxemar version 1.2. In particular, water compositions are available for KLX03, KLX04 and KAV04A. Only samples that are considered 'representative' or 'less representative data but suitable when used with caution' have been considered for calibration. Data from below 1 km is still only available for KLX02, the next deepest is –914 m in KLX04, and since Brine is not seen in significant proportion until about –900 m, then the data on the dense saline water is quite sparse. Thus, there is a risk of bias if we base the calibration of salinity on just the one or two deep boreholes.

Salinity is calculated from the sum of the major ion concentrations. The analytical error on each major ion concentration is about ± 5%.

6.2 Water types, major ions and isotopes in boreholes

The reference water mixing fractions provide us with several different tracers that have entered the groundwater system at different times and with different densities. This allows us to quantify sensitivities to initial conditions, boundary conditions and hydraulic properties, which would not be possible with salinity data alone.

6.2.1 Data

Transport of four reference waters (non-chemically reactive fluids) was simulated in the CONNECTFLOW groundwater flow model. These reference waters have been identified by the hydrogeochemistry group from previous site investigations as well as Oskarshamn site-specific data /SKB 2006/. Their representative composition of element concentrations and isotopic values (e.g. Na, Cl, $\delta^{18}O$, δD, ^{3}H) has been analysed as given in Table 5-1.

Using this information and assuming non-reactive mixing, it is possible to make a linear conversion from mixing fractions to element concentrations and isotopic values at any point in the model. As explained in Section 2.5, the main reason for performing simulations using the mixing fractions as the transported entities rather than element concentrations is that it is more straightforward to define boundary and initial conditions in terms of the evolution of different water types rather than chemical compositions. However, the output from a CONNECTFLOW simulation can readily be presented as either mixing fractions or as element concentrations and isotopic values for comparison with measured data from boreholes. For example, the fraction of each water type at a borehole can also be simulated using CONNECTFLOW and compared to the Multivariate Mixing and Mass-balance (M3) mixing fractions. The M3 approach takes samples from a borehole and uses 'principal component analysis' to calculate the fraction of each water type present in a sample

/Laaksoharju et al. 1999/. However, this approach has at least a 10% margin of error on each M3 mixing fraction. This margin is significant when several of the four reference waters are present since the cumulative error for all waters becomes large. Further, the error associated with a particular sample varies down boreholes depending on the primary reference waters present, which leads to artificial spikes in the reference water profiles down the borehole. For this reason the major ions and environmental isotopes are also used in the calibration since they represent 'raw' data. However, caution has to be used here also since while some chemical constituents, like Cl and $\delta^{18}O$, are transported conservatively (i.e. no chemical reaction takes place during transport), others are likely to be non-conservative, like SO_4, which can be affected by chemical and microbial processes. Mg is not strictly a conservative element either, but it is a useful indicator to differentiate between Brine at depth (low Mg concentration) and shallower Littorina water with high Mg concentration. The environmental isotopes δD and $\delta^{18}O$ help to differentiate between Glacial and Meteoric reference waters, and to some extent $\delta^{18}O$ can be used to distinguish the saline reference waters (Brine from Littorina).

6.2.2 Calibration targets

The main calibration target of coupled groundwater flow and reference water transport then is to compare the mixing fractions along the boreholes. The comparison is done in a visual way by comparing the trend for mixing fractions along the whole length of borehole with the interpreted field-data. It is done this way, rather than defining some sort of objective function only at the data points, so as to gain an understanding of the broader mixing pattern at a variety of depths.

6.2.3 Uncertainties in data

In view of the various uncertainties in the hydro-geochemical data, calibration of the CONNECTFLOW model is considered against as many of the measured data as possible. In particular, the calibration of CONNECTFLOW considers the most conservative, and representative, measured data (Cl, $\delta^{18}O$ and Mg), and the water types with larger fractions in the M3 mixing approach (where the 10% error margin is less significant). The measurement error on $\delta^{18}O$ is approximately ± 0.2‰, and ± 1‰ on δD. The analytical error on each major ion concentration is about ± 5%.

All data provided by ChemNet is considered representative, but some data is judged to be the best or most representative. This classification has been used by the geochemists to highlight their highest quality samples with a complete set of major ion and isotope analytical data, charge balance of ± 5%, and less than 1% drilling water. Other data provided as part of the S1.2 data delivery has been removed from the L1.2 data delivery since it is considered less representative. Also, some of the representative data is sourced from percussion drilled boreholes under pumped rather than natural inflow conditions. To distinguish between these different categories of sample quality, different symbols are used to plot the data values when compared to the simulations:

- For the best representative samples filled squares are used to show the data.
- For other representative samples shaded squares are used to show the data.
- For samples from nearby percussion drilled holes filled triangles are used to show the data.
- For KLX02 and KAV01, the L1.2 data is supplemented with some S1.2 data and these are showns as an asterix symbol.

Extra data has been incorporated from S1.2 for KLX02 and KAV01 since it was felt that this data appears consistent with the representative data and helps fill some gaps in the representative data to give a more meaningful comparison for these two boreholes. It is noted that some of this less representative data is used in the L1.2 hydrogeochemistry report /SKB 2006/.

6.3 Hydraulic conductivity in boreholes

In developing the Hydro-DFN, the DFN hydraulic properties were matched against relatively small scale measurements, i.e. individual flow anomalies from PFL-f or 5 m test intervals for PSS. A further testing of the models is possible by considering the ECPM hydraulic properties on larger scales.

6.3.1 Data

PSS data gives interpreted hydraulic conductivity measurements generally on 5 m, 20 m and 100 m scales. This is provided for KLX01, KLX02, KSH01A, KSH02, KSH03A and KAV01. Since the regional-scale model has an element-size of either 50 m or 100 m, then it is most appropriate to compare the hydraulic conductivity in the model simulations to the 100 m PSS intervals. Where 100 m intervals are not available, then the hydraulic conductivity from several shorter intervals has been averaged (i.e. assuming radial flow) to give an equivalent 100 m interval. For each borehole, the PSS data typically covers from –100 m to either –600 m or –1,000 m, i.e. about 6–10 intervals. Comparisons of this type have already been illustrated in Figure 5-15.

6.3.2 Calibration targets

The calibration against the hydraulic conductivities is performed by plotting the distribution in the model along with the PSS data with axes of elevation and Log(K_{eff}). It is expected that the hydraulic conductivities should be of comparable magnitude and, in particular, high values corresponding to large deterministic DZs should match closely as they have been conditioned in the HCD data interpretation.

6.3.3 Uncertainties in data

There are several uncertainties associated with the PSS data. Firstly, these are single-hole measurements and so there are issues relating to the borehole skin, or other localised effects such as the test only evaluates part of the zone adjacent to the borehole. There are then interpretation uncertainties. For example, two alternative methods have been used in the PSS interpretation, based on either the Moye or 2D radial transient flow assumptions. The transient evaluation is considered to "filter out" the effect of the skin factor. There are also some intervals in which there have been problems in making the single-hole test. In these cases a small hydraulic conductivity is given and so it is not always clear if this is a realistic value. Hence, in doing the comparison we might expect the overall magnitude of hydraulic conductivity to agree, with perhaps the high values to be in closer agreement, and lower values may indicate tighter areas although these are more uncertain.

7 Regional model – flow simulations

The SKB Task Description (TD) required that modelling be performed in two main phases:

1. Model the groundwater flow from the last glaciation up to present with different boundary conditions and hydraulic properties, and compare with measured TDS and calculated mixing proportions.
   a. Part of the purpose is to motivate the size of the model and applied boundary conditions.
   b. The effects of discretisation should be tested and be a part of the motivation for grid size and assigned grid properties.
2. Select representative cases from Phase 1 and perform flow-path calculations based on the present boundary conditions. Calculate Darcy velocities and hydraulic conductivity for selected areas.

In the SKB Task Description, a table was given with a number of different approaches for modelling the Hydraulic Conductor Domain (HCD) and the Hydraulic Rock Domain (HRD). The HCD is specified by data deliveries from the RVS group and by properties in spreadsheets. For the HRD, both a homogeneous approach and an approach based on the Hydro-DFN were tested. Three different depth dependency functions for both the HCD and the HRD were given. The TD states that these should be tested to find the best combination. Calibration was initially performed against PSS data to obtain hydraulic properties and then later against chemistry data to fine-tune the hydraulic properties and the transport parameters. The influence of the model size was also addressed by performing modelling using the potential natural boundaries that could give stable results for the site-scale mixing fractions and groundwater flow-paths. The consistency in the modelling results moving from one size to the other was then assessed.

In summary, hydraulic properties, initial conditions and boundary conditions that could give consistent simulations of the present-day salinity and mixing fractions were considered.

This section describes the sensitivity analysis performed with CONNECTFLOW in matching the salinity and mixing fractions. The predictions of transient flow and groundwater flow-paths for some calibrated cases are presented in Chapters 8 and 9.

7.1 Methodology

Figure 7-1 shows a schematic overview of the modelling workflow used in the project. The starting point is the Hydro-DFN conceptual model and the associated fracture properties. This can be used to obtain the statistics of block-scale properties or to construct a regional-scale DFN, which may be upscaled to produce an ECPM model. The resulting ECPM model has HRD hydraulic properties consistent with a realisation of the underlying DFN data. Initially, simple homogeneous models of the HRD can be used to help understand the importance of parameter assignment within the HCD and transport parameters such as flow-wetted surface and diffusion accessible porosity. However, ultimately, more complex stochastic models based on a DFN concept must be used. These stochastic models provide a more realistic representation of the heterogeneity that characterises the HRD. This means combining the regional-scale ECPM model with representations of the HCD and HSD. Finally, simulations of transient groundwater flow and reference water transport provide the calibration targets and required transport performance measures.

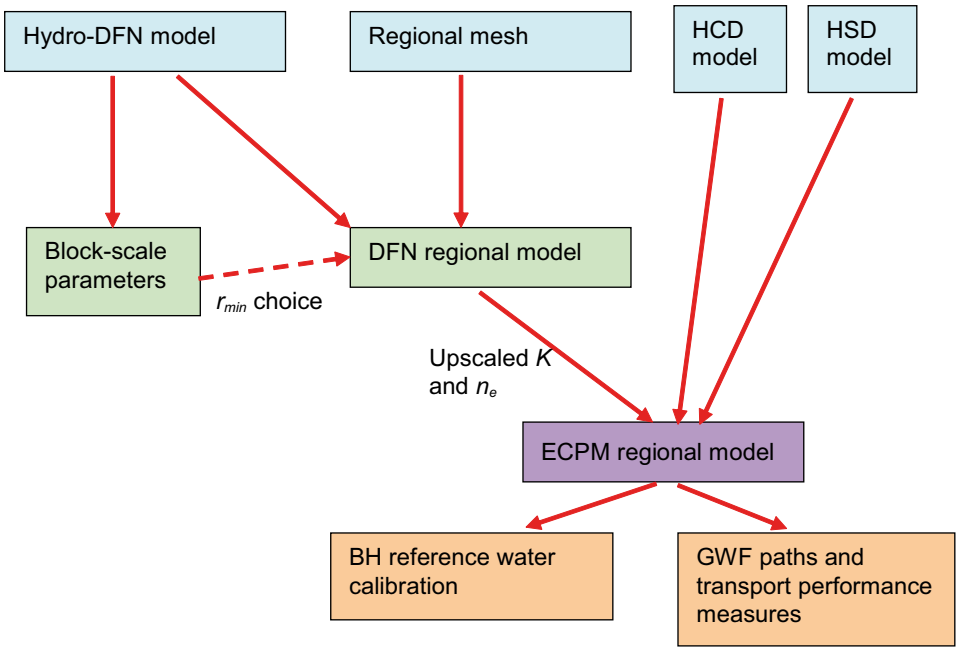

Figure 7-1. *A schematic workflow for the CONNECTFLOW modelling.*

The calibration is performed by plotting profiles of each of the 4 reference water fractions, salinity and isotope ratios down each borehole. The transport performance measures are processed as statistics over an ensemble of particles released from many points in the local-scale or site-scale areas to give histograms and tables. Several model variants were created to quantify the sensitivities to a number of key issues such as hydraulic properties, initial and boundary conditions.

Based on the SKB Task Description and experience gained in previous SDM studies, a number of options were tested in the modelling. A list is given below to illustrate some of the different options that were addressed or need to be addressed in future studies, for example SR-Can L1.2 or when more data are available.

Model domain (MD)

1. Full regional model domain based on catchment areas
2. Smaller regional model.

Initial conditions (IC)

1. Reference case mixing ratios: Glacial melt water conditions between ground surface and an elevation of –700 m, decreasing to 0% at –1,500 m. Between –700 m and –1,500 m elevation the Brine increases linearly from 0% to 100%. (corresponds to S1.2 results).
2. Glacial melt water conditions between ground surface and –300 m elevation, decreasing to 0% at –1,500 m. Between –300 m and –1,500 m elevation the Brine increases linearly from 0% to 100%.

Boundary conditions (BC)

1. Specified head: topographic including lake surfaces.
2. Specified head: watertable (see Section 5.5).
   a. Lowest possible watertable.
   b. Increased watertable (+ 30% of difference between topographic and lowest watertable).
   c. Increased watertable (+ 60% of difference between topographic and lowest watertable).
3. Flux condition: 165 mm/year, 82 mm/year or less.

HSD

1. Homogenous, 3 layer model with uniform thickness (1 m per layer) and properties.
2. Refined 3 layer representation using overburden model from SurfaceNet /Werner et al. 2005/.

HCD

1. All zones, step function (0 to –300 m, –300 m to –600 m, < –600 m) conditioned at boreholes.
2. All zones, power-law ($T = a(-z)^b$) conditioned at boreholes.
3. All zones, exponential function ($T = ae^{-bz}$) conditioned at boreholes.

HCD confidence levels

1. High confidence zones only.
2. High and medium confidence zones only.

HCD stochastic properties

1. Stochastic, realisation 1.
2. Stochastic, realisation 2.
3. Stochastic, realisation 3.

HCD kinematic porosities

1. Kinematic porosities as suggested in a data delivery: $0.46T^{0.5}/W$, where W is the thickness of zone.
2. Kinematic porosites scaled such that the max porosity is 10^{-2}, and the minimum is about 10^{-6}.
3. Kinematic porosity 10^{-3} for $W < 100$ m and 10^{-2} for $W \geq 100$ m.

HRD hydraulic conductivities

1. Homogenous, based on PSS data.
2. Homogenous, based on Hydro-DFN median values.

3. ECPM based on Hydro-DFN base case, semi-correlated, realisation 1.
4. ECPM based on Hydro-DFN base case, semi-correlated, realisation 2.
5. ECPM based Hydro-DFN base case, semi-correlated, realisation 3.
6. ECPM based on Hydro-DFN base case, correlated, realisation 1.
7. ECPM based on Hydro-DFN base case, uncorrelated, realisation 1.
8. ECPM based on Hydro-DFN variant, semi-correlated, with anisotropy in T between fracture sets.
9. ECPM based on Hydro-DFN variant, semi-correlated, with lower transmissivity below –600 m elevation.
10. Exponential properties ($K = ae^{-bz}$).

For variants 3–8, an additional variant considered was the elevation used for the step change in Hydro-DFN parameters. In the development of the Hydro-DFN, an elevation of –300 m was used. However, there is some uncertainty over the appropriate depth for this transition (see Subsection 5.9.3) and so for the regional modelling, some cases were performed using the same Hydro-DFN parameters but with the step change at –200 m.

HRD transport properties

Diffusion coefficient

1. Reference case (Byegård): 1.5×10^{-13} m^2/s.
2. Alternative 1 (ChemNet): 3.1×10^{-13} m^2/s.
3. Alternative 2 for sensitivity study: 5.0×10^{-13} m^2/s.

Flow-wetted surface

1. Reference case: $a_r = 1$ below –200 m; $a_r = 2.0$ (HRD(A2)) or 1.5 (elsewhere) above –200 m.
2. $a_r = 1$ below –300 m; $a_r = 2.0$ (HRD(A2)) or 1.5 (elsewhere) above –300 m.
3. Calculated from PFL-f data (see Table 5-15).

Matrix diffusion length

1. Reference case: For elevations below –200 m, $L_D = 1.0$ m. For elevations above –200 m, $L_D = 0.5$ m for HRD(A2), $L_D = 1.0$ m for HRD(D,E,M), and $L_D = 0.7$ m elsewhere.
2. Matrix diffusion length taken as $1/a_r$: $L_D = 1.0$ m below –300 m; $L_D = 0.5$ m for HRD(A2) or 0.7 m (elsewhere) above –300 m.
3. Dispersion lengths taken as minimal for grid size: $a_l = 40$ m, $a_t = 5$ m.

Diffusion accessible porosity

1. Reference case (Byegård upper limit) 5.9×10^{-3}.
2. Alternative (Byegård mean) 3.6×10^{-3}.

Kinematic porosity

1. Reference case: $n_{e,b}$ from upscaled regional-scale DFN, semi-correlated T model. The 10th percentile values for the 20 m block scale kinematic porosity obtained from the appropriate Hydro-DFN are used as minima of $n_{e,b}$.
2. 10^{-4} above –300 m, 10^{-5} below –300 m.
3. 10^{-4} above –200 m, 10^{-5} below –200 m.

Based on the list above, a multitude of cases have been performed and analysed. In general, the smaller regional model has been used in the screening process to search for promising combinations of the listed modelling options. The most promising cases are then propagated to a larger model domain to test whether the results are insensitive to the domain size in terms of chemical profiles and general behaviour of particle pathlines and exit locations. However, some minor differences in the pathlines may be expected due to boundary effects, e.g. the odd particle that is transported close to the inner model boundary. As an illustration of the multitude of cases performed, a selection is given in Table 7-1 below. The reference case is highlighted in blue. For each of the other cases, only those properties that differ significantly from the reference case properties are given.

Table 7-1. A selection of cases with main properties, model region and purpose. The reference case is highlighted in blue.

Case	Properties	Region	Purpose/Comments
L12_HCD1P3_HRD1_HSD1_ BC1_MD1_IC1	BC: Topographic head boundary condition; HRD: Homogenous, step model A for each subarea.	Large	Homogeneous HRD model used as starting point.
L12_HCD1P3_HRD1_HSD1_ BC1_MD2_IC1	BC: Topographic head boundary condition; HRD: Homogenous, step model A for each subarea.	Small	Homogeneous HRD model used as starting point.
L12_HCD1P3C2_HRD1_ HSD1_BC1_MD2_IC1	BC: Topographic head boundary condition; HRD: Homogenous, step model A for each subarea; HCD: Low confidence zones removed.	Small	Influence of deformation zones.
L12_HCD1P3S1_HRD1_ HSD1_BC1_MD2_IC1	BC: Topographic head boundary condition; HRD: Homogenous, step model A for each subarea; HCD: Stochastic properties, realisation 1.	Small	Influence of stochastic properties for deformation zones.
L12_HCD1P3_HRD1_HSD2_ BC1_MD2_IC1	BC: Topographic head boundary condition; HRD: Homogenous, step model A for each subarea; HSD: Overburden model.	Small	Influence of overburden model.
L12_HCD1P3_HRD1_HSD2_ BC4_MD2_IC1	BC: Flux; HSD: Overburden model.	Small	Test overburden model with flux boundary condition.
L12_HCD1P3_HRD1F1_ HSD1_BC1_MD2_IC1	BC: Topographic head boundary condition; HRD: Homogenous, step model A for each subarea; a_r from PFL-f data.	Small	Influence of flow-wetted-surface.
L12_HCD1P3_HRD1MP1_ HSD1_BC1_MD2_IC1	BC: Topographic head boundary condition; HRD: Homogenous, step model A for each subarea; lower diffusion accessible porosity.	Small	Influence of diffusion accessible porosity.

Case	Properties	Region	Purpose/Comments
L12_HCD1P3_HRD1D2_ HSD1_BC1_MD2_IC1	BC: Topographic head boundary condition; HRD: Homogenous, step model A for each subarea; Alternative 1 (higher) diffusion coefficient.	Small	Influence of matrix diffusion.
L12_HCD1P3_HRD1_HSD1_ BC2_MD2_IC1	BC: Watertable +60% boundary condition; HRD: Homogenous, step model A for each subarea.	Small	Influence of boundary condition.
L12_HCD3P3_HRD7_HSD1_ BC1_MD2_IC1	HRD: Exponential depth dependency; HCD: Exponential depth dependency, porosity depdendent on zone thickness only.	Small	Influence of depth trend.
L12_HCD3P3C2_HRD7_ HSD1_BC1_MD2_IC1	HRD: Exponential depth dependency; HCD: Exponential depth dependency; porosity depdendent on zone thickness only; low confidence HCDs removed.	Small	Influence of deformation zones.
L12_HCD3P3_HRD7_HSD2_ BC1_MD2_IC1	HRD: Exponential depth dependency; HCD: Exponential depth dependency; HSD: Overburden model.	Small	Influence of overburden model together with the exponential depth dependency.
L12_HCD1P3_HRD3a_HSD1_ BC1_MD2_IC1	HRD: K and $n_{e,b}$ from upscaled DFN (semi-correlated T model, isotropic case) realisation 1, step change at z = –300 m.	Small	Influence of isotropy in T between fracture sets in underlying Hydro-DFN models.
L12_HCD1P3_HRD3a_ddKha-lf_ani_HSD1_BC3_MD2_IC1		Small	Influence of model domain.
L12_HCD1P3_HRD3a_ddKha-lf_ani_HSD1_BC1_MD1_IC1	BC: Topographic head boundary condition.	Large	Influence of boundary conditions.
L12_HCD1P3_HRD3a_ddKha-lf_ani_HSD1_BC2_MD1_IC1	BC: Watertable +60% boundary condition.	Large	Influence of boundary conditions.
L12_HCD1P3_HRD3a_ani_ HSD1_BC3_MD1_IC1	HRD: No step change in K at z = –600 m.		In this case, there is too much flushing of brine at depth – a reduction in K below –600 m improves results.
L12_HCD1P3_HRD3a_ddKha-lf_ani_HSD1_BC3_MD1_IC1	BC: Watertable +30% boundary condition; HRD: K and $n_{e,b}$ from upscaled DFN (semi-correlated T model with lower T in Set_A and Set_B) realisation 1, step change in Hydro-DFN properties at z = –200 m; step change in K at –600 m; HCD: step change model for T; porosity dependent on zone thickness only; includes all zones. HSD: Homogenous.	Large	Reference case
L12_HCD1P3_HRD3b_ddKha-lf_ani_HSD1_BC3_MD1_IC1	Realisation 2 of upscaled DFN.		Sensitivity to different realisations.
L12_HCD1P3_HRD3c_ddKha-lf_ani_HSD1_BC3_MD1_IC1	Realisation 3 of upscaled DFN.		Sensitivity to different realisations.
L12_HCD1P3_HRD4_ddKhalf_ ani_HSD1_BC3_MD1_IC1	K and $n_{e,b}$ from upscaled DFN (correlated T model with lower T in Set_A and Set_B) realisation 1, step change in Hydro-DFN properties at z = –200 m.	Large	Test of different transmissivity model.
L12_HCD1P3_HRD5_ddKhalf_ ani_HSD1_BC3_MD1_IC1	K and $n_{e,b}$ from upscaled DFN (uncorrelated T model with lower T in Set_A and Set_B) realisation 1, step change in Hydro-DFN properties at z = –200 m.	Large	Test of different transmissivity model.

7.2 Summary of applied regional model cases

The key variants simulated by CONNECTFLOW modelling were:

- Model domain size.
- Initial and boundary conditions for flow and reference water transport.
- Hydro-DFN parameters.
- Hydraulic properties of HRD and HCD.
- Transport parameters for RMD and flow-path calculations.

Several model cases were constructed to quantify and illustrate the effects of each of these variants. During the initial stages of the modelling, a significant number of other cases were created on route to gaining an understanding of how individual model parameters affected the calibration, and ultimately what ranges of parameters gave a reasonable match to the field-data. Not all of these steps are reported here since they are of limited interest. Instead, the approach was to define a reference case that gives a reasonable match, and then consider variants about this to illustrate the sensitivity to the various issues. For Sections 7.5 to 7.9, the cases considered are grouped into these key variants to give structure to the discussions.

The reference case properties and conditions are summarised in Table 7-2. A selection of the cases considered is given in Table 7-1, with the reference case highlighted in blue. The names of the variants were chosen to denote the data version, HCD model, HRD model, HSD model, boundary conditions, model domain and initial conditions. Each of the key issues and associated variants are discussed in terms of the hydro-geochemical calibration results in the sub-sections following.

Table 7-2. Description of the reference case.

Property	Description	Uncertainties and parameter ranges
Domain	Extended regional model domain with 50 m element-size embedded grid in Laxemar, Simpevarp and Ävrö release areas, and 100 m element-size elsewhere.	
Initial condition	Initial condition is set to full glacial melt water conditions between ground surface and an elevation of –700 m; then linear gradient to no Glacial and full Brine at –1,500 m elavation. Between –700 m and –1,500 m elevation, the Brine increases linearly from 0 to 100%. Below –1,500 m elevation, a full Brine condition is applied.	Brine at shallower depths in Simpevarp subarea?
Top surface flow boundary condition	Top-surface head equals simulated watertable +30% of the difference between the simulated watertable and the topographic surface (see Figure 5-3).	Watertable level or flux boundary condition.
Top surface waters	Surface groundwaters are: Glacial and Littorina during early Baltic Ice Lake, Yoldia Sea and Ancylus Lake periods; Meteoric water and Littorina during the Littorina Sea and current Baltic Sea phases. The provided sea-water salinity history is used to determine relative fractions of Littorina and Meteoric waters at the top surface of the model offshore.	
Density and viscosity	Density and viscosity a function of salinity (transient), temperature (fixed), and total pressure (transient).	
Tranmissivity model	Hydraulic properties obtained from an upscaled regional-scale DFN that is based on the semi-correlated cases of the Hydro-DFN models.	Alternative T models are correlated or uncorrelated.

Property	Description	Uncertainties and parameter ranges
Anisotropy	Anisotropy has been introduced by decreasing the transmissivity of fracture sets Set_A and Set_B by a factor of 10.	Anisotropy has not been fully investigated. Other possibilities include increasing transmissivity of Set_C.
HCD confidence	HCD included all zones.	Alternative is exclusion of low confidence zones.
Depth dependency	HRD: The underlying DFN has a step change in properties according to the Hydro-DFN, although a transition elevation of –200 m is used instead of –300 m. For all HRD except HRD(A2), the upscaled conductivity is then reduced by half an order of magnitude below an elevation of –600 m. HCD: Implemented as a step function in elevation (0 to –300 m, –300 m to –600 m, < –600 m), conditioned at boreholes against measured transmissivities.	Borehole data suggests that levels of the two step changes could be within the ranges –200 m to –350 m and –500 m to –650 m. Alternative depth trend functions for HRD and HCD are exponential and power-law.
HSD	Homogeneous 3 layer HSD of uniform 1 m thickness per layer.	Overburden model from /Werner et al. 2005/ with uncertainty in hydraulic conductivities.
Flow-wetted surface and Matrix diffusion length	Flow-wetted-surface (FWS) per unit volume for RMD above –200 m elevation: a_r = 2.0 m^2/m^3.for HRD(A2), a_r = 1.0 m^2/m^3.for HRD(D,E,M), a_r = 1.5 m^2/m^3 elsewhere. For all rock domains below –200 m elevation, a_r = 1.0 m^2/m^3. Matrix diffusion length into matrix blocks above –200 m elevation, L_D = 0.5 m for HRD(A2), L_D = 1.0 m for HRD(D,E,M), L_D = 0.7 m elsewhere, and L_D = 1.0 m for all rock domains below –200 m elevation.	Other possibilities are FWS based on PFL-f or $P32_c$ analysis.
Kinematic porosity	HRD kinematic porosity is taken from the upscaled regional-scale DFN that is based on the semi-correlated cases of the Hydro-DFN models. However, the 10th percentile values for the 20 m block scale kinematic porosity obtained from the appropriate Hydro-DFN are used as minima of $n_{e,b}$. HCD porosity 10^{-3} for zone thickness W < 100 m and 10^{-2} for W ≥ 100 m	An alternative for HCD is a depth-dependent porosity based on the transmissivity and thickness of the zones.
Diffusion accessible porosity	Diffusion accessible porosity from Byegård upper limit n_m = 5.9 10^{-3}.	1.3×10^{-3}–5.9 10^{-3} (Byegård)
Diffusion coefficient	Intrinsic diffusion coefficient into matrix D_e = 1.5 10^{-13} m^2/s.	1.5 10^{-13} (Byegård) –3.1 10^{-13} (ChemNet)
Dispersion lengths	a_l = 40 m, a_t = 5 m	

7.3 Comparison of hydraulic properties for Hydro-DFN based regional-scale models

Firstly, it is useful to provide an illustration of how hydraulic conductivity is represented in the ECPM models based on the Hydro-DFN. By plotting the profile of effective hydraulic conductivity (geometric mean of three axial components) along a line section through the model corresponding to the borehole trajectory, a comparison can be made with the measured hydraulic conductivity. It should be noted that this should be treated as no more than a qualitative comparison since the borehole measurements are an interpretation of radial flow through the immediate volume around the borehole and will depend heavily on the particular fractures, their properties and connectivity that intersect the borehole. In contrast, the

modelled values are upscaled values for a 50 m grid block based on the equivalent properties averaged over the block volume. In addition, the HRD component is an unconditioned stochastic realisation, although the HCD component has been conditioned (see Section 5.8).

Figure 7-2 and Figure 7-3 show two realisations of the model for six of the boreholes in the local-scale area. Note: that the intervals in the model are only 50 m compared with 100 m for the PSS data and hence one might expect more heterogeneity in the model than in the data, which seems to hold in some areas. Generally, one can see that values are of the right order of magnitude, have a consistent level of heterogeneity, and depth trend. The plots also show that there is considerable variability between the realisations, up to 3 orders of magnitude in places, due to heterogeneity in the HRD. Therefore, one should consider more than one realisation in the palaeo-hydrogeology calibration to quantify the sensitivity to the individual realisation. Here, three realisations were performed of the reference case.

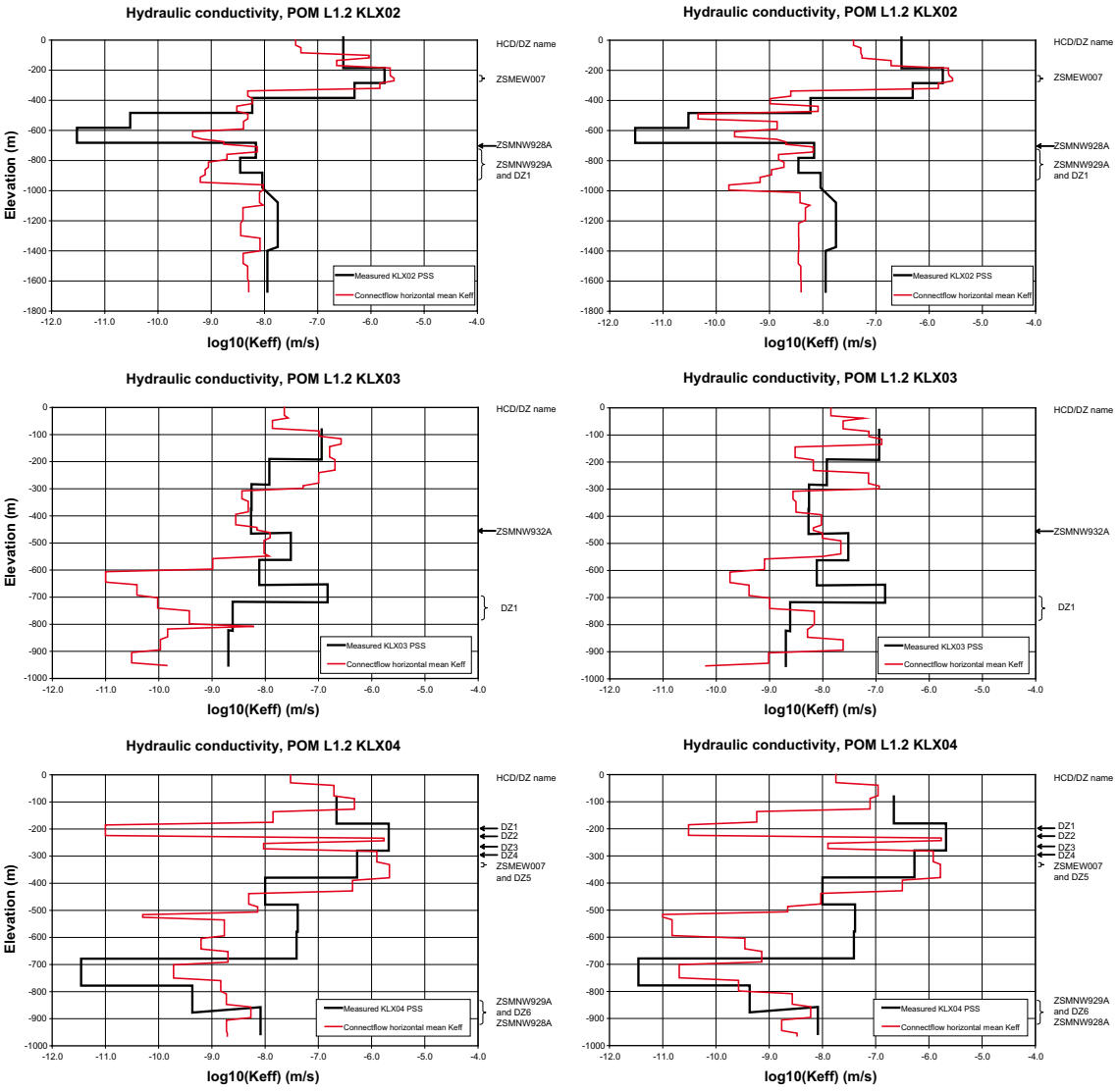

Figure 7-2. *Comparison of hydraulic properties along KLX02 and KLX03, KLX04 for the large regional model using a semi-correlated transmissivity model. Realisation 1 (left), and Realisation 2 (right). The hydraulic conductivity profile in the model is shown by red lines and compared with measured 100 m interval PSS data in black.*

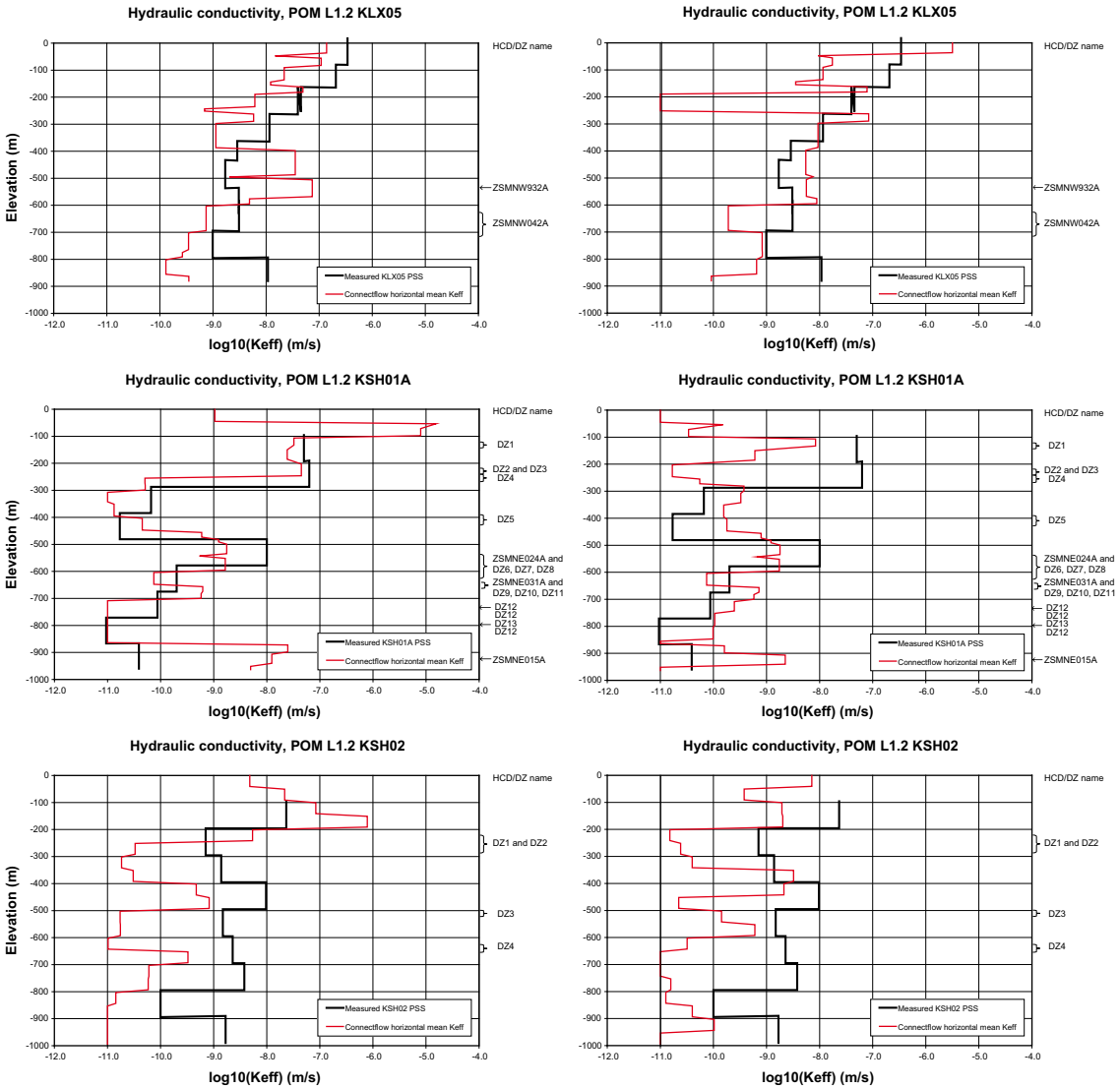

Figure 7-3. *Comparison of hydraulic properties along KLX05, KSH01A and KSH02 for the large regional model using a semi-correlated transmissivity model. Realisation 1 (left), and Realisation 2 (right). The hydraulic conductivity profile in the model is shown by red lines and compared with measured 100 m interval PSS data in black.*

7.4 Palaeo-hydrogeology calibration of the reference case

Using the extended regional model domain for transient coupled groundwater flow and reference water transport, a calibration process resulted in the reference case properties listed in Section 7.2.

Initially, localised changes to the hydraulic properties of individual RVS DZs observed in or near the boreholes were made to fit PSS data. The model was then fine-tuned to give a better match to the reference water mixing fractions and concentration profiles. The main changes required were to change the watertable model to reduce the driving heads, and use the Hydro-DFN variant case with anisotropy between the fracture sets. Although it is likely that the models could be fine-tuned further considering local conditions and parameters rather than just global ones, it is outside the time-frame of the current study. Even if a perfect match is not obtained, it is still possible to increase the level of knowledge on model response and influence of modelling approaches, by the model variations performed.

Further, it is important to note that the calibration does not lead to a unique model that is consistent with observations. Rather, it identifies combinations of hydraulic and transport characteristic features and values consistent with the site data and conversely, identifies combinations of settings unlikely to occur in reality. Presently, the reference case is denoted L12_HCD1P3_ddKhalf_ani_HRD3a_HSD1_BC3_MD1_IC1.

7.4.1 Reference waters

Figure 7-4 to Figure 7-11 show the calibration of the reference case against the interpreted 4 reference water profiles for the calibration boreholes. These calculations were performed with RMD and so the mixing fraction in both the fracture system and diffusion accessible porewater (matrix) are shown. It should be noted that the embedded grid had higher resolution of 50 m for the Laxemar, Simpevarp and Ävrö boreholes, but is coarser, 100 m, around Äspö.

For the Laxemar boreholes, Figure 7-4 shows that in KLX01 the model predicts the mixing zone to be too deep, suggesting that the model has either too much hydraulic conductivity at depth or too little at the surface, which would have the effect of focussing flow much higher. The match for KLX02 in Figure 7-5 is more interesting since the borehole has much more data and goes deeper. The transition from Brine to Meteoric water occurs at approximately the correct depth and a similarly steep slope. The spikes in Littorina and Glacial waters also occur at approximately the correct depth.

Results for the Simpevarp boreholes KSH01A, KSH02 and KSH03A are shown in Figure 7-6 to Figure 7-8. For KSH01A, the mixing zone is much higher, presumably because it is near the coast. The match for this borehole is generally good. The data point at about –550 m suggests more Glacial water than Littorina, which is consistent with the model prediction. The model suggests the mixing fractions vary rapidly with depth due to the presence of ZSMNE024A and other deformation zones. Hence, results are quite sensitivite at this depth and also because several waters are present, then the M3 analysis is likely to be more uncertain here. For KSH02, the model prediction for the transition from Meteoric to Glacial water is reasonable, as are the levels of Brine, Glacial and Littorina waters at depth, as shown in Figure 7-7. KSH03A only has data points near the surface, but nevertheless is a good match, illustrated in Figure 7-8.

For Ävrö, KAV01 has data points near the surface and at about –550 m. As shown in Figure 7-9, the model predicts the mixing zone at about the right depth, but suggests slightly more Littorina than Glacial water, though again it is within the M3 uncertainty magnitude. This location of the transition zone may be associated with the DZs ZSMNE012A, DZ1, DZ2 and DZ3, which the borehole intersects between about –400 m and –580 m elevation as indicated in Figure 7-9. If these DZs had too high a transmissivity, then model would have predicted too much flushing.

Figure 7-10 to Figure 7-13 show the calibration at the Äspö boreholes. For KAS02, the model predicts the mixing zone at about the right depth, but at 200–500 m depth there is too little Glacial and too much Littorina compared to the M3 data. Similar results are seen in KAS03 with spike of Littorina water not seen in the M3 analysis. The M3 profiles in these boreholes suggest a vertically homogenised mixture over large depth ranges. It is hard to envisage how this could occur under natural conditions since it would require the Littorina pulse to mix with the Glacial water uniformly as it sinks, for example. There is reasonable agreement between M3 data and the model for KAS04 and KAS06. In KAS04 the model predicts more Littorina than Glacial, as with KAS02.

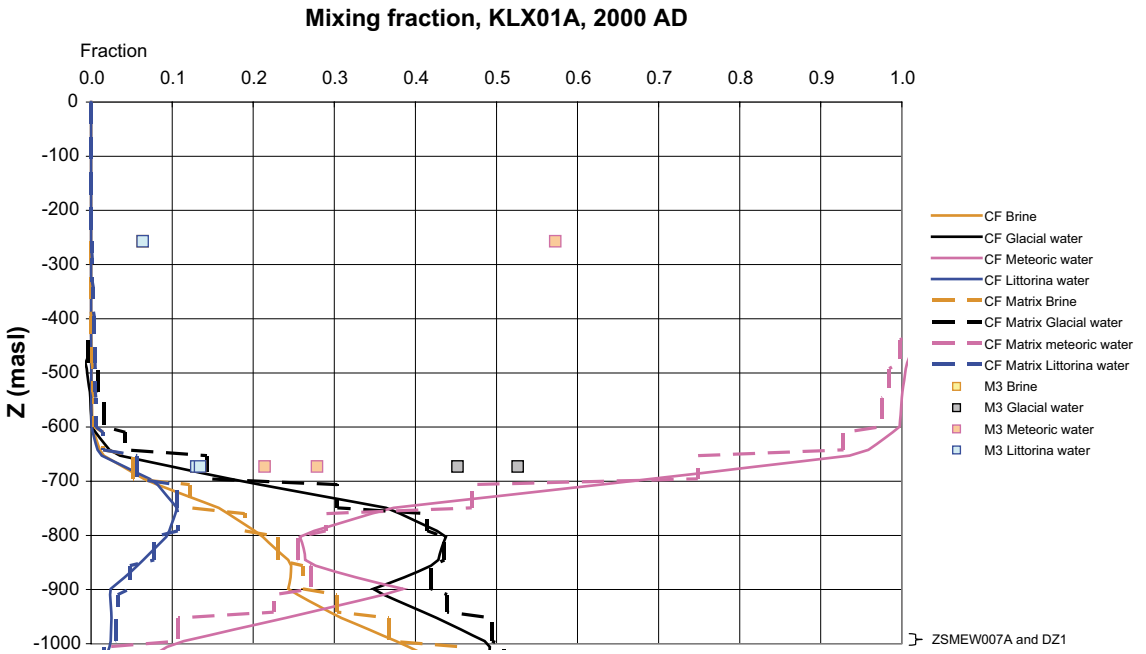

Figure 7-4. *Comparison of 4 reference water fractions in KLX01 for the reference case. The mixing fractions in the fracture system are shown by solid lines, in the matrix it is dashed, and the data by points. Only representative data is shown. Dark filled shapes are considered the best data.*

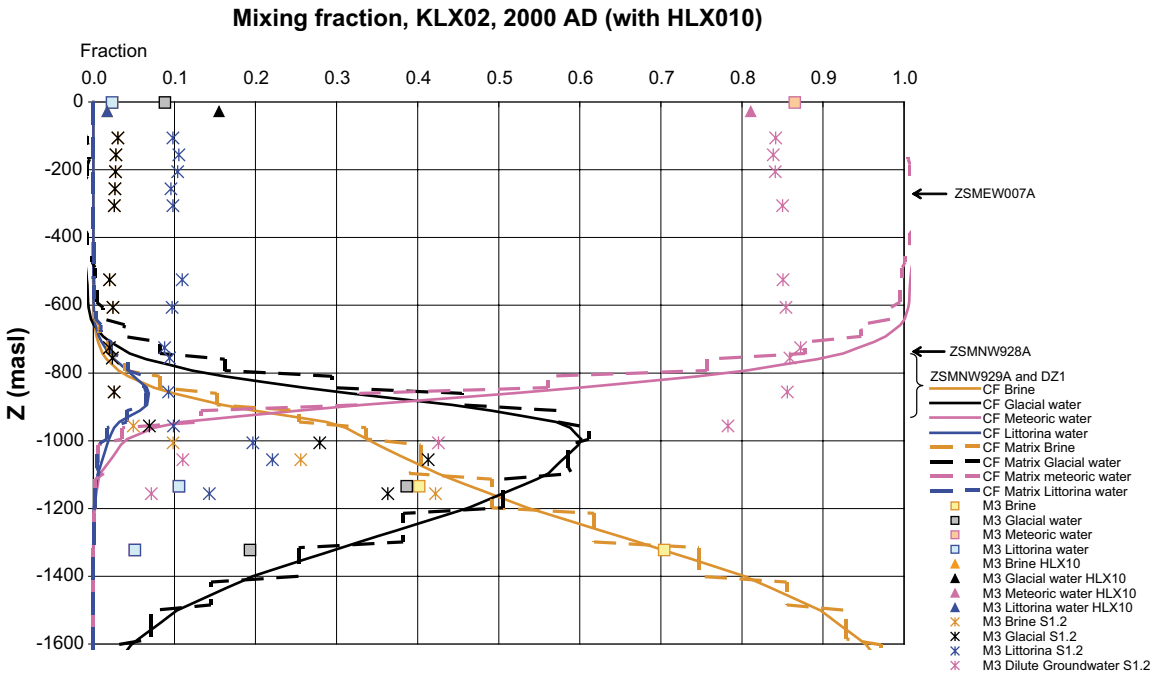

Figure 7-5. *Comparison of 4 reference water fractions in KLX02 for the reference case. The mixing fractions in the fracture system are shown by solid lines, in the matrix it is dashed, and the data by points. The representative data is shown as filled shapes and some S1.2 data are included as an asterix.*

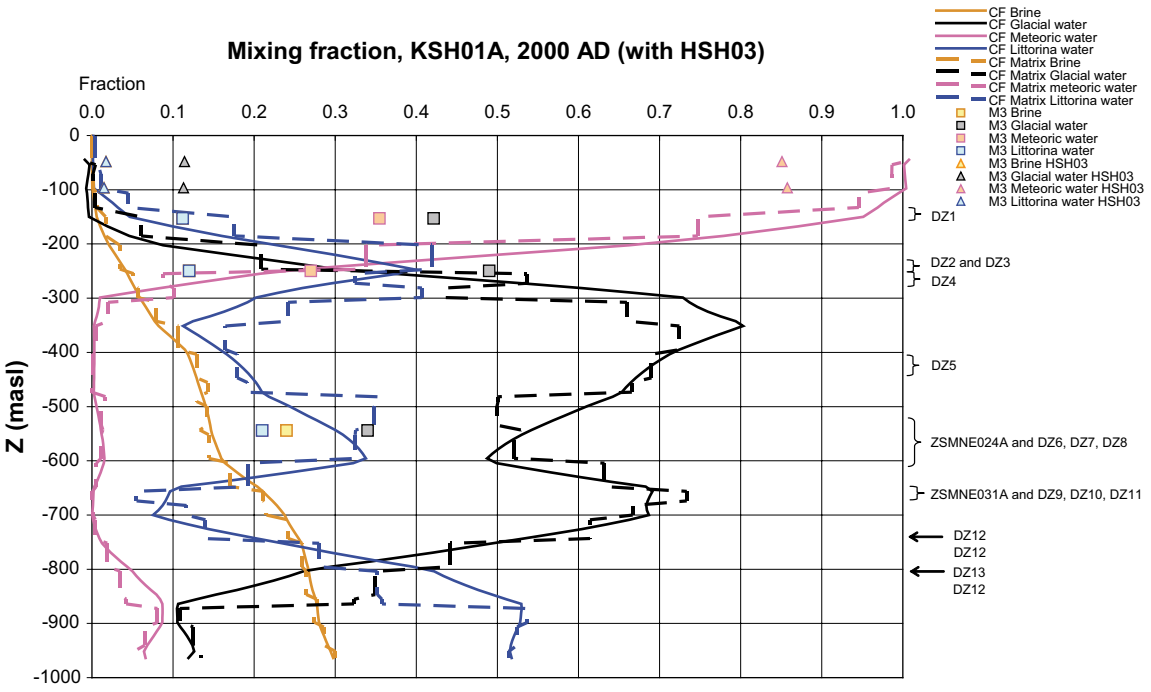

Figure 7-6. *Comparison of 4 reference water fractions in KSH01A for the reference case. The mixing fractions in the fracture system are shown by solid lines, in the matrix it is dashed, and the data by points. Only representative data is shown. Dark filled shapes are considered the best data.*

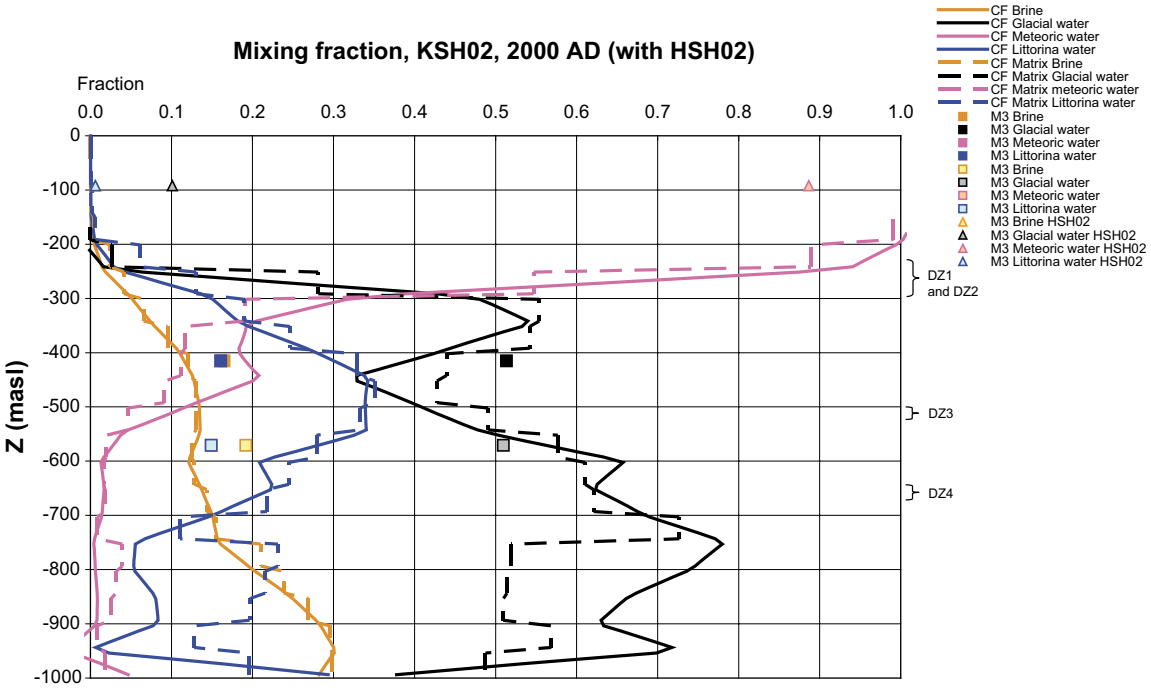

Figure 7-7. *Comparison of 4 reference water fractions in KSH02 for the reference case. The mixing fractions in the fracture system are shown by solid lines, in the matrix it is dashed, and the data by points. Only representative data is shown. Dark filled shapes are considered the best data.*

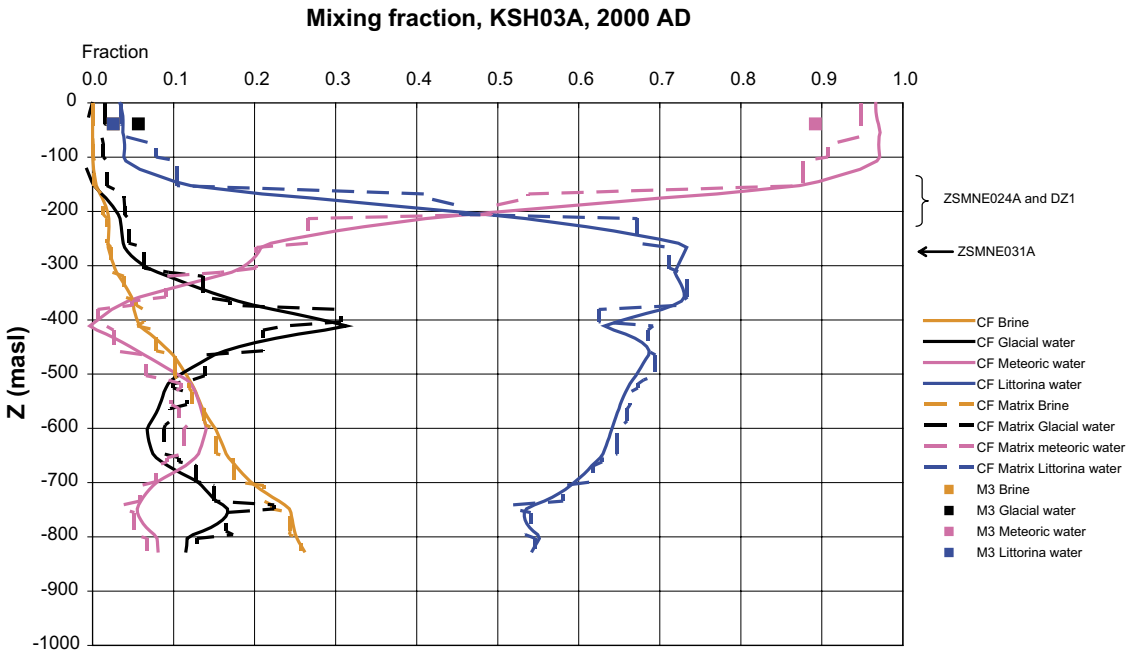

Figure 7-8. *Comparison of 4 reference water fractions in KSH03A for the reference case. The mixing fractions in the fracture system are shown by solid lines, in the matrix it is dashed, and the data by points. Only representative data is shown. Dark filled shapes are considered the best data.*

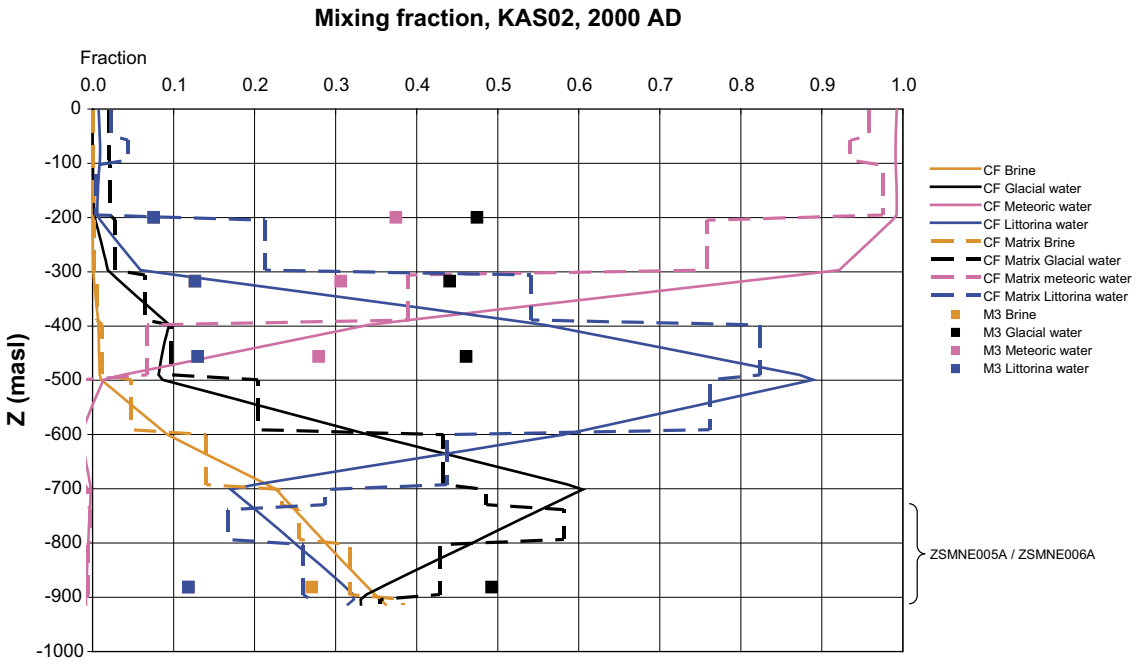

Figure 7-9. *Comparison of 4 reference water fractions in KAV01 for the reference case. The mixing fractions in the fracture system are shown by solid lines, in the matrix it is dashed, and the data by points. The representative data is shown as filled points and some S1.2 data are included as an asterix. Dark filled shapes are considered the best data.*

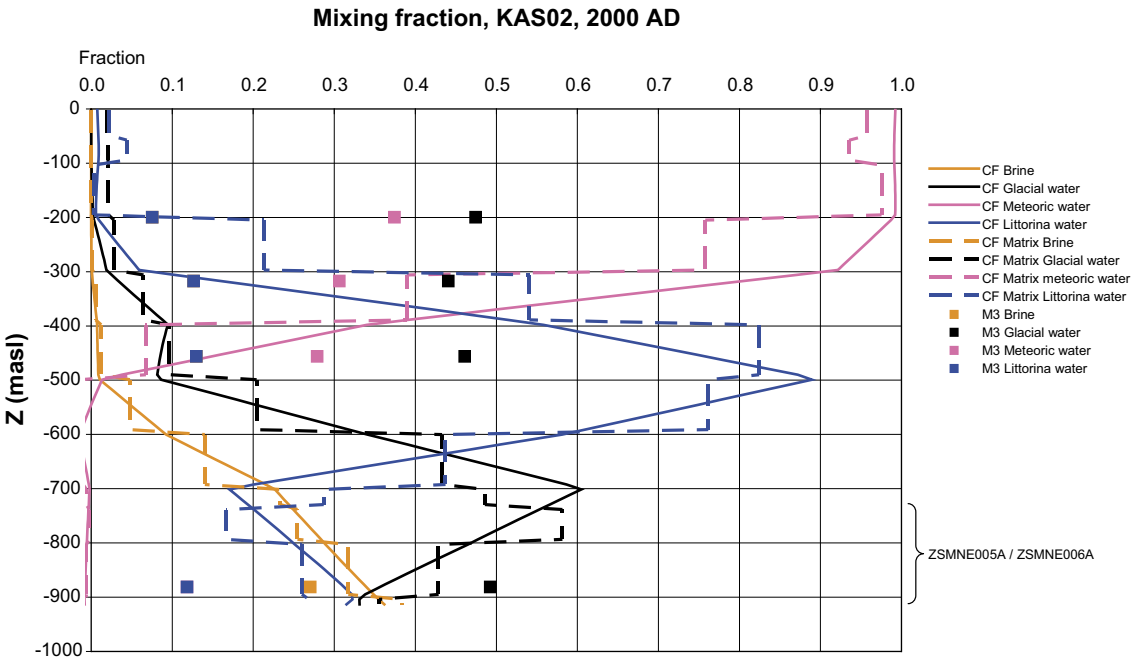

Figure 7-10. *Comparison of 4 reference water fractions in KAS02 for the reference case. The mixing fractions in the fracture system are shown by solid lines, in the matrix it is dashed, and the data by points. Only representative data is shown. Dark filled shapes are considered the best data.*

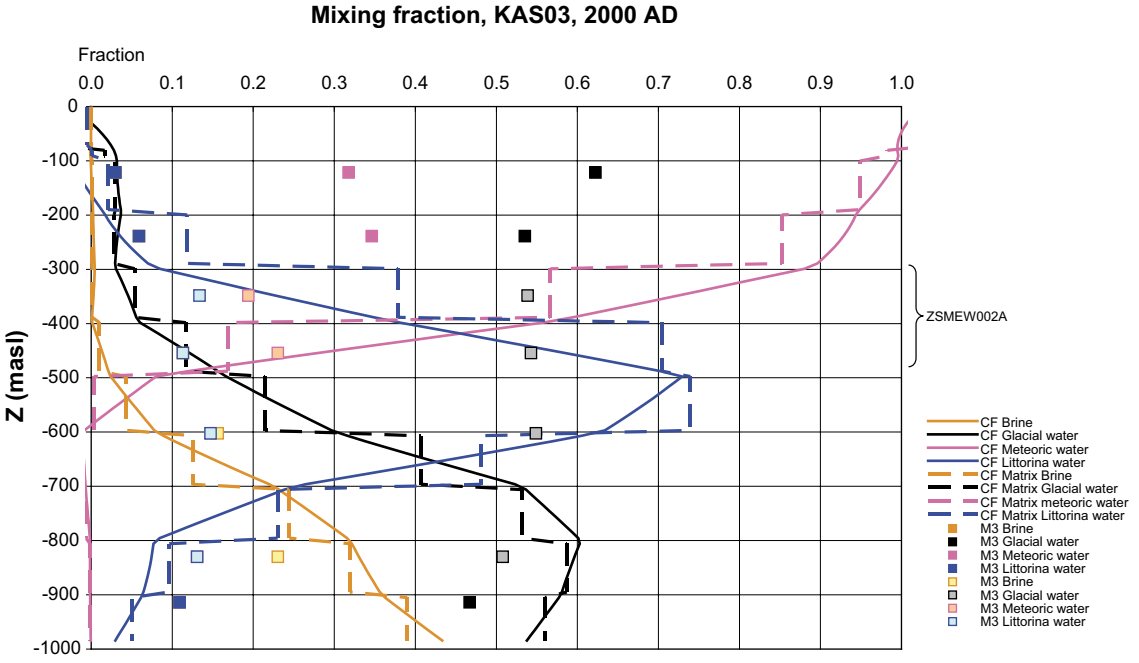

Figure 7-11. *Comparison of 4 reference water fractions in KAS03 for the reference case. The mixing fractions in the fracture system are shown by solid lines, in the matrix it is dashed, and the data by points. Only representative data is shown. Dark filled shapes are considered the best data.*

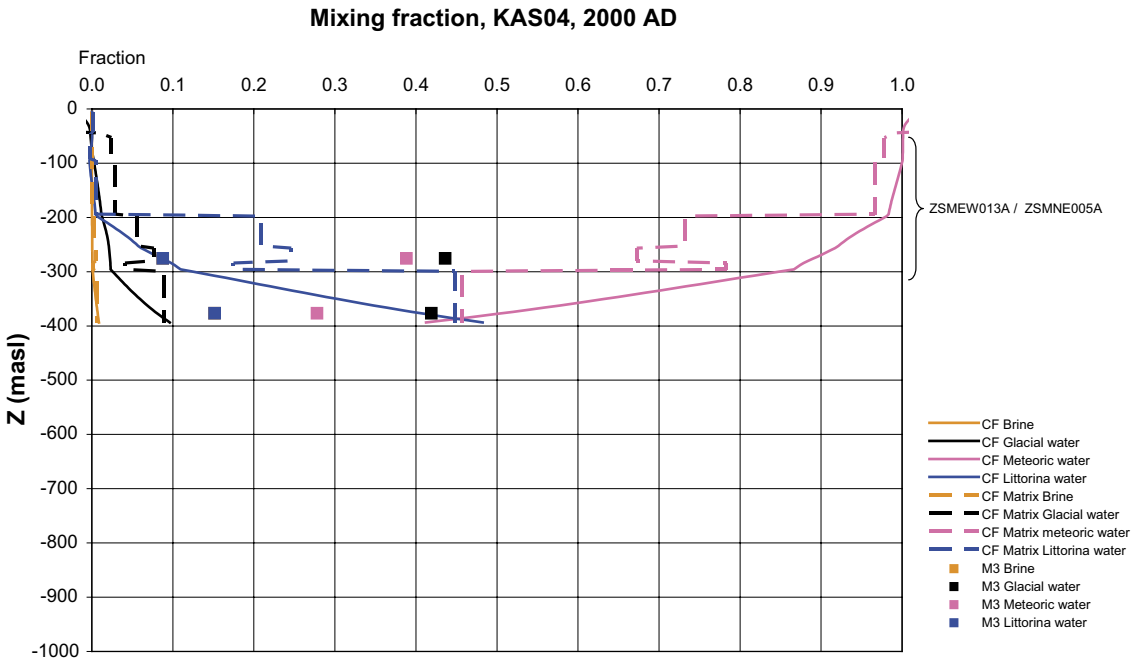

Figure 7-12. *Comparison of 4 reference water fractions in KAS04 for the reference case. The mixing fractions in the fracture system are shown by solid lines, in the matrix it is dashed, and the data by points. Only representative data is shown. Dark filled shapes are considered the best data.*

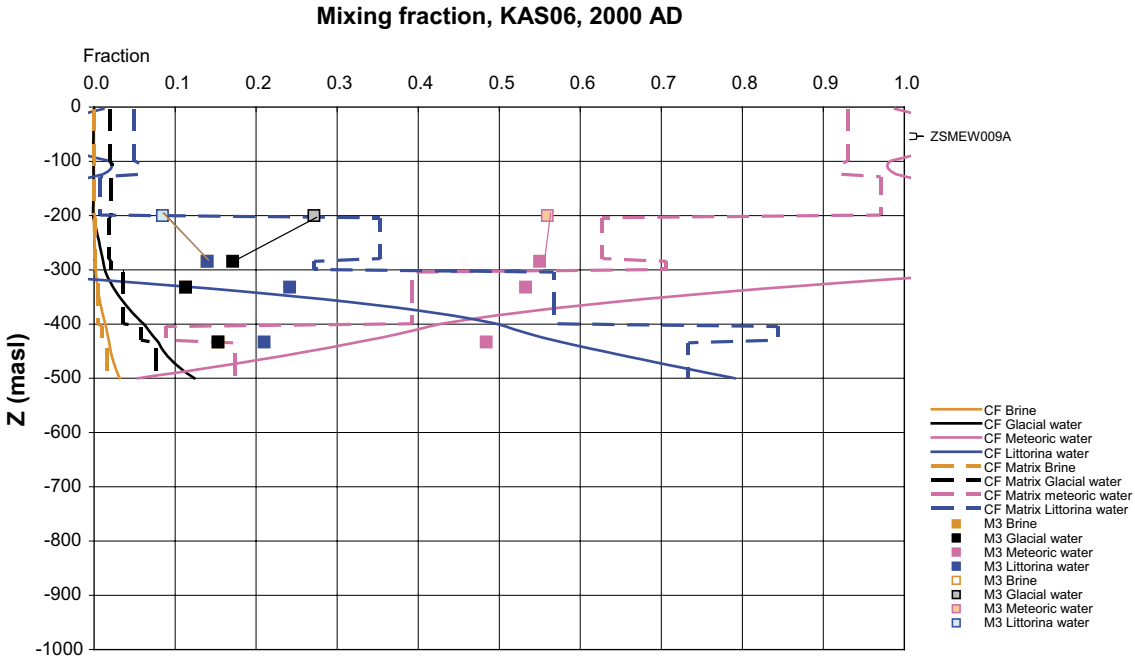

Figure 7-13. *Comparison of 4 reference water fractions in KAS06 for the reference case. The mixing fractions in the fracture system are shown by solid lines, in the matrix it is dashed, and the data by points. Only representative data is shown. Dark filled shapes are considered the best data.*

7.4.2 Salinity

Salinity closely follows the profile of Brine, although there is also a contribution from the Littorina reference water. Figure 7-14 shows the comparison for salinity between the reference case simulation and the data for boreholes KLX01, KLX02, KLX03 and KLX04. In Figure 7-15, the modelling results are compared to the measured values for KSH01A, KSH02 and KSH03A. The boreholes mentioned could be used to illustrate the differences observed in moving from coastal (KSH01A, KSH02 and KSH03A) to inland (KLX01), and further inland (KLX02, KLX03 and KLX04). The relative depths of salinity for the series of boreholes are generally good for the KLX and KSH boreholes, and they seem to have the right sort of slopes.

For Äspo, the modelling results are compared to the measured values in Figure 7-16. For KAS02 and KAS03, the model predicts a higher salinity than the measured data below an elevation of about –600 m. Both the measured data and the model results indicate a sharp increase in the proportion of Brine below this elevation (see Figure 7-10 and Figure 7-11). However, for KAS02, the model predicts a higher proportion of Littorina than the measured data, and for KAS03 the combined proportions of Littorina and Brine are higher in the model results than in the measured data. This results in a higher salinity predicted by the model for these boreholes.

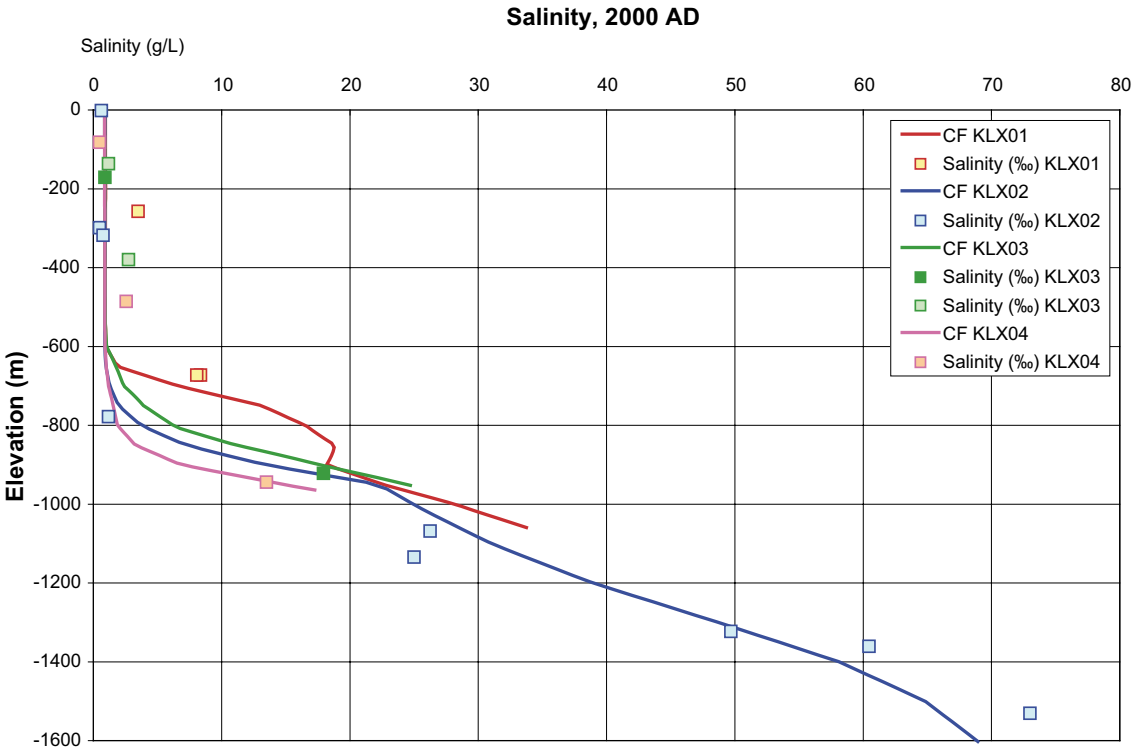

Figure 7-14. *Comparison of salinity in KLX01, KLX02, KLX03 and KLX04 for the reference case. The salinity in the fracture system is shown by solid lines, and the data by points. Only representative data is shown. Dark filled shapes are considered the best data.*

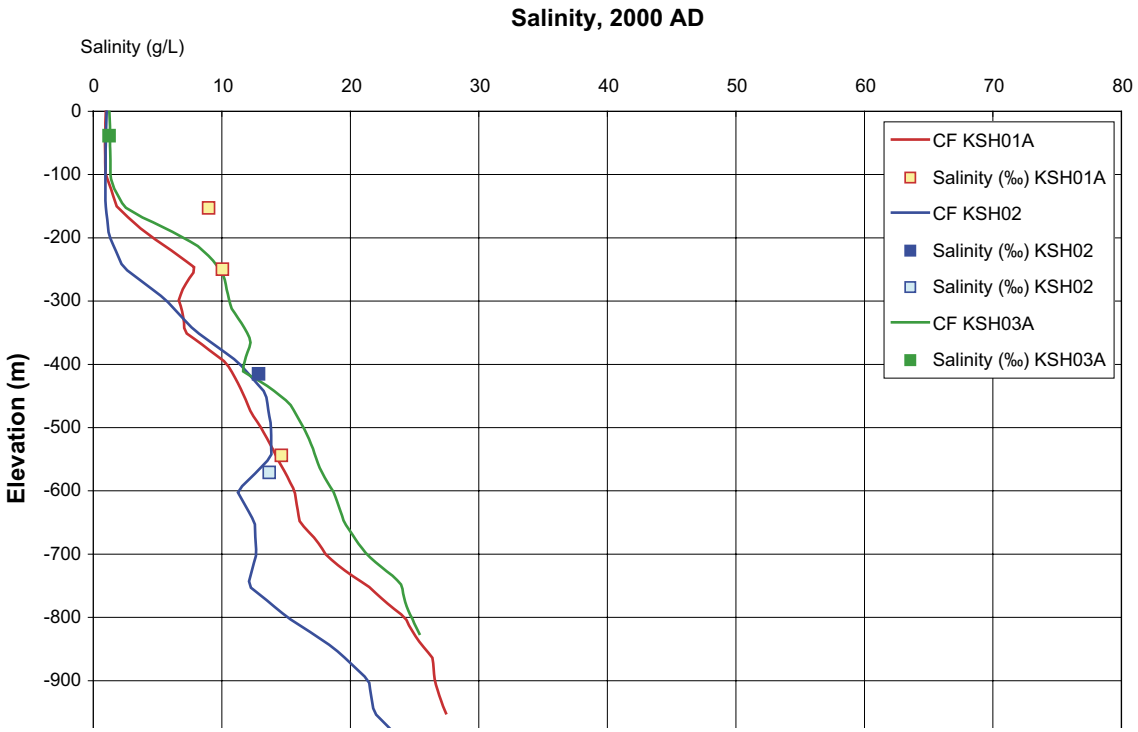

Figure 7-15. *Comparison of salinity in KSH01A, KSH02 and KSH03A for the reference case. The salinity in the fracture system is shown by solid lines, and the data by points. Only representative data is shown. Dark filled shapes are considered the best data.*

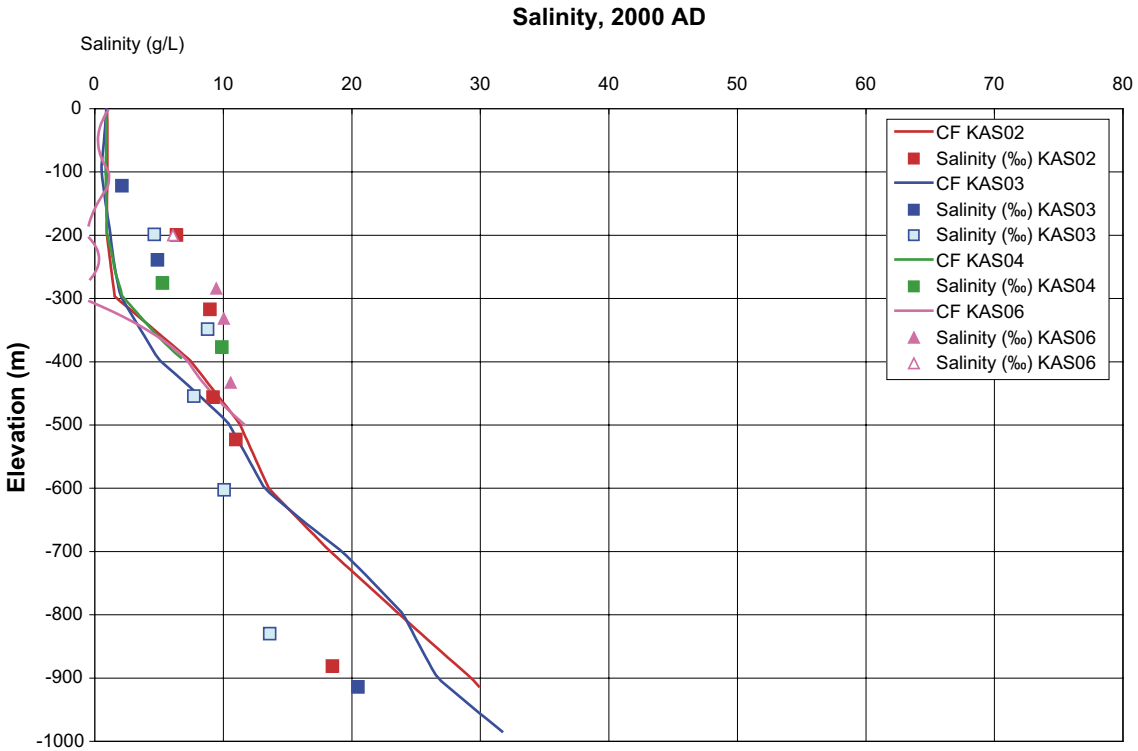

Figure 7-16. *Comparison of salinity in KAS02, KAS03, KAS04 and KAS06 for the reference case. The salinity in the fracture system is shown by solid lines, and the data by points. Only representative data is shown. Dark filled shapes are considered the best data.*

7.4.3 Environmental isotopes

As well as comparing the interpreted hydrogeochemistry from the M3 approach, a comparison was made with the environmental isotopes, using them as conservative tracers. The Oxygen-18 isotope ratios are shown for boreholes KLX01, KLX02, KLX03 and KLX04 in Figure 7-17; KSH01A, KSH02 and KSH03A are shown in Figure 7-18, KAV01 and KAV04A in Figure 7-19; and KAS02, KAS03, KAS04 and KAS06 in Figure 7-20. High negative values of $\delta^{18}O$ are associated with Glacial water. For example, the model at KLX02 predicts the right sort of shape of profile, but there is a little too much Glacial water at depth, whereas the model is not predicting enough Glacial in the upper part of KLX04 due to too much mixing in the model near this borehole. Pockets of Glacial water in KAS02 and KAS04 do not seem to be reproduced in the model. The model simulations agree best with the observed chemistry in KAS06. Still, in general, the shapes of the profiles down the boreholes seem to mirror that of the data.

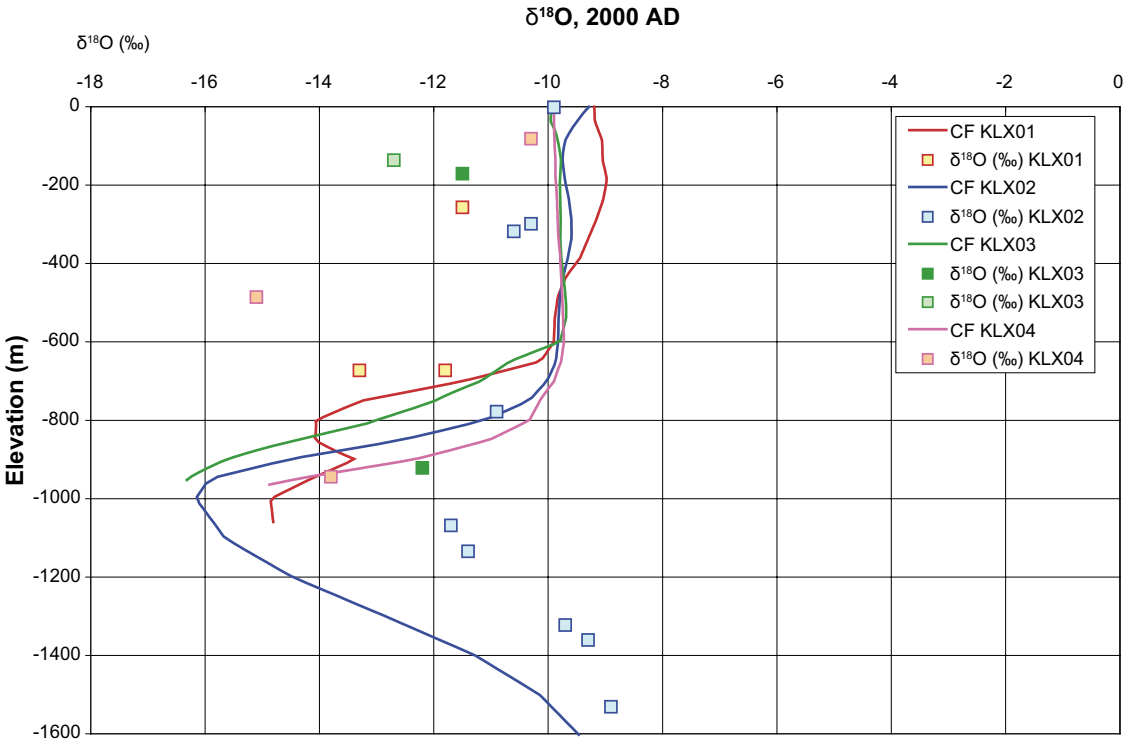

Figure 7-17. *Comparison of Oxygen isotope ratio $\delta^{18}O$ in KLX01, KLX02, KLX03 and KLX04 for the reference case. $\delta^{18}O$ in the simulated fracture system are shown by solid lines, and the data by points. Only representative data is shown. Dark filled shapes are considered the best data.*

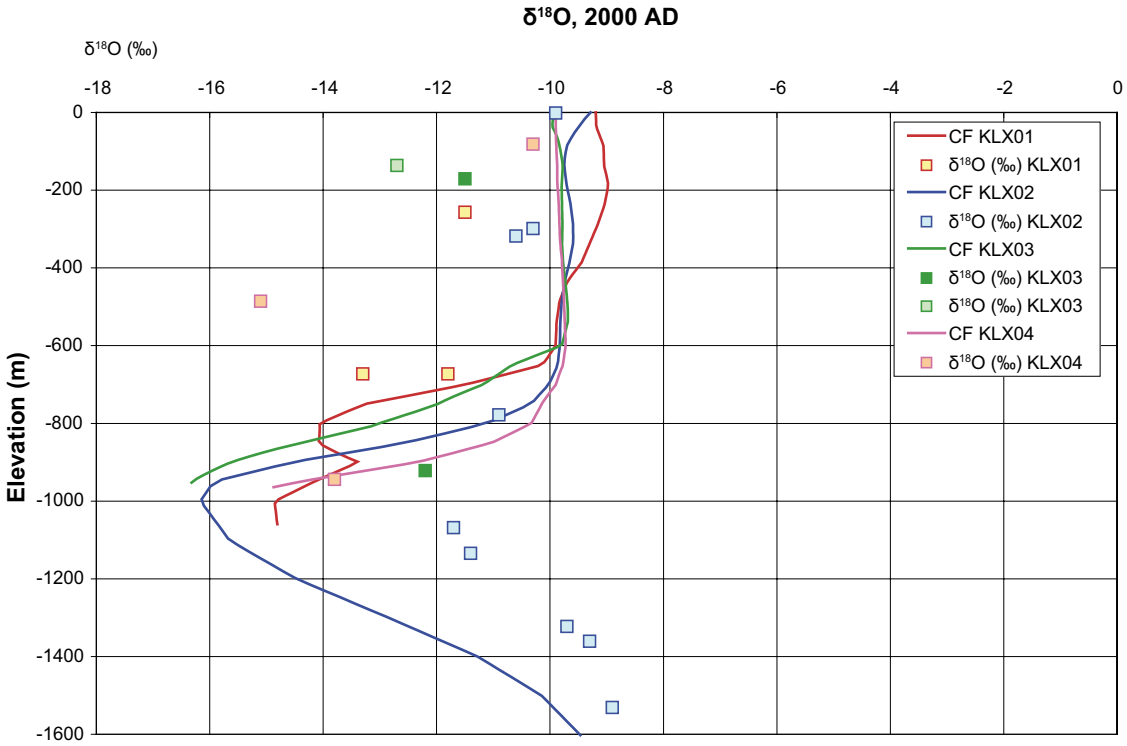

Figure 7-18. *Comparison of Oxygen isotope ratio $\delta^{18}O$ in KSH01A, KSH02 and KSH03A for the reference case. $\delta^{18}O$ in the simulated fracture system are shown by solid lines, and the data by points. Only representative data is shown. Dark filled shapes are considered the best data.*

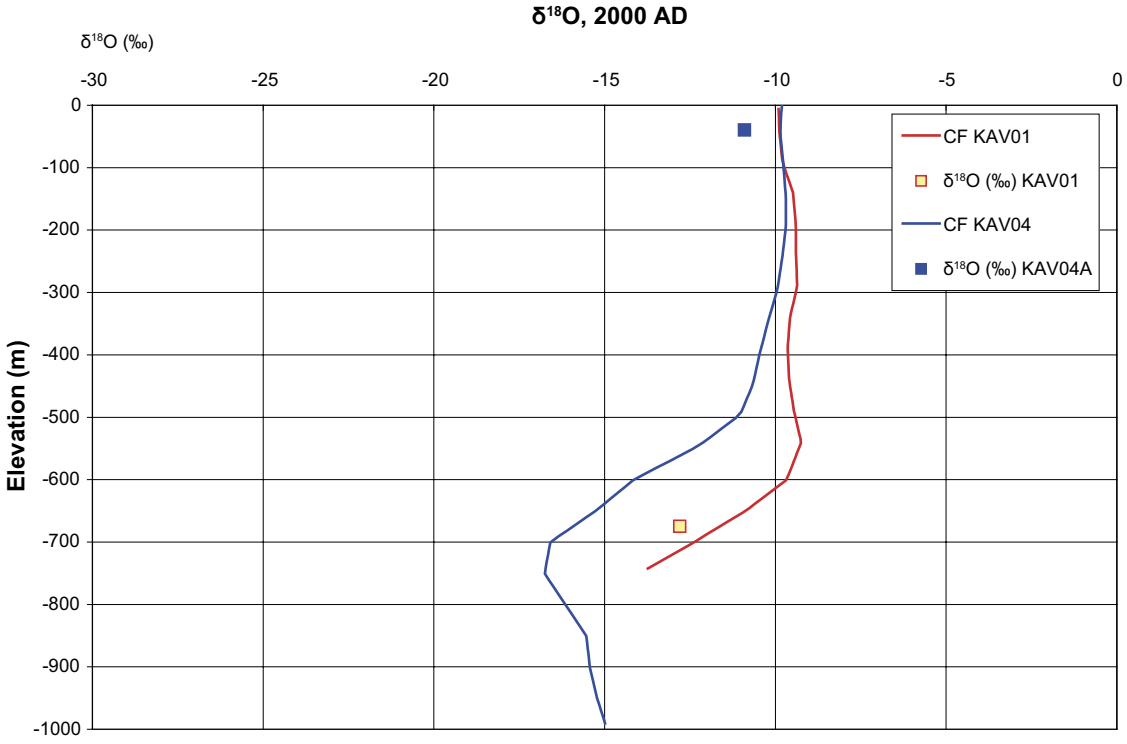

Figure 7-19. *Comparison of Oxygen isotope ratio $\delta^{18}O$ in KAV01 and KAV04A for the reference case. $\delta^{18}O$ in the simulated fracture system are shown by solid lines, and the data by points. Only representative data is shown. Dark filled shapes are considered the best data.*

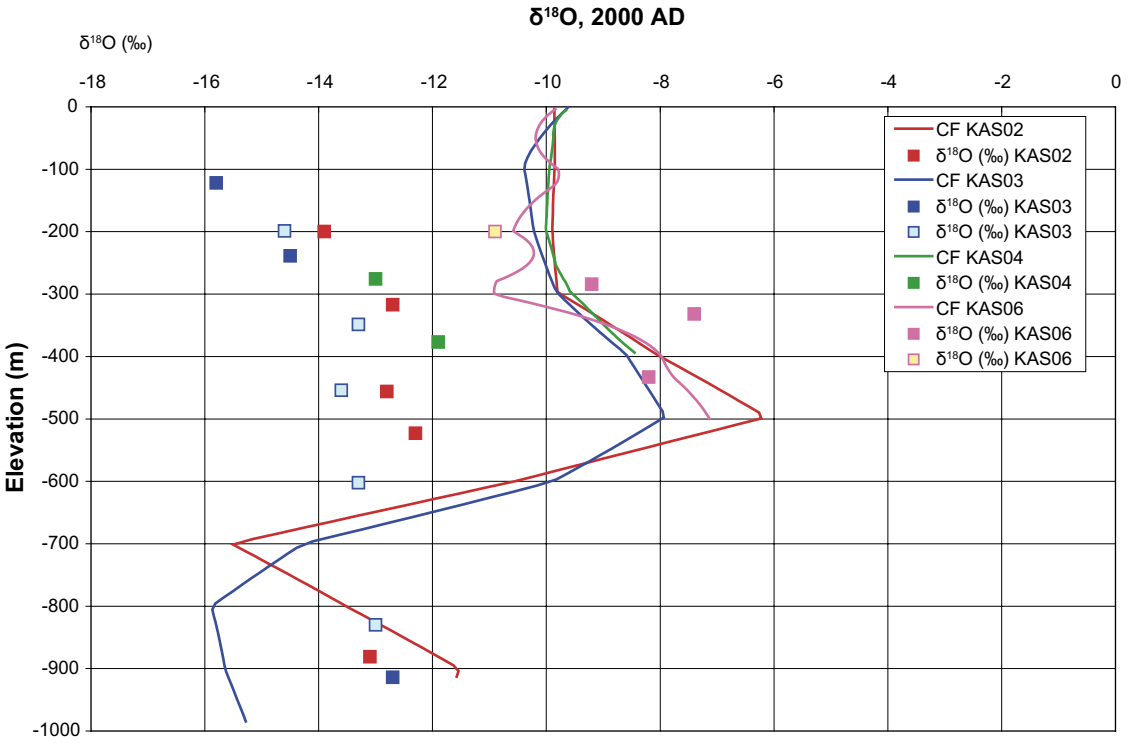

Figure 7-20. *Comparison of Oxygen isotope ratio $\delta^{18}O$ in KAS02, KAS03, KAS04 and KAS06 for the reference case. $\delta^{18}O$ in the simulated fracture system are shown by solid lines, and the data by points. Dark filled shapes are considered the best data.*

7.5 Sensitivity to the size of the regional model domain

The extended regional model domain was used for the reference case and several variant cases. Other variant cases were performed using the smaller regional model domain. A comparison was made between the results obtained from the reference case and those obtained from a variant case in which the smaller regional model domain was used but all other parameters were identical to the reference case. This comparison illustrated that the sensitivity of the predicted reference water mixing fractions to the model domain size is low and confirmed that the smaller regional model may be used for calibrating the model in terms of the reference water mixing fractions. This is useful because the smaller model demands less computational effort and so enables testing of more variants.

7.6 Sensitivity to initial and boundary conditions

7.6.1 Initial Brine condition

The variant initial condition specified brine at shallower depths, increasing linearly between –300 m elevation and –1,500 m elevation instead of between –700 m elevation and –1,500 m elevation as specified in the reference case. This improved the match for reference water mixing fractions for Simpevarp and Ävrö but gave a slightly worse match for Laxemar as it reduced the amount of Glacial water seen in the boreholes. However, within the ranges tested here, the initial condition had a low effect on the results.

7.6.2 Level of watertable

In the reference case, the head on the top surface of the model was specified according to the simulated minimum watertable +30% of the difference between the minimum watertable and the topographic height. To test the sensitivity to the watertable level, two variant cases with different watertable levels were considered: watertable at topographic height; minimum watertable +60% of the difference between the simulated watertable and the topographic height. The level of the watertable has a high effect on the results. A lower watertable results in reduced flow and flushing, and hence a better match to the reference water distribution. As an example, the salinity in the Laxemar boreholes for the case with the watertable at the topographic surface is shown in Figure 7-21 to illustrate how the salinity is significantly deeper in this case. A similarly large effect is seen in the Simpevarp and Äspö boreholes.

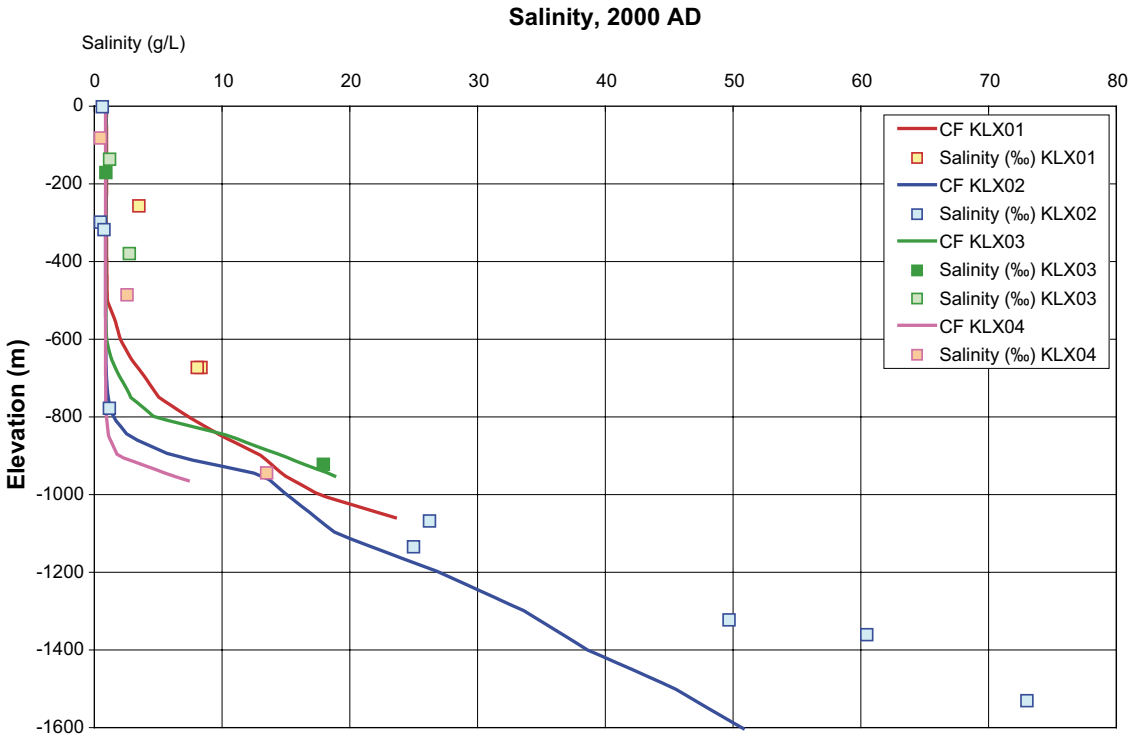

Figure 7-21. *Comparison of salinity in KLX01, KLX02, KLX03 and KLX04 for the case with a watertable at topographic height. The salinity in the fracture system is shown by solid lines, and the data by points. Only representative data is shown. Dark filled shapes are considered the best data.*

7.6.3 Flux boundary condition – specified potential recharge

A flux boundary condition was specified on the top surface of the model using the method described in Section 2.6. The sensitivity to the potential groundwater recharge was tested by running cases with 165 mm/year potential recharge and 82 mm/year potential recharge. At 165 mm/year the calculated head is close to ground surface making the results very similar to the case with head set to the topographic height. Reducing the potential recharge by half to 82 mm/year had a significant effect on the hydrogeochemistry profiles and improved the profiles in the calibration boreholes, but the results are still some way from a good match at Laxemar. However, it did show that the sensitivity to the potential recharge is high, and perhaps reducing the potential recharge to just a few tens of mm/year would give a good match and results similar to those for the approximated watertables. In some ways, developing a calibration based on a flux type boundary condition may give more insight than approximating the watertable, but it requires more time to calibrate the potential recharge and overburden properties. Surface hydrology modelling for Laxemar /Werner et al. 2005/ gives some useful water balance components to compare with. They suggest a potential recharge into the soil that varies between about 140 mm/year in the elevated recharge areas to about 40 mm/year in lower areas, and a specific discharge in the sub-soil of about 15–30 mm/year.

In principle, the spatial distribution of recharge could be obtained directly from the MIKE-SHE surface hydrology modelling that represents the hydro-meteorological processes in detail by coupling it to the CONNECTFLOW hydrogeological. However, to study the palaeo-hydrogeology over tens of thousands of years, one would need to develop surface hydrology models over consistent timescales, which would require development. Other approaches currently under investigation are to use a head dependent recharge rate, as described in Section 2.6, along with unsaturated flow to remove high flows in the near surface under recharge areas where there are high hydraulic conductivities; or to add a thin highly conductive top layer along with unsaturated flow to model surface run-off.

7.5 Sensitivity to DFN model parameters and data interpretation

The variants for the DFN model include:

- Comparison of three realisations using a semi-correlated transmissivity model with anisotropy.
- A correlated transmissivity model.
- An uncorrelated transmissivity model.
- An isotropic model.

7.5.1 DFN Realisations 1, 2 and 3

To quantify the effect of the stochastic nature of the HRD properties on the predicted borehole reference water profiles, three different DFN realisations of the reference case (i.e. the Hydro-DFN variant with the semi-correlated transmissivity model and anisotropy) were considered. This might be expected to give fractures in different positions and with different properties in the boreholes, for example.

A comparison of the predicted reference water profiles indicated that the stochastic effect of the DFN model on the regional flow pattern can sometimes give significant localised effects in the boreholes. Hence, there is probably sufficient difference to require at least a few realisations to perform the calibration, and possibly calculation of the transport performance measures. For example, the first realisation gave the best predictions of $\delta^{18}O$ in the KSH boreholes; realisation 2 gave the best predictions of $\delta^{18}O$ in the KLX and KAS boreholes; realisation1 gave the best prediction of salinity in KSH02. Apart from this, many similar features occur in all three realisations and the results are generally less sensitive in the Laxemar subarea, but this may just be because the model consistently predicts for all realisations that the upper parts of the bedrock have been flushed with meteoric water due to the higher topography in the area. Comparisons between all three realisations of salinity and $\delta^{18}O$ in the KLX, KSH and KAS boreholes are presented in Figure 7-22 to Figure 7-25.

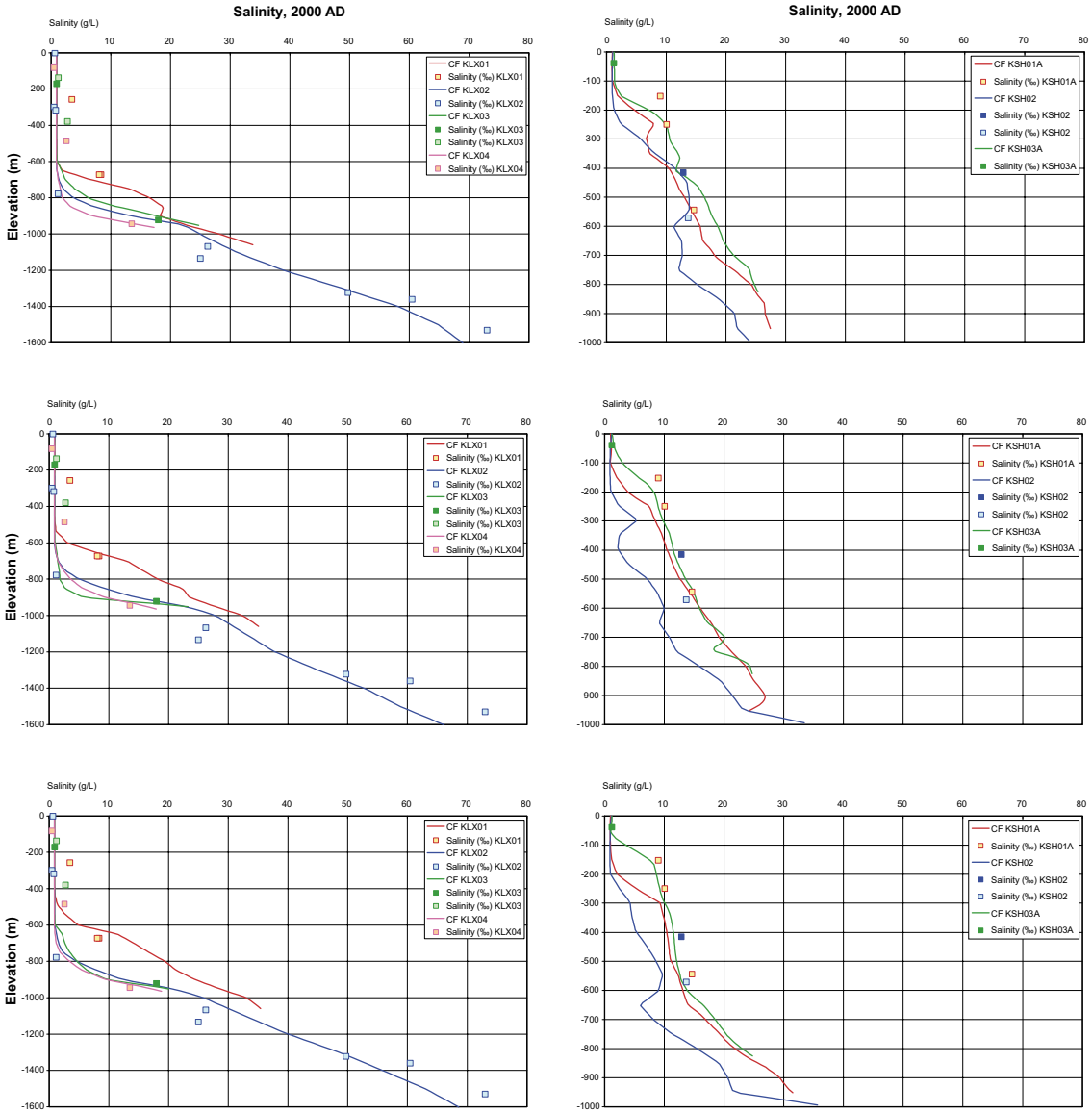

Figure 7-22. *Comparison of salinity in Laxemar (left) and Simpevarp (right) boreholes for realisations 1,2 and 3 (top to bottom) of the reference case. The salinity in the fracture system is shown by solid lines, and the data by points. Only representative data is shown. Dark filled shapes are considered the best data.*

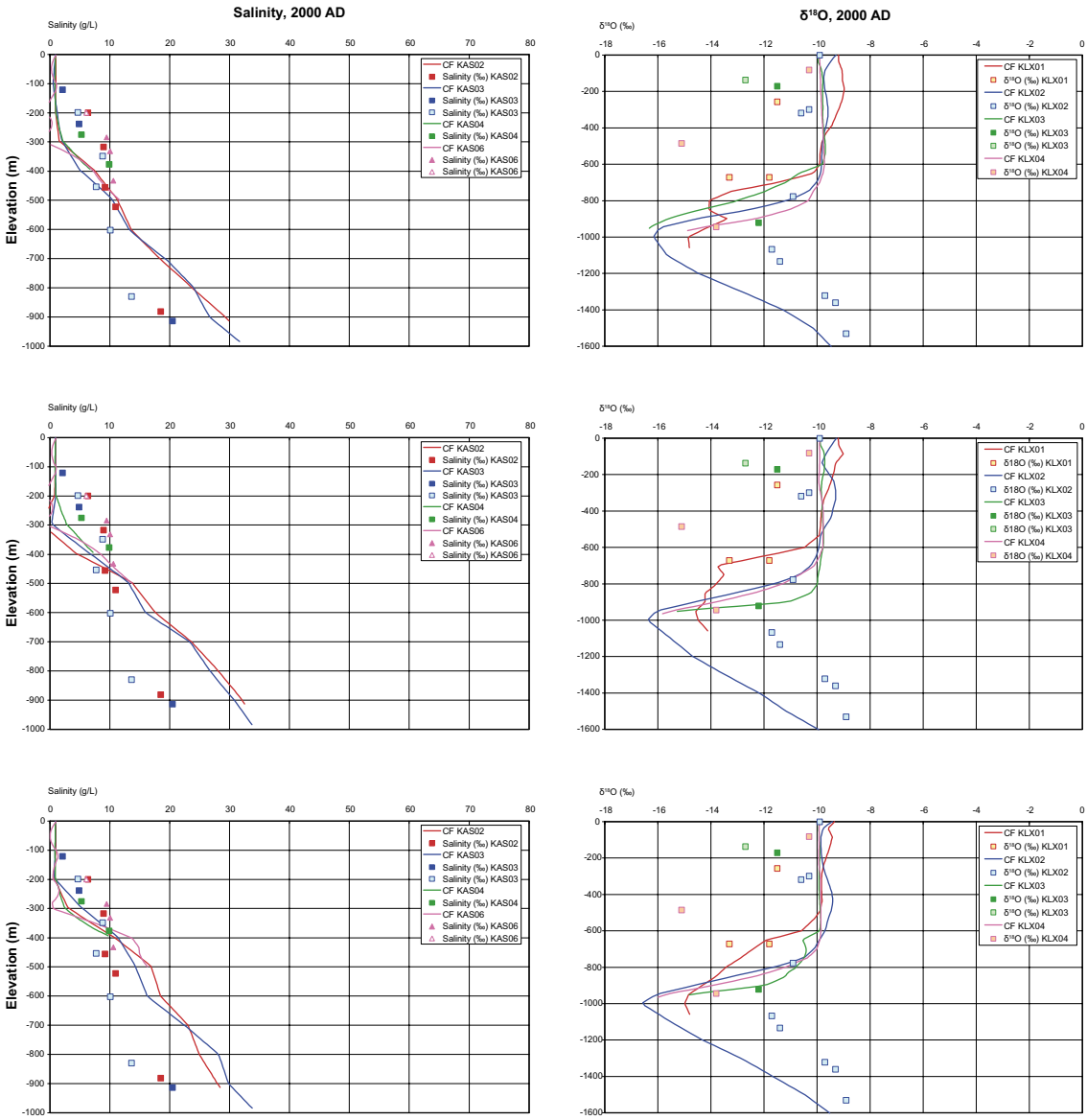

Figure 7-23. *Comparison of salinity in Äspö boreholes (left) and $\delta^{18}O$ in Laxemar boreholes (right) for realisations 1,2 and 3 (top to bottom) of the reference case. The model simulation in the fracture system is shown by solid lines, and the data by points. Only representative data is shown. Dark filled shapes are considered the best data.*

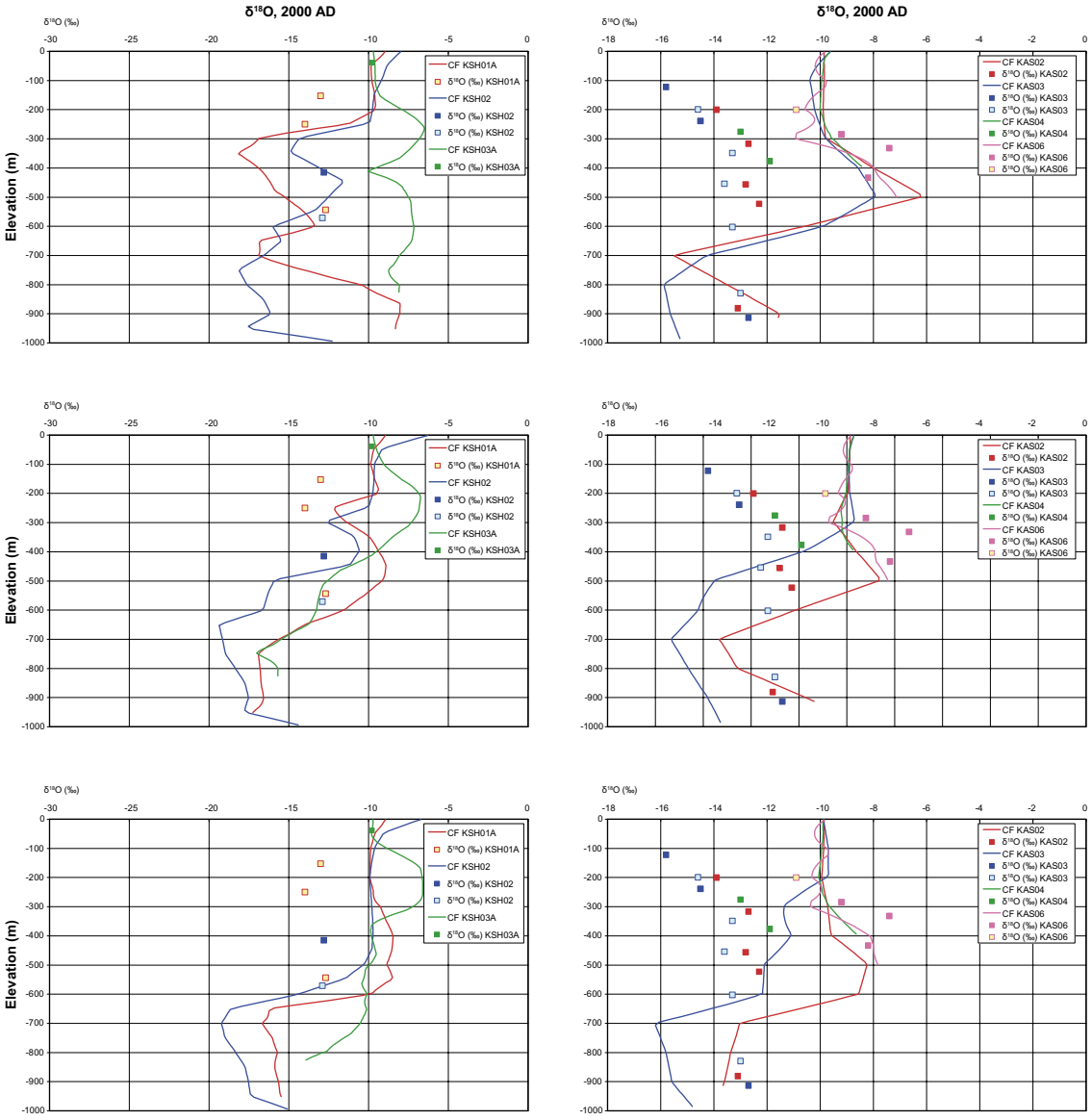

Figure 7-24. *Comparison of Oxygen isotope ratio $\delta^{18}O$ in Simpevarp (left) and Äspö (right) boreholes for realisations 1,2 and 3 (top to bottom) of the reference case. $\delta^{18}O$ in the simulated fracture system are shown by solid lines, and the data by points. Only representative data is shown. Dark filled shapes are considered the best data.*

7.5.2 Correlated transmissivity

The reference case and the other two realisations described above all use a semi-correlated relationship between transmissivity and fracture size. In order to test the sensitivity to the transmissivity model, one realisation with a correlated *T* model with anisotropy was considered. This model has less variability in the hydraulic conductivity of the HRD than the semi-correlated model. The correlated model shows distinct differences in the model predictions of hydrogeochemistry in the boreholes, but the results are qualitatively similar in terms of the types of reference waters present and the depth of any Littorina or Glacial pockets. The only other significant effect is slightly less flushing of Brine at depth in KLX01 and KLX04. This suggests that in the semi-correlated model, the process of adding a stochastic component to the transmissivity is sometimes enhancing flow at large depths,

probably due to the increased heterogeneity. Perhaps the results suggest that the spread in fracture transmissivity for the semi-correlated *T* model decreases at large depths around 1 km, which would seem physical given the increase in stress at depth.

7.5.3 Uncorrelated transmissivity

An uncorrelated *T* model was also considered. This model generally gives less spatial variability in the block-scale hydraulic conductivity of the HRD. Results are qualitatively the same as for the semi-correlated case. However, there are some improvements in the match at Laxemar, for example in the salinity in the KAS boreholes, but the match is worse in the Äspö area for Glacial water. Hence, it is not possible to promote one *T* model over another based on the palaeo-hydrogology since the differences between the predictions are small are certainly not greater than the variation between individual realisations of any one *T* model. The results merely confirm that each of the transmissivity models has been conditioned consistently to the same hydraulic data, and so predict bulk hydraulic properties of very similar magnitude. Therefore, the three *T* models should be retained at this stage in the absence of better evidence and to scope uncertainty.

7.5.4 Isotropic DFN model

In the reference case, an anisotropic DFN model was created by decreasing the transmissivity of the vertical sets Set_A and Set_B by a factor of 10. This was found to give a significant improvement in the hydrogeochemistry calibration within the Laxemar subarea over a model with an isotropic transmissivity model across all fracture sets, as was the starting point for the regional modelling. The results are less sensitive in other areas since they have been exposed to flushing by meteoric water for less time. The isotropic case is more conductive, especially vertically, compared to Realisation 1 of the anisotropic case (described in Subsection 7.7.1), which uses the same random fracture population. A comparison of the reference water profiles showed that more brine is flushed out in the isotropic case, even using the boundary condition variant with the lowest watertable. It is concluded that a match cannot be obtained for the Simpevarp subarea using an isotropic case unless the minimum watertable is also used, and then the match is considerably poorer than the anisotropic case. In general, inclusion of anisotropy between the transmissivity of the fracture sets results in a better match.

7.6 Sensitivity to hydraulic properties and concepts of HCD, HRD and HSD

The variants of the hydraulic properties of the HCD, HRD and HSD include:

- Low confidence deformation zones removed.
- Depth dependency models.
- Stochastic HCD models.
- Overburden models.

7.6.1 HCD Case with high and medium confidence zones

In the reference case there are 200 DZs including high, medium and low confidence zones. The effect of excluding the low confidence zones was tested. Removing the low confidence zones has a small effect on the hydrogeochemistry calibration as compared to the reference case.

7.6.2 Depth dependency models for HCD and HRD

For the HRD, the reference case uses upscaled hydraulic properties from a stochastic DFN that has a step change in fracture transmissivity at an elevation of –200 m. In the resulting ECPM model, a further step change in properties is introduced by reducing the conductivity below –600 m by half an order of magnitude. The sensitivity to these step changes is discussed below.

A possible range for the elevation of the step change in fracture properties is between about –350 m to –200 m based on variability between boreholes. Originally, the step change in both HRD and HCD was located at –300 m. This was moved up to –200 m in the HRD since it was found to give an improved calibration on hydrogeochemistry in the Simpevarp and Äspö areas. The step change model used for the HCD remains at –300 m in the reference case.

The motivation for introducing the step change in conductivity at –600 m was to try to improve the match to salinity at depth, mainly the profile in KLX02, and to reduce the overall tendency to displace the Brine at depth. A half order of magnitude change was found to be sufficient to see a significant improvement in salinity profiles in the Laxemar subarea. This may be seen by comparing the salinity profiles obtained from a variant case in which there is no step change at –600 m (Figure 7-25) with the corresponding reference case results (Figure 7-14). Considering the 100 m PSS interval data discussed in Section 5.9, this decrease in conductivity below –600 m is well within the levels of uncertainty.

Initial sensitivity studies for a homogeneous HRD model – not based on a DFN – used a step change, a power-law or an exponential depth-trend function for both HRD and HCD (see Subsection 5.9.2). None of these homogeneous models gave a good match in either the Laxemar or Äspö areas since they tended to predict either Glacial pockets were flushed by meteoric water at Laxemar, or Littorina pockets were flushed at Äspö. This is probably a result of the lack heterogeneity or anisotropy leading to an unrealistically high degree of connectivity within the regional-scale model. In order to obtain a match with a homogeneous model, the hydraulic conductivity of the HRD had to be reduced significantly at depth to values far below those supported by the PSS 100 m interval data. The power-law and exponential depth-dependencies gave similar results.

7.6.3 Stochastic HCD case

In the reference case, the properties within each zone were uniform. For some variant cases with stochastic HCD properties, the zones were triangulated on a 200 m length scale and transmissivity was sampled from a lognormal distribution truncated at ± 2 standard deviations. For the reference water profiles, this affected both the depth of the mixing zone and the relative fractions of reference waters. Overall, this had a large effect on the results, and hence should be given further consideration for its effect on performance safety assessment.

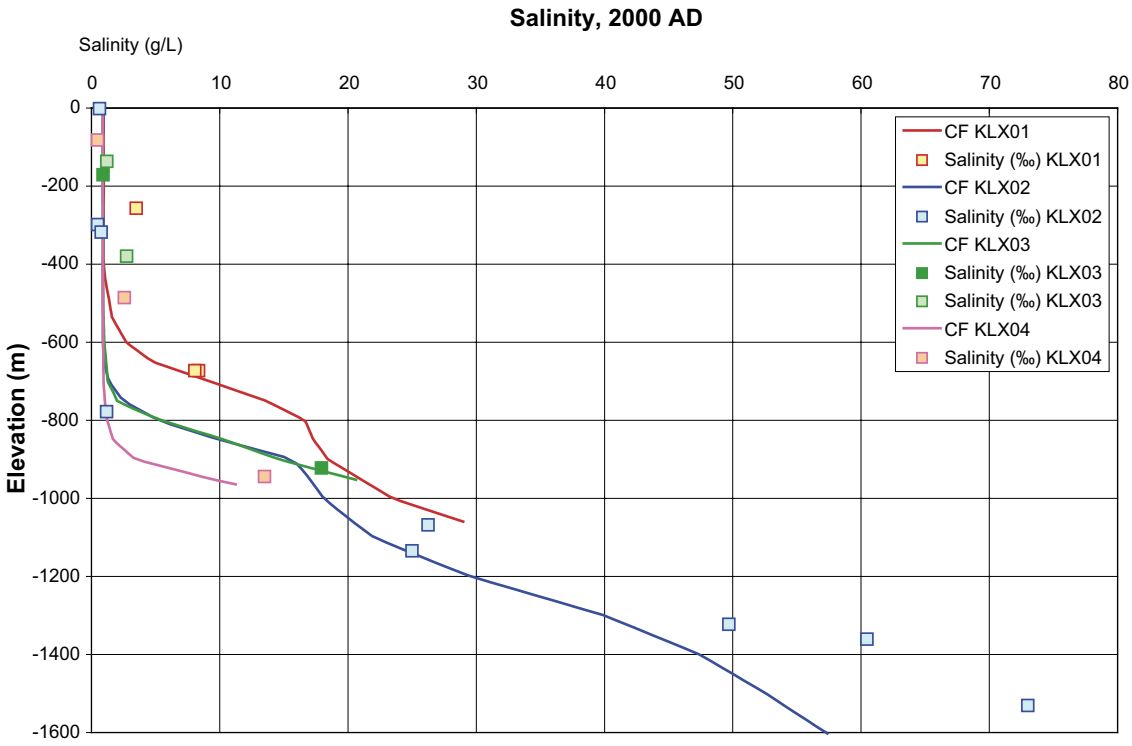

Figure 7-25. *Comparison of salinity in KLX01, KLX02, KLX03 and KLX04 for the variant on the reference case in which there is no step change in conductivity at –600 m elevation. The salinity in the fracture system is shown by solid lines, and the data by points. Only representative data is shown.*

Some preliminary results are shown in Figure 7-26 for salinity and Oxygen isotope ratio in the Laxemar for 3 realisations of the HCD model. In this case the standard deviation values given in the analysis of the single-hole interperetations of HCD transmissivity were reduced by half an order of magnitude otherwise the results deviated a long way from the data. The figures show some of the boreholes like KLX01 are quite sensitive to having stochastic variations within the HCD. KLX01 is cut by the ZSMEW007A RVS DZ at around –1,000 m elevation. This modelling concept of the large deformation zones will be tested more thoroughly in the future.

7.6.4 Soil domain model

The reference case used a HSD model consisting of three homogenous layers each of a constant 1 m thickness. A model approach using a sophisticated HSD model based on Quaternary deposits and stratigraphy maps provided by the SurfacNet Group /Werner et al. 2005/ was also considered in a variant case (HSD2). For the Laxemar boreholes, only small differences were seen due to the fact that the cover is generally more conductive than the bedrock so it has limited effect on heads in the bedrock, at least fro a specified head type boundary condition. It is perhaps more important when specify a flux type boundary condition, but still it is likely to be less important for flow in the bedrock at deeper levels. A flux type boundary condition will be investigated more in future studies.

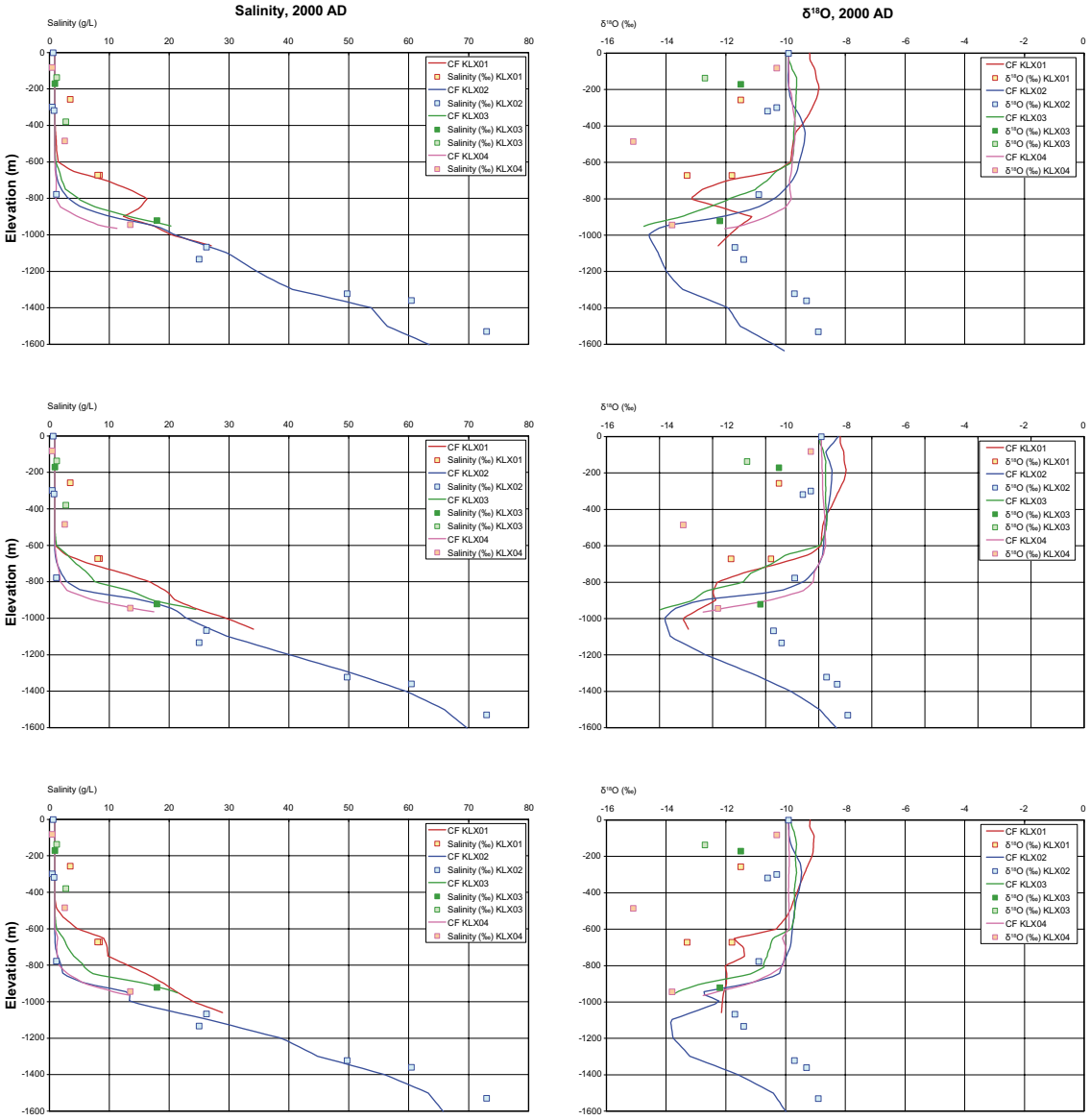

Figure 7-26. *Comparison of salinity (left) and Oxygen isotope ratio $\delta^{18}O$ (right) in the Laxemar boreholes for 3 realisations of the HCD. Values in the simulated fracture system are shown by solid lines, and the data by points. Only representative data is shown. Dark filled shapes are considered the best data.*

7.7 Sensitivity to transport properties

The variants of the transport properties of the HRD include:

- Flow-wetted-surface.
- Diffusion accessible porosity.
- Intrinsic diffusivity.

The flow-wetted surface may play an important role in the retardation of solutes, since it determines the available area for diffusion from the flowing water into the matrix. Within the range tested in this study, a moderate effect on the results has been observed. Also, the diffusion accessible porosity and the intrinsic diffusivity have a moderate to low effect on the results.

7.7.1 Flow-wetted-surface, a_r based on PFL-f data

In this variant case, the flow-wetted surface area was based on PFL-f data. This gives different a_r values for each HRD, and the a_r value is generally lower than that used in the reference case (see Table 5-15). Compared to the reference case, the mixing zone for reference water fractions in the fracture system is at a shallower depth, most notably for the Laxemar boreholes. Higher values of a_r are required in the deep rock than are suggested by the PFL flow anomaly data to give good diffusive exchange between the fracture and matrix systems to achieve equilibrium in the reference water concentrations. **This would suggest that advective flow in fractures below the PFL-f detection limit contributes to transport of solutes on the timescale of hundreds to thousands of years**. In conclusion, the flow-wetted surface area has a high effect on the results.

7.7.2 Lower diffusion accessible porosity

The effect of lowering diffusion accessible porosity was expected to be similar to the effect of lowering the flow-wetted surface. However, within the range tested here (see Table 5-8), the diffusion accessible porosity had a low effect on the results.

7.7.3 Higher diffusion coefficient

The effect of increasing diffusion accessible porosity was expected to reduce the time for the fracture and matrix system to reach equilibrium, but not to affect the capacity of RMD. This was confirmed by modelling since, within the range tested here (see Table 5-9), the diffusion coefficient had a very low effect on the results.

7.8 Summary of modelled cases and main conclusions from the calibration

In the previous study of S1.2 using approximately the same region, /Hartley et al. 2005a/ obtained good matches with the measured concentration profiles and the calculated mixing fractions. In that study, the hydraulic properties were based on measurements made for boreholes near and around the Simpevarp peninsula. For the L1.2 modelling, borehole data from the Laxemar subarea were also taken into account, resulting in areas of higher conductivity than were present in the S1.2 regional-scale models.

The higher hydraulic conductivities lead to model predictions that tended to flush the system more quickly with Meteoric water than the chemistry data would suggest. This created more of a challenge to obtain a calibrated model than for S1.2. Many attempts were made to obtain a better match, including calibration of hydraulic properties, testing HCD, HRD and HSD model concepts and transport parameter variations, but still a good match was difficult to obtain. It was particularly difficult to obtain a match in the Simpevarp sub-area due to the relatively high hydraulic conductivities suggested by the flow-tests which lead to model predictions of solute transport more rapid than indicated by the hydrogeo-chemistry data. To reconcile these difficulties, it was found necessary to reduce the driving forces, i.e. consider alternative flow boundary conditions. Hence, the key step in achieving a match is to lower the modelled watertable below the topographic surface, either by approximating a watertable based on surface water elevations or using a specified flux type boundary condition with reduced infiltration to the deep hydrogeology. The best match was obtained with the watertable based on the approximated minimum watertable form surface water heights plus 30% of the difference between topography and the minimum watertable.

The use of a flux type boundary condition suggested that this is equivalent to a potential groundwater recharge of a few tens of mm/year. Other important steps in achieving a calibration using the Hydro-DFN derived for Laxemar were to introduce anisotropy in transmissivity between the stochastic fracture sets by reducing transmissivity in the vertical sets orthogonal to the maximum in situ stress, and to increase the flow-wetted surface above that suggested by the PFL-anomaly data. Overall parameter sensitivity of the modelled hydrogeochemistry profiles in site boreholes is summarised in Table 7-3.

Table 7-3. Summary of relative sensitivities based on modelled variants for parameter variations within probable ranges.

Variant	Relative sensitivity
Model domain size	Low
Initial condition	Low
Top surface flow boundary condition	High
DFN realisation	Moderate
Transmissivity model	Moderate
Anisotropy	High
HCD confidence	Low
Depth dependency (HRD)	Moderate
Stochastic HCD	High (Indicative results – more simulations needed)
HSD	Low (need to simulate QD model combined with flux boundary condition)
Flow-wetted surface	High
Diffusion accessible porosity	Low
Diffusion coefficient	Low

7.9 Conclusions on suitable hydraulic parameter representation with uncertainties

7.9.1 Suitable model domain

The large regional-scale model, based on several water catchments, and the smaller model give similar results for the concentration profiles in the boreholes. The size of the smaller model is based on previous studies of the area. Although the model size may have some impact on the exit locations of a small proportion of particles, overall the model size has a low effect on the results.

7.9.2 Initial and boundary conditions

The flow boundary conditions on the top surface of the model have a considerable impact on the results and a watertable several metres below the topographic surface gives the best calibration results against hydrogeochemistry. Within the tested range of the initial conditions, the effect on the reference water concentration profiles is low.

7.9.3 HCD, HRD, HSD properties

The use of homogeneous models for hydraulic conductivity using depth dependency trends based on the PSS data all resulted in a poor match against the hydro-geochemical data. For such models, a calibration could only be achieved using a hydraulic conductivity in the

deep rock over an order of magnitude less than measured values. Using the Hydro-DFN base case gave interval conductivities consistent with the PSS 100 m interval data, and when anisotropy was introduced by reducing the transmissivity in the sub-vertical fracture sets Set_A and Set_B (see Subsection 3.8.2), an improved match with hydrogeochemistry was obtained. The Hydro-DFN gives a stochastic model of the HRD properties and there is uncertainty in the relationship between fracture transmissivity and size. Sensitivities to the individual realisation and *T*-model are both moderate in terms of the effect on the chemistry profiles in boreholes. The flow-wetted surface of the HRD has a strong effect on solute transport for variations in the range a_r = 0.1–1 m^2/m^3 with the best calibration results obtained for higher values. This suggests advective flow in fractures below the PFL-f detection limit has a significant effect on solute transport under natural flow conditions over hundreds to thousands of years, enhancing the effect of rock matrix diffusion.

The use of different depth dependencies for the HCD had a low to moderate effect on the results in terms of concentration profiles. By increasing the kinematic porosity values in HCD, a moderate effect on the results is obtained which improved the calibration results marginally. Removing low confidence zones from the model did not have a significant effect on the results. Spatial variability within the HCD seems to have a large effect of the hydrogeochemistry and one would also expect on transport performance measures. This particular aspect needs further investigation in future studies.

The complex Quaternary Deposits model of the HSD had little effect on the hydrogeochemistry and flow-path performance measures. Only localised effects on recharge and discharge areas at the surface were experienced. This is likely to be due to the use of a specified head boundary condition on the top surface of the model. Subsequent calculations, within safety assessment, will combine this complex HSD model with unsaturated flow equations in the near-surface and specified flux boundary conditions to identify the range of potential groundwater recharge that give consistency with the hydrogeochemistry data. The quaternary deposits and their properties may then play a more important role as they could limit recharge/discharge from some HCD overlain by Gytta and clay.

For the reference case, the underlying DFN model was initially based on the Hydro-DFN base case with a semi-correlated *T* model. However, during the regional modelling studies, modifications were made to the DFN prescription to achieve a better calibration against borehole hydrogeochemistry. The final Hydro-DFN regional case parameters used for the reference case are summarised in Table 7-4 to Table 7-7.

Table 7-4. Description of the Hydro-DFN regional case input parameters using the 'k_r fit' parameters for KLX04 matched to all hydraulic data (Rock Domain A), with all other parameters taken from the Geo-DFN.

Fracture set name	Orientation set pole: (trend, plunge), concentration	Fracture radius model power-law (r_0, k_r)	Intensity P_{32} (m^2/m^3); valid radius interval (r_{min}, r_{max})	Relative intensity of P32	Semi-correlated transmissivity model parameters *(a,b,σ)*
Set_A	(338.1, 4.5) 13.06	(0.28, 2.73)	Above –200 m: 50% of open = 1.70	0.18	(3.5 10^{-9}, 1.0, 0.9) z > –200 (3.5 10^{-10}, 1.0, 0.9) –200 > z > –600 (1.1 10^{-10}, 1.0, 0.9) z < –600
Set_B	(100.4, 0.2) 19.62	(0.28, 2.83)	Below –200 m: 35% of open = 1.19	0.19	
Set_C	(212.9, 0.9) 10.46	(0.28, 2.73)	(0.28, 564)	0.19	(3.5 10^{-8}, 1.0, 0.9) z > –200 (3.5 10^{-9}, 1.0, 0.9) –200 > z > –600 (1.1 10^{-9}, 1.0, 0.9) z < –600
Set_d	(3.3, 62.1) 10.13	(0.28, 2.76)		0.27	
Set_f	(243, 24.4) 23.52	(0.40, 3.6)		0.17	

Table 7-5. Description of the Hydro-DFN regional case input parameters using the 'k_r fit' parameters for KLX03 (Rock Domains: M(A), M(D) and D), with all other parameters taken from the Geo-DFN.

Fracture set name	Orientation set pole: (trend, plunge), concentration	Fracture radius model power-law (r_0, k_r)	Intensity P_{32} (m^2/m^3); valid radius interval (r_{min}, r_{max})	Relative intensity of P32	Semi-correlated transmissivity model parameters *(a,b,σ)*
Set_A	(338.1, 4.5) 13.06	(0.28, 2.63)	Above –200 m: 60% of open = 0.84	0.22	($1.8\ 10^{-9}$, 1.0, 0.9) z > 200
					($3.5\ 10^{-10}$, 1.0, 0.9) –200 > z > –600
Set_B	(100.4, 0.2) 19.62	(0.28, 2.68)	Below –200 m: 30% of open = 0.42	0.15	($1.1\ 10^{-10}$, 1.0, 0.9) z < –600
Set_C	(212.9, 0.9) 10.46	(0.28, 2.59)	(0.28, 564)	0.17	($1.8\ 10^{-8}$, 1.0, 0.9) z > 200
					($3.5\ 10^{-9}$, 1.0, 0.9) –200 > z > –600
Set_d	(3.3, 62.1) 10.13	(0.28, 2.63)		0.36	($1.1\ 10^{-9}$, 1.0, 0.9) z < –600
Set_f	(243, 24.4) 23.52	(0.40, 3.6)		0.09	

Table 7-6. Description of the Hydro-DFN regional case input parameters using the 'k_r fit' parameters for KSH01A (Rock Domains: B and C), with all other input parameters taken from the Geo-DFN.

Fracture set name	Orientation set pole: (trend, plunge), concentration	Fracture radius model power-law (r_0, k_r)	Intensity P_{32} (m^2/m^3); valid radius interval (r_{min}, r_{max})	Relative intensity of P32	Semi-correlated transmissivity model parameters *(a,b,σ)*
Set_A	(330.3, 6.1) 16.80	(0.28, 2.77)	Above –200 m: 27% of open = 1.40	0.24	($1.4\ 10^{-9}$, 1.2, 0.9) z > 200
					($1.6\ 10^{-11}$, 0.8, 0.9) –200 > z > –600
Set_B	(284.6, 0.6) 10.78	(0.28, 2.91)	Below –200 m: 27% of open = 1.40	0.15	($5.1\ 10^{-12}$, 0.8, 0.9) z < –600
Set_C	(201.8, 3.7) 14.60	(0.28, 2.92)	(0.28, 564)	0.26	$1.4\ 10^{-8}$, 1.2, 0.9) z > 200
					($1.6\ 10^{-10}$, 0.8, 0.9) –200 > z > –600
Set_d	(84.6, 81.8) 6.98	(0.28, 2.87)		0.26	($5.1\ 10^{-11}$, 0.8, 0.9) z < –600
Set_f	(67.1, 15.5) 11.73	(0.21, 3.27)		0.10	

Table 7-7. Description of the Hydro-DFN regional case input parameters using the 'k_r fit' parameters for KAV04A (Rock Domains: A and C around Ävrö and Äspö), with all other input parameters taken from the Geo-DFN.

Fracture set name	Orientation set pole: (trend, plunge), concentration	Fracture radius model power-law (r_0, k_r)	Intensity P_{32} (m^2/m^3); valid radius interval (r_{min}, r_{max})	Relative intensity of P32	Semi-correlated transmissivity model parameters *(a,b,σ)*
Set_A	(330.3, 6.1) 16.80	(0.28, 2.78)	Above –200 m: 28% of open = 1.43	0.24	($4.5\ 10^{-9}$, 0.7, 0.9) z > –200
					($7.5\ 10^{-9}$, 0.7, 0.9) z < –200
Set_B	(284.6, 0.6) 10.78	(0.28, 2.87)	Below –200 m: 22% of open = 1.13	0.16	
Set_C	(201.8, 3.7) 14.60	(0.28, 2.90)	(0.28, 564)	0.22	($4.5\ 10^{-8}$, 0.7, 0.9) z > –200
					($7.5\ 10^{-8}$, 0.7, 0.9) z < –200
Set_d	(84.6, 81.8) 6.98	(0.28, 2.85)		0.27	
Set_f	(67.1, 15.5) 11.73	(0.21, 3.27)		0.11	

8 Description of Past evolution

The simulations use a start time of 8000 BC and a final time of 10,000 years, i.e. to 2000 AD, corresponding to present-day conditions. At 8000 BC, the last glaciation had ended and the entire modelled area is assumed to be covered with melted ice, here referred to as Glacial water. Initially, there are only two types of water in the model. The upper part of the model is filled with Glacial water and underneath this there is an increasing fraction of Brine. As discussed previously, there are two different initial conditions used for the Brine distribution at 8000 BC.

8.1 Reference case

The past evolution of the four reference waters, namely Brine, Littorina, Meteoric water and Glacial water, is shown in Figure 8-1 and Figure 8-2. The distributions of the different water types are presented in vertical slices at three times corresponding to: 5000 BC, 0 BC and 2000 AD (present-day). The fraction of each water type is calculated and the sum of the fractions of the four water types equals one. The corresponding TDS distributions are presented in Figure 8-3.

During the first 2,000 years the shore level continues to rise, see Figure 5-9. This creates an increased pressure head over the eastern part of the model, pushing the Glacial water deeper into the model displacing the Brine at depth. The Littorina pulse, starting at 6500 BC, is clearly visible in the upper part of the model at 5000 BC. Because the entire area is covered by sea at 5000 BC, no Meteoric water is found in the model at this time.

As soon as the first parts of the modelled area start to rise above the sea-level, the Meteoric water also contributes to the fresh water load into the model. The land-rise can easily be observed in Figure 8-2 in the part of the modelled area (west) where the Meteoric water has penetrated into the model, displacing the Glacial water near the upper surface and pushing it out toward the sea. The Brine is slowly mixing with Meteoric water and being transported toward the sea and up through the bedrock, driven by the land-rise. At 2000 AD, Littorina water is almost only found in the Baltic Sea as Meteoric water has flushed out all earlier pulses of Littorina that managed to penetrate into the model. Only a few minor pockets of Littorina water persist onshore at relatively low concentrations. As for the Glacial water, the situation is rather different. Glacial water of high concentrations can still be found in lenses deep down in the model at elevations of around –300 m to –1,000 m. These areas correspond to relatively low permeability rocks with low advective velocities.

The TDS distribution is the result of mixing between the four reference waters, which has a time varying concentration of salt. The shape of the TDS distribution, seen in Figure 8-3, suggests that the dominant part of the salt originates from the Brine. Naturally there is a greater contribution from Littorina water off-shore.

The distribution of the vertical Darcy velocity, presented in Figure 8-3, shows a highly heterogeneous flow field. The general pattern of the flow field changes from having more flows directed upwards (discharge) as long as the sea water dominates the top surface of the model, to having more flows directed downwards (recharge) as the land rises above the sea and meteoric water is allowed to penetrate into the model. The interface between the fresh water and the Brine is also observed as the level where the vertical flow changes direction. This is seen at 5000 BC, in particular.

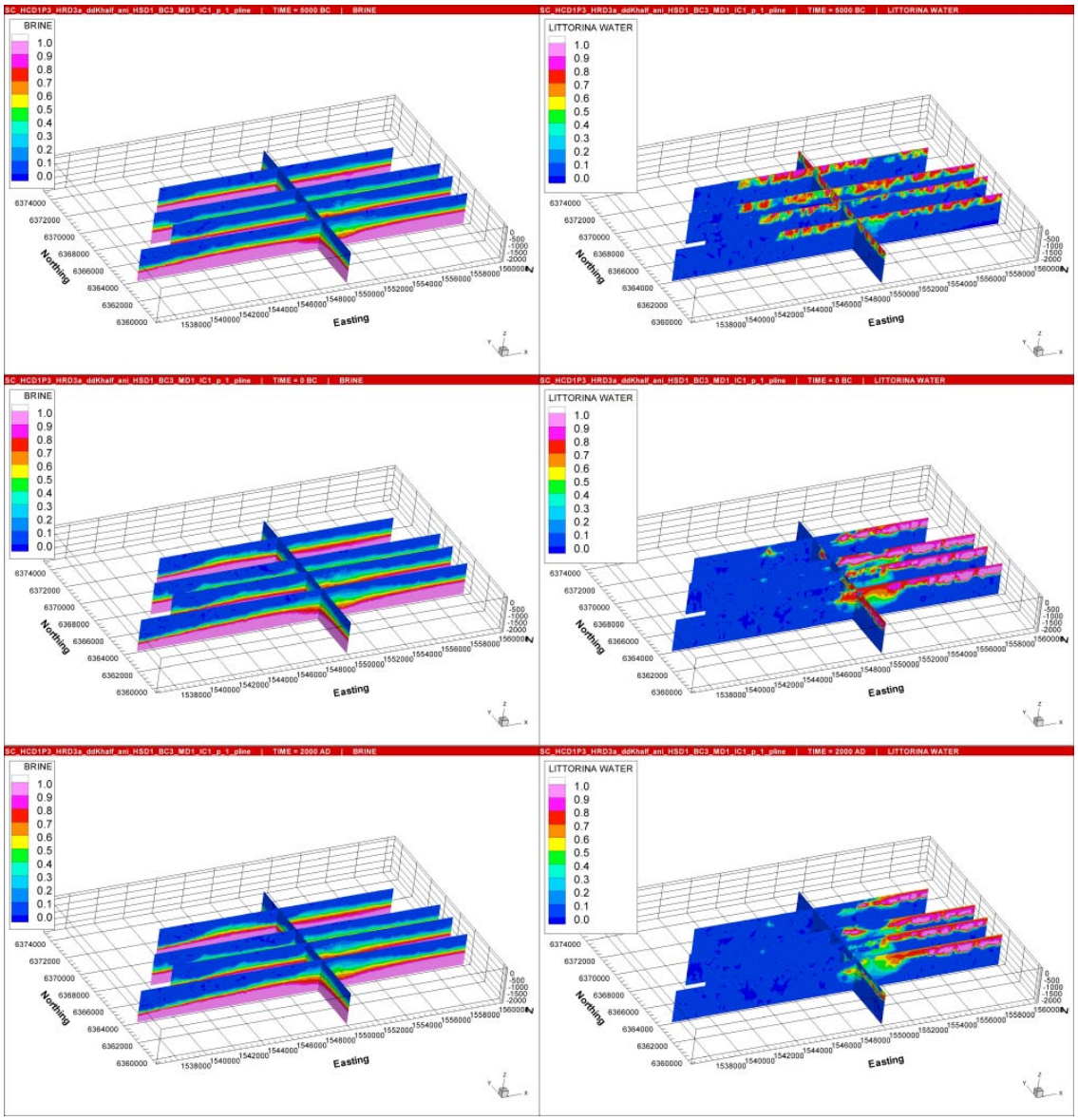

Figure 8-1. *Distribution of Brine (left) and Littorina water (right) in vertical slices at times equal to (from top to bottom) 5000 BC, 0 BC and 2000 AD (present-day), for the reference case.*

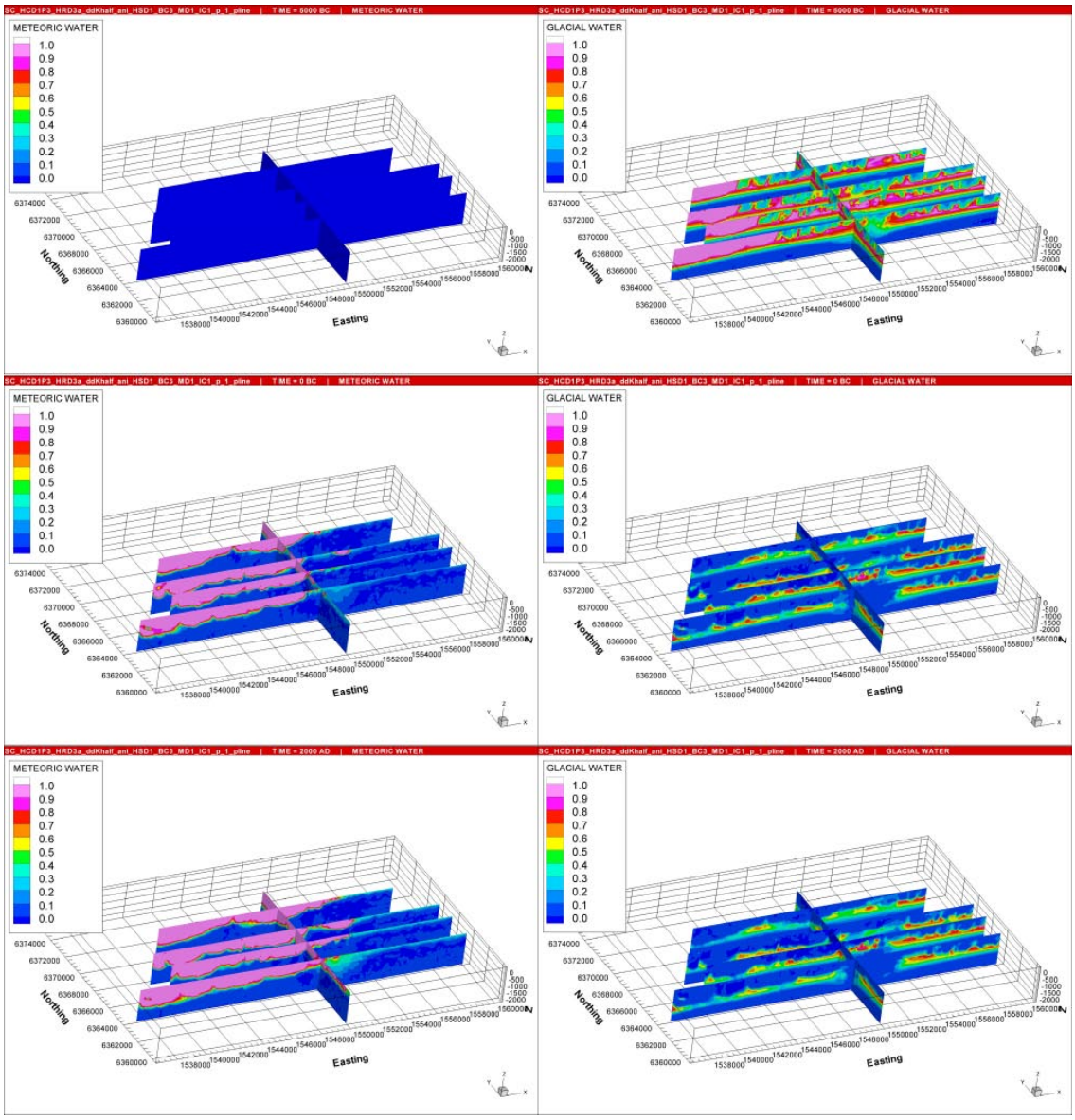

Figure 8-2. *Distribution of Meteoric water (left) and Glacial water (right) in vertical slices at times equal to (from top to bottom) 5000 BC, 0 BC and 2000 AD (present-day), for the reference case.*

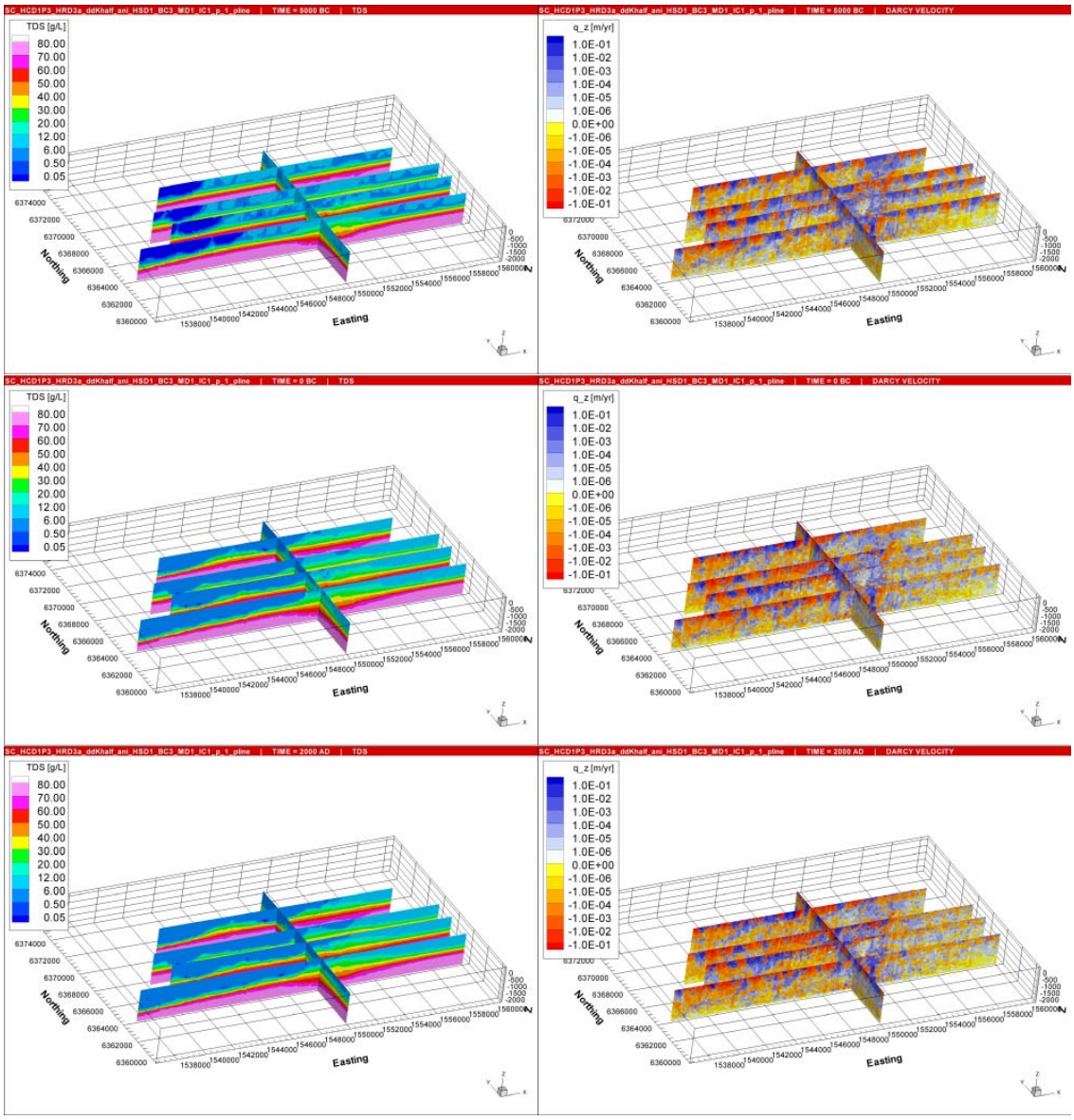

Figure 8-3. *Distribution of TDS (left) and the vertical Darcy velocity, q_z (right), in vertical slices at times equal to (from top to bottom) 5000 BC, 0 BC and 2000 AD (present-day), for the reference case.*

9 Description of the present-day flow conditions

9.1 Methodology

A selection of the most relevant modelled cases is presented in this section. Results representing the present-day flow conditions, i.e. 2000 AD (the final time-step in the simulations) are shown in terms of flow-paths (particle exit locations), distributions of F-factor, and regional distributions of reference waters and recharge and discharge rates. The purpose of the flow-path analysis is two-fold. Firstly, it provides a set of Performance Measures (PMs) for quantifying the current groundwater flow situation. These PMs can be used to compare variants and quantify uncertainties. Secondly, the identification of discharge areas is important for the Preliminary Safety Evaluation (PSE). Here we present various illustrations of groundwater flow-paths and give a summary of statistics of safety assessment PMs for several cases in Appendix C as a preliminary indication of PM sensitivity. These results should be viewed as preliminary indications of discharge areas since transport pathways will be studied in more detail using DFN models as part of SR-Can for L1.2. Experience from SR-Can for F1.2 leads us to anticipate potentially shorter paths using DFN simulations due to the reduced continuity inherent in sparse fracture networks compared to CPM models. Due to the massive amount of graphical output generated from the simulations, the number of figures presented in this report is limited to the reference case and other cases selected to illustrate the sensitivities to particular variants.

9.2 Reference case

This section presents the results for the reference case, which was developed from the calibration against the reference water mixing interpreted from borehole water samples to give a reasonable match in the global sense. Hydraulic parameters, initial conditions and boundary conditions obtained for the reference case formed the basis for the subsequent sensitivity study.

9.2.1 Flow-paths

In Figure 9-1 the distribution of the $\log_{10}$(F-factor) at particle starting locations in the local-scale release area for the reference case is presented. The Laxemar (left) and Simpevarp (right) release areas are shown as smaller black rectangles for orientation. Blue indicates higher F-factor. It is clear that the characteristics of the two release areas are quite different. Even though there are some particles with very high F-factors in Laxemar, the median value of the F-factor is actually significantly higher in the Simpevarp subarea. This is expected as the effective conductivity of the rock is lower in Simpevarp subarea. The areas containing particles with high F-factors generally coincide with areas having larger pressure heads, i.e. recharge areas.

In Figure 9-2 the distribution of $\log_{10}$(F-factor) at particle exit locations for the ensemble of particles released in the local-scale area for the reference case is presented. It is evident that the path-length of the released particles is generally quite short. Despite using a watertable below the topographic surface, the effects of the topography are still clearly present over the entire area. Even if the grid refinement could be improved, the localised flows are present as a result of the topography and the heterogeneity in the bedrock. Most released particles exit

inside or very close to the local-scale release area. It is also clear that the areas with very high F-factors at particle starting locations, shown in Figure 9-1, contain no exit locations. The exit locations are, as expected, located close to the shoreline and in the valleys with lower topographic elevation in the area. There are two main valleys confining the Laxemar release area from the north and from the south. Due to the topographic elevation, most of the Laxemar release area acts as a recharge area. Some particles released in the southern part of Laxemar actually exit to the west of the local-scale release area. This might look strange since the overall head gradient is directed to the east, but a combination of local topographic low points close to the release area and the presence of a deformation zone provides pathways a short distance to the east.

Only a few particles find their way out of the model further away. It should also be noted that a couple of particles reach the northern boundary close to the shoreline. This suggests that the boundary is placed too close to the release area and that the model domain size should be increased. However, the number of particles reaching this boundary is very small and so it is not considered to be of any importance for the results. Increasing the size of the model domain would increase the already long solve times for the calculations.

In Figure 9-3 the exit locations of the particles released from Laxemar (coloured in blue) and Simpevarp (coloured in red) are shown for comparison of discharge from the two different release areas. Figure 9-4 shows a close-up view of Figure 9-3. The predominant exit locations of the particles released from the Laxemar release area are the valleys to the north and south of the Laxemar release area and the area along the shoreline between Äspö and Hålö. Compared to the Simpevarp release area, the particles released from the Laxemar release area go more northerly. The main exit locations for the particles released from the Simpevarp release area are found around the Simpevarp peninsula and north of Hålö. A group of particles reach further south along the shoreline.

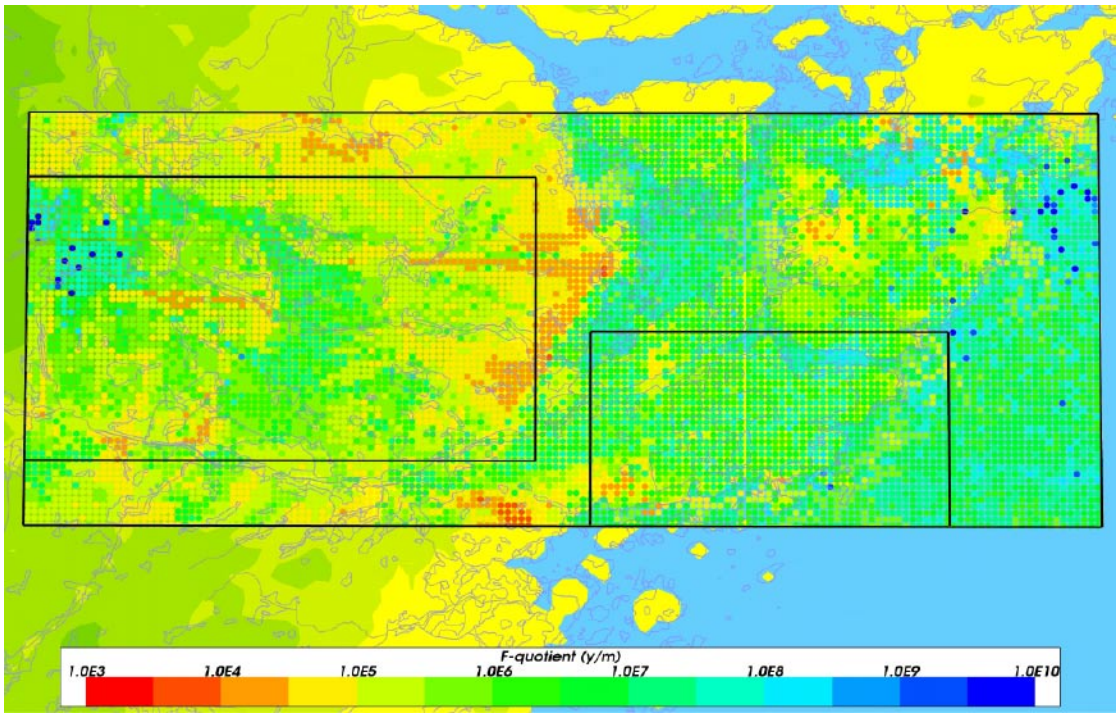

Figure 9-1. *Distribution of F-factor (Log10) at particle starting locations in the local-scale release area (large black rectangle) for the reference case. The Laxemar (left) and Simpevarp (right) release areas are shown as smaller black rectangles for orientation. The outlines of surface water bodies and streams are superimposed in blue. The background colours show groundwater head.*

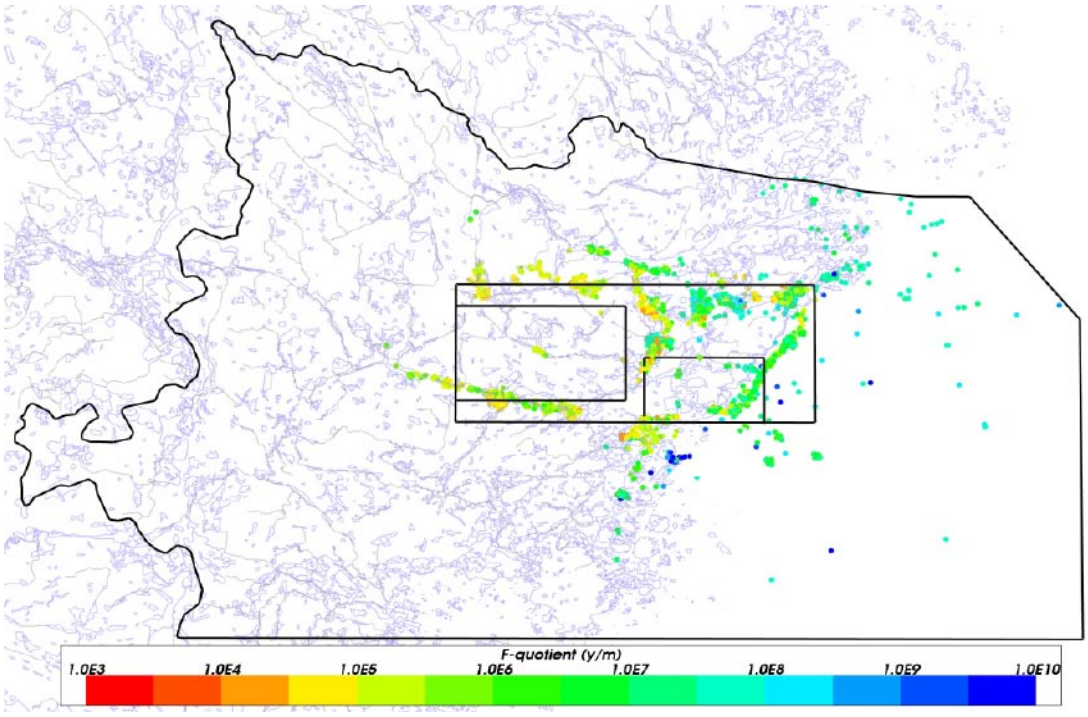

Figure 9-2. *Distribution of F-factor (Log10) at particle exit locations for the ensemble of particles released in the local-scale release area for the reference case. Black polygons are showing the large-regional model domain (curved), the local-scale (large black rectangle), the Laxemar (left small rectangle) and the Simpevarp release areas (right small rectangle) for the reference case. The outlines of surface water bodies and streams are superimposed in blue.*

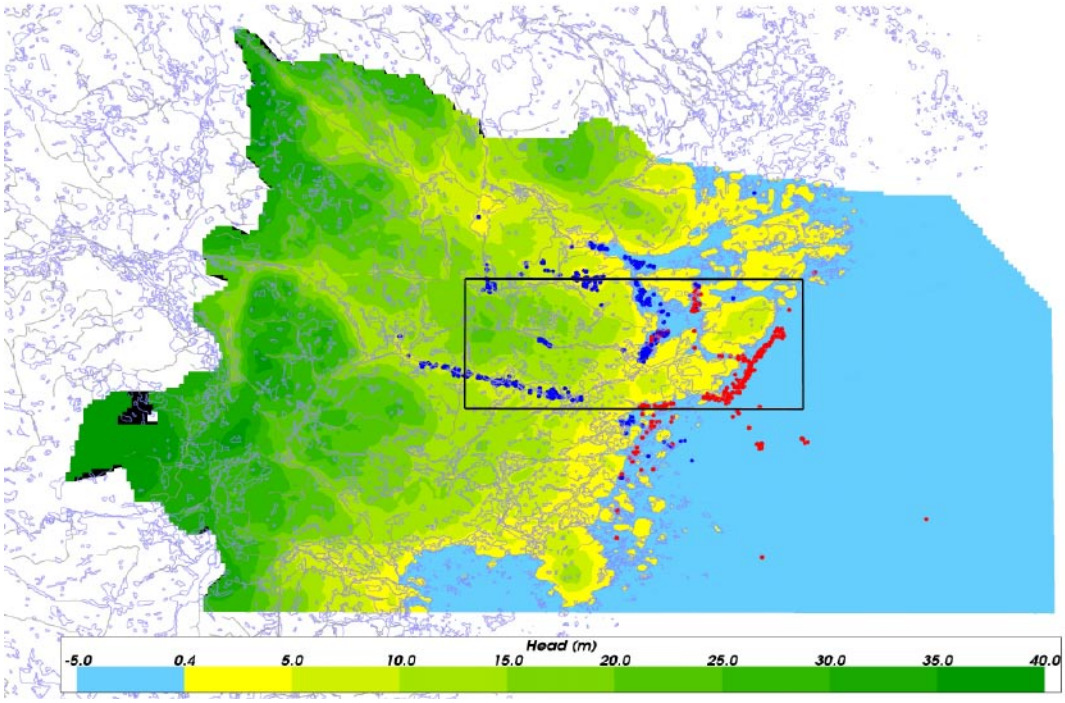

Figure 9-3. *Particle exit locations in the local-scale release area for the reference case. Particles released from the Laxemar release area are coloured in blue and particles from the Simpevarp release area are coloured in red. The local-scale release area (black rectangle) is shown for orientation. The outlines of surface water bodies and streams are superimposed in blue. The background colours show groundwater head.*

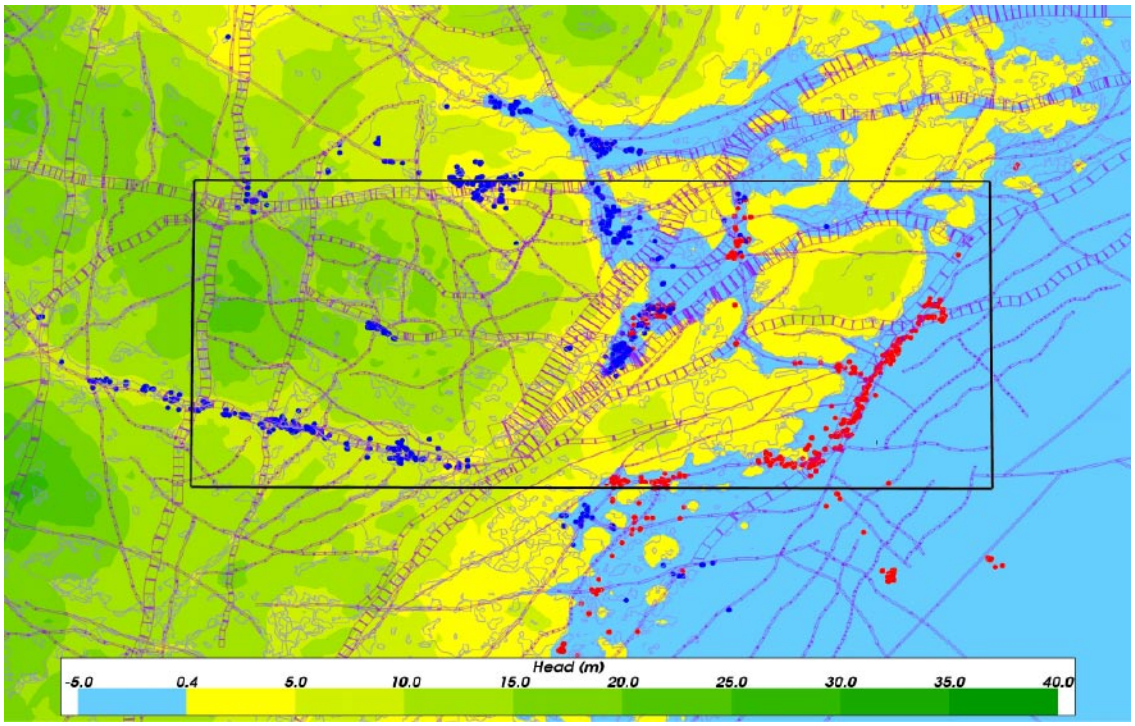

Figure 9-4. *Close-up view of particle exit locations in the local-scale release area for the reference case. Particles released from the Laxemar release area are coloured in blue and particles from the Simpevarp release area are coloured in red. The local-scale release area (black rectangle) and HCD (purple) are shown for orientation. Because of the limited view, not all particles are shown in the picture. The outlines of surface water bodies and streams are superimposed in blue. The background colours show groundwater head.*

9.2.2 Regional distribution of reference waters

In Figure 9-5 to Figure 9-7, the present-day distributions of the four reference waters Brine, Littorina, Meteoric water and Glacial water, are presented in vertical and horizontal slices. At –500 m no Brine is found in the western part of the modelled area. In the eastern part, however, the Brine fraction is about 20–30%, corresponding to a TDS of 14–21 g/l. At a depth of –1,000 m the fraction of Brine is about 50% in the eastern part, corresponding to a TDS of about 35 g/l, while the western part of the modelled area still contains freshwater originating from the Meteoric water and Glacial water.

Littorina water is only present in the eastern part of the modelled area underneath the sea. Due to the very low flowing velocities in the rock underneath the sea, the older Littorina water remains at depth for a long period of time. In the remaining rock there are just a few small pockets of Littorina water present at around –1,000 m elevation at 2000 AD.

Water originating from the Meteoric water penetrates the rock down to about –2,000 m elevation in the western area where land first rose above the sea-level. In the upper horizontal slices (–10 m and –100 m), the Meteoric water covers almost the entire model domain since the dominant part of the model has risen above the sea at present-day.

The Glacial water that covered the upper part of the model at 8000 BC has been displaced by Meteoric water and Littorina waters in the western part of the model. In the eastern part however, there is still Glacial water present at depths of –500 m to –1,500 m in both the Laxemar and Simpevarp subareas.

In Figure 9-8 and Figure 9-9, cross-sections along the WNW-ESE through KLX04 and KSH01A (left column) and SSW-NNE through KLX04 and KLX06 (right column), are shown for the present-day distribution of the reference waters and the TDS for comparison with interpretations made by the ChemNet Group. The Brine is generally found deep in the model, apart from the area around KSH01A which is situated close to the Baltic Sea. The Brine is slowly displaced by the Meteoric water from the west to the east. Littorina is only found around KSH01A and has been flushed-out elsewhere. The penetration of Meteoric water is also clearly observed in Figure 9-8 and the effects of the top boundary condition can be seen. Areas corresponding to the marine water surrounding the islands have higher Littorina fractions, whilst the area corresponding to the Simpevarp peninsula shows infiltration of Meteoric water at the top. Pockets of Glacial water can be seen between KLX04 and KSH01A.

The distribution of TDS shown in Figure 9-9 is broadly confirmed by the ChemNet Group and adds to the credibility of the modelling results.

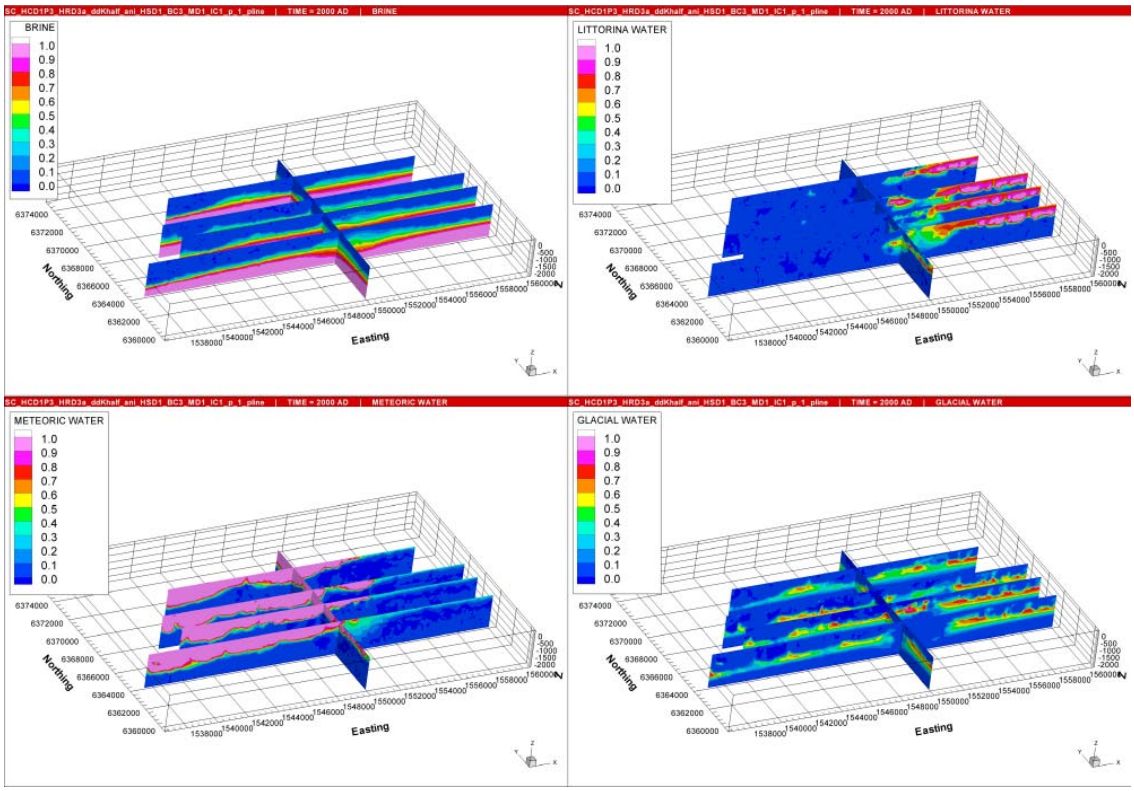

Figure 9-5. *Present-day distribution of the reference waters Brine (top left), Littorina water (top right), Meteoric water (bottom left) and Glacial water (bottom right) in vertical slices, for the reference case.*

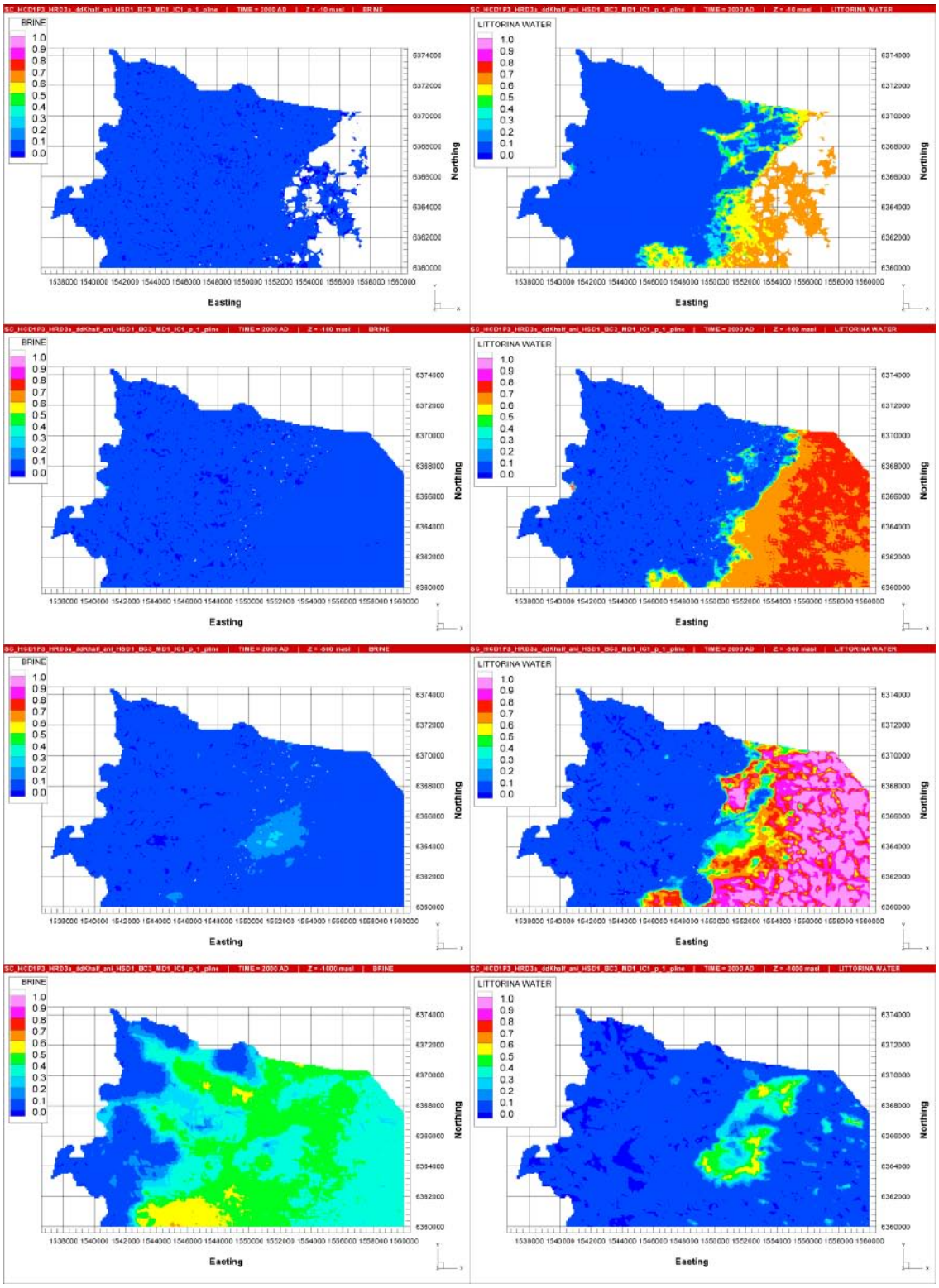

Figure 9-6. *Present-day distribution of Brine (left) and Littorina water (right) in horizontal slices at elevations (from top to bottom) –10 m, –100 m, –500 m and –1,000 m, for the reference case.*

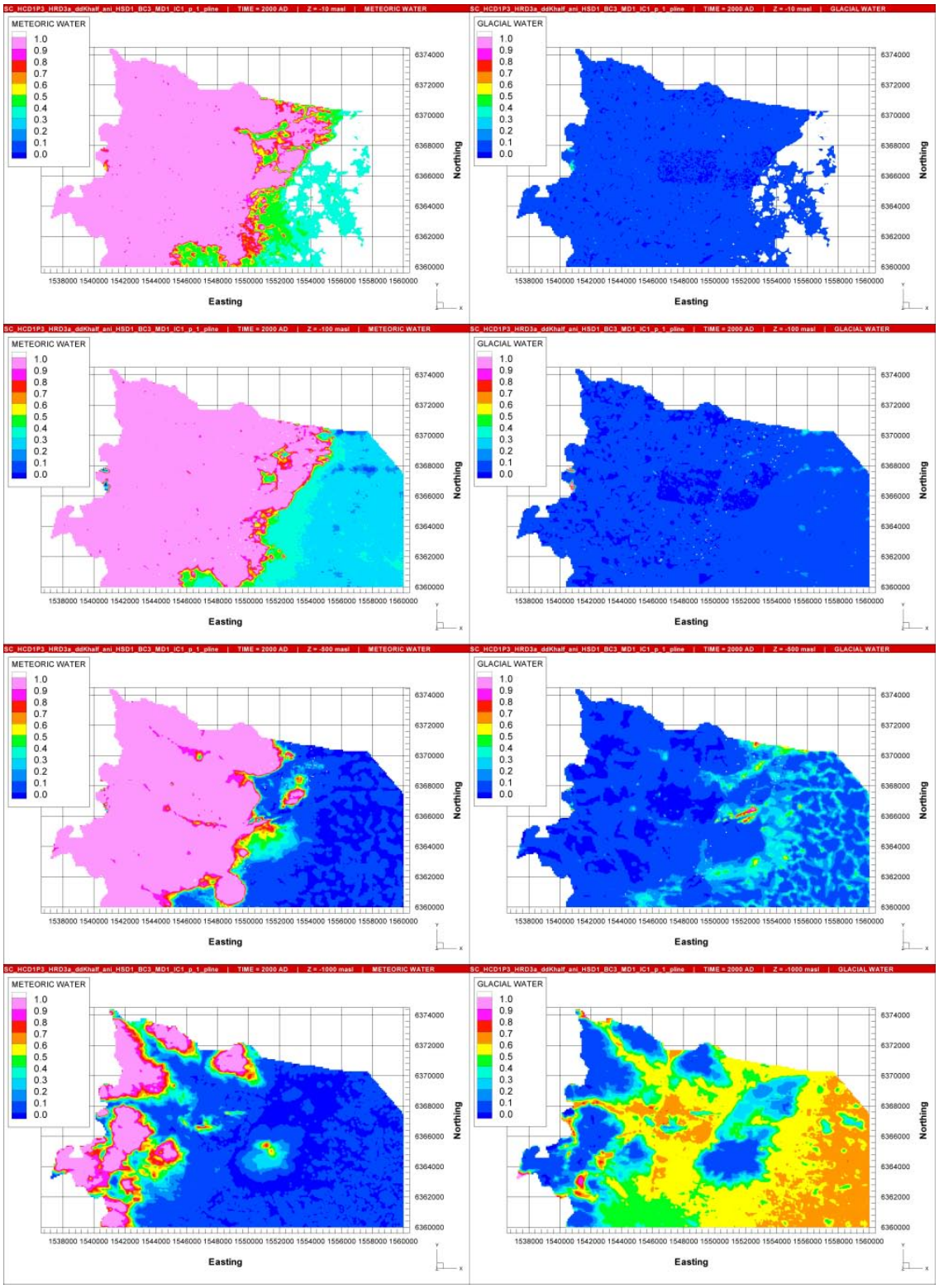

Figure 9-7. *Present-day distribution of Meteoric water (left) and Glacial water (right) in horizontal slices at elevations (from top to bottom) –10 m, –100 m, –500 m and –1,000 m, for the reference case.*

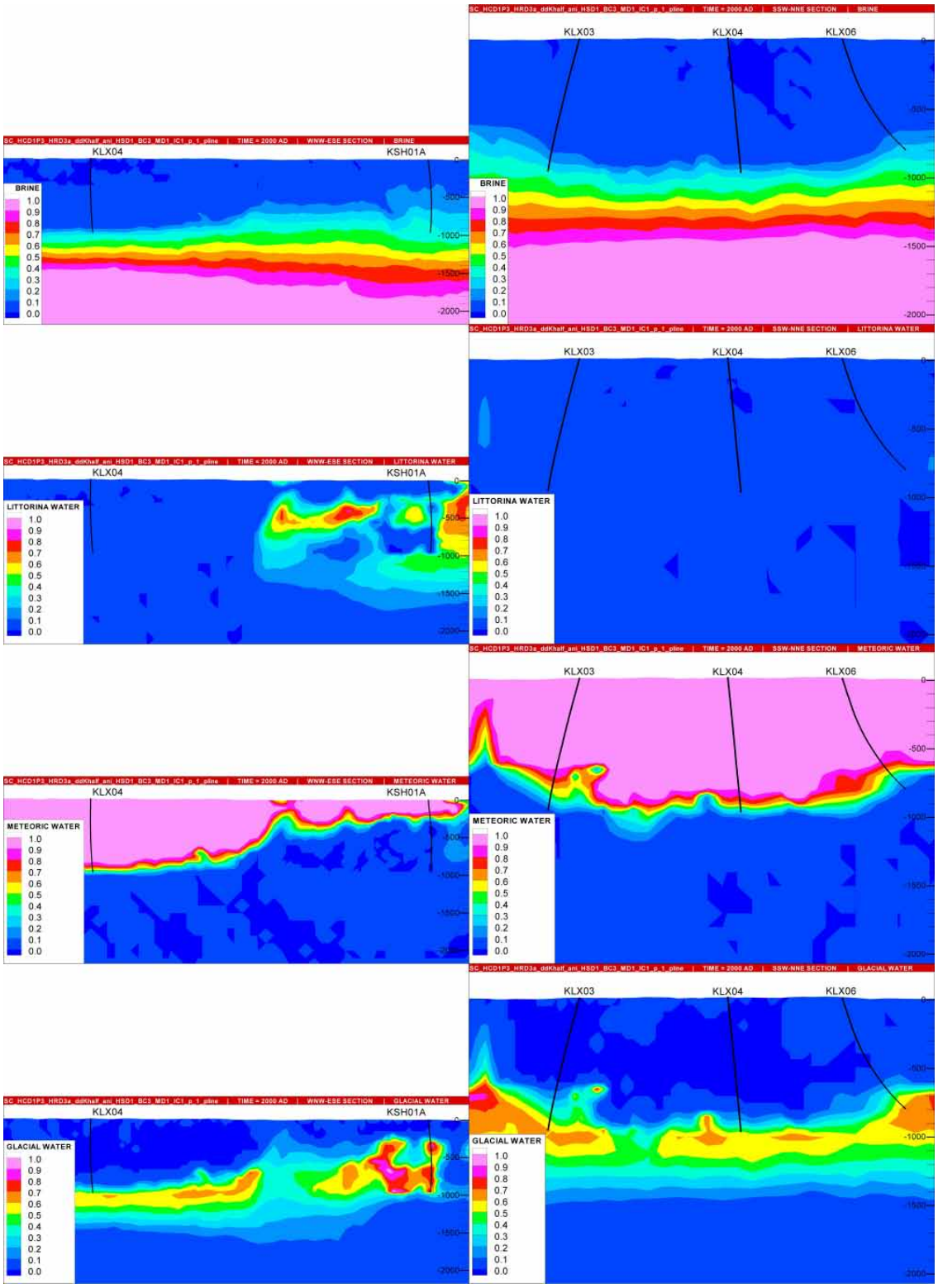

Figure 9-8. *Cross-sections along the WNW-ESE (left column) and SSW-NNE (right column) transects, showing the present-day distribution of the reference waters (from top to bottom) Brine, Littorina, Meteoric water and Glacial water, for the reference case.*

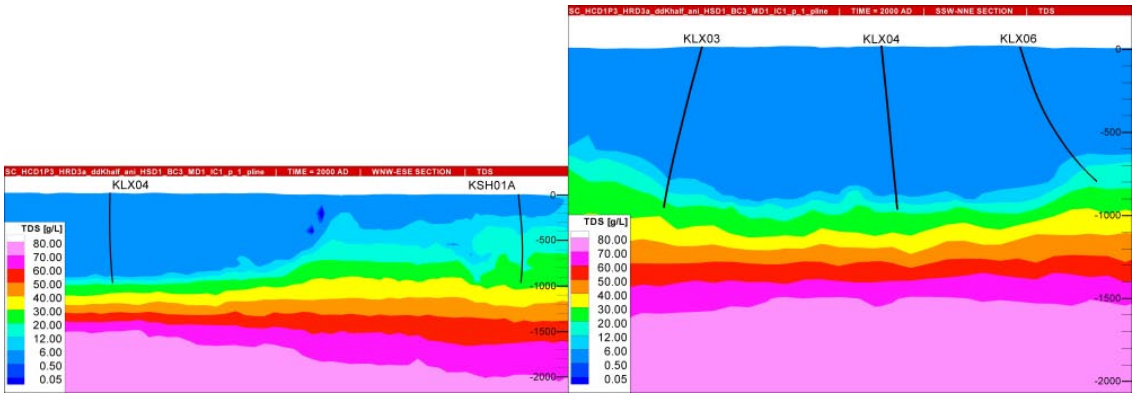

Figure 9-9. *Cross-sections along the WNW-ESE (left column) and SSW-NNE (right column) transects, showing the present-day distribution of TDS, for the reference case.*

9.2.3 Recharge and discharge

In Figure 9-10 the vertical Darcy velocity distribution under present-day flow conditions is presented in horizontal slices. Close to the surface at –10 m there are more downward flows (recharge), at a rate of around 0.1 m/year which reduces to about 0.01 m/year at –100 m elevation. The discharge is located to the Baltic Sea in the eastern part of the modelled area and around deformation zones and valleys onshore. In the deformation zones, the vertical Darcy velocity is around 0.1 m/year. The flow-field near the surface is very heterogeneous indicating localised flow-cells. At –500 m, the flow-rates are generally around 0.01–0.0001 m/year in both the recharge and discharge areas. This is one to two orders of magnitude lower than for the flow-rates above –100 m. The flow-field also tends to be more homogeneous at this depth and so it is easier to distinguish the areas of recharge and discharge for the deep hydrogeology. For both the Laxemar and Simpevarp release areas, flow is mainly downwards, which is promising from a safety assessment point of view. At –1,000 m, the flow-rates are generally less than 0.0001 m/year.

In Figure 9-11 and Figure 9-12, the recharge (red) and discharge (blue) locations for particles released in the local-scale area for the reference case are shown. As discussed previously, the discharge areas are located along the shoreline and in a few valleys onshore. The recharge areas are calculated by back-tracking of particles in the velocity-field until they reach the surface. That is, pathlines are calculated in the normal way, but by reversing the sign of the velocity vector so that particles can be started at repository depth (–500 m elevation) and then tracked upstream to their eventual recharge location. This method uses the variable-density velocity-field calculated in the finite-element scheme to obtain a single pathline per particle. It does not consider the convergence or divergence of pathlines, although particles are released on a dense grid of points to give an indication of the heterogeneity of flow-paths. Hence, the recharge points are the upstream starting points on the top surface for the flow-paths going through the release area. They help identify the area of influence, both upstream and downstream, for the release area, and hence confirm if the model domain is of sufficient extent.

The recharge areas are associated with several topographic highs both inside and outside the local-scale release area. Generally the recharge areas are found well inside the model domain suggesting that the regional water divides are an appropriate choice. All the major islands (Äspö, Ävrö and Hålö) together with the Simpevarp peninsula act as recharge areas, as does the central investigation area at Laxemar. A few recharge areas that influence the Laxemar subarea are located at hills several kilometres to the west and

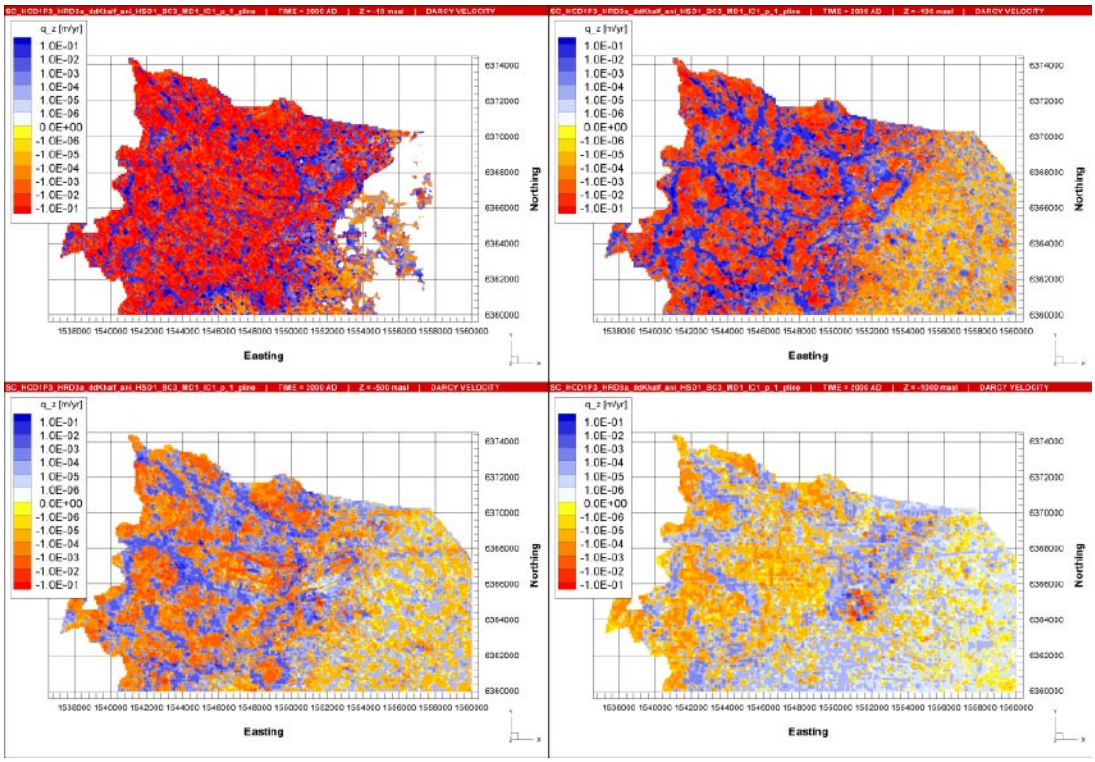

Figure 9-10. *Present-day distribution of the vertical Darcy velocity, qz, in horizontal slices at elevations –10 m (top left), –100 m (top right), –500 m (bottom left) and –1,000 m (bottom right), for the reference case.*

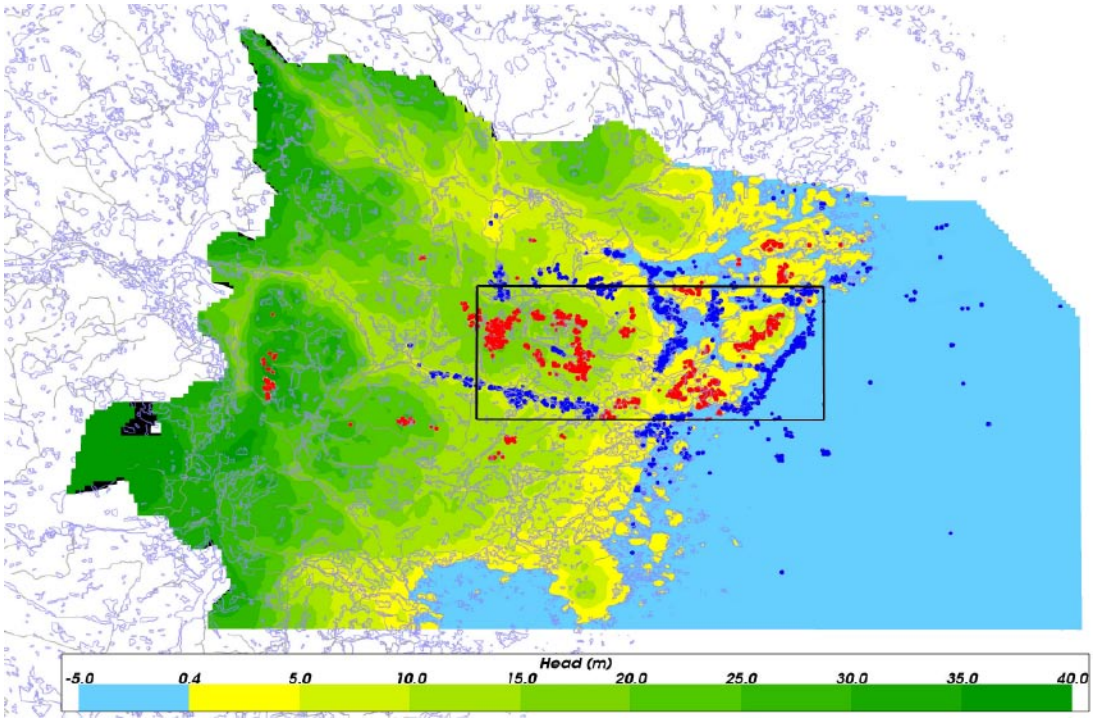

Figure 9-11. *Recharge (red) and discharge (blue) locations for particles released in the local-scale area for the reference case. The local-scale release area (black rectangle) is shown for orientation. The recharge points are the upstream start points on the model surface for flow-paths through the release area. The discharge points are the equivalent downstream exit points. The outlines of surface water bodies and streams are superimposed in blue. The background colours show groundwater head.*

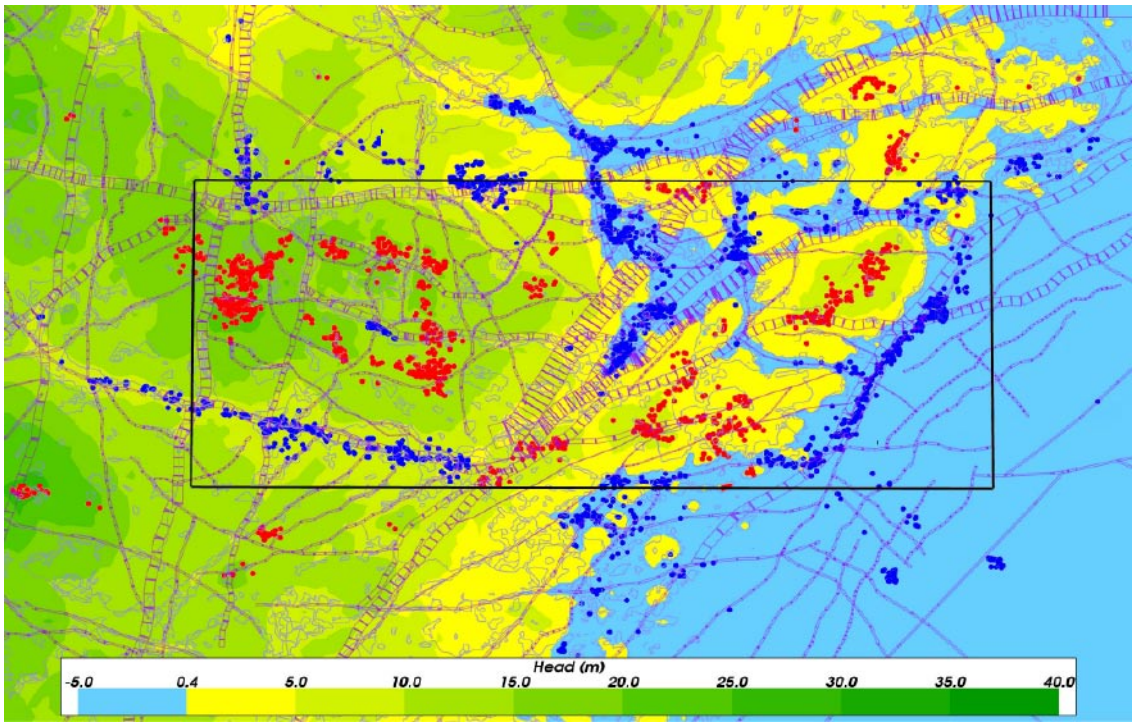

Figure 9-12. *Close-up view of recharge (red) and discharge (blue) for particles released in the local-scale area for the reference case. The recharge points are the upstream start points on the model surface for flow-paths through the release area. The local-scale release area (black rectangle) and HCD (purple) are shown for orientation. Because of the limited view, not all particles are shown in the picture. The outlines of surface water bodies and streams are superimposed in blue. The background colours show groundwater head.*

southwest. One might notice a considerable number of recharge points found out in the sea east of Simpevarp and Ävrö. The explanation for this behaviour is that a significant number of particles released within the local-scale area are actually underneath the sea (all starting positions coloured blue inside the local scale release area, see Figure 9-12). The flow velocities underneath the sea are generally very slow (see Figure 9-11). However, following the methodology described above, particles are tracked from areas where sea water gently infiltrates the bedrock due to buoyancy forces, towards the the overall global pressure minima at the shoreline. Therefore, particles started underneath the sea will tend to have recharge locations further out in the sea. Hence, these recharge positions are of little interest. Discharge areas are located mainly in valleys to the south and north of Laxemar together with the shoreline, especially south of Äspö. There is also a very minor discharge area associated with a small stream in the centre of the Laxemar subarea.

9.3 Sensitivities to flow boundary conditions

9.3.1 The intermediate watertable case

In the intermediate watertable case, a higher watertable is used compared to the reference case. The watertable used to assign the specified head at the top surface was calculated as the lowest possible groundwatertable +60% of difference between the lowest level and the topography (est_gvy_06). It should be noted that this case did not give as good a match to the borehole hydrogeochemistry as the reference case.

The intermediate watertable case predicts slightly lower F-factors compared to the reference case (see Figure 9-13), presumably due to increased pressure differences at the surface, which increase flow velocities. The differences are however small and the same conclusions as for the reference case apply for this case as well. Figure 9-14 shows the locations of discharge areas for this case. Qualitatively the discharge areas are similar to the reference case (see Figure 9-4), but here the discharge areas seem to be more concentrated. This is thought to be because in the reference case the watertable is considered to lie at the lowest possible realistic elevation, giving a smoother surface head profile and hence more diffuse discharge locations. In the intermediate case, topographic undulations are more emphasised leading to more distinct minima in the watertable surface, which act to attract a greater number of particles.

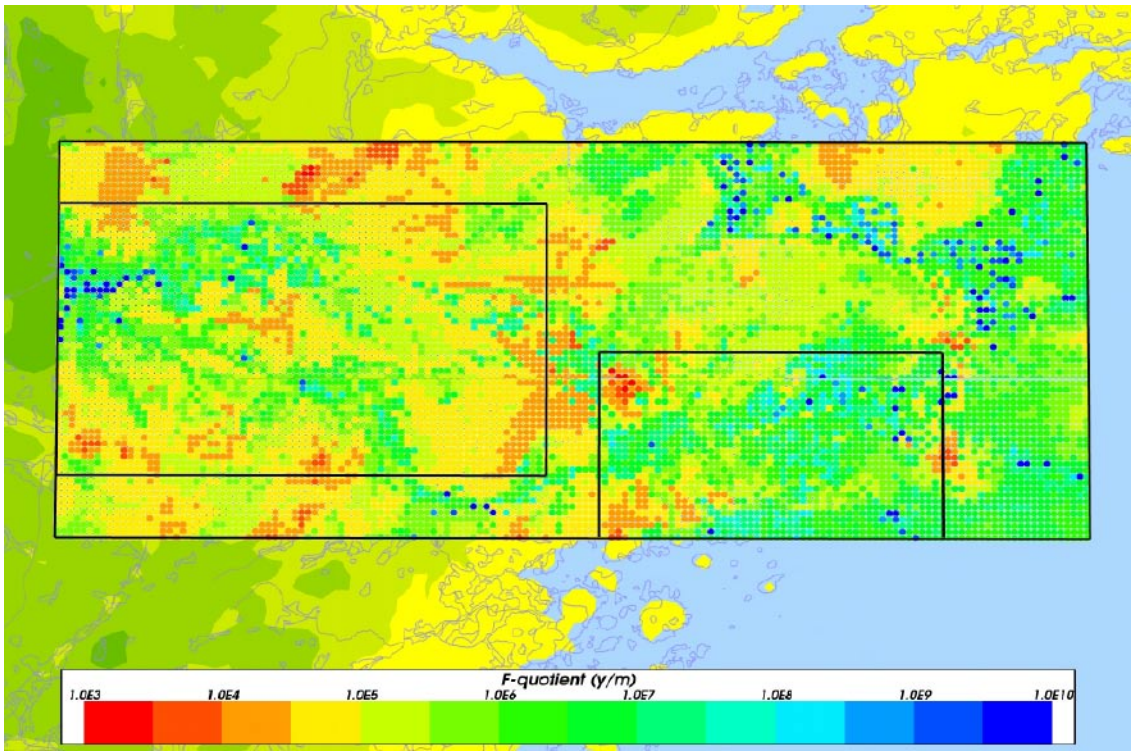

Figure 9-13. *Distribution of F-factor (Log10) at particle starting locations in the local-scale release area (large black rectangle) for the intermediate watertable case. The Laxemar (left) and Simpevarp (right) release areas are shown as smaller black rectangles for orientation. The outlines of surface water bodies and streams are superimposed in blue. The background colours show groundwater head.*

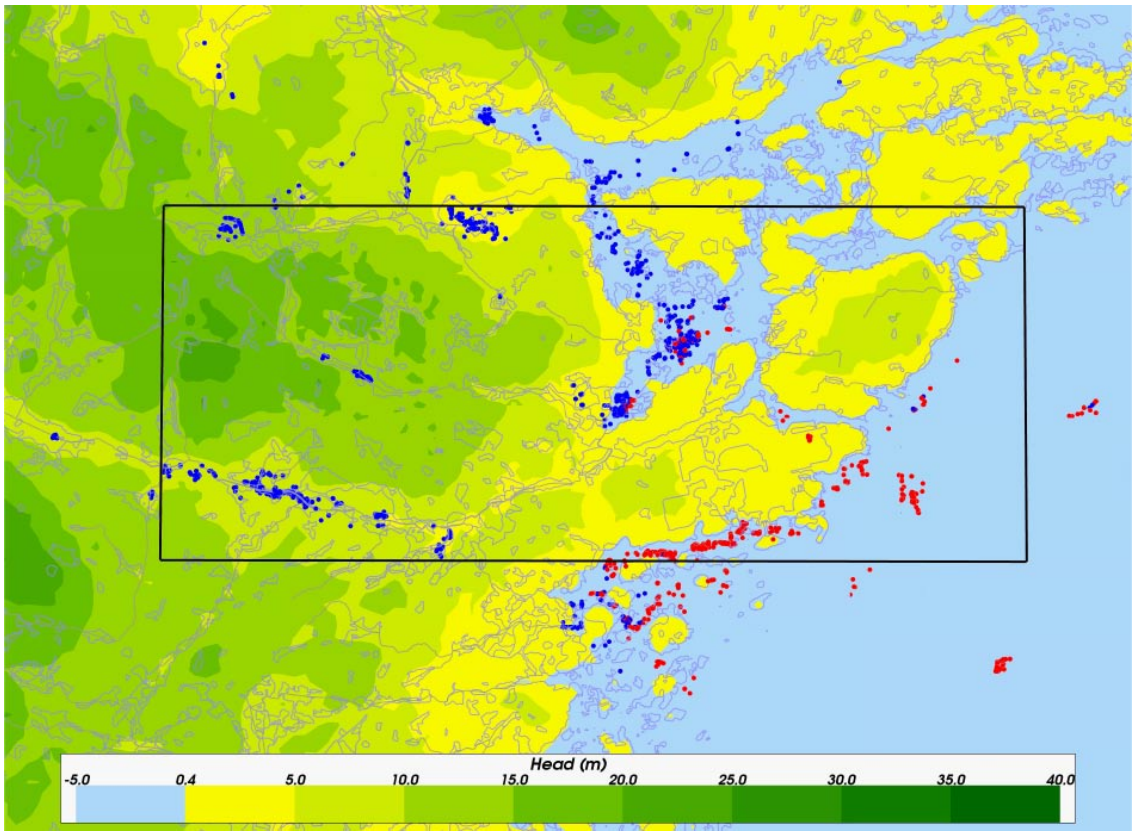

Figure 9-14. *Close-up view of particle exit locations in the local-scale release area for the intermediate watertable case. Particles released from the Laxemar release area are coloured in blue and particles from the Simpevarp release area are coloured in red. The local-scale release area (black rectangle) is shown for orientation. Because of the limited view, not all particles are shown in the picture. The outlines of surface water bodies and streams are superimposed in blue. The background colours show groundwater head.*

9.4 The topographic head case

In this case, a topographic head is used to assign the specified head at the top surface. It should be noted that this case did not give as good a match to the borehole hydrogeochemistry as the reference case.

In Figure 9-15 the distribution of the $\log_{10}$(F-factor) at particle starting locations in the local-scale release area for the topographic head case is presented. The Laxemar (left) and Simpevarp (right) release areas are shown as smaller black rectangles for orientation. Red colour indicates higher F-factor. The topographic head case suggests slightly lower F-factors compared to both the reference case and the intermediate watertable case (compare with Figure 9-1). The differences for the Simpevarp release area are small, but for the Laxemar-area the median F-factor is 0.7 logarithmic units lower compared to the reference case.

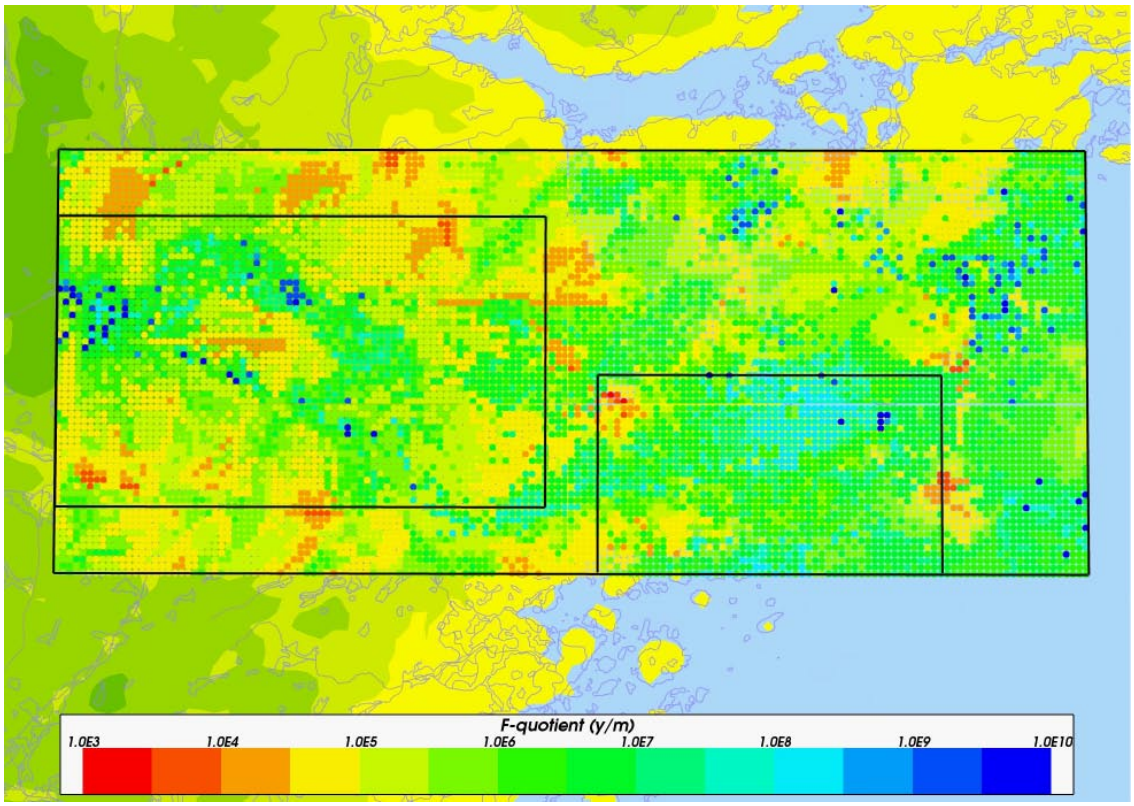

Figure 9-15. *Distribution of F-factor (Log10) at particle starting locations in the local-scale release area (large black rectangle) for the topographic head case. The Laxemar (left) and Simpevarp (right) release areas are shown as smaller black rectangles for orientation. The outlines of surface water bodies and streams are superimposed in blue. The background colours show groundwater head.*

The exit locations for the two different release areas, Laxemar and Simpevarp, are shown in Figure 9-16. Some differences can be found in the distribution of exit locations but the main conclusions from the reference case still apply. Again, the discharge areas seem to be more concentrated than in the reference case and very similar to the intermediate watertable case. Another difference is that a few more particles reach further out to sea for the topographic head case.

9.5 Conclusions

- The characteristics of the two different release areas, Laxemar and Simpevarp, are quite different. Even though there are some particles with very high F-factors in Laxemar, the median value of the F-factor is significantly higher in the Simpevarp area. This is expected as the effective conductivity of the rock is lower in Simpevarp. The areas containing particles with high F-factors generally coincide with recharge areas.
- The path-length of the released particles is generally quite short. Localised flows are present as a result of the topography and the heterogeneous bedrock. Most released particles exit inside or very close to the local-scale release area, and the extent of flow-paths at repository depth has a median of only about 1 km (see Appendix C.2). The exit locations are located close to the shoreline and in the valleys with lower topographic elevation in the area. Due to the topographic elevation, most of the Laxemar release area is beneath a recharge area.

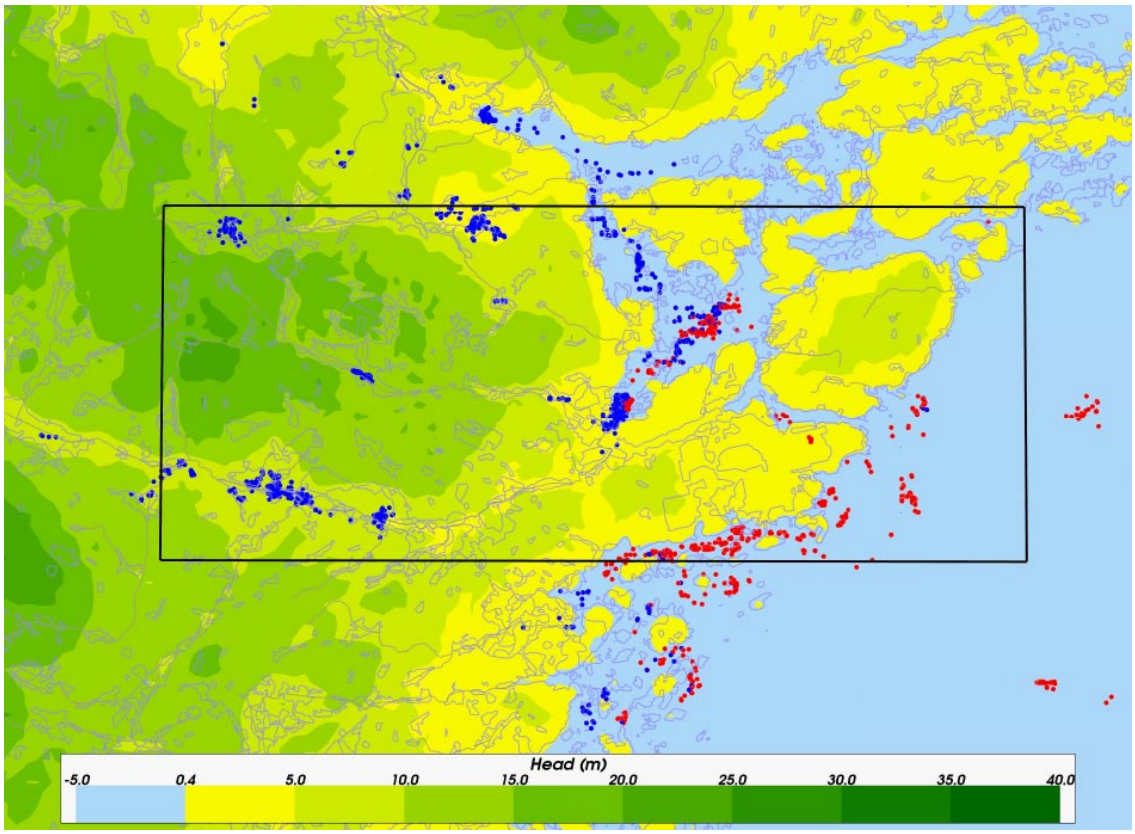

Figure 9-16. *Close-up view of particle exit locations in the local-scale release area for the topographic head case. Particles released from the Laxemar release area are coloured in blue and particles form the Simpevarp release area are coloured in red. The local-scale release area (black rectangle) is shown for orientation. Because of the limited view, not all particles are shown in the picture. The outlines of surface water bodies and streams are superimposed in blue. The background colours show groundwater head.*

- The discharge areas are located close to the shoreline and in a few valleys onshore. The recharge areas (obtained by back-tracking of particles in the velocity-field until they reach the surface), are associated with several topographic highs both inside and outside the local-scale release area. The recharge areas are found well inside the model domain suggesting that the regional water divides are an appropriate choice. The recharge area for the Laxemar release area is mostly directly above the site. A few recharge areas that influence the Laxemar subarea are located at hills several kilometres to the west and southwest. All the major islands (Äspö, Ävrö and Hålö) together with the Simpevarp peninsula act as recharge areas.
- The predominant exit locations of the particles released from the Laxemar area are the valleys north and south of the Laxemar release area and close to the shoreline between Äspö and Hålö. There is only one very minor discharge area at the centre of the Laxemar subarea, associated with a small stream. Compared to the Simpevarp release area, the particles released from the Laxemar area go more northerly. The main exit locations for the particles released from the Simpevarp area are found around the Simpevarp peninsula and north of Hålö.
- There are only a few particles with long paths. A couple of particles reach the northern boundary close to the shoreline, suggesting that the boundary is possibly placed too close to the release area, and that the model domain size should be increased. However, since the number of particles reaching this boundary is very small, this is not considered to be of any importance to the results.

- The distribution of salinity (TDS) is broadly confirmed by the ChemNet Group and adds credibility to the modelling results.
- Close to the surface at –10 m the flows are mainly downwards (recharge) at a rate of around 0.01 to 0.1 m/year, reducing to about 0.001 to 0.01 m/year at –100 m elevation. The discharge is directed to the Baltic Sea in the eastern part of the modelled area and around deformation zones and valleys on-shore. In the deformation zones, the vertical Darcy velocity is around 0.1 m/year. The flow-field near the surface is very heterogeneous indicating localised flow cells. At –500 m, the flow-rates are generally around 0.01–0.0001 m/year in the recharge as well as in the discharge areas. The flow-field also tends to be more homogeneous at this depth. At –1,000 m, the flow-rates are generally less than 0.0001 m/year.
- The model is sensitive to the top surface boundary condition governed by the position of the watertable. Three different top boundary conditions were considered, which are based on different watertable levels. The case with the lowest watertable gives the best match to the hydrogeochemistry data at the boreholes. However, in terms of flow-path statistics and exit locations, there are only small differences in results between the three boundary conditions. The main difference being that the F-factor for the Laxemar release area is significantly lower for the case where the watertable is held at the topographic surface. For the Simpevarp release area the differences in performance measures are smaller. The exit locations have similar locations for all three watertable levels, although the discharge locations are more diffuse for the case with the lowest watertable. The lack of sensitivity of the exit locations is to be expected since all three cases are based on the same topographic surface, if slightly smoothed for the lower watertable levels. Therefore, the positions of head maxima and minima are unchanged, although the head gradients are modified. These results indicate that more effort should be put on studying/quantifying the groundwater recharge.

10 Discussion and general conclusions

10.1 Summary of main conclusions and feedback to other disciplines

From the Hydro-DFN study:

- The fracture size distributions for open fractures were derived within this study rather than using those provided by the Geo-DFN due to problems of coordination with the final Geo-DFN. Here, a minimum radius of 0.28 m was assumed and power-law shape parameters were derived for each set and each rock domain by matching the P32 values for open fractures in the boreholes with the deterministic deformation zones. The values derived are broadly consistent with the final values derived in the Geo-DFN, but the discrepancy leaves an uncertainty as to the most representative model for fracture size distribution. Although the nature of fracturing is heavily sensitive to the fracture size distribution, it is felt that ultimately the calculation of flow within the Hydro-DFN is less sensitive once all other parameters – open fracture intensity and transmissivity – have been constrained by conditioning on hydrogeological data.
- The methodology developed for integrating the PFL-f and PSS hydraulic data with the geological fracture interpretation as part of the S1.2 and F1.2 modelling has been further enhanced here. The noteworthy improvements have been representing depth variations in fracture parameters, modelling larger domains, and improving the analysis of flows within individual fracture sets.
- Three different relationships between transmissivity and size have been considered, and all three can be made to give a reasonable match to the hydrogeological data. The semi-correlated model gives a slightly better match and a more realistic relationship.
- For KLX04, difficulties were encountered in developing a model that matched the bi-modal behaviour observed in the hydrogeological data. This bi-modal nature was observed in the PSS 5 m interval data and the PFL-f data. It is thought that this arises due to swarms of relatively high transmissivity stochastic fractures within single intervals. Such behaviour is difficult to reproduce in a model that assumes a Poisson spatial process and a continuous distribution of fractures as defined by size and transmissivity. Such behaviour was not evident in the transmissivity distribution of individual fractures in the PFL-anomaly data for any of the other boreholes considered, and the other borehole with 5 m PSS interval data, KSH01A, did not show a bi-modal behaviour. This should be studied in future boreholes where short interval PSS data is provided.
- The spatial variability between boreholes means the uncertainty in how representative it is to extrapolate a single borehole to an entire rock domain needs to be quantified. For example, comparing KLX04 in the Ävrö granite with more recent data since the L1.2 data freeze from KLX08 would suggest the values might be about half an order of magnitude too high compared to the bedrock away from large deformation zones.
- The PFL-f data gives some indication that the sub-vertical sets Set_A and Set_B are 0.5 to 1.0 orders of magnitude lower in transmissivity than Set_C and Set_d. Further, Set_C could have transmissivity 0.5 to 1.0 orders of magnitude higher than Set_d. At the moment these results are speculative being based on an analysis of KLX04 only. However, it should be understood that we may have under-estimated the importance of anisotropy in opting for a simplified model with the same transmissivity relationships for all sets. It is recommended that more consideration be given to hydraulic anisotropy between fracture sets when analysing PFL-f data from additional boreholes. Also the

quantity of flow data from sub-vertical fractures is limited in vertical boreholes such as KLX04. The use of inclined boreholes with different trends may inform more on the anisotropy between sets.

- Matching hydraulic data for all boreholes gives higher values for the median effective hydraulic conductivity, $\log(K_{eff})$ above –300 m, than below –300 m elevation. Median $\log(K_{eff})$ in the Ävrö granite (HRD(A)) is between –6.6 to –7.1 above –300 m, and –8.0 to –8.5 below –300 m elevation.
- Generally the 20 m block shows similar or lower median effective hydraulic conductivity, K_{eff} than the 100 m block. In all cases and all boreholes, the spread of the effective hydraulic conductivity is higher for the 20 m block scale than for the 100 m block-scale because there is a greater amount of averaging over individual fractures on the 100 m scale.
- Regional anisotropy with strike towards NW-SE has been shown for all cases for KLX04. For KLX03, the regional anisotropy has WNW-ESE strike direction. For KSH01A, the regional anisotropy has W-E strike direction. For KAV04A the regional anisotropy has an ENE-WSW strike direction.
- As expected, lower kinematic porosity values are obtained in the simulations matched to hydraulic data below –300 m than above –300 m elevation. Median $\log(n_e)$ in the Ävrö granite (HRD(A)) is between –3.4 to –4.1 above –300 m, and –3.9 to –4.1 below –300 m elevation.
- It is recommended that steps be taken to avoid some of the problems encountered in the coordination of the Geo-DFN and the Hydro-DFN. This could be achieved by tighter integration between Geology and Hydrogeology. In particular, evidence from the hydrogeological data that may address uncertainties in the geological data should be incorporated in the Geo-DFN.

From the regional flow modelling and calibration against hydrogeochemistry:

- The large regional-scale model based on several water catchments and the smaller model give similar results for the concentration profiles in the boreholes. However, the larger catchments based domain is necessary to study the recharge and discharge areas relevant to the Laxemar and Simpevarp release areas.
- The flow boundary conditions on the top surface of the model have a considerable impact on the results and a watertable often several metres below the topographic surface gives the best calibration results against hydrogeochemistry. Using a lower watertable below the topographic surface was found to be vital ingredient in achieving a calibrated model. Other ways of applying a lower watertable were considered based on a specified flux type boundary condition. This suggested a maximum potential groundwater recharge of a few tens of mm/year would give a reasonable match. It is suggested that this be compared with the potential recharge to bedrock calculated by the SurfaceNet Group.
- Another key step in the calibration against hydrogeochemistry was to introduce anisotropy between the transmissivity of the fracture sets. This was implemented as a reduction in the transmissivity of Set_A and Set_B by a factor 10 compared to the original isotropic parameters suggested in the Hydro-DFN. This makes physical sense since both sets are oriented perpendicular to the maximum horizontal stress and was considered as an option in the conditioning of the Hydro-DFN for KLX04. The result gave a marked improvement in the calibration even for a topographic head, although the best results were obtained with a combination of anisotropy and the lowest watertable case.
- A further step in achieving a calibrated model was in the transport parameters. It was necessary to delay deep infiltration of meteoric waters by choosing a diffusion accessible porosity at the high end of measured values and allowing good access to this porosity by

setting a flow-wetted surface of the bedrock in the range a_r around 1 m^2/m^3 or more. This suggests advective flow in fractures below the PFL-f detection limit has a significant effect on solute transport under natural flow conditions over hundreds to thousands of years, enhancing the effect of rock matrix diffusion.

- Finally, to improve the calibration in terms of reducing the flushing of Brine at large depths (e.g. towards the base of KLX02, below about 1,000 m), the fracture transmissivity as parameterised by the Hydro-DFN was reduced by half an order of magnitude below an elevation of –600 m.
- It is worth noting that initial attempts to calibrate homogeneous models for hydraulic conductivity using depth dependency trends based on the PSS data all resulted in a poor match against the hydro-geochemical data. For such models a calibration could only be achieved using a hydraulic conductivity in the deep rock over order of magnitude less than measured values. In contrast, the Hydro-DFN gave heterogeneous hydraulic properties that resulted in a model both consistent with PSS interval conductivities and gave a reasonable match with hydrogeochemistry was obtained.
- Sensitivities of the palaeo-hydrogeology to the various model components can be ranked as follows. The sensitivity to the surface flow boundary condition, anisotropy and flow-wetted surfaces are high. More moderate sensitivities were found for HCD depth dependence, HCD stochastic variability and kinematic porosity, transmissivity model and DFN realisation. Low sensitivities were found for the initial condition, domain, HCD confidence, diffusion accessible porosity, HRD kinematic porosity, overburden properties and diffusion coefficient.
- The distribution of salinity (TDS) is broadly confirmed by the ChemNet Group and adds credibility to the modelling results.
- Close to the surface at –10 m the flows are mainly downwards (recharge) at a rate of around 0.01 to 0. 1 m/year, reducing to about 0.001 to 0.01 m/year at –100 m elevation. The discharge is directed to the Baltic Sea in the eastern part of the modelled area and around deformation zones and valleys onshore. In the deformation zones, the vertical Darcy velocity is around 0.1 m/year. The flow-field near the surface is very heterogeneous, indicating localised flow cells. At –500 m, the flow-rates are generally around 0.01–0.0001 m/year in the recharge as well as the discharge areas. The flow-field also tends to be more homogeneous at this depth. At –1,000 m, the flow-rates are generally less than 0.0001 m/year.

A series of transport calculations were performed for each of the variants considered to provide guidance for the Preliminary Safety Evaluation (PSE). These results are reported in Appendix C as plots and tables of statistics. On the basis of these results, the following conclusions are drawn:

- The characteristics of the two different release areas, Laxemar and Simpevarp, are quite different. Even though there are some particles with very high F-factors in Laxemar, the median value of the F-factor at Laxemar is significantly lower with a median $\mathrm{Log}_{10}(F_r)$ of 5.5 year/m than in the Simpevarp area with median $\mathrm{Log}_{10}(F_r)$ of 6.8 year/m. This is expected as the effective conductivity of the rock is lower in Simpevarp. The areas containing particles with high F-factors generally coincide with recharge areas.
- The path-length of the released particles is generally quite short. Localised flows are present as a result of the topography and the heterogeneous bedrock. Most released particles exit inside or very close to the local-scale release area. The exit locations are located close to the shoreline and in the valleys with lower topographic elevation in the area. Due to the topographic elevation, most of the Laxemar release area is beneath a recharge area.

- The recharge areas (obtained by back-tracking of particles in the velocity-field until they reach the surface), are associated with several topographic highs both inside and outside the local-scale release area. The recharge areas are found well inside the model domain suggesting that the regional water divides are an appropriate choice. The recharge area for the Laxemar release area is mostly directly above the site. A few recharge areas that influence the Laxemar site are located at hills several kilometres to the west and southwest. All the major islands (Äspö, Ävrö and Hålö) together with the Simpevarp peninsula act as recharge areas.
- The predominant exit locations of the particles released from the Laxemar release area are the valleys north and south of the Laxemar release area and the area close to the shoreline between Äspö and Hålö. There is only one very minor discharge area at the centre of the Laxemar area, associated with a small stream. Compared to the Simpevarp release area, the particles released from the Laxemar release area go more northerly. The main exit locations for the particles released from the Simpevarp release area are found around the Simpevarp peninsula and north of Hålö.

10.1 Conclusions and recommendations for further investigations and simulations

10.1.1 Recommendations for Safety Assessment simulations in SR-Can L1.2

Important uncertainties that we recommend for further consideration in the SR-Can Safety Assessment calculations are:

- The effect of including heterogeneity within each deformation zone. From the SKB Task Description, an appropriate scale for the correlation of properties within zones is about 50–200 m, and the standard deviation should be about one order of magnitude. Such a model needs to be checked against the hydro-geochemical data and this may require some adjustment to parameters. Several realisations of the HCD model should then be used to quantify the sensitivity to stochastic properties.
- The effect of anisotropy between the fracture sets seems to have an important effect on palaeo-hydrogeology. Some variants with alternative anisotropy models may be need to be considered such as a higher transmissivity in Set_C and an isotropic case.
- More attention needs to be given to the flow-wetted surface. The current values used in the model are relatively high compared to those derived from the PFL-f data. Some variants that have lower values for flow-wetted surface whilst maintaining a match to the hydro-geochemical data need to be considered as it is not conservative to assume high values of flow-wetted surface.
- The kinematic porosity in the rock mass, which is derived from the fracture transport aperture, has a weak influence on palaeo-hydrogeology and so it is not well calibrated. However, transport aperture has an effect on travel-time, and so it may have a more significant effect on Safety Assessment.
- The top surface flow boundary condition has been shown to be important in this study and the calibrated model uses a derived watertable based on present-day surface water bodies. It may be worth using a non-linear flux-type boundary condition to calculate the watertable automatically based on a specified potential groundwater recharge and the site hydrogeology.

- Further work is required on combining the overburden model with alternative watertable models. In addition, and in coordination with SurfaceNet, some variants on hydraulic properties of the HSD may be suitable as they could have an effect on discharge areas and hence the Biosphere modelling.

10.1.2 Recommendations for further investigations

This study has suggested some issues on which to focus further acquisition of site data:

- The use of inclined boreholes with different trends (< 60°) would provide a better basis for studies of relative anisotropy between fracture sets.
- Flow data from other boreholes with PFL-f and PSS data will help bound the variability of hydraulic properties within the main rock domains and hence bound the uncertainty in extrapolating properties from boreholes to rock domains.
- The importance of the depth trend in hydraulic properties also suggests that flow data from other boreholes with PFL-f and PSS data would provide a better basis for characterising this feature.
- PSS 5 m interval data from another borehole at Laxemar would help confirm whether the fracture transmissivity displays a bi-modal behaviour as partly suggested by the lower section of KLX04, or whether this was just a unique feature in KLX04.
- The performance of cross-hole/interference tests as a basis for testing the Hydro-DFN models developed is important for the process of confidence building. However, it is accept that the hydraulic response in such tests often tends to be dominated by a few transmissive features rather than measure the background fracture system, and so careful planning is required. Vertical cross-hole or intra-hole tests could also help compare vertical flow with horizontal cross-hole and radial flow.
- The importance of the position of the watertable suggests more data should be acquired on the surface hydrology in terms of groundwater levels and the potential groundwater recharge. This suggests further cooperation between the HydroNet and SurfaceNet Groups.
- More hydrogeochemical data around repository depth between –300 m to –600 m would assist the regional model calibration around repository depth, and help inform of depth dependency in hydraulic properties. Of particular interest is to confirm the existence of Glacial water (or low $\delta^{18}O$) at these depths as it would suggest greater heterogeneity and possibly lower vertical hydarulic conductivities. Appropriate locations for acquiring such data are under recharge areas where one expects vertical flushing by Meteoric water. The existence of a Littorina signature is of more interest in lower lying areas in the valleys to the north and south of the Laxemar subarea, in the topographic low at the centre of the site and in the south east corner of the Laxemar subarea. More data on the deep brine would help identify the lower extent of groundwater flow. Possibly this could be aided by a 3D profile of salinity interpreted from transient electromagnetic remote sensing data.
- The ChemNet group has started to provide information on the chemistry in the diffusion accessible porosity and to compare this with that in the fracture system. This is encouraged, and further work will help address uncertainties in the connection between the two porosities and transport parameters such as flow-wetted surface.

References

Andersson J, 2003. Site descriptive modelling – strategy for integrated evaluation, SKB R-03-05, Svensk Kärnbränslehantering AB.

Bour O, Davy P, Darcel C, Odling N E, 2002. A statistical scaling model for fracture network geometry, with validation on a multi-scale mapping of a joint network (Hornelen Basin, Norway). Journal Geophysical Research, 107(6), doi: 10.1029/2001JB000176.

Byegård J, Gustavsson E, 2006. Bedrock transport properties. Preliminary site description Laxemar subarea – version 1.2, SKB R-06-27, Svensk Kärnbränslehantering AB.

Carrera J, Sanchez-Vila X, Benet I, Medina A, Galarza G, Guimera J, 1998. On Matrix Diffusion: Formulations, Solution Methods and Quantitative Effects, Hydrogeology Journal, 6, No 1, 178–190.

Craig H, 1961. Isotope variations in meteoric waters. Science, 133: 1702–1703.

Darcel C, Davy P, Bour O, De Dreuzy J-R, 2004. Alternative DFN model based on initial site investigations at Simpevarp, SKB R-04-76, Svensk Kärnbränslehantering AB.

De Dreuzy J-R, Davy P, Bour O, 2001. Hydraulic properties of two-dimensional fracture networks following a power-law length distribution, Water Resources Research, 37, No 8, 2065–2078.

Dershowitz W, Winberg A, Hermanson J, Byegård J, Tullborg E-L, Andersson P, Mazurek M, 2003. Äspö Hard Rock Laboratory. Äspö Task Force on modelling of groundwater flow and transport of solutes – Task 6C – A semi-synthetic model of block scale conductive structures at the Äspö HRL, SKB IPR-03-13, Svensk Kärnbränslehantering AB.

Follin S, Stigsson M, Svensson U, 2006. Hydrogeological DFN modelling using structural and hydraulic data from KLX04. Preliminary site description Laxemar subarea – version 1.2. SKB R-06-24, Svensk Kärnbränslehantering AB.

Forssman I, Zetterlund M, Forsmark T, Rhén I, 2005a. Oskarshamn site investigation. Correlation of Posiva Flow Log anomalies to core mapped features in KSH01A, KSH02A and KAV01. SKB P-05-65, Svensk Kärnbränslehantering AB.

Forssman I, Zetterlund M, Forsmark T, Rhén I, 2005b. Oskarshamn site investigation. Correlation of Posiva Flow Log anomalies to core mapped features in KLX02, KLX03, KLX04, KAV04A and KAV04b. SKB P-05-241, Svensk Kärnbränslehantering AB.

Hartley L, Hoch A, Hunter F, Jackson P, Marsic N, 2005a. Regional hydrogeological simulations – Numerical modelling using Connectflow, Preliminary site description Simpevarp subarea – version 1.2, SKB R-05-12, Svensk Kärnbränslehantering AB.

Hartley L, Cox I, Hunter F, Jackson P, Joyce S, Swift B, Gylling B, Marsic N, 2005b. Regional hydrogeological simulations for Forsmark– numerical modelling using Connectflow, Preliminary site description Forsmark area – version 1.2, SKB R-05-32, Svensk Kärnbränslehantering AB.

Hartley L, Hoch A, Jackson P, Joyce S, McCarthy R, Rodwell R, Swift B, Marsic N, 2006. Groundwater flow and transport modelling during the temperate period for the SR-Can assessment: Forsmark area – version 1.2. SKB R-06-?? (in manuscript), Svensk Kärnbränslehantering AB.

Hermansson J, Forsberg O, Fox A, La Point P, 2005. Statistical model of fractures and deformation zones: Preliminary site description, Laxemar subarea, version 1.2, SKB R-05-45, Svensk Kärnbränslehantering AB.

Hoch A R, Jackson C P, 2004. Rock-matrix diffusion in transport of salinity. Implementation in CONNECTFLOW, SKB R-04-78, Svensk Kärnbränslehantering AB.

Jackson C P, Hoch A R, Todman S J, 2000. Self-consistency of a heterogeneous continuum porous medium representation of a fractured medium, Water Resources Research, 36, No 1, 189–202.

Kestin J, Khalifa H E, Correia R J, 1981. Tables of dynamic and kinematic viscosity of aqueous NaCl solutions in the temperature range 20–150°C and the pressure range 0.1–35 MPa, J.Phys. Chem. Ref. Data Vol 10, No 1.

Laaksoharju et al. 1999. Multivariate Mixing and Mass Balance (M3) Calculations, A New Tool for Decoding Hydrogeochemical Information, Applied Geochemistry 14, 861–871, (1999).

La Pointe P R, Wallmann P and Follin S, 1995. Estimation of Effective Block Conductivities Based on Discrete Network Analyses Using Data from the Äspö Site, Tech. Rep. SKB TR-95-15, Svensk Kärnbränslehantering AB.

Marsic N, Hartley L J, Jackson C P, Poole M J, Morvik A, 2001. Development of Hydrogeological Modelling Tools Based on NAMMU, SKB R-01-49, Svensk Kärnbränslehantering AB.

Marsily G, 1986. Quantitive Hydrology, Groundwater Hydrology for Engineers. Academic Press, Inc., London.

Nyman H, 2005. Depth and stratigraphy of Quaternary deposits: Preliminary site description, Laxemar subarea – version 1.2, SKB R-05-454, Svensk Kärnbränslehantering AB.

Rhén I, Gustafson G, Stansfors, R, Wikberg P, 1997. Äspö HRL – Geoscientific evaluation 1997/5. Models based on site characterization 1986–1995. SKB TR-97-06, Svensk Kärnbränslehantering AB.

Rhén I, Forsmark T, 2001. Äspö Hard Rock Laboratory, Prototype repository, Hydrogeology, Summary report of investigations before the operation phase. SKB IPR-01-65, Svensk Kärnbränslehantering AB.

Rhén I, Forsmark T, Forssman I, Zetterlund M, 2006. Hydrogeological single-hole interpretation of KLX02, KLX03, KLX04, KAV04A and KAV04b, Preliminary site description, Laxemar subarea – version 1.2, SKB R-06-21, Svensk Kärnbränslehantering AB.

Serco Assurance, 2005a. CONNECTFLOW Release 9.0 Technical Summary Document, Serco Assurance Report SA/ENV/CONNECTFLOW/15.

Serco Assurance, 2005b. NAMMU Release 9.0 Technical Summary Document, Serco Assurance Report SA/ENV/CONNECTFLOW/8.

Serco Assurance, 2005c. NAPSAC Release 9.0 Technical Summary Document, Serco Assurance Report SA/ENV/CONNECTFLOW/12.

SKB, 2000. Geoscientific programme for investigation and evaluation of sites for the deep repository, SKB TR-00-20, Svensk Kärnbränslehantering AB.

SKB, 2001. Site Investigations. Investigation methods and general execution programme, SKB TR-01-29, Svensk Kärnbränslehantering AB.

SKB, 2004. Hydrogeochemical evaluation of the Simpevarp area, model version 1.2, SKB R-04-74, Svensk Kärnbränslehantering AB.

SKB, 2005. Preliminary site description, Simpevarp subarea – version 1.2, SKB R-05-08, Svensk Kärnbränslehantering AB.

SKB, 2006. Hydrogeochemical Evaluation, Preliminary site description, Laxemar subarea – version 1.2, SKB R-06-12, Svensk Kärnbränslehantering AB.

Terzaghi R, 1965. Sources of error in joint surveys. Geotechnique 15(3): 287–304.

Tullborg E-L, Larson S Å, 1984. $\delta^{18}O$ and $\delta^{13}C$ for limestones,calcite fissure infillings and calcite precipitates from Sweden. Geologiska Föreningens i Stockholm Förhandlingar, 106, 127–130.

Werner K, Bosson E, Berglund S, 2005. Laxemar 1.2. Background report for climate, surface hydrology and near-surface hydrogeology. SKB R-05-61, Svensk Kärnbränslehantering AB.

Westman P, Wastegård S, Schoning K, Gustafsson B, Omstedt A, 1999. Salinity change in the Baltic Sea during the last 8500 years: evidence, causes and models. SKB TR-99-38, Svensk Kärnbränslehantering AB.

Appendix A

Analysis of hydrogeological data

A.1 KLX02, Orientation and transmissivity of PFL-anomalies

The orientation of features located closest to each PFL-anomaly has been plotted for KLX02 (Figure A-1 and Figure A-2). All the features within a certain distance (< 0.5 m) of each PFL-anomaly are shown; coloured by measured transmissivity, as well as flow anomalies associated with the deformation zones DZ1. Although there is no obvious dominating orientation of conductive fractures, the highest flows are found in Set_B. The transmissivity of each flowing feature has been plotted against elevation for the PFL-anomalies (Figure A-3). Flow is noted throughout the borehole but is greatest at shallow elevations (< 350 m).

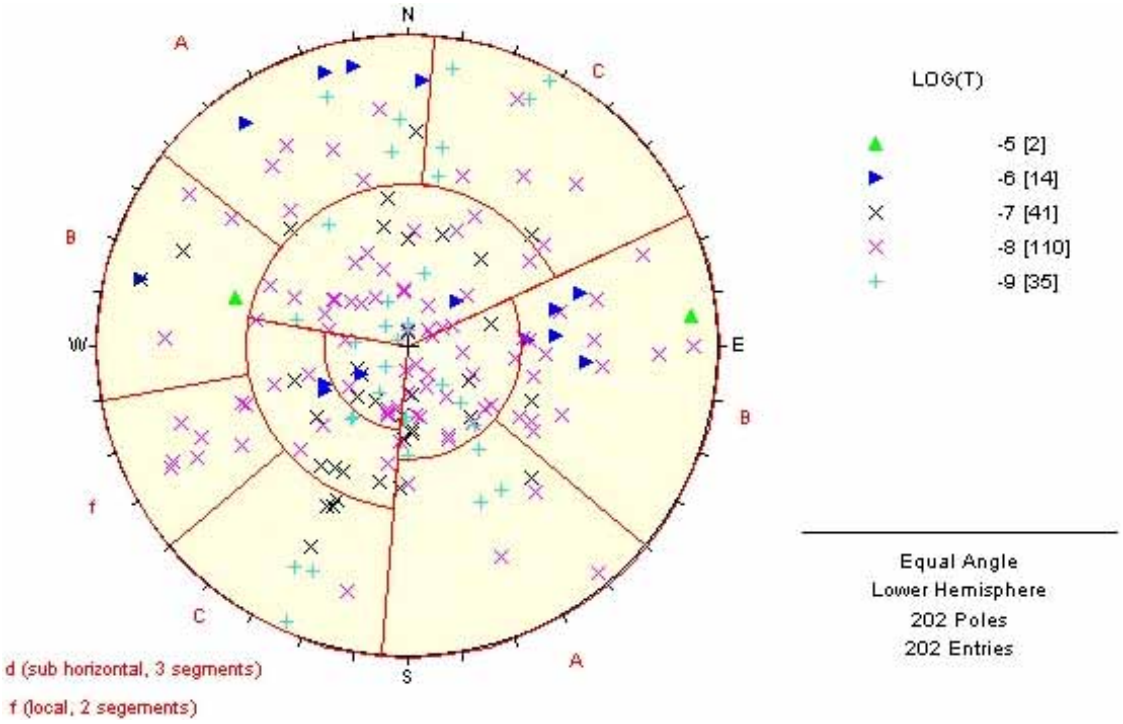

Figure A-1. *Orientations of the pole to fractures associated with PFL-anomalies in KLX02, for all fractures (including DZ's). Fractures are coloured by magnitude of the transmissivity of the PFL-anomaly. The set divisions and the names of each set are superimposed in red.*

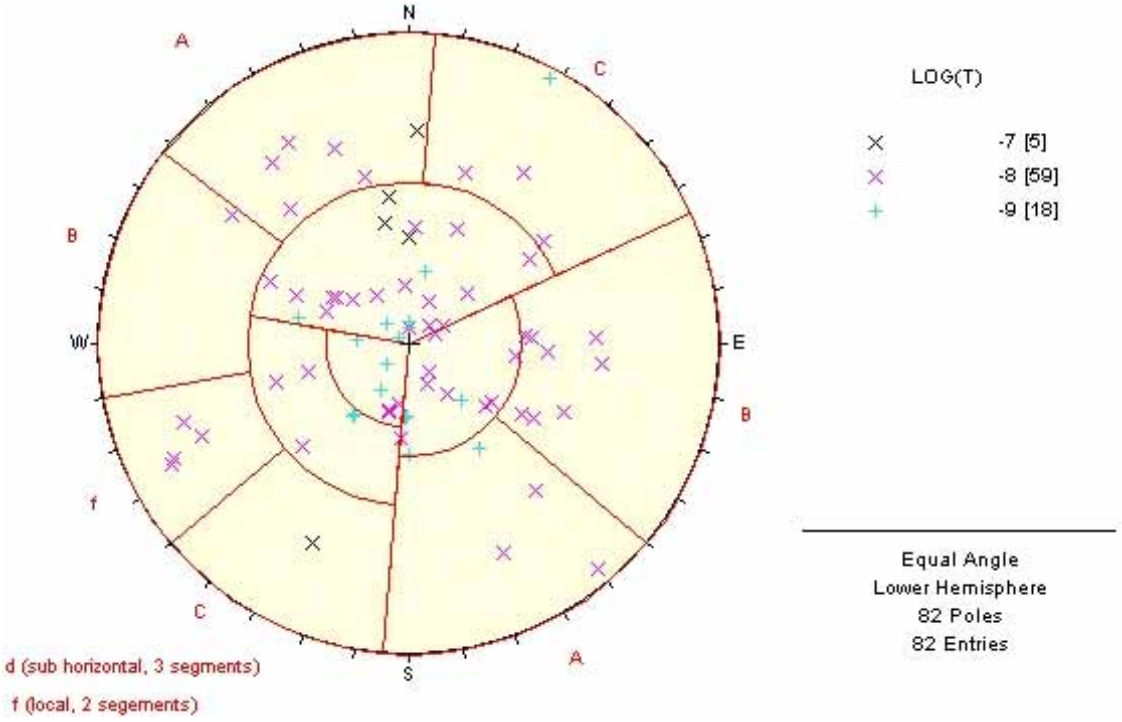

Figure A-2. *Orientations of the pole to fractures associated with PFL-anomalies in KLX02, for the deformation zones (DZ1). Fractures are coloured by magnitude of the transmissivity of the PFL-anomaly. The set divisions and the names of each set are superimposed in red.*

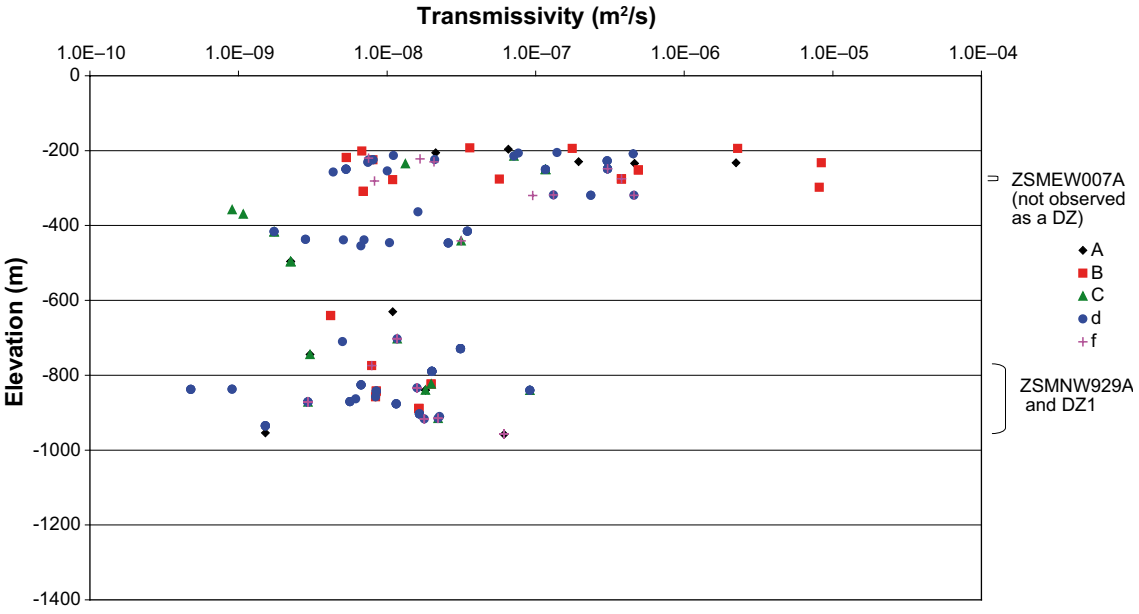

Figure A-3. *Transmissivity of PFL-anomalies against elevation for KLX02. Each PFL-anomaly is coloured by fracture set. The colouring depends on the orientation of the closest fracture(s), hence one PFL-anomaly may have more than one associated orientation if there are several close fractures. Only data down to –1,000 m elevation are shown.*

A.2 KLX03, Orientation and transmissivity of PFL-anomalies

The orientation of features located closest to each PFL-anomaly has been plotted for KLX03 (Figure A-4 and Figure A-5). All the features within a certain distance (< 0.5 m) of each PFL-anomaly are shown, coloured by measured transmissivity, as well as flow anomalies associated with DZ1. It is clear from these figures that the dominating conductive fractures are sub-horizontal or steeply dipping features with strike to the NW. The transmissivity of each flowing feature has been plotted against elevation for the PFL-anomalies (Figure A-6), and for 100 m PSS data (Figure A-7). 5 m and 20 m PSS data were not available in this data freeze. Flow is noted throughout the borehole, with the most transmissive flows observed in the sub-horizontal set (Set_d). Flow is greatest at shallow elevations (< 300 m), and near DZ1. The 100 m PSS data shows flow at all elevations.

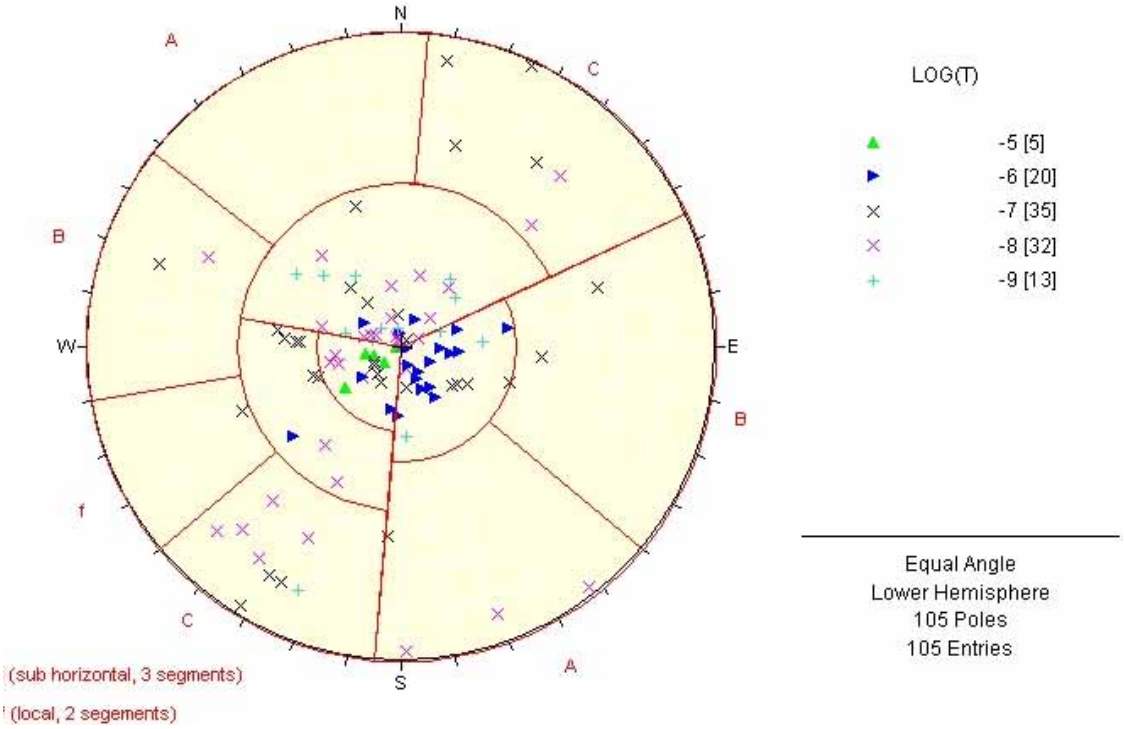

Figure A-4. *Orientations of the pole to fractures associated with PFL-anomalies in KLX03, for all fractures (including DZ's). Fractures are coloured by magnitude of the transmissivity of the PFL-anomaly. The set divisions and the names of each set are superimposed in red.*

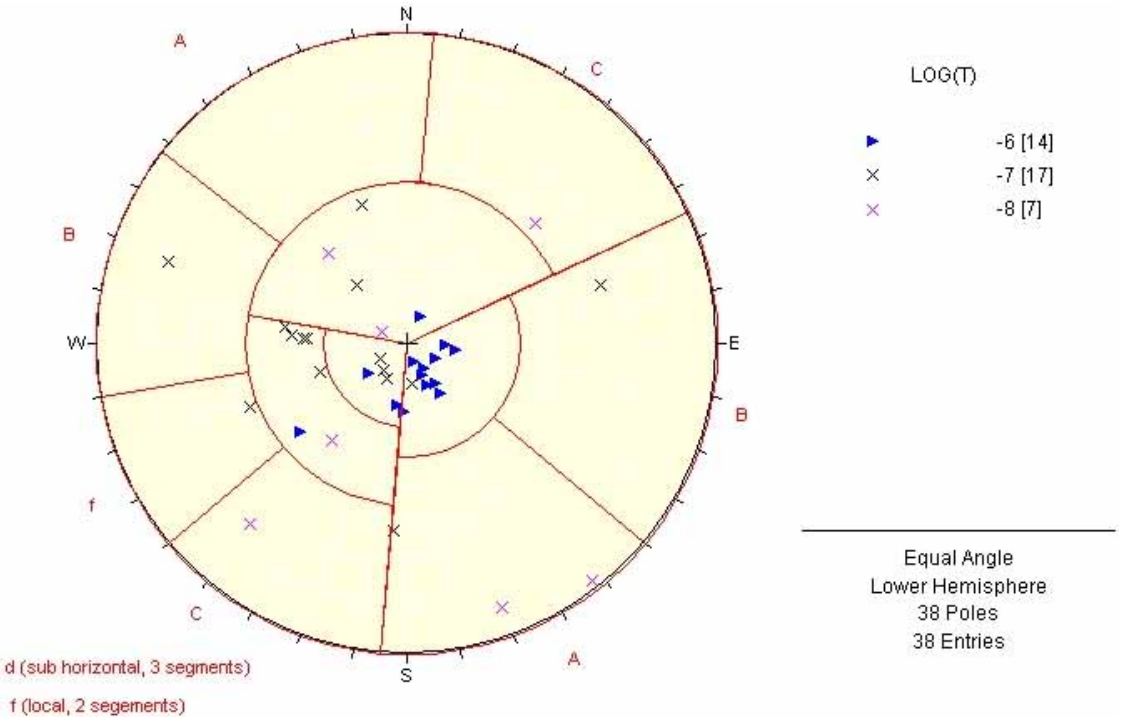

Figure A-5. *Orientations of the pole to fractures associated with PFL-anomalies in KLX03, for the deformation zones (DZ1). Fractures are coloured by magnitude of the transmissivity of the PFL-anomaly. The set divisions and the names of each set are superimposed in red.*

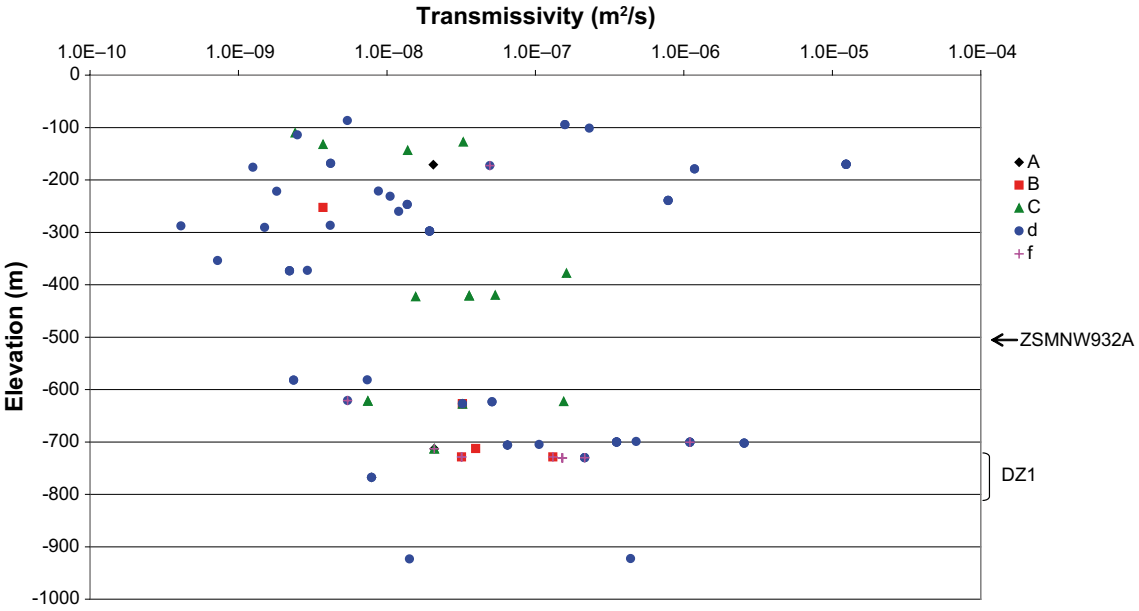

Figure A-6. *Transmissivity of PFL-anomalies against elevation for KLX03. Each PFL-anomaly is coloured by fracture set. The colouring depends on the orientation of the closest fracture(s), hence one PFL-anomaly may have more than one associated orientation if there are several close fractures.*

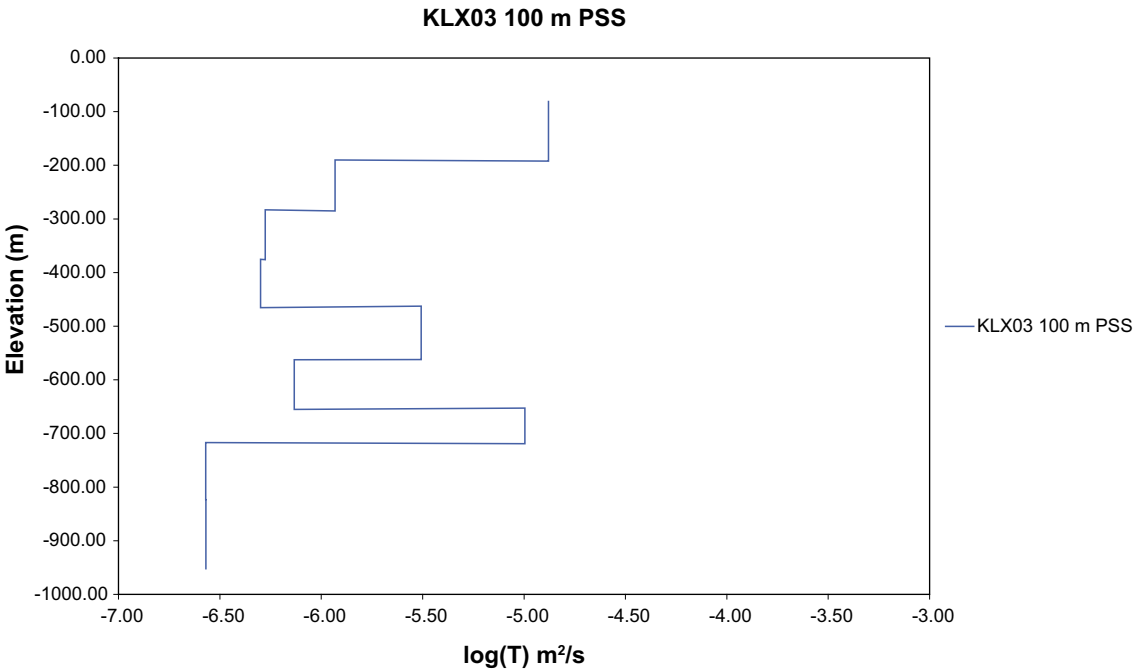

Figure A-7. *Transmissivity of 100 m borehole intervals with measurable flow recorded by PSS in KLX03.*

A.3 KSH01A, Orientation and transmissivity of PFL-anomalies

The orientation of features located closest to each PFL-anomaly has been plotted for KSH01A (Figure A-8 and Figure A-9). All the features nearest each PFL-anomaly (< 0.5 m) are shown, coloured by measured transmissivity, as well as flow anomalies associated the deformation zones. It is clear from these figures that the dominating conductive fractures are sub-horizontal. The transmissivity of each flowing feature has been plotted against elevation for the PFL-anomalies (Figure A-10). Flow is noted down to –700 m elevation, (no data below –700 m elevation). The most transmissive flows are observed in the sub-horizontal set (Set_d). PSS measurements for KSH01A are shown in Figure A-11.

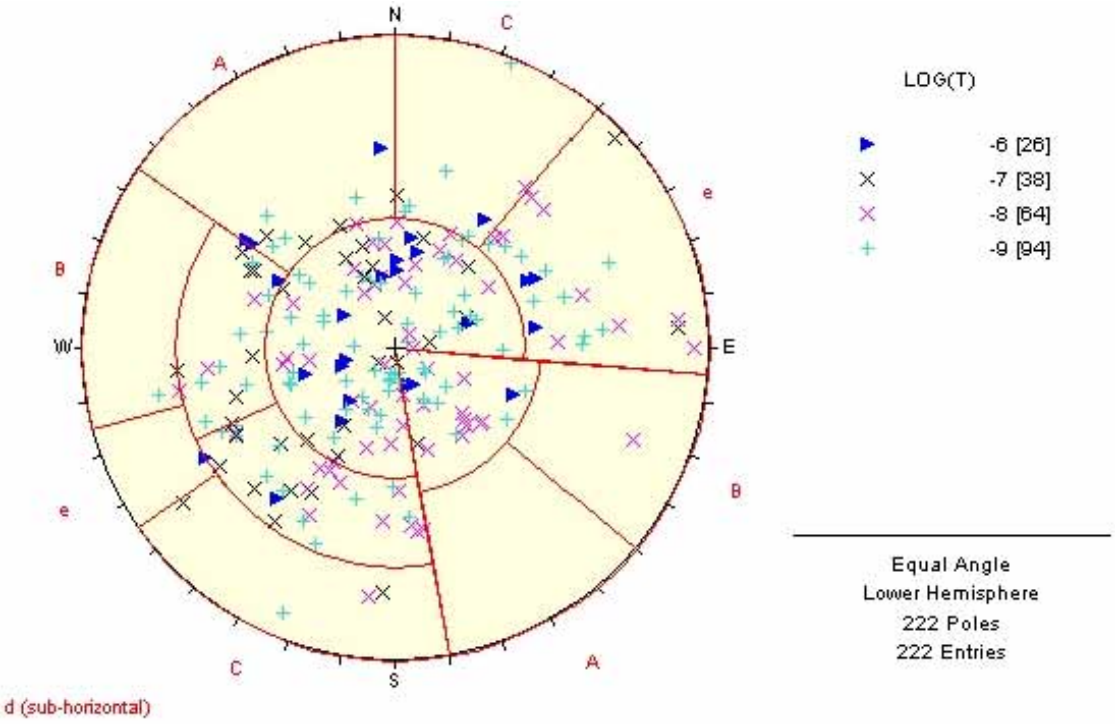

Figure A-8. *Orientations of the pole to fractures associated with PFL-anomalies in KSH01A, for all fractures (including DZ's). Fractures are coloured by magnitude of the transmissivity of the PFL-anomaly. The set divisions and the names of each set are superimposed in red.*

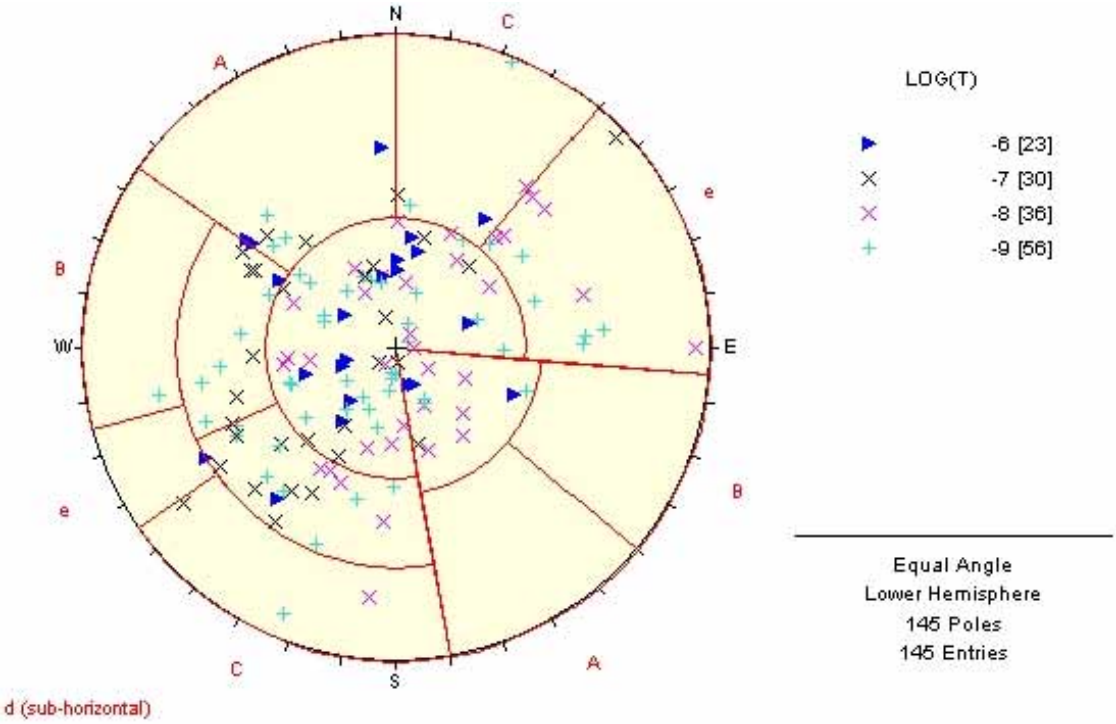

Figure A-9. *Orientations of the pole to fractures associated with PFL-anomalies in KSH01A, for the deformation zones (DZ1 to DZ13). Fractures are coloured by magnitude of the transmissivity of the PFL-anomaly. The set divisions and the names of each set are superimposed in red.*

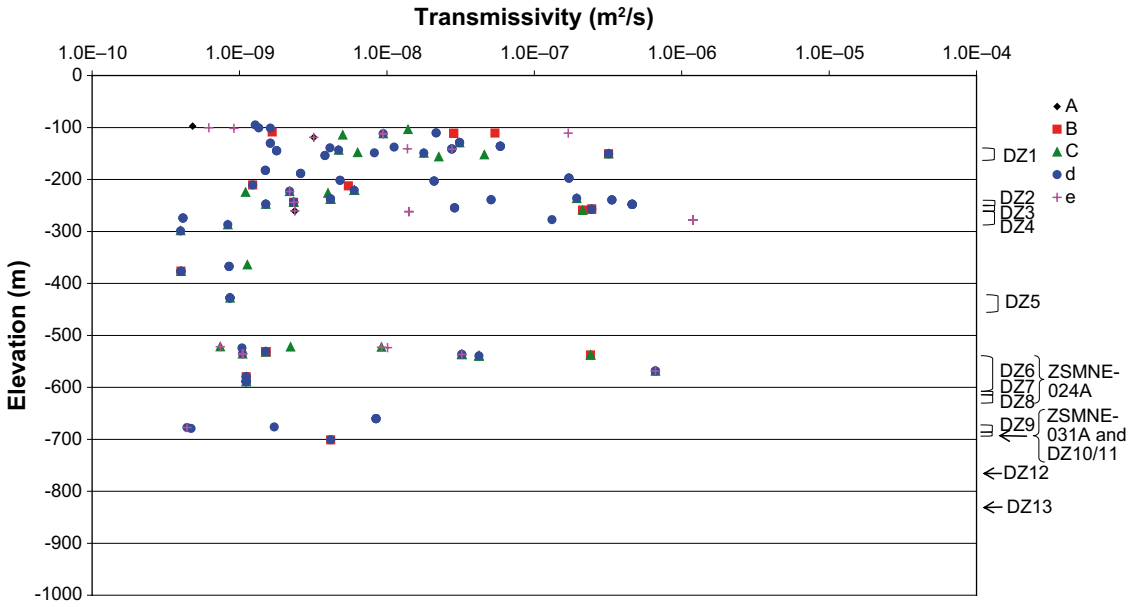

Figure A-10. *Transmissivity of PFL-anomalies against elevation for KSH01A. Each PFL-anomaly is coloured by fracture set. The colouring depends on the orientation of the closest fracture(s), hence one PFL-anomaly may have more than one associated orientation if there are several close fractures.*

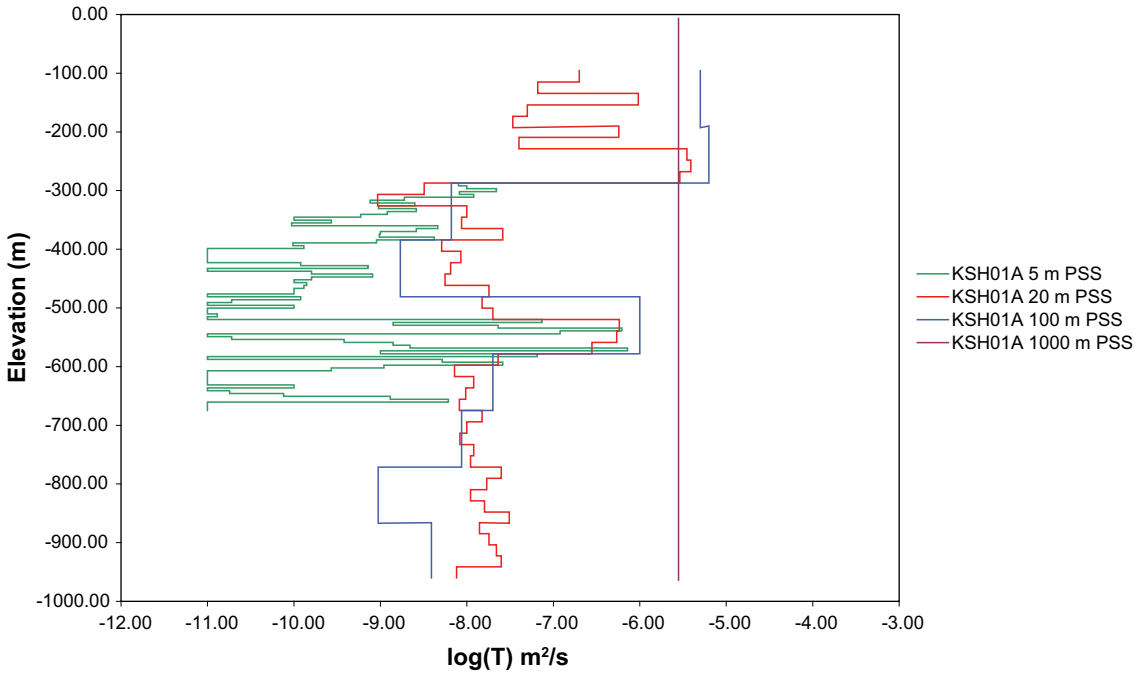

Figure A-11. *Transmissivity of 5 m, 20 m, 100 m and 1,000 m borehole intervals with measurable flow recorded by PSS in KSH01A.*

A.4 KSH02, Orientation and transmissivity of PFL-anomalies

The orientation of features located closest to each PFL-anomaly has been plotted for KSH02 (Figure A-12 and Figure A-13). All the features nearest each PFL-anomaly (< 0.5 m) are shown, coloured by measured transmissivity, as well as flow anomalies associated the deformation zones. It is clear from these figures that the dominating conductive fractures are sub-horizontal, with most of the higher flows in the deformation zones. The transmissivity of each flowing feature has been plotted against elevation for the PFL-anomalies (Figure A-14). Flow is noted down at all elevations, with greater flows observed above –200 m elevation. The most transmissive flows are observed in the sub-horizontal set (Set_d). PSS measurements for KSH02 are shown in Figure A-15.

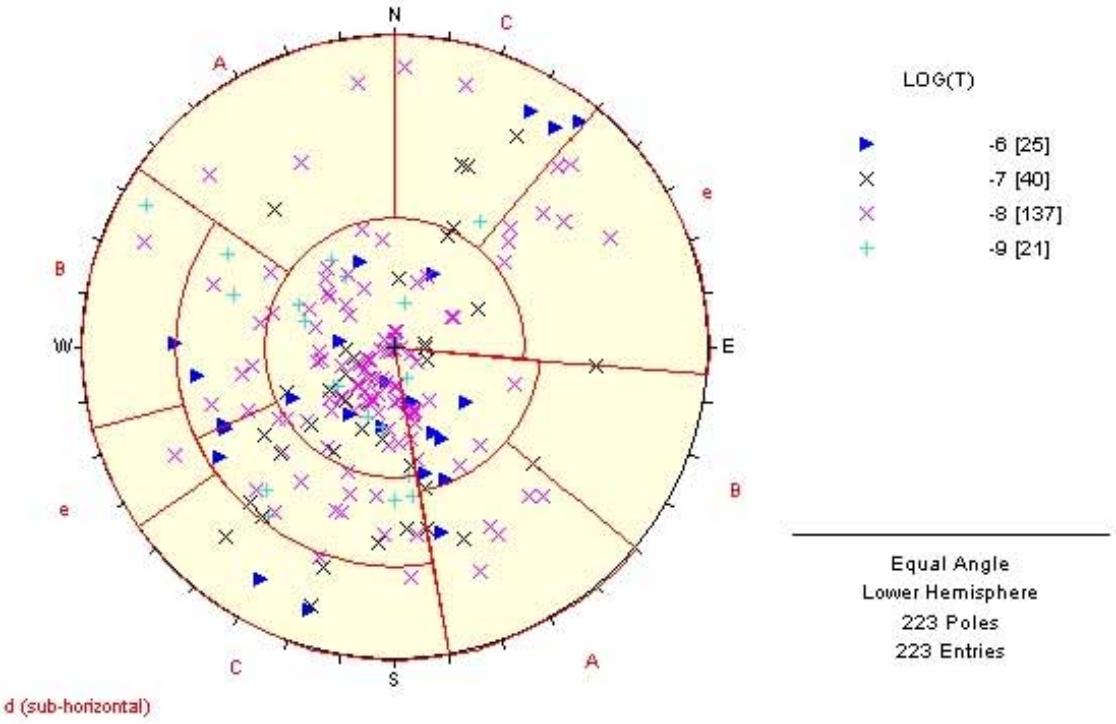

Figure A-12. *Orientations of the pole to fractures associated with PFL-anomalies in KSH02, for all fractures (including DZ's). Fractures are coloured by magnitude of the transmissivity of the PFL-anomaly. The set divisions and the names of each set are superimposed in red.*

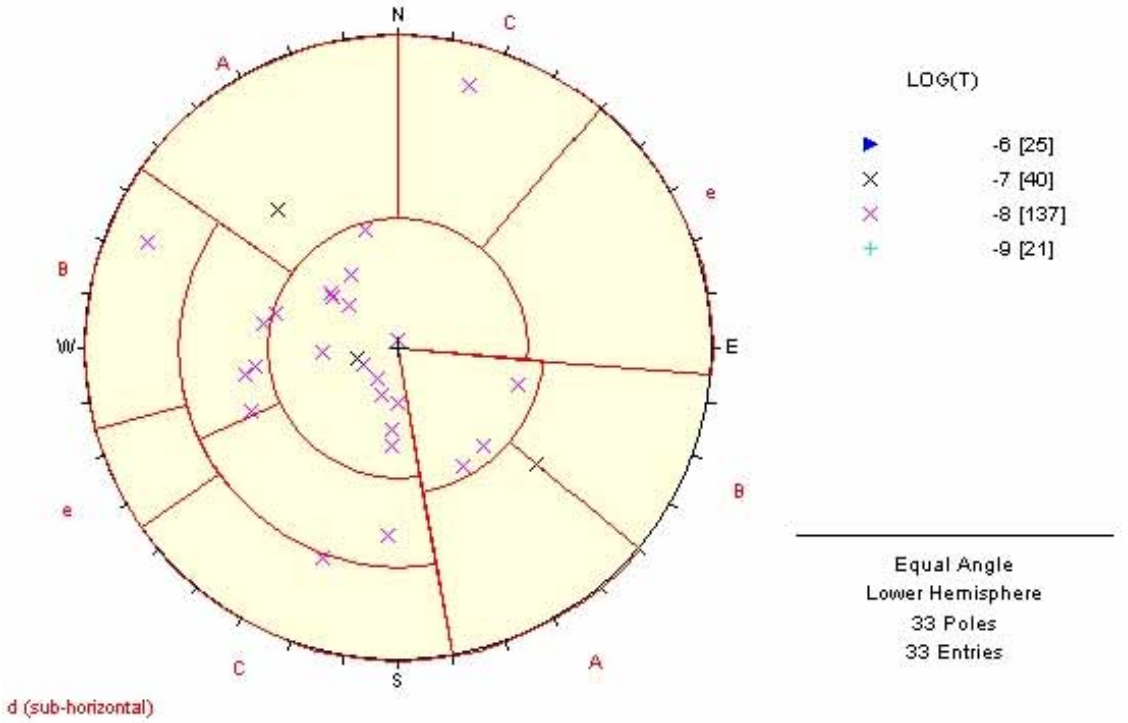

Figure A-13. *Orientations of the pole to fractures associated with PFL-anomalies in KSH02, for the deformation zones (DZ1 to DZ4). Fractures are coloured by magnitude of the transmissivity of the PFL-anomaly. The set divisions and the names of each set are superimposed in red.*

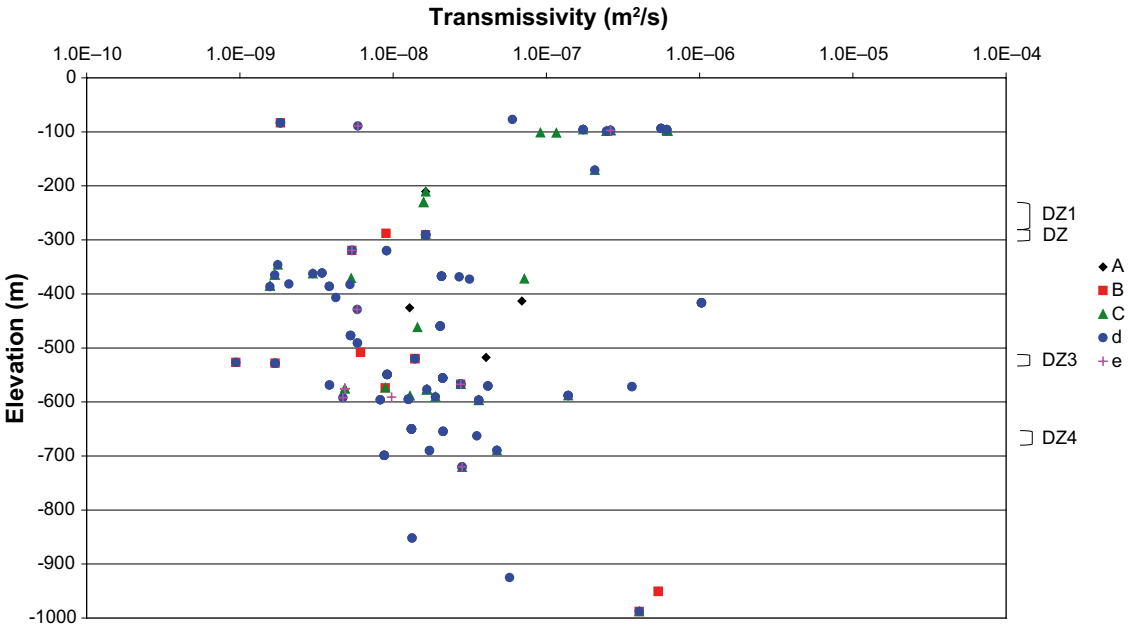

Figure A-14. *Transmissivity of PFL-anomalies against elevation for KSH02. Each PFL-anomaly is coloured by fracture set. The colouring depends on the orientation of the closest fracture(s), hence one PFL-anomaly may have more than one associated orientation if there are several close fractures.*

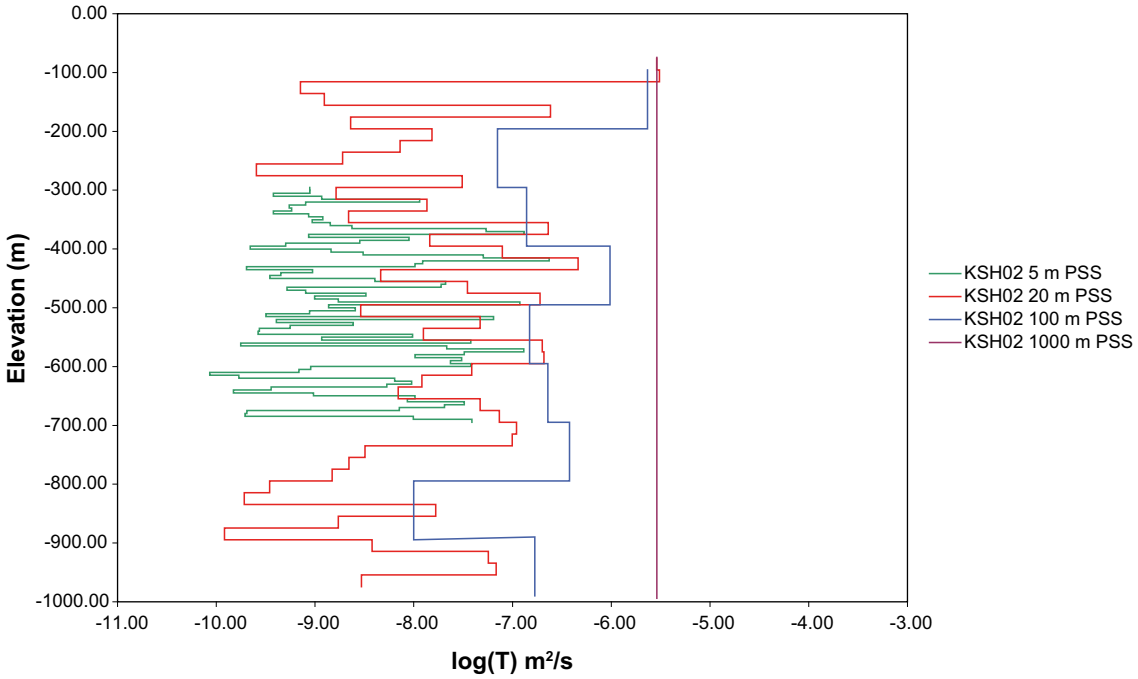

Figure A-15. *Transmissivity of 5 m, 20 m, 100 m and 1,000 m borehole intervals with measurable flow recorded by PSS in KSH02.*

A.5 KAV01, Orientation and transmissivity of PFL-anomalies

The orientation of features located closest to each PFL-anomaly has been plotted for KAV01 (Figure A-16 and Figure A-17). All the features within 0.5 m of each PFL-anomaly are shown; coloured by measured transmissivity, as well as anomalies associated the deformation zones. The dominating conductive fractures are sub-horizontal or steeply dipping features with strike to the NE (Set_A). The transmissivity of each flowing feature has been plotted against elevation for the PFL-anomalies (Figure A-18). Flow is noted above –660 m elevation (no data below –600 m elevation), with the most transmissive flows observed in the sub-horizontal set (Set_d). Flow is greatest near to ZSMNE012A (DZ1, DZ2 and DZ3). There are no PSS measurements for KAV01.

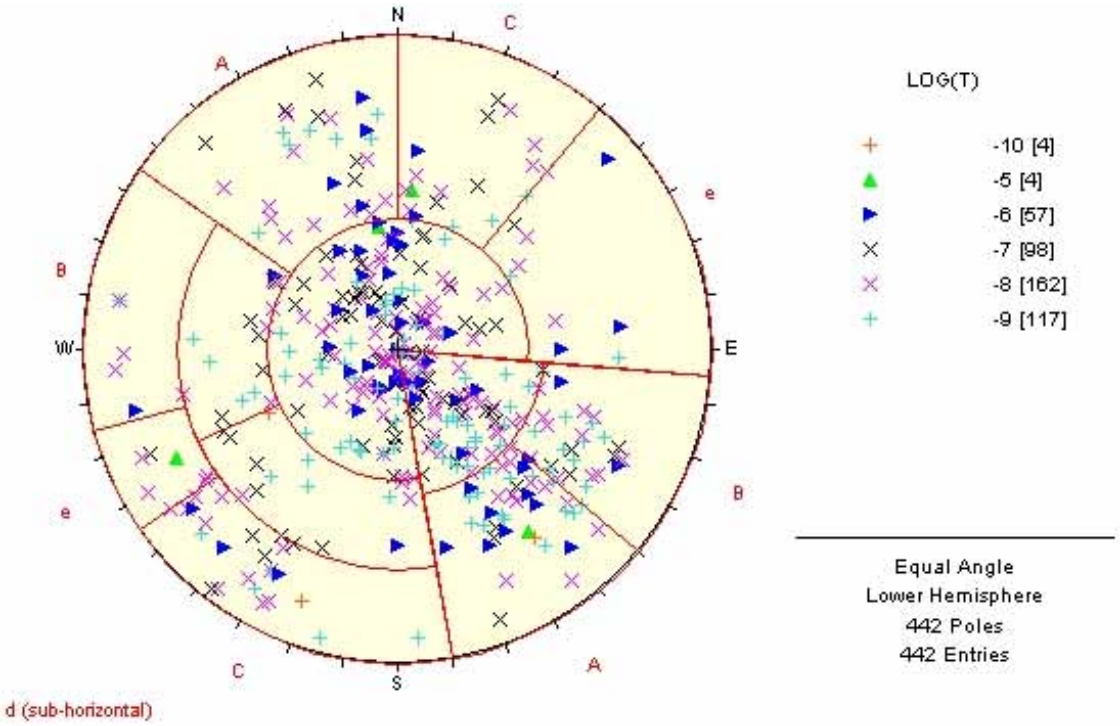

Figure A-16. *Orientations of the pole to fractures associated with PFL-anomalies in KAV01, for all fractures (including DZ's). Fractures are coloured by magnitude of the transmissivity of the PFL-anomaly. The set divisions and the names of each set are superimposed in red.*

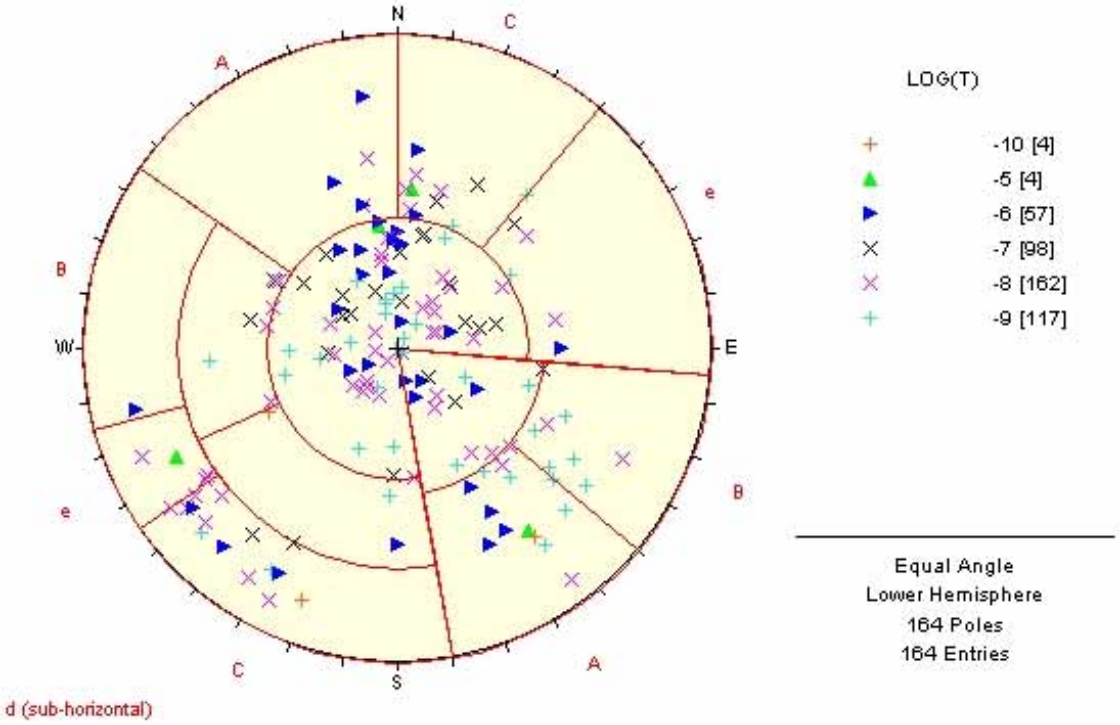

Figure A-17. *Orientations of the pole to fractures associated with PFL-anomalies in KAV01, for the deformation zones (DZ1, DZ2 and DZ3). Fractures are coloured by magnitude of the transmissivity of the PFL-anomaly. The set divisions and the names of each set are superimposed in red.*

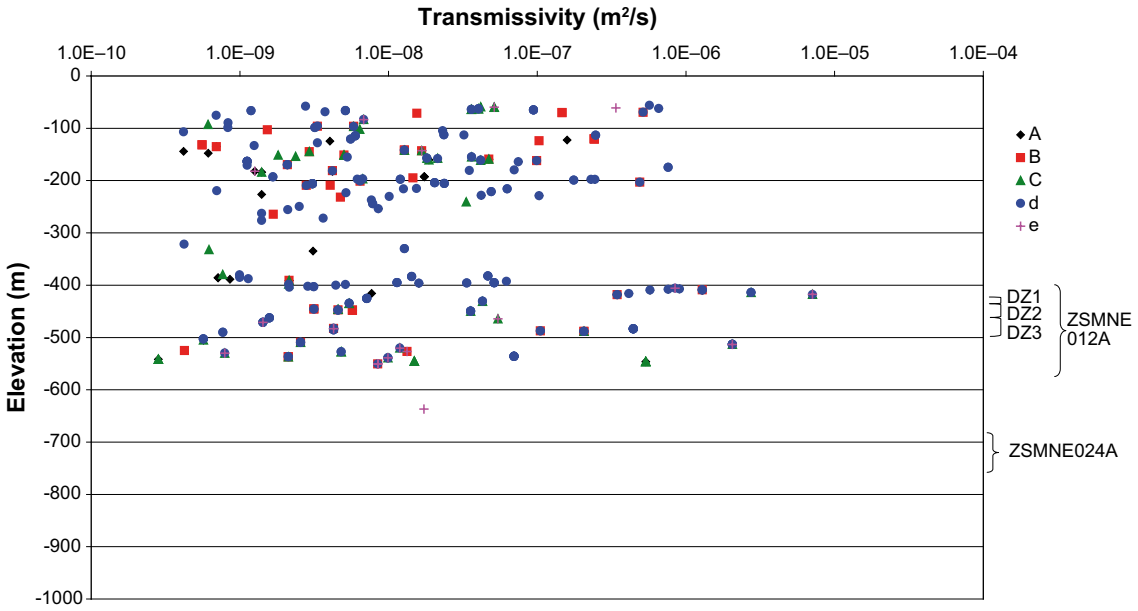

Figure A-18. *Transmissivity of PFL-anomalies against elevation for KAV01. Each PFL-anomaly is coloured by fracture set. The colouring depends on the orientation of the closest fracture(s), hence one PFL-anomaly may have more than one associated orientation if there are several close fractures.*

A.6 KAV04A, Orientation and transmissivity of PFL-anomalies

The orientation of features located closest to each PFL-anomaly has been plotted for KAV04A/B (Figure A-19). All the features within 0.5 m of each PFL-anomaly are shown, coloured by measured transmissivity. There is only one flow anomalies associated the deformation zone (DZ1), oriented in Set_B with log(T) of 10^{-7} m^2/s. The dominating conductive fractures are sub-horizontal or steeply dipping features with strike to the NE (Set_A). The transmissivity of each flowing feature has been plotted against elevation for the PFL-anomalies (Figure A-20). Flow is noted down to –840 m elevation, with much flow in KAV04B (above –90 m elevation) (no data below –850 m elevation). The most transmissive flows are observed in the sub-horizontal set (Set_d). There are no PSS measurements for KAV04A/B.

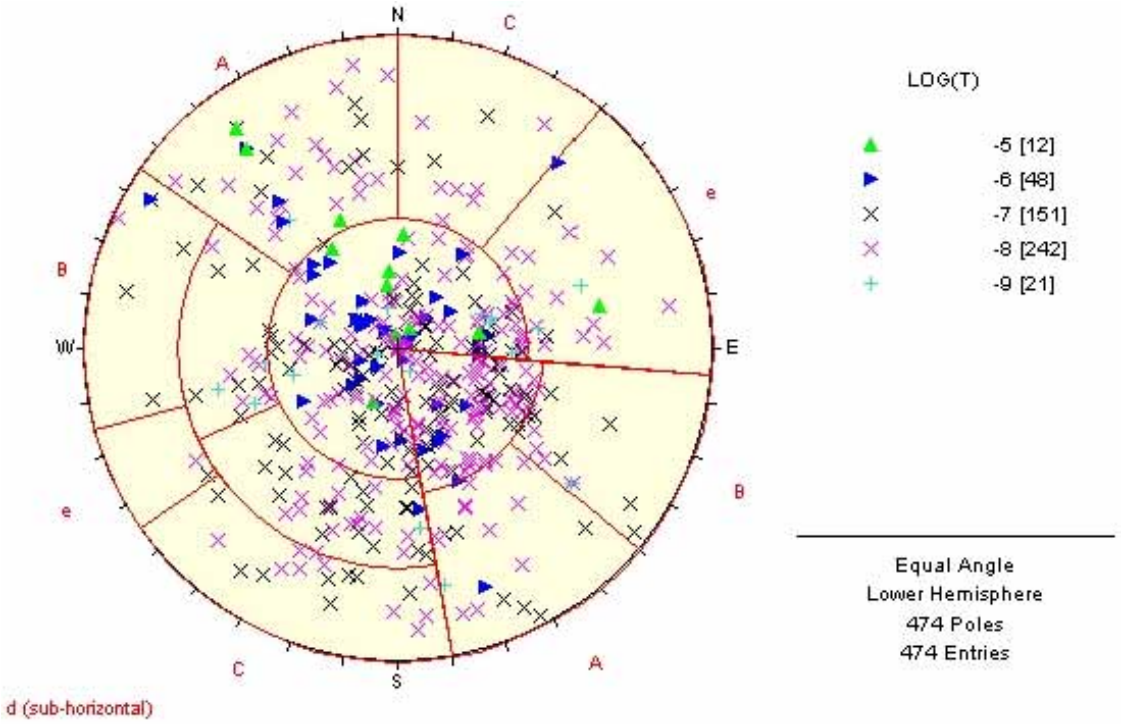

Figure A-19. *Orientations of the pole to fractures associated with PFL-anomalies in KAV04A/B, for all fractures (including DZ's). Fractures are coloured by magnitude of the transmissivity of the PFL-anomaly. The set divisions and the names of each set are superimposed in red.*

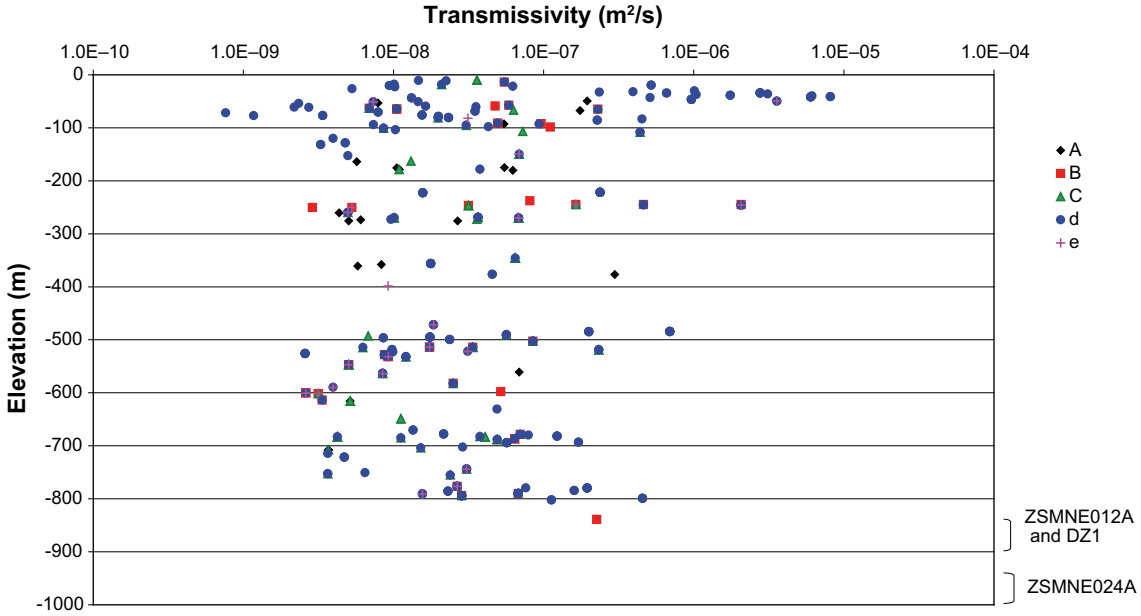

Figure A-20. *Transmissivity of PFL-anomalies against elevation for KAV04A/B. Each PFL-anomaly is coloured by fracture set. The colouring depends on the orientation of the closest fracture(s), hence one PFL-anomaly may have more than one associated orientation if there are several close fractures. KAV04B is shown by flow anomalies shallower than –90 m elevation; KAV04A is represented by flow anomalies deeper than –90 m elevation.*

Appendix B

DFN simulations for KLX03, KSH01A and KAV04A

The following sections detail the DFN models constructed for KLX03, KSH01A and KAV04A. The methodology that has been followed is described in Section 3.6 to Section 3.8

B.1 DFN simulations for KLX03

For the simulations, KLX03 was modelled as vertical with length of 988 m. Two realisations of the DFN model are shown in Figure B-1 with all fractures included and a 400 m diameter model domain surrounding KLX03. The smaller-scale fractures (fracture radii between r_0 and 5.6 m) generated only within a region with a 40 m square horizontal cross-section around KLX03 is shown in Figure B-2. Similar models were used to perform the flow simulations. Figure B-3 shows connected fractures for three realisations of the DFN model around borehole KLX03.

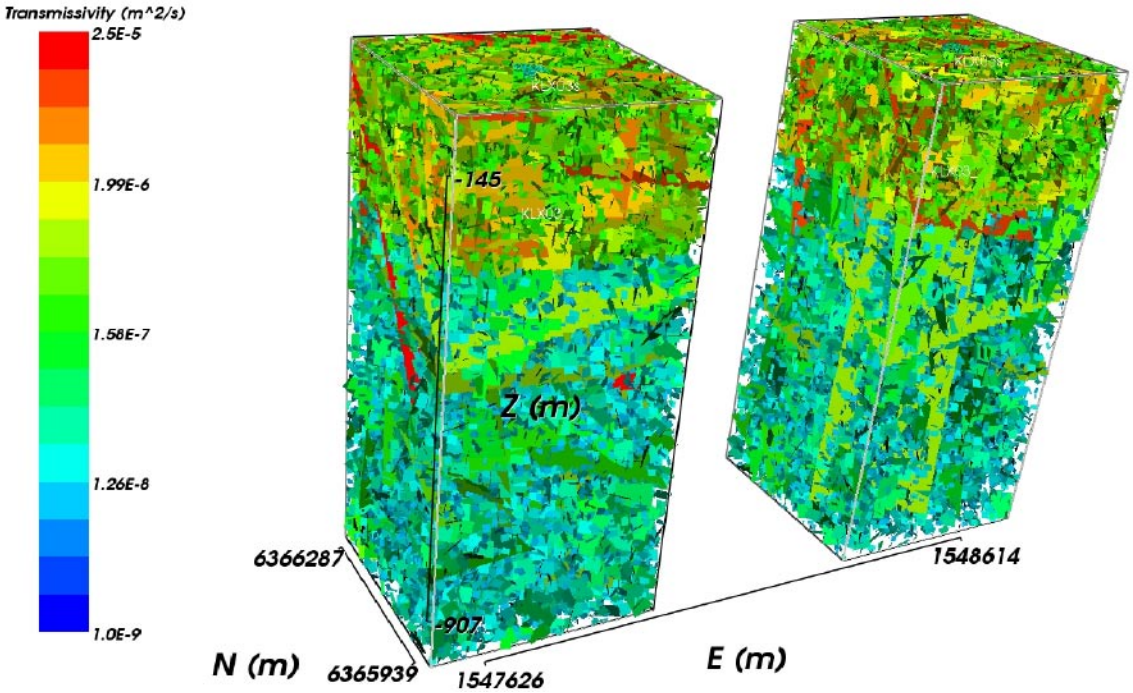

Figure B-1. *Two realisations of the DFN for a domain of 400 m square cross-section and 1,088 m length around borehole KLX03. All fractures are shown and coloured by log(T) (in this case T is correlated to r using a power-law distribution).*

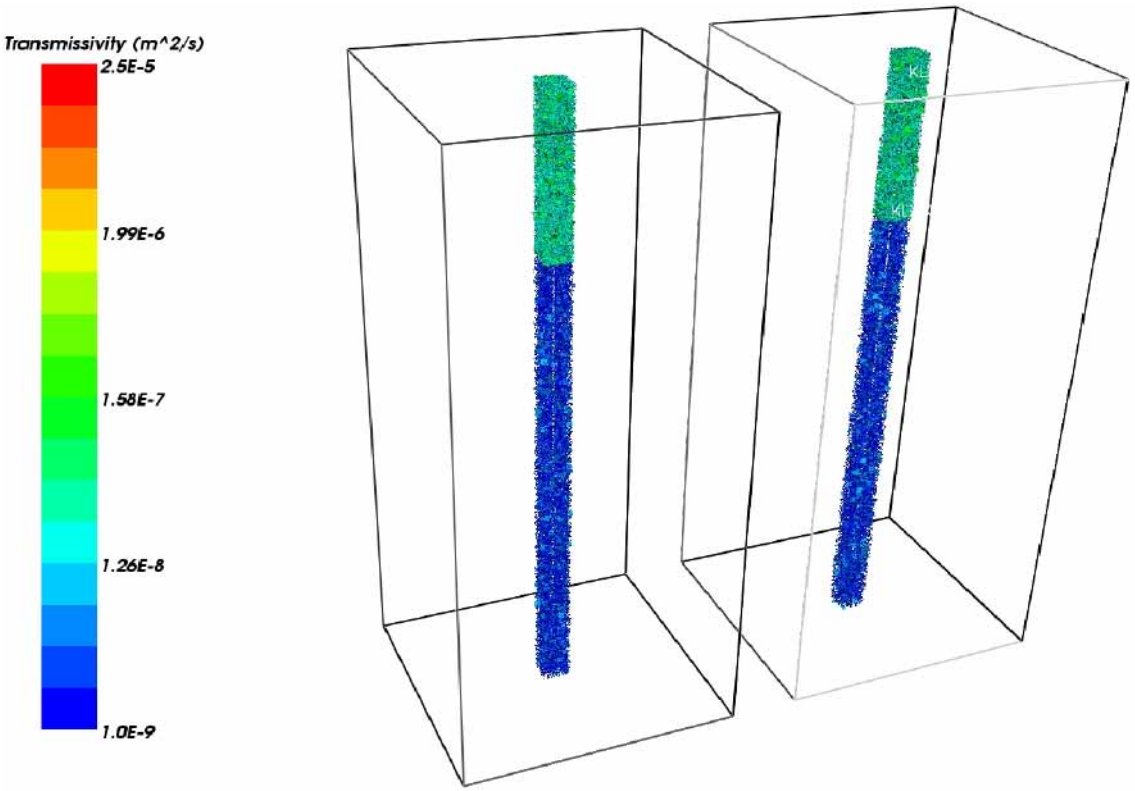

Figure B-2. *Two realisations of the DFN showing just the small-scale fractures generated within a region of 40 m square cross-section around borehole KLX03. Fractures are coloured by log(T) (in this case T is correlated to r using a power-law distribution).*

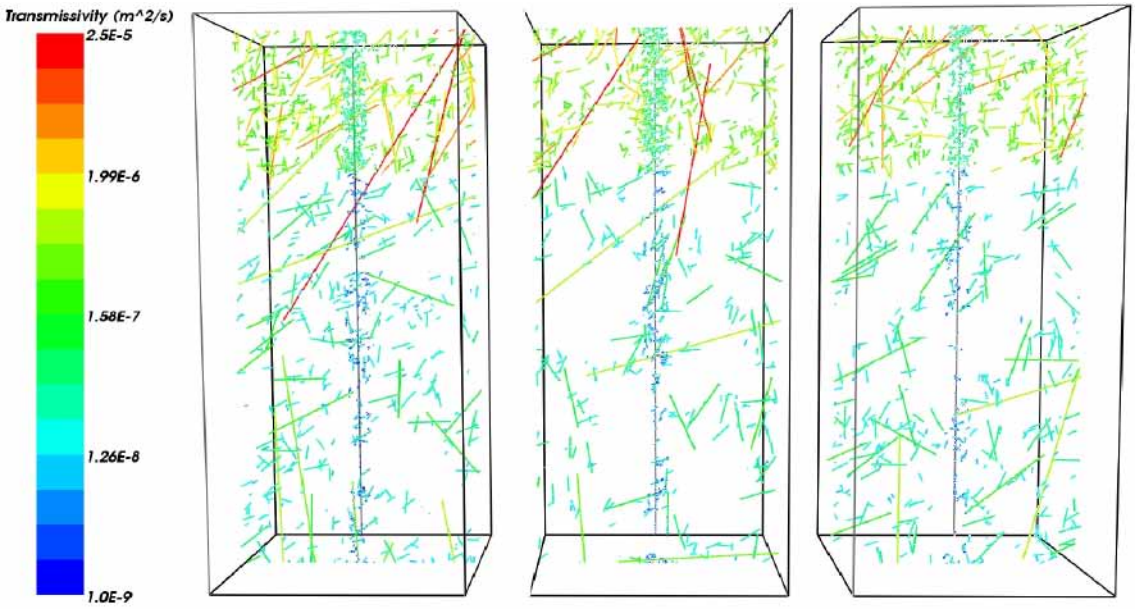

Figure B-3. *Three realisations of the DFN around borehole KLX03 showing only the connected fractures on a vertical N-S slice. Fractures are coloured by log(T) (in this case T is correlated to r using a power-law distribution).*

B.1.1 Conditioning the simulated flow-rate against PFL-f data for KLX03

Each transmissivity model has been matched against the distribution of flow-rate of individual PFL-anomalies, for the 'k_r fit' cases above –300 m and below –300 m, for each of the correlated, semi-correlated and uncorrelated transmissivity cases (Figure B-4, Figure B-7, Figure B-10, Figure B-12, Figure B-14, Figure B-16). There is no PSS data for KLX03. The orientation of the simulated flowing features in each fracture set has also been compared to the orientation of the closest features to each PFL-anomaly for the same cases (Figure B-5, Figure B-8, Figure B-11, Figure B-13, Figure B-15, Figure B-17). The fracture orientation plots show the point of the median, minimum and maximum flow-rate associated with each set. One realisation of the simulated flowing features is plotted as a stereonet in Figure B-6 for below –300 m and Figure B-9 for above –300 m elevation and the complete borehole length. These figures can be compared with the measured flows in Appendix A.2.

These figures show that the simulated flow-rate distribution is reasonably well matched against the PFL flow anomalies in the range above the detection limit around 3 10^{-9} m^3/s. The data suggests the high flows are predominantly in Set_C and Set_d. The simulations are consistent in predicting more flow and higher flow is associated with Set_d, but tends to suggest too many PFL-anomalies in Set_A and Set_B.

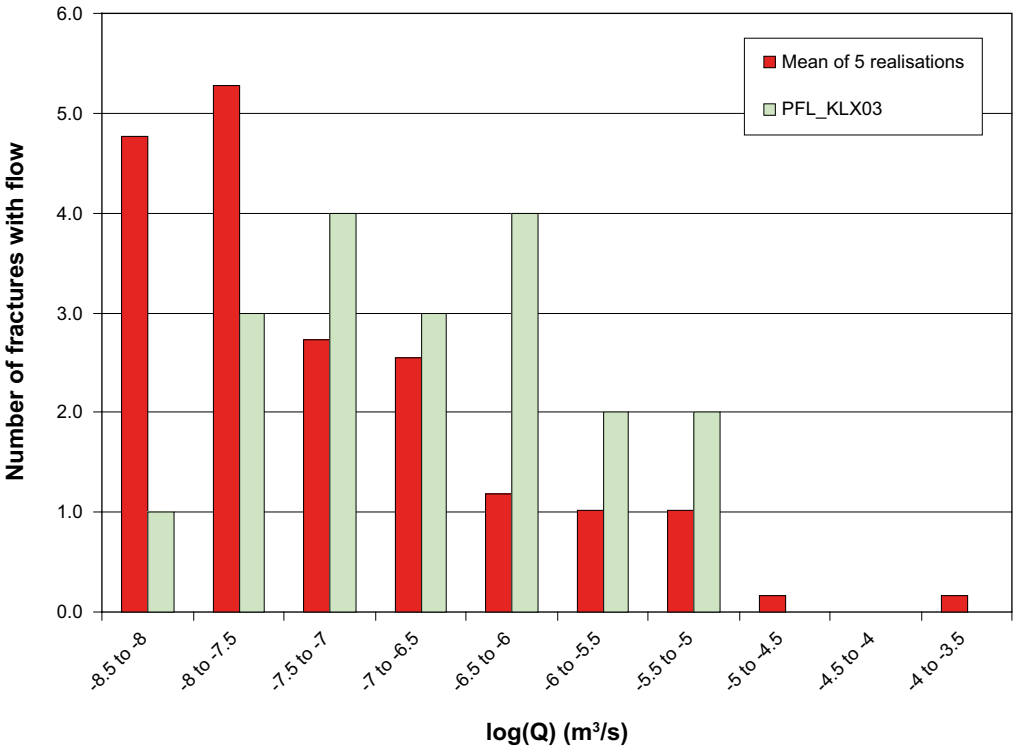

Figure B-4. *Histogram of Log(Q) flow-rate to borehole, for the mean of five realisations compared to the PFL-anomaly data for KLX03 below –300 m. Here, the correlated T distribution is used, from the matched PFL-f and PSS transmissivity with 30% of P32.*

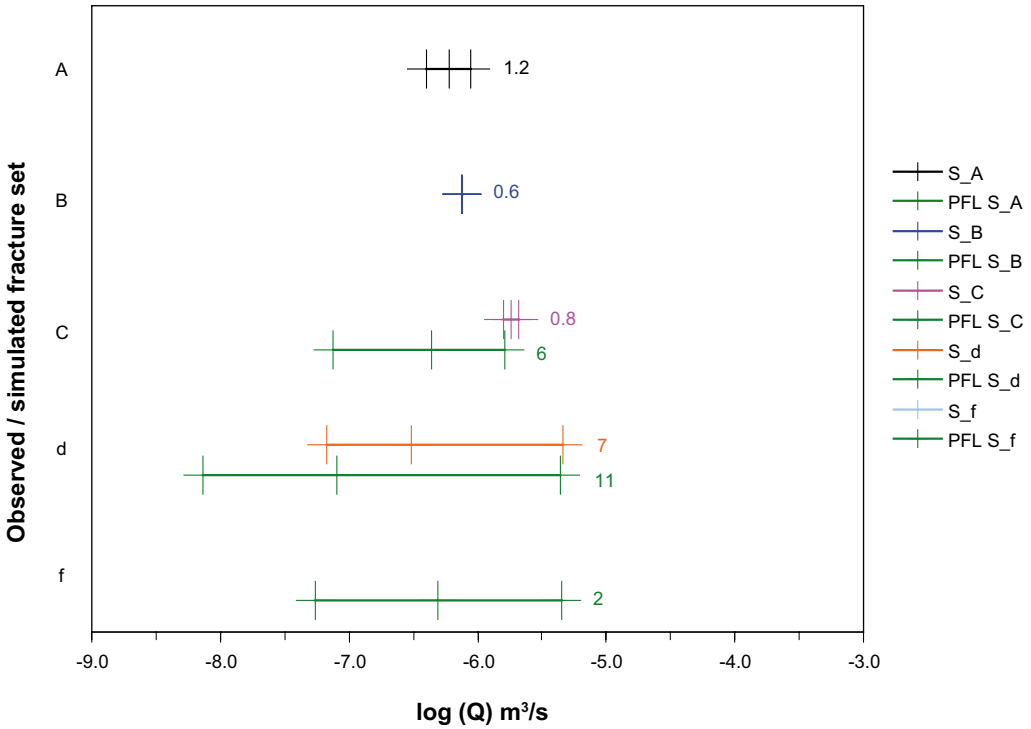

Figure B-5. *Plot of Log(Q) flow-rate to borehole, for the mean of five realisations compared to the PFL-anomaly data for KLX03 below –300 m. The flow in each fracture set is shown, with vertical bars marking the minimum, median and maximum flow-rates. Here, the correlated T distribution is used, from the matched PFL-f and PSS transmissivity with 30% of P32.*

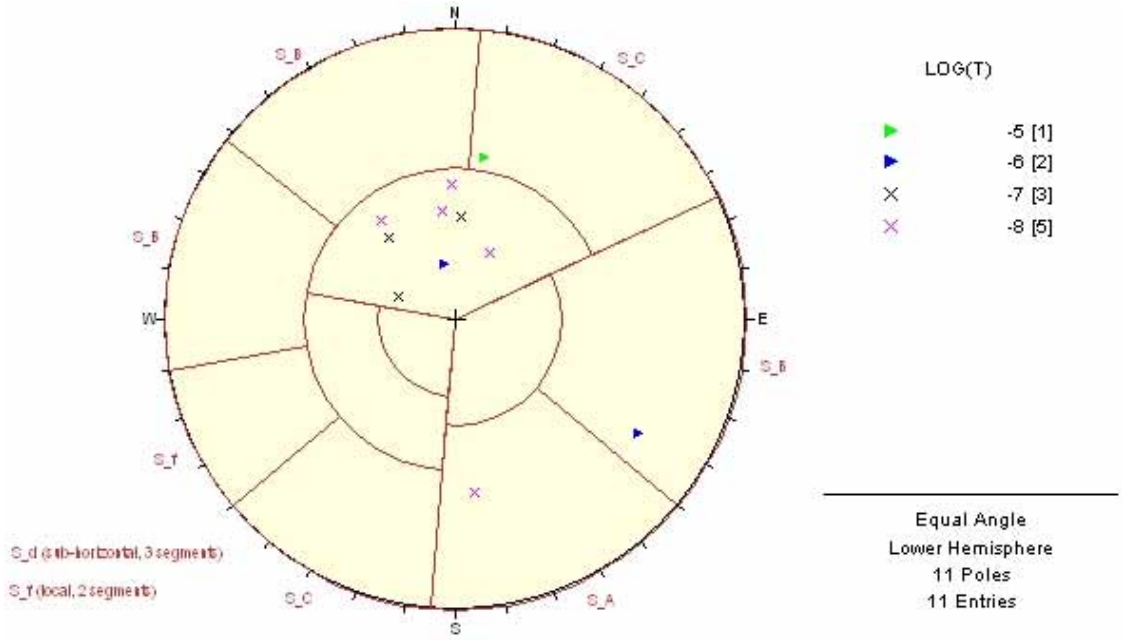

Figure B-6. *Orientations of the simulated flowing features for the correlated case for KLX03 below –300 m. One realisation is shown. Symbols are coloured according to log of transmissivity of each flowing feature (m^2 s^{-1}).*

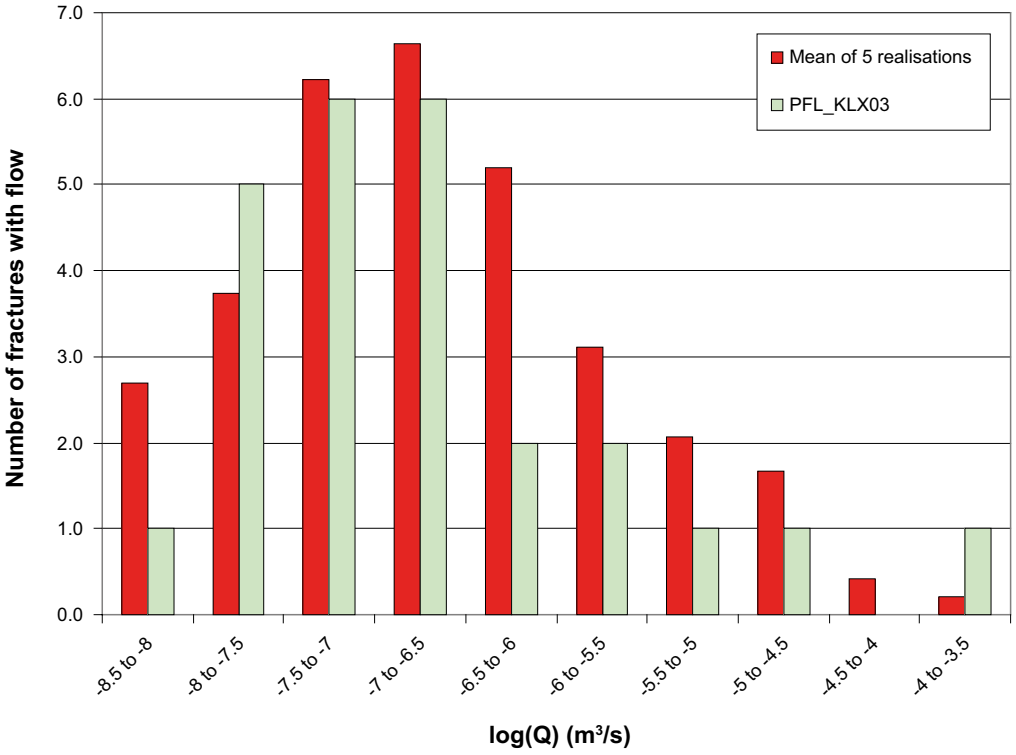

Figure B-7. *Histogram of Log(Q) flow-rate to borehole, for the mean of five realisations compared to the PFL-anomaly data for KLX03 above –300 m. Here, the correlated T distribution is used, from the matched PFL-f and PSS transmissivity with 60% of P32.*

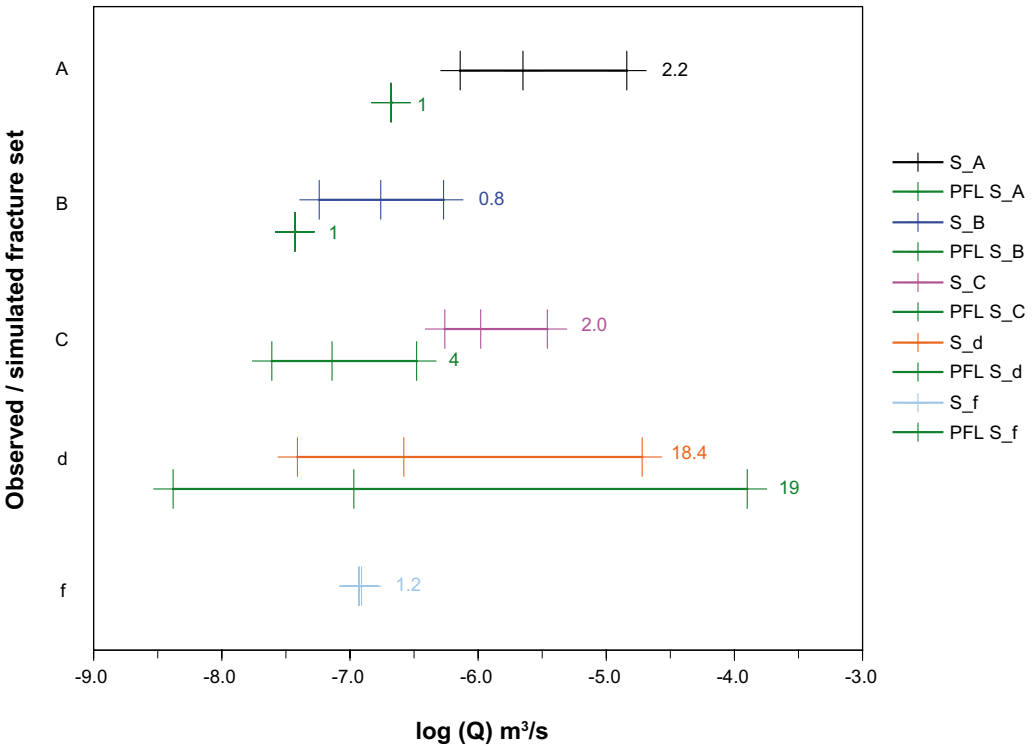

Figure B-8. *Plot of Log(Q) flow-rate to borehole, for the mean of five realisations compared to the PFL-anomaly data for KLX03 above –300 m. The flow in each fracture set is shown, with vertical bars marking the minimum, median and maximum flow-rates. Here, the correlated T distribution is used, from the matched PFL-f and PSS transmissivity with 60% of P32.*

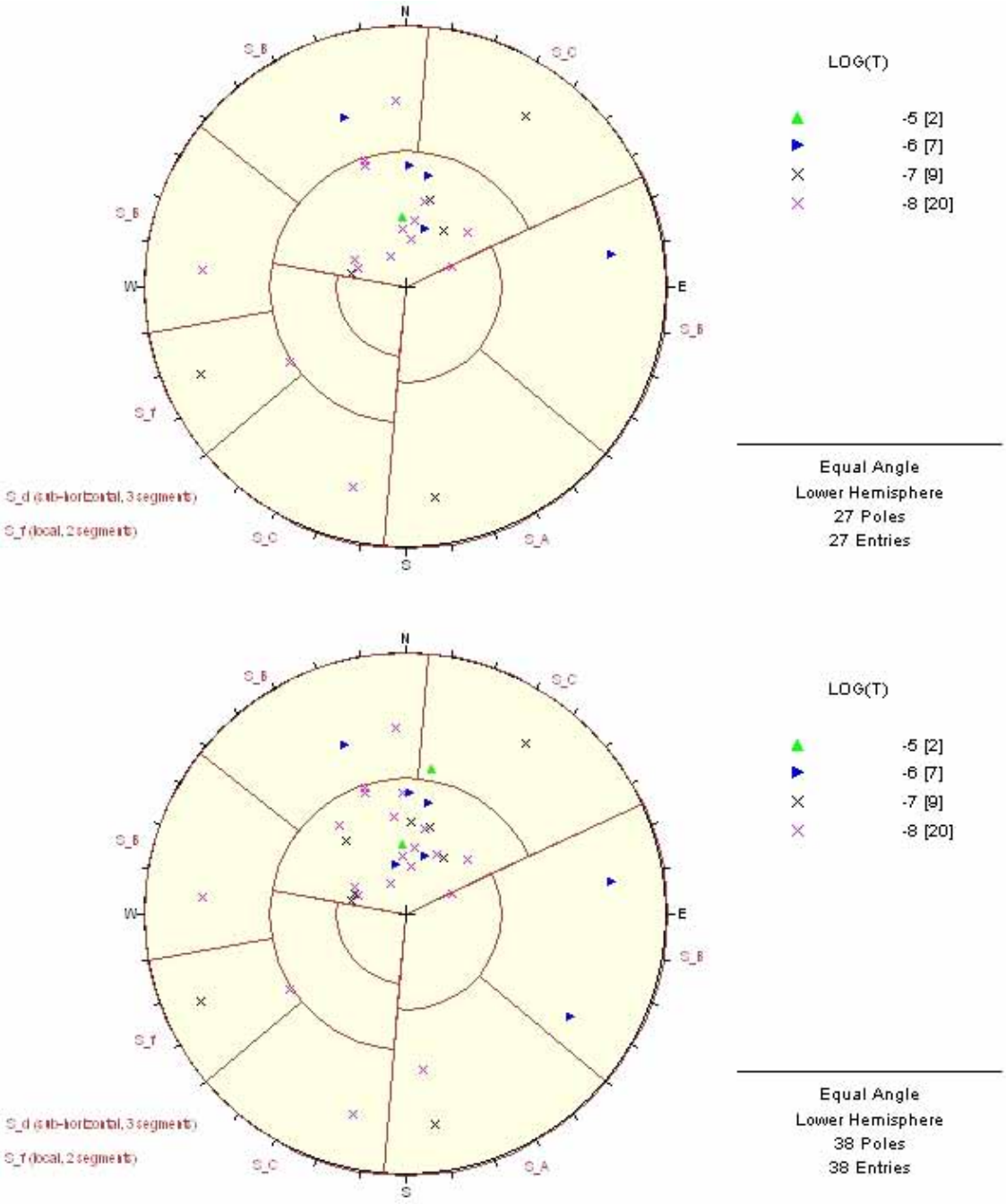

Figure B-9. *Orientations of the simulated flowing features for the correlated case for KLX03 above –300 m (top), and the complete length of KLX03 (bottom). One realisation is shown. Symbols are coloured according to log of transmissivity of each flowing feature ($m^2\ s^{-1}$).*

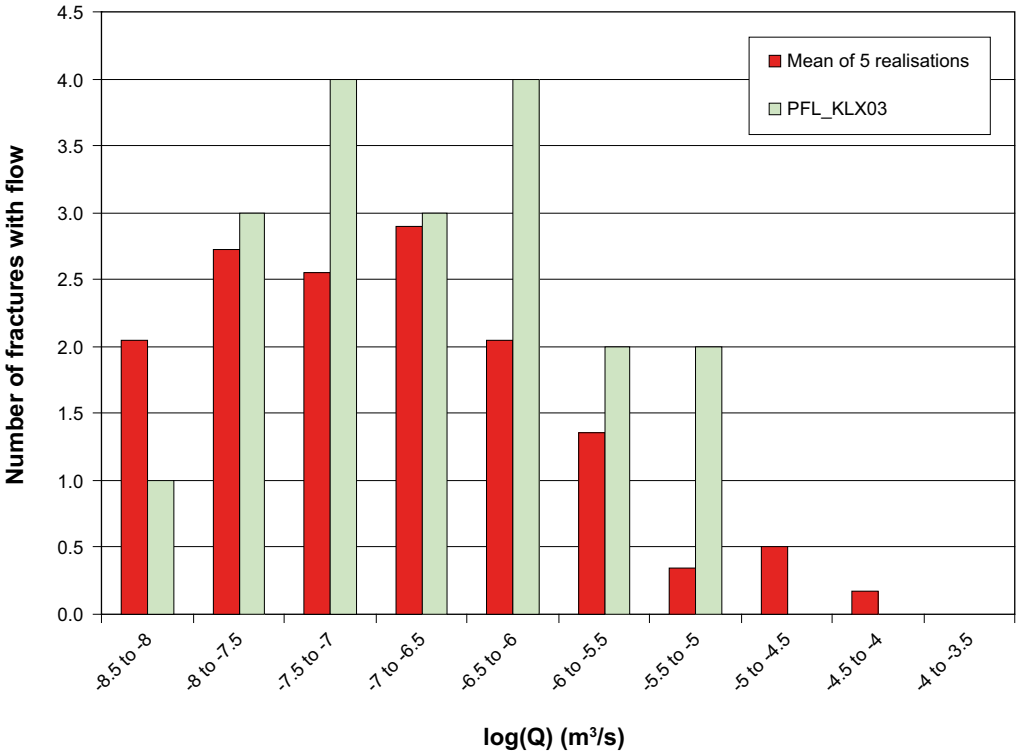

Figure B-10. *Histogram of Log(Q) flow-rate to borehole, for the mean of five realisations compared to the PFL-anomaly data for KLX03 below –300 m. Here, the semi-correlated T distribution is used, from the matched PFL-f and PSS transmissivity with 30% of P32.*

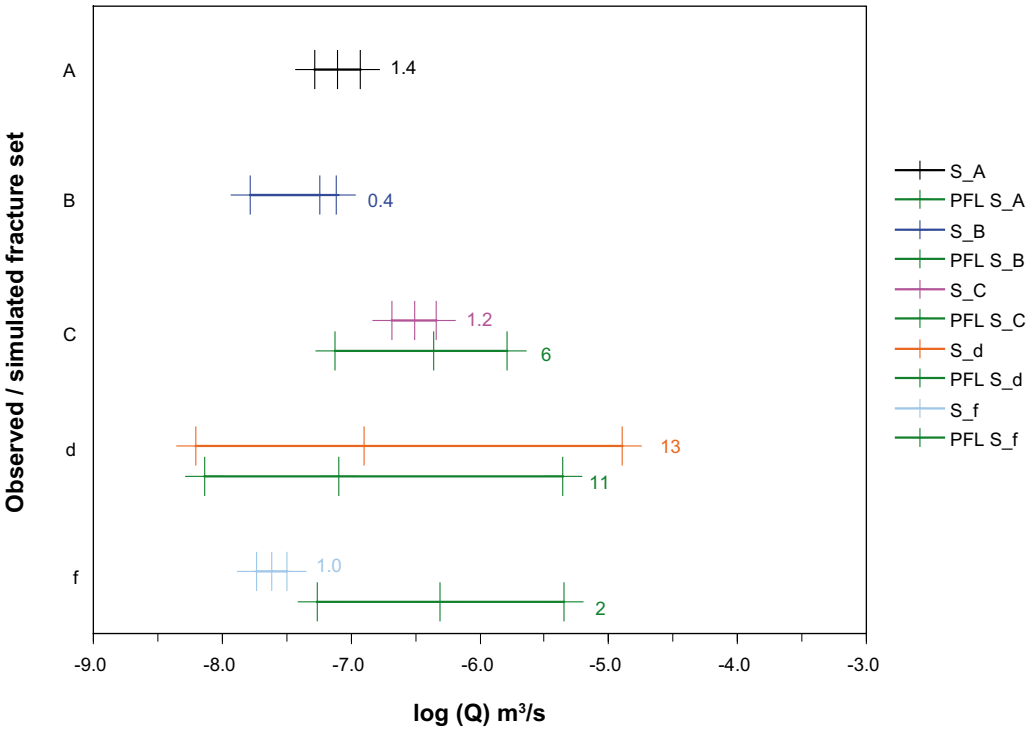

Figure B-11. *Plot of Log(Q) flow-rate to borehole, for the mean of five realisations compared to the PFL-anomaly data for KLX03 below –300 m. The flow in each fracture set is shown, with vertical bars marking the minimum, median and maximum flow-rates. Here, the semi-correlated T distribution is used, from the matched PFL-f and PSS transmissivity with 30% of P32.*

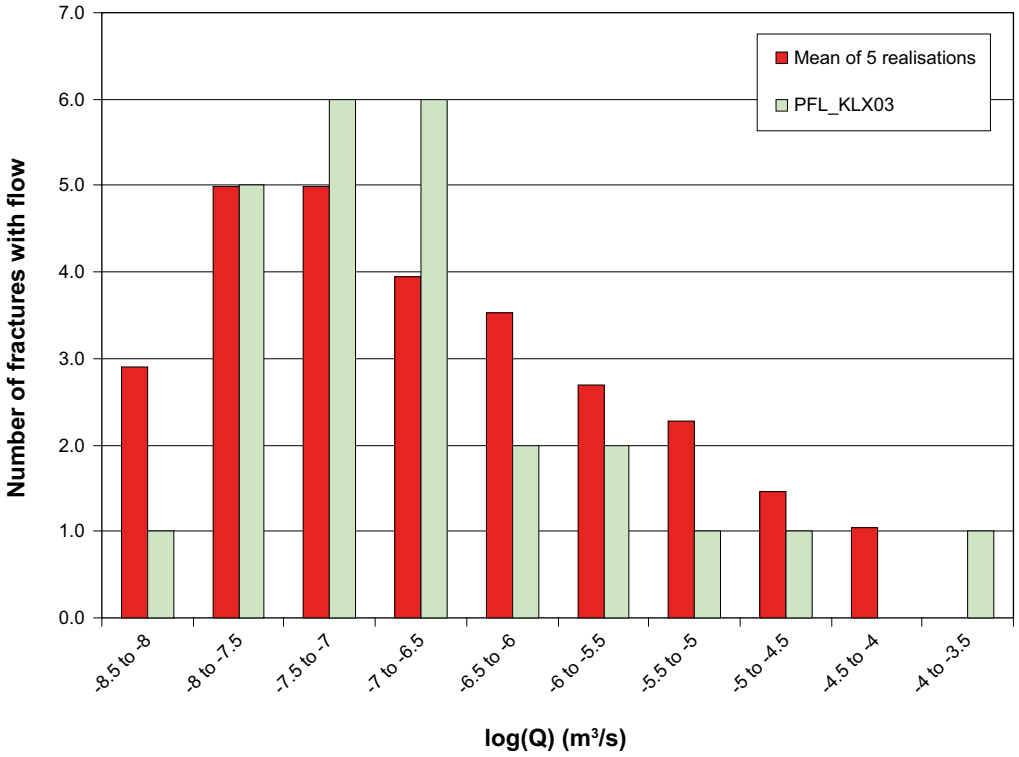

Figure B-12. *Histogram of Log(Q) flow-rate to borehole, for the mean of five realisations compared to the PFL-anomaly data for KLX03 above –300 m. Here, the semi-correlated T distribution is used, from the matched PFL-f and PSS transmissivity with 60% of P32.*

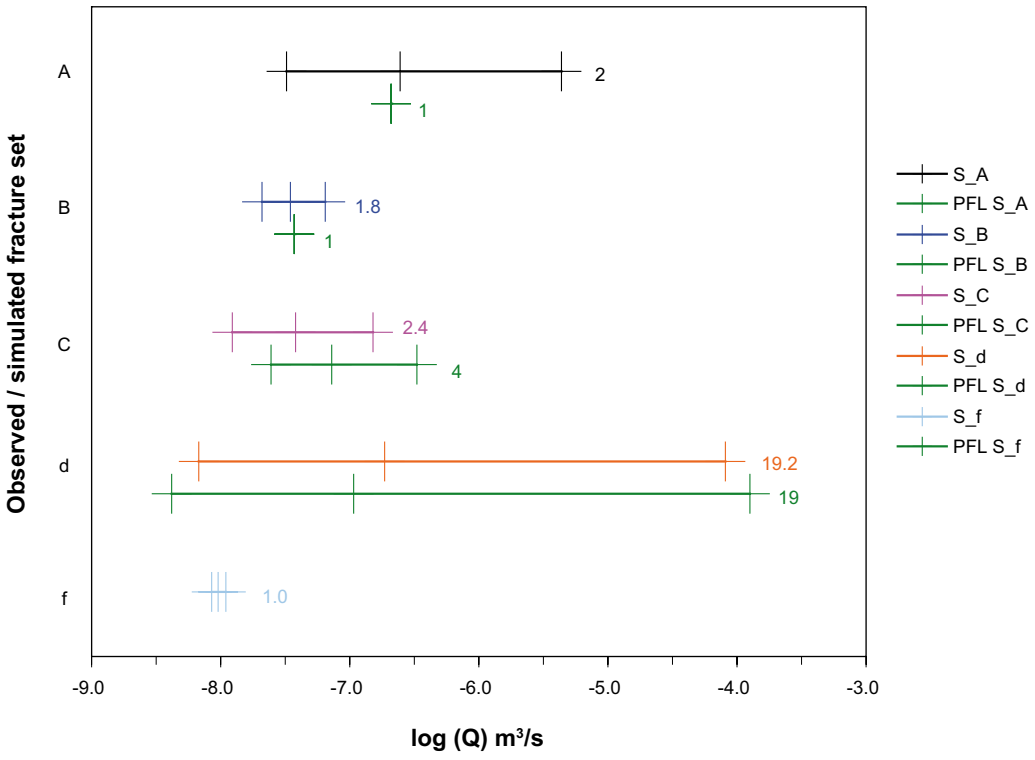

Figure B-13. *Plot of Log(Q) flow-rate to borehole, for the mean of five realisations compared to the PFL-anomaly data for KLX03 above –300 m. The flow in each fracture set is shown, with vertical bars marking the minimum, median and maximum flow-rates. Here, the semi-correlated T distribution is used, from the matched PFL-f and PSS transmissivity with 60% of P32.*

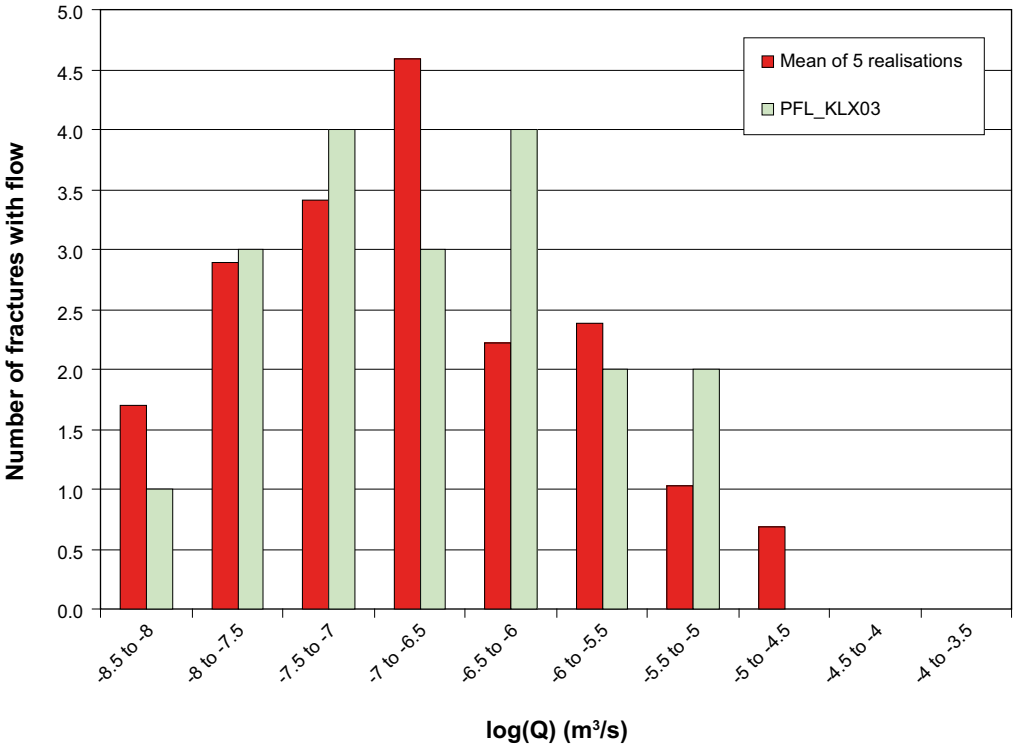

Figure B-14. *Histogram of Log(Q) flow-rate to borehole, for the mean of five realisations compared to the PFL-anomaly data for KLX03 below –300 m. Here, the uncorrelated T distribution is used, from the matched PFL-f and PSS transmissivity with 30% of P32.*

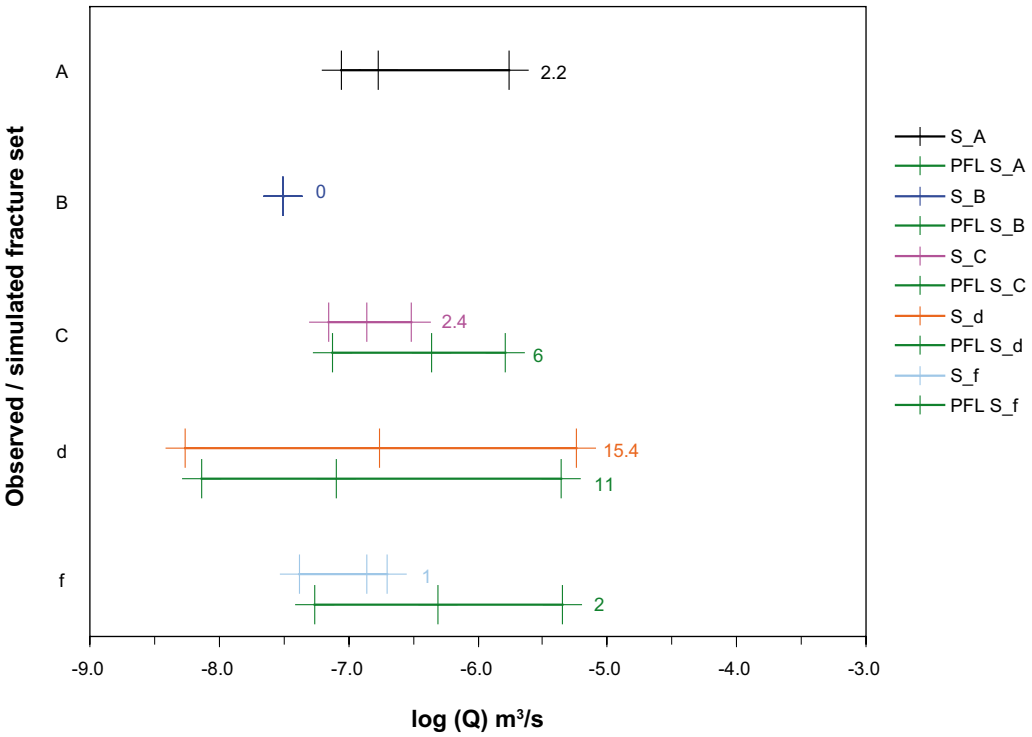

Figure B-15. *Plot of Log(Q) flow-rate to borehole, for the mean of five realisations compared to the PFL-anomaly data for KLX03 below –300 m. The flow in each fracture set is shown, with vertical bars marking the minimum, median and maximum flow-rates. Here, the uncorrelated T distribution is used, from the matched PFL-f and PSS transmissivity with 30% of P32.*

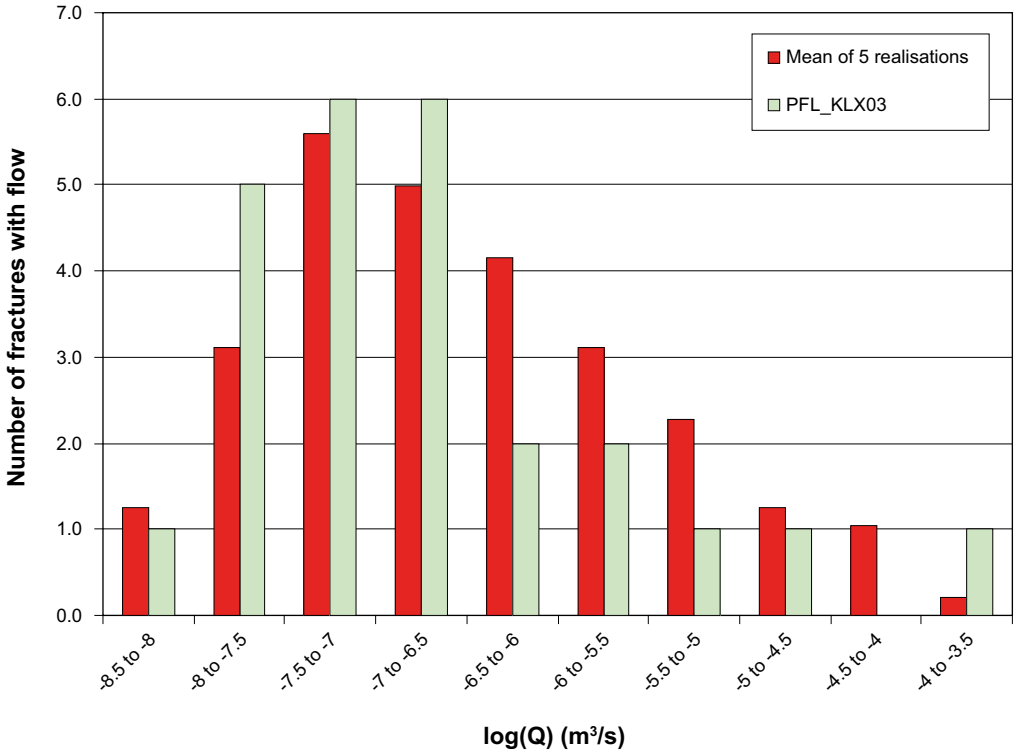

Figure B-16. *Histogram of Log(Q) flow-rate to borehole, for the mean of five realisations compared to the PFL-anomaly data for KLX03 above –300 m. Here, the uncorrelated T distribution is used, from the matched PFL-f and PSS transmissivity with 60% of P32.*

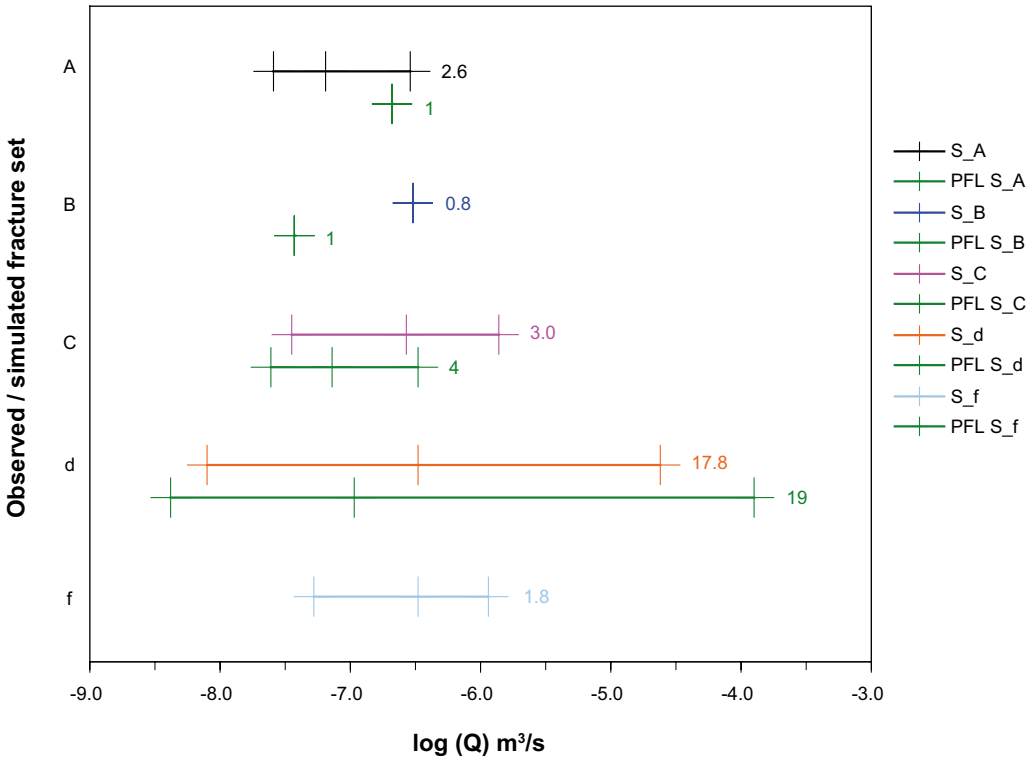

Figure B-17. *Plot of Log(Q) flow-rate to borehole, for the mean of five realisations compared to the PFL-anomaly data for KLX03 above –300 m. The flow in each fracture set is shown, with vertical bars marking the minimum, median and maximum flow-rates. Here, the uncorrelated T distribution is used, from the matched PFL-f and PSS transmissivity with 60% of P32.*

B.2 DFN simulations for KSH01A

For the simulations, KSH01A was modelled as inclined (75°) with length of 998 m. Two realisations of the DFN model are shown in Figure B-18 with all fractures included and a 400 m diameter model domain surrounding the borehole. The smaller-scale fractures (fracture radii between r_0 and 5.6 m) generated only within a region with a 40 m square horizontal cross-section around KSH01A is shown in Figure B-19. Similar models were used to perform the flow simulations. Figure B-20 shows connected fractures for three realisations of the DFN model around borehole KSH01A.

B.2.1 Conditioning transmissivity for KSH01A

Transmissivity distributions were matched the 'k_r fit' cases below –300 m and above –300 m for the correlated, semi-correlated and uncorrelated models for KSH01A. The main objectives were to match the average total flow over 5 realisations to the data, and to qualitatively match the distribution of transmissivity between borehole intervals. PSS was available for fewer intervals than for the PFL-f data, so the frequency of the PSS data was re-normalised to a consistent total length with the PFL-f data and simulations. PSS data was not available for all depths at the highest resolution (5 m intervals) so a comparison has also been made for the 20 m PSS data, using the best match parameters from the simulation against 5 m data (Figure B-22).

Figure 3-18 to Figure 3-20 show the comparison with the data for the final matched models for each transmissivity model (correlated, semi-correlated and uncorrelated). These figures show that the simulated transmissivity distribution is reasonably well matched against the PFL flow anomalies in the range above the detection limit around 3 10^{-9} m^3/s.

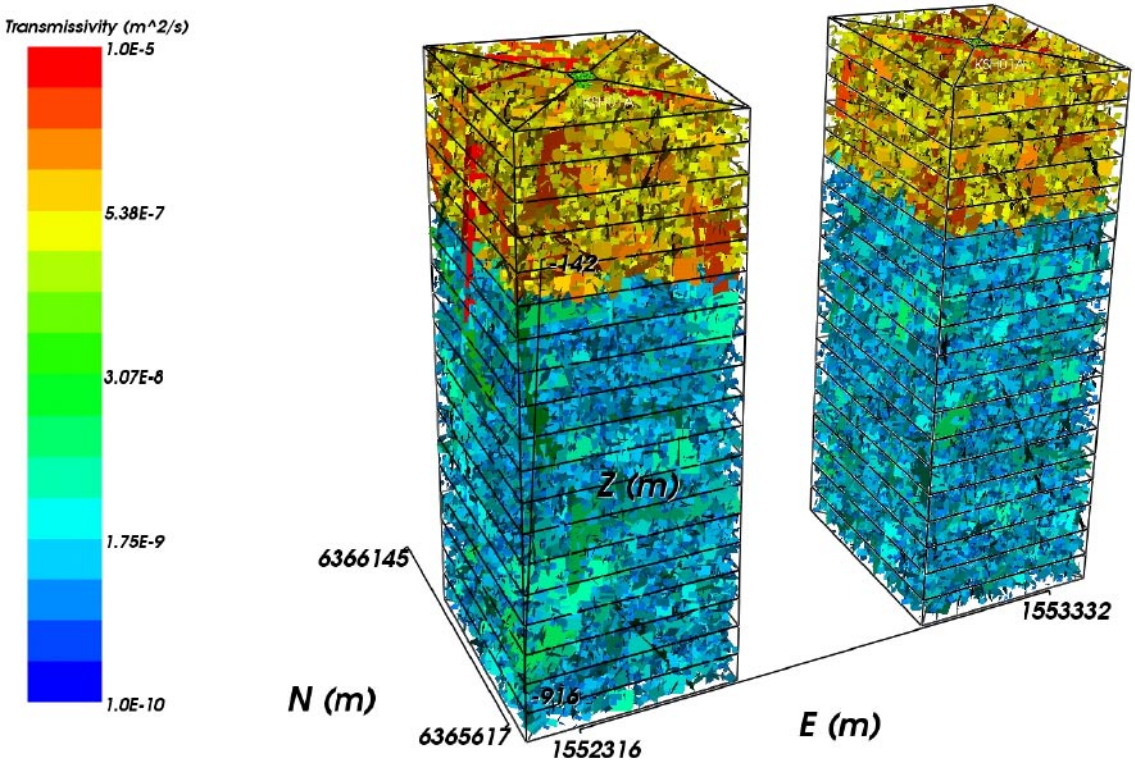

Figure B-18. *Two realisations of the DFN for a domain of 400 m square cross-section and 1,098 m length around borehole KSH01A. All fractures are shown and coloured by log(T) (in this case T is correlated to r using a power-law distribution).*

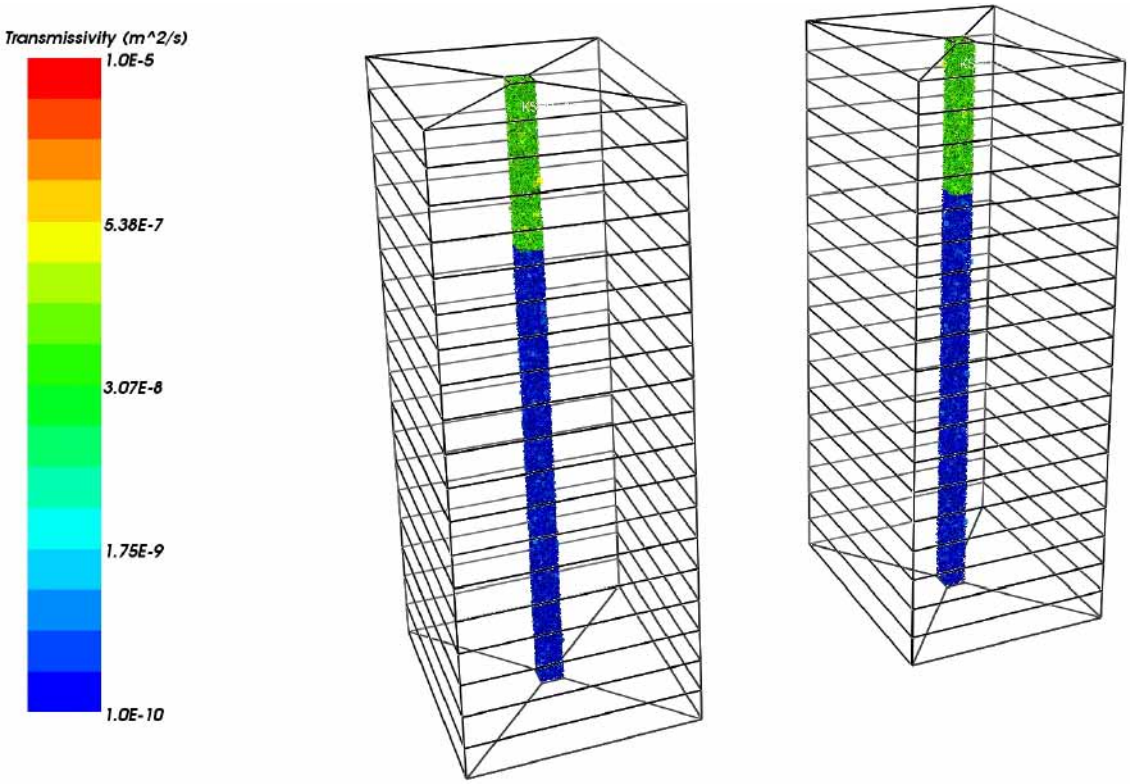

Figure B-19. *Two realisations of the DFN showing just the small-scale fractures generated within a region of 40 m square cross-section around borehole KSH01A. Fractures are coloured by log(T) (in this case T is correlated to r using a power-law distribution).*

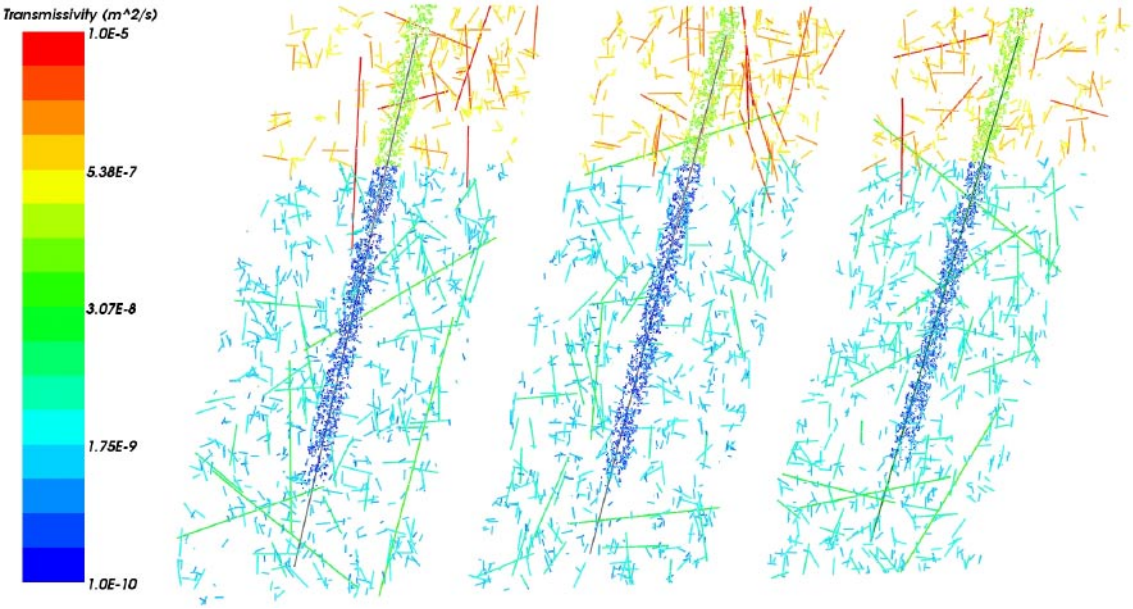

Figure B-20. *Three realisations of the DFN around borehole KSH01A showing only the connected fractures on a vertical N-S slice. Fractures are coloured by log(T) (in this case T is correlated to r using a power-law distribution).*

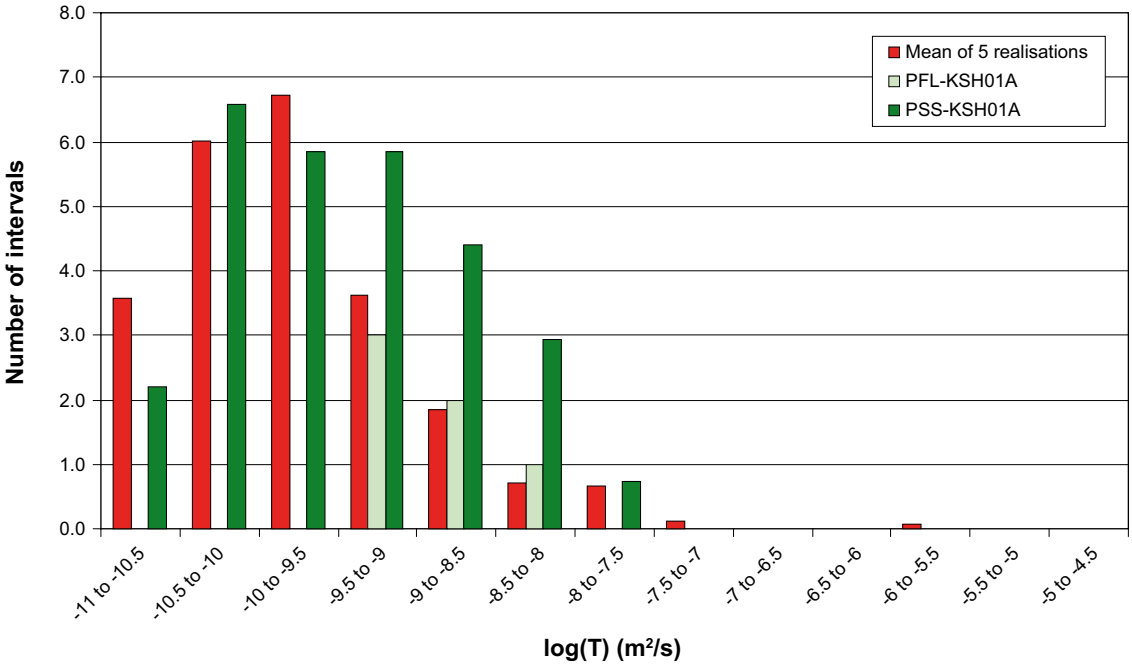

Figure B-21. *Histogram of Log(T) in 5 m intervals for the mean of 5 realisations of the correlated T distribution compared with the PFL-anomaly and PSS data for KSH01A below –300 m. This case is based on 27% of open and partly-open fractures.*

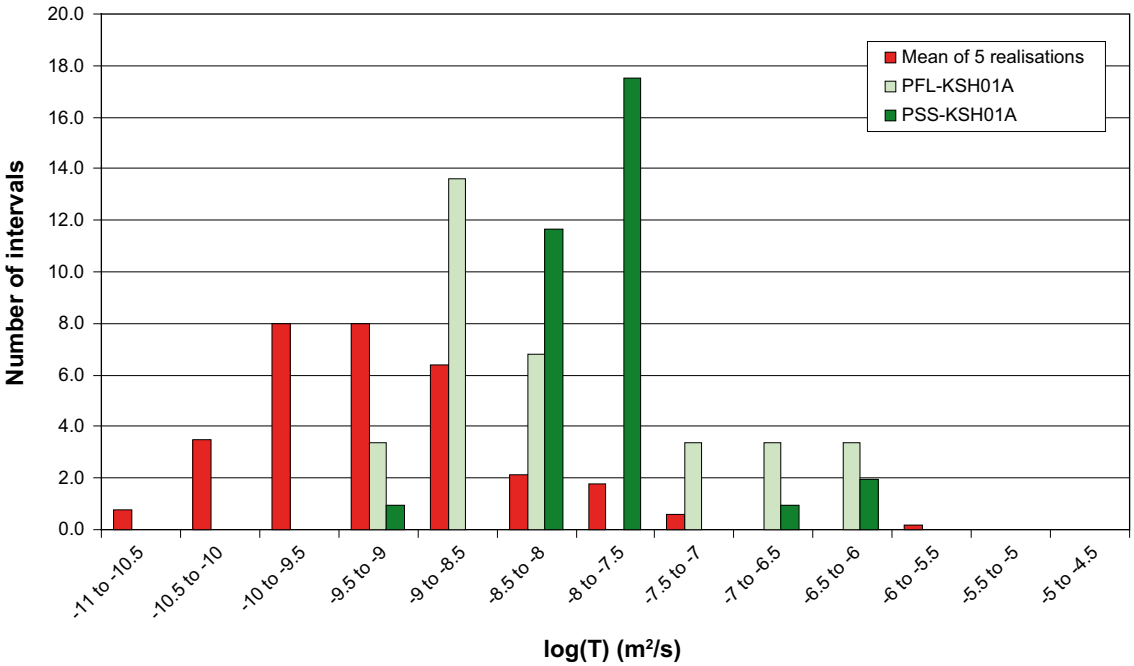

Figure B-22. *Histogram of Log(T) in 20 m intervals for the mean of 5 realisations of the correlated T distribution compared with the PFL-anomaly and PSS data for KSH01A below –300 m. This case is based on 27% of open and partly-open fractures.*

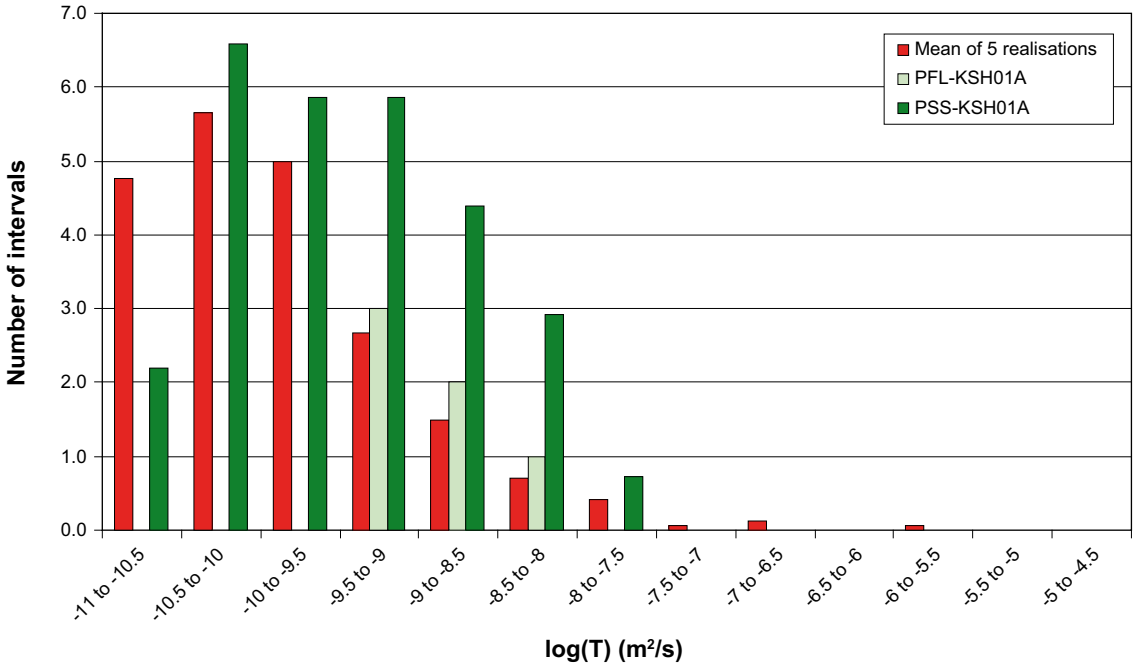

Figure B-23. *Histogram of Log(T) in 5 m intervals for the mean of 5 realisations of the semi-correlated T distribution compared with the PFL-anomaly and PSS data for KSH01A below –300 m. This case is based on 27% of open and partly-open fractures.*

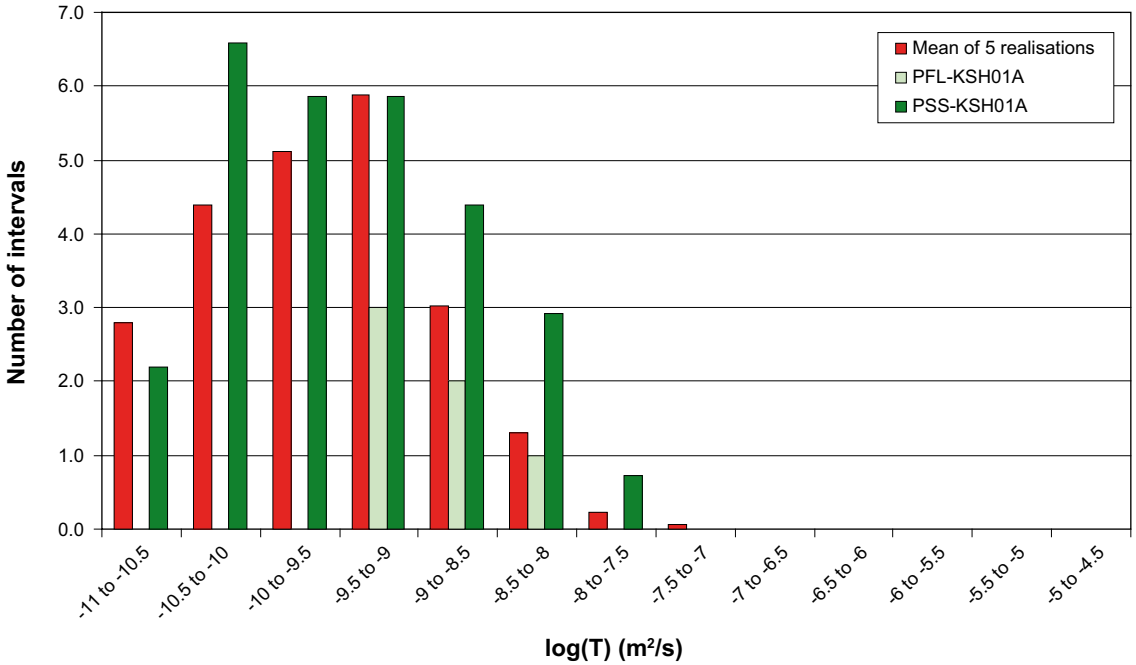

Figure B-24. *Histogram of Log(T) in 5 m intervals for the mean of 5 realisations of the uncorrelated T distribution compared with the PFL-anomaly and PSS data for KSH01A below –300 m. This case is based on 27% of open and partly-open fractures.*

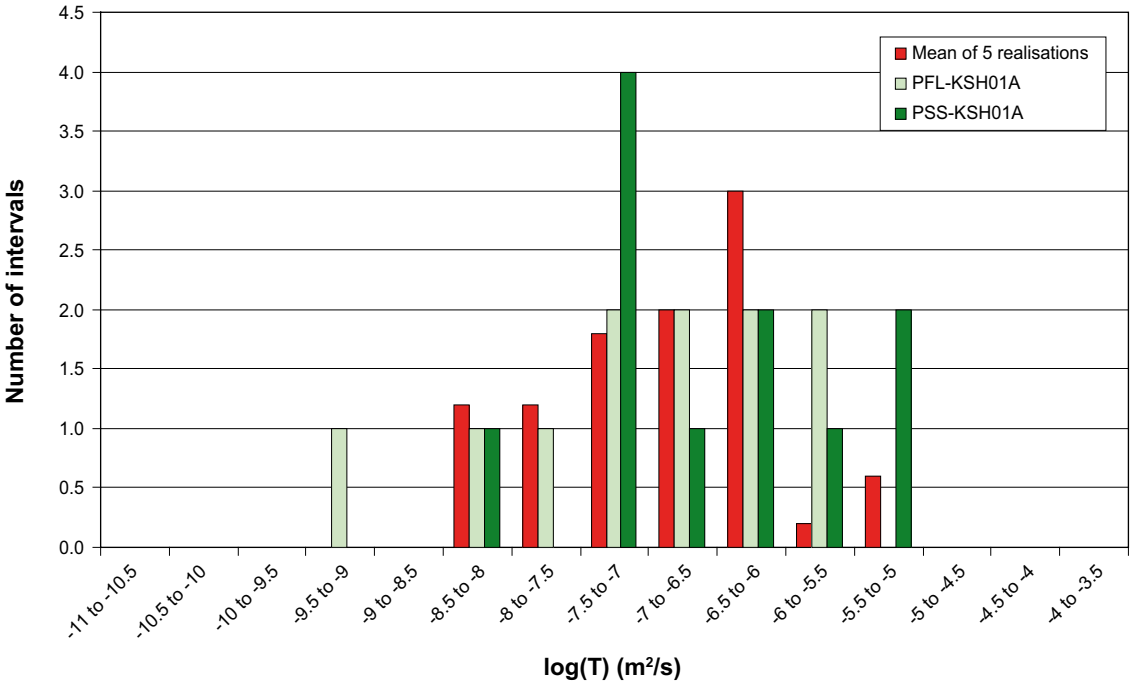

Figure B-25. *Histogram of Log(T) in 5 m intervals for the mean of 5 realisations of the correlated T distribution compared with the PFL-anomaly and PSS data for KSH01A above –300 m. This case is based on 27% of open and partly-open fractures.*

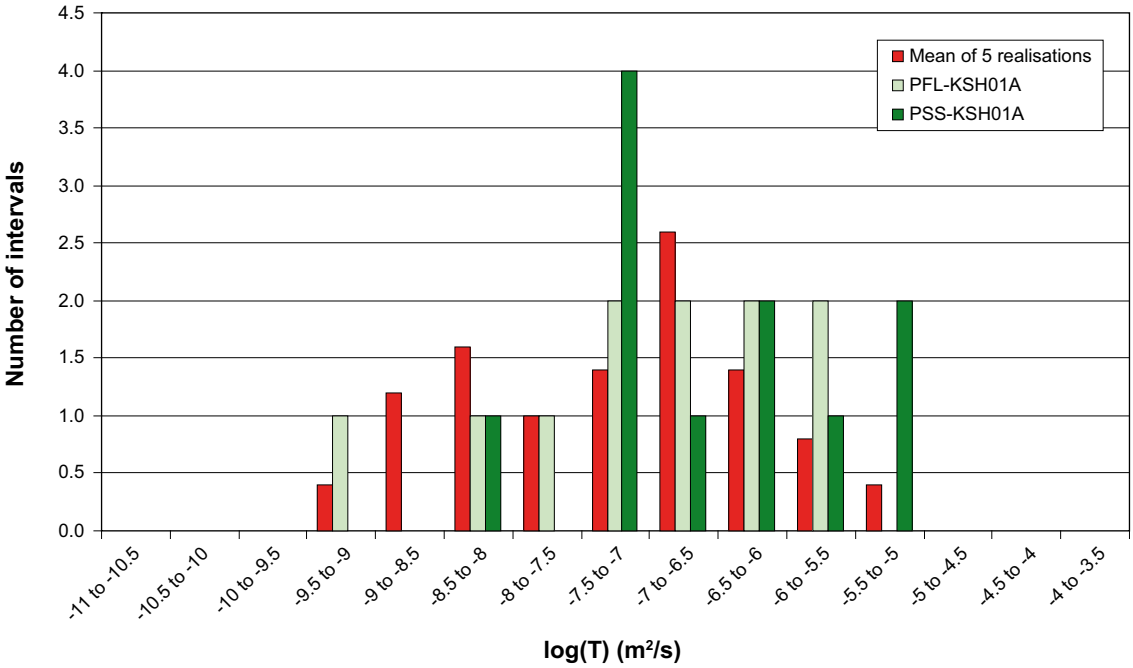

Figure B-26. *Histogram of Log(T) in 5 m intervals for the mean of 5 realisations of the semi-correlated T distribution compared with the PFL-anomaly and PSS data for KSH01A above –300 m. This case is based on 27% of open and partly-open fractures.*

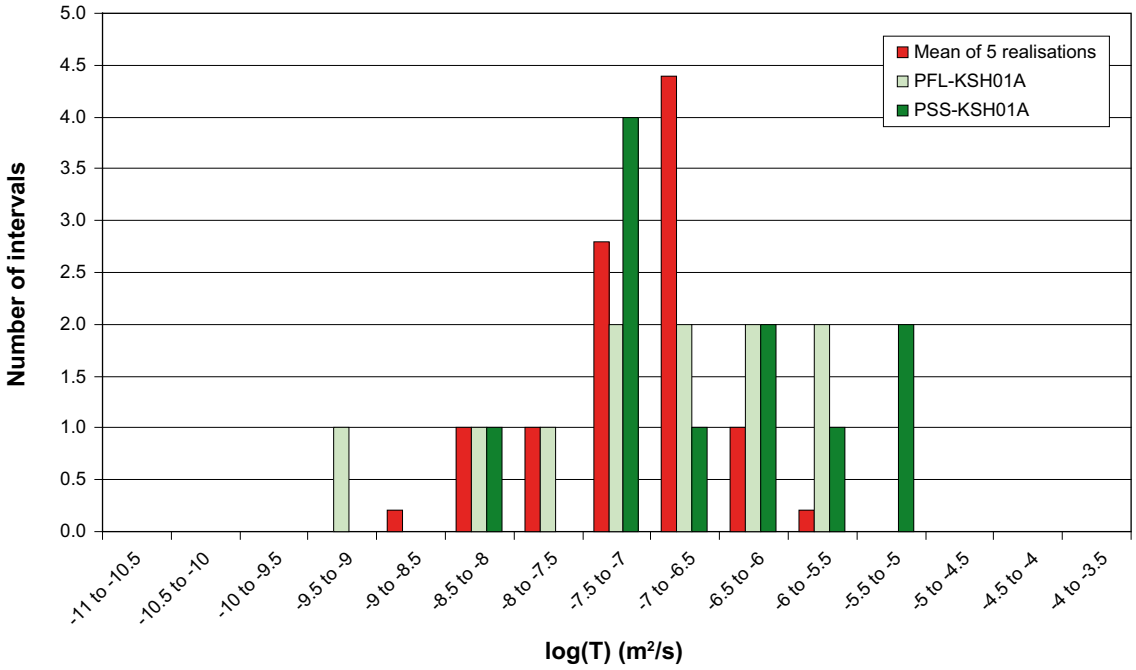

Figure B-27. *Histogram of Log(T) in 5 m intervals for the mean of 5 realisations of the uncorrelated T distribution compared with the PFL-anomaly and PSS data for KSH01A above –300 m. This case is based on 27% of open and partly-open fractures.*

B.2.2 Checking the simulated flow-rate against PFL-f data for KSH01A

The best fit parameters for each transmissivity model have been checked against the distribution of flow-rate of individual PFL-anomalies, for the 'k_r fit' cases below –300 m and above –300 m, for each of the correlated, semi-correlated and uncorrelated transmissivity cases (Figure B-28, Figure B-31, Figure B-34, Figure B-36, Figure B-38, Figure B-40).The orientation of the simulated flowing features in each fracture set has also been compared to the orientation of the closest features to each PFL-anomaly for the same cases (Figure B-29, Figure B-32, Figure B-35, Figure B-37, Figure B-39, Figure B-41). The fracture orientation plots show the point of the median, minimum and maximum flow-rate associated with each set. One realisation of the simulated flowing features is plotted as a stereonet in Figure B-30 for below –300 m, and Figure B-33 for above –300 m elevation and the complete borehole length. These figures can be compared with the measured flows in Appendix A.3.

These figures show that the simulated flow-rate distribution is slightly higher than the PFL flow anomalies, for the 'k_r fit' cases below –300 m, in the range above the detection limit around 3 10^{-9} m^3/s. However, the simulated flow-rate distribution for the 'k_r fit' cases below –300 m is reasonable compared to the PFL flow anomalies. The data suggests the high flows are predominantly in Set_d in both cases. For both cases, the simulations are consistent in predicting too high flows in Set_A although no flows have been measured below –300 m elevation, and above –300 m elevation only one flow has been measured.

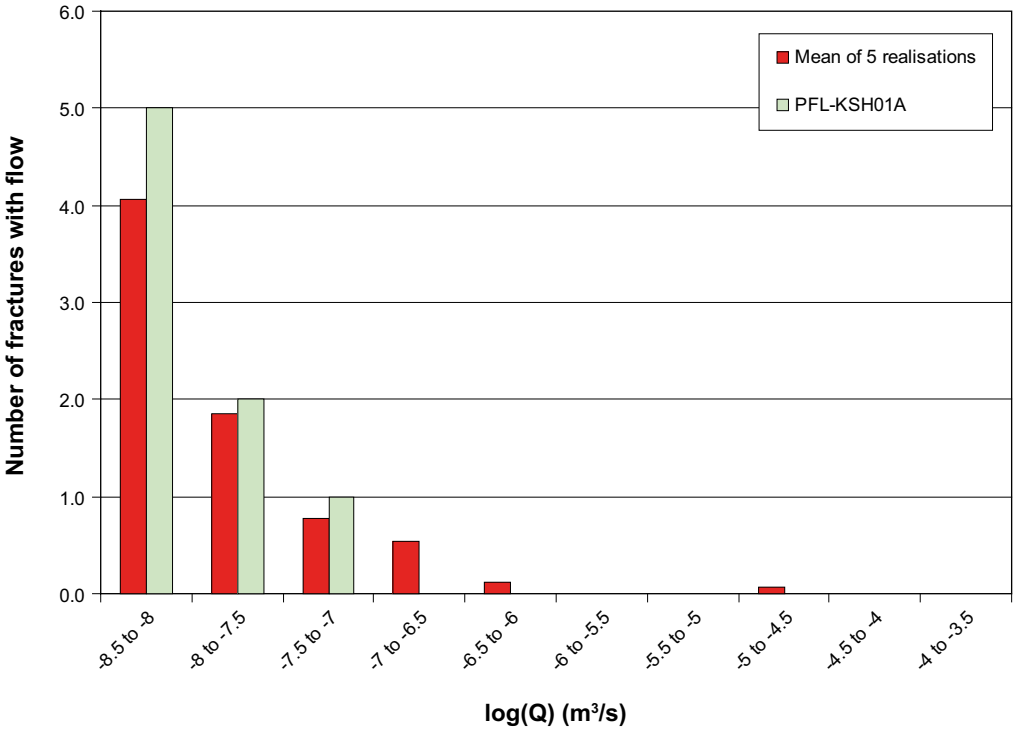

Figure B-28. *Histogram of Log(Q) flow-rate to borehole, for the mean of five realisations compared to the PFL-anomaly data for KSH01A below –300 m. Here, the correlated T distribution is used, from the matched PFL-f and PSS transmissivity with 27% of P32.*

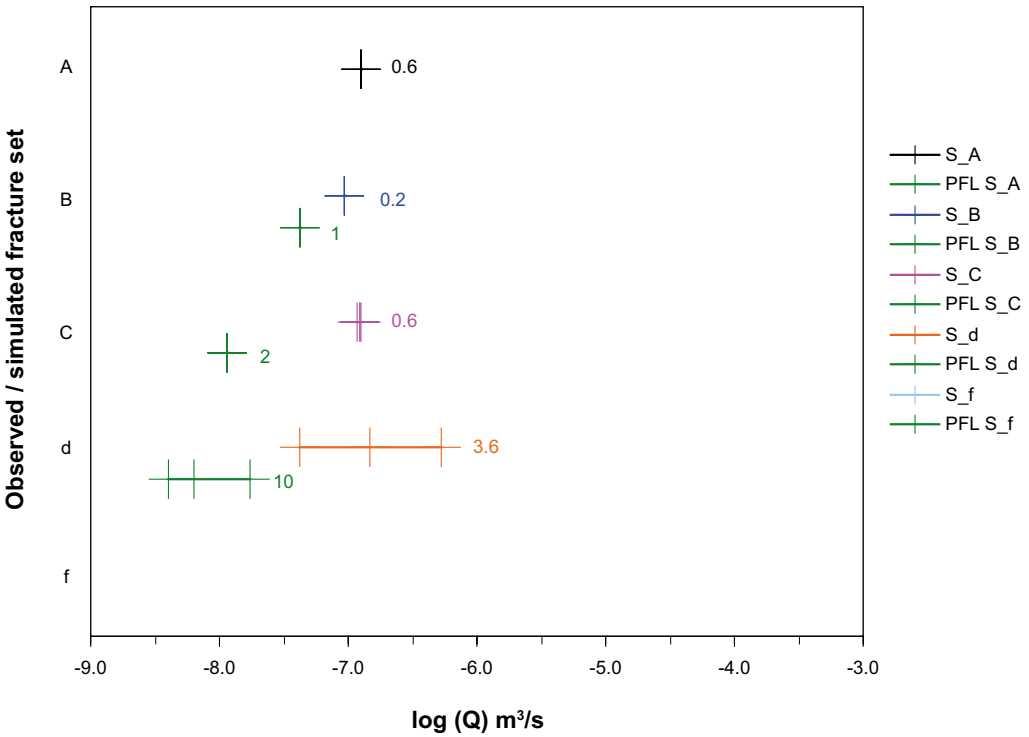

Figure B-29. *Plot of Log(Q) flow-rate to borehole, for the mean of five realisations compared to the PFL-anomaly data for KSH01A below –300 m. The flow in each fracture set is shown, with vertical bars marking the minimum, median and maximum flow-rates. Here, the correlated T distribution is used, from the matched PFL-f and PSS transmissivity with 27% of P32.*

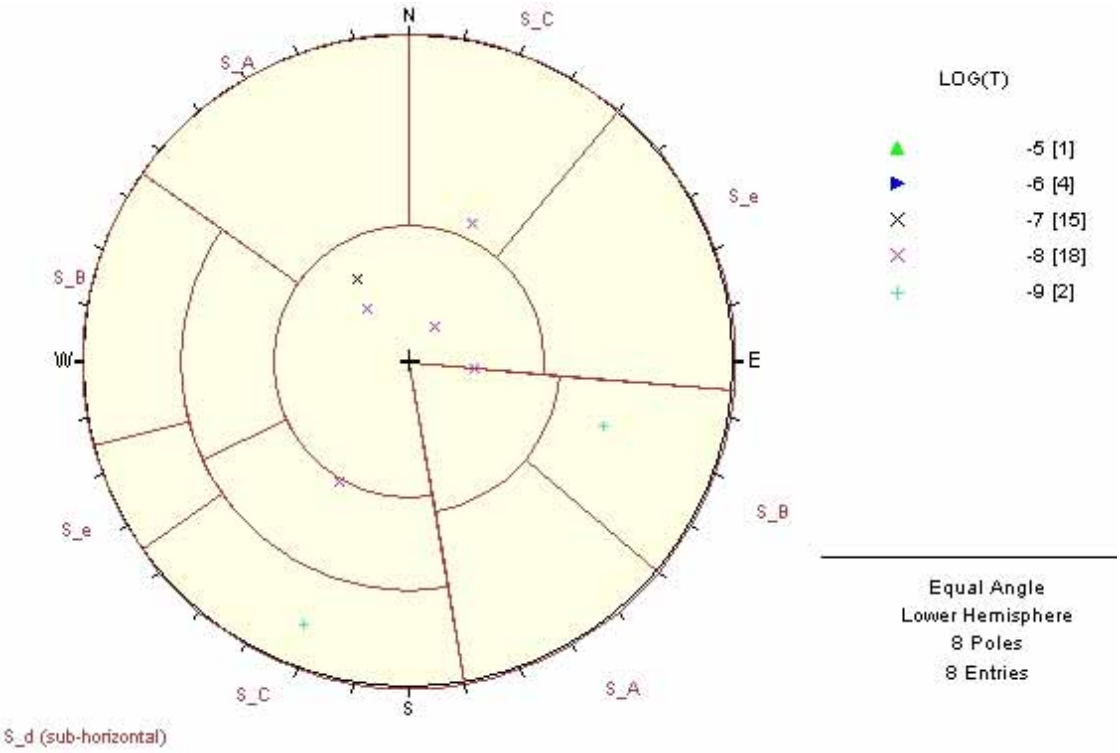

Figure B-30. *Orientations of the simulated flowing features for the correlated case for KSH01A below –300 m. One realisation is shown. Symbols are coloured according to log of transmissivity of each flowing feature (m^2 s^{-1}).*

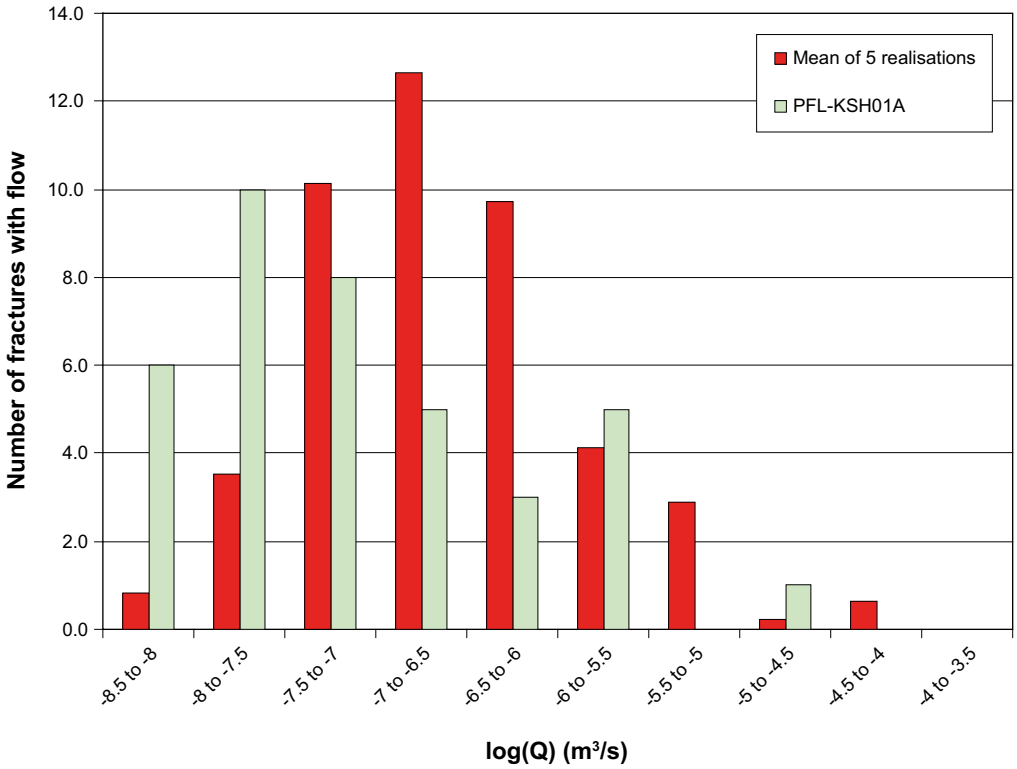

Figure B-31. *Histogram of Log(Q) flow-rate to borehole, for the mean of five realisations compared to the PFL-anomaly data for KSH01A above –300 m. Here, the correlated T distribution is used, from the matched PFL-f and PSS transmissivity with 27% of P32.*

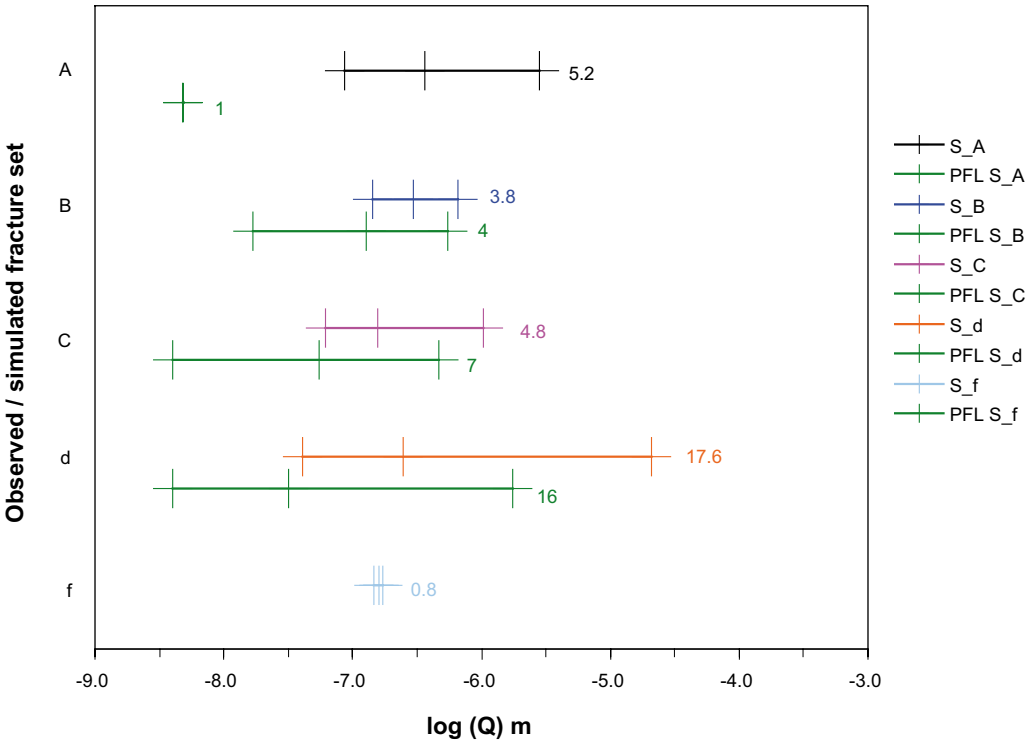

Figure B-32. *Plot of Log(Q) flow-rate to borehole, for the mean of five realisations compared to the PFL-anomaly data for KSH01A above –300 m. The flow in each fracture set is shown, with vertical bars marking the minimum, median and maximum flow-rates. Here, the correlated T distribution is used, from the matched PFL-f and PSS transmissivity with 27% of P32.*

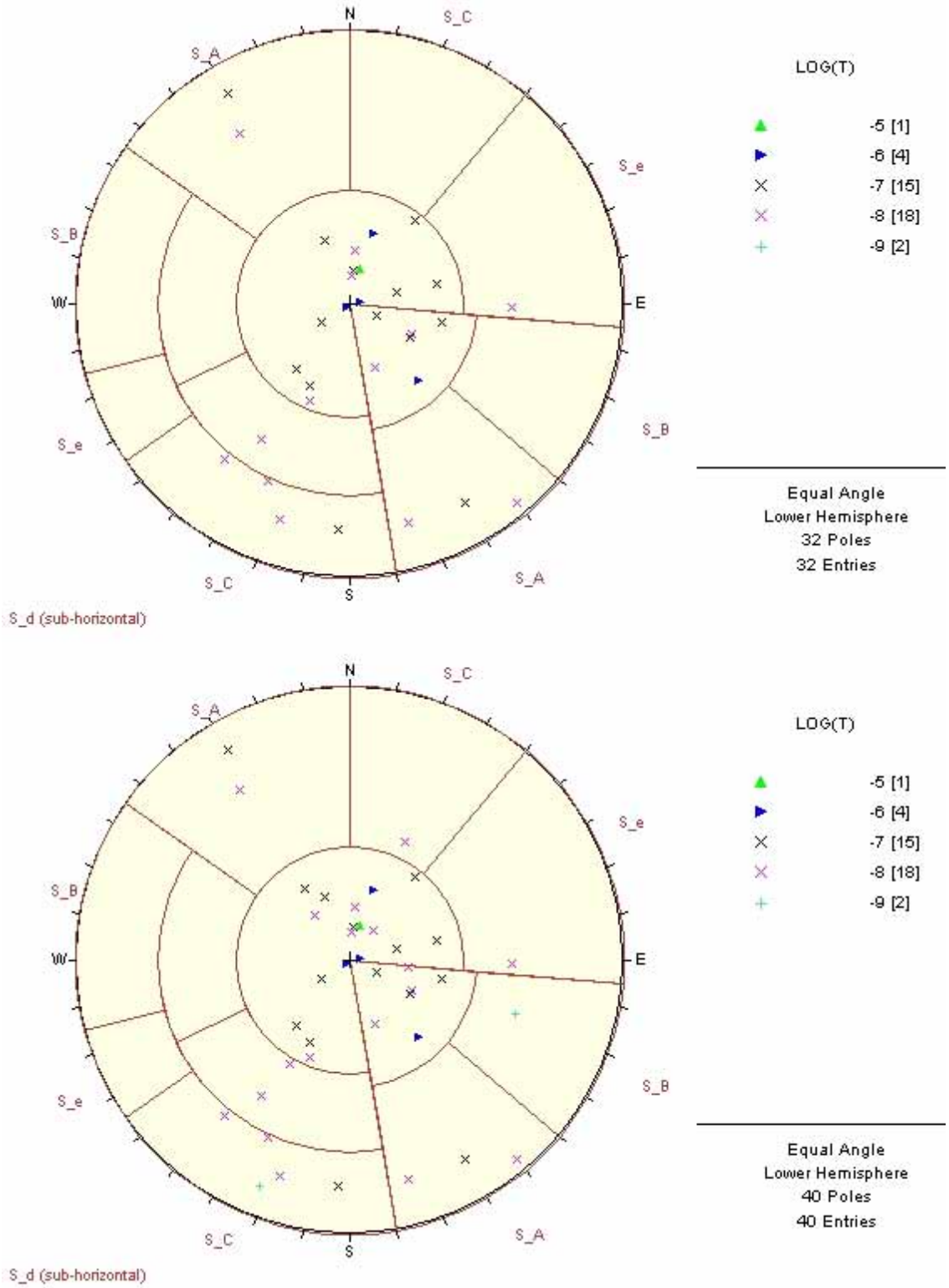

Figure B-33. *Orientations of the simulated flowing features for the correlated case for KSH01A above –300 m (top), and the complete length of KSH01A (bottom). One realisation is shown. Symbols are coloured according to log of transmissivity of each flowing feature (m^2 s^{-1}).*

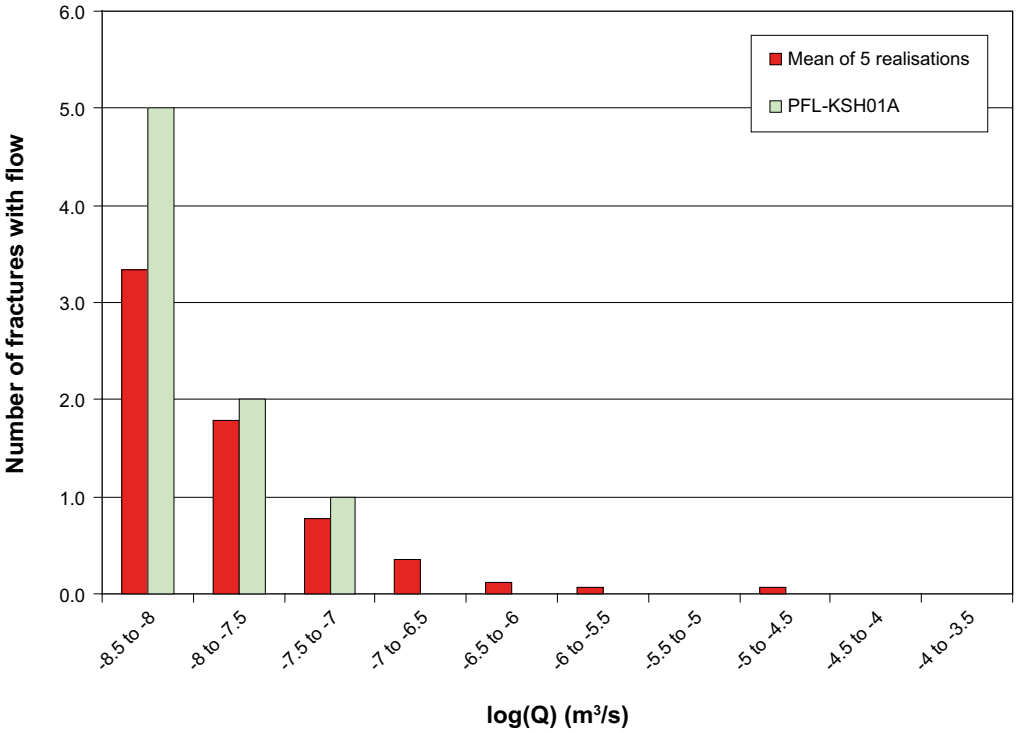

Figure B-34. *Histogram of Log(Q) flow-rate to borehole, for the mean of five realisations compared to the PFL-anomaly data for KSH01A below –300 m. Here, the semi-correlated T distribution is used, from the matched PFL-f and PSS transmissivity with 27% of P32.*

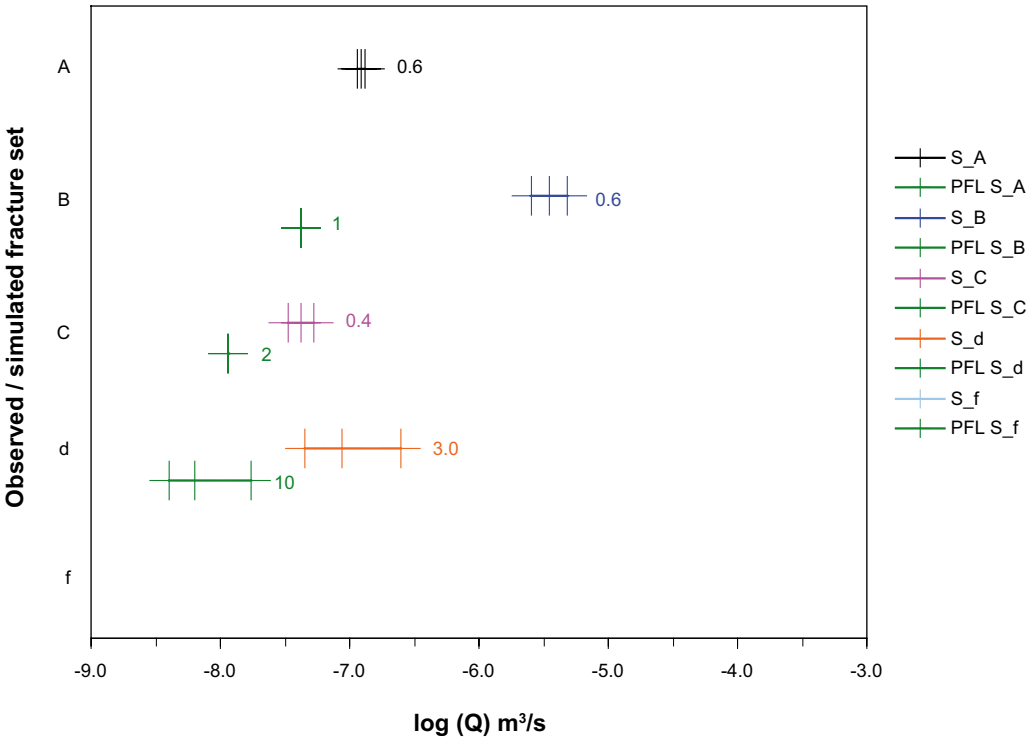

Figure B-35. *Plot of Log(Q) flow-rate to borehole, for the mean of five realisations compared to the PFL-anomaly data for KSH01A below –300 m. The flow in each fracture set is shown, with vertical bars marking the minimum, median and maximum flow-rates. Here, the semi-correlated T distribution is used, from the matched PFL-f and PSS transmissivity with 27% of P32.*

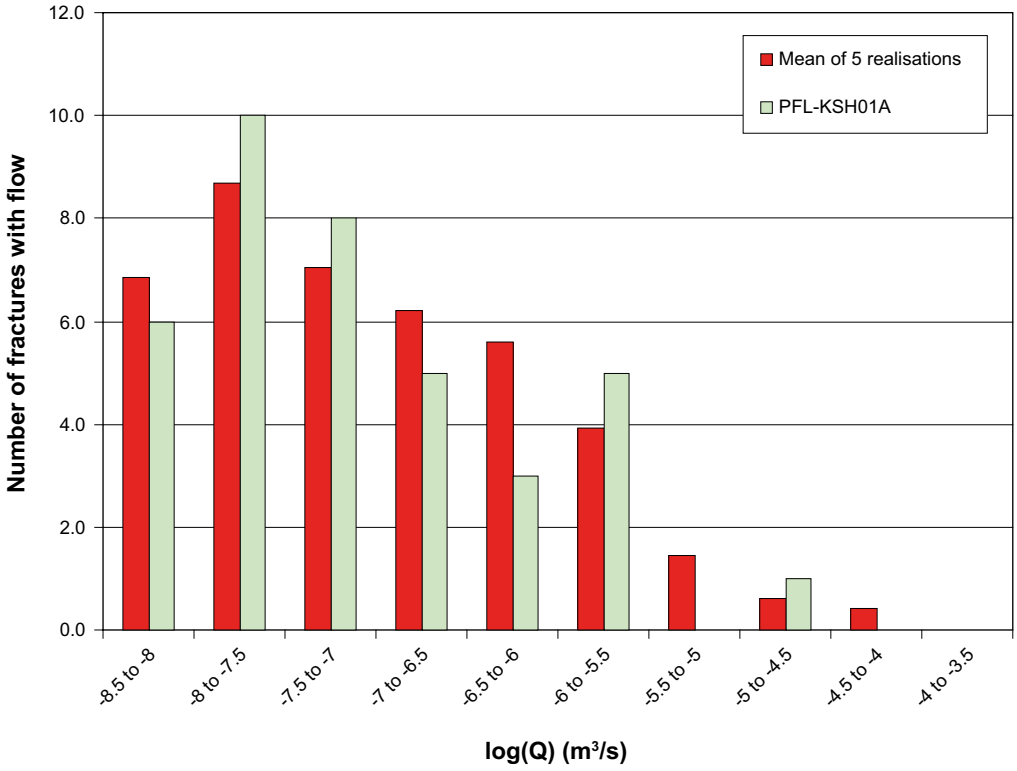

Figure B-36. *Histogram of Log(Q) flow-rate to borehole, for the mean of five realisations compared to the PFL-anomaly data for KSH01A above –300 m. Here, the semi-correlated T distribution is used, from the matched PFL-f and PSS transmissivity with 27% of P32.*

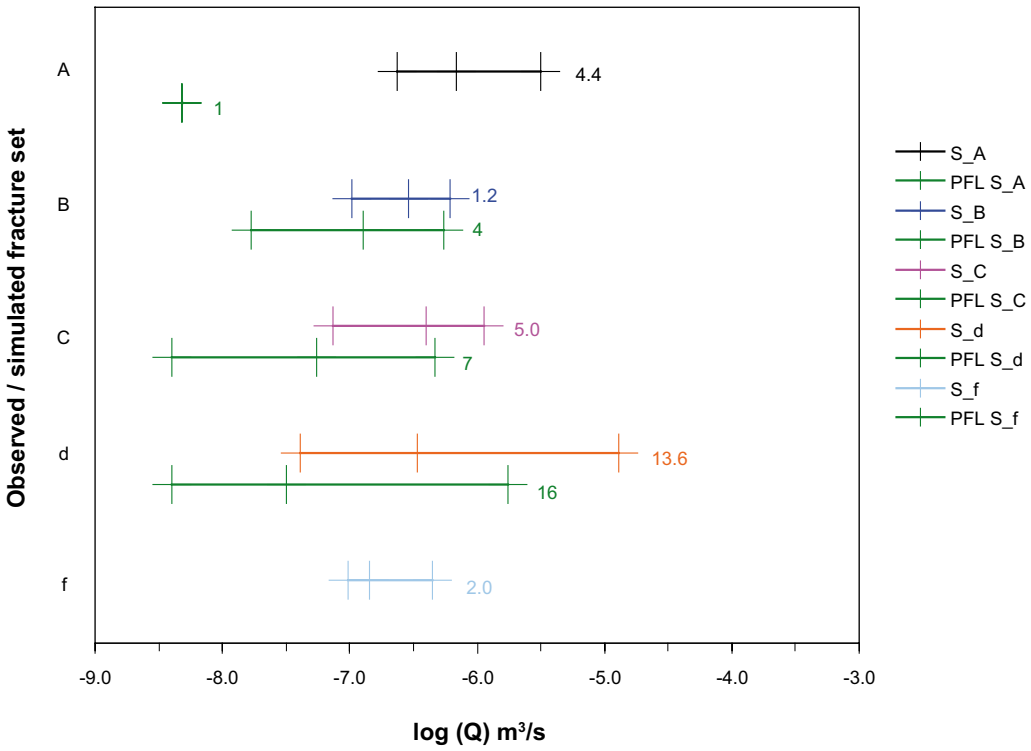

Figure B-37. *Plot of Log(Q) flow-rate to borehole, for the mean of five realisations compared to the PFL-anomaly data for KSH01A above –300 m. The flow in each fracture set is shown, with vertical bars marking the minimum, median and maximum flow-rates. Here, the semi-correlated T distribution is used, from the matched PFL-f and PSS transmissivity with 27% of P32.*

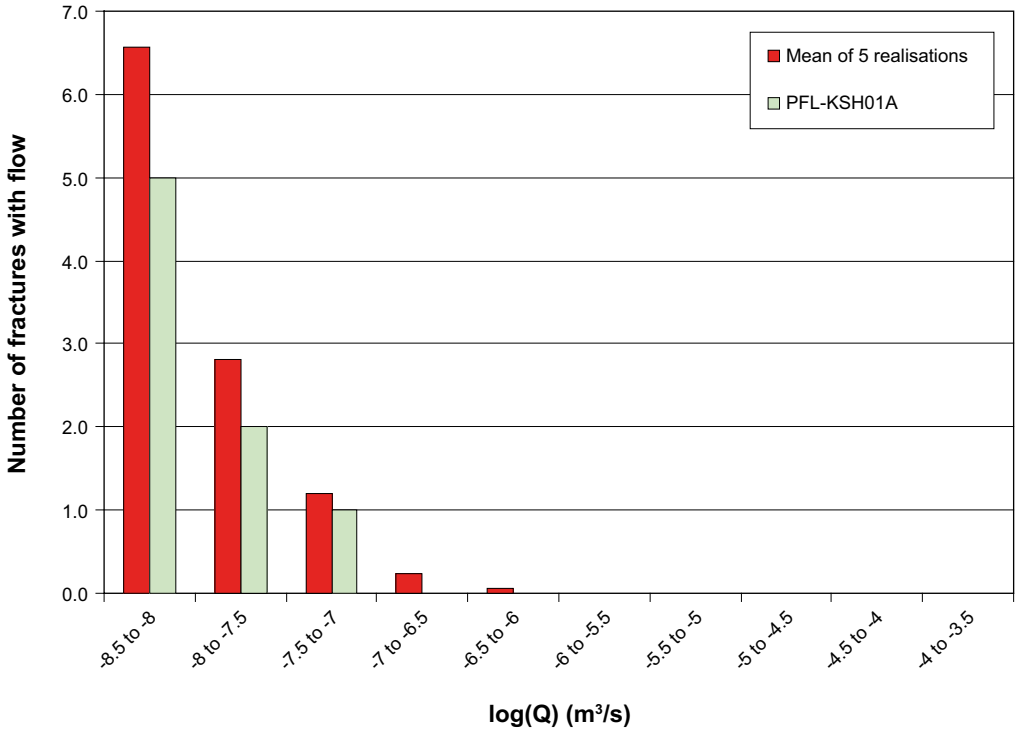

Figure B-38. *Histogram of Log(Q) flow-rate to borehole, for the mean of five realisations compared to the PFL-anomaly data for KSH01A below –300 m. Here, the uncorrelated T distribution is used, from the matched PFL-f and PSS transmissivity with 27% of P32.*

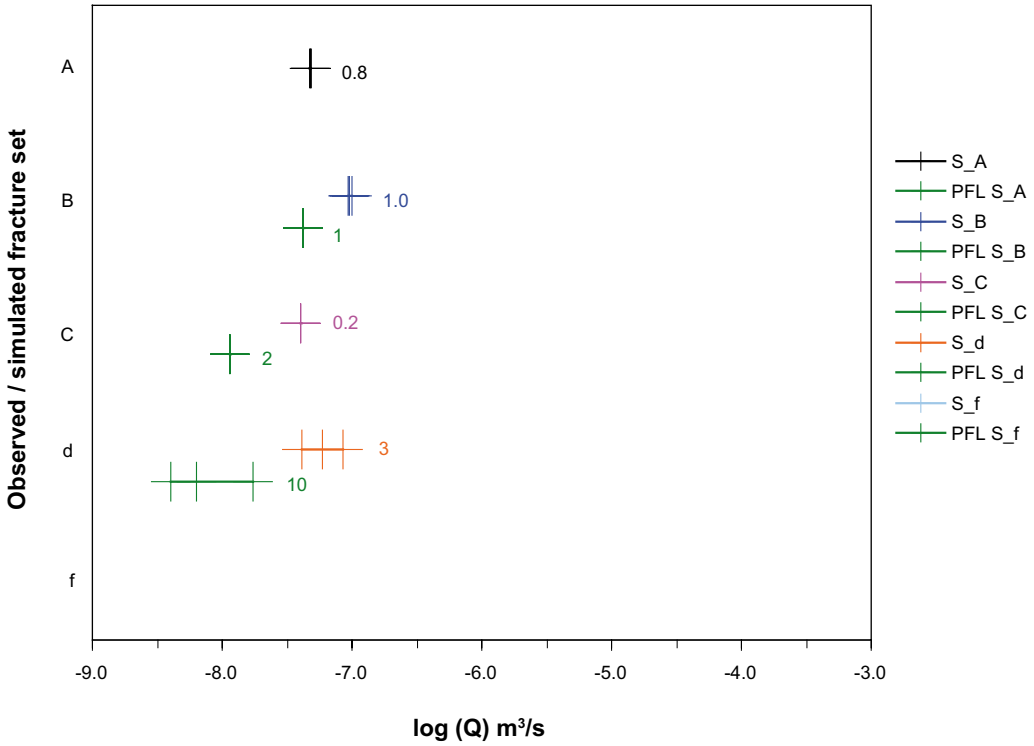

Figure B-39. *Plot of Log(Q) flow-rate to borehole, for the mean of five realisations compared to the PFL-anomaly data for KSH01A below –300 m. The flow in each fracture set is shown, with vertical bars marking the minimum, median and maximum flow-rates. Here, the uncorrelated T distribution is used, from the matched PFL-f and PSS transmissivity with 27% of P32.*

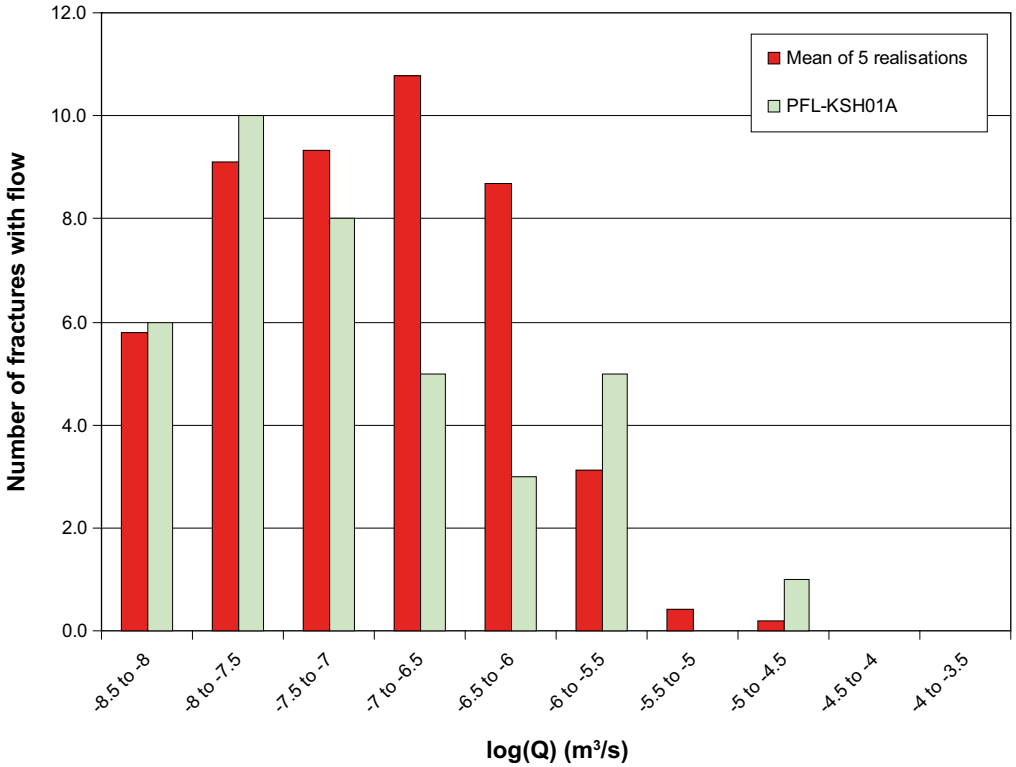

Figure B-40. *Histogram of Log(Q) flow-rate to borehole, for the mean of five realisations compared to the PFL-anomaly data for KSH01A above –300 m. Here, the uncorrelated T distribution is used, from the matched PFL-f and PSS transmissivity with 27% of P32.*

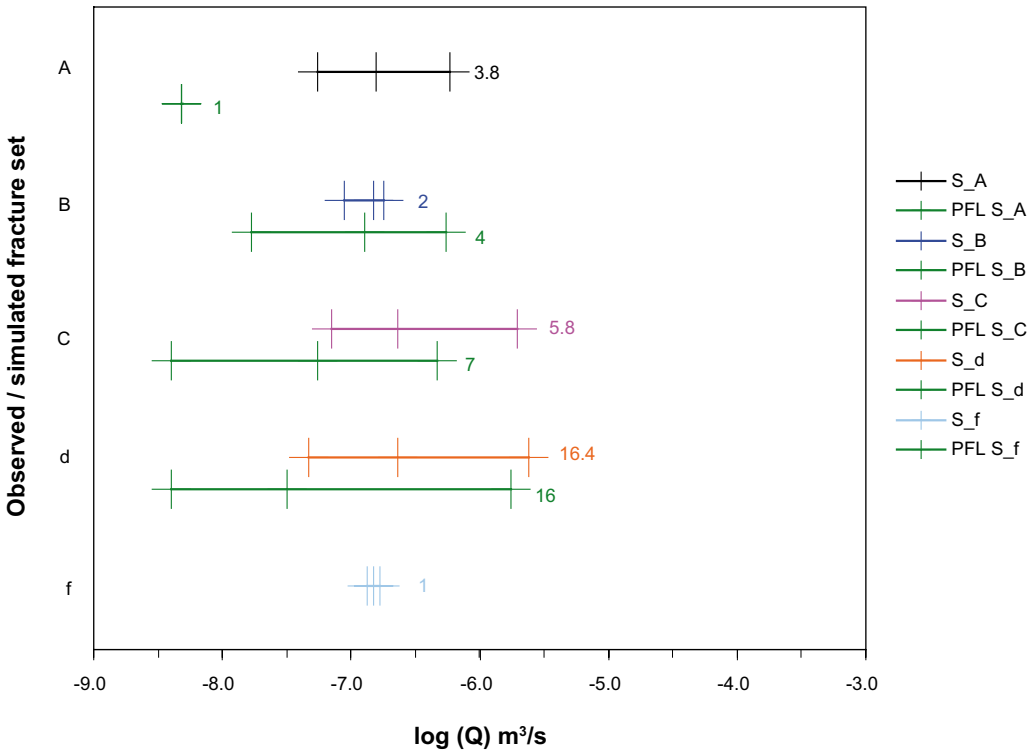

Figure B-41. *Plot of Log(Q) flow-rate to borehole, for the mean of five realisations compared to the PFL-anomaly data for KSH01A above –300 m. The flow in each fracture set is shown, with vertical bars marking the minimum, median and maximum flow-rates. Here, the uncorrelated T distribution is used, from the matched PFL-f and PSS transmissivity with 27% of P32.*

B.3 DFN simulations for KAV04A

For the simulations, KAV04A was modelled as vertical with length of 900 m. Two realisations of the DFN model are shown in Figure B-42 with all fractures included and a 400 m diameter model domain surrounding KAV04A. The smaller-scale fractures (fracture radii between r_0 and 5.6 m) generated only within a region with a 40 m square horizontal cross-section around KAV04A is shown in Figure B-43. Similar models were used to perform the flow simulations. Figure B-44 shows connected fractures for three realisations of the DFN model around borehole KAV04A.

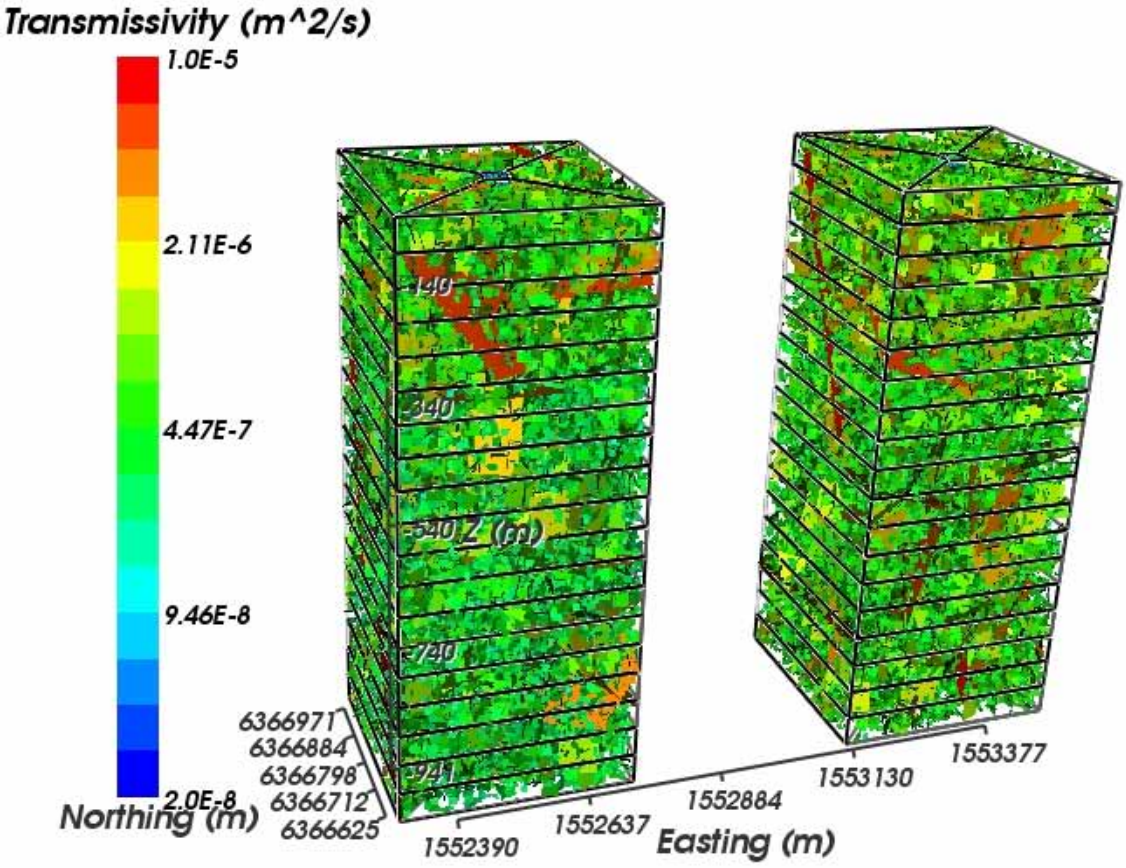

Figure B-42. *Two realisations of the DFN for a domain of 400 m square cross-section and 1,000 m length around borehole KAV04A. All fractures are shown and coloured by log(T) (in this case T is correlated to r using a power-law distribution).*

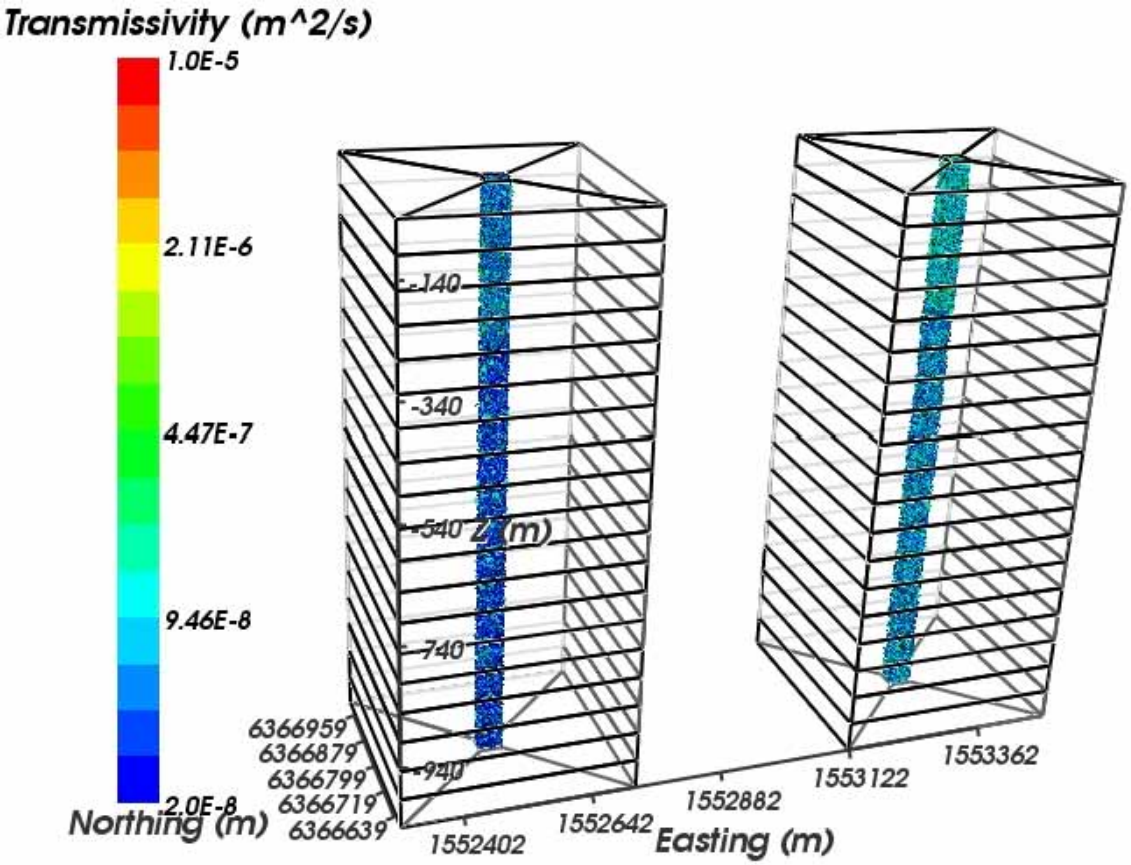

Figure B-43. *Two realisations of the DFN showing just the small-scale fractures generated within a region of 40 m square cross-section around borehole KAV04A. Fractures are coloured by log(T) (in this case T is correlated to r using a power-law distribution).*

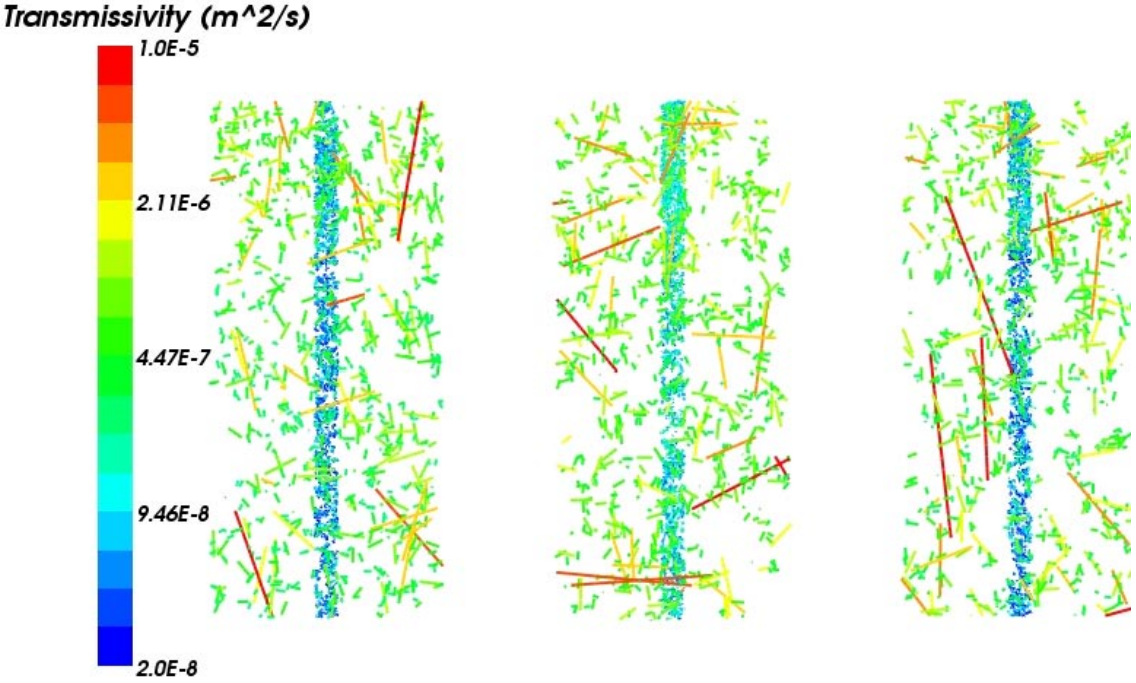

Figure B-44. *Three realisations of the DFN around borehole KAV04A showing only the connected fractures on a vertical N-S slice. Fractures are coloured by log(T) (in this case T is correlated to r using a power-law distribution).*

B.1.1 Conditioning the simulated flow-rate against PFL-f data for KAV04A

Each transmissivity model has been matched against the distribution of flow-rate of individual PFL-anomalies, for the 'k_r fit' cases above –300 m and below –300 m, for each of the correlated, semi-correlated and uncorrelated transmissivity cases (Figure B-45, Figure B-48, Figure B-51, Figure B-53, Figure B-55, Figure B-57). There is no PSS data for KAV04A. The orientation of the simulated flowing features in each fracture set has also been compared to the orientation of the closest features to each PFL-f anomaly for the same cases (Figure B-46, Figure B-49, Figure B-52, Figure B-54, Figure B-56, Figure B-58). The fracture orientation plots show the point of the median, minimum and maximum flow-rate associated with each set. One realisation of the simulated flowing features is plotted as a stereonet in Figure B-47 for below –300 m, and Figure B-50 for above –300 m elevation and the complete borehole length. These figures can be compared with the measured flows in Appendix A.6.

These figures show that the simulated flow-rate distribution is reasonably well matched against the PFL flow anomalies in the range above the detection limit around 3 10^{-8} m^3/s. The data for the 'k_r fit' case below –300 m suggest the high flows are predominantly in Set_C and Set_A; while the 'k_r fit' case above –300 m has more evenly spread flows in Set_A, Set_B, Set_C and Set_d. The simulations are reasonable for the 'k_r fit' case below –300 m in predicting higher flows for Set_A and Set_d, however Set_B and Set_C are over-predicted. The simulations for the 'k_r fit' case above –300 m show reasonable predictions for fracture sets with high flow.

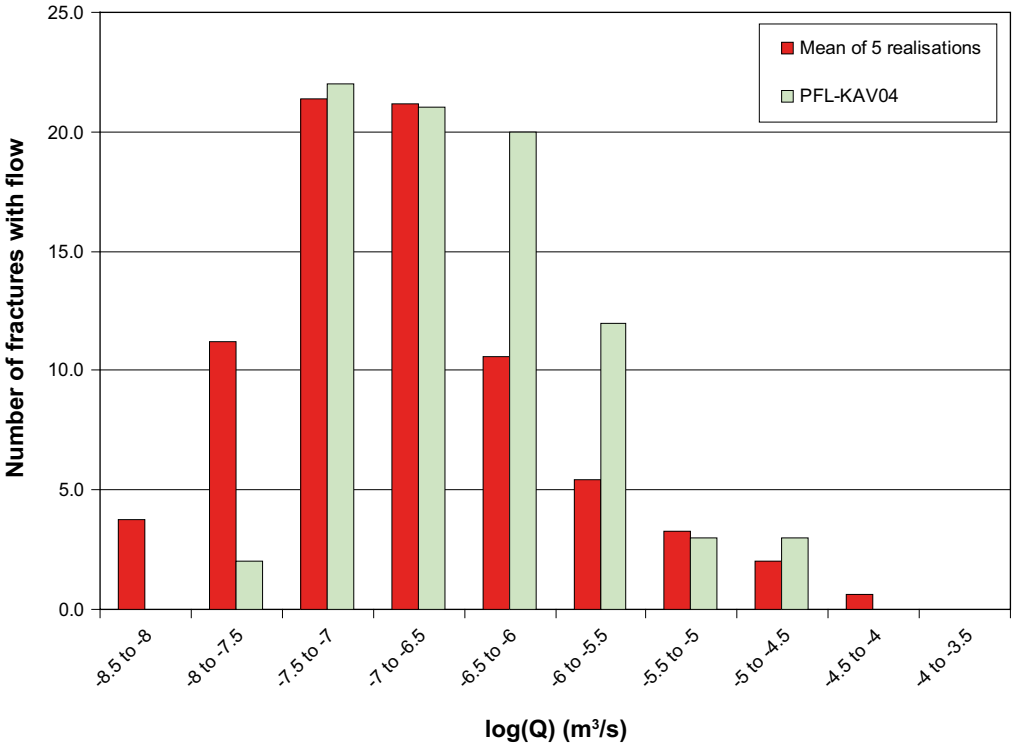

Figure B-45. *Plot of Histogram of Log(Q) flow-rate to borehole, for the mean of five realisations compared to the PFL-anomaly data for KAV04A below –300 m. Here, the correlated T distribution is used, from the matched PFL-f and PSS transmissivity with 22% of P32.*

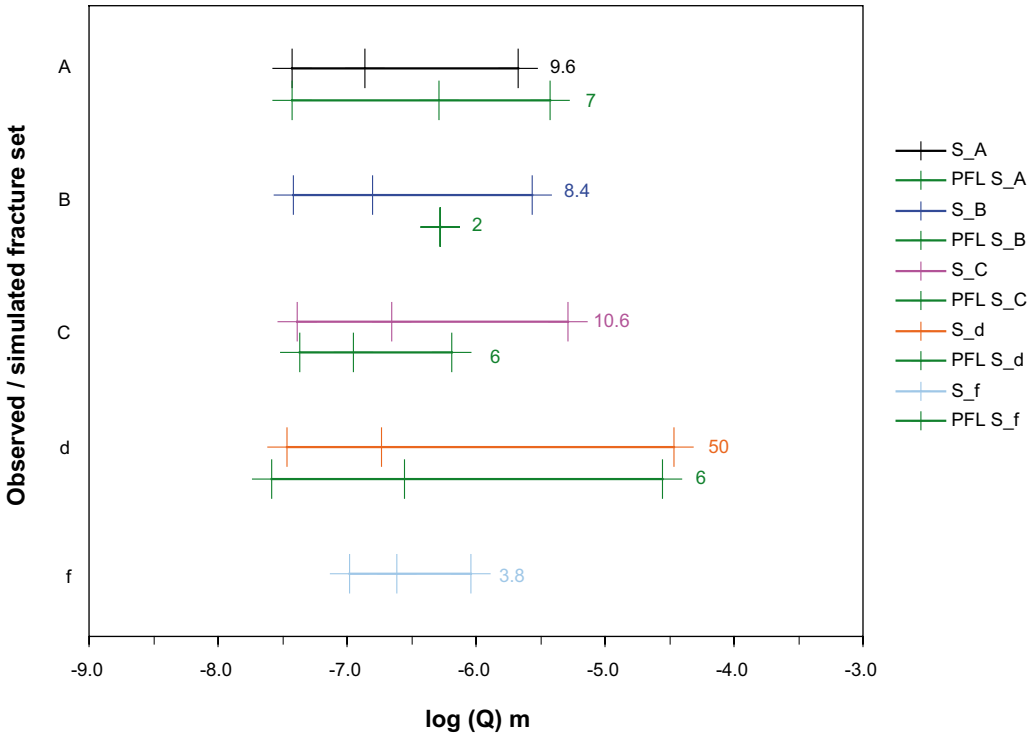

Figure B-46. *Plot of Log(Q) flow-rate to borehole, for the mean of five realisations compared to the PFL-anomaly data for KAV04A below –300 m. The flow in each fracture set is shown, with vertical bars marking the minimum, median and maximum flow-rates. Here, the correlated T distribution is used, from the matched PFL-f and PSS transmissivity with 22% of P32.*

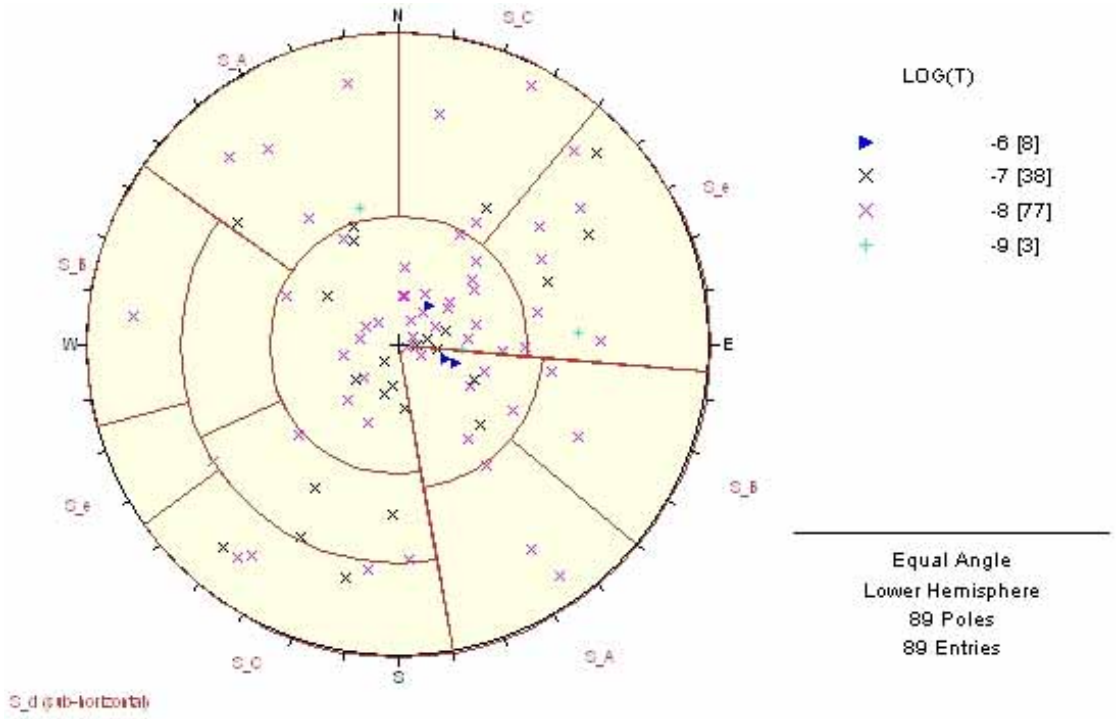

Figure B-47. *Orientations of the simulated flowing features for the correlated case for KAV04A below –300 m. One realisation is shown. Symbols are coloured according to log of transmissivity of each flowing feature (m^2 s^{-1}).*

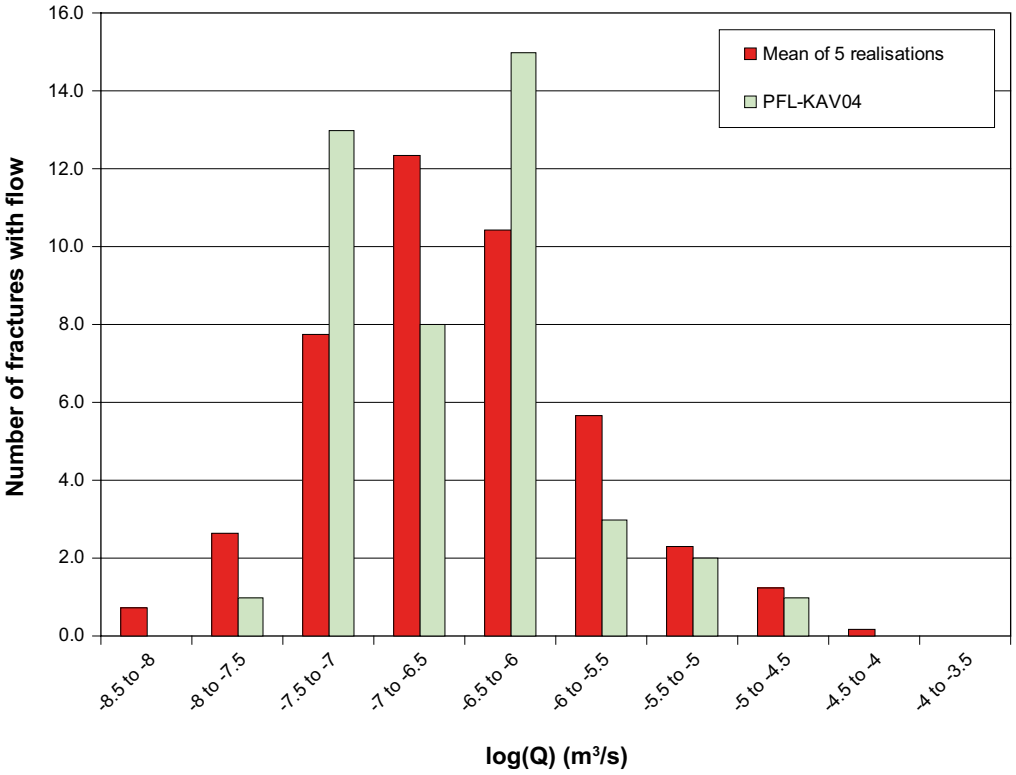

Figure B-48. *Plot of Histogram of Log(Q) flow-rate to borehole, for the mean of five realisations compared to the PFL-anomaly data for KAV04A above –300 m. Here, the correlated T distribution is used, from the matched PFL-f and PSS transmissivity with 28% of P32.*

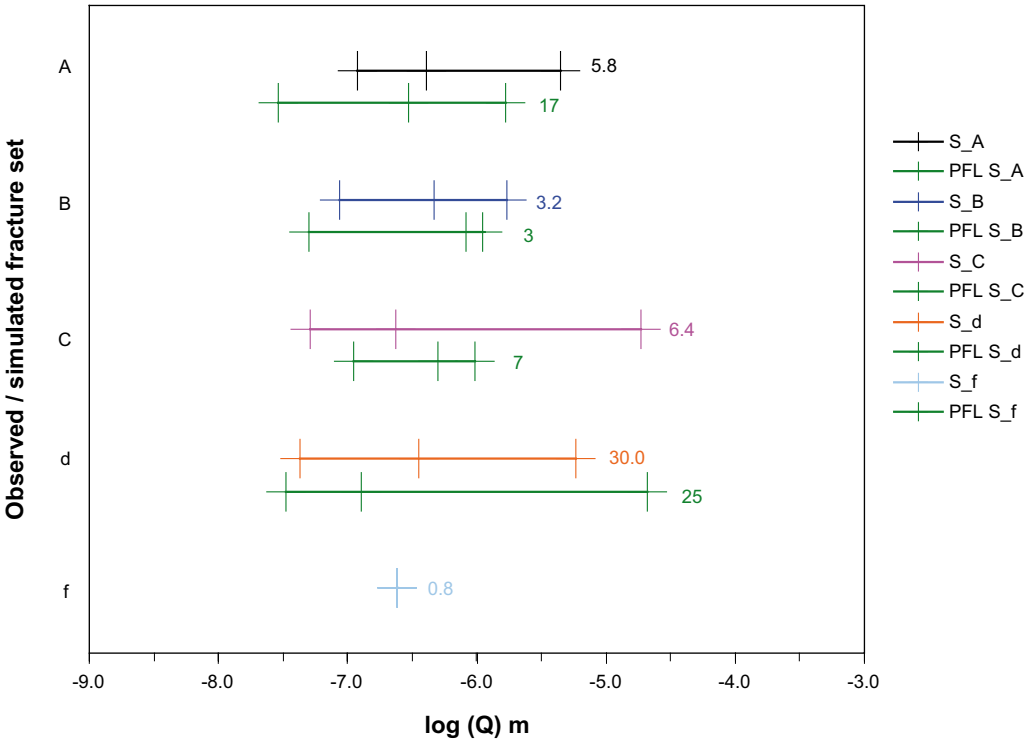

Figure B-49. *Plot of Log(Q) flow-rate to borehole, for the mean of five realisations compared to the PFL-anomaly data for KAV04A above –300 m. The flow in each fracture set is shown, with vertical bars marking the minimum, median and maximum flow-rates. Here, the correlated T distribution is used, from the matched PFL-f and PSS transmissivity with 28% of P32.*

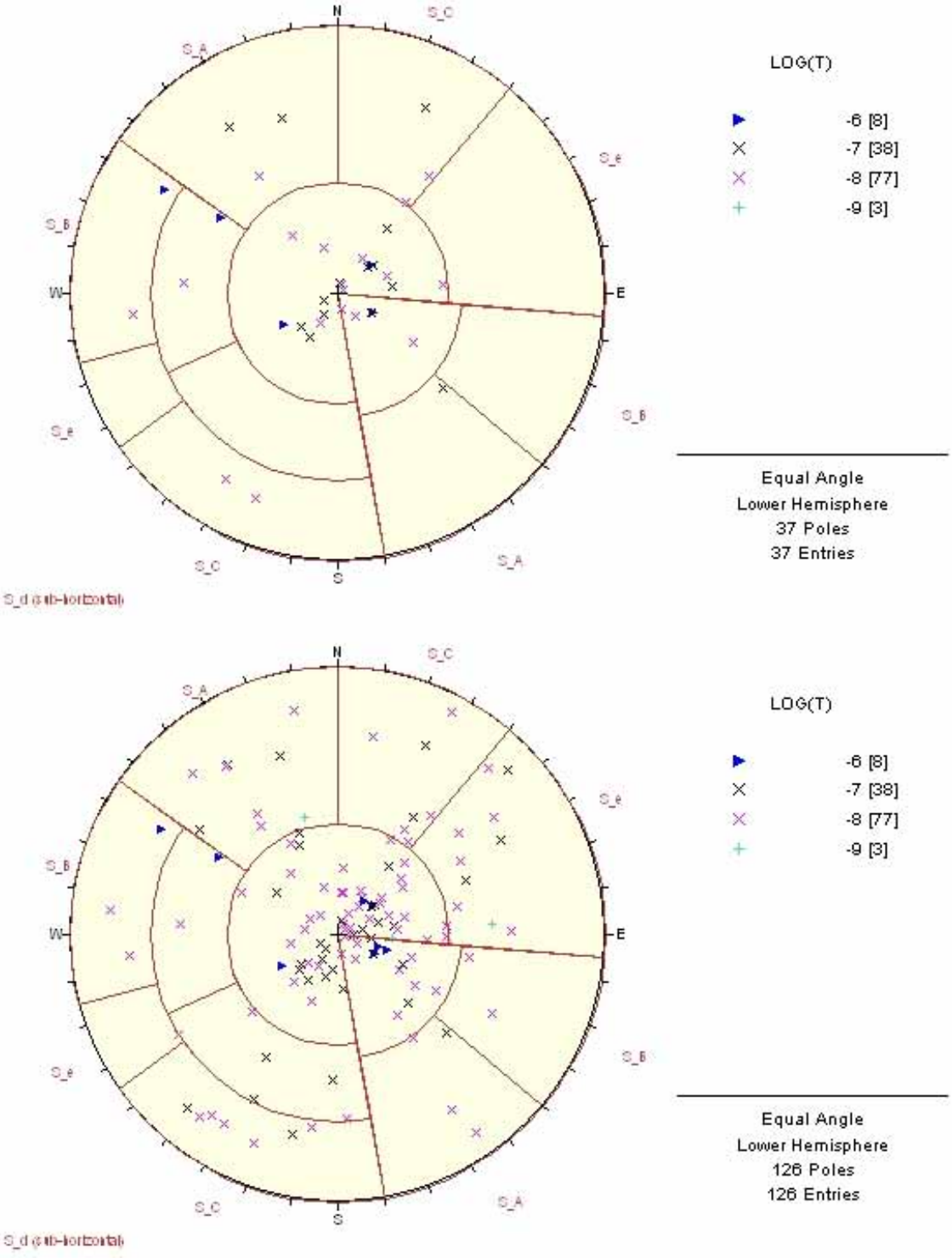

Figure B-50. *Orientations of the simulated flowing features for the correlated case for KAV04A above –300 m (top), and the complete length of KAV04A (bottom). One realisation is shown. Symbols are coloured according to log of transmissivity of each flowing feature (m^2 s^{-1}).*

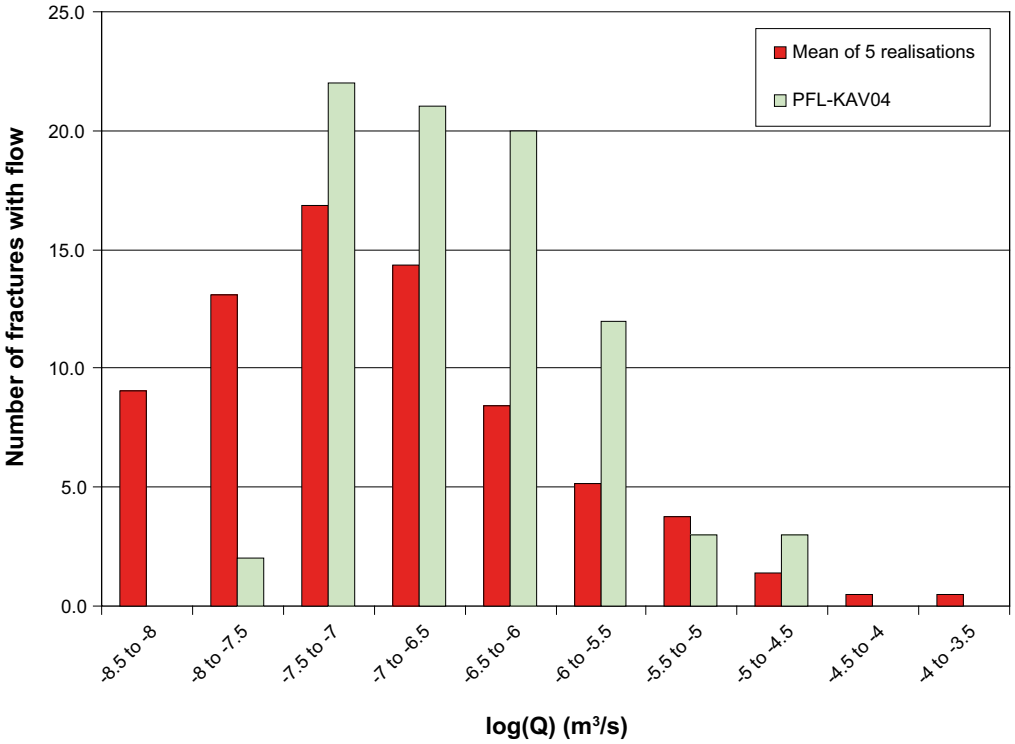

Figure B-51. *Plot of Histogram of Log(Q) flow-rate to borehole, for the mean of five realisations compared to the PFL-anomaly data for KAV04A below –300 m. Here, the semi-correlated T distribution is used, from the matched PFL-f and PSS transmissivity with 22% of P32.*

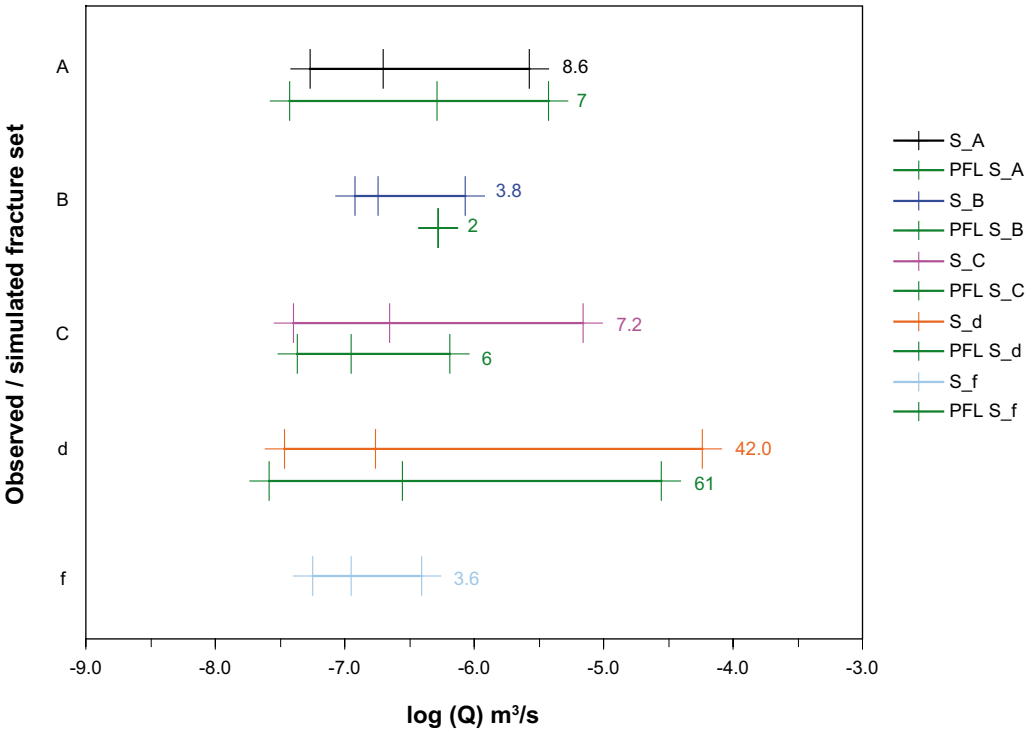

Figure B-52. *Plot of Log(Q) flow-rate to borehole, for the mean of five realisations compared to the PFL-anomaly data for KAV04A below –300 m. The flow in each fracture set is shown, with vertical bars marking the minimum, median and maximum flow-rates. Here, the semi-correlated T distribution is used, from the matched PFL-f and PSS transmissivity with 22% of P32.*

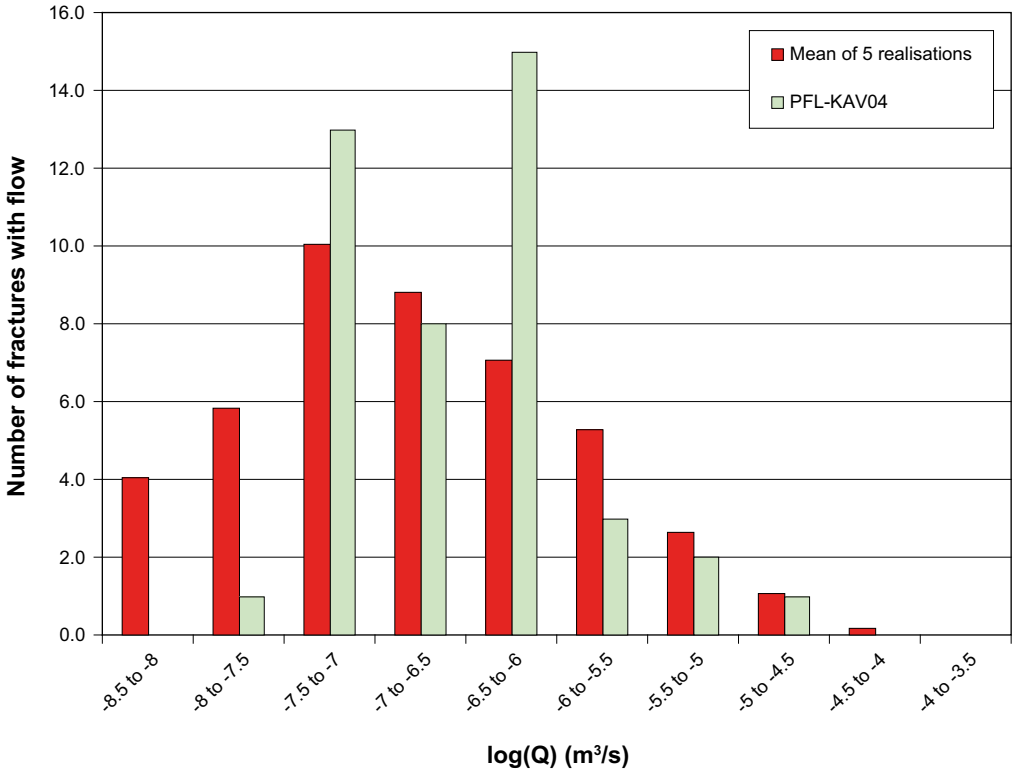

Figure B-53. *Plot of Histogram of Log(Q) flow-rate to borehole, for the mean of five realisations compared to the PFL-anomaly data for KAV04A above –300 m. Here, the semi-correlated T distribution is used, from the matched PFL-f and PSS transmissivity with 28% of P32.*

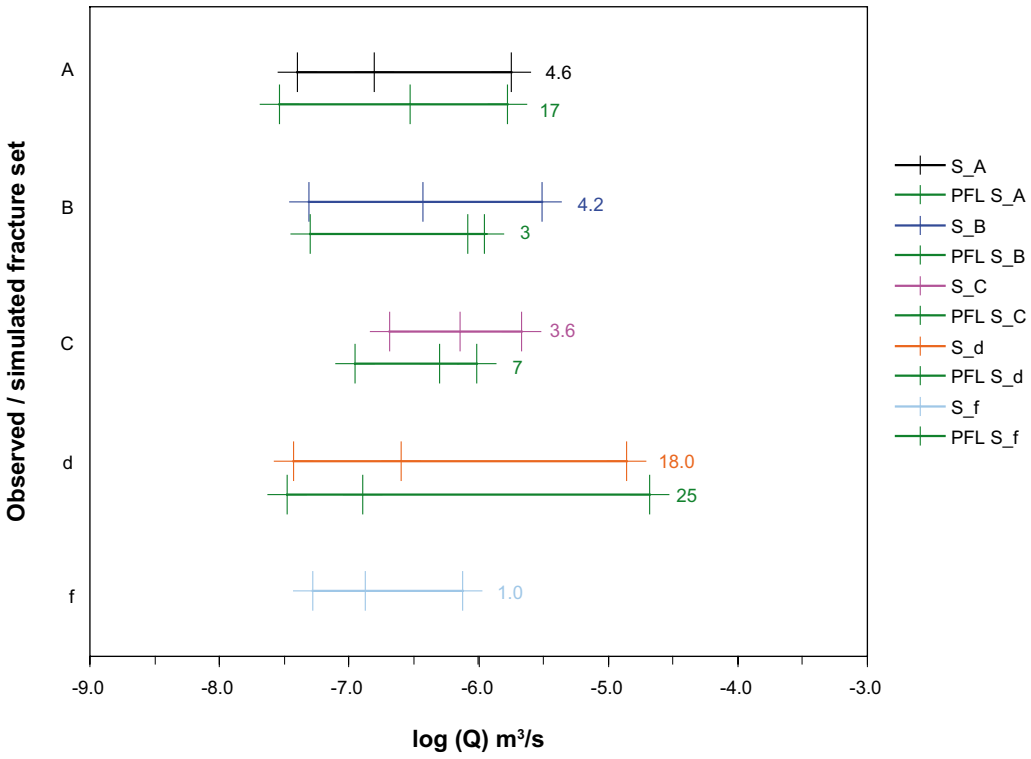

Figure B-54. *Plot of Log(Q) flow-rate to borehole, for the mean of five realisations compared to the PFL-anomaly data for KAV04A above –300 m. The flow in each fracture set is shown, with vertical bars marking the minimum, median and maximum flow-rates. Here, the semi-correlated T distribution is used, from the matched PFL-f and PSS transmissivity with 28% of P32.*

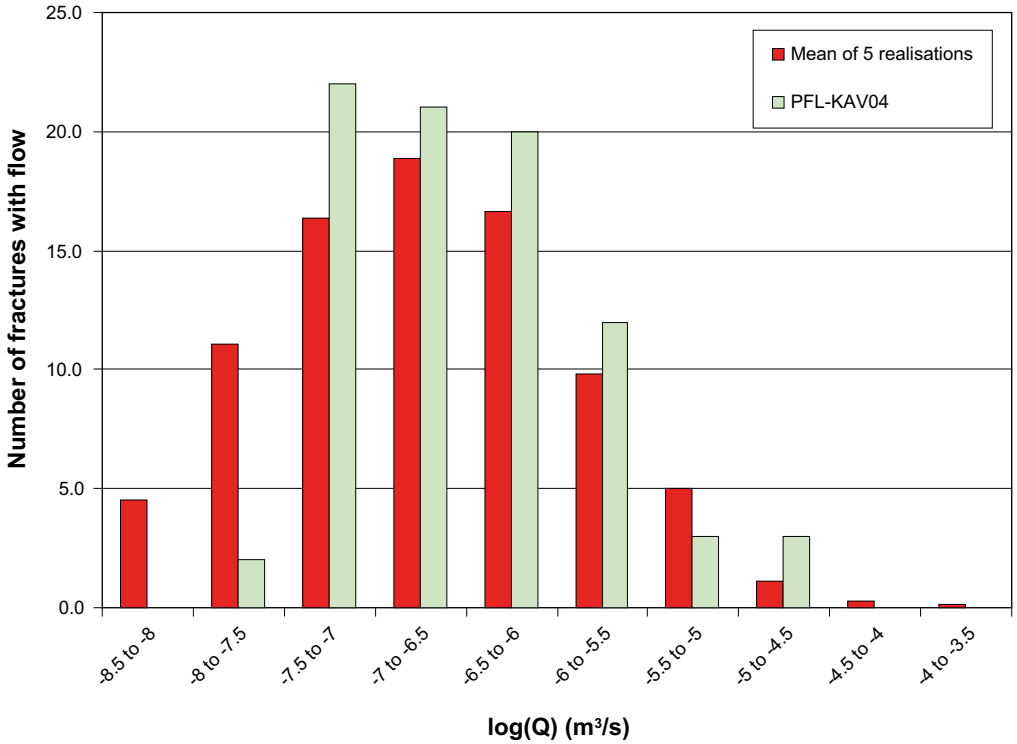

Figure B-55. *Plot of Histogram of Log(Q) flow-rate to borehole, for the mean of five realisations compared to the PFL-anomaly data for KAV04A below –300 m. Here, the uncorrelated T distribution is used, from the matched PFL-f and PSS transmissivity with 22% of P32.*

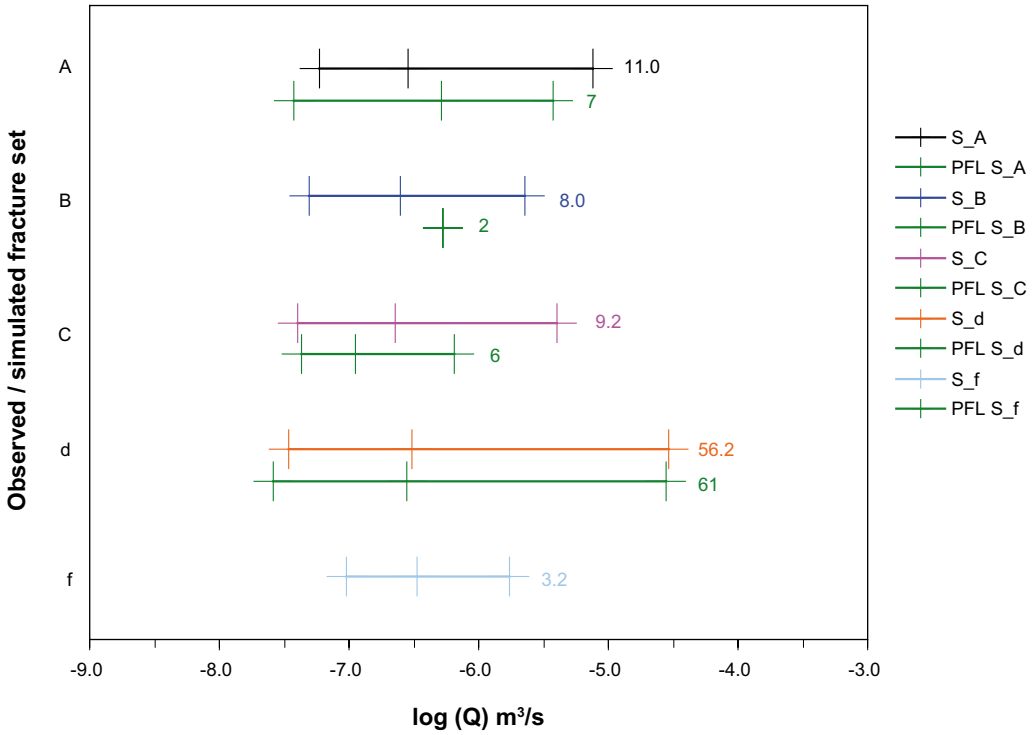

Figure B-56. *Plot of Log(Q) flow-rate to borehole, for the mean of five realisations compared to the PFL-anomaly data for KAV04A below –300 m. The flow in each fracture set is shown, with vertical bars marking the minimum, median and maximum flow-rates. Here, the uncorrelated T distribution is used, from the matched PFL-f and PSS transmissivity with 22% of P32.*

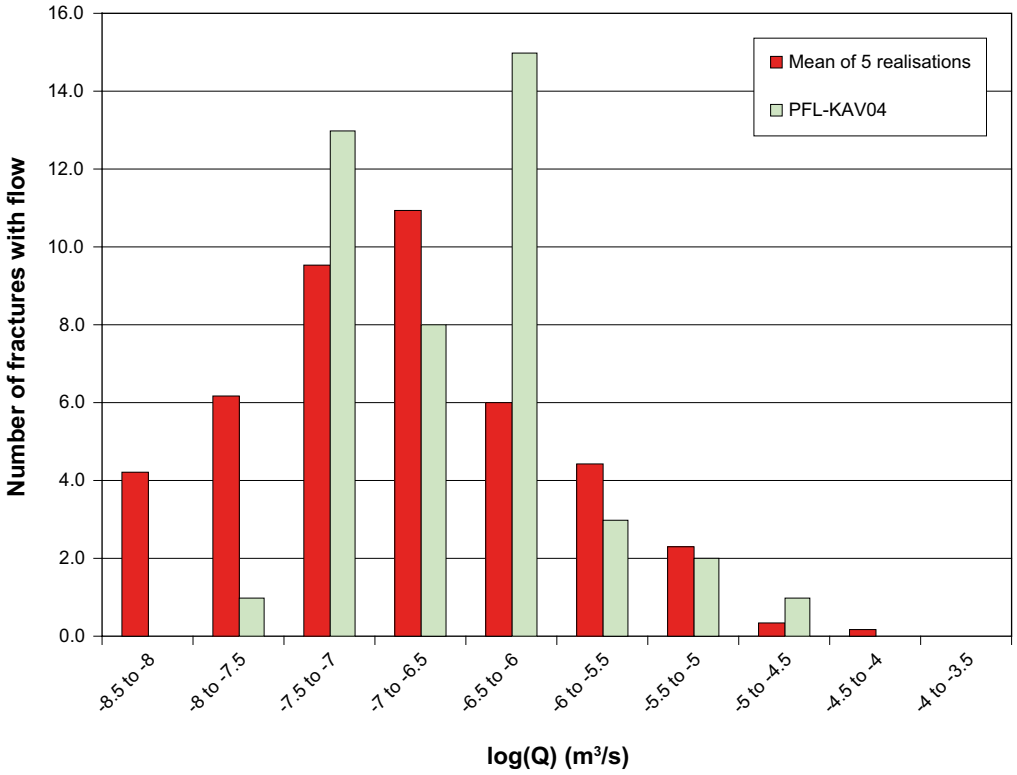

Figure B-57. *Plot of Histogram of Log(Q) flow-rate to borehole, for the mean of five realisations compared to the PFL-anomaly data for KAV04A above –300 m. Here, the uncorrelated T distribution is used, from the matched PFL-f and PSS transmissivity with 28% of P32.*

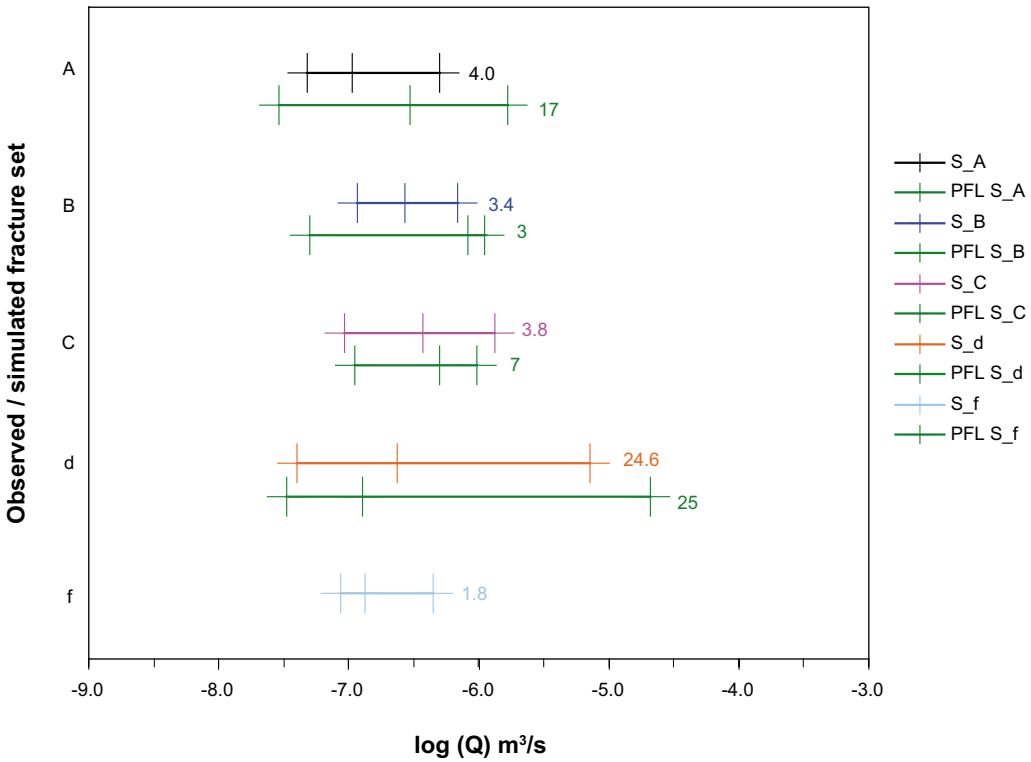

Figure B-58. *Plot of Log(Q) flow-rate to borehole, for the mean of five realisations compared to the PFL-anomaly data for KAV04A above –300 m. The flow in each fracture set is shown, with vertical bars marking the minimum, median and maximum flow-rates. Here, the uncorrelated T distribution is used, from the matched PFL-f and PSS transmissivity with 28% of P32.*

Appendix C

Description of transport properties of the present-day flow paths

C.1 Methodology

The general approach to characterising transport properties is to track particles advected by the present-day flow-field and to record the travel time (t_r), initial Darcy-velocity (canister flux, U_r), F-factor (F_r) and path length (L_r) (See Section 2.7). The subscript "*r*" is here used to denote that the particle is transported in the rock and is introduced for consistency with the coming SR-Can study for Laxemar. The particles are released within a rectangle corresponding to the local-scale, Laxemar or Simpevarp release areas at –500 m elevation and with a spacing of 50 m. The number of released particles in the local-scale is 10,205, in the Laxemar release area 3,375 and in the Simpevarp release area 1,643. Statistics are given as percentiles and the first four moments (Mean, Variance, Skewness and Kurtosis) to measure the shape of the distributions rather than just assume they are symmetric Gaussian.

C.2 Reference case

In Figure C-1 to Figure C-6 the statistical results for the reference case are shown as scatter plots and histograms for the four calculated performance measures travel time (t_r), canister flux (U_r, Darcy velocity), F-factor (F_r) and path length (L_r). The results presented in Figure C-1 and Figure C-4 are based on the ensemble of particles released within the local-scale release area. In Figure C-2 and Figure C-5 the results are based on particles released within the Simpevarp release area only. In Figure C-3 and Figure C-6 the results are based on particles released within the Laxemar release area only. The results demonstrate approximately uni-modal behaviour (normal distribution). The different rock properties inside the local-scale do however have an impact on the results. Separating the data from the two areas Simpevarp and Laxemar it becomes clear that the two areas show quite different statistics indicating differences in the structural model.

The statistical summaries for the reference case are presented in Table C-1 to Table C-3, where the statistics are calculated for numbers in $\log_{10}$ space. The results presented are based on the ensemble of particles released in the local-scale release area. To quantify the differences between Simpevarp and Laxemar statistics were also calculated for the two sites separately. The performance measure statistics are presented in Table C-2 and Table C-3 for the two sites individually. The medians of both t_r and F_r are about one order of magnitude lower for the Laxemar release area than for Simpevarp. Correspondingly, the median of U_r is about one order of magnitude higher in the Laxemar area.

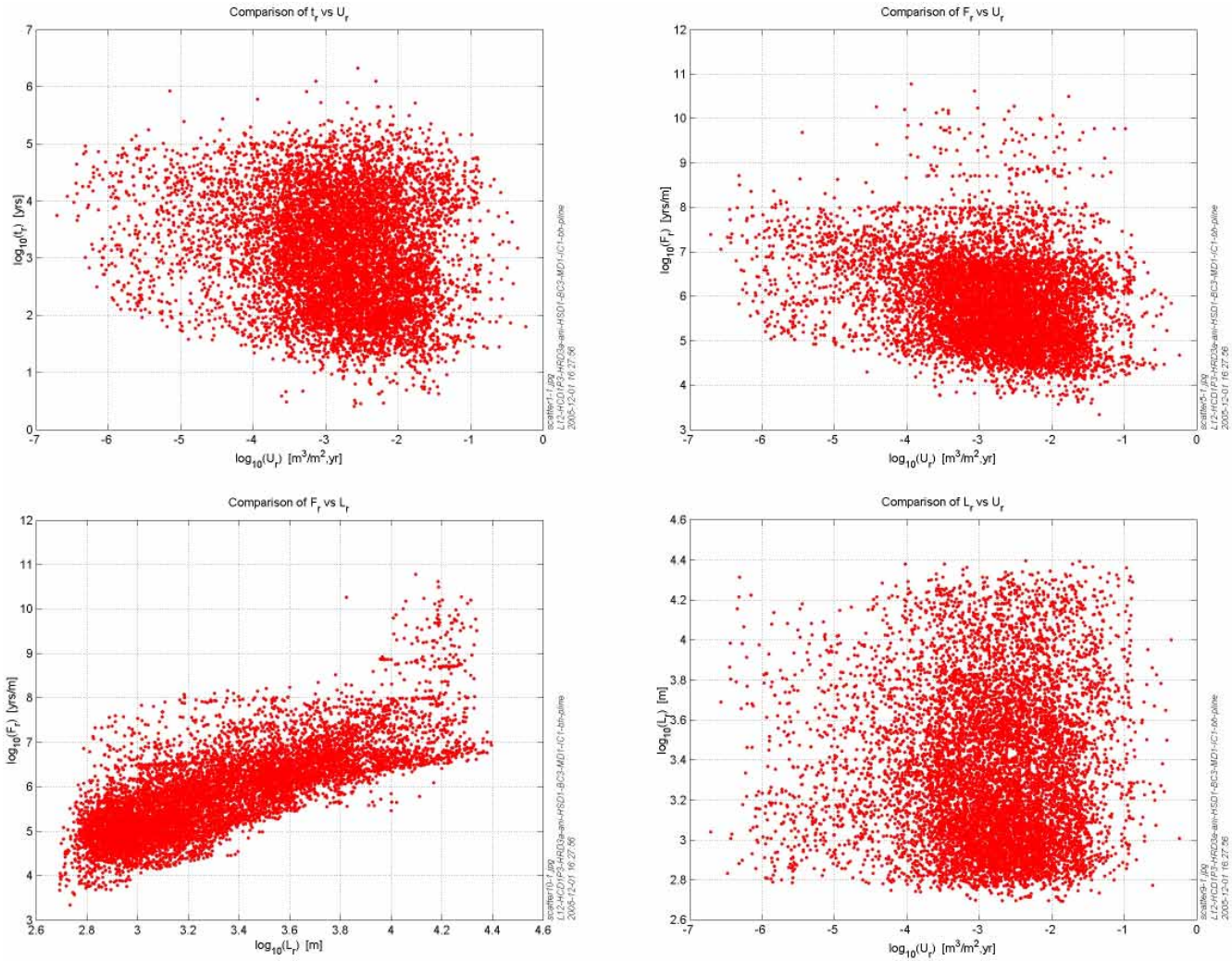

Figure C-1. *Scatter plots with different combinations of the calculated performance measures (t_r, U_r, F_r and L_r). Statistics shown for the ensemble of particles released in the local-scale release area for the reference case.*

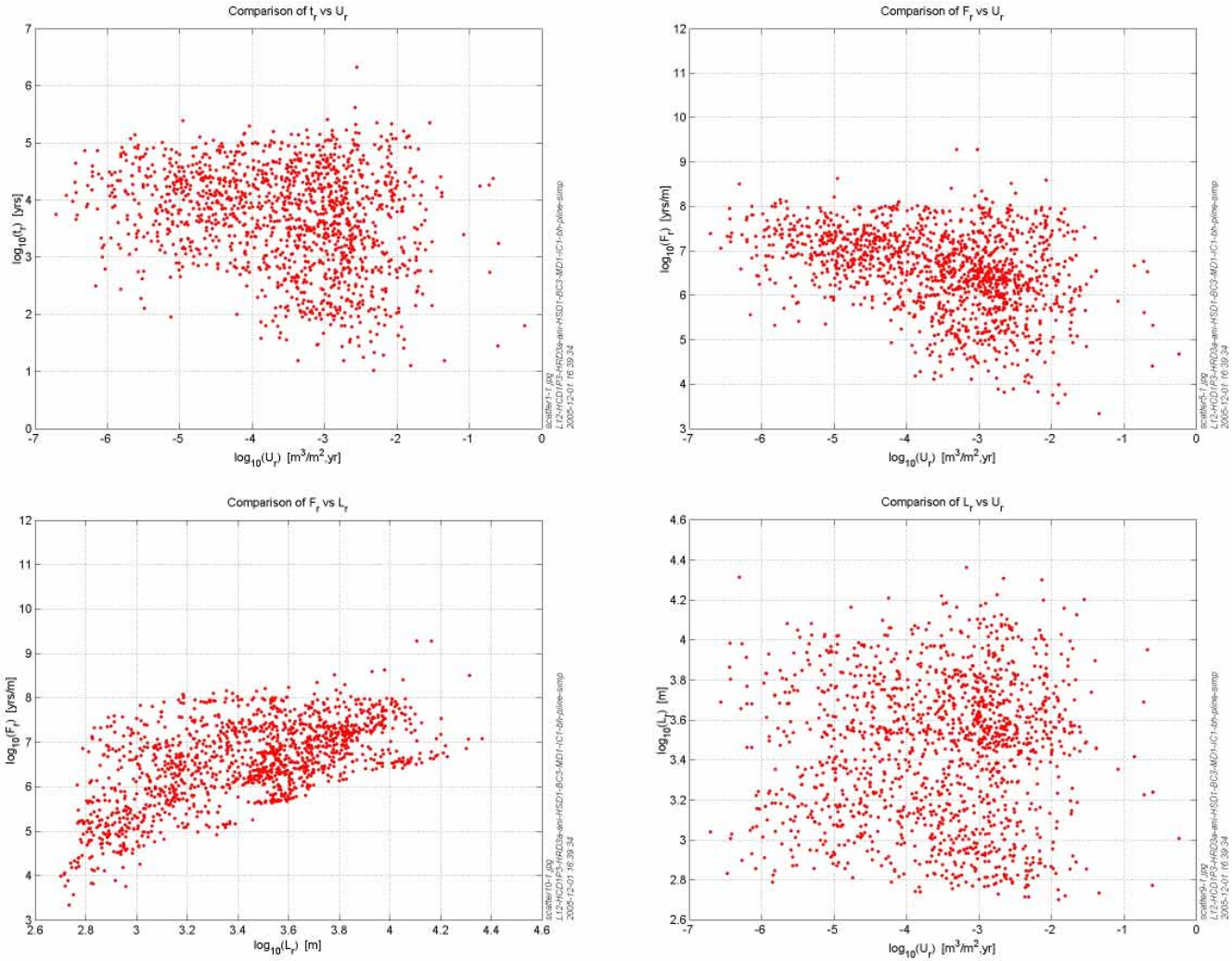

Figure C-2. *Scatter plots with different combinations of the calculated performance measures (t_r, U_r, F_r and L_r). Statistics shown for the reference case for particles released within the Simpevarp release area.*

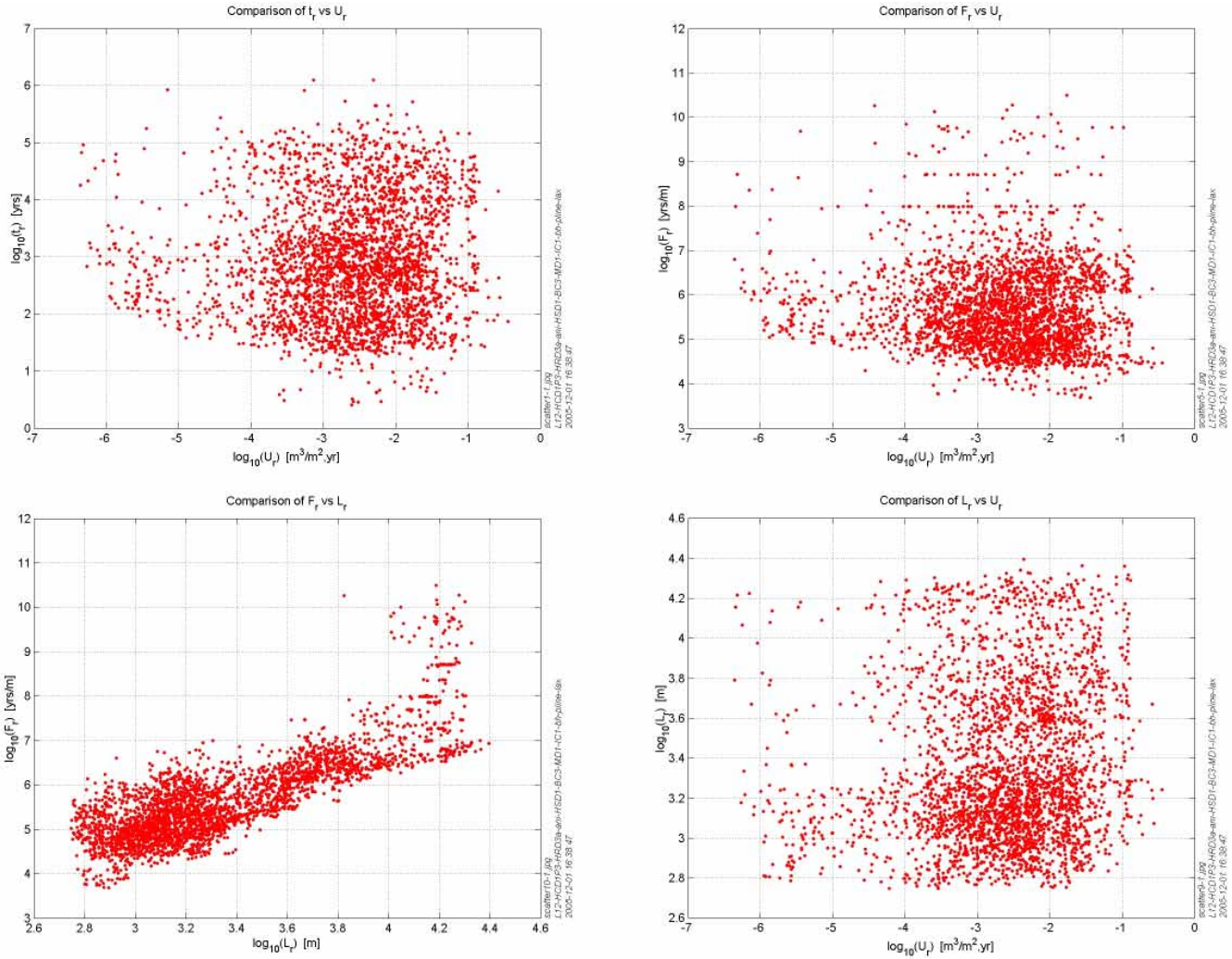

Figure C-3. *Scatter plots with different combinations of the calculated performance measures (t_r, U_r, F_r and L_r). Statistics shown for the reference case for particles released within the Laxemar release area.*

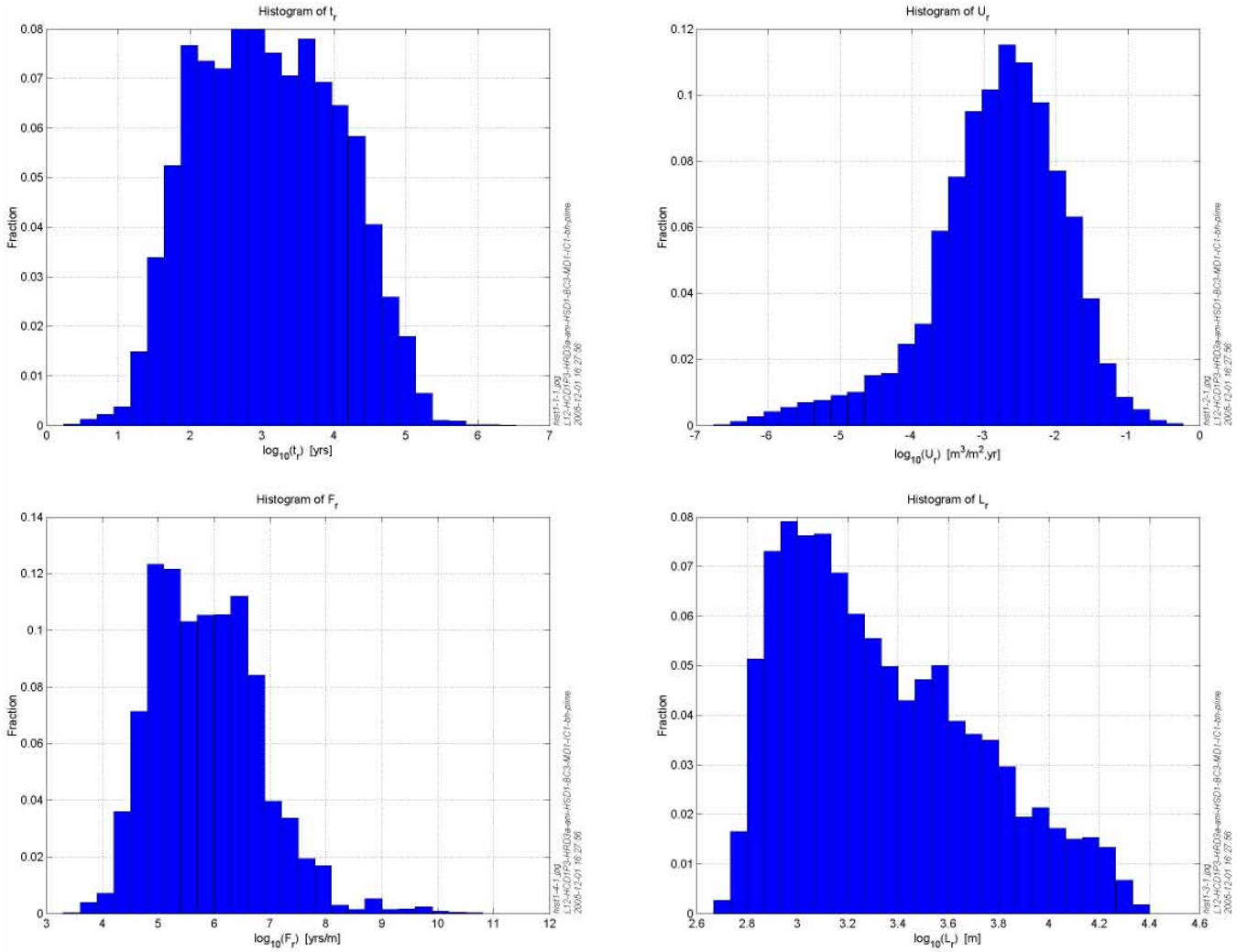

Figure C-4. *Histograms of the calculated performance measures (t_r, U_r, F_r and L_r). Statistics shown for the ensemble of particles released in the local-scale release area for the reference case.*

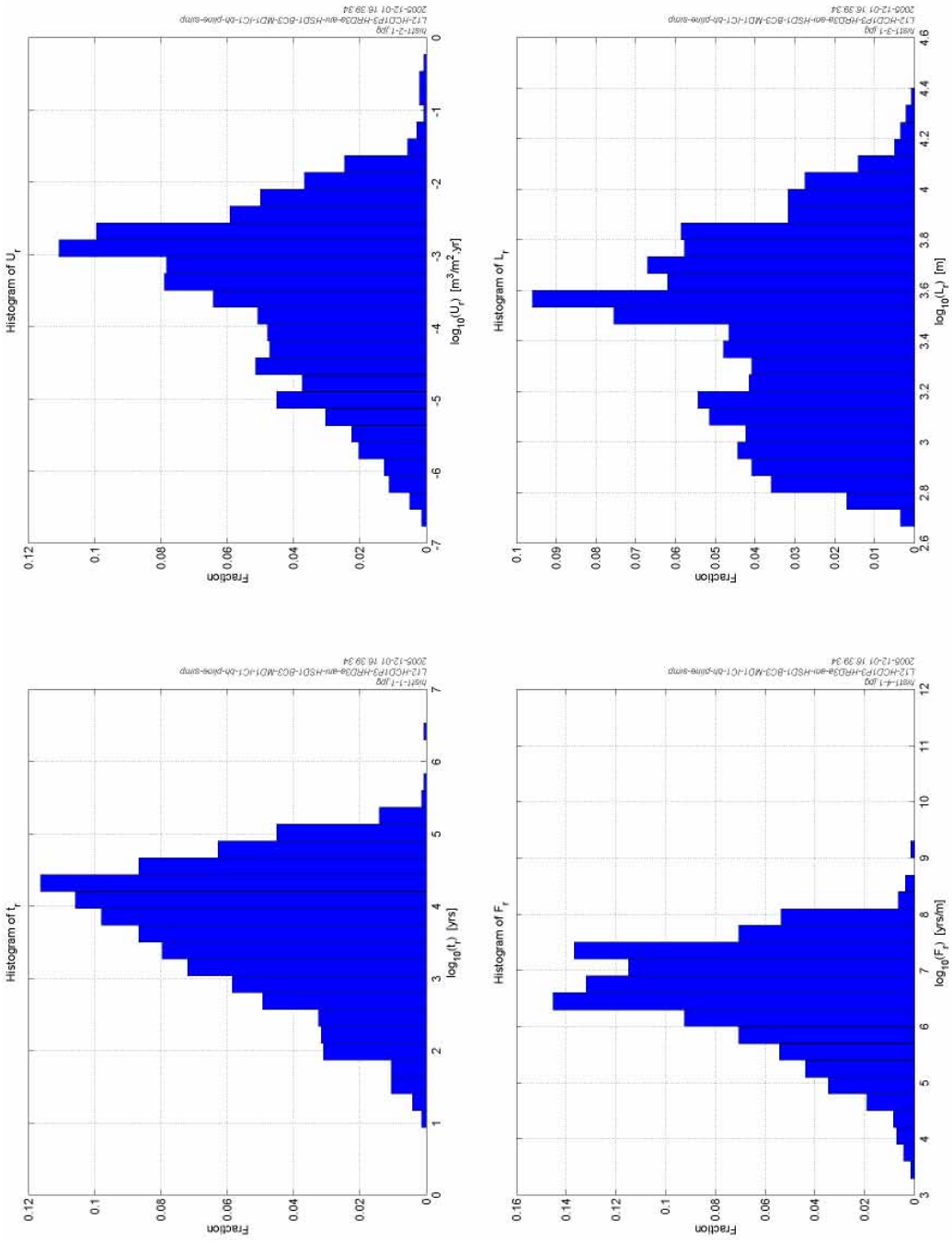

Figure C-5. *Histograms of the calculated performance measures (t_r, U_r, F_r and L_r). Statistics shown for the reference case for particles released within the Simpevarp release area.*

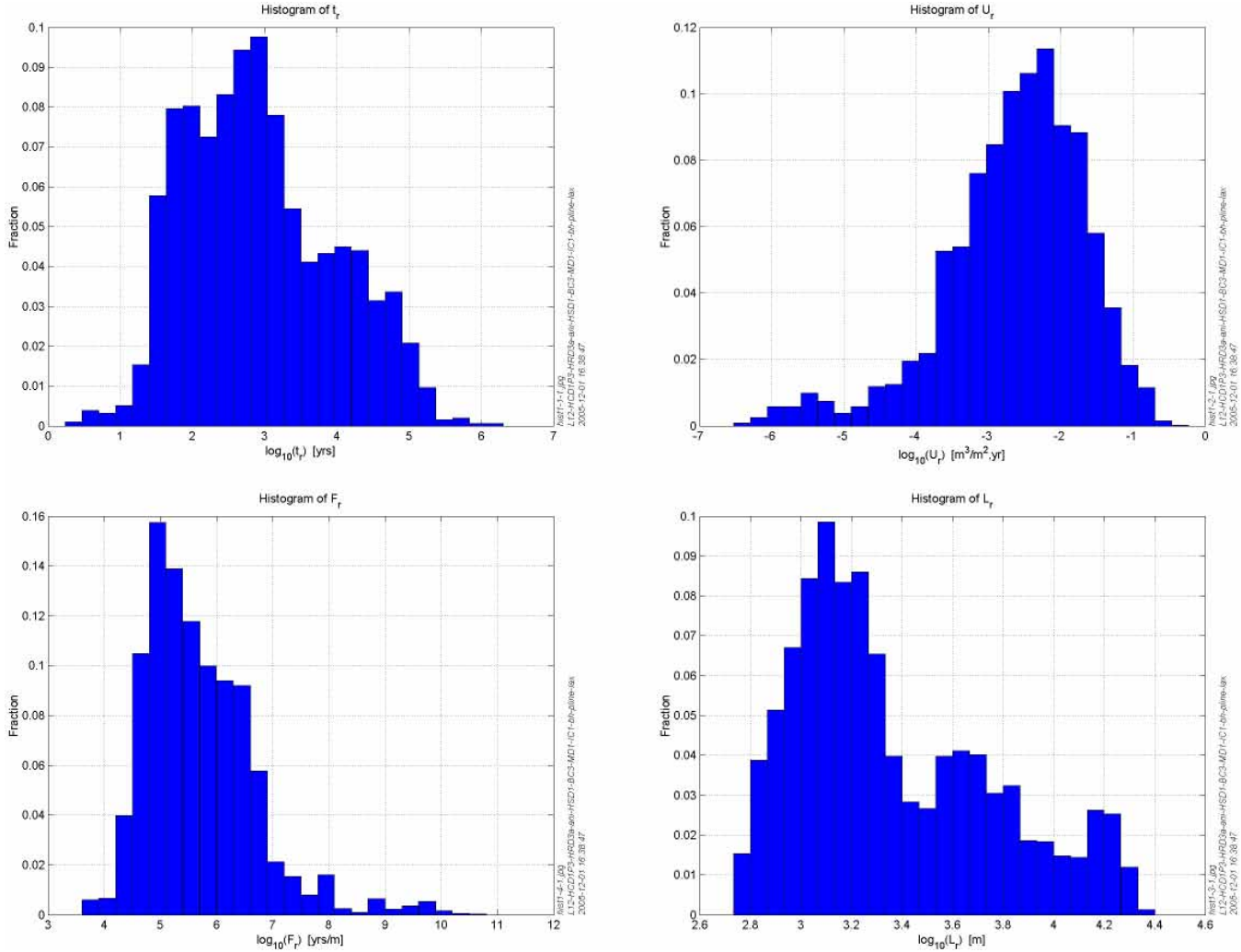

Figure C-6. *Histograms of the calculated performance measures (t_r, U_r, F_r and L_r). Statistics shown for the reference case for the particles released within the Laxemar release area.*

Table C-1. Statistical summary of the calculated performance measures (t_r, U_r, F_r and L_r) for the ensemble of particles released in the local-scale release area for the reference case.

Statistical entity	$\text{Log}_{10}(t_r)$	$\text{Log}_{10}(U_r)$	$\text{Log}_{10}(F_r)$	$\text{Log}_{10}(L_r)$
Mean	3.094	–2.825	5.870	3.337
Median	3.063	–2.726	5.796	3.261
5th percentile	1.592	–4.603	4.514	2.845
25th percentile	2.303	–3.312	5.119	3.024
75th percentile	3.846	–2.199	6.492	3.599
95th percentile	4.697	–1.517	7.556	4.077
Std dev	0.975	0.933	0.969	0.381
Variance	0.950	0.871	0.939	0.145
Skewness	0.090	–0.813	0.726	0.606
Kurtosis	–0.776	1.220	1.061	–0.512
Min value	0.406	–7.257	3.340	2.693
Max value	6.328	–0.236	10.778	4.396
Fraction OK	0.922	1.000	0.922	0.922

Table C-2. Statistical summary of the calculated performance measures (t_r, U_r, F_r and L_r) for the Simpevarp release area for the reference case.

Statistical entity	$\text{Log}_{10}(t_r)$	$\text{Log}_{10}(U_r)$	$\text{Log}_{10}(F_r)$	$\text{Log}_{10}(L_r)$
Mean	3.688	–3.499	6.563	3.446
Median	3.830	–3.282	6.655	3.500
5th percentile	2.064	–5.575	4.921	2.856
25th percentile	3.117	–4.258	6.032	3.151
75th percentile	4.357	–2.695	7.240	3.712
95th percentile	4.948	–1.964	7.876	4.008
Std dev	0.881	1.111	0.901	0.356
Variance	0.776	1.234	0.811	0.126
Skewness	–0.475	–0.467	–0.539	–0.097
Kurtosis	–0.345	–0.252	0.114	–0.863
Min value	1.015	–7.257	3.340	2.703
Max value	6.328	–0.236	9.283	4.364
Fraction OK	0.863	1.000	0.863	0.863

Table C-3. Statistical summary of the calculated performance measures (t_r, U_r, F_r and L_r) for the Laxemar release area for the reference case.

Statistical entity	$Log_{10}(t_r)$	$Log_{10}(U_r)$	$Log_{10}(F_r)$	$Log_{10}(L_r)$
Mean	2.923	–2.639	5.691	3.361
Median	2.806	–2.513	5.497	3.246
5th percentile	1.487	–4.476	4.493	2.861
25th percentile	2.111	–3.141	4.975	3.062
75th percentile	3.635	–1.974	6.260	3.639
95th percentile	4.803	–1.306	7.454	4.171
Std dev	1.024	0.976	0.986	0.393
Variance	1.049	0.953	0.973	0.155
Skewness	0.387	–0.951	1.312	0.722
Kurtosis	–0.536	1.393	2.848	–0.449
Min value	0.406	–6.364	3.686	2.748
Max value	6.102	–0.446	10.500	4.396
Fraction OK	0.923	1.000	0.923	0.923

C.3 The intermediate watertable case

The statistical summaries for the intermediate watertable case are presented in Table C-4 to Table C-6, where the statistics are calculated for numbers in $\log_{10}$ space. The results presented are based on the ensemble of particles released in the local-scale release area. To quantify the differences between Simpevarp and Laxemar statistics were also calculated for the two sites separately. The performance measure statistics are presented in Table C-5 and Table C-6 for the two sites individually. The medians of both t_r and F_r are about one order of magnitude lower for the Laxemar release area than for Simpevarp. Correspondingly, the median of U_r is about one order of magnitude higher in the Laxemar area. The F-factors are slightly lower for the intermediate watertable case compared to the reference case.

Table C-4. Statistical summary of the calculated performance measures (t_r, U_r, F_r and L_r) for the ensemble of particles released in the local-scale release area for the intermediate watertable case.

Statistical entity	$Log_{10}(t_r)$	$Log_{10}(U_r)$	$Log_{10}(F_r)$	$Log_{10}(L_r)$
Mean	3.011	–2.748	5.740	3.312
Median	2.974	–2.649	5.626	3.231
5th percentile	1.547	–4.432	4.491	2.835
25th percentile	2.220	–3.239	5.020	3.002
75th percentile	3.717	–2.134	6.386	3.560
95th percentile	4.625	–1.487	7.332	4.032
Std dev	0.970	0.900	0.927	0.375
Variance	0.942	0.810	0.859	0.141
Skewness	0.172	–0.793	0.767	0.635
Kurtosis	–0.752	1.195	1.128	–0.529
Min value	0.311	–6.989	3.231	2.693
Max value	6.167	–0.247	11.123	4.361
Fraction OK	0.928	1.000	0.928	0.928

C.4 The topographic head case

The statistical summaries for the topographic head case are presented in Table C-7 to Table C-9, where the statistics are calculated for numbers in $\log_{10}$ space. The results presented are based on the ensemble of particles released in the local-scale release area. To quantify the differences between Simpevarp and Laxemar statistics were also calculated for the two sites separately. The performance measure statistics are presented in Table C-8 and Table C-9 for the two sites individually. The medians of both t_r and F_r are almost one order of magnitude lower for the Laxemar release area than for Simpevarp. Correspondingly, the median of U_r is higher in the Laxemar area. The F-factors are lower for the topographic head case compared to the reference case. For the Laxemar release area in particular the median F-factor is 0.7 logarithmic units lower in the topographic head case.

Table C-5. Statistical summary of the calculated performance measures (t_r, U_r, F_r and L_r) for the Simpevarp release area for the intermediate watertable case.

Statistical entity	$\log_{10}(t_r)$	$\log_{10}(U_r)$	$\log_{10}(F_r)$	$\log_{10}(L_r)$
Mean	3.481	–3.326	6.319	3.314
Median	3.503	–3.144	6.379	3.287
5th percentile	1.805	–5.290	4.677	2.817
25th percentile	2.871	–3.981	5.752	3.025
75th percentile	4.152	–2.573	6.923	3.559
95th percentile	4.991	–1.912	7.854	3.944
Std dev	0.951	1.039	0.941	0.357
Variance	0.905	1.080	0.885	0.127
Skewness	–0.163	–0.561	–0.078	0.430
Kurtosis	–0.564	0.025	0.374	–0.584
Min value	0.952	–6.989	3.231	2.703
Max value	5.960	–0.247	10.168	4.333
Fraction OK	0.733	1.000	0.733	0.733

Table C-6. Statistical summary of the calculated performance measures (t_r, U_r, F_r and L_r) for the Laxemar release area for the intermediate watertable case.

Statistical entity	$\log_{10}(t_r)$	$\log_{10}(U_r)$	$\log_{10}(F_r)$	$\log_{10}(L_r)$
Mean	2.914	–2.605	5.636	3.341
Median	2.786	–2.497	5.433	3.240
5th percentile	1.484	–4.396	4.503	2.843
25th percentile	2.112	–3.119	4.955	3.055
75th percentile	3.568	–1.943	6.260	3.621
95th percentile	4.637	–1.283	7.316	4.042
Std dev	1.018	0.959	0.923	0.374
Variance	1.035	0.920	0.851	0.140
Skewness	0.363	–0.906	1.097	0.582
Kurtosis	–0.745	1.250	2.108	–0.663
Min value	0.311	–6.257	3.727	2.722
Max value	5.525	–0.427	10.368	4.326
Fraction OK	0.986	1.000	0.986	0.986

Table C-7. Statistical summary of the calculated performance measures (t_r, U_r, F_r and L_r) for the ensemble of particles released in the local-scale release area for the topographic head case.

Statistical entity	$\text{Log}_{10}(t_r)$	$\text{Log}_{10}(U_r)$	$\text{Log}_{10}(F_r)$	$\text{Log}_{10}(L_r)$
Mean	2.785	–2.834	5.516	3.255
Median	2.709	–2.693	5.329	3.185
5th percentile	1.449	–4.876	4.338	2.834
25th percentile	2.095	–3.393	4.820	2.998
75th percentile	3.347	–2.117	6.089	3.444
95th percentile	4.562	–1.450	7.175	3.926
Std dev	0.922	1.030	0.940	0.333
Variance	0.849	1.061	0.883	0.111
Skewness	0.440	–0.825	1.116	0.855
Kurtosis	–0.105	0.915	2.162	0.254
Min value	0.293	–7.224	3.166	2.694
Max value	6.020	–0.285	10.509	4.358
Fraction OK	0.942	1.000	0.942	0.942

Table C-8. Statistical summary of the calculated performance measures (t_r, U_r, F_r and L_r) for the Simpevarp release area for the topographic head case.

Statistical entity	$\text{Log}_{10}(t_r)$	$\text{Log}_{10}(U_r)$	$\text{Log}_{10}(F_r)$	$\text{Log}_{10}(L_r)$
Mean	3.273	–3.316	6.056	3.270
Median	3.283	–3.074	5.996	3.210
5th percentile	1.556	–5.570	4.344	2.810
25th percentile	2.559	–4.051	5.320	2.990
75th percentile	4.012	–2.413	6.851	3.533
95th percentile	4.822	–1.766	7.678	3.897
Std dev	1.008	1.167	1.053	0.341
Variance	1.016	1.362	1.109	0.117
Skewness	–0.061	–0.603	0.218	0.553
Kurtosis	–0.623	–0.234	0.017	–0.420
Min value	0.792	–7.224	3.166	2.697
Max value	6.020	–0.521	9.891	4.283
Fraction OK	0.870	1.000	0.870	0.870

Table C-9. Statistical summary of the calculated performance measures (t_r, U_r, F_r and L_r) for the Laxemar release area for the topographic head case.

Statistical entity	$Log_{10}(t_r)$	$Log_{10}(U_r)$	$Log_{10}(F_r)$	$Log_{10}(L_r)$
Mean	2.599	–2.771	5.333	3.244
Median	2.522	–2.537	5.123	3.188
5th percentile	1.403	–5.444	4.384	2.821
25th percentile	2.000	–3.366	4.757	3.032
75th percentile	2.979	–1.979	5.777	3.396
95th percentile	4.509	–1.288	6.922	3.886
Std dev	0.866	1.151	0.831	0.305
Variance	0.751	1.325	0.691	0.093
Skewness	0.815	–0.935	1.617	0.865
Kurtosis	0.861	0.820	4.730	0.529
Min value	0.293	–6.590	3.786	2.717
Max value	5.571	–0.431	10.462	4.358
Fraction OK	0.977	1.000	0.977	0.977

C.5 Reduced K below –600 m elevation case

The statistical summaries for the variant with a hydraulic conductivity reduced by half an order of magnitude below –600 m elevation are presented in Table C-10 to Table C-12, where the statistics are calculated for numbers in log_{10}-space. The results presented are based on the ensemble of particles released in the local-scale release area. To quantify the differences between Simpevarp and Laxemar statistics were also calculated for the two sites separately. The performance measure statistics are presented in Table C-11 and Table C-12 for the two sites individually. The median F-factor is only very slightly lower than in the reference case.

Table C-10. Statistical summary of the calculated performance measures (t_r, U_r, F_r and L_r) for the ensemble of particles released in the local-scale release area for the case with a reduced K below –600 m elevation.

Statistical entity	$Log_{10}(t_r)$	$Log_{10}(U_r)$	$Log_{10}(F_r)$	$Log_{10}(L_r)$
Mean	3.134	–2.811	5.899	3.344
Median	3.108	–2.718	5.773	3.253
5th percentile	1.580	–4.544	4.512	2.846
25th percentile	2.283	–3.284	5.107	3.023
75th percentile	3.996	–2.186	6.635	3.618
95th percentile	4.726	–1.516	7.490	4.085
Std dev	1.022	0.927	0.968	0.389
Variance	1.044	0.858	0.936	0.151
Skewness	0.060	–0.829	0.381	0.624
Kurtosis	–0.974	1.303	–0.340	–0.565
Min value	0.466	–7.099	3.319	2.726
Max value	5.734	–0.275	10.128	4.405
Fraction OK	0.894	1.000	0.894	0.894

Table C-11. Statistical summary of the calculated performance measures (t_r, U_r, F_r and L_r) for the Simpevarp release area for the case with a reduced K below –600 m elevation.

Statistical entity	$Log_{10}(t_r)$	$Log_{10}(U_r)$	$Log_{10}(F_r)$	$Log_{10}(L_r)$
Mean	3.869	–3.550	6.709	3.463
Median	4.026	–3.440	6.826	3.473
5th percentile	2.175	–5.530	5.010	2.865
25th percentile	3.368	–4.297	6.242	3.189
75th percentile	4.477	–2.760	7.319	3.737
95th percentile	5.009	–1.964	7.894	4.055
Std dev	0.843	1.087	0.863	0.365
Variance	0.711	1.182	0.744	0.133
Skewness	–0.731	–0.380	–0.586	0.033
Kurtosis	0.075	–0.203	0.500	–0.784
Min value	1.170	–7.099	3.319	2.730
Max value	5.734	–0.509	9.672	4.378
Fraction OK	0.823	1.000	0.823	0.823

Table C-12. Statistical summary of the calculated performance measures (t_r, U_r, F_r and L_r) for the Laxemar release area for the case with a reduced K below –600 m elevation.

Statistical entity	$Log_{10}(t_r)$	$Log_{10}(U_r)$	$Log_{10}(F_r)$	$Log_{10}(L_r)$
Mean	2.852	–2.641	5.593	3.323
Median	2.746	–2.518	5.421	3.218
5th percentile	1.470	–4.500	4.482	2.850
25th percentile	2.052	–3.147	4.945	3.044
75th percentile	3.381	–1.985	6.139	3.565
95th percentile	4.815	–1.302	7.277	4.074
Std dev	1.013	0.975	0.853	0.375
Variance	1.026	0.951	0.727	0.140
Skewness	0.516	–0.953	0.707	0.827
Kurtosis	–0.362	1.410	0.296	–0.183
Min value	0.466	–6.431	3.701	2.726
Max value	5.613	–0.438	9.974	4.384
Fraction OK	0.904	1.000	0.904	0.904

C.6 Second realisation of Hydro-DFN

The statistical summaries for the second realisation of the Hydro-DFN are presented in Table C-13 to Table C-15, where the statistics are calculated for numbers in log_{10}-space. The results presented are based on the ensemble of particles released in the local-scale release area. To quantify the differences between Simpevarp and Laxemar statistics were also calculated for the two sites separately. The performance measure statistics are presented in Table C-14 and Table C-15 for the two sites individually. The median F-factor is slightly higher by 0.3 in log_{10}-space than in the reference case.

Table C-13. Statistical summary of the calculated performance measures (t_r, U_r, F_r and L_r) for the ensemble of particles released in the local-scale release area for the second realisation of the Hydro-DFN.

Statistical entity	$Log_{10}(t_r)$	$Log_{10}(U_r)$	$Log_{10}(F_r)$	$Log_{10}(L_r)$
Mean	3.305	–2.927	6.013	3.423
Median	3.329	–2.845	6.001	3.359
5th percentile	1.681	–4.630	4.539	2.845
25th percentile	2.479	–3.439	5.211	3.043
75th percentile	4.164	–2.306	6.663	3.799
95th percentile	4.849	–1.522	7.598	4.153
Std dev	1.022	0.944	1.021	0.428
Variance	1.045	0.891	1.043	0.183
Skewness	–0.106	–0.734	0.556	0.297
Kurtosis	–0.871	1.160	0.646	–1.148
Min value	0.049	–7.236	3.098	2.702
Max value	6.444	–0.265	10.249	4.368
Fraction OK	0.808	1.000	0.808	0.808

Table C-14. Statistical summary of the calculated performance measures (t_r, U_r, F_r and L_r) for the Simpevarp release area for the second realisation of the Hydro-DFN.

Statistical entity	$Log_{10}(t_r)$	$Log_{10}(U_r)$	$Log_{10}(F_r)$	$Log_{10}(L_r)$
Mean	4.146	–3.573	6.970	3.680
Median	4.204	–3.449	7.035	3.742
5th percentile	2.860	–5.672	5.657	2.990
25th percentile	3.788	–4.345	6.481	3.404
75th percentile	4.634	–2.662	7.445	3.997
95th percentile	5.225	–1.926	8.101	4.198
Std dev	0.725	1.161	0.778	0.377
Variance	0.525	1.349	0.605	0.142
Skewness	–0.852	–0.429	0.061	–0.433
Kurtosis	1.317	–0.424	1.684	–0.776
Min value	1.127	–7.236	4.031	2.771
Max value	5.687	–1.080	10.157	4.323
Fraction OK	0.626	1.000	0.626	0.626

Table C-15. Statistical summary of the calculated performance measures (t_r, U_r, F_r and L_r) for the Laxemar release area for the second realisation of the Hydro-DFN.

Statistical entity	$Log_{10}(t_r)$	$Log_{10}(U_r)$	$Log_{10}(F_r)$	$Log_{10}(L_r)$
Mean	3.202	–2.704	5.913	3.447
Median	3.062	–2.613	5.829	3.350
5th percentile	1.598	–4.371	4.527	2.865
25th percentile	2.382	–3.281	5.144	3.066
75th percentile	4.137	–2.040	6.597	3.843
95th percentile	4.794	–1.306	7.393	4.140
Std dev	1.032	0.975	1.003	0.424
Variance	1.065	0.950	1.006	0.180
Skewness	0.010	–0.770	0.814	0.228
Kurtosis	–0.947	1.092	1.733	–1.278
Min value	0.049	–6.311	3.098	2.737
Max value	5.683	–0.265	10.249	4.357
Fraction OK	0.927	1.000	0.927	0.927

C.7 Third realisation of Hydro-DFN

The statistical summaries for the third realisation of the Hydro-DFN are presented in Table C-16 to Table C-18, where the statistics are calculated for numbers in log_{10}-space. The results presented are based on the ensemble of particles released in the local-scale release area. To quantify the differences between Simpevarp and Laxemar statistics were also calculated for the two sites separately. The performance measure statistics are presented in Table C-17 and Table C-18 for the two sites individually. The median F-factor is slightly higher by 0.2 in log_{10}-space than in the reference case.

Table C-16. Statistical summary of the calculated performance measures (t_r, U_r, F_r and L_r) for the ensemble of particles released in the local-scale release area for the third realisation of the Hydro-DFN.

Statistical entity	$Log_{10}(t_r)$	$Log_{10}(U_r)$	$Log_{10}(F_r)$	$Log_{10}(L_r)$
Mean	3.175	–2.876	5.969	3.418
Median	3.218	–2.782	5.926	3.337
5th percentile	1.547	–4.747	4.459	2.852
25th percentile	2.338	–3.367	5.130	3.041
75th percentile	4.003	–2.224	6.715	3.785
95th percentile	4.741	–1.505	7.588	4.135
Std dev	1.012	0.967	1.036	0.422
Variance	1.025	0.936	1.074	0.178
Skewness	–0.121	–0.848	0.416	0.307
Kurtosis	–0.828	1.293	0.153	–1.175
Min value	0.066	–7.318	3.129	2.718
Max value	5.829	–0.463	10.277	4.381
Fraction OK	0.845	1.000	0.845	0.845

Table C-17. Statistical summary of the calculated performance measures (t_r, U_r, F_r and L_r) for the Simpevarp release area for the third realisation of the Hydro-DFN.

Statistical entity	$Log_{10}(t_r)$	$Log_{10}(U_r)$	$Log_{10}(F_r)$	$Log_{10}(L_r)$
Mean	3.880	–3.463	6.892	3.607
Median	3.930	–3.240	6.936	3.648
5th percentile	2.513	–5.815	5.497	2.895
25th percentile	3.426	–4.456	6.457	3.358
75th percentile	4.438	–2.479	7.415	3.900
95th percentile	5.029	–1.653	8.014	4.147
Std dev	0.778	1.310	0.805	0.369
Variance	0.606	1.716	0.648	0.137
Skewness	–0.654	–0.356	–0.327	–0.394
Kurtosis	0.692	–0.543	1.804	–0.615
Min value	0.845	–7.318	3.779	2.727
Max value	5.648	–0.463	10.011	4.310
Fraction OK	0.720	1.000	0.720	0.720

Table C-18. Statistical summary of the calculated performance measures (t_r, U_r, F_r and L_r) for the Laxemar release area for the third realisation of the Hydro-DFN.

Statistical entity	$Log_{10}(t_r)$	$Log_{10}(U_r)$	$Log_{10}(F_r)$	$Log_{10}(L_r)$
Mean	3.015	–2.677	5.738	3.401
Median	2.900	–2.573	5.603	3.259
5th percentile	1.503	–4.460	4.496	2.887
25th percentile	2.191	–3.213	4.996	3.063
75th percentile	4.004	–2.003	6.367	3.757
95th percentile	4.665	–1.317	7.212	4.125
Std dev	1.022	0.983	0.933	0.406
Variance	1.044	0.966	0.870	0.165
Skewness	0.186	–0.867	0.755	0.466
Kurtosis	–1.040	1.222	0.745	–1.088
Min value	0.621	–6.432	3.905	2.737
Max value	5.424	–0.480	9.920	4.314
Fraction OK	0.917	1.000	0.917	0.917

C.8 Correlated transmissivity model

In Figure C-1 to Figure C-6 the statistical results for the reference case are shown as scatter plots and histograms for the four calculated performance measures travel time (t_r), canister flux (U_r, Darcy velocity), F-factor (F_r) and path length (L_r). The results presented in Figure C-1 and Figure C-4 are based on the ensemble of particles released within the local-scale release area. In Figure C-2 and Figure C-5 the results are based on particles released within the Simpevarp release area only. In Figure C-3 and Figure C-6 the results are based on particles released within the Laxemar release area only. The results demonstrate approximately uni-modal behaviour (normal distribution). The different rock properties inside the local-scale do however have an impact on the results. Separating the data from the two subareas Simpevarp and Laxemar, it becomes clear that the two areas show quite different statistics, indicating differences in the structural model.

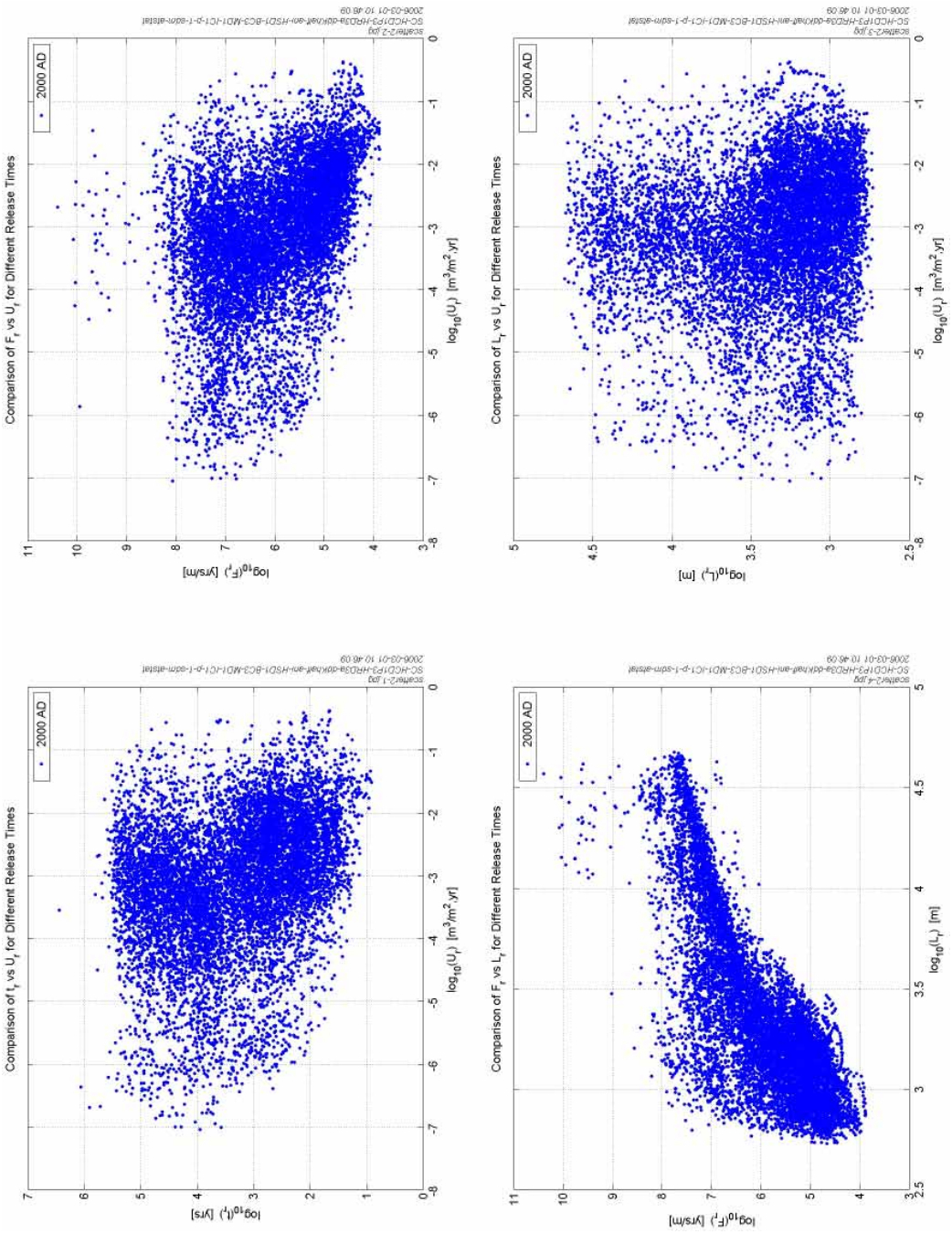

Figure C-7. *Scatter plots with different combinations of the calculated performance measures (t_r, U_r, F_r and L_r). Statistics shown for the ensemble of particles released in the local-scale release area for the reference case.*

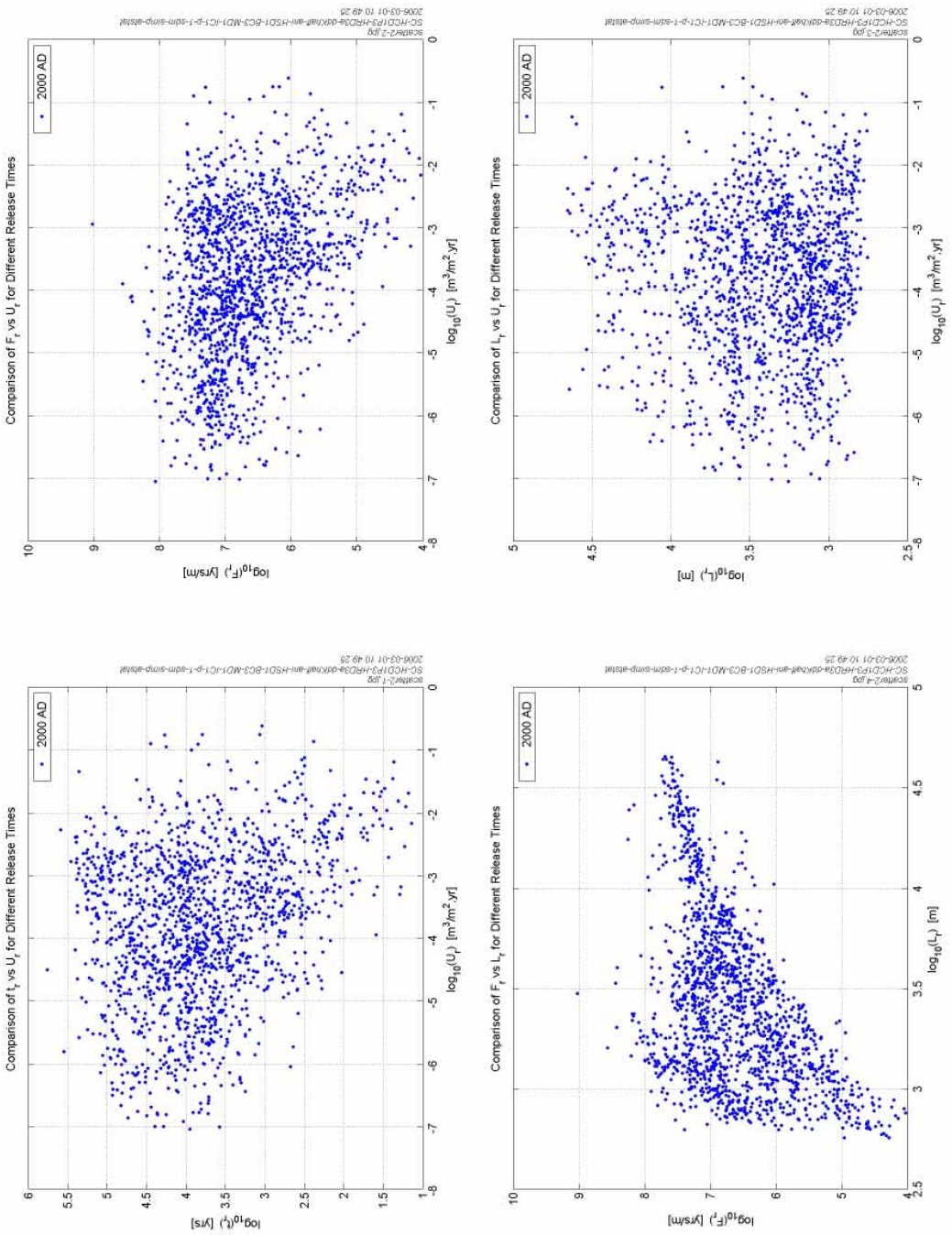

Figure C-8. *Scatter plots with different combinations of the calculated performance measures (t_r, U_r, F_r and L_r). Statistics shown for the reference case for particles released within the Simpevarp release area.*

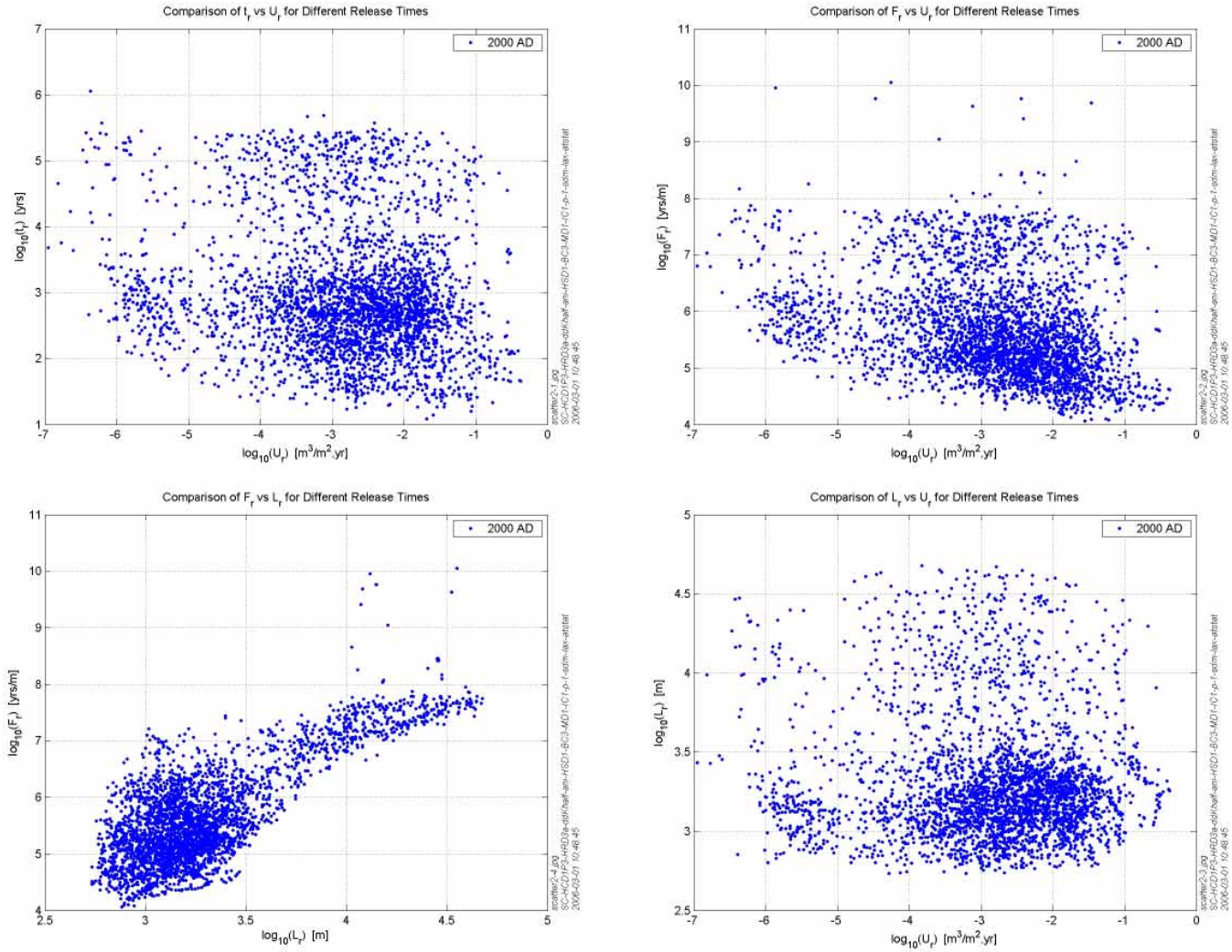

Figure C-9. *Scatter plots with different combinations of the calculated performance measures (t_r, U_r, F_r and L_r). Statistics shown for the reference case for particles released within the Laxemar release area.*

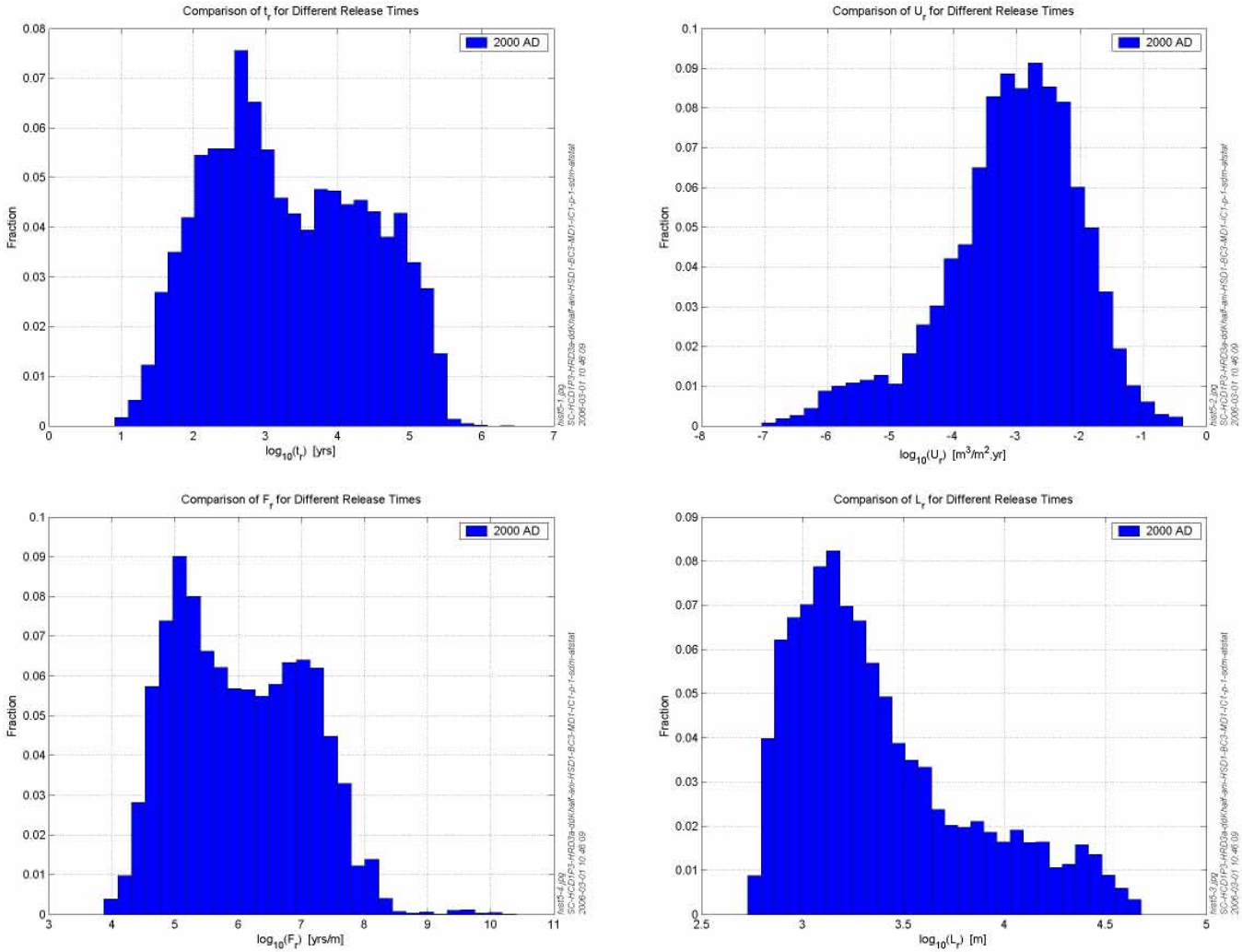

Figure C-10. *Histograms of the calculated performance measures (t_r, U_r, F_r and L_r). Statistics shown for the ensemble of particles released in the local-scale release area for the reference case.*

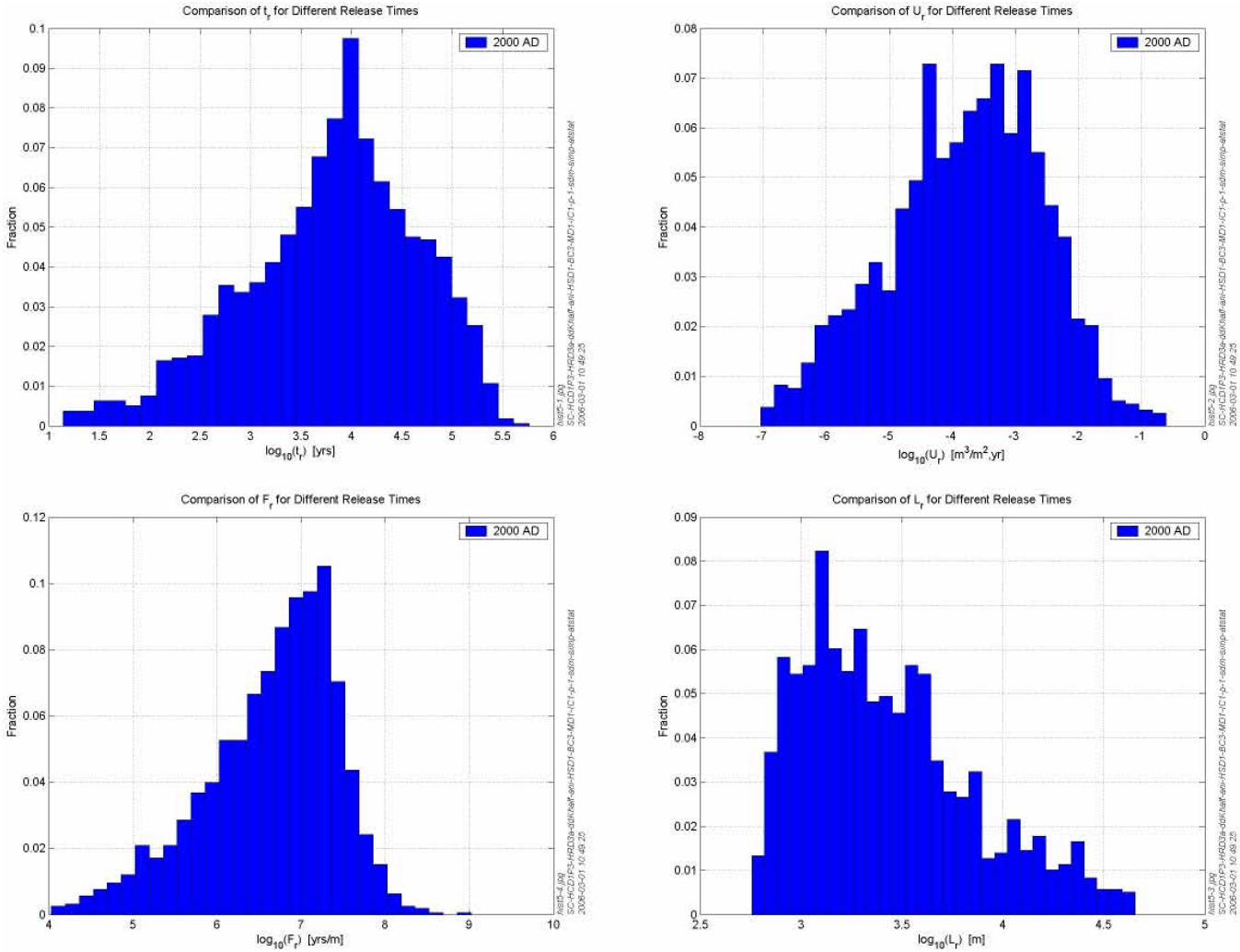

Figure C-11. *Histograms of the calculated performance measures (t_r, U_r, F_r and L_r). Statistics shown for the reference case for particles released within the Simpevarp release area.*

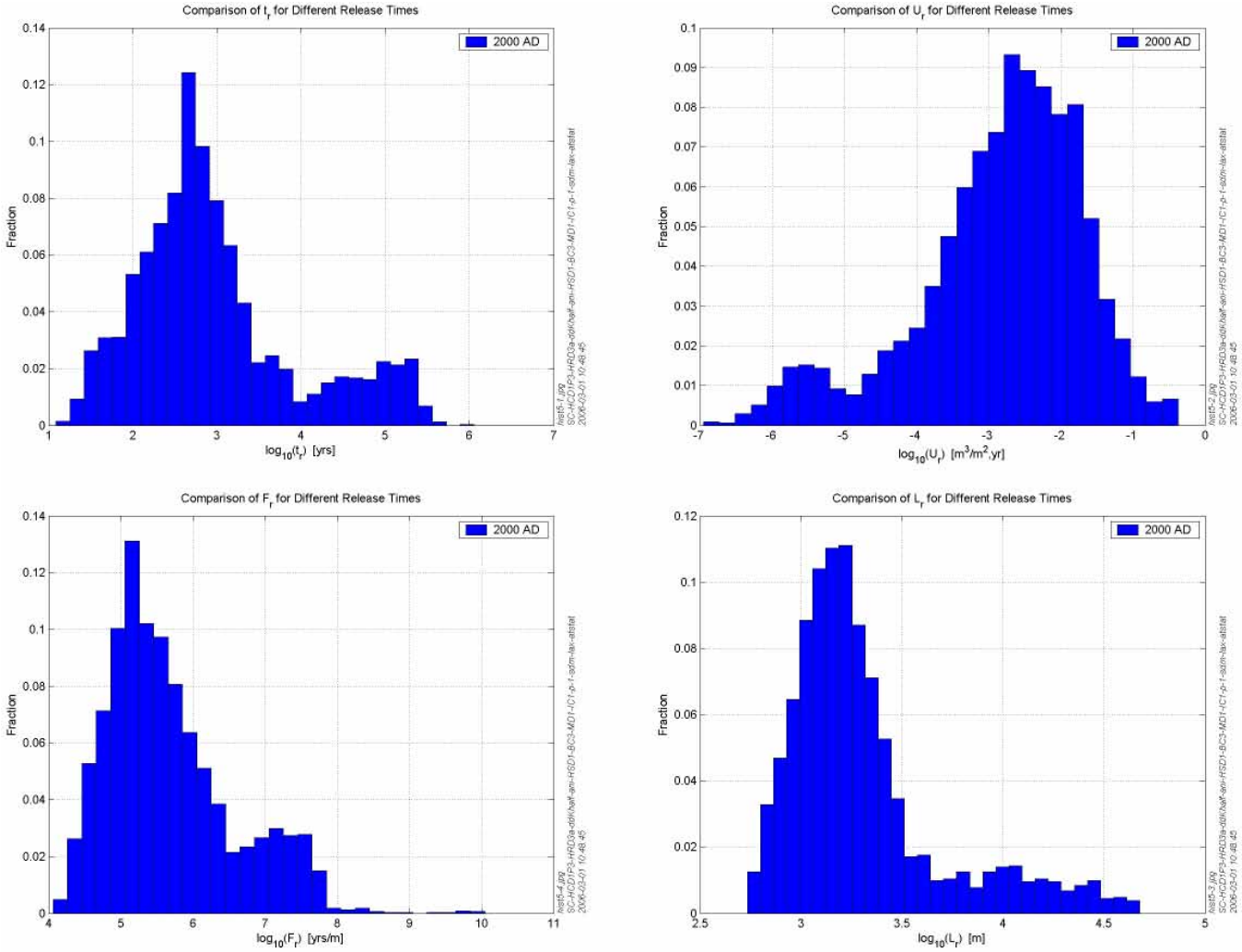

Figure C-12. *Histograms of the calculated performance measures (t_r, U_r, F_r and L_r). Statistics shown for the reference case for the particles released within the Laxemar release area.*

The statistical summaries for the reference case are presented in Table C-1 to Table C-3, where the statistics are calculated for numbers in $\log_{10}$ space. The results presented are based on the ensemble of particles released in the local-scale release area. To quantify the differences between Simpevarp and Laxemar, statistics were also calculated for the two sites separately. The performance measure statistics are presented in Table C-2 and Table C-3 for the two sites individually. The medians of both t_r and F_r are about one order of magnitude lower for the Laxemar release area than for Simpevarp. Correspondingly, the median of U_r is about one order of magnitude higher in the Laxemar area.

Table C-19. Statistical summary of the calculated performance measures (t_r, U_r, F_r and L_r) for the ensemble of particles released in the local-scale release area for the reference case.

Statistical entity	$\log_{10}(t_r)$	$\log_{10}(U_r)$	$\log_{10}(F_r)$	$\log_{10}(L_r)$
Mean	3.314	–3.091	6.033	3.389
Median	3.179	–2.975	5.954	3.270
5th percentile	1.674	–5.277	4.568	2.863
25th percentile	2.447	–3.660	5.149	3.057
75th percentile	4.223	–2.339	6.885	3.619
95th percentile	5.121	–1.568	7.664	4.341
Std dev	1.088	1.085	1.031	0.443
Variance	1.183	1.178	1.062	0.196
Skewness	0.157	–0.699	0.296	0.931
Kurtosis	–1.018	0.582	–0.649	0.034
Min value	0.915	–7.041	3.875	2.731
Max value	6.444	–0.375	10.400	4.677
Fraction OK	0.980	1.000	0.980	0.980

Table C-20. Statistical summary of the calculated performance measures (t_r, U_r, F_r and L_r) for the Simpevarp release area for the reference case.

Statistical entity	$\log_{10}(t_r)$	$\log_{10}(U_r)$	$\log_{10}(F_r)$	$\log_{10}(L_r)$
Mean	3.801	–3.784	6.643	3.427
Median	3.894	–3.676	6.783	3.350
5th percentile	2.239	–5.993	5.094	2.881
25th percentile	3.256	–4.591	6.159	3.097
75th percentile	4.411	–2.860	7.230	3.668
95th percentile	5.081	–1.912	7.699	4.286
Std dev	0.857	1.224	0.789	0.422
Variance	0.734	1.497	0.622	0.178
Skewness	–0.478	–0.246	–0.687	0.743
Kurtosis	–0.091	–0.403	0.215	–0.117
Min value	1.143	–7.041	4.029	2.755
Max value	5.760	–0.567	9.021	4.655
Fraction OK	0.961	1.000	0.961	0.961

Table C-21. Statistical summary of the calculated performance measures (t_r, U_r, F_r and L_r) for the Laxemar release area for the reference case.

Statistical entity	$Log_{10}(t_r)$	$Log_{10}(U_r)$	$Log_{10}(F_r)$	$Log_{10}(L_r)$
Mean	2.969	–2.843	5.675	3.308
Median	2.763	–2.666	5.480	3.210
5th percentile	1.670	–5.400	4.555	2.873
25th percentile	2.337	–3.403	5.049	3.061
75th percentile	3.318	–2.030	6.127	3.403
95th percentile	5.083	–1.291	7.461	4.204
Std dev	0.964	1.163	0.882	0.386
Variance	0.930	1.353	0.779	0.149
Skewness	0.908	–0.855	0.939	1.464
Kurtosis	0.262	0.590	0.682	1.788
Min value	1.090	–6.951	4.061	2.734
Max value	6.057	–0.375	10.045	4.677
Fraction OK	0.992	1.000	0.992	0.992

C.9 No step change in K at –600 m elevation case

The statistical summaries for the variant without a step change (decrease) in hydraulic conductivity at –600 m elevation are presented in Table C-10 to Table C-12, where the statistics are calculated for numbers in log_{10}-space. The results presented are based on the ensemble of particles released in the local-scale release area. To quantify the differences between Simpevarp and Laxemar, statistics were also calculated for the two sites separately. The performance measure statistics are presented in Table C-11 and Table C-12 for the two sites individually. For the ensemble of particles released in the local-scale release area and for the Laxemar release area, the median F-factor is very slightly lower than in the reference case. However, for the Simpevarp release area the median F-factor is very slightly higher than in the reference case.

Table C-22. Statistical summary of the calculated performance measures (t_r, U_r, F_r and L_r) for the ensemble of particles released in the local-scale release area for the case with no step change in K at –600 m elevation.

Statistical entity	$Log_{10}(t_r)$	$Log_{10}(U_r)$	$Log_{10}(F_r)$	$Log_{10}(L_r)$
Mean	3.303	–3.081	6.019	3.390
Median	3.104	–2.963	5.895	3.274
5th percentile	1.672	–5.287	4.551	2.868
25th percentile	2.452	–3.622	5.149	3.065
75th percentile	4.237	–2.344	6.854	3.642
95th percentile	5.158	–1.582	7.655	4.289
Std dev	1.115	1.080	1.053	0.431
Variance	1.244	1.166	1.108	0.186
Skewness	0.305	–0.765	0.481	0.917
Kurtosis	–0.834	0.775	–0.124	0.160
Min value	0.913	–7.285	3.870	2.696
Max value	6.395	–0.383	10.509	4.737
Fraction OK	0.968	1.000	0.968	0.968

Table C-23. Statistical summary of the calculated performance measures (t_r, U_r, F_r and L_r) for the Simpevarp release area for the case with no step change in K at –600 m elevation.

Statistical entity	$Log_{10}(t_r)$	$Log_{10}(U_r)$	$Log_{10}(F_r)$	$Log_{10}(L_r)$
Mean	4.016	–3.888	6.820	3.527
Median	4.009	–3.804	6.875	3.491
5th percentile	2.315	–6.063	5.233	2.897
25th percentile	3.338	–4.755	6.252	3.188
75th percentile	4.747	–2.980	7.388	3.795
95th percentile	5.444	–1.940	8.306	4.369
Std dev	0.982	1.245	0.877	0.435
Variance	0.965	1.551	0.770	0.189
Skewness	–0.164	–0.174	–0.251	0.520
Kurtosis	–0.193	–0.435	0.175	–0.288
Min value	1.155	–7.285	4.045	2.763
Max value	6.395	–0.570	10.146	4.721
Fraction OK	0.967	1.000	0.967	0.967

Table C-24. Statistical summary of the calculated performance measures (t_r, U_r, F_r and L_r) for the Laxemar release area for the case with no step change in K at –600 m elevation.

Statistical entity	$Log_{10}(t_r)$	$Log_{10}(U_r)$	$Log_{10}(F_r)$	$Log_{10}(L_r)$
Mean	2.906	–2.831	5.668	3.305
Median	2.765	–2.642	5.493	3.215
5th percentile	1.686	–5.431	4.535	2.868
25th percentile	2.371	–3.385	5.026	3.054
75th percentile	3.258	–2.024	6.114	3.438
95th percentile	4.875	–1.311	7.374	4.180
Std dev	0.867	1.154	0.933	0.378
Variance	0.752	1.332	0.870	0.143
Skewness	0.908	–0.866	1.536	1.437
Kurtosis	0.750	0.600	3.768	2.020
Min value	0.993	–7.012	4.053	2.730
Max value	5.634	–0.383	10.509	4.724
Fraction OK	0.985	1.000	0.985	0.985

C.10 Second realisation of Hydro-DFN

The statistical summaries for the second realisation of the Hydro-DFN are presented in Table C-13 to Table C-15, where the statistics are calculated for numbers in log_{10}-space. The results presented are based on the ensemble of particles released in the local-scale release area. To quantify the differences between Simpevarp and Laxemar, statistics were also calculated for the two sites separately. The performance measure statistics are presented in Table C-14 and Table C-15 for the two sites individually. For the local-scale release area, the median F-factor is slightly higher, by about 0.2 in log_{10}-space, than in the reference case.

Table C-25. Statistical summary of the calculated performance measures (t_r, U_r, F_r and L_r) for the ensemble of particles released in the local-scale release area for the second realisation of the Hydro-DFN.

Statistical entity	$Log_{10}(t_r)$	$Log_{10}(U_r)$	$Log_{10}(F_r)$	$Log_{10}(L_r)$
Mean	3.419	–3.217	6.224	3.443
Median	3.314	–3.104	6.190	3.377
5th percentile	1.629	–5.432	4.550	2.856
25th percentile	2.494	–3.842	5.258	3.072
75th percentile	4.505	–2.430	7.121	3.791
95th percentile	5.243	–1.597	8.017	4.164
Std dev	1.172	1.130	1.151	0.428
Variance	1.372	1.277	1.325	0.183
Skewness	0.088	–0.596	0.301	0.348
Kurtosis	–1.010	0.444	–0.460	–0.918
Min value	0.413	–7.623	3.427	2.729
Max value	6.391	–0.236	10.137	4.634
Fraction OK	0.974	1.000	0.974	0.974

Table C-26. Statistical summary of the calculated performance measures (t_r, U_r, F_r and L_r) for the Simpevarp release area for the second realisation of the Hydro-DFN.

Statistical entity	$Log_{10}(t_r)$	$Log_{10}(U_r)$	$Log_{10}(F_r)$	$Log_{10}(L_r)$
Mean	4.192	–4.053	7.173	3.543
Median	4.504	–4.081	7.312	3.518
5th percentile	2.246	–6.012	5.296	2.918
25th percentile	3.534	–4.804	6.659	3.199
75th percentile	4.949	–3.170	7.793	3.874
95th percentile	5.426	–2.115	8.496	4.196
Std dev	1.016	1.185	1.002	0.414
Variance	1.033	1.404	1.005	0.171
Skewness	–0.885	–0.195	–0.542	0.180
Kurtosis	0.282	–0.170	1.471	–0.940
Min value	0.901	–7.623	3.427	2.763
Max value	6.230	–1.223	10.137	4.614
Fraction OK	0.945	1.000	0.945	0.945

Table C-27. Statistical summary of the calculated performance measures (t_r, U_r, F_r and L_r) for the Laxemar release area for the second realisation of the Hydro-DFN.

Statistical entity	$Log_{10}(t_r)$	$Log_{10}(U_r)$	$Log_{10}(F_r)$	$Log_{10}(L_r)$
Mean	2.960	–2.923	5.708	3.283
Median	2.769	–2.678	5.461	3.173
5th percentile	1.586	–5.599	4.548	2.845
25th percentile	2.270	–3.556	5.025	3.025
75th percentile	3.337	–2.065	6.188	3.420
95th percentile	5.188	–1.332	7.527	4.113
Std dev	1.046	1.219	0.947	0.384
Variance	1.094	1.486	0.897	0.148
Skewness	0.893	–0.819	0.939	1.282
Kurtosis	0.355	0.307	0.382	1.157
Min value	0.413	–6.674	3.719	2.729
Max value	6.308	–0.393	9.443	4.634
Fraction OK	0.982	1.000	0.982	0.982

C.11 Correlated transmissivity model

The statistical summaries for the case with a correlated transmissivity Hydro-DFN are presented in Table C-28 to Table C-30, where the statistics are calculated for numbers in log_{10}-space. The results presented are based on the ensemble of particles released in the local-scale release area. To quantify the differences between Simpevarp and Laxemar, statistics were also calculated for the two sites separately. The performance measure statistics are presented in Table C-29 and Table C-30 for the two sites individually. The median F-factor for the local-scale release area is about the same as that in the reference case.

Table C-28. Statistical summary of the calculated performance measures (t_r, U_r, F_r and L_r) for the ensemble of particles released in the local-scale release area for the correlated transmissivity Hydro-DFN model.

Statistical entity	$Log_{10}(t_r)$	$Log_{10}(U_r)$	$Log_{10}(F_r)$	$Log_{10}(L_r)$
Mean	3.262	–3.248	5.993	3.392
Median	3.083	–3.172	5.866	3.274
5th percentile	1.683	–5.334	4.477	2.855
25th percentile	2.364	–3.870	5.111	3.049
75th percentile	4.176	–2.490	6.753	3.712
95th percentile	5.176	–1.690	7.788	4.228
Std dev	1.111	1.073	1.076	0.432
Variance	1.235	1.151	1.157	0.187
Skewness	0.262	–0.564	0.531	0.741
Kurtosis	–0.897	0.519	0.023	–0.346
Min value	0.398	–7.490	3.821	2.746
Max value	6.401	–0.389	10.642	4.702
Fraction OK	0.881	1.000	0.881	0.881

Table C-29. Statistical summary of the calculated performance measures (t_r, U_r, F_r and L_r) for the Simpevarp release area for the correlated transmissivity Hydro-DFN model.

Statistical entity	$Log_{10}(t_r)$	$Log_{10}(U_r)$	$Log_{10}(F_r)$	$Log_{10}(L_r)$
Mean	4.320	–3.999	7.160	3.740
Median	4.450	–3.860	7.182	3.835
5th percentile	2.607	–6.030	5.642	2.878
25th percentile	3.860	–4.737	6.755	3.417
75th percentile	4.923	–3.145	7.584	4.033
95th percentile	5.541	–2.317	8.278	4.437
Std dev	0.867	1.138	0.813	0.464
Variance	0.752	1.294	0.661	0.216
Skewness	–0.711	–0.412	0.044	–0.459
Kurtosis	0.419	–0.412	3.030	–0.598
Min value	1.413	–7.322	4.354	2.764
Max value	6.401	–1.541	10.611	4.683
Fraction OK	0.827	1.000	0.827	0.827

Table C-30. Statistical summary of the calculated performance measures (t_r, U_r, F_r and L_r) for the Laxemar release area for the for the correlated transmissivity Hydro-DFN model.

Statistical entity	$Log_{10}(t_r)$	$Log_{10}(U_r)$	$Log_{10}(F_r)$	$Log_{10}(L_r)$
Mean	2.784	–2.975	5.494	3.239
Median	2.619	–2.801	5.337	3.190
5th percentile	1.680	–5.500	4.477	2.850
25th percentile	2.253	–3.647	4.946	3.045
75th percentile	3.115	–2.146	5.853	3.335
95th percentile	4.897	–1.355	7.326	3.959
Std dev	0.872	1.164	0.786	0.320
Variance	0.760	1.356	0.618	0.103
Skewness	1.219	–0.678	1.040	1.717
Kurtosis	1.739	0.273	0.780	3.776
Min value	0.736	–6.836	4.076	2.754
Max value	5.818	–0.389	8.049	4.661
Fraction OK	0.945	1.000	0.945	0.945